UNIVERSIDADE DE LISBOA
INSTITUTO SUPERIOR TÉCNICO

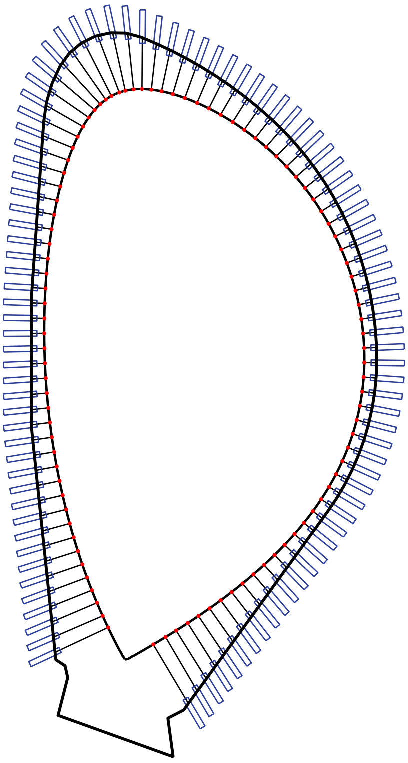

# Assessment of reflectometry diagnostics for DEMO

**Emanuel Alves Ricardo**

**Supervisor:** Doctor Filipe José Fernandes Manuel da Silva
**Co-supervisors:** Doctor Stéphane Heuraux
Doctor Bruno Miguel Soares Gonçalves

Thesis approved in public session to obtain the PhD Degree in **Physics**
**Jury final classification: Pass with Distinction**

**2021**

UNIVERSIDADE DE LISBOA
INSTITUTO SUPERIOR TÉCNICO

# Assessment of reflectometry diagnostics for DEMO

**Emanuel Alves Ricardo**

**Supervisor:** Doctor Filipe José Fernandes Manuel da Silva
**Co-supervisors:** Doctor Stéphane Heuraux
Doctor Bruno Miguel Soares Gonçalves

Thesis approved in public session to obtain the PhD Degree in **Physics**
**Jury final classification: Pass with Distinction**

## Jury

**Chairperson:** Doctor Luís Paulo da Mota Capitão Lemos Alves, Instituto Superior Técnico, Universidade de Lisboa

**Members of the committee:**

Doctor Wolfgang Biel, Institut für Energie- und Klimaforschung (IEK), Forschungszentrum Jülich GmbH, Germany

Doctor Carlos Alberto Nogueira Garcia da Silva, Instituto Superior Técnico, Universidade de Lisboa

Doctor Roland Sabot, CEA - Commissariat a l'énergie atomique et aux energies alternatives, France

Doctor António Guilherme Pereira Ehrhardt Gonçalves Silva, Instituto Superior Técnico, Universidade de Lisboa

Doctor Filipe José Fernandes Manuel da Silva, Instituto Superior Técnico, Universidade de Lisboa

**Funding Institutions**
Fundação para a Ciência e a Tecnologia, EUROfusion

**2021**

# Acknowledgements

This dissertation would not have been successfully completed without the help of my supervisors, of my family and of my friends, for whom I am forever grateful.

First of all I would like to express my gratitude to my supervisors, who turned out this research work possible. I thank Dr. Filipe José Fernandes Manuel da Silva for introducing me in the field of reflectometry simulation, for giving me the opportunity to work on this extraordinary project and for constantly supporting and guiding me during this long journey. I thank Dr. Stéphane Heuraux for being always available to support, to give advices, to discuss reflectometry and share his knowledge. I thank Dr. Bruno Miguel Soares Gonçalves for introducing me to IPFN and plasma diagnostics, for his trust on my work and for his support.

I would like to thank all my colleagues from IPFN in particular the Reflectometry Group, for all their help and for the excellent work environment they provided me. I thank to Jorge Santos and António Silva for their advices, support and collaboration on this project. I thank Dr. Maria Emília Manso for teach me experimental techniques in reflectometry, for her support and encouragement.

I am also in debt to my high school teacher Ana Sofia for introducing me to the fascinating world of physics and for transmitting me the taste for scientific knowledge that years later would be concretized in this work.

I would like to acknowledge all my friends and family, in particular my parents Marília and Luís, my brother Dinis, Lourdes and Susana for their constant support and encouragement. To them I dedicate this thesis.

Thank you all.

Lisboa, Junho de 2021
Emanuel Alves Ricardo

# Abstract

DEMO will be the first prototype of a fusion power plant. Unlike experimental tokamaks like ITER, only the necessary diagnostics for machine protection and plasma control will be implemented. One of the fundamental measurements is the position and shape of the last closed magnetic surface, typically measured with the magnetic diagnostics. One of the major issues of its implementation in DEMO is the integration drifts that can occur during the steady state operation due to the high levels of nuclear radiation. This can lead to a wrong plasma position estimation, putting the operation at risk. The prime candidate to complement or substitute the magnetic diagnostics in DEMO is the microwave reflectometry. By sweeping the frequency of the probing beam, microwave reflectometry is capable of measuring the electron density profile. As the density is directly linked to the magnetic flux surfaces these measurements give access to the magnetic configuration, providing its local radial position. The O-mode propagation is independent from the magnetic field, being ideal for replacing the magnetic diagnostics.

The DEMO plasma position reflectometer (DEMO PPR) consists a system of multi-reflectometers distributed poloidaly along the wall at different positions that will provide the separatrix reconstruction. The optimization of a PPR system requires the simulation of the measurement process for different poloidal views, emitting angles, antenna assemblies and plasma configurations. The final system must be optimized for the operation scenario and be stable under the possible deviations to its equilibrium that can occur during the discharges. For now, the DEMO PPR is in an early development stage and there are many questions that need to be investigated before reaching its final design.

In this work we study the process of optimization of PPR systems with a general approach, taking into account the future changes in the geometry and plasma scenario. The important variables of a general multiple reflectometers system were identified and the techniques and the procedure to its optimization were developed. The simulation of such systems is in general a complex task that requires the definition of several different regions of interest and testing different antenna models and plasmas, which is a very demanding task from the computational point of view and of necessary time to write the simulation scripts. For this reason, we developed the structure of a high-level framework for multiple reflectometry simulations that is capable of automate all the simulation process of a multiple reflectometers system for the REFMUL* codes, a family of full-wave FDTD codes that has been used for reflectometry simulations. The user defines the configuration files of the system geometry and plasma, the probing bands and the dependence between the main variables of the problem. A main script creates all the necessary models and necessary scripts to manage and run all the simulations in the HPCs.

Using the developed framework, we optimized the DEMO PPR system using the official DEMO scenario from EUROfusion database. We defined 100 different positions around the tokamak (gaps) and two different configurations were tested. In the first one, the antennas were aligned perpendicularly with the wall. This configuration has advantages from the point of view of the implementation of the antennas. However, the results shown that there are positions in the top of the machine and in the divertor region that have a very poor measurement performance due to the flux lines configuration and in some cases the signal is totally lost. In the second configuration, the antennas were aligned perpendicularly to the separatrix. In this case, since the direction of the probing beam is approximately parallel to the density gradient, a better measurement performance is expected. The results confirmed this principle, improving the results in several positions. At the divertor region, some of the reflectometers continued to have a poor measurement performance, being necessary to sweep the probing angle to verify if there is an optimized configuration.

One of the problems associated with the optimization is that is necessary to extract the round trip group delay and the amplitude of the detected signal for many different reflectometer configurations, with a brute-force approach. The analysis of the simulation results requires the manual adjustment of the data analysis parameters, as the filter cutoff frequency or the signal delay. Using the principle that a slow varying group delay has a minimum standard deviation if it is well filtered, we developed an automatized version of the the I/Q detection, designed as IQA method. With this technique, it was possible sweeping the probing angle at all the positions and select the optimized configuration in useful time. The maximum average detected amplitude shown to be a good selection criteria for the optimized configuration. The results show that, with the exception of some positions in the divertor region, there is an optimized configuration with low position error ($< 1$ cm) and the power losses minimized.

With the optimized configuration, the stability of the system was tested for plasma displacements of 5 (reference case) and 15 cm (limit case, corresponding to a disruption). The results show that the system is stable for 5 cm plasma displacements in different directions (0°, 90°, 180° and 270°). For displacements of 15 cm, the positions at the top of the machine can reach errors above the requirement (2 cm), being necessary the study of the effect of these measurements in the separatrix reconstruction.

The effect of turbulence in reflectometry measurements was studied in one gap of the equatorial region, in the high field side. Due to the lack of information on the turbulence properties of DEMO plasmas, the fluctuations were defined with an analytical model. A Kolmogorov-like spectrum was used to generate 400 random plasma samples for 16 different levels of amplitude ($1 - 16\%$), compatible with the order of values observed in the experiments. Using the IQA algorithm, the principal statistical parameters were calculated. The results show that for higher levels of turbulence ($> 5\%$), the mean position error becomes negative due to the change of the effective cutoff position. This effect occurs for all the frequencies, leading to an accumulative error that can affect the position measurement in the order of accuracy requirements. As we increase the level of turbulence, the power losses increase, which can be a problem for the positions with higher plasma-wall distance. In order to prove the reliability of the entire system, it is necessary to apply the same procedure to the other positions of the system, which requires a huge amount of computation time on HPCs to be done.

The techniques and the algorithms developed in this work can be applied in other processes which involve the analysis of a high number of reflectometry simulations, including studies with other reflectometry techniques.

**Keywords:** DEMO diagnostics; Microwave diagnostics; Microwave reflectometry; Plasma position reflectometry; Optimization of reflectometry systems.

# Resumo

O DEMO será o primeiro protótipo de uma estação elétrica de fusão nuclear. Ao contrário dos tokamaks experimentais como o ITER, apenas os diagnósticos necessários para a proteção da máquina e controlo do plasma serão implementados. Uma das medidas fundamentais é a posição do plasma e a forma da última superfície magnética fechada, tipicamente medida com os diagnósticos magnéticos. O problema da sua implementação no DEMO são os grandes desvios associados à integração dos sinais que podem ocorrer durante a operação devido aos elevados níveis de radiação. Este fenómeno pode levar à estimativa errada da posição do plasma, colocando toda a operação em risco. O candidato principal para complementar ou substituir os diagnósticos magnéticos no DEMO é a reflectometria de microondas. Varrendo a frequência do sinal emitido, a reflectometria de micro-ondas consegue medir o perfil de densidade electrónica do plasma. Uma vez que a densidade electrónica está ligada directamente às superfícies de fluxo magnético, as medidas de reflectometria dão acesso à configuração magnética, permitindo medir a sua localização. A propagação em modo O é independente do campo magnético, o que o torna ideal para substituir os diagnósticos magnéticos.

O reflectómetro de posição do DEMO (DEMO PPR) consiste num sistema de múltiplos reflectómetros distribuídos poloidalmente ao longo da parede da máquina em diferentes posições que será responsável pela reconstrução da separatriz. A otimização deste tipo de sistemas requere a simulação do processo de medida para diferentes vistas poloidais, anglos de emissão, geometrias de antena e configurações de plasma. O sistema final deve ser otimizado para o cenário base de operação e ser estável em relação aos possíveis desvios que possam ocorrer durante as descargas. O deslocamento do plasma, a turbulência ou atividade MHD são fenómenos que podem ocorrer durante o confinamento do plasma, sendo necessário perceber a sua influência na performance das medidas. Por agora, o DEMO PPR está no seu estado inicial de desenvolvimento e há várias questões que precisam de ser investigadas antes de atingir o seu desenho final.

Neste trabalho, nós estudamos o processo de otimização de sistemas PPR com uma abordagem geral, tendo em conta as mudanças futuras que possam ocorrer na geometria da máquina ou no plasma. As variáveis importantes de um sistema de vários reflectometros arbitrário foram identificadas e as técnicas e procedimentos para o otimizar foram desenvolvidos. A simulação destes sistemas é em geral uma tarefa complicada que envolve a definição de várias regiões de simulação e testar diferentes modelos de antenas e plasmas, o que é exigente do ponto de vista computacional e do tempo necessário para escrever os scripts para as simulações. Por esta razão, desenvolvemos um framework de suporte a múltiplas simulações de reflectometria que é capaz de automatizar todo o processo de simulação de um sistema de múltiplos reflectómetros para os códigos REFMUL*, uma família de códigos FDTD que tem sido usada para simulações de reflectometria. O utilizador define os ficheiros de configuração da geometria do sistema e do plasma, as bandas e a dependência entre as variáveis principais do problema. Depois, um script gera todos os modelos e scripts necessários para gerir e executar as simulações nos HPCs.

Com a framework desenvolvida, o DEMO PPR foi otimizado usando o cenário de plasma da base de dados oficial da EUROfusion. 100 diferentes posições foram definidas ao longo da parede da máquina (gaps) e testámos duas configurações diferentes. Na primeira configuração, as antenas foram alinhadas perpendicularmente à parede. Esta configuração tem vantagens do ponto de vista da implementação das antenas. No entanto, os resultados mostram que existem posições no topo da máquina e na região do divertor que têm uma fraca performance de medida e em alguns casos o sinal é totalmente perdido. Na segunda configuração, as antenas foram alinhadas perpendicularmente à separatriz. Neste caso, uma vez que a direção do feixe emitido é aproximadamente paralelo ao gradiente da densidade, é expectável a diminuição do erro da medida. Os resultados confirmaram este princípio, melhorando as medidas em várias posições. Na região do topo e no divertor algumas posições continuaram a ter uma fraca performance de medida, sendo necessário variar o ângulo de emissão para verificar se existe uma configuração otimizada.

Um dos problemas associado à otimização é que é necessário extrair a derivada de fase e calcular a amplitude detetada para muitas configurações diferentes. A análise dos resultados das simulações requerem o ajustamento manual dos parâmetros da análise dados, como a frequência de corte dos filtros ou o atraso do sinal recebido. Usando o princípio que um perfil de atraso de grupo que varie de forma lenta tem um desvio padrão mínimo se estiver bem filtrado, a deteção I/Q foi automatizada, denominando-se algoritmo IQA. Com esta técnica, foi possível analisar todas as simulações num tempo aceitável e selecionar a configuração otimizada. A máxima amplitude média mostrou ser um bom critério de selecção para a configuração otimizada. Os resultados mostram que, com exceção de algumas posições na zona do divertor, há uma configuração otimizada onde as medidas têm um erro baixo ($< 1$ cm) e minimizam as perdas de sinal.

Com a configuração otimizada, a estabilidade do sistema foi testada para deslocamentos de plasma em várias direcções (0°, 90°, 180° e 270°). Os resultados mostram que o sistema é estável para deslocamentos macroscópicos na ordem dos 5 cm.

O efeito da turbulência nas medidas de reflectometria foi também estudado numa posição equatorial do lado interior da máquina. Devido à falta de informação sobre as propriedades da turbulência dos plasmas do DEMO, as flutuações foram definidas com um modelo analítico. Um espectro do tipo Kolmogorov foi utilizado para gerar 400 amostras aleatórias de plasma para 16 diferentes níveis de amplitude ($1 - 16\%$), compatíveis com a ordem de valores observados em tokamaks. Os resultados mostram que para maiores níveis de turbulência ($> 5\%$), o erro da posição torna-se negativo devido à mudança da posição da camada de corte. Este efeito ocorre para todas as frequências, levando ao erro acumulativo que pode afetar a mediação da posição na ordem do valor limite do erro. Consoante o nível de turbulência é aumentado, a perda de potência detetada aumenta, o que pode ser um problema nas posições onde a distância plasma-parede é maior. De forma a comprovar a confiabilidade de todo o sistema, é necessário aplicar o mesmo procedimento nas restantes posições do sistema, o que envolve um elevado esforço computacional.

As técnicas e os algoritmos desenvolvidos neste trabalho podem ser aplicados noutros estudos que envolvam a análise de um elevado número de simulações, incluindo estudos que envolvam outros tipos de reflectometria.

**Keywords:** Diagnósticos do DEMO; Diagnósticos de microondas; Reflectometria; Reflectometria de posição; Otimização de sistemas de reflectometria.

# Acronyms

**2D** Two dimensions

**3D** Three dimensions

**ADC** Analog-to-Digital Converters

**ASDEX** Axially Symmetric Divertor Experiment

**DC** Diagnostic and Control system

**DEMO** DEMOnstration power plant

**DEMO PPR** DEMO Plasma Position Reflectometer

**DTT** Divertor Test Tokamak

**EDW** Electron Drift Waves

**ELM** Edge Localized modes

**EMP** Electromagnetic performance team

**EOF** End of Flat Top

**ETB** External Transport Barrier

**EXP** Experimental team

**FEM** Finite Element Method

**FB** Full-Band

**FDTD** Finite-Difference Time-Domain

**FMCW** Frequency Modulated Continuous Wave

**FSP** Fixed Separatrix Position optimization

**FWP** Fixed Wall Position optimization

**GDP** Gross Domestic Product

**HDI** Human Development Index

**HFS** High field side

**HPC** High Performance Computing

**ICF** Inertial confinement fusion

**ITB** Internal Transport Barriers

**ITG** Ion Temperature Gradient

**ITER** International Thermonuclear Experimental Reactor

**IQ** In-phase and Quadrature

**IQA** Automated IQ method

**JET** Joint European Tokamak

**LCMS** Last Closed Magnetic Surface

**LFS** Low field side

**LO** Local oscillator

**LTI** Linear Time-Invariant

**NBI** Neutral Beam Injection

**MHD** Magnetohydrodynamics

**MRS** Multiple Reflectometer Systems

**MRSF** Multiple Reflectometer Systems Framework

**PML** Perfect Matched Layer

**PPR** Plasma Position Reflectometer

**RAM** Random-Access Memory

**REFMUL*** REFMUL family of codes

**RF** radio-frequency

**ROI** Region Of Interest

**SD** Simulation Directory

**SFFT** Sliding Fast Fourier Transform

**SOF** Start of the Flap Top

**SOL** Scrape-Off Layer

**TEM** Trapped Electron Modes

**TLM** Transmission Line Matrix Method

**TMP** Thermomechanical performance team

**UTS** Unidirectional Transparent Source

**WKB** Wentzel–Kramers–Brillouin

**XYK** The Xu-Yuan Kernel

# Contents

# Chapter 1

# Context

## 1.1 Nuclear fusion

### 1.1.1 The need for fusion energy

Energy is an essential good to human health and well-being. It is one of the most important elements of the economic growth since many production and consumption activities involve energy conversion. Modern societies depend on energy for producing food, heating and lighting homes, operating industrial facilities, transportation, communication, technology, and other activities. In general, life quality requires a substantial energy consumption and this is possible if it is readily available at a reasonable good price [1, 2, 3].

Despite of all the development of energy technology, the humanity is facing an energy problem at the present days, and the situation is getting worst [1]. The energy demand is increasing due to different reasons, and an unsustainable scenario of energy shortage and global environmental pollution can be reached in the next years if no effective action starts. The first factor contributing to the increase of the energy demand is the increasing human population. Figure 1.1 (left) shows the world human population estimates from 1800 to 2100, with the estimated range of future population after 2020 [4]. In the best scenario case, the population in 2100 is approximately the same. However, in the worst case scenario, the population maintains the same growth rate and the population doubles. If the average life standards are the same, this requires, at least, the double of the energy consumption, which implies an adequate energy demand. Another factor is the energy access in the rapidly industrializing and developing countries [1]. Figure 1.1 (right) shows a study of the human development index (HDI), total primary energy footprint per capita, relative population and gross domestic product (GDP) per capita of selected countries, during 1995–2008. In the current context of globalization, the energy required to maintain a high level of development is underestimated by the total primary energy demand since part of the energy is used to sustain the welfare of developed countries. The best indicator is the energy footprint, the energy consumed worldwide to produce the goods and services demanded by that country. Increasing the footprint of the developing countries and the rapidly industrializing countries is required as necessary condition to achieve the HDI and GPD values of the developed countries [5]. Following the reference, it is concluded that the minimum total primary energy footprint per capita to achieve a high level of development is 33% higher than current world's per capita energy use [5]. These countries are also the most populated, making the problem even more difficult. In the developing countries, on the other hand, there is a continuous search for new technological solutions

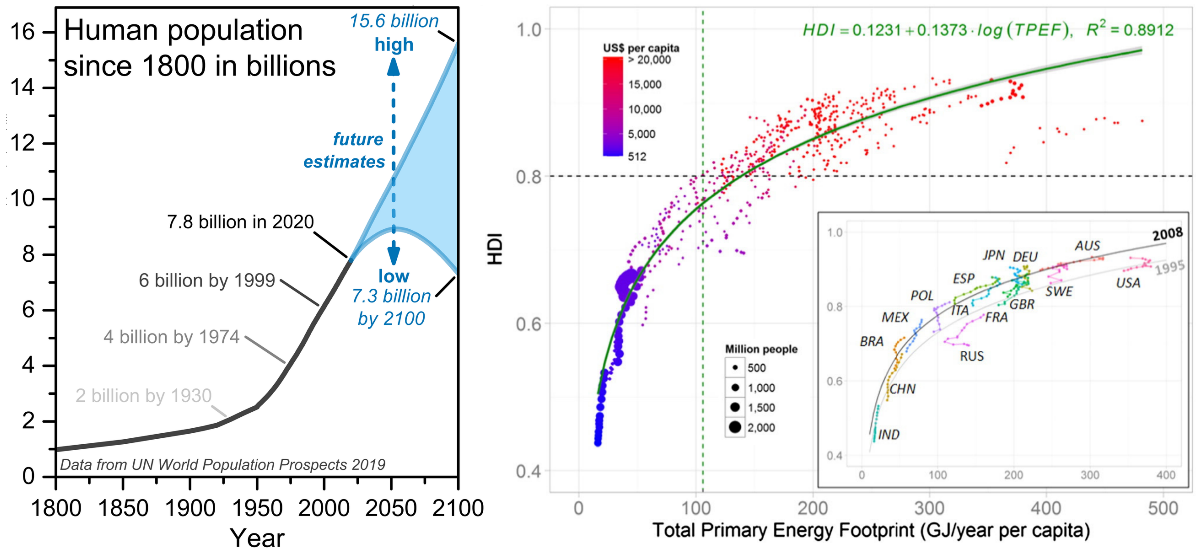

Figure 1.1: World human population estimates from 1800 to 2100, with estimated range of future population after 2020 based on "high" and "low" scenarios. Data from the United Nations projections in 2019 [6, 4] (left). The human development index (HDI), total primary energy footprint per capita, population and GDP per capita of selected countries, during the years 1995–2008 [5] (right).

that contribute to the improvement of the life standard, resulting also in more energy consumption. A detailed analysis on the existing forms of energy production concludes that, with the increase of the population and of the energy demanding per capita, there is no economically viable and environmentally friendly long-term solution.

Energy sources are classified in three categories: fossil fuels, nuclear fuels, and sunlight, which drivers directly or indirectly the different renewables (e.g. wind energy, hydropower, solar) [7, 8, 9]. Energy use in society begins with the natural source and passes through several intermediate processes for refinement or conversion to a different form, finally reaching a consumer, where it is used in some purpose like transportation, house heating or electricity. The evolution of the energy consumption in the world by source is shown in figure 1.2 (left) and the world electricity consumption in figure 1.2 (right). It is clear that fossil fuels are the most used energy source in the world. They are cheap, safe to transport in general, easy to store, abundant, reliable. A considerable part of this energy is used to produce electricity, a form of energy which has increasing its demand over the last years. The fossil fuels are not, however, the solution to the energy demand problem. They are harmful to the environment and public health due to the greenhouse gases emitted during the process. The estimations preview reserves in the order of a few decades for oil and gas and approximately a century for the coal [10]. In the renewables the environmental impact is reduced and the reserve problems are nonexistent, but they have other disadvantages. They are more expensive, intermittent, require storage and are limited by the local resources. In contrast, nuclear fission can supply as much energy as it is available in a continuous rate. It is safe and, similarly to the renewables, does not emit polluting gases. Estimations preview reserves in the order of several hundred years. But fission centrals have also some disadvantages. They have an expensive cost and cannot react fast to changes in electricity demand. The waste is radioactive and a safe disposal is very difficult and expensive. There are also other environmental issues

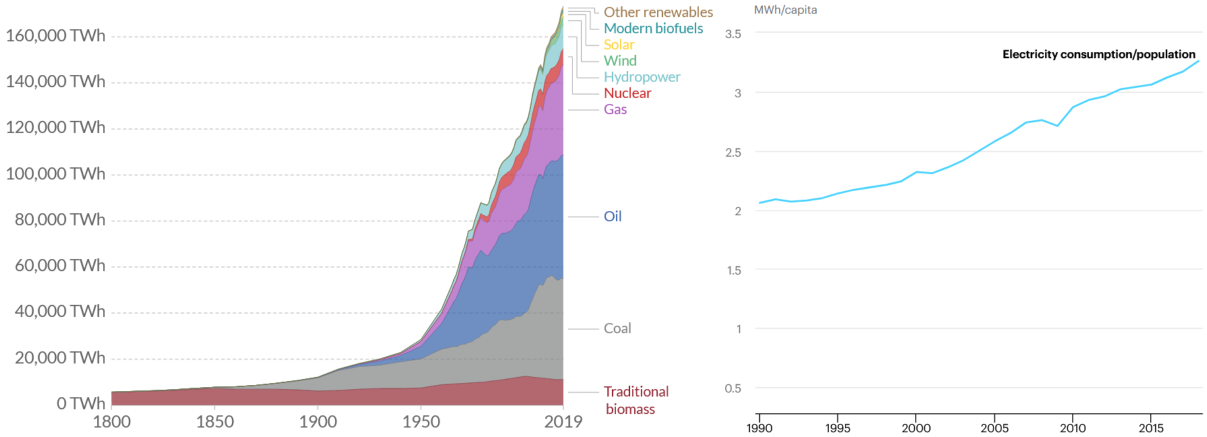

Figure 1.2: Global primary energy consumption by source source in the World [11] (left). Electricity consumption per capita in the world, 1990-2018 [1] (right).

related with the fuel transport and impact on local ecosystems. The most viable solution to the energy problem in the short/medium term is foreseen to be a combination of nuclear with renewables, along with promoting more efficient energy use. In the long term, nuclear fusion is the only solution. Nuclear fusion energy has the necessary features in terms of reserves, safety, environmental impact, reliability, and can provide electric power uninterruptedly. Although the process of producing energy with nuclear fusion reactions is well known, there are many scientific challenges that need to be solved to have a continuous and sustainable process of energy production. The most promising technique involves the confinement of the fuel inside a vacuum vessel with intense magnetic fields at temperatures in the order of $100 - 150$ million °C, in such way that there are no losses to the environment.

Since the 1950s, scientists and engineers of the world's fusion research program work together to solve the fusion challenges one by one. As final goal, an economically competitive power plant will integrate all the developed solutions and introduce fusion in the world energy market [8]. As result of the last decades of research and of the collaboration of 35 nations, the International Thermonuclear Experimental Reactor (ITER) is being built in Cadarache, France [12]. ITER is one of the most ambitious research energy projects in the world and pretends to develop and validate the necessary technology for a fusion power plant. With the know-how to have a continuous and sustainable energy production, the European (EU) long-term strategy towards fusion energy is the development of a DEMOnstration Power Plant (DEMO) as the final step between the ITER experiment and a commercial fusion power plant [13].

While there any many open questions that will be clear after ITER results, some problems are inherent and exclusive to DEMO and are starting to be addressed. In particular, the development of the plasma diagnostic and control (D&C) system. This work is contextualized in the study and design of the DEMO Plasma Position Reflectometry (DEMO PPR), a diagnostic system based on microwave reflectometry that is expected to substitute or complement the magnetic diagnostics in the measurement of the plasma position and shape during the long pulses of operation in DEMO.

In this chapter we make an introduction on how the energy is produced in the reactor, the principal characteristics of ITER and DEMO are reviewed and the problems of DEMO PPR that are addressed in the following chapters of this dissertation are introduced.

### 1.1.2 The basics of nuclear fusion

The atom is the basic unit from which ordinary matter is constituted. The electromagnetic force is responsible for holding the electrons (negative charge) and the nucleus (positive charge). At the atom's nucleus scale ($10^{-15}$ m), the strong nuclear force overcomes the electric repulsion of protons and is responsible for holding the protons (p) and the neutrons (n) together. Nuclear reactions result from the strong, electromagnetic or weak interactions between different nuclei or particles [14, 15, 16]. After the interaction, new nuclei or particles are formed. A nuclear reaction is represented in the form

$$\mathrm{A}_1 + \mathrm{A}_2 \rightarrow \mathrm{A}_3 + ... + \mathrm{A}_k + ... + \mathrm{A}_N + \text{ energy}, \tag{1.1}$$

where $\mathrm{A}_k$ is the involved nucleus or particle. The reaction energy represents the mass that is converted into energy by the Einstein's famous relation $E = mc^2$,

$$E = [(m_{\mathrm{A}_1} + m_{\mathrm{A}_2}) - (m_{\mathrm{A}_3} + ... + m_{\mathrm{A}_k} + ... + m_{\mathrm{A}_N})]c^2. \tag{1.2}$$

The conversion factor, $c$, is the speed of light in vacuum. This relation represents the decrease in biding energy (nuclear potential energy) of the nuclei between the final and initial states. The mass $M$ of a nucleus with $N$ protons and $Z$ neutrons is given by $M = Nm_p + Zm_n - E_B/c^2$, where $E_B$ is the binding energy [17]. The total number of nucleons $A$ is the sum of the number of protons and neutrons, $A = Z + N$. Figure 1.3 shows the nuclear binding energy per nucleon ($E_B/A$) as function of the atomic number of the dominant form of each element.

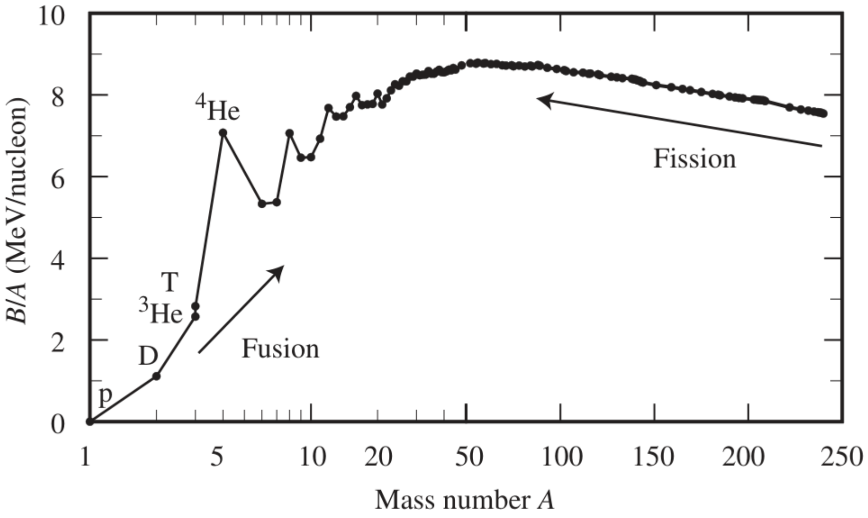

Figure 1.3: Nuclear binding energy per nucleon as function of the mass number of the dominant form of each element [18].

Due to the shape of the binding energy curve, nuclear reactions are most readily initiated for either heavy elements (fission) or light elements (fusion). In the nuclear fission reactions, the nucleus of an atom splits into two or more smaller nuclei, releasing a very large amount of energy and often gamma radiation. The usual method of processing fission energy is to bombard an atom of $U^{235}$ (uranium isotope) with a slow neutron. This reaction produces fragments with energy in the order of several MeV and new neutrons that can be used to start another reaction [19]. Nuclear fission power stations control a chain of these reactions at the correct rate to produce energy from the nuclear fuel according with its needs. In the nuclear fusion reactions the opposite phenomena occurs. Two or more atomic nuclei are combined and form different nucleus and subatomic particles.

Nuclear fusion powers the sun and other stars from the universe and is responsible for the evolution of life on Earth [20, 21, 22]. Ordinary Hydrogen (${}^1_1$H) is the most abundant element in the sun's core as well in the universe. With its extreme gravitational field, high densities (150 g/cm$^3$) and temperatures (15 million degrees Celsius), the sun is a natural self-confined fusion reactor where different reactions occur and produce the energy. The existing high temperatures ensure there is enough kinetic energy to overcome the Coulomb barrier and fuse the nuclei. A chain of reactions, called the proton-proton chain, occurs in the sun, transforming ionized hydrogen (proton) in ionized helium (${}^4_2$He, or $\alpha$ particles) and releasing energy. To make controlled fusion on earth on a smaller scale, many challenges related with the hot fuel contention turn the process much more complicated. In the sun, the fuel confinement is done by the gravitational field. The reactions are also different, taking into account the availability of the fuel and the ease of the fusion processes [8, 23]. The interesting and advantageous reactions for controlled fusion on earth are:

$$\begin{gathered}
{}^2_1\mathrm{D} + {}^2_1\mathrm{D} \longrightarrow {}^3_2\mathrm{He}(0.82\ \mathrm{MeV}) + \mathrm{n}(2.45\ \mathrm{MeV}) \\
{}^2_1\mathrm{D} + {}^2_1\mathrm{D} \longrightarrow {}^3_1\mathrm{T}(1.01\ \mathrm{MeV}) + {}^1_1\mathrm{H}(3.02\ \mathrm{MeV}) \\
{}^2_1\mathrm{D} + {}^3_2\mathrm{He} \longrightarrow {}^4_2\mathrm{He}(3.6\ \mathrm{MeV}) + {}^1_1\mathrm{H}(14.7\ \mathrm{MeV}) \\
{}^2_1\mathrm{D} + {}^3_1\mathrm{T} \longrightarrow {}^4_2\mathrm{He}(3.5\ \mathrm{MeV}) + \mathrm{n}(14.1\ \mathrm{MeV}) \\
{}^3_1\mathrm{T} + {}^3_1\mathrm{T} \longrightarrow {}^4_2\mathrm{He} + 2\mathrm{n} + 11.33\ \mathrm{MeV}
\end{gathered}$$

Figure 1.4 shows the cross section and the averaged reactivity of each process.

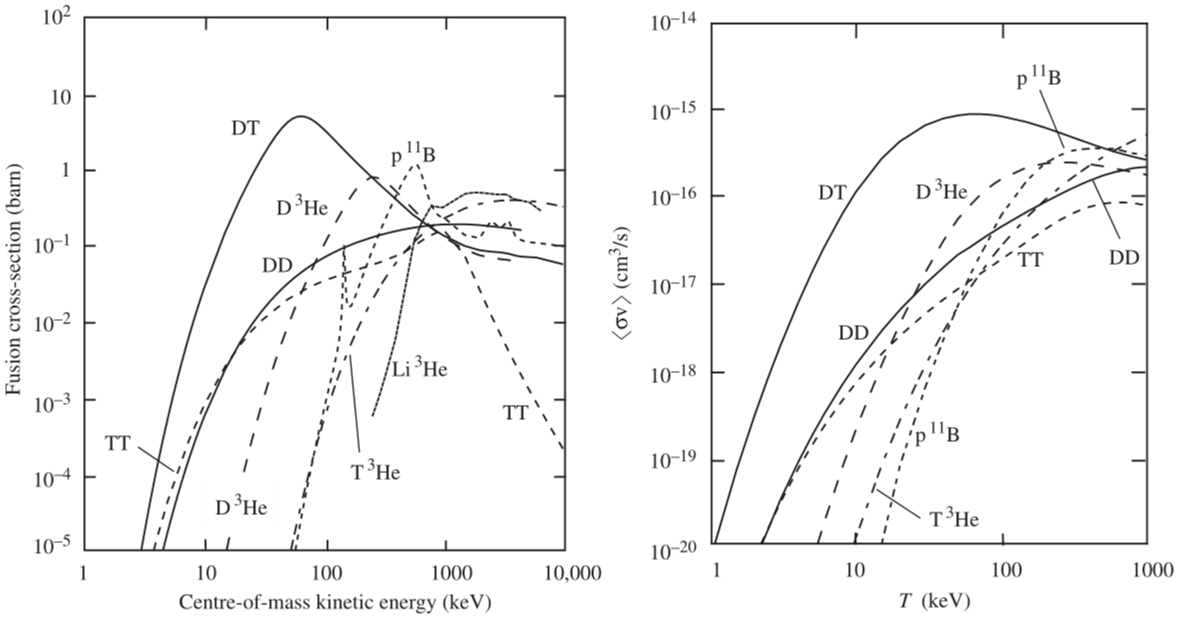

Figure 1.4: Cross section of the interesting fusion reactions [22] (left). Reactivity of the interesting fusion reactions [22] (right). Calculated for a Maxwellian distribution.

The cross section $\sigma$ characterizes the probability of the reaction to occur. It is the projection of the interaction region to the motion of the incident particle and depends on the center-of-mass energy of the incident particles and on the nature of the interaction. Classically, the cross section of a nuclear fusion reaction in the order of the nucleus cross section if the kinetic energy is enough to overcome the electric barrier (Coulomb cutoff). In practice, its form is explained by the quantum mechanical effects (tunneling effect, resonance, high speed decay). The reactivity, defined as

$$\langle\sigma v\rangle = \frac{1}{n_1 n_2}\int\int f_1(\mathbf{v}_1) f_2(\mathbf{v}_2)\sigma_{1,2}(|\mathbf{v}_1 - \mathbf{v}_2|)|\mathbf{v}_1 - \mathbf{v}_2| d\mathbf{v}_1 d\mathbf{v}_2, \tag{1.3}$$

is the reaction probability per unit of time and unit of density averaged over the velocity distribution functions $f_1(\mathbf{v}_1)$ and $f_2(\mathbf{v}_2)$ of the fused species. The distribution function characterizes the number of particles in a elementary volume $d\mathbf{r}d\mathbf{v}$ of the phase space $(\mathbf{r}, \mathbf{v})$. $n_1$ and $n_2$ are the respective local densities of the 1 and 2 species. With this definition, the fusion power rate $S_f$ of the reaction is directly calculated by

$$S_f = E_f n_1 n_2 \langle\sigma v\rangle\,. \tag{1.4}$$

The values of figure 1.4 are obtained assuming a Maxwellian velocity distribution $f_j$ of each colliding specie $j$ at the same temperature $T$,

$$f_j(v) = n_j\left(\frac{m_j}{2\pi k_B T}\right)\exp\left(-\frac{m_j v^2}{2k_B T}\right), \tag{1.5}$$

where $k_B$ is the Boltzman constant and $m_j$ the mass of the specie. The temperature is given in keV, by $T_{\mathrm{keV}} = 10^{-3}\,(k_B/e)\,T$. Here $e$ is the elementary electron charge. In a generic situation, $f_j(\mathbf{v})$ is deviated from the Maxwellian distribution. For proposes of evaluating the basic conditions of the fusion reactors, this assumption is sufficient.

The most desirable reaction for a fusion machine is the DD reaction. Deuterium is very abundant and could be easily extracted from the ocean, providing a unlimited supply of inexpensive fuel. However, as observed in the cross section and reactivity of each reaction, it is one the most difficult to initiate. Consequently, the focus of the current fusion research is the DT reaction. At the necessary temperatures, in the order of 15 keV, most of the nuclei are ionized, and the fuel is in the plasma state. The challenge of a nuclear fusion reactor is to confine the fuel at the necessary conditions in the plasma state to obtain the desired fusion power continuously during the operation time.

### 1.1.3 Plasma, the fourth state of matter

Plasma state is one of the four fundamental states of matter. Depending on the substance temperature, each state of matter (solid, liquid, gas, plasma) is distinguished by the equilibrium between the thermal energy and the inter-particle binding forces [8]. If sufficient energy is provided to a molecular gas, they are dissociated in atoms as result of the collisions. At a given temperature there is enough energy to overcome the electronic binding energy, the atoms become ionized (the charges are separated specially). Each charged particle interacts simultaneously with a large number of other particles of the medium, resulting in important characteristic phenomena. Charged particles create electromagnetic fields, and are affected by the electromagnetic fields created by the other particles of the medium. A particle of mass $m$ and charge $q$ under the influence of an electric field $\mathbf{E}(\mathbf{r}, t)$ and magnetic field $\mathbf{B}(\mathbf{r}, t)$ experiences a Lorentz force $\mathbf{F}$ of

$$\mathbf{F} = \frac{\mathrm{d}\mathbf{p}}{\mathrm{d}t} = q[\mathbf{E} + \mathbf{v}\times\mathbf{B}], \tag{1.6}$$

where $\mathbf{p} = \gamma m \mathbf{v}$ is the relativistic momentum, with $\gamma = 1/\sqrt{1-(v/c)^2}$. Taking the limit $v << c$, the classic form of the equation is obtained, with $\mathbf{p} = m\mathbf{v}$. The electric fields produced by the charges are described by the Maxwell equations,

$$\nabla \cdot \mathbf{E} = \frac{\rho}{\varepsilon_0} \tag{1.7}$$

$$\nabla \cdot \mathbf{B} = 0 \tag{1.8}$$

$$\nabla \times \mathbf{E} = -\frac{\partial \mathbf{B}}{\partial t} \tag{1.9}$$

$$\nabla \times \mathbf{B} = \mu_0 \left( \mathbf{J} + \varepsilon_0 \frac{\partial \mathbf{B}}{\partial t} \right), \tag{1.10}$$

where $\rho(\mathbf{r}, t) = \sum_j^N q_j \delta(\mathbf{r}_j, t)$ is the total charge density and $\mathbf{J} = \sum_j^N q_j \delta(\mathbf{r}_j, t)\mathbf{v}_j$ the total current density of a system composed by $N$ particles. If the medium exhibit the conditions of collective behavior, it is classified as a plasma [24, 25, 8, 26].

The first criterion is the macroscopic neutrality. If there is no external disturbance, the number of ions and electrons in a macroscopic volume is approximately the same. When a microscopic charge variation occurs, the potential energy resulting from the coulomb forces are enormous compared to the kinetic energy and the resulting internal charge fields tend to restore the charge neutrality. This collective behavior is described by an oscillation of characteristic frequency know as the plasma frequency $\omega_{pe}$,

$$\omega_{pe} = \left( \frac{n_e e^2}{m_e \varepsilon_0} \right)^{1/2}. \tag{1.11}$$

Another important plasma parameter is the Debye length. It characterizes the distance over which the potential created by a charge is felt by the other particles. When a particle of charge $Q$ is inserted in a plasma, the local electric potential has a decaying different from the Coulomb potential, proportional to $(Q/r)\exp(-r/\lambda_D)$. The decay length $\lambda_D$ is known as the Debye length, given by

$$\lambda_D = \left( \frac{\varepsilon_0 k_B T}{e^2 n_e} \right)^{1/2}. \tag{1.12}$$

This effect is called Debye shielding and it defines the order of distance over which fluctuating electric potentials appear in the plasma. For higher distances, the electric fields of the individual charged particles cancel each other and can be classified as electrically neutral. The second criterion to describe as plasma is that the characteristic length of the medium $L$ should be greater than the Debye length, $L > \lambda_D$. This means that, by approximation, each charge of the plasma interacts collectively only with the charges that are inside of a sphere of radius $\lambda_D$, known as the Debye sphere. The collective behavior occurs if there is sufficient electrons in the Debye sphere, $n_e \lambda_D^3 >> 1$, corresponding to the third criterion to a medium be a plasma. The last criterion for the existence of a plasma is having a plasma frequency much higher than the collisions with the neutral species, $\omega_{pe} > 2\pi\nu_{en}$. Here $\nu_{en}$ is the neutral collision frequency. Otherwise, the electrons are forced to become in equilibrium with the neutrals, and the medium has a behavior similar to a neutral gas. The Coulomb collisions are the predominant collisional mechanism.

It is estimated that more than 99% of the visible matter in the universe is in plasma state, however, plasmas are almost not present on earth naturally (e.g. lightning). To create a plasma artificially, the medium has to be heated with enough temperature and confined during the desired time, so the energy is not lost to the environment.

### 1.1.4 Plasma confinement and fusion reactors

There are basically two ways to confine a plasma in a reactor: inertially and magnetically. Inertial confinement fusion (ICF) uses high energy laser beams of light, electrons or ions to initiate nuclear fusion reactions by heating and compressing small solid fuel pellets [27, 18, 28, 29]. They have a size comparable to a pinhead (sub mm range) and contain some milligrams of fuel with the optimal mix of deuterium and tritium already prepared. The fusion reactions inside the pellet take place in a very short time and this process is repeated periodically. In the magnetic confinement, the ionized nuclei and the electrons existing in the fuel are spatially confined by strong magnetic fields, following the principle that magnetic fields force charged particles into helical orbits following the field lines [30]. The challenge of magnetic confinement is to find a suitable configuration of magnetic fields lines so that most of the particles stay on closed orbits and never escape from the confinement region. The magnetic fields do not interact with the high energetic neutrons resulting from the fusion reactions, they escape from the confinement zone and its power can be extracted externally. The helium particles that are generated are also confined by the magnetic field, and have an influence in the plasma behavior, keeping its neutrality.

Different magnetic configurations were tested over the last years of research in different experiences around the world [8, 30]. The three main configurations are the Tokamak [23, 30], the Stellarator [31, 30] and the Reverse Pinch Field [32], based on a toroidal geometry. The Tokamak has shown to be the one with most promising results in terms of plasma confinement. Consequently, the current fusion research is focused in the Tokamak configuration. Inertial confinement stills on research but has shown to be less attractive than the magnetic confinement to be used in a power plant. The other configurations, specially Stellarators, are still making improvements to compete with Tokamaks.

The DT reactors requires a continuous supply of tritium. Tritium is a radioactive isotope with a half-life of 12.6 years that does not occur naturally in nature. This problem is solved using the reaction neutrons to interact with lithium, producing tritium. This concept is called tritium breeding and the nuclear reactions of primary interest are

$$ {}^{6}_{3}\mathrm{L} + \mathrm{n(slow)} \longrightarrow {}^{4}_{2}\mathrm{He} + {}^{3}_{1}\mathrm{T} + 4.8\ \mathrm{MeV} $$

$$ {}^{7}_{3}\mathrm{L} + \mathrm{n(fast)} \longrightarrow {}^{4}_{2}\mathrm{He} + {}^{3}_{1}\mathrm{T} - 2.5\ \mathrm{MeV}. $$

The first reaction is much easier to initiate and as a result dominates the breeding process [23, 8]. Lithium has the advantage of be very abundant in the earth, with reserves sufficiently large to last thousands of years. Figure 1.5 (left) shows the concept of a generic magnetic DT fusion power plant. The reactor consists of a toroidal plasma surrounded by a first wall, a blanket and shield, the superconducting magnets that create the necessary magnetic field, and all the necessary additional technology as measurement systems (plasma diagnostics) or heating systems. The fuel is supplied and the tritium breeding occurs in the blankets to produce tritium. The blankets also capture the neutrons and their energy in the coolant flowing into it. The produced energy is then converted to electricity with the help of a steam-turbine generator. Figure 1.5 (right) shows a simple schematic model of a blanket-and-shield sector.

The first wall is the first layer of material having contact with the flux of particles, designed to withstand the heat flux from the plasma. The blanket is composed by the neutron multiplier, moderator and breeder. The neutron multiplier is required to create excess neutrons to replace losses in the blanket and is typically made of beryllium (Be) and lead (Pb). After the multiplier there is a moderator to slow down the fast neutrons

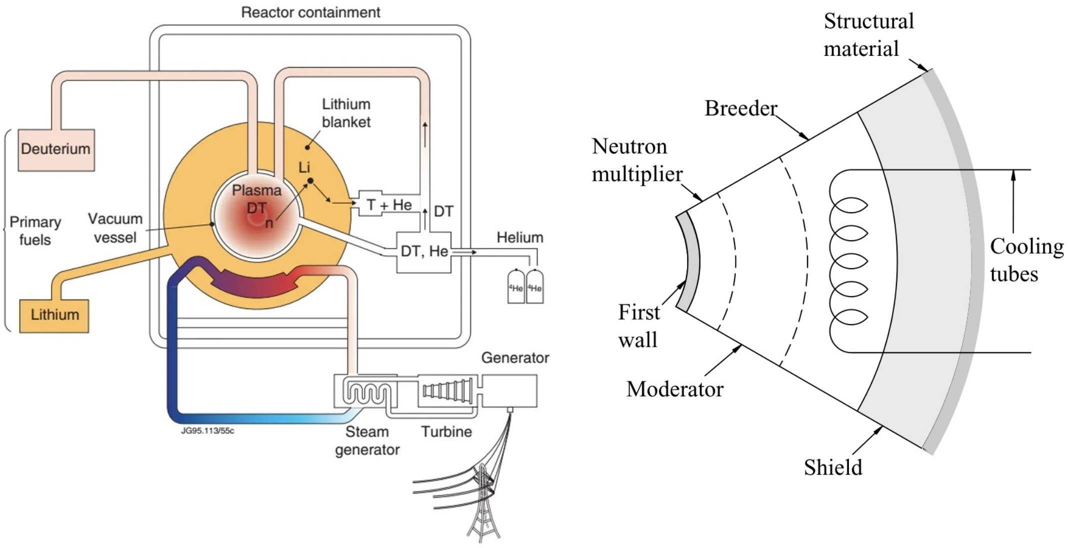

Figure 1.5: Schematic of a fusion reactor [33] (left). Schematic model of a first wall, blanket and shield sector [8] (right).

to a thermal energy compatible with the $^{6}_{3}\text{L}$ reaction. The tritium breeding process can then occur in a region containing a substantial amount of lithium. A set of liquid or gas cooling tubes are also embedded in the blanket. The role of these cooling systems is to transport the heat resulting from the slowing down of energetic particles to the thermal conversion system where the electricity is produced. Around the blanket, there is a shield with the purpose of absorbing any neutrons or gamma rays that escape the blanket. Its absorption must be very effective because the superconducting coils have to be thermally protected to operate at the required low temperatures.

### 1.1.5 Lawson criteria, ignition and breakheaven

The plasma confinement quality is characterized by the energy confinement time, $\tau_E$, and corresponds to the relaxation time at which the plasma internal energy $U$ is lost due energy transport, $\tau_E = U/S_k$, where $S_k$ is the rate of the losses. When the plasma is heated and reaches the necessary density and temperature, the steady state is maintained to produce a continuous output power. This is possible if the rate of energy losses is equal to the energy input. One important calculation is the minimum density $n$, temperature $T$ and confinement time $\tau_E$ to have net steady state energy output in a fusion reactor. This can be estimated with a plasma in thermodynamic equilibrium composed by a mix of deuterium and tritium, characterized by a density $n = 2n_D = 2n_T = n_e$, at the same temperature $T = T_D = T_T = T_e$ and with a plasma pressure $p = 2nT$, as done in [8, 23].

The plasma energy is lost to the environment through conduction (mass) or radiation (light). The radiation losses correspond essentially to the Bremsstrahlung radiation. From the electromagnetic theory we know that accelerated charges emit radiation and lose energy with this process. Bremsstrahlung radiation is emitted during the Coulomb collisions and occurs over a continuous range of frequencies, typically in the ultraviolet or soft x-ray region. These photons have a low probability of being absorbed in the plasma and the energy is lost from the system, corresponding to a power rate proportional to $n_i n_e T_e^{1/2}$. The two mechanisms of energy production are the alpha particles and the external heating systems. The alpha particles (ionized helium) are still confined by the magnetic field after the reaction occurs and are in thermal equilibrium with the other species. Its power rate is denoted by $S_\alpha = \frac{1}{4}E_\alpha n^2 \langle \sigma v \rangle$. From the final balance equation, $S_k + S_B = S_h + S_\alpha$, the Lawson criterion is obtained,

$$nT\tau_E \gtrapprox f_\alpha K_I \frac{T_k^2}{\langle \sigma v \rangle} \text{ atm s.} \tag{1.13}$$

Here $K_I = 0.055$, $S_h$ is the external heating power rate and $f_\alpha$ is the fraction of inserted energy in the system due to the alpha particles heating, $f_\alpha = S_\alpha/(S_\alpha + S_h)$. The ignition corresponds to the case with no external heating applied to the plasma ($f_\alpha = 1$). The minimizing value of triple product is obtained for $T_{min} = 15$ keV, corresponding to a minimum confinement time $(nT\tau_E)_I$ in the order of $10^{21}$ keV m$^{-3}$ s. Magnetic confinement confines plasmas with densities of $10^{20}$ m$^{-3}$ and therefore needs confinement times in the order of the second. When the plasma is externally heated is sub-ignited and the minimum confinement time is reduced by $f_\alpha$.

One important parameter to describe a fusion reactor is the gain factor $Q$,

$$Q = \frac{P_{\text{fus}}}{P_{\text{heat}}}, \tag{1.14}$$

where $P_{\text{heat}}$ and $P_{\text{fus}}$ are the input heating power and the output fusion power, respectively. The engineering gain factor, $Q_E$, corresponds to the net gain factor taking into account the efficiency of the heating and thermochemical systems. The breakeven of a fusion reactor is reached when $Q = 1$. For higher values, the reaction is sustainable and it is possible to have fusion machine producing more electricity than the output. A commercial solution, however, needs to have higher values of gain factor to be economically sustainable and interesting. Figure 1.6 shows the fusion triple product achieved on different magnetic fusion experiences, with the respective break-heaven and ignition limits.

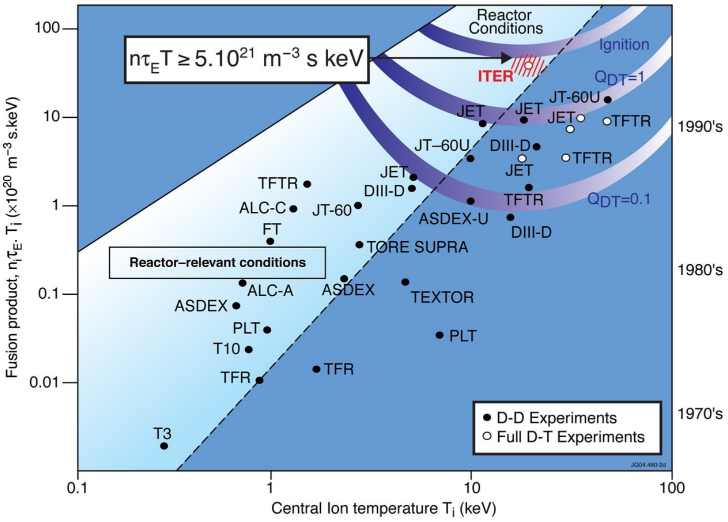

Figure 1.6: The evolution of the fusion triple product [34]

The present experimental devices machines have now achieved their limits of the fusion triple product. Although the fusion triple product attained has increased by a factor of $10^5$ over the past 30 years, it still falls short of breakeven conditions. The current record is held by Joint European Torus (JET) tokamak, in Culham (UK), which generated 16 MW of fusion power from 24 MW of input heating power. One of the ITER principal objectives is the demonstration of the ignition and the breakheaven points [12].

## 1.2 Tokamaks

### 1.2.1 Plasma dynamics

The knowledge of the plasma dynamics is essential to understand how to confine it. The simplest model would be knowing its initial positions and find the solution described by the Maxwell equations and the equation of motion of each particle as discussed in section 1.1.3. Unfortunately, this model does not work. Firstly, it is not enough to describe the physical processes of the plasma confinement in a fusion reactor since many physical processes are not included (e.g. ionization and recombination) and some of them would require quantum mechanics to be properly described. Secondly, this approach is not solvable analytically for the number of particles involved. Solving it with a super computer would would take impractical times to simulate even with a basic plasma configuration. To make progress in plasma physics, theoretical models which can be solved and tractable analytically or computationally is required.

There are basically three main approaches that are useful to modulate the plasma behavior: the single particle dynamics, the plasma kinetic theory and the fluid theory. There are also different models that are derived from them. Each one has a different level of complexity and can explain different phenomena in its scale of validity. The deductions of the different models here presented are found in [35, 30, 25, 8].

#### Single particle theory

The single particle theory consists in the analysis of the single-particle orbits under the presence of electric and magnetic fixed fields and extrapolate its behavior to the whole plasma. Here we describe the basic orbits necessary in the development of this work. The first important result is that magnetic fields do not create work. The variation of kinetic energy depends exclusively of the electric field, $\frac{d}{dt}E_k \propto (\mathbf{v} \cdot \mathbf{E})$. If a charged particle is subjected to a constant magnetic field $\mathbf{B}$, the classic version of the equation of motion (equation 1.6, for $\gamma = 1$) becomes:

$$m\frac{d\mathbf{v}}{dt} = q[\mathbf{v} \times \mathbf{B}]. \tag{1.15}$$

Decomposing the velocity in a parallel and perpendicular component to the magnetic field, $\mathbf{v} = \mathbf{v}_{\parallel} + \mathbf{v}_{\perp}$, two different equations are obtained for each component. Taking Cartesian coordinates for simplicity and $\mathbf{B} = (0, 0, B)$, the solution of equation of motion 1.15 is

$$[x(t), y(t), z(t)] = [x_g + \rho_L \sin(\omega_c t \pm \phi), y_g \mp \rho_L \cos(\omega_c t \pm \phi), v_{\parallel} t + z_0]. \tag{1.16}$$

In the perpendicular direction, the motion is circular with a center at $(x_g, y_g) = (x_0 + \rho_L \sin\phi, y_0 - \rho_L \cos\phi)$, where $(x_0, y_0)$ is the initial position and $\phi$ the phase. The frequency $\omega_c$ of the circular motion is called the cyclotron frequency,

$$\omega_c = \frac{|q|B}{m}. \tag{1.17}$$

The radius $\rho_L$ is known as the Larmor radius, and is given by $\rho_L = v_{\perp}/\omega_c$. The upper signal of the $[x(t), y(t)]$ solutions correspond to negative charge and the lower to the positives. Negative charge particles rotate clockwise and positive charge particles rotate anticlockwise. The circular motion in a magnetic field is fundamental in plasma confinement. Since the velocity keeps constant along the magnetic field direction and the perpendicular motion is circular, charged particles tend to follow magnetic lines. This is the main idea behind using magnetic fields to confine plasmas.

The relativistic effects have impact in some plasma quantities in the context of nuclear fusion. They almost often increase the complexity of the analytical descriptions. In the case of the circular motion they change the the cyclotron frequency is affected by a factor $\gamma^{-1}$, making the difference for high speed particles. Due to the increasing level of complexity, only the classic versions of the problems are presented in this work. If relativistic effects are needed to take into account, its use is mentioned.

When the particle is under the presence of an additional constant force, **F**, the guiding center drifts in the perpendicular direction. The drift velocity is given by

$$\mathbf{v}_D = \frac{\mathbf{F} \times \mathbf{B}}{qB^2}. \tag{1.18}$$

Drifts are one of the fundamental mechanisms affecting the confinement and transport of particles and energy because particles may follow orbits in undesired directions. The three main drifts in the context of the single particle model are:

$$\mathbf{v}_D = \mathbf{v}_{\mathbf{E}\times\mathbf{B}} + \mathbf{v}_{\nabla B} + \mathbf{v}_\kappa = \frac{[\mathbf{E} \times \mathbf{B}]}{B^2} + \frac{mv_\perp^2}{2qB}\frac{\mathbf{B} \times \nabla B}{B^2} + \frac{mv_\parallel^2}{qB}\frac{\mathbf{B} \times \nabla B}{B^2}, \tag{1.19}$$

The first term corresponds to the drift ($\mathbf{v}_{\mathbf{E}\times\mathbf{B}}$) that occurs for constant electric field. This drift has no dependence on the charge, so the ions and the electrons move in the same direction. The second and third term correspond to the gradient ($\mathbf{v}_{\nabla B}$) and the curvature ($\mathbf{v}_\kappa$) magnetic drifts that occur when the magnetic field changes and depend on the particle's charge. For small variations ($\delta\mathbf{B} << \mathbf{rB}$), the magnetic field can be expressed by a Taylor expansion, $\mathbf{B}(\mathbf{r}) = \mathbf{B}_0 + \mathbf{r} \cdot (\nabla\mathbf{B})$. In this case, the effect of the magnetic field can be seen as a constant force that corresponds to the average force over the gyration period. These drifts must be counterbalanced in a magnetic confinement device. The orbit theory is useful but is limited in many contexts due to the influence of the particle on its surroundings is not taken into account.

### Plasma kinetic theory

Plasma kinetic theory describes the plasma statistically in scales above the Debye length. It assumes that each specie $j$ is described by a distribution function $f_j(\mathbf{r}, \mathbf{v}, t)$ that contains information on the number of particles that exist in a small phase space volume element $d\mathbf{r}d\mathbf{v}$ centered at $\mathbf{r}$ and $\mathbf{v}$. The local charge density is obtained given by integrating in the velocity space,

$$n_j(\mathbf{r}, t) = \int_{\mathbf{v}} f_j(\mathbf{r}, \mathbf{v}, t)d\mathbf{v}, \tag{1.20}$$

The Fokker-Planck equation describes the evolution of the distribution function,

$$\frac{\partial f_j}{\partial t} + \mathbf{v} \cdot \frac{\partial f_j}{\partial \mathbf{r}} + \frac{1}{m_j}[\mathbf{F}_{ext} + q_j(\mathbf{E} + \mathbf{v} \times \mathbf{B})] \cdot \frac{\partial f_j}{\partial \mathbf{v}} = \sum_\beta C(f_j, f_\beta), \tag{1.21}$$

where the right term is the variation of the distribution function due to the collisions or other phenomena (e. g. particle creation) and $\mathbf{F}_{ext}$ is any other external force apart from the Lorentz force. The macroscopic variables correspond to averaged quantities obtained from the distribution function. The macroscopic fluid velocity is given

$$\mathbf{u}_j(\mathbf{r}, t) = \frac{1}{n_j(\mathbf{r}, t)} \int_{\mathbf{v}} \mathbf{v} f_j(\mathbf{r}, \mathbf{v}, t)d\mathbf{v}. \tag{1.22}$$

The model is completed with the Maxwell equations, where the macroscopic currents are used. If no collisions take in place, this term is zero and the equation is called Vlasov equation. The equilibrium solution of the Vlasov for the case in which there is no external forces is a Maxwellian distribution of the particle's velocities. Other forms of the Fokker-Planck equation are also used in the study of plasma dynamics. One of the examples is the gyro-kinetic theory, which reduces the Fokker-Planck to six dimensions instead of the seven (3 spatial, 3 velocity, and time) by averaging the gyromotion [36]. This leads to consume much less computational time which turns this framework very useful in simulations, in particularly in the study of turbulence phenomena covered in this chapter.

### Fluid theory

Fluid theory equations are derived from kinetic theory and describe the evolution of the macroscopic quantities. Although a plasma differs from a normal fluid due to the presence of collective effects and low rates of collisions, this theory works very well and leads to many important results. The equations are obtained by integrating the Fokker-Planck over the velocity space with moments in the form $M^{(N)}_{jil..k}(\mathbf{r},t) = \int_{\mathbf{v}} v_i v_l ... v_k f_j(\mathbf{r},\mathbf{v},t) d\mathbf{v}$. The continuity equation is obtained by taking the 0th moment,

$$\frac{\partial n_j}{\partial t} + \nabla \cdot (n_j \mathbf{u}_j) = 0. \tag{1.23}$$

Introducing the thermal motion velocity as $\mathbf{w} = \mathbf{v} - \mathbf{u}_j$, different macroscopic quantities of interest are defined. The pressure tensor is defined as

$$\mathbf{P}_j = m_\alpha n_j \langle \mathbf{w} w \rangle = \mathbf{\Pi}_j + p_j \mathbf{I} \tag{1.24}$$

where the scalar pressure is $p_j = \frac{1}{3} m_j n_j \langle w^2 \rangle$ and $\mathbf{\Pi_j}$ is the anisotropic part. The $\langle h \rangle$ operator is a moment $\int h f_j d\mathbf{v}$ divided by the density $n_j$. The temperature is calculated from the scalar pressure, $T_j = (p_j/n_j)$. The first moment gives the momentum equation,

$$m_j n_j \frac{dn_j}{dt} \mathbf{u}_j = q_j n_j [\mathbf{E} + \mathbf{u}_j \times \mathbf{B}] - \nabla \cdot \mathbf{P}_j + \sum_{\beta \neq j} \mathbf{R}_{j\beta} \tag{1.25}$$

where $\mathbf{R}_j = \int m_j \mathbf{w} C(f_j, f_\beta) d\mathbf{w}$ is the mean momentum transferred between particles due to the friction of collisions. The second moment gives the energy equation,

$$n_j \left[ \frac{d}{dt} \left( \frac{1}{2} m_j u_j^2 + \frac{3}{2} T_j \right) \right] - q_j n_j \mathbf{u}_j \cdot \mathbf{E} + \nabla \cdot (\mathbf{u}_j \cdot \mathbf{P}_j + \mathbf{q}) = Q_j + \mathbf{u}_j \cdot \mathbf{R}_j \tag{1.26}$$

where the time derivative is the convective derivative, $\mathbf{q}_j = \frac{1}{2} m_j n_j \langle w^2 \mathbf{w} \rangle$ is the heat flux due to random motion and $Q_j = \int \frac{1}{2} m_j w^2 C(f_j, f_\beta) d\mathbf{w}$ is the mean heat transferred between particles due to the friction of collisions. Additionally to the fluid equations, the Maxwell equations describe the electromagnetic fields. Many phenomena like radiation, creation of particles, fusion, and plasma-boundary interactions are not included in this description. New terms need to be included if a more detailed model is required.

### Single fluid theory - ideal MHD equations

The ideal Magnetohydrodynamics equations (MHD equations) provide a single-fluid description of macroscopic plasma phenomena characterized by long-wavelength and low-frequency. Some phenomena, like micro instabilities, classical and anomalous transport, radiation, plasma-wall interactions, need a kinetic or multiple fluid description to be treated. However, ideal MHD theory is very accurate to understand how can a magnetic geometry provide forces to hold a plasma in equilibrium and what are the most stable geometries. Despite its simplicity, experimental results demonstrate that ideal MHD provides a very accurate description of most macroscopic plasma behavior.

Ideal MHD theory assumes a plasma composed by two species, the ions and the electrons, and uses the fluid and the Maxwell equations. The equations are

$$\frac{\partial \rho}{\partial t} + \nabla \cdot (\rho \mathbf{v}) = 0 \tag{1.27}$$

$$\rho \frac{d\mathbf{v}}{dt} = \mathbf{J} \times \mathbf{B} - \nabla p \tag{1.28}$$

$$\frac{d}{dt}\left(\frac{p}{\rho^{\gamma}}\right) = 0 \tag{1.29}$$

$$\mathbf{E} + \mathbf{v} \times \mathbf{B} = 0 \tag{1.30}$$

$$\nabla \times \mathbf{E} = -\frac{\partial \mathbf{B}}{\partial t} \tag{1.31}$$

$$\nabla \times \mathbf{B} = \mu_0 \mathbf{J} \tag{1.32}$$

$$\nabla \cdot \mathbf{B} = 0. \tag{1.33}$$

They are valid in regimes with (I) non-relativistic characteristic thermal velocities and phase velocities ($\omega/k, V_{th} << c$), (II) characteristic frequencies much lower than the plasma frequency ($\omega << \omega_{pe}$), (II) characteristic length much longer than the Debye length ($L >> \lambda_D$), (IV) small resistivity, small gyro radius ($\rho_i << L$) and (V) high collisionality. The single fluid variables are the density $n = n_i = n_e$, the current $\mathbf{J} = en(\mathbf{u}_i - \mathbf{u}_e)$, the mass density $\rho = m_i n$, the fluid velocity $\mathbf{v} = \mathbf{u}_i$, the temperature $T = (T_i + T_e)/2$ and the pressure $p = p_i + p_e = 2nT$. The subscript indexes design the ion ($i$) and electron ($e$) species. The model assumes an adiabatic plasma and the the energy fluid equation becomes 1.29, with $\gamma = 5/3$. The collisions of each specie rapidly transform the distribution function into a Maxwellian form giving rise to an isotropic pressure. The non ideal MHD (with the resistivity included) and other derivations from the fluid theory are not in the scope of this work, being available in the literature [30, 35].

### 1.2.2 MHD equilibrium and magnetic surfaces

There are two important aspects in the design of a magnetic configuration: equilibrium and stability. Equilibrium consists in a state where the macroscopic properties are stationary and located at the confinement zone. The stability is its capacity of returning to the equilibrium state when a disturbance in occurs. If the configuration is not stable, it is not possible to have a continuous operation. The equilibrium is lost and the energy can reach the wall in critical quantities. The equilibrium conditions are obtained removing the time dependent terms from the ideal MHD equations. The momentum equation becomes

$$\mathbf{J} \times \mathbf{B} = \nabla p, \tag{1.34}$$

which means that the local equilibrium is found by balancing the magnetic force with the pressure gradient. This shows that when a plasma column is created, it has tendency to contract radially until the balance between the inward force created by the existing magnetic field and the outward pressure gradient force is achieved (Bennett pinch effect).

The most common magnetic fusion concepts use a reactor with the shape of a torus, so the magnetic fields remain closed inside the toroidal device and do not intersect the chamber. In the open ended devices, a great part of the energy is lost perpendicularly and parallel to the magnetic field.

An important result from ideal MHD equilibrium are the geometrical conditions of the current and magnetic field. From the dot product of the equilibrium equation 1.34 with $\mathbf{B}$, one obtains

$$\mathbf{B} \cdot \nabla p = 0. \tag{1.35}$$

Therefore, the magnetic field lines lie on a set of closed toroidal surfaces of constant pressure. A similar relation is obtained by the dot product of $\mathbf{J}$ with the same equation,

$$\mathbf{J} \cdot \nabla p = 0, \tag{1.36}$$

implying that current lines also lie on the constant pressure surfaces. These toroidal surfaces of constant pressure are also called toroidal magnetic surfaces or magnetic flux surfaces. Figure 1.7 shows the representation of these conditions in a torus section.

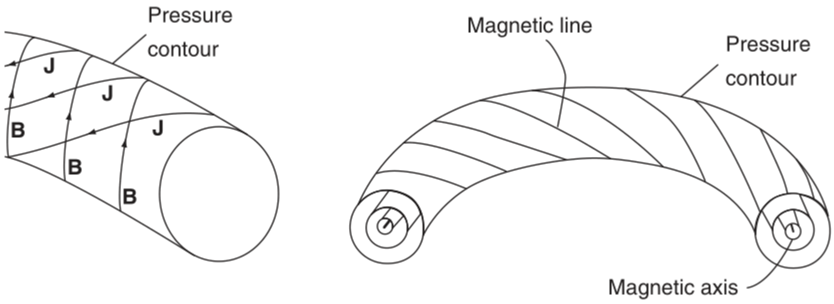

Figure 1.7: Current and magnetic field lying on the pressure surface (left). Different magnetic surfaces of a torus with the magnetic lines and the magnetic axis (right) [30].

In a general well-confined equilibrium, the pressure is maximum at the center of the poloidal cross section (section of the torus). The magnetic axis is the limit when the surfaces are approximated by a line.

### 1.2.3 Grad–Shafranov equation

The Grad–Shafranov equation is a two-dimensional, non-linear, partial differential equation obtained from the ideal MHD equations [37]. Using toroidal coordinates (right-handed cylindrical coordinates $[R, \phi, Z]$, the derivative of any function of $\phi$ is zero. The magnetic field and the current are given by

$$\mathbf{B} = B_\phi \mathbf{e}_\phi + \mathbf{B_p} = \frac{F}{R}\mathbf{e}_\phi + \frac{1}{R}\nabla\Psi \times \mathbf{e}_\phi \tag{1.37}$$

$$\mu_0 \mathbf{J} = \mu_0 J_\phi \mathbf{e}_\phi + \frac{1}{R}\nabla(RB_\phi) \times \mathbf{e}_\phi \tag{1.38}$$

where $F = RB_\phi$ and $\Psi = RA_\phi$, being $A_\phi$ the component of the vector potential $\mathbf{A}$ which verifies $\mathbf{B} = \nabla \times \mathbf{A}$. The flux function $\Psi$ is related with the poloidal flux $\Psi_p$ by

$$\Psi_{pol}(R, Z) = \int_0^{2\pi} d\phi \int_{R_m}^{R} R' B_Z(R', 0) dR' = 2\pi\Psi(R, Z). \tag{1.39}$$

where $R_m$ is the magnetic axis and the integration constant is chosen so $\Psi(R_m, 0) = 0$. The poloidal flux $\Psi_p(R, Z)$ is the flux through the circle with its center at $R = 0$ lying in the z-plane and having $(R, Z)$ on its boundary. From equations 1.35 and 1.36, we get $p = p(\Psi)$ and $F = F(\Psi)$. The magnetic field 1.37 and current 1.38 inserted in the balance force equation 1.34 yields the Grad-Shafranov equation,

$$\Delta^*\Psi = R^2\nabla \cdot \frac{\nabla\Psi}{R^2} = R\frac{\partial}{\partial R}\left(\frac{1}{R}\frac{\partial\Psi}{\partial R}\right) + \frac{\partial^2\Psi}{\partial Z^2} = -\mu_0 R^2\frac{dp}{d\Psi} - F(\Psi)\frac{dF}{d\Psi} \tag{1.40}$$

The nature of the equilibrium of the toroidal symmetric devices (e.g., tokamak, reversed field pinch, etc.) is determined by the choice of the $p(\Psi)$ and $F(\Psi)$ functions.

### 1.2.4 The basics of tokamaks

Many Magnetic configurations based on macroscopic MHD equilibrium and stability were proposed and studied over the last years of fusion research. The two most promising concepts are the tokamak [23, 30] and the stellarator [31, 30]. All of them are 2D axisymmetric toroidal configurations, with the exception of the stellarator, which is a 3D configuration. One of the stellarator advantages is being the only concept not requiring toroidal current drive. It has, however, a more complicated magnet configuration which increases its complexity and cost [38]. Tokamaks have been studied the most and have achieved the best performance. They have the best balance between having attractive confinement physics and technological attractiveness, being the reason why ITER will be a tokamak. Figure 1.8 shows a schematic view of both configurations.

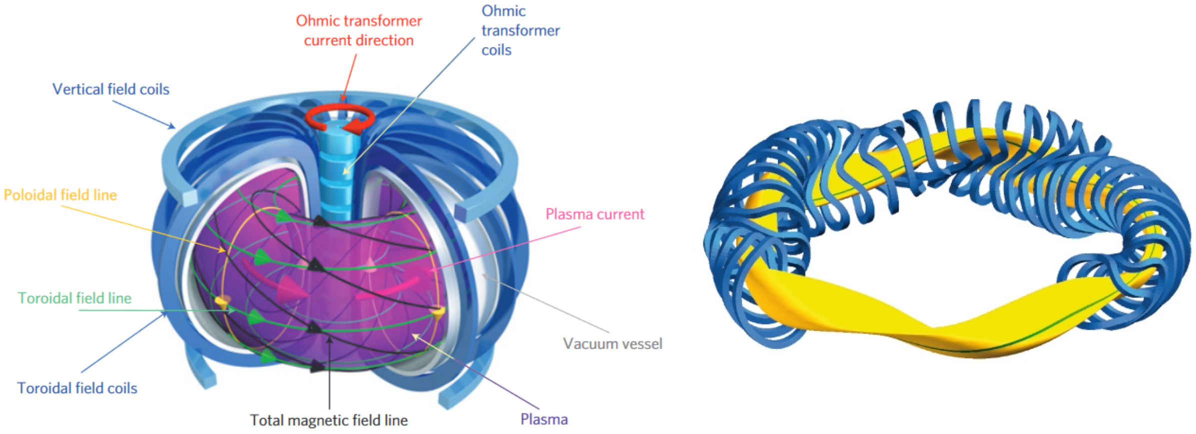

Figure 1.8: Schematic view of the tokamak configuration (left) [39]. Schematic view of the stellarator configuration (right) [40].

The Tokamak configuration was proposed by Sakharov and Tamm in 1950. The word comes from the Russian **TO**roidol'naya **KA**mera s **MA**gnitinymi **K**atushkami, which means toroidal chamber with magnetic coils. In this configuration, the plasma confinement is achieved by combining magnetic fields generated by external coils and by current flowing in the plasma. The principal magnetic field is the toroidal field, $B_\phi$, produced by the poloidal coils placed around the torus. Its intensity is function of the distance from the major axis, $R$, according with

$$\oint \mathbf{B} \cdot d\mathbf{l} = 2\pi R B_\phi = \mu_0 I_c \Rightarrow B_\phi = \frac{\mu_0 I_c}{2\pi R} = \frac{B_0 R_0}{R}, \tag{1.41}$$

where $I_c$ is the total current passing in the coils. It is convenient the use of a toroidal coordinate system, where $R = R_0 + r\cos\theta$, $Z = r\sin\theta$ and $0 < r < a$ [41]. In this case, $R_0$ corresponds to the major radius (torus axis) and $a$ is the minor radius of the tokamak. The ratio $R_0/a$ is called the aspect ratio of the torus.

The toroidal field is not, however, able to counterbalance the pressure gradient by itself. Due to this variation with $R$, the magnetic gradient $\nabla B$ causes the ions and electrons to drift vertically in opposite directions (see equation 1.19). The resulting charge separation results in a vertical electric field, which in combination with the toroidal magnetic field leads to a radial outward $\mathbf{E} \times \mathbf{B}$ drift of the plasma. Thus, no equilibrium force exists to keep the plasma confined. Since for particles in the inner edge of the torus (known as High field side, HFS) this drift is directed to the plasma axis and for those closer to the outer edge (Low field side, LFS) is directed to the wall, the solution to avoid this drift is twisting magnetic field lines along the toroidal direction. This can be done adding a poloidal magnetic field component $\mathbf{B}_\theta$, as seen in figure 1.8.

In the stellarators, the poloidal field is generated by external coils. In tokamaks, this field is induced by a transformer (see figure 1.8). The inner central solenoid acts as the primary circuit and the plasma column forms the secondary. By ramping up the current, the induced electric field creates the plasma current and heats the plasma through ohmic heating. The plasma discharge duration is thus limited to the solenoid capacity for steady state operation, being one of the principal tokamak disadvantages. The geometry of the field lines is described by the safety factor, $q$, defined as the ratio between the number of complete toroidal circuits a field line must make before to complete a poloidal circuit. This parameter plays an important role in the plasma stability. Another fundamental quantity is the ratio of the plasma pressure by the magnetic pressure,

$$\beta = \frac{p}{B^2/2\mu_0}, \tag{1.42}$$

where $B$ is the magnetic field. Higher $\beta$ is favorable for the economic point of view, but it is more difficult to achieve experimentally.

Additional coils are required to balance the outward forces resulting from the toroidal geometry and to shape the plasma [30]. An array of coils (vertical field coils) outside the vessel creates the necessary vertical magnetic field to help to contain the plasma (see figure 1.8). By changing the intensity of the different magnetic fields produced by these coils, the plasma can be shaped, moved up or down, in or out, and create field nulls, i.e. X-points (point in space at which the poloidal field has zero magnitude).

There are two fundamental mechanisms of isolating the confinement zone from the wall, preventing that the thermal energy is lost and cause damage to the wall materials. The first one is using a limiter surface, in which the plasma is bounded by a specific material limiter inside the vessel. The second one is using a poloidal divertor magnetic configuration. This configuration protects the surrounding walls from thermal and neutronic loads and allows the control of the plasma particles to the divertor zone, where the heat and ash produced by the fusion reaction is extracted and the contamination is minimized. The divertor configuration has proved to be more favorable for good plasma confinement than the limiter configuration. Figure 1.9 (left) shows the Single and Double null divertor configurations. The most common is the Single null, where the plasma is round at the top and forms an X-point at the bottom divertor position. Figure 1.9 (right) shows the representation of this plasma shape in a toroidal section.

The Last Closed Magnetic Surface (LCMS) is known as plasma separatrix and separates the confinement region where the lines are closed from the region where opened field lines

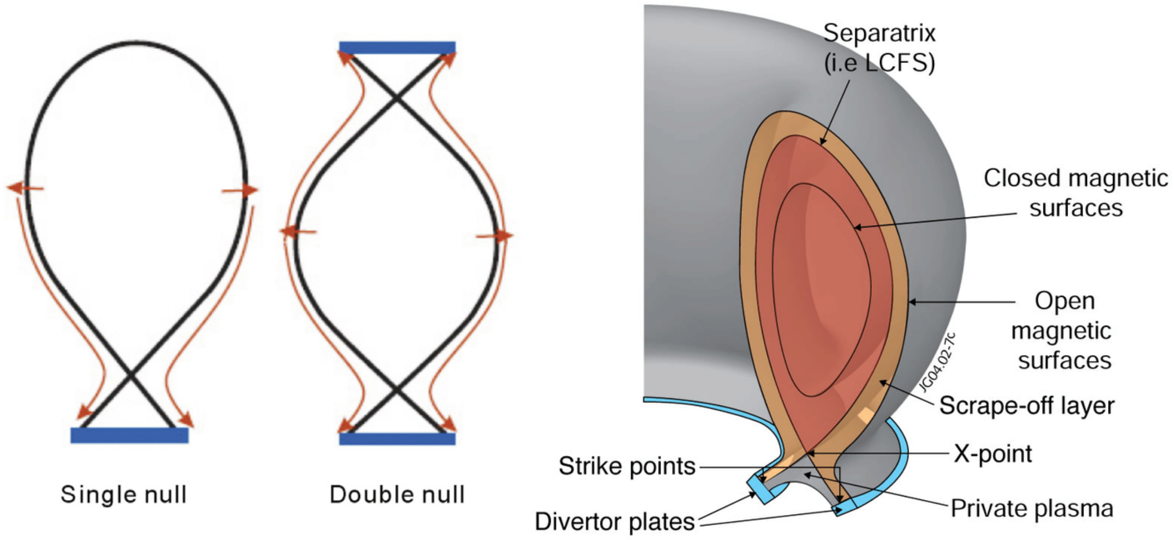
Single null

Double null

Figure 1.9: (left) Single and Double Null plasma shape. Adapted from [38]. (right) Tokamak divertor configuration [42].

connect to material surfaces. The poloidal flux $\Psi(R, Z)$ is usually normalized to the value at the separatrix, $\Psi_s$, through the transformation

$$\rho_{pol} = \sqrt{\frac{\Psi_{pol} - \Psi_c}{\Psi_{sep} - \Psi_c}}, \tag{1.43}$$

where $\Psi_c$ is the higher magnetic flux at the center of the plasma. The Scrape-Off Layer (SOL) is the plasma region outside the separatrix ($\rho > 1$) characterized by open field lines. The SOL absorbs most of the plasma exhaust (particles and heat) and transports it along the field lines to the divertor plates. In contrast to the plasma core, where it is required to have hot temperatures, in the SOL it is desirable to have the plasma cold in the SOL region to reduce melting, impurity generation, and other unwanted plasma-surface interactions. Typically the plasma density assumes an exponential decay in the radial direction in this region since the particle losses are not compensated. For the typical experiments, this value is of a few centimeters [43]. Under high density and low plasma current conditions, a shoulder can be formed in the SOL [44, 45]. The decay lengths of temperature, pressure, power, and other variables are different.

Due to the nature of the plasmas, different waves of particles and fields can be excited and propagate in the medium. These waves are formed by perturbing the plasma parameters from the equilibrium, leading to the usual wave phenomena. Plasma instabilities occur when the perturbations can growth and lead to an unstable behavior. Many ideal or resistive MHD instabilities can occur in tokamaks (Kink modes, Ballooning mode, Magnetic islands, etc.). The guaranty of the MHD stability is crucial in the operation of a tokamak plasma, otherwise the confinement is lost. By understanding the behavior of each instability, is possible to find the necessary conditions to suppress it. This topic is not fully covered in this work, but the bibliography on the subject is extensive [46, 47].

Fusion plasmas require heating methods to reach the desired temperatures and to compensate the losses [8]. In a tokamak, the plasma current required for equilibrium heats the plasma. This method becomes ineffective at high temperatures because the Spitzer resistivity decreases with the plasma temperature $\eta_{\parallel} \sim T_e^{-3/2}$. At about 3 keV, the resistive heating alone cannot overcome the radiation power loss and the plasma cannot get hotter. The two main additional heating methods are the neutral beam injection (NBI heating) and radio-frequency waves (RF heating). In the NBI heating very powerful beams of neutral particles (typically of the same plasma species) are tangentially injected the the plasma. The neutral particles are not affected by the confinement fields and are ionized by collisions with the plasma particles becoming part of the plasma and transferring its energy in the further interactions. The beam velocity is enough to reach the plasma core and heat the plasma locally. In the RF heating, electromagnetic waves at resonant frequencies are used to transfer energy to the particles. The resonant frequencies occur when parallel Doppler shifted frequency is equal to an harmonic of the cyclotron frequency,

$$\omega = k_{\parallel} v_{\parallel} + l\Omega_c \quad l = 0, 1, 2, ... \tag{1.44}$$

and therefore depends on the magnetic field of the device. If the resonant interaction is made with the ions it is called Ion cyclotron resonance heating (ICRH) while if its with the electrons, Electron cyclotron heating (ECRH). The absorption location is controlled in order to be more effective and to avoid reflection on the wall or damage in the plasma facing components. These heating methods are technologically developed to heat the plasma with powers in the order of several tens of MW during steady state operations.

All the operation in a tokamak is driven by a control system which takes decisions according to the plasma state and to what is intended in the discharge. The plasma state is measured by the plasma diagnostics [48, 49]. They are essential for understanding and developing plasma technology, providing the database for fusion research. The perturbation of the plasma properties and the effect of the plasma particles in the instruments must be minimized to ensure the continuation of the operation.

Figure 1.10 shows the interior of the vacuum vessel of JET (Joint European Tokamak) [50]. At the left side, we see the Be tiles protecting the first wall, the diagnostics and the divertor plates at the bottom. At the right, a plasma picture taken during a discharge is shown. The visible light corresponds to the low temperature zones, near the wall.

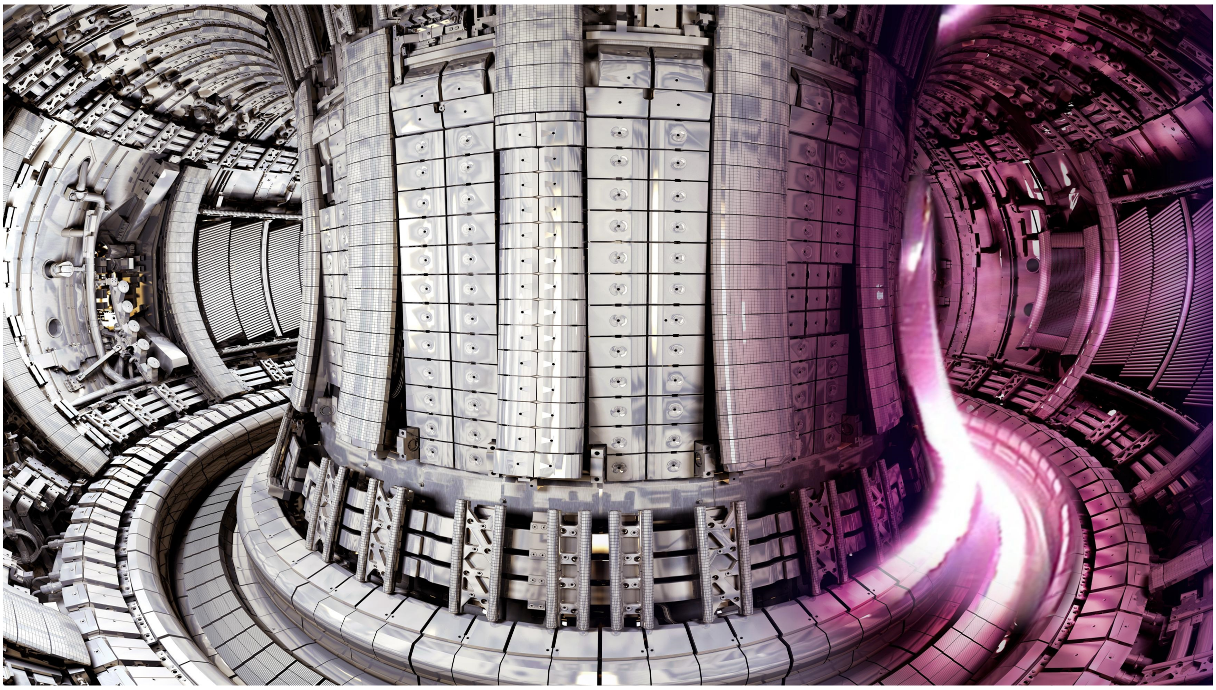

Figure 1.10: The interior of the vacuum vessel of JET with and without plasma [50].

### 1.2.5 Plasma turbulence and micro instabilities

In an ideal equilibrium state, the plasma parameters are constant during the discharge and have a well defined spatial profile. In contrast, experimental plasmas in equilibrium conditions show fluctuations in all the parameters such as density $\delta n$, temperature $\delta T$, velocity $\delta \mathbf{u}$ or magnetic field $\delta \mathbf{B}$. These fluctuations are characterized by a wide range of frequencies from a few Hz to MHz and by irregular spacial structures with characteristic dimensions. Its amplitude level is typically given in percentage of the unperturbed parameter, for example and changes according to the region of the plasma (SOL, edge and core). This phenomena is known as plasma turbulence, and is induced by incoherent motion appearing from micro-instabilities (see figure 1.11).

Although the turbulent transport processes are not fully understood, it is very clear that they affect the plasma confinement and are responsible for the experimental radial transport compared to the neoclassical transport previsions [51, 52]. Understanding the dynamics of the turbulent transport and know how to control and suppress it is one of the major areas of research in fusion. With the help of gyro-kinetic codes such as GYSELA [53], GYRO [54], GENE [55] or GEMR ([56], the turbulence properties can be simulated. These simulations are very demanding from the point of computational power and rely on several approximations. Unfortunately, with the existing turbulence models there is difference between measurements and simulation results. Figure 1.11 shows the snapshot of the density fluctuations from the GYRO code where is possible to observe irregular structures and its dependence on the poloidal region.

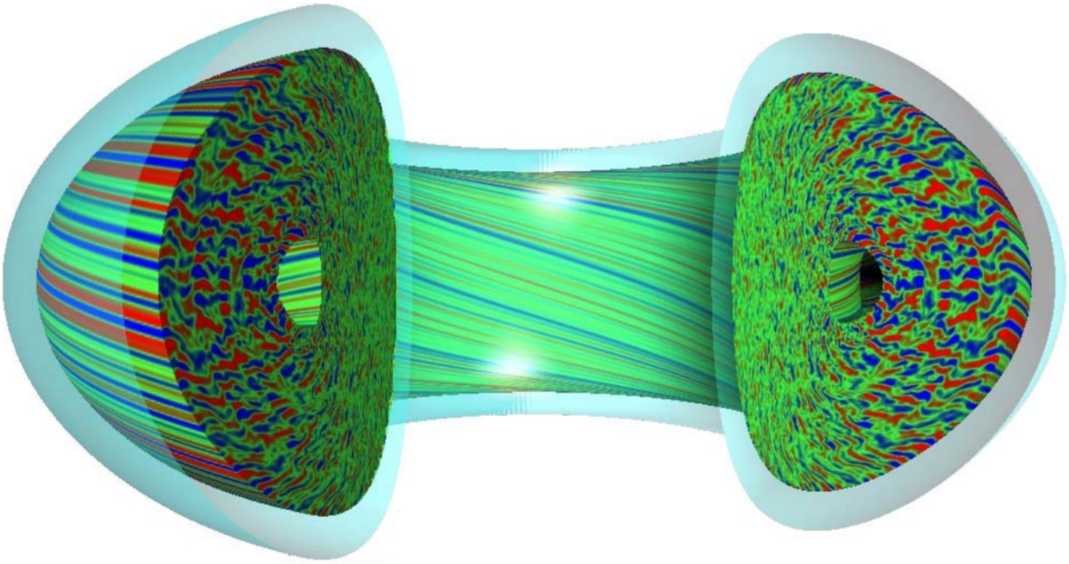

Figure 1.11: Snapshot of the density fluctuations from the simulation of a turbulent plasma with the GYRO code [57, 58].

The original image sequence shows the evolution of these structures over time and the motion of these structures between different layers. In a fluid this irregular dynamics exists when it is subjected to external forces. The transition to a turbulent state can be shown with an incompressible $(\nabla \cdot \mathbf{u})$ neutral fluid governed by the Navier-Stokes equation,

$$\rho_m \left( \frac{\partial \mathbf{u}}{\partial} + (\mathbf{u} \cdot \nabla)\mathbf{u} \right) = -\nabla p + \mu \Delta \mathbf{u}. \tag{1.45}$$

Here $\rho_m$ is the mass density, $\mathbf{u}$ the fluid velocity field, $p$ the pressure and $\mu$ the viscosity of the fluid. The behavior of the system depends on a fundamental parameter, the Reynolds number $Re = u_0 l_0 \rho_m / \mu$. It is defined as the ratio of inertial forces (second term of the left side of equation 1.45) to the viscous forces (last term), obtained with the dimensionless Navier-Stokes equation for the characteristic system scales ($u_0$ is the characteristic velocity and $l_0$ the characteristic length). For low values of Reynold number, $Re << 1$, the flow is laminar (smooth and clear behavior). For intermediate values, $Re \sim 1$, the formation of eddies (Karman vortex streets) occurs due to the instability of the flow associated with the inertial forces [59, 60]. A fully turbulent state is developed at very high Reynold number number, $Re >> 1$. A similar phenomena occurs in the plasmas, although its dynamic is totally different. Plasmas are formed by multiple fluids of charged particles interacting between each-other by complex electromagnetic interactions. Different instabilities can be present and induce the turbulent behavior.

One important characteristic of a turbulent system is the transference of the energy $E(k)$ from an instability towards different scales. When the energy is transferred from larger to smaller scales, it is known as a direct cascade. When it is transferred from the smaller to the larger, it is an inverse cascade. In 1941 Kolmogorov published the K41-theory in which he derived an equation for the spectral energy per unit wavenumber resulting from the injection of an instability at the characteristic wavenumber $k_{\text{inj}}$. For $k > k_{\text{inj}}$, the energy distribution has an inverse cascade and assumes a dependence in the form $E(k) \sim k^{5/3}$, being confirmed by the experiments on fluids [61]. However there is a substantial difference when this is applied to a problem like magnetic plasma confinement. The transport along the magnetic lines is much faster compared to the drifts in the perpendicular direction, resulting in anisotropic 2D turbulent structures (see figure 1.11). The spectral energy distribution for this case was studied in by Krainchan in 1971 [62], obtaining an energy distribution in the form $E(k) \sim k^{-5/3}$ for $k < k_{\text{inj}}$ and $E(k) \sim k^{-3}$ for $k > k_{\text{inj}}$. Figure 1.12 shows the spectral energy per wavenumber unit for 3D turbulence (left) and 2D turbulence (right). For this case, there is a direct and an inverse cascade. In real plasmas different injection scales can exist at the same time coming from different micro-instabilities and some assumptions are not the same of fluids, modifying the final spectrum [63, 64, 65].

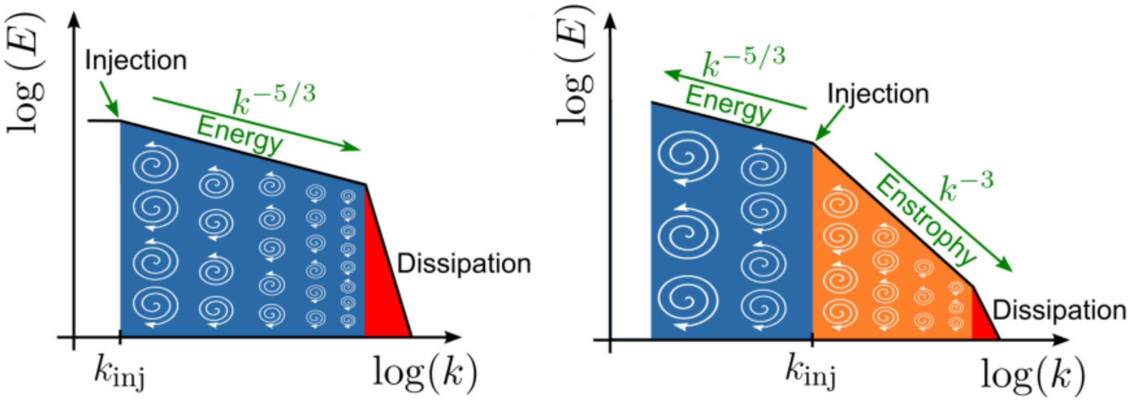

Figure 1.12: Spectral energy per wavenumber unit for (left) 3D turbulence and (right) 3D turbulence [66].

These instabilities occur due to inhomogeneities in the plasma. The most dominant effects are the gradients of temperature, density, pressure and current density. They are described by its growing rate. In the linear regimes, also present in states of fully developed turbulence [67], the growing scale can be found analytically, giving an important ideia of the dependence form and of the characteristic scales.

Different regions of the machine tend to have different micro-instabilities, leading to different local turbulence spectra (see figure 1.11). The normalized logarithmic density gradient $R/L_n = -R\nabla \log(n)$ and normalized logarithmic temperature gradients $R/T_{e,i} = -R\nabla \log(T_{e,i})$ are two important parameters in the characterization of each one. The most dominant ones are presented. The electron drift waves (EDW) dominate the edge region of the plasma ($0.95 < \rho < 1$), where $\nabla \log(n)/\nabla \log(T_{e,i}) \gtrsim 2$ [68, 69, 70]. The growth rate is maximum for $k_\perp \rho_S \sim 1$, where $\rho_S = (m_i T_e)^{1/2}/eB$ is known as the drift wave scale. This corresponds to its characteristic scale. In the core region ($\rho < 0.95$), where typically $\nabla \log(T_{e,i})/\nabla \log(n) > 1$, two modes are dominant. The trapped electron modes (TEM) are driven by the electron temperature gradient $R/L_{T_e}$ and have a spatial growth rate of $k_\perp \rho_S \sim 0.3$. The ion temperature gradient (ITG) modes driven by the ion temperature gradient $R/L_{T_i}$, are stabilized by the $R/L_n$ and have a spatial growth rates of $k_\perp \rho_S \sim 0.3$. Due to the inverse dependence of the characteristic scales on the magnetic field, HFS tends to have smaller characteristic scales when comparing with the LFS as shown in figure 1.11.

### 1.2.6 Energy transport and H-mode confinement

The temperature and density gradients existing in the plasma edge drive the energy transport ($\propto -n\nabla T$) and particle transport ($\propto -\nabla n$) in the radial direction. The collisions cause a random distribution of the velocity, originating particle transport between the different magnetic surfaces and creating a source of energy loss. In tokamaks, the classical transport diffusion coefficient prediction needs to be modified due to the inhomogeneous magnetic field. The magnetic field changes along the magnetic field line and can trap particles in magnetic mirrors (the so-called banana orbits). The neoclassical transport theory has this effect into account and gives corrected expressions for the diffusion coefficients [8]. Unfortunately, the experimental measured transport is significantly higher than the previsions from the neoclassic theory. This discrepancy is known as anomalous transport and can be explained due to the turbulent transport of particles, caused by small-scale fluctuations in parameters. If only the neoclassic transport existed, the ignition triple product would have been already achieved in present fusion devices because turbulence enhances transport by at minimum an order of magnitude higher the neoclassical coefficient.

Different confinement levels, known as regimes, are observed in tokamaks (and also in other configurations as the stellarators). In 1982, Friedrich Wagner discovered the H-mode (High-confinement mode) confinement regime accidentally in ASDEX [71]. Above a threshold heating power ($P_{LH}$), an External Transport Barrier (ETB) characterized by steepening plasma gradients and by a significant reduction of the level of fluctuations and turbulent transport appears spontaneously at the edge of the plasma, increasing the confinement time [72, 73]. A knee-point in the pressure profile known as the pedestal is formed around $\rho \sim 0.9 - 1$. Before the power limit, confinement is generally low, being called the L-mode (Low-confinement mode) scenario. The H-mode confinement time is improved by a considerable factor, representing a major improvement for the community. Figure 1.13 (left) shows the density profile in the transition between the L and H mode, including the exponential density decay at the SOL as mentioned previously. After decades of research, the exact explanation for the ETB formation and turbulence suppression is still not fully understood. Plasma scientists believe the high auxiliary power strongly sheared flow velocities in the edge due to an existing localized radial electric field that acts as a micro-turbulence stabilizer.

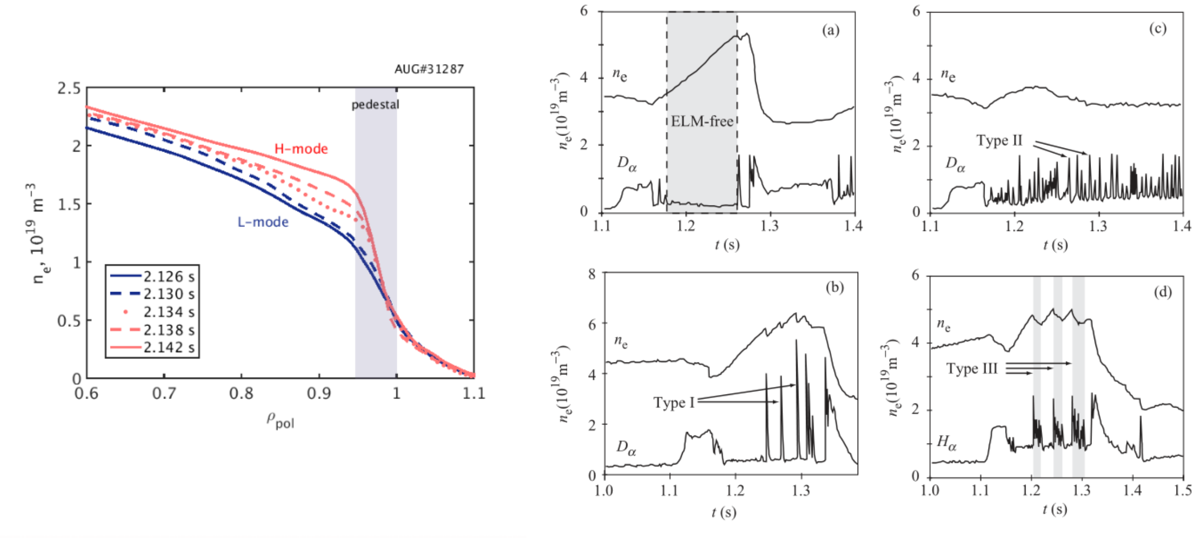

Figure 1.13: L-H transition [74] (left). Different ELM behavior (ASDEX) [8] (right).

During the H-mode operation, a phenomena known as Edge Localized Modes, ELMs, leads to a quasi-periodic violent ETB relaxation phenomena when the edge pressure gradient reaches a limit, acting as a pressure relief valve. This results in sudden losses of heat and particles, impacting the confinement and the plasma-facing components. After an occurrence, the radial heat and particle transport from restore the plasma pressure on a time scale of a few ms until the next event occurs. There are different types of ELM behavior (Free, Type I, Type II, Type III) [8]. Each type depends on the frequency and intensity. They are represented in figure 1.13 (right) by the repetitive bursts in $D_\alpha$ or $H_\alpha$ emission (fast-ion spectroscopy), indicating an increasing particle transport from the plasma to the divertor. The ideal operation would be ELM free (Quiescient H-mode [75]). However this is typically a transient behavior leading to increased edge density and impurities. ELMs with moderate amplitude bursts and higher frequency are preferred over lower frequency ELMs with higher losses. Other advanced operation regimes with internal transport barriers (ITB) have been developed over the last years, with the aim of finding the best regime for the future machines. Understanding ELMs and advanced operation scenarios is another major challenge of the plasma scientists.

## 1.3 On the way to the fusion power plant

### 1.3.1 ITER, the International Thermonuclear Experimental Reactor

ITER, which in Latin means *the way*, is an International Thermonuclear Experimental Reactor that is being built next to the Cadarache facility in Saint-Paul-lès-Durance, in Provence, southern France [12]. Considered one of the most challenger projects of this century, ITER is a collaboration of 35 nations around the world to build the world's largest and most advanced tokamak.

With the aim of advancing fusion science and preparing the way for the fusion power plants of the future, the machine has been designed to:

1. Produce 500 MW of fusion power with a gain of $Q = 10$ (The world's record from JET is $Q = 0.67$). Operate in steady state during long periods of time.
2. Study the plasma physics under conditions similar to the future power plants ($R_0 = 6$ m, $a = 2$ m, $B_0 = 5.3$ T, $\langle T_e \rangle = 8.8$ KeV, $\langle n_e \rangle = 10.1 \times 10^{19}$ m$^{-3}$).
3. Test the necessary fusion technologies such as tritium breeding, heating, control, diagnostics, cryogenics and remote maintenance.
4. Achieve ignition with a deuterium-tritium plasma.
5. Demonstrate the safety characteristics of a fusion device.

Figure 1.14 shows a schematic view of the device and a poloidal view of the vessel.

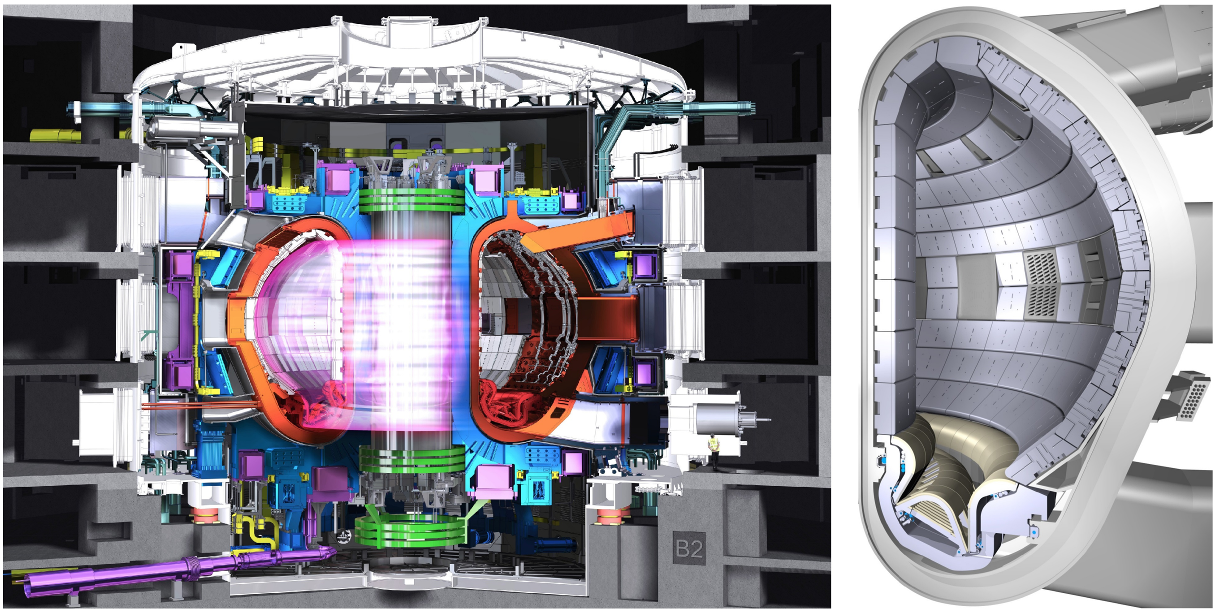

Figure 1.14: Schematic view of the device (left). Poloidal view of the vessel [12] (right).

The vacuum vessel provides a high-vacuum level for the plasma, acts as the primary confinement barrier for radioactivity and support the in-vessel components such as the blanket or the divertor. Different openings, known as ports, provide access for remote handling operations, diagnostics, heating, and vacuum systems. It has an outer diameter of 19.4 meters, 11.4 meters high and weigh approximately 5,200 tonnes. This allows to have a plasma volume of 800 m$^3$ (ten times larger than the largest operating tokamak - JET), providing unique experimental conditions for fusion scientists. The inner wall is covered by 440 blanket modules that protect the steel structure and the superconducting toroidal field magnets from the heat and high-energy neutrons produced by the fusion reactions. The neutron energy is transformed into heat energy and collected by the water cooling systems designed to remove more than 736 MW of thermal power. Since this is an experimental reactor, this energy will not be used for electrical power production. The superconductors are manufactured from niobium-tin (Nb3Sn) or niobium-titanium (Nb-Ti) and will cooled with super-critical helium at 4 K (-269°C) to produce the necessary magnetic fields to initiate, confine, shape and control the plasma in steady state. All these components and the supporting systems are installed inside the cryostat, the largest stainless steel high-vacuum pressure chamber ever built (16,000 m$^3$). It will provide the necessary vacuum to the chamber and the access will be restricted to for cooling systems, magnet feeders, auxiliary heating, diagnostics, and maintenance systems. As an experimental machine for technology testing, ITER will be equipped with an array of many different plasma diagnostics for control and to learn plasma physics.

The ITER operation will require an input heating power of 50 MW to reach the expected gain values. This will be achieved with three different external heating systems: (i) two neutral beam injectors delivering a deuterium beam of 16.5 MW each, a ion cyclotron heating system with a frequency of 40 to 55 MHz generating 20 MW and an electron cyclotron resonance heating system composed by 24 gyrotrons of 1 MW of power each one at the frequency of 170 GHz.

### 1.3.2 DEMO, the DEMOnstration power station

DEMO (DEMOnstration power station) is a proposed nuclear fusion power station that is intended to be the step between ITER and the first commercial fusion power plant [76, 77]. DEMO must use the acquired ITER know-how to demonstrate only the necessary technology for controlling a more powerful plasma and for generating electricity continuously and in a rapid and reliable manner. According to the European Fusion Programme, DEMO will enter in operation about the middle of this century. For now, it is just a concept. The results of the next years of research will be crucial to make its design.

Most of the DEMO studies are based on the tokamak concept but DEMO stellarators are also being considered [77]. Although there is no consensus on the exact final DEMO plasma scenario and reactor parameters, different designs with the tokamak magnetic configuration have been studied with major radius in the order of 6-9 m and fusion thermal powers in the order of 2-5 GW [77, 78, 79, 80]. The current design assumes a major radius of 9 m, minor radius of 2.9 m, a toroidal magnetic field of $5-6$ T and a net electrical output power of 500 MW [13]. These values of power are predicted assuming a standard ELMy H mode scenario, but it is expected that the final DEMO scenario should have no ELMs (or only very low energy ELMs). Figure 1.15 (right) shows the dimensions comparison between ITER, the current DEMO geometry, and other relevant tokamaks.

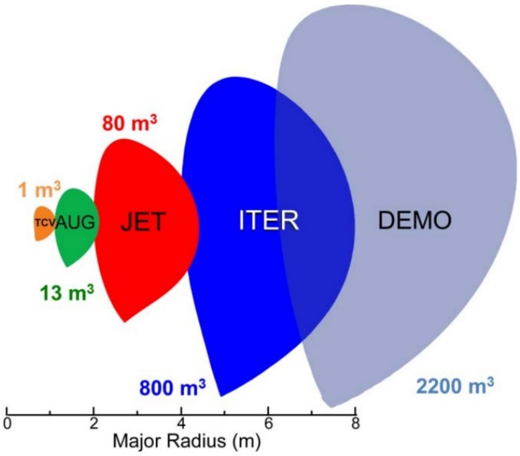

Figure 1.15: Dimensions of relevant tokamaks compared with ITER and DEMO [81].

While there any many open questions that will only be clear with the ITER results, there are some aspects that are inherent to DEMO and are starting to be addressed. In particular, the development of the plasma diagnostic and control (D&C) system [78, 13]. The plasma control is a vital function of any magnetic fusion device. The process of controlling a plasma consists in implementing the necessary scientific and technological knowledge in the machine to create, sustain and terminate a tokamak discharge with the required parameters [82]. This requires plasma diagnostics with the necessary accuracy and temporal resolution to measure the plasma state. The main function of the control system is the machine protection. In the particular case of the fusion machines, a single failure of the plasma control system may immediately cause damage to the machine and in have a tremendous economic consequences. When the conditions for machine protection are fulfilled, the other systems can actuate to achieve the desired plasma parameters. If they are not, the system immediately starts the procedure to suppress the encountered problem or shut down the discharge if needed.

There are three main requirements that the DEMO D&C system must fulfill simultaneously:

- High reliability - the future power plants will operate continuously during his lifetime. The DEMO D&C system must be robust sufficiently to provide reliable measurements during its operation. A single failure may result in loss of confinement or ultimately disruptions.
- High accuracy - in order to maximize the output power, a high accuracy is needed to operate near the machine operational limits.
- Fast controls - Systems must act fast in case of unforeseen transient events (e.g. component failure).

On the other hand, there are many adverse limiting conditions that interfere with the diagnostic systems and difficult its design:

- Space restrictions - diagnostic systems are limited to the geometry constrains, especially the vessel components. Versatile diagnostics are preferred.
- Adverse fusion conditions - DEMO will have an extremely harsh fusion environment. The neutron and gamma radiation, heat loads, erosion and deposition effects will be much stronger than on ITER. This may result in limited performance of the measurements.
- Different plasma scenario - The plasma parameters existing on the DEMO scenario may affect the diagnostic measurements in a different way of the ITER plasmas.

Finding a solution to the implementation of the systems that fulfills these conditions needs to be done in a generic way, taking into account the uncertainties of the plasma scenario and machine geometry. The improvement of the controllability of the DEMO plasma will be made using advanced control techniques which aim to provide a fast state description of the plasma based on the diagnostic measurements or model-based predictions. In the diagnostics, each specific problem of each diagnostic is being identified and studied with the help of simulations and of experiments in the current experimental machines. In the current development status this is being carried out only in the stationary phase [13]. In the next years, after the results of the initial stage, the ramp-up and ramp-down phases and other aspects as the control of instabilities, emergency actions or disruption mitigation will need to be investigated in more detail.

## 1.4 Plasma position control in DEMO

### 1.4.1 Plasma position control with magnetic diagnostics

Of all the controllable variables, the plasma position and shape play a fundamental role in the control of a fusion plasma. A minimum plasma-wall distance must be maintained during the operation so that the first wall is protected from the direct contact with the hot plasma. On the other hand, the shape control of the plasma is essential to achieve the optimizing scenario. Physically, the spatial distribution of plasma particles is directly identified by the density profile and the magnetic equilibrium by the existing magnetic field configuration inside the vessel. Finding the position and shape of the plasma, is finding the separatrix of the magnetic configuration. It is inside its shape ($\rho < 1$) that most of the particles are confined.

In present tokamaks the measurement of the plasma position and shape is usually performed with the magnetic diagnostics. These diagnostics provide many other important parameters of current plasma experiments such as the plasma current, the loop voltage or the plasma stored energy [48]. They consist in simple loops and coils installed at appropriate positions on the tokamak. When the magnetic field varies inside the loops, a voltage proportional to the magnetic flux is obtained at the circuit terminals. The fields are obtaining by integrating these signals. The location of the separatrix is then estimated using magnetic equilibrium reconstruction codes. Their accuracy in the edge is typically in the order of 1 cm, which is adequate for the purpose.

The implementation of the magnetics in DEMO faces several problems related with the existing adverse fusion conditions [13]. Firstly, the possible changes in the electrical and mechanical properties of the wires induced by the high levels of nuclear and gamma radiation and the ability to maintain the different sensors when the structure has becomes radioactive. Secondly, the drifts caused by small thermo-electric voltages and operational amplifier offset currents that can occur during the DEMO long pulses. Since these diagnostics require the integration of the electric signals, the error accumulation results in the wrong separatrix position and shape estimation, putting all the operation at risk. For this reason, alternative methods of determining the position are being studied.

### 1.4.2 Plasma position control with reflectometry

The prime candidate to complement or substitute the magnetic diagnostics in DEMO is microwave reflectometry [13]. By sweeping the frequency of the probing beam and detecting the reflected signal from the plasma, microwave reflectometry is capable of measuring the electron density profile at the probing line of view [83]. In the context of the position control this measure is not, however, directly representative of the separatrix position and shape. The estimated positions rely on different assumptions or on external measurements. With the separatrix density known, its position can be directly inferred from the density profile. As the density is directly linked to the magnetic flux surfaces, $n = n(\rho)$, these measurements give access to the magnetic configuration, providing its local radial position. The frequency is swept in a very short time scale, being possible to follow the time evolution of the iso-density layer position on very short time scale below the fastest time scale associated to MHD events [82]. This diagnostic is capable of being totally independent of the magnetic measurements due to the fact that one of the possible propagation modes (O-mode) is independent on the magnetic field. Furthermore, microwave reflectometry is known by its reduced access, robustness and reliability, fulfilling the needs/requirements to the operation in a fusion reactor with the necessary spatial ($\sim 1$ cm) and temporal ($\sim 10$ $\mu$s) resolution. It is also a versatile diagnostic regarding the spatial constraints. The only in-vessel components are the antennas used to probe the plasma and to detect the reflected signal and the waveguides. Furthermore, the waveguides can be bended according with the available geometry [84]. The signals are then detected and analyzed some meters away from the reactor. Other reliable diagnostics were considered to measure density profiles in the future machines, as example the Li-beam plasma spectroscopy or the Thomson scattering. The absence of in-vessel elements such as mirrors and sensors and the high spatial and temporal resolution makes microwave reflectometry the preferred diagnostic amongst the viable candidates [82].

The use of reflectometry to measure the plasma position has been experimentally validated in real-time on ASDEX-Upgrade [85] and continues to be a research topic [86, 87]. Figure 1.16 shows one of the demonstration discharge where is possible to see the reflectometry measurement following the targeting positions of the position controller in comparison with the magnetic measurements.

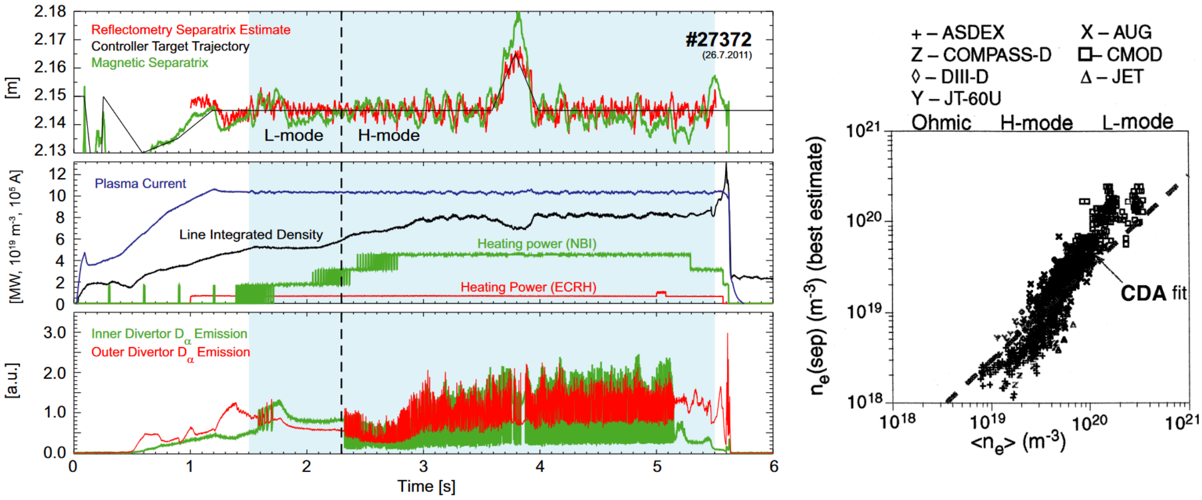

Figure 1.16: Time traces of the position controller target trajectory and of the magnetic and reflectometric separatrix positions during a plasma position reflectometry demonstration discharge. Reflectometry based control was performed during the shaded period [85] (left). Dependence of the separatrix density on the linear average density for several tokamaks and operating regimes [88] (right).

The density separatrix can be known using an empirical scaling relating the plasma line average density, $\bar{n}_e$, and the density at the separatrix, $n_{sep}$. The scaling constant depends on the the confinement mode (Ohmic/L-mode/H–mode), as described in [85, 88] and shown in figure 1.16 (right). In practice, the averaged density is obtained with interferometry, another microwave diagnostic independent from the magnetic field. In interferometry, a beam of coherent radiation passes through the plasma and changes the phase proportionally to the $F(Z)$ function, $\phi \propto F(Z) = \int n_e \sqrt{(Z^2 + R^2)} dR$. Using multiple lines of sights, the reconstruction of the electron density profile is given by $n_e(r) = -(1/\pi) \int_r^a \frac{d}{dy} [F(Z)] \frac{dy}{\sqrt{r^2 - y^2}}$. This diagnostic been used on present day experimental devices and has a well developed technology [48, 49]. However it does not provide the spatial resolution required for the possible advanced control scenarios.

Alternatively, if the density profile is known from the edge to the SOL, the separatrix point can be identified directly in the density profile with physical considerations.

### 1.4.3 The DEMO plasma position reflectometer (PPR)

The DEMO plasma position reflectometer (DEMO PPR) will be a system of multi-reflectometers distributed poloidaly along the DEMO wall to provide measurements of different separatrix points used to reconstruct accurately its shape. Up to now, the DEMO PPR is just a concept in the development stage and many questions need to be investigated before reaching its final design. One fundamental question of this system is the minimum number of measurements required to reconstruct the separatrix shape. This problem has been already studied with a purely geometric approach [89]. Using a deformable template based on B-splines, the final curve is found by minimizing the distance between a limited number of estimated and measured points along the reflectometer lines of sight. The official DEMO 2015 models from the EUROfusion database were used as input. The study concluded that:

1. The method is more robust with respect to a synthetic random measurement error (10 cm) than to a reduction in the measurement number.
2. Using 15 measurements seems to be adequate for a reliable reconstruction.

On the other hand, the maximum number of measurements is limited by the geometrical constraints. The in-vessel microwave components (waveguides and antennas) and the cooling systems are limited to the available space in the vessel and by the area of the ports. One important design aspect is the integration of such systems. In this context, an innovative concept consisting in the integration of several groups of antennas and waveguides into a full poloidal section with the water cooled liquid lead breading blanket is currently under consideration [90]. Studies are being conducted testing different cooling systems and microwave components implementations. The components are expected to be made of EUROFER, the same material used in the blanket structure, which limits the maximum allowable operation temperatures to 550°C [91]. The antennas and the waveguides will be made of tungsten. Thermochemical simulations show the the need of a cylindrical cavity with a diameter and length in the order of 10 cm$^3$ between the antenna mouth and the wall surface to be possible cooling the system to the order of the required temperatures.

With respect to the measurement performance of the system, a first assessment of microwave diagnostics has been made in [92]. The study concluded that for the considered scenario (2015 model) the O mode reflectometry measurements can be used in the LFS and HFS with special attention on the possible low gradients. At the other positions of the machine, the electromagnetic performance is unknown. Since reflectometry model assumes a slab plasma geometry, these regions can be submitted to an intrinsic and systematic measurement errors. In fact, this is a fundamental question of DEMO PPR.

The experimental validation of these regions is in-existent and difficult to achieve. The measurement performance depends on the reflectometer geometry and on the plasma shape. The DEMO geometry and the expected plasma scenarios will be unique, making the experimental validations of the system in other machine difficult. Besides that, the physical implementation of such systems in the existing machines is also very difficult due to the spacial constraints already defined during its construction. In this context, reflectometry simulations are fundamental. They allow to assess the measuring capabilities of the experimental devices and to predict the performance of future ones. In this work, the electromagnetic performance of the DEMO PPR will be studied using numerical simulations.

### 1.4.4 Thesis goals and outline

This dissertation has two main goals. The first one is the study the electromagnetic performance of the DEMO plasma position reflectometer in the different locations of the machine. The second is the development of the necessary techniques and to correct the measured signals and find an optimized solution for a preliminary design of the system using the available DEMO models. These goals include:

1. Assess the measuring capabilities of the system under DEMO baseline scenario including the effect of the poloidal divergence and curvature for the positions away from the equatorial plane.
2. Evaluate the amplitude and frequency dynamic range of the signals in the different frequency bands and find solutions for the optimization of the system in the locations where the measurements are associated to higher errors.
3. Evaluate the sensitivity and robustness of the measurements of gaps to movements of the plasma column, including the radial and vertical displacement events.
4. Estimate the impact in the measurements of turbulence and other deviations to the equilibrium.
5. Estimate the effects of the blanket modules reflections on the measurements.
6. Generate a database of signals corresponding to each possible situation and the respective necessary processing techniques to rebuild the density profiles and extract the plasma position.

The techniques used to solve these problems must be developed as general as possible to any tokamak geometry and plasma shape, adapting to the future DEMO models. To model the interaction of the probing beam with the plasma, REFMULF, a 2D full-wave Maxwell full-polarization Finite-Difference Time-Domain (FDTD) code for reflectometry simulation, is used [93, 94].

This thesis is structured as follows: In chapter two, the theoretical aspects of plasma position reflectometry are introduced. The third chapter addresses the numerical simulations and the description of the data analysis methods that are used in the context of reflectometry simulations. The fourth chapter contains the simulation results and the new developed methods. And finally, the last chapter, mentions the conclusions and highlights, describes the future work, the opened questions, and the application of the developed work in other projects.

# Chapter 2

# Microwave Reflectometry

## 2.1 Brief introduction to microwave reflectometry

### 2.1.1 Microwave reflectometry for fusion plasma diagnostics

Microwave reflectometry is a plasma diagnostic based on the RADAR principle (RAdio Detection And Ranging [95]). RADAR systems use the phenomena of reflection of electromagnetic waves on materials of considerable electrical conductivity (e.g. metals, seawater, wet ground) to measure the physical properties such as the velocity or position of a target. In a similar way, reflectometry uses the reflection of electromagnetic waves in a plasma to measure some of its properties. The principal difference to the RADAR systems is the nature of the wave propagation before the target (plasma layers). For most of the RADAR applications, the refractive index of the propagating medium is constant, making the analysis of the detected signals easier. In a plasma, the refractive index changes during the propagation. This results in more complicated expressions to deduce the plasma properties from the measured signals. One of the current application of reflectometry is the measurement of electron density profiles. By sweeping the frequency in the range $0 - F$ and measuring the round-trip time-delay between the emission and the detection for each frequency, one can estimate the position $r_c(F)$ of the reflecting layer associated to the cutoff density $n_c(F)$. The polarization and the frequencies are chosen according to the application, making sure the cutoff occurs during the propagation.

Microwave reflectometry was developed during the 1960s in the context of ionospheric studies to determine the altitude of the atmospheric density layers [96, 97]. In 1961 was suggested as a plasma diagnostic to measure electron density profiles in tokamak plasmas [98]. For the typical plasma parameters this involves probing the plasma with frequencies in the order of tens to hundreds of GHz. Although this technique looks very attractive, it presented several technical challenges during the first years of experimental implementation. Since the emission and reflection occurs in a very short time scale, in the order of a few nanoseconds, it was difficult to obtain measurements with the necessary band width since the electron density profile cannot change substantially during the sweeping time. The potential of this technique was only possible with the advances of the microwave technology and the development of broadband swept microwave sources. In 1982, a fast swept frequency microwave reflectometry system was proposed to measure electron density profiles in tokamak experiments [99]. The first electron density profiles were obtained a few years later in the TFR [100] and JET tokamaks [101]. Since there, more exactly due to the possibility to use solid state microwave sources, reflectometry systems have been developed and studied in large tokamaks such as Tore Supra, ASDEX [102], JET [103], DIII-D [104] and other experimental machines. Over the last decades, reflectometry became a rapidly an expanding field, accompanied by the evolution of the numerical simulations and theoretical works. Different reflectometry techniques have been developed, such as the Doppler reflectometry [105] or the correlation reflectometry [106]. The control of the plasma position with reflectometry has been demonstrated in ASDEX-U [85].

Reflectometry has several advantages for fusion plasmas: (i) it provides measurements of many different plasma parameters with the necessary temporal ($\sim 10\ \mu$s) and spatial ($\sim 1$ cm) resolutions, (ii) it requires a reduced access compared to other electron density diagnostic techniques like interferometry or Thomson scattering, (iii) it is versatil and (iv) robust under the fusion environment conditions [107, 108]. For these reasons, microwave reflectometry is now considered one of the key diagnostics for DEMO and the future fusion machines, being the principal candidate to substitute or complement the magnetic diagnostics in the position measurements during the expected long-pulse operations [13].

### 2.1.2 The principle of microwave reflectometry

The concept of reflectometry is illustrated in figure 2.1.

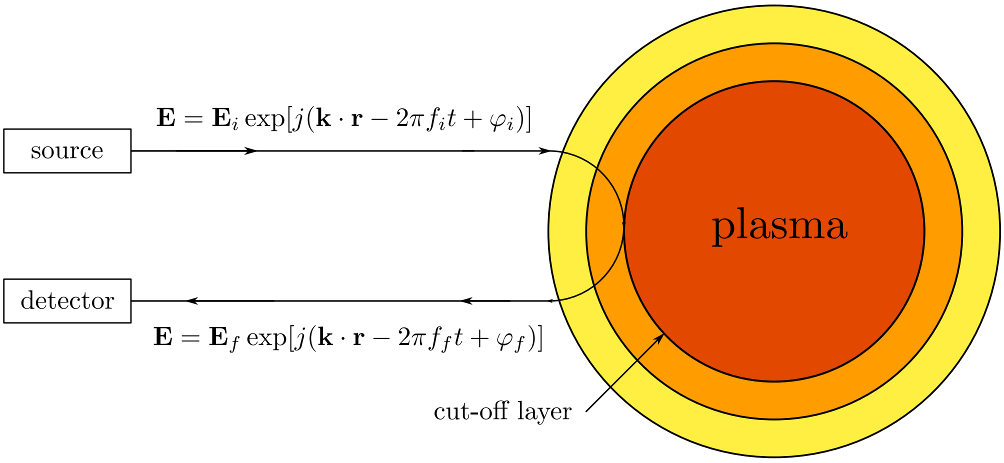

Figure 2.1: The concept of microwave reflectometry.

A monochromatic and stationary electromagnetic wave with an initial state $\mathbf{S_i} = (E_i, f_i, \varphi_i)$ characterized by an amplitude $E_i$, a probing frequency $f_i$ and an initial phase $\varphi_i$ is emitted by a microwave source. The wave propagates thought the plasma and interacts with the charged species until reaches the critical layer, where it is totally reflected backwards. When it reaches the detector, it is characterized by a final state, $\mathbf{S_f} = (E_f, \omega_f, \varphi_f)$, resulting from the nature of the plasma-wave interaction (the same variables with $f$ subscript). A reflectometry measurement consists in apply the necessary hardware techniques to know these two states ($\mathbf{S_i}$ and $\mathbf{S_f}$), the difference, or part of them (e.g. only the phase difference, $\varphi = \varphi_f - \varphi_i$). The estimation of a parameter of the plasma is obtained by writing it analytically as a function of the initial and final states or by a combination of states from multiple processes of measurement with the help of a physical model. This involves describing the propagation of the electromagnetic waves in the microwave components of the system (e.g. antennas, waveguides), in the vacuum and in the plasma. The ways of extracting the different plasma parameters by this concept represent a different technique of reflectometry.

### 2.1.3 Topics of wave propagation in the context of reflectometry

#### Macroscopic Maxwell equations

The behavior of electromagnetic fields in the plasma and in the microwave components of the reflectometry systems is described by the macroscopic Maxwell equations [109, 48],

$$\nabla \cdot \mathbf{D} = \rho \qquad \text{(Gauss' electric field law)} \tag{2.1}$$

$$\nabla \cdot \mathbf{B} = 0 \qquad \text{(Gauss' magnetic field law)} \tag{2.2}$$

$$\nabla \times \mathbf{E} = -\frac{\partial \mathbf{B}}{\partial t} \qquad \text{(Faraday's induction law)} \tag{2.3}$$

$$\nabla \times \mathbf{H} = \mathbf{J} + \frac{\partial \mathbf{D}}{\partial t} \qquad \text{(Ampère's law),} \tag{2.4}$$

where **E** is the electric field, **B** is the magnetic field, **D** is the displacement field, **H** is the magnetizing field, $\rho$ is the electric charge, **J** the electric current density. The displacement and the magnetizing field describe the polarization and magnetization effects, characteristic of each macroscopic medium. They are defined by

$$\mathbf{D} = \varepsilon_0 \mathbf{E} + \mathbf{P} \tag{2.5}$$

$$\mathbf{H} = \frac{1}{\mu_0}\mathbf{B} - \mathbf{M}, \tag{2.6}$$

where **P** is the electric polarization vector and **M** the magnetic polarization vector.

#### Linear description of the materials and Ohm's law

In many cases, the polarization and magnetization are linear functions, simplifying the description of the problems. In this case we have

$$\mathbf{D} = \boldsymbol{\varepsilon} \cdot \mathbf{E} \tag{2.7}$$

$$\mathbf{B} = \boldsymbol{\mu} \cdot \mathbf{H} \tag{2.8}$$

where $\boldsymbol{\varepsilon}$ is the electric permittivity tensor and $\boldsymbol{\mu}$ is the magnetic permeability tensor. Another important characteristic of a medium is the conductivity which measure of a material's ability to conduct electric current density. If it is a linear conducting medium, the induced current density is written in the form

$$\mathbf{J} = \boldsymbol{\sigma} \cdot \mathbf{E}, \tag{2.9}$$

where $\boldsymbol{\sigma}$ is the conductivity tensor. This equation is known as the Ohm's law. As it is shown in section 2.2.1, the plasma can be described approximately as a linear conductor medium without polarization ($\boldsymbol{\varepsilon} = \varepsilon_0 \boldsymbol{I}$) or magnetization ($\boldsymbol{\mu} = \mu_0 \boldsymbol{I}$).

#### Propagation of the electromagnetic field

A wave is a solution of a perturbated equilibrium resulting of small variations of its physical parameter(s). In the case of the electromagnetic waves, the wave equation is established from the Maxwell equations. The simplest case is the propagation in vacuum, where there is no polarization or magnetization effects, electric current or charge perturbation. The total electric field consists in the sum of the equilibrium term $\mathbf{E}_0$ with the perturbation $\mathbf{E}$. Taking the curl of the Faraday's induction law and the Ampère's law, and the curl of the curl identity $\nabla \times (\nabla \times \mathbf{E}) = \nabla(\nabla \cdot \mathbf{E}) - \nabla^2\mathbf{E}$, and $\nabla \cdot \mathbf{E} = 0$, the propagation of the electric field in vacuum is given by the equation:

$$\nabla^2\mathbf{E} = \frac{1}{c^2}\frac{\partial^2\mathbf{E}}{\partial t^2}, \tag{2.10}$$

where $c = 1/\sqrt{\varepsilon_0\mu_0}$ is the speed of light in vacuum [110]. The propagation of the magnetic field is described by the same differential equation. For a general media with finite perturbations, the wave equations are difficult to solve. Fortunately, when the wave equation results from a linear analysis, the treatment is easier and, in many cases, leads to analytical descriptions of the phenomena of propagation. Due to the linearity, a linear combination of solutions is also a solution. The perturbation can be functional decomposed, being the wave equation valid for each component. The Fourier decomposition is typically used for this purpose, in which the wave is written as a sum of plane waves, in the form $\mathbf{E}(\mathbf{k}, \omega)e^{j(\mathbf{k}\cdot\mathbf{r}-\omega t)}$. The electric field perturbation is written as

$$\mathbf{E}(\mathbf{r}, t) = \int\int \mathbf{E}(\mathbf{k}, \omega)e^{j(\mathbf{k}\cdot\mathbf{r}-\omega t)}d\mathbf{k}d\omega, \tag{2.11}$$

where

$$\mathbf{E}(\mathbf{k}, \omega) = \int\int \mathbf{E}(\mathbf{r}, t)e^{-j(\mathbf{k}\cdot\mathbf{r}-\omega t)}d\mathbf{r}dt \tag{2.12}$$

is the Fourier transform. With this description, the propagation is described as a relation between $\mathbf{k}$ and $\omega$ of each Fourier mode,

$$D(\mathbf{k}, \omega) = 0, \tag{2.13}$$

known as the dispersion relation. For the propagation in vacuum described by equation 2.10, the dispersion relation results in $k^2 = c^2\omega^2$. This corresponds to two solutions, propagation in the positive direction, $k = \omega c$, and propagation in the negative direction, $k = -c\omega$. In general the solutions of the dispersion relation are in the complex plane. The real component describes the oscillation and the imaginary component the increase or decrease of the amplitude of the wave due to some physical mechanism (for example energy losses due to collisions). If $\mathbf{k}_R = 0$, the wave is evanescent. The phase velocity $\mathbf{v}_{ph}$ measures the velocity of propagation of a point characterized by constant phase ($\phi = \mathbf{k}\cdot\mathbf{r} - \omega t$), $\omega$ and $\mathbf{k}$,and is defined by

$$\mathbf{v}_{ph} = \left.\frac{d\mathbf{r}}{dt}\right|_{d\phi=0} = \frac{\omega}{k}\frac{\mathbf{k}}{k}. \tag{2.14}$$

The refractive index characterizes how close the phase velocity of a medium is from the speed of light,

$$\mathbf{N} = \frac{c}{v_{ph}}\frac{\mathbf{k}}{k} = \frac{c}{\omega}\mathbf{k}. \tag{2.15}$$

For the case of the propagation in vacuum, each Fourier component travels at the same phase absolute velocity speed, $v_{ph} = c$. Thus, the initial perturbation keeps its shape during the propagation. The solution of the wave equation is an arbitrary perturbation propagating in the phase velocity direction, $\mathbf{E}(\mathbf{r}, t) = \mathbf{E}(\mathbf{r} - \mathbf{v}_{ph} t, 0)$, or a sum of multiple perturbations propagating in different directions with $v_{ph} = c$. In a general propagation phenomena, each component travels at a different speed, and the shape of the perturbation changes (dispersion). In this case, the group velocity is a good approximation for the propagation velocity of a group of waves described by a characteristic wavenumber $k_0$. Expanding $\omega(\mathbf{k})$ around $\mathbf{k}_0$ with the Taylor series, the evolution of the group is

$$\begin{aligned} \mathbf{E}(\mathbf{r}, t) &= \int_{-\infty}^{\infty} \mathbf{E}(\mathbf{k}, \omega) e^{j(\mathbf{k}\cdot\mathbf{r} - \omega(\mathbf{k})t)} d\mathbf{k} d\omega \simeq \int_{-\infty}^{\infty} \mathbf{E}(\mathbf{k}, \omega) e^{j(\mathbf{k}\cdot\mathbf{r} - [\omega_{\mathbf{k}_0} + \nabla\omega(\mathbf{k} - \mathbf{k}_0)]t)} d\mathbf{k} d\omega \\ &= \left[e^{j(\omega_{\mathbf{k}_0} t - \nabla\omega\cdot\mathbf{k}_0 t)}\right] \int_{-\infty}^{\infty} \mathbf{E}(\mathbf{k}, \omega) e^{j[\mathbf{k}(\mathbf{r} - \nabla\omega t)]} d\mathbf{k} d\omega = e^{j\theta(t)} \mathbf{E}(\mathbf{r} - \nabla\omega t, t = 0). \end{aligned} \tag{2.16}$$

Therefore, the group velocity is

$$\mathbf{v}_g = \nabla\omega(\mathbf{k}), \tag{2.17}$$

independently of the spacial distribution of the initial pulse. In the case of the propagation in vacuum, the group velocity is constant and equal to the speed of light. Assuming a homogeneous non-dispersive media with constant group velocity (constant refractive index) and by measuring the round-trip time-delay of a group of waves ($\tau_g$) between the emission and the detection of the reflected signal, the distance of the object is estimated by $d = v_g(\tau_g/2)$. In a plasma the group velocity is not constant, resulting in a more complicated expressions to obtain the position of the reflecting layer.

### Reflection of electromagnetic waves

The phenomena of reflection occurs when there is a transition between different media [109]. The Maxwell equations establish the conditions in the material interface,

$$\mathbf{n}_{12} \cdot (\mathbf{D}_2 - \mathbf{D}_1) = \rho_S \tag{2.18}$$

$$\mathbf{n}_{12} \cdot (\mathbf{B}_2 - \mathbf{B}_1) = 0 \tag{2.19}$$

$$\mathbf{n}_{12} \times (\mathbf{E}_2 - \mathbf{E}_1) = 0 \tag{2.20}$$

$$\mathbf{n}_{12} \times (\mathbf{H}_2 - \mathbf{H}_1) = \mathbf{J}_S \tag{2.21}$$

where $\mathbf{n}_{12}$ is a normal vector from medium 1 to medium 2, $\rho_S$ and $\mathbf{J}_S$ are the electric charge and current density defined in the material interface. When a plane wave reaches an interface between two media, a reflected and a transmitted wave are be formed. The ratio between the amplitude and the phase of the reflected wave with the incident wave is given by the reflection coefficient $R$, and of the transmitted wave with the incident wave by the transmitting coefficient $T$. If the medium of incidence is a perfect conductor ($\sigma \to \infty$), where the electric field is zero by definition, the wave is totally reflected, with $T = 0$ and $R = 1$. In fact, this is the principle behind the conduction of electromagnetic energy [111], which is crucial to transport the probing beam from the outside to the vessel.

Based in the fundamental concepts of wave propagation discussed in these topics, the next section review the main mechanisms of wave propagation in the plasma in the context of reflectometry. In section 2.3 the principal experimental aspects of reflectometry are discussed, from the basic constitution of a reflectometry setup, to the data processing techniques. The last section is dedicated to the plasma position reflectometry technique and the aspects to have in consideration in the design and optimization of a plasma position reflectometer, which is the main topic of this dissertation.

## 2.2 Fundamental mechanisms of wave propagation in the plasma

### 2.2.1 The homogeneous magnetized plasma dispersion relation

Due to the complexity of the plasma-wave interaction, the study of the propagation of electromagnetic waves in the plasma is done with different approximations. These approximations allow to obtain analytical models to relate the initial and final states of the wave, leading to the estimation of the plasma parameters when the validity conditions are fulfilled. The simplest model considers the plasma as an infinite homogeneous medium magnetized by a strong uniform magnetic field $\mathbf{B}_0$ and uses the first order theory of electromagnetic waves to derive the dispersion relation. Since real plasmas are inhomogeneous, this model does not describes the propagation accurately. However, it gives a picture of how the electric field propagates locally, allowing the calculation of the dispersion relation. In the case of a slow varying refractive index, the plasma can be approximated as a succession of homogeneous layers, where these relations are valid. The total electromagnetic field considered by this model is

$$\mathbf{E} = \mathbf{E}_1(\mathbf{r}, t) \tag{2.22}$$

$$\mathbf{B} = \mathbf{B}_0 + \mathbf{B}_1(\mathbf{r}, t), \tag{2.23}$$

where $\mathbf{E}_1$ and $\mathbf{B}_1$ correspond to the propagating signal (perturbation), with $\mathbf{B}_1 << \mathbf{B}_0$. The effect of the plasma is expressed by the current term of the Ampère's law, $\mathbf{J}$. The polarization and magnetization effects are neglected ($\boldsymbol{\varepsilon} = \varepsilon_0 \mathbf{I}$ and $\boldsymbol{\mu} = \mu_0 \mathbf{I}$). The propagation equation of the electric field is derived taking the curl of the Faraday's induction law and the partial derivative with respect to time of the Ampère's law,

$$\nabla \times [\nabla \times \mathbf{E}] + \mu_0 \frac{\partial}{\partial t} \left( \mathbf{J} + \varepsilon_0 \mu_0 \frac{\partial \mathbf{E}}{\partial t} \right) = 0. \tag{2.24}$$

If the Ohm's law is valid, the equation 2.24 is linear and can be Fourier analyzed. The result is the algebraic wave equation

$$\mathbf{M} \cdot \mathbf{E} = \left[ \mathbf{kk} - k^2 \mathbf{I} + \frac{\omega^2}{c^2} \left( \mathbf{I} + \frac{j}{\varepsilon_0 \omega} \boldsymbol{\sigma}(\mathbf{k}, \omega) \right) \right] \cdot \mathbf{E} = 0, \tag{2.25}$$

where the conductivity $\boldsymbol{\sigma}(\mathbf{k}, \omega)$ is relative to a Fourier component. Mathematically, the plasma can be described by an equivalent relative electric permittivity of

$$\boldsymbol{\varepsilon}(\mathbf{k}, \omega) = \mathbf{I} + \frac{j}{\varepsilon_0 \omega} \boldsymbol{\sigma}(\mathbf{k}, \omega), \tag{2.26}$$

as it was a linear dielectric material. The existence of non-trivial solutions ($\mathbf{E} \neq 0$) of equation 2.25 allows to obtain the general expression for the dispersion relation,

$$D(\mathbf{k}, \omega) = \det \left[ \mathbf{kk} - k^2 \mathbf{I} + \frac{\omega^2}{c^2} \boldsymbol{\varepsilon}(\mathbf{k}, \omega) \right] = \det [\mathbf{M}] = 0 \tag{2.27}$$

In Cartesian coordinates, equation 2.24 becomes

$$\mathbf{M} \cdot \mathbf{E} = \begin{pmatrix} k_x k_x - k^2 + \frac{\omega^2}{c^2} \varepsilon_{xx} & k_x k_y - k^2 + \frac{\omega^2}{c^2} \varepsilon_{xy} & k_x k_z - k^2 + \frac{\omega^2}{c^2} \varepsilon_{xz} \\ k_y k_x - k^2 + \frac{\omega^2}{c^2} \varepsilon_{yx} & k_y k_y - k^2 + \frac{\omega^2}{c^2} \varepsilon_{yy} & k_y k_z - k^2 + \frac{\omega^2}{c^2} \varepsilon_{yz} \\ k_z k_x - k^2 + \frac{\omega^2}{c^2} \varepsilon_{zx} & k_z k_y - k^2 + \frac{\omega^2}{c^2} \varepsilon_{zy} & k_z k_z - k^2 + \frac{\omega^2}{c^2} \varepsilon_{zz} \end{pmatrix} \begin{pmatrix} E_x \\ E_y \\ E_z \end{pmatrix} = 0. \tag{2.28}$$

Using $\mathbf{B}_0 = (0, 0, B_0)$ and $\mathbf{k} = (k \sin\theta, 0, k\cos\theta)$ in a Cartesian coordinate system without loss of generality, equation 2.28 yields

$$\mathbf{M}\cdot\mathbf{E} = \begin{pmatrix} \varepsilon_{xx} - N^2\cos^2\theta & \varepsilon_{xy} & \varepsilon_{xz} + N^2\sin\theta\cos\theta \\ \varepsilon_{yx} & \varepsilon_{yy} - N^2 & \varepsilon_{yz} \\ \varepsilon_{zx} + N^2\sin\theta\cos\theta & \varepsilon_{zy} & \varepsilon_{zz} - N^2\sin^2\theta \end{pmatrix} \begin{pmatrix} E_x \\ E_y \\ E_z \end{pmatrix} = 0. \tag{2.29}$$

The calculation of the dielectric constant implies the use of a model to describe the plasma dynamics and find the conductivity. In the context of the reflectometry and other microwave diagnostics, the cold plasma approximation is typically used to describe the plasma-wave interaction. The fluid equations describe the plasma responses induced by the wave, leading to an analytical solution of the conductivity tensor. The kinetic theory is important to include the effects of the velocity distribution function (thermal effects). However, this approach produces complicated expressions for the plasma permittivity, even for a Maxwellian distribution. Fortunately, for the high frequencies that are used to probe the plasma (∼GHz), the hot plasma effects are negligible. For temperatures above 5 keV, the relativistic effects generate plasma frequencies down shift and need to be taken into account [112]. The reader can find the details of the equations that are derived in this section and the full treatment of the plasma waves in the classic bibliography, [46, 97, 113, 110, 114].

### 2.2.2 The cold plasma model to express permittivity tensor components

The cold plasma model relies in two physical approximations:

- The thermal electron velocity $v_{th}$ is much smaller than the phase velocity of the wave, $v_{ph}$. The pressure term in the equations for fluid motion is neglected.
- The frequency of the wave is assumed to be much higher than the ion cyclotron frequency ($\omega > \omega_{ci}$). The ions are considered motionless due to their high inertia. Only the electrons interact with the perturbing electromagnetic field.

Under these approximations the electron fluid motion equation (equation 1.24) is

$$m_e n_e \left[\frac{\partial \mathbf{v}_e}{\partial t} + (\mathbf{v}_e \cdot \nabla)\,\mathbf{v}_e\right] = -e n_e(\mathbf{E} + \mathbf{v}_e \times \mathbf{B}) - \nu m_e \mathbf{v}_e, \tag{2.30}$$

where the last term represents the variation of momentum due to the collisions, being $\nu$ the collision frequency. The plasma density and velocity quantities are perturbed by the electromagnetic fields and are written in the form:

$$n_e = n_0 + n_1(\mathbf{r}, t) \tag{2.31}$$

$$\mathbf{v}_e = \mathbf{v}_0 + \mathbf{v}_1(\mathbf{r}, t), \tag{2.32}$$

where $n_0$ and $\mathbf{v}_0$ are the equilibrium density and velocity. Substituting $n_e$, $\mathbf{v}_e$ and the electromagnetic fields given by equations 2.22-2.23 in the Faraday's induction law, Ampère's law, on equation 2.30, and neglecting the second order terms $\mathbf{v}_1 \times \mathbf{B}_1$ and $(\mathbf{v}_1 \cdot \nabla)\cdot \mathbf{v}_1$ to linearize the equations, one obtains

$$\mathbf{k} \times \mathbf{E}_1 = \omega \mathbf{B}_1 \tag{2.33}$$

$$i\mathbf{k} \times \mathbf{B}_1 = \mu_0(-e n_0 \mathbf{v}_1 - i\omega\varepsilon_0 \mathbf{E}_1) \tag{2.34}$$

$$-i\omega m_e \mathbf{v}_1 = -e(\mathbf{E}_1 + \mathbf{v}_1 \times \mathbf{B}_0) - \nu m_e \mathbf{v}_1, \tag{2.35}$$

resulting in the relation between the perturbed velocity and the electromagnetic field,

$$\begin{pmatrix} v_{1x} \\ v_{1y} \\ v_{1z} \end{pmatrix} = -j\frac{e}{m_e U(U^2-Y^2)} \begin{pmatrix} U^2 & -jUY & 0 \\ jUY & U^2 & 0 \\ 0 & 0 & (U^2-Y^2) \end{pmatrix} \begin{pmatrix} E_x \\ E_y \\ E_z \end{pmatrix}, \tag{2.36}$$

where

$$U = 1 + j\frac{\nu}{\omega} \tag{2.37}$$

$$Y = \frac{\omega_c}{\omega}. \tag{2.38}$$

From equation 2.36, the conductivity is directly calculated by $\mathbf{j}_1 = -en_e\mathbf{v}_1 = \boldsymbol{\sigma}\mathbf{E}_1$ and the cold plasma dielectric tensor (equation 2.26) is written in the form [113]

$$\boldsymbol{\varepsilon} = \begin{pmatrix} S & -iD & 0 \\ iD & S & 0 \\ 0 & 0 & P \end{pmatrix}, \tag{2.39}$$

with

$$X = \left(\frac{\omega_p}{\omega}\right)^2 \tag{2.40}$$

$$S = 1 - \frac{XU}{U^2-Y^2} \tag{2.41}$$

$$D = -\frac{XY}{U^2-Y^2} \tag{2.42}$$

$$P = 1 - \frac{X}{U}. \tag{2.43}$$

As the frequency increases ($\omega \to \infty$), $S \to 1$, $P \to 1$ and $D \to 0$. Under these conditions the plasma is seen as a transparent medium similar to vacuum ($\boldsymbol{\varepsilon}_{ij} \to \delta_{ij}$, the Kronecker delta). Applying the dielectric tensor of equation 2.39 to equation 2.27, the dispersion relation is obtained,

$$\begin{aligned} 0 &= N^4(S\sin^2\theta + P\cos^2\theta) - N^2[(S^2-D^2)\sin^2\theta + SP(1+\cos^2\theta)] + P(S^2-D^2) \\ &= N^4(S\sin^2\theta + P\cos^2\theta) - N^2[RL\sin^2\theta + SP(1+\cos^2\theta)] + PRL \\ &= N^4A - N^2B + C, \end{aligned} \tag{2.44}$$

where $R = (S+D)$ and $L = (S-D)$. The two roots of this equation,

$$\begin{aligned} N^2 &= \frac{1}{2A}\left(B \pm \frac{1}{2A}\sqrt{B^2-4AC}\right) \\ &= 1 - \frac{X}{U - \frac{Y^2\sin^2\theta}{2(U-X)} \pm \left[\frac{Y^4\sin^4\theta}{4(U-X)^2} + Y^2\cos^2\theta\right]^{1/2}}, \end{aligned} \tag{2.45}$$

correspond to two different configurations of the electric field, the propagation modes. This is known as the Altar-Appleton-Hartree equation, initially derived to describe the propagation of electromagnetic waves in the ionosphere [96]. The ± signals obtained by the square root of $N^2$ correspond to different directions of propagation. In the context of fusion plasmas, the collision frequency is usually neglected when compared with the high frequencies of the wave. In this case, since $B^2 - 4AC = (RL-PS)^2\sin^4\theta + 4D^2P^2\cos^2\theta$

is always positive, the refractive index is always real or purely imaginary. This means that the wave propagates or has a time-evolution exhibiting an exponential behavior (evanescent or growing in the case of an unstable system). Each mode is characterized by different cutoff ($N \to 0$, $\lambda \to \infty$, $\mathbf{v}_{ph} \to \infty$, $\mathbf{v}_g \to 0$) and absorption ($N \to \infty$, $\lambda \to 0$, $\mathbf{v}_{ph} \to 0$, $\mathbf{v}_g \to \infty$) frequencies, which determine the transition between the regions where propagation is allowed ($N_R > 0$) and where it is not ($N_I > 0$). The frequency bands where propagation does not occur, are called the stop bands. Unfortunately, the case of arbitrary direction cannot be provide tractable expressions. The solutions are represented in the Clemmow-Mullaly-Allis (CMA) diagrams [46, 113]. The cases of interest with simplified expressions are the parallel ($\theta = 0°$) and perpendicular propagation ($\theta = 90°$).

### Parallel propagation, $\mathbf{k} \parallel \mathbf{B}_0$

When the propagation is parallel to the equilibrium magnetic field ($\theta = 0°$), the two solutions of equation 2.45 are:

$$N_L^2 = 1 - \frac{X}{1+Y} = S - D = L = 1 - \frac{\omega_p^2}{\omega(\omega+\omega_c)} \tag{2.46}$$

$$N_R^2 = 1 - \frac{X}{1-Y} = S + D = R = 1 - \frac{\omega_p^2}{\omega(\omega-\omega_c)} \tag{2.47}$$

The first refractive index, $N_L^2 = L$, corresponds to the left-hand polarized mode (L-wave) and the second one, $N_R^2 = R$, to the right-hand polarized mode (R-mode). The polarization is obtained with the equation 2.29, for $\theta = 0°$. In the case of longitudinal electric field ($E_x = E_y = 0$, $E_z \neq 0$), the solution requires $P = 0$. This corresponds to the Langmuir oscillation at the plasma frequency, $\omega = \omega_p$. For purely transverse electric field case ($E_x \neq 0$, $E_y \neq 0$, $E_z = 0$), the ratio of the $x$-$y$ electric field components is

$$\frac{E_x}{E_y} = i\frac{D}{S - N_{L,R}^2} = \pm i \tag{2.48}$$

In the L-wave mode the electric field components have a phase shift of $\pi/2$, rotating in the counterclockwise direction. The R-wave mode has a phase shift of $-\pi/2$, rotating in the clockwise direction. Depending on the polarization of the wave, the refractive index is different (Faraday effect). Each mode has different cutoffs. The L-wave cutoff ($\omega_L$) is given by $N_L^2 = L = 0$, and the R-wave cutoff ($\omega_R$) is given by $N_R^2 = R = 0$:

$$\omega_L = \frac{1}{2}\left[\sqrt{(\omega_c^2 + 4\omega_p^2)} - \omega_c\right] \tag{2.49}$$

$$\omega_R = \frac{1}{2}\left[\sqrt{(\omega_c^2 + 4\omega_p^2)} + \omega_c\right] = \omega_L + \omega_c \tag{2.50}$$

Below $\omega_L$, there is no propagation for the L-wave. Since for the R-wave the electric field rotates in the direction of the electron gyro-motion, there is a resonance at $\omega = \omega_c$. The wave propagates in the $0 - \omega_c$ range and above the $\omega_R$ cutoff.

### Perpendicular propagation, $\mathbf{k} \perp \mathbf{B}_0$

For the case of perpendicular propagation ($\theta = 90°$), equation 2.44 yields two modes, the Ordinary mode (O-mode),

$$N_O^2 = \varepsilon_{zz} = P = 1 - X = 1 - \frac{\omega_p^2}{\omega^2} \tag{2.51}$$

and the extraordinary mode (X-mode),

$$N_X^2 = \varepsilon_{yy} - \frac{\varepsilon_{yx}\varepsilon_{xy}}{\varepsilon_{xx}} = \frac{S^2 - D^2}{S} = 1 - \frac{X(1-X)}{1-X-Y^2} = \frac{(\omega^2-\omega_L^2)(\omega^2-\omega_R^2)}{\omega^2(\omega^2-\omega_{uh}^2)}, \tag{2.52}$$

where $\omega_{uh}^2 = \omega_p^2 + \omega_c^2$ is the upper hybrid frequency. Equation 2.29 becomes

$$\begin{pmatrix} S & -iD & 0 \\ iD & S-N^2 & 0 \\ 0 & 0 & P-N^2 \end{pmatrix} \begin{pmatrix} E_x \\ E_y \\ E_z \end{pmatrix} = 0 \tag{2.53}$$

In the O-mode, the electric field has the direction of the magnetic field ($E_x = 0, E_y = 0, E_z \neq 0$). Since the induced motion is in the magnetic field direction the dispersion relation is not dependent on the magnetic field ($\mathbf{v}\times\mathbf{B} = 0$). The O-mode has a cutoff for $\omega = \omega_p$ and only propagates for frequencies above ($\omega > \omega_p$). In the X-mode, the electric field only exists in the direction perpendicular to the magnetic field ($E_x \neq 0$, $E_y \neq 0$, $E_z = 0$). The ratio of the electric field components is obtained with equation 2.53,

$$\frac{E_x}{E_y} = i\frac{D}{S}, \tag{2.54}$$

defining the polarization of the launched wave. Since the wave is rotating in the $x$-$y$ plane and propagating in the x-direction, the X-mode is partially transverse and partially longitudinal. For $\omega \rightarrow \omega_{uh}$, it becomes purely longitudinal. The X-mode has two cutoffs, one at $\omega = \omega_L$ and th other at $\omega = \omega_R$. The wave propagates in the range $\omega_L - \omega_{uh}$ and above $\omega_R$. They are referred to the lower ($\omega_{LCR}$) and upper cutoff ($\omega_{UCR}$) regions, respectively. There is a resonance at the upper hybrid frequency, $\omega = \omega_{uh}$. Figure 2.2 shows the positive (propagation) and negative (evanescent) $N^2$ regions of each mode.

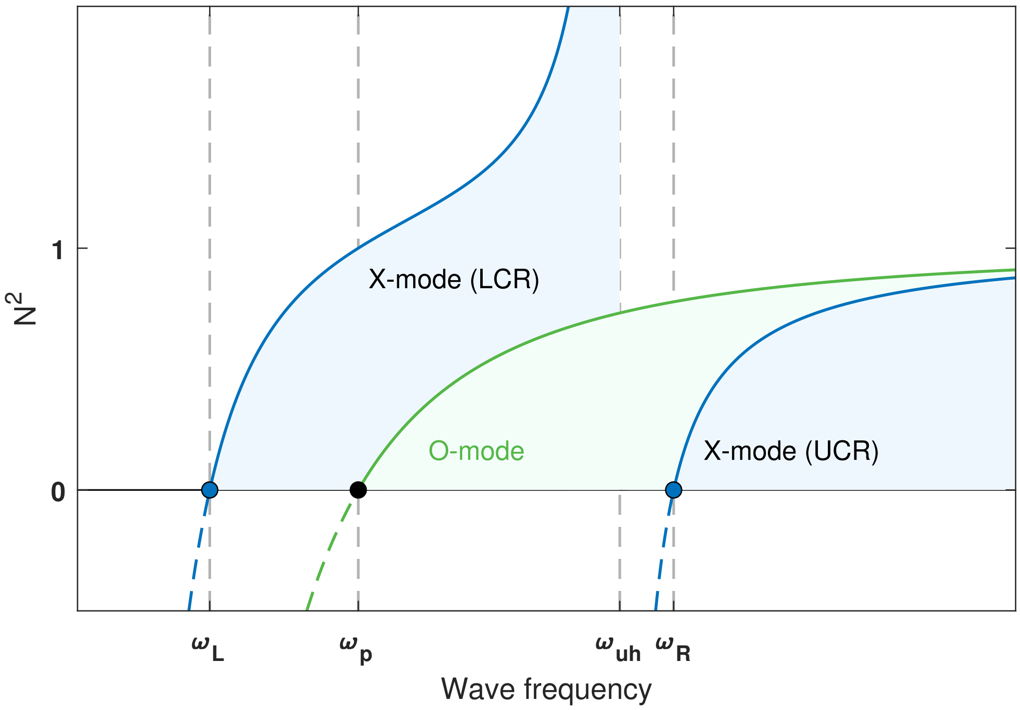

Figure 2.2: Propagation (line) and evanescent (dashed) regions of the O- and X-mode.

In the context of reflectometry, the propagation perpendicular to the magnetic field is favorable from the experimental point of view. In the typical applications (ionosphere, magnetic fusion devices), the density gradient is perpendicular to the magnetic field. If the emission is parallel to the density gradient (perpendicular to the magnetic field), the plasma can be seen approximately as as successive set of homogeneous slab layers. Using one dimensional full wave analysis it is possible to derive the theoretical models for density profile measurement and other applications of reflectometry.

### 2.2.3 One dimensional full wave analysis

The cold plasma model describes the plasma by an equivalent dielectric tensor dependent on the density and on the magnetic field. In a real plasma these quantities are inhomogeneous and vary in time. In the case of slow time variations of the plasma parameters, the propagation equation 2.24 becomes

$$\nabla \times [\nabla \times \mathbf{E}(\omega, \mathbf{r}, t)] - \frac{\omega^2}{c^2}\boldsymbol{\varepsilon}(\omega, \mathbf{r}, t) \cdot \mathbf{E}(\omega, \mathbf{r}, t) = 0. \tag{2.55}$$

In the Cartesian coordinates, the equations of each component of the electric field are

$$\frac{\partial^2 E_y}{\partial x \partial y} + \frac{\partial^2 E_z}{\partial x \partial z} - \frac{\partial^2 E_x}{\partial^2 y} - \frac{\partial^2 E_x}{\partial^2 z} = \frac{\omega^2}{c^2}\left[\varepsilon_{xx} E_x + \varepsilon_{xy} E_y\right], \tag{2.56}$$

$$\frac{\partial^2 E_x}{\partial y \partial x} + \frac{\partial^2 E_z}{\partial y \partial z} - \frac{\partial^2 E_y}{\partial^2 x} - \frac{\partial^2 E_y}{\partial^2 z} = \frac{\omega^2}{c^2}\left[\varepsilon_{yx} E_x + \varepsilon_{yy} E_y\right], \tag{2.57}$$

$$\frac{\partial^2 E_x}{\partial z \partial x} + \frac{\partial^2 E_y}{\partial z \partial y} - \frac{\partial^2 E_z}{\partial^2 x} - \frac{\partial^2 E_z}{\partial^2 y} = \frac{\omega^2}{c^2}\varepsilon_{zz} E_z, \tag{2.58}$$

This system of equations has no analytical solution for a generic dielectric tensor. However, if the plasma gradients are perpendicular to magnetic field and parallel to the direction of propagation, the equation can be treated for a static plasma. In the selected geometry, the propagation occurs in the $x$ cartesian axis, implying the density is a function of $x$,

$$n(\mathbf{r}) = n(x) \rightarrow \nabla n(x) = \frac{\partial n(x)}{\partial x}\mathbf{e}_x. \tag{2.59}$$

The propagation should be in the same direction of the increasing density ($\omega > \omega_p$), so the signal of the gradient and of the propagation is the same. For the O-mode case, the equation becomes

$$\left[\frac{d^2}{dx^2} + \frac{\omega^2}{c^2}\varepsilon_{zz}(x)\right] E_z = 0. \tag{2.60}$$

In the X-mode, if the magnetic field varies in the $x$ direction,

$$B_z(\mathbf{r}) = B_z(x) \rightarrow \nabla B_z(x) = \frac{\partial B_z(x)}{\partial x}\mathbf{e}_x, \tag{2.61}$$

the equations 2.56 and 2.57 yield

$$\left[\frac{d^2}{dx^2} + \frac{\omega^2}{c^2}\left(\varepsilon_{yy}(x) - \frac{\varepsilon_{yx}(x)\varepsilon_{xy}(x)}{\varepsilon_{xx}(x)}\right)\right] E_y = 0. \tag{2.62}$$

These conditions can be found in different situations, such as in the equatorial plane of a tokamak or in the vertical probing of the ionosphere. In both cases, O-mode (equation

2.60) and X-mode (equation 2.62), the behavior of the electric field component is described by the Helmoltz equation,

$$\frac{d^2E(x)}{dx^2} + k^2(x)E(x) = 0 \tag{2.63}$$

where

$$k(x) = \frac{c}{\omega}N(x). \tag{2.64}$$

The local wavenumber and depends on the chosen mode. For O-mode $k(x)$ is

$$k_O^2(x) = \frac{c^2}{\omega^2}N_O(x) = k_0^2\left(1 - \frac{\omega_p^2(x)}{\omega^2}\right) = k_0^2\left(1 - \frac{n_e(x)}{n_c}\right) \tag{2.65}$$

where $k_0 = \omega/c$ is the vacuum wavenumber and $n_c$ is the cutoff density, given by

$$n_c = \frac{\varepsilon_0 m_e}{e^2}\omega^2. \tag{2.66}$$

This density is deduced from $\omega = \omega_p$ for which the O-mode index becomes 0, corresponding to a cutoff by definition. For the X-mode the local wavenumber is

$$k_X^2(x) = \frac{c^2}{\omega^2}N_X^2(x) = k_0^2\left[1 - \frac{\omega_p^2(x)(\omega^2 - \omega_p^2(x))}{\omega^2(\omega^2 - \omega_c^2(x) - \omega_p^2(x))}\right], \tag{2.67}$$

and the propagation depends on the cutoff region (see figure 2.2).

### 2.2.4 The WKB approximation

Although the Helmholtz equation has no analytical solution, the WKB (Wentzel-Kramer-Brillouin) method provides an approximate solution for the case of a slow varying wavenumber/refractive index [35]. With this condition, it is expectable a solution nearly plane wave in the form $E(x) = A(x)e^{jS(x)}$, where $A(x)$ is assumed to vary slowly and $S(x) = k(x)x$ varies rapidly. The Helmholtz equation becomes

$$\left[\frac{\partial^2 A}{\partial x^2} + 2j\frac{\partial A}{\partial x}\frac{\partial S}{\partial x} + A\left(k^2 - \left(\frac{\partial S}{\partial x}\right)^2 + j\frac{\partial^2 S}{\partial^2 x}\right)\right]e^{jS} = 0. \tag{2.68}$$

Neglecting the derivatives of $A(x)$ and the second derivative of $S$, equation 2.68 yields

$$\frac{\partial S}{\partial x} = \pm k(x) \rightarrow S(x) = \pm\int_{x_0}^{x} k(x')dx'. \tag{2.69}$$

With this result, the next order, where only the second derivative of $A(x)$ of equation 2.68 is neglected, yields

$$2j\frac{\partial S}{\partial x}\frac{\partial A}{\partial x} + j\frac{\partial S}{\partial x^2}A = 0 \rightarrow A = \frac{E_0}{\sqrt{k(x)}}. \tag{2.70}$$

The WKB solution for the electric field is

$$E(x) = \sqrt{\frac{E_0}{N(x)}}e^{\pm j\frac{\omega}{c}\int_{x_0}^{x} N(x')dx'}, \tag{2.71}$$

which corresponds to an integration over the refractive index. This means that the total phase shift is obtained by summing the infinitesimal phase variations of the successive set of infinitesimal homogeneous layers. In fact, the WKB approximation is the first term of the expansion (see reference [97]) of the electric field in the form

$$E(x) = \left[E_{(0)}(x) + \frac{c}{\omega}E_{(1)}(x) + \frac{c^2}{\omega^2}E_{(2)}(x) + ...\right] \exp\left[-j\frac{\omega}{c}\Phi(x)\right] \tag{2.72}$$

Substituting the field expansion in the propagation equation gives

$$E_{(0)}(x) = \frac{C}{\sqrt{N(x)}}, \tag{2.73}$$

$$E_{(1)}(x) = \frac{1}{\sqrt{N(x)}}\int_{x_0}^{x}\frac{1}{2j\sqrt{N(x)}}\frac{\partial^2 E_{(0)}(x)}{\partial^2 t}dx. \tag{2.74}$$

The WKB validity condition is defined by the condition $|E_{(0)}| >> (c/\omega)|E_{(1)}|$, which is equivalent to

$$\left|\frac{dk(x)}{dx}\right| << k^2(x) \Leftrightarrow \frac{1}{k_0 N^2}\left|\frac{dN(x)}{dx}\right| << 1. \tag{2.75}$$

This condition is not valid at the cutoff, with $N \to 0$. The analytical model of reflectometry considers the cutoff region as a dielectric constant varying linearly with the position, where an analytical solution of the electric field can be found.

### 2.2.5 Electric field at the cutoff

If the plasma dielectric constant is a linear function, the Helmoltz equation can be written in the form of the Airy's equation, which has an exact solution. Expanding $N^2(x)$ around the cutoff position $x_c$, one obtains

$$N^2(x) = \underbrace{N^2(x_c)}_{=0} + \left.\frac{dN^2}{dx}\right|_{x_c}(x - x_c) + \mathcal{O}(x - x_c)^2 \simeq -D_\varepsilon(x - x_c) \tag{2.76}$$

$D_\varepsilon$ is the absolute derivative of the dielectric constant at $x_c$. In order to have an exact solution for the field in this region, we proceed with a change of variable in the form $\xi = \beta^{1/3}(x - x_c)$, with $\beta = k_0^2 D_\varepsilon$. The wave equation is now transformed into the Airy equation,

$$\frac{d^2E(x)}{d\xi^2} = \xi E(x). \tag{2.77}$$

The solution of the Airy equation is

$$E(\xi) = C_0 Ai(\xi) + C_1 Bi(\xi) \tag{2.78}$$

where $A_i(\xi)$ and $B_i(\xi)$ are the Airy function (first kind and second kind, respectively),

$$Ai(\xi) = \frac{1}{\pi}\int_0^\infty \cos\left(\frac{t^3}{3} + \xi t\right) dt \tag{2.79}$$

$$Bi(\xi) = \frac{1}{\pi}\int_0^\infty \left[\exp\left(-\frac{t^3}{3} + \xi t\right) + \sin\left(\frac{t^3}{3} + \xi t\right)\right] dt, \tag{2.80}$$

and $C_0$ and $C_1$ are the boundary constants. Only the Airy function of the first kind ($Ai(\xi)$) has physical meaning. The second term, proportional to $Bi(\xi)$, goes to $\infty$ when $\xi \to 0$. Therefore, the solution is

$$E(x) = C_0 Ai\left[\beta^{1/3}(x - x_c)\right]. \tag{2.81}$$

Figure 2.3 shows the plot of the $A_i(\xi)$ function and the respective asymptotic behavior.

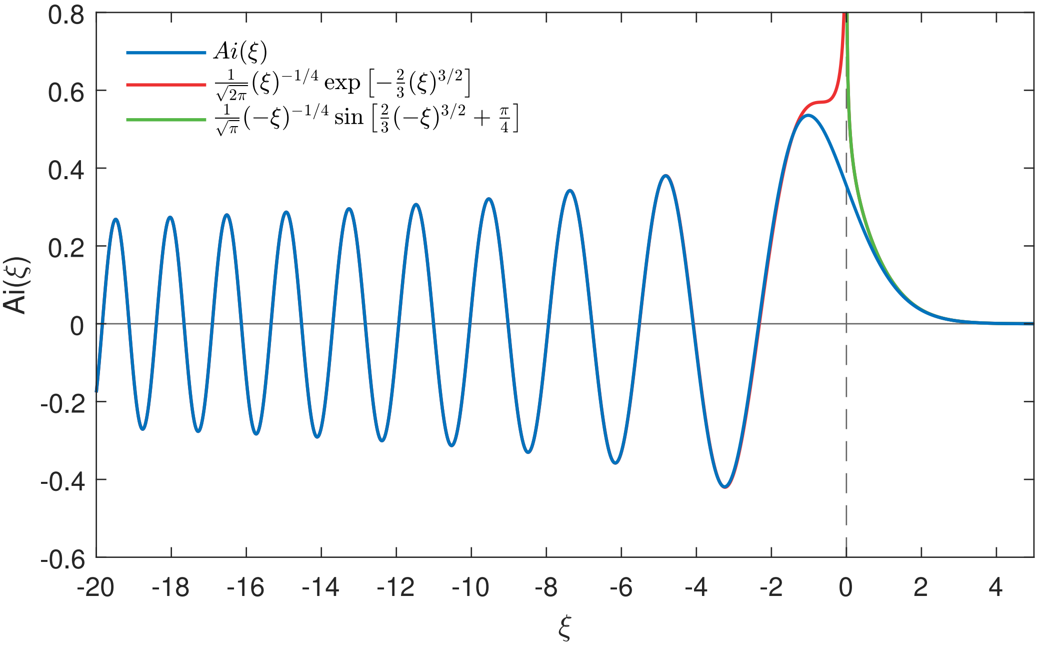

Figure 2.3: Airy function and the respective asymptotic behavior.

The solution is a standing wave created by the continuous interference of the incident and reflected waves. The Airy function has an exponential decay the asymptotic behavior

$$Ai(\xi) \sim \frac{1}{2\sqrt{\pi}}\xi^{-1/4}\exp\left[-\frac{2}{3}\xi^{3/2}\right] \tag{2.82}$$

when $\xi \to \infty$ and

$$Ai(\xi) \sim \frac{1}{\sqrt{\pi}}(-\xi)^{-1/4}\sin\left[\frac{2}{3}(-\xi)^{3/2} + \frac{\pi}{4}\right] \tag{2.83}$$

when $\xi \to -\infty$, as shown in the figure 2.3. The solution is an exponential decay for $x >> x_c$ and an oscillatory form for $x << x_c$. The error is smaller than 1% for $|\xi| \leq 5$.

### 2.2.6 The round-trip phase shift and time delay

One of the fundamental quantity in reflectometry is the difference of phase $\varphi$ between the initial (emission) and final state (detection) that the wave suffers during the propagation, $\varphi = \varphi_f - \varphi_i$. The model for its relation with the plasma parameters is calculated directly from the results of the one dimensional full wave analysis. The propagation in the plasma is divided in four regions, as shown in figure 2.4. The wave is sent at the antenna position $x_a$ (initial point of reference for the propagation), propagates in vacuum (region I), until the initial plasma position, $x_p$. The plasma is assumed to correspond to a slow varying refractive index, validating the condition 2.75. The wave propagates (region II) and reaches the cutoff layer (region III). The layer has a width of $\Delta$, centered at $x_c$. After the cutoff layer (region IV), the field becomes evanescent and the plasma is assumed to be described by a slow varying refractive index, similarly to the region II.

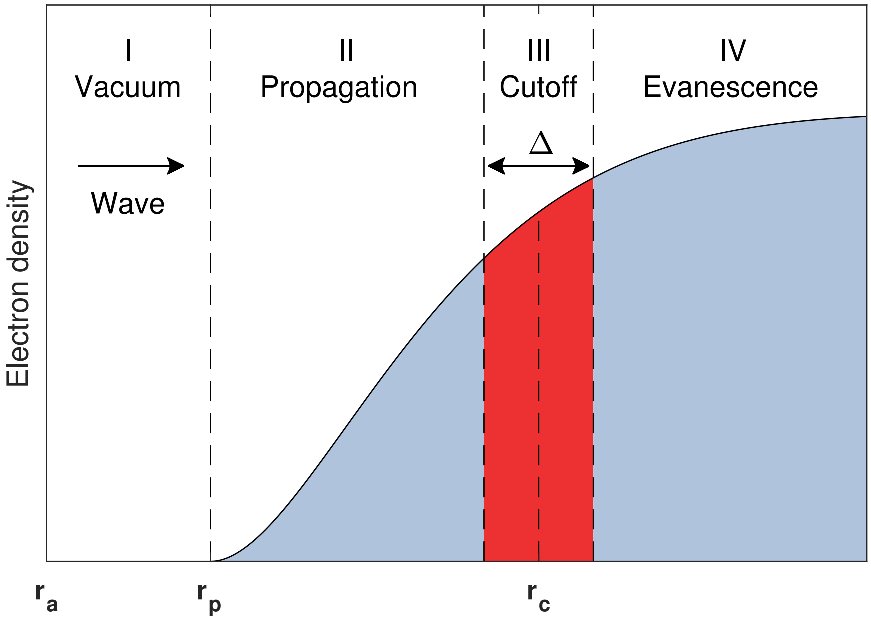

Figure 2.4: Propagation in the different regions of the plasma. The plasma shape, the cutoff layer and the signal propagation are merely representative and do not correspond to any specific case of propagation.

The total phase-shift of the process of propagation between the antenna and the plasma is $\varphi_p = \varphi_I + \varphi_{II} + \varphi_{III} + \varphi_{IV}$. In the context of the experiments, it is necessary to include two additional phase shifts. The first is relative to the propagation between the source located at $x_s$ and the antenna position ($\varphi_m = \phi_{x_s \to x_a}$). The second, between the antenna position and the detector, located at $x_d$ ($\varphi_{x_a \to x_d}$). The total phase shift is

$$\varphi = \varphi_{x_s \to x_a} + \varphi_{x_a \to x_d} + \varphi_I + \varphi_{II} + \varphi_{III} + \varphi_{IV}, \tag{2.84}$$

We now analyze each region in detail and find the phase shift contribution of each one.

### Region I - propagation in vacuum

The wave propagates in vacuum along a distance of $x_p - x_a$. Using $N(x) = 1$ in the Helmholtz equation, we obtain the electric field with the form

$$E_I(x) = A_1 e^{jk_0 x} + A_2 e^{-jk_0 x} \tag{2.85}$$

where $k_0 = \omega/c$ and $A_1$ and $A_2$ are, respectively, the amplitude of the wave propagating in the positive and in the negative direction. The phase shift between the position $x_i$ and $x_f$ is directly calculated by $\phi_{x_i \to x_f} = k_0(x_f - x_i)$. The total phase shift associated to the propagation in vacuum is

$$\varphi_I(f) = \varphi_{x_a \to x_p}(f) + \varphi_{x_p \to x_a}(f) = 2\varphi_{x_a \to x_p}(f) = \frac{4\pi}{c} f(x_p - x_a) \tag{2.86}$$

Notice that this term includes the phase shift of the emitted and the reflected wave.

### Region II - propagation in the plasma

In this region, we admit a slow varying refractive index, so we can use the WKB approximation. From equation 2.71, the electric field has the form

$$E_{II}(x) = \frac{A_3}{\sqrt{N(x,f)}} e^{jk_0 \int_{x_p}^{x_c-\Delta/2} N(x',f)dx'} + \frac{A_4}{\sqrt{N(x,f)}} e^{-jk_0 \int_{x_p}^{x-\Delta/2} N(x',f)dx'} \tag{2.87}$$

where $A_3$ and $A_4$ are the amplitudes. Note that $N(x = x_p, f) = 1$. Assuming the condition 2.75 valid, the round trip phase shift for this region is

$$\varphi_{II} = 2\varphi_{x_p \to x_c-\Delta/2} = \frac{4\pi f}{c} \int_{x_p}^{x_c-\Delta/2} N(x',f)dx'. \tag{2.88}$$

### Region III - cutoff layer

In the cutoff layer, the WKB approximation is no longer valid ($N \to 0$). If the dielectric tensor is approximated by a linear function, the solution is in the form of equation 2.81,

$$E_{III}(x) = A_5 Ai\left[-\beta^{2/3}(x - x_c)\right]. \tag{2.89}$$

At the position $x = x_c - \Delta/2$ the WKB solution matches the Airy's function by a small error. The field is described by the asymptotic expansion given in equation 2.83. Using $N = (\beta^{\frac{1}{3}}/k_0)\sqrt{-\xi}$ and $dx = \beta^{-1/3}d\xi$, it is shown that

$$k_0 \int_{x_c-\Delta/2}^{x_c} N(x',f)dx' = k_0 \int_{\xi(x_c-\Delta/2)}^{0} \sqrt{-\xi}d\xi = \frac{2}{3}\left[-\xi(x-\Delta/2)\right]^{3/2}. \tag{2.90}$$

Using this equality, the phase shift in the cutoff layer is calculated by

$$\varphi_{III} = 2\phi_{x_c \to x_c-\Delta/2} = 2\left[\frac{2}{3}\left[-\xi(x-\Delta/2)\right]^{3/2} - \frac{\pi}{4}\right] = k_0 \int_{x_c-\Delta/2}^{x_c} N(x',f)dx' - \frac{\pi}{2}. \tag{2.91}$$

This can also be obtained from writing the asymptotic limit as

$$\begin{aligned} E_{III}(x) &= A_5(-\xi)^{-1/4}\left[\frac{e^{j(\frac{2}{3}(-\xi)^{3/2}+\frac{\pi}{4})} - e^{-j(\frac{2}{3}(-\xi)^{3/2}+\frac{\pi}{4})}}{2j}\right] \\ &= A_5'(-\xi)^{-1/4}\left[e^{-j(\frac{2}{3}(-\xi)^{3/2})} - je^{j(\frac{2}{3}(-\xi)^{3/2})}\right]. \end{aligned} \tag{2.92}$$

By comparing the WKB solution with the last term of this equation, we conclude that the reflected wave has a phase-shift of $\pi/2$ and a reflection coefficient of $R = 1$. The wave is totally reflected. Using the identity

$$\sqrt{-\xi} = \frac{1}{\pi\left[Ai^2(\xi) + Bi^2(\xi)\right]} = \frac{1}{\pi \mathrm{M}^2(\xi)}, \tag{2.93}$$

the Airy's wavenumber, $k_A$, is defined as

$$k_A = k(\xi = 0) = \frac{\beta^{\frac{1}{3}}}{\pi \mathrm{M}^2(0)} = 0.63(k_0^2 D_\varepsilon)^{\frac{1}{3}} \tag{2.94}$$

The Airy's wavelength $\lambda_A$ is the wavelength at the cutoff layer [115],

$$\lambda_A = \frac{2\pi}{k_A} \tag{2.95}$$

From the initial plasma position the wavelength increases until reach the maximum value, at the cutoff layer. The width of the layer is estimated by

$$\Delta = \beta^{-1/3}\Delta\xi = \Delta\xi k_0^{-2/3} D_\varepsilon^{-1/3} = \Delta\xi \left(\frac{c}{\omega}\right)^{2/3} D_\varepsilon^{-1/3}. \tag{2.96}$$

For the O-mode the layer width is

$$\Delta = \Delta\xi \left(\frac{c}{\omega}\right)^{2/3} \left[\frac{1}{n_c}\frac{\mathrm{d}n_e(x)}{\mathrm{d}x}\bigg|_{x_c}\right]^{-1/3} = \Delta\xi \left(\frac{c}{\omega}\right)^{2/3} L_n^{1/3}, \tag{2.97}$$

where $L_n$ is the density gradient length. There are different assumptions for $\Delta\xi$ in the literature. For example in [49], the authors assume $\Delta\xi = 1.6$, corresponding to the difference of positions of the half maximum of $Ai^2(\xi)$.

### Region IV - evanescent wave

In this region the refractive index is purely imaginary ($N = jN_I$) and the WKB approximation gives an exponential decay. The electric field has the form

$$E_{IV}(x) = \frac{A_6}{\sqrt{N(x,f)}} e^{-k_0 \int_{x_c+\Delta/2}^{x} N_I(x',f)dx'} \tag{2.98}$$

The wave is evanescent and there is no phase term.

### The total phase shift

The total phase shift is

$$\begin{aligned} \varphi(f) &= \varphi_I(f) + \varphi_{II}(f) + \varphi_{III}(f) + \varphi_{IV}(f) \\ &= \frac{4\pi}{c} f(x_p - x_a) + \frac{4\pi}{c} f \int_{x_p}^{x_c(f)-\Delta/2} N(x,f)dx + \frac{4\pi}{c} f \int_{x_c(f)-\Delta/2}^{x_c(f)} N(x,f)dx - \frac{\pi}{2} \\ &= \underbrace{\frac{4\pi}{c} f(x_p - x_a)}_{\text{vacuum}} + \underbrace{\frac{4\pi}{c} f \int_{x_p}^{x_c(f)} N(x,f)dx - \frac{\pi}{2}}_{\text{plasma}}. \end{aligned} \tag{2.99}$$

The phase shift due to the propagation between the source/detector and the antenna is not included. The plasma contribution can be written in the form

$$\varphi_p(f) = 2\int_{x_p}^{x_c(f)} k(x,f)dx - \frac{\pi}{2}. \tag{2.100}$$

In general, the local wavenumber/refractive index is unknown. For a density profile in the form

$$n_e(x) = n_e(x_M)\left(\frac{x - x_0}{x_M - x_0}\right)^s \quad , s > 0 \tag{2.101}$$

the O-mode refractive index has an analytical form [116, 94]:

$$\varphi = \frac{4\pi^{3/2}\Gamma\left(\frac{2}{s}\right)(x_M - x_0)}{c\Gamma\left(\frac{2}{s}+\frac{1}{2}\right)} \left(\frac{f}{\frac{2}{s}+1}\right)\left(\frac{f}{f_M}\right)^{2/s}. \tag{2.102}$$

Here, $f_M$ is the cutoff frequency associated with $n_e(x_M)$.

### The round-trip time-delay

The expression for the phase difference assumes a monochromatic plane wave in stationary state. From the experimental point of view, it is convenient the evaluation of the round-trip time-delay of a wave train. As discussed in section 2.3, the time delay is fundamental to invert the equation 2.99 and find the density profile. Firstly, the group velocity (equation 2.17) is written as function of the refractive index,

$$\mathbf{v}_g = \left[ \left( \frac{\partial k_x}{\partial \omega} \right)^{-1}, \left( \frac{\partial k_y}{\partial \omega} \right)^{-1}, \left( \frac{\partial k_z}{\partial \omega} \right)^{-1} \right] = \left[ \frac{c}{\frac{\partial}{\partial \omega}[\omega N_x]}, \frac{c}{\frac{\partial}{\partial \omega}[\omega N_y]}, \frac{c}{\frac{\partial}{\partial \omega}[\omega N_z]} \right] \tag{2.103}$$

In the considered geometry, only the first component is different from zero. Using this form of the group velocity, the group delay is

$$\tau_g(f) = 2 \int_{x_p}^{x_c} \frac{1}{v_g(x)} dx = \frac{2}{c} \int_{x_p}^{x_c} \frac{c}{v_g(x)} dx = \frac{2}{c} \int_{x_p}^{x_c(f)} \frac{\partial}{\partial \omega} \left[ \omega N(x) \right] dx. \tag{2.104}$$

Taking the derivative of the equation 2.99 excluding the propagation in vacuum, one obtains

$$\frac{\partial \varphi}{\partial f} = \frac{4\pi}{c} \int_{x_p}^{x_c(f)} \frac{\partial}{\partial f} \left[ f N(x) \right] dx \tag{2.105}$$

Equation 2.104 and 2.105 are related by a $2\pi$ factor,

$$\tau_g(f) = \frac{1}{2\pi} \frac{\partial \varphi}{\partial f} = \frac{\partial \varphi}{\partial \omega} \tag{2.106}$$

In section 2.3, it is demonstrated that the measurement of the density profile is done measuring the group delay for several frequencies. The total group-delay between the emission and the detection of the signal is

$$\tau(f) = \tau_{x_s \to x_a}(f) + \tau_{x_a \to x_d}(f) + \frac{4\pi}{c}(x_p - x_a) + \frac{4\pi}{c} f \int_{x_p}^{x_c(f)} \frac{\partial}{\partial f} \left[ f N(x) \right] dx \tag{2.107}$$

where $\tau_{x_s \to x_a}(f)$ is the time delay between the emission and the antenna position and $\tau_{x_a \to x_d}(f)$ between the antenna and the detection point. These time delays are dependent of the microwave components that constitute the measurement system. In a real experiment, the system is calibrated so that the terms from the propagation in the vacuum and plasma can be partially extracted.

### The measurement error

Each measurement has an error associated that corresponds to the difference between the real value of the parameter and the measured one. The cause of the error can be the hardware (experimental) or due to the physical model does not describe the propagation phenomena accurately (intrinsic). In this section we analyze some possible causes for second type error in magnetic confinement experiments.

The approximate solution of the phase and group delay was derived under three main assumptions intrinsically connected to the used model: (i) cold plasma model, (ii) plane wave approximation, (iii) frozen plasma, (iv) one dimensional slow varying plasma and (v) reflection at a linear dielectric. There are many situations where these conditions are not fulfilled. This introduces a measurement error, since the measured phase shift and the round-trip time-delay of the wave do not correspond to the theoretical prediction. If the measurement produces a significant error in the estimated plasma parameter, the diagnostic is not viable for the desired application. Another effect that is not considered in the model are the losses of power of the probing beam. In the one dimensional model the wave is totally reflected backwards. In a real experiment only a part of the emitted power is detected, depending on the receiving antenna geometry and on the fraction of power that is scattered by the plasma to different directions.

The density profile is, in general, a function of the space and time. In a real experiment, many different phenomena contribute to the variance local or macroscopic, of the density profile/magnetic field. The total electron density can be written as the sum of the smooth density profile $n_0$ with the variant density profile component:

$$n_e(\mathbf{r},t) = \underbrace{n_0(\mathbf{r},t)}_{\text{smooth profile}} + \underbrace{\sum_j \tilde{n}_e^j(\mathbf{r},t)}_{\text{variant component}}. \tag{2.108}$$

The variant component of the density profile is the sum of all the deformations/perturbations $\tilde{n}_e^j$ induced by the different physical phenomena (labeled by $j$) that can occur during the discharge. In steady state, it is expected that the smooth density profile corresponds to the MHD equilibrium scenario.

During the propagation in such irregular plasmas, many different phenomena occur to the probing wave, such as refraction, diffraction scattering or resonance absorption, leading to changes in the propagation path and in the wave characteristics. The effect of the time variation of the plasma parameters can be solved if the measurements are done in a small scale of time. The plasma is considered frozen and all the fluctuations are considered spatial, inducing an intrinsic error assumed to be negligible in first approximation. However, the macroscopic plasma shape and the spacial structure of the different perturbations are intrinsic to any plasma experiment, and only part of them can be controlled. This has an impact in the validity of the one dimensional slow varying plasma approximation, since the slab plasma assumption can be no longer valid.

Confining a plasma requires closed magnetic surfaces, implying, in general, some degree of curvature and divergence of the isodensity density lines and gradients with variable direction along the propagation line. This is an intrinsic effect of every plasma equilibrium, and cannot be avoided by any confinement mechanism. During the ramp-up and ramp-down phases of the discharge the equilibrium plasma shape is being formed, which can be even more complicated to probe in the validity conditions. Apart from the equilibrium plasma shape, other phenomena such as turbulence and MHD instabilities (e.g. vertical plasma displacements or ELMs) are responsible for introducing significant local or macroscopical variations in the density profiles during the discharges [93], affecting the propagation of the probing beam.

Although there is no analytical solution of the propagation equation for a general density profile characterized by turbulent fluctuations, the propagation of the probing beam profile can be analyzed within the frame of the perturbation theory. In fact, the results of the application of perturbation theory in reflectometry have been used to measure plasma parameters such as the density fluctuations level or the turbulence spectrum. The next topic of this section is dedicated to the propagation in a turbulent plasma.

Apart from the shape of the plasma and the different density profile perturbations, there are other phenomena that puts the first three conditions of validity of the reflectometry model in cause, modifying the propagation. In the case of high temperatures (> 5 keV), the cold plasma model does not describe the dielectric tensor of the plasma properly due to the relativistic effects, as mentioned before. A correction to the cutoffs needs to be implemented to obtain accurate results. Furthermore, although the measurements can be done in very short time scales to consider the density profile practically static, in some cases the Doppler effect can affect the propagation. These physical mechanisms are discussed in the last topic of this section.

The plane wave approximation is also no longer valid in real experiments. The geometry of the measuring system determines the shape of the probing beam, although it can be approximated by a plane wave in a limited region. The reflected beam that is not detected can eventually be reflected in the surrounding structure (e.g. blanket) and forms multiple plasma-wall reflections. These reflections can be detected later, contributing to an inaccurate measurement if the data processing cannot reject them. The different sources of error in the context of the position measurement are listed and analyzed in the last section of this chapter.

### 2.2.7 Wave propagation in a turbulent plasma

In the study of turbulence the total density (equation 2.108) is denoted as

$$n_e(\mathbf{r},t) = n_0(\mathbf{r},t) + \tilde{n}_e(\mathbf{r},t), \tag{2.109}$$

where $n_0(\mathbf{r},t)$ is the unperturbed density profile and $\tilde{n}_e(\mathbf{r},t)$ is the perturbation induced by the turbulence, representing the density fluctuations. $\delta n_e(\mathbf{r},t)$ is typically used as the amplitude of the perturbations. The fluctuations are locally characterized by a spectrum $S(\mathbf{k},t)$ and by a level/amplitude, in relation to the unperturbed plasma. The local level/amplitude of fluctuations is defined as the ratio

$$A_{trb} = \frac{\delta n_e}{n_0}, \tag{2.110}$$

usually given in percentage. Some authors use the root mean squared value instead of the amplitude. In a tokamak, this ratio is in the order of 1% in the core and can reach values in the order of $10-30\%$ in the edge [117]. When the amplitude of the turbulent density fluctuations is much lower than the unperturbed plasma ($\delta n_e << n_0$) the Born approximation can be applied. The characteristic times of turbulence are lower than the timescales associated to the macroscopic plasma phenomena ($\sim$ 1 ms). Turbulence is considered, in general, a random phenomena. In steady state, is expected that the averaged density profile tends to the equilibrium configuration, $< n_e >= n_0$. In a similar way, the total magnetic field is written as a sum of the unperturbed/equilibrium term with the fluctuation term, $\mathbf{B}(\mathbf{r},t)$. Recent experiments show that the magnetic fluctuations effect in the propagation of the X-mode is typically low [118]. For simplicity it is assumed that the perturbations come from the density fluctuations.

The total phase-shift due to the propagation in the turbulence plasma can be written as

$$\varphi = \varphi_0 + \tilde{\varphi}, \tag{2.111}$$

where $\varphi_0$ is the phase associated with the unperturbed density profile corresponding to an average value and $\tilde{\varphi}$ is the phase fluctuation induced by the perturbations [48]. In the typical plasmas, the 3D effects of the plasma-wave interactions are important to take into consideration. The experimental observation of large-amplitude fluctuations of the reflected wave suggests that the multi-dimensional effects play an important role and need to be taken into account in an accurate description of the propagation in turbulent plasmas [47]. From the physical point of view, the reflected wave is no longer a plane wave after interacting with the cutoff layer, making this process very difficult to describe mathematically. Multiple waves coming from different directions and positions, with different phases and intensities, reach the detector at the same time, changing the interpretation of the measurement. However the one-dimensional models are essential to treat the problem mathematically and understand part of the physics involved in the process. The simplest model for the phase perturbation assumes the phase fluctuations are directly estimated from equation 2.100. Only the fluctuation with size structure much larger than the local wavelength can be described. The fluctuations in the plasma dielectric constant are included in the total wavenumber, $k(x) = k_0(x) + \tilde{k}(x)$. The perturbed phase shift is

$$\varphi = 2\int_{x_a}^{x_c} k(x')dx' = \underbrace{2\int_{x_a}^{x_c} k_0(x')dx'}_{\varphi_0} + \underbrace{2\int_{x_a}^{x_c} \tilde{k}(x')dx'}_{\tilde{\varphi}} \tag{2.112}$$

The calculation of $\tilde{\varphi}$ depends on $\tilde{k}$, that has a different expression for each mode of propagation. The fluctuations on the local wavenumber are related to the local density perturbation, $\tilde{k}(x) = (\partial k(x)/\partial n_e)\delta\tilde{n}_e(x)$. For the O-mode case, the phase fluctuation is

$$\tilde{\varphi}_O(x_c) = -\left(\frac{\omega}{c}\right)\int_{x_p}^{x_c} \frac{\tilde{n}_e}{n_c}\frac{1}{\sqrt{1-(n_0/n_c)}}dx' = -k_0\int_{x_p}^{x_c} N_O^{-1}\frac{\tilde{n}_e}{n_c}dx'. \tag{2.113}$$

This expression corresponds to the second order term of Taylor expansion of the integral term of equation 2.100,

$$\begin{aligned}\tilde{\varphi}_O &= 2k_0\int_{x_p}^{x_c}\sqrt{1-\frac{(n_0+\tilde{n}_e)}{n_c}}dx' \\ &\underbrace{\simeq}_{\sqrt{a-x}\simeq\sqrt{a}-x/(2\sqrt{a})} 2k_0\int_{x_p}^{x_c}\sqrt{1-\frac{n_0}{n_c}}dx' - k_0\int_{x_p}^{x_c}\frac{\tilde{n}_e}{n_c}\frac{1}{\sqrt{1-(n_0/n_c)}}dx'.\end{aligned} \tag{2.114}$$

This equation shows that the wave records the effect of the different fluctuations along the propagation path, and due to the denominator approaching zero at $n_e = n_c$, it is expected that most of the contribution comes from near the cutoff position. For high amplitude large perturbations, the fluctuations may change the cutoff position, $x_c$, resulting in a characteristic phase fluctuations also associated to the cutoff region [119]. The question of the localization of the phase fluctuations is in fact, one important topic of the reflectometry theory. Different experiments shown the confirmation of the localization of the fluctuations in the cutoff region [120, 121]. However, theoretical studies predicted that the Bragg scattering could be the dominant mechanism inducing fluctuations in the phase [122], contradicting the localization of the perturbations in the cutoff layer. This difference between the predictions and the experiments lead to consider the 2D effects as the principal cause of discrepancy, without success. In [123] it has been shown analytically with the Born approximation that the localization is dependent on the fluctuation wavenumber and on the Airy's wavenumber, clarifying the problem. Before discussing these results, the Bragg scattering is introduced.

### Bragg resonant scattering

When an electromagnetic wave with a frequency $\omega_i$ and a wavenumber $k_i$ propagates in an inhomogeneous plasma with density fluctuations characterized by a wavenumber $k_f$ and frequency $\omega_f$, part of the energy can be scattered in different directions. This phenomena, called Bragg scattering, is similar to what occurs in crystals with the X-rays [124]. The Bragg rule describe the condition at which the coupling between incident wave and the turbulence is maximum [125],

$$\omega_s = \omega_i \pm \omega_f \tag{2.115}$$

$$\mathbf{k}_s = \mathbf{k}_i \pm \mathbf{k}_f, \tag{2.116}$$

where $\omega_s$ and $k_s$ are the frequency and wave-number of the scattered wave. Note that we should distinguish the main reflection from the cutoff layer and the backscattered waves from the density fluctuations that follow the Bragg rule. Since $\omega_f << \omega_i$ (less or up to MHz compared with tens of GHz of the probing wave) and $\omega_i \simeq \omega_s$, the dispersion relation of the plasma requires locally $|k_i| \simeq |k_s|$. The scattering angle ($\theta$) follows the Bragg's rule,

$$k_f = 2k_i \sin\left(\frac{\theta}{2}\right). \tag{2.117}$$

For normal incidence in 1D, which is the relevant condition in most of the reflectometry applications, if the incident wavevector is colinear to the wavenumber, equation 2.116 becomes

$$k_f(x_B) = 2k_i(x_B), \tag{2.118}$$

and $\mathbf{k}_d = \pm\mathbf{k}_i$ (from equation 2.116). $x_B$ is the position at which this condition is verified. These two solutions correspond to the Bragg backscattering (-) and to the forward scattering (+). The Bragg backscattering of the probing wave before the cutoff lead to phase fluctuations in the detected signal. As a first approximation, the forward scattering usually does not contribute significantly to the perturbation of the reflected signal in the one dimensional model. However it is known that non-linear effects from forward scattering can also affect the reflectometry signal in the 2D approach [126].

During the propagation in one-dimension, if there is a position $x_B$ where this condition is full-filled, there will be a resonant response of the phase and the phase fluctuations may not be localized in the cutoff [123, 127]. In a fusion plasma, where a spectrum of turbulence is present, this condition can occur multiple times during the propagation in different positions, leading to a final phase shift, whose the localization is not at the cutoff. Using the Born approximation, it is possible to obtain analytical descriptions of the scattered field phase and amplitude, allowing a better understanding of what happens to the probing beam when it is in the presence of turbulent structures. Before going further in the important results from the studies that have been made within the frame of the perturbation theory, we analyze the solution of the Mathieu equation.

### Mathieu equation

The complexity of the process of interaction of the fluctuations with the probing wave is illustrated with a simple model of a monochromatic perturbation centered at $x_f$ [128]. The total refractive index is

$$N = N_0 + \tilde{N} = N_0[1 + a_f \sin(k_f(x - x_f - w_f))], \tag{2.119}$$

where $a_f$ is the relative amplitude of the fluctuation, $w_f$ is half width and $x \in [x_f - w_f, x_f + w_f]$. The unperturbed refractive index is in general a function of the position, but here it is being described locally, at the $x_f$ position, taken as constant. By the proper change of variables with $\xi = \frac{\pi}{4} - \frac{1}{2}k_f(x - x_f - w_f)$, the Helmholtz equation is written in the form

$$\frac{d^2E}{d\xi^2} + (p - 2q\cos(2\xi))E = 0, \tag{2.120}$$

where $p$ and $q$ represent the the normalized position and amplitude of the fluctuations, which is dependent on the mode. For O-mode we have

$$p = 4\frac{\omega^2}{k_f^2c^2}N_O^2(x_f) \tag{2.121}$$

$$q = 2a_f\frac{\omega_p^2(x_f)}{k_f^2c^2}. \tag{2.122}$$

For the X-mode, the expressions depend if the perturbations are of density or of the magnetic field (see [128]). Equation 2.120 is known as the Mathieu equation. The solution of this equation can be expressed by an infinite progression of functions $a_i(q)$ and $b_i(q)$

$$a_1(q) = 1 + q - \frac{q^2}{8} - \frac{q^3}{64} - \frac{q^4}{1536} + ... \qquad a_2(q) = 4 + \frac{5q^2}{12} - \frac{763q^4}{13824} + ... \tag{2.123}$$

$$b_1(q) = 1 - q - \frac{q^2}{8} + \frac{q^3}{64} - \frac{q^4}{1536} + ... \qquad b_2(q) = 4 + \frac{5q^2}{12} - \frac{763q^4}{13824} + ... \tag{2.124}$$

The solution is stable in the intervals defined by $a_i < p < b_{i+1}$ and unstable for $b_i < p < a_i$, according to figure 2.5

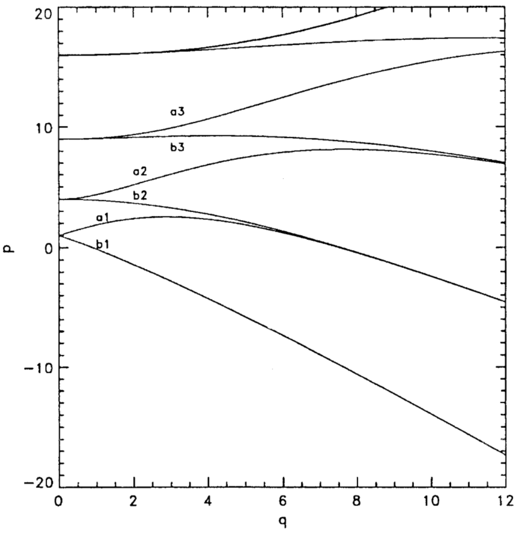

Figure 2.5: Representation of the $a_i$ and $b_i$ functions in the diagram $(p, q)$. The solution is stable in the intervals defined by $a_i < p < b_{i+1}$ and unstable for $b_i < p < a_i$. Adapted from [128].

Note that only an unstable region exists for a very low level of turbulence ($q \sim 0$), corresponding to the previously written Bragg scattering condition. For higher amplitudes of turbulence, different unstable regions are possible, demonstrating the complexity of the propagation in a turbulent medium [129].

### Born approximation

In [130] the author finds the general expression for the perturbed electric $\tilde{E}$ field using the Born approximation, valid for small perturbations. This allows the calculation of the contribution of the scattering to the phase-shift. Starting from Helmholtz equation, a differential equation dependent on the zero order solution $E_0$ is obtained for the perturbed electric field $\tilde{E}$,

$$\frac{d^2E}{dx^2} + [k^2(x) + \tilde{k^2}(x)]E = 0 \rightarrow \frac{d^2\tilde{E}}{dx^2} + k^2\tilde{E} = -\tilde{k^2}E_0, \tag{2.125}$$

where $\tilde{k^2}$ represents the fluctuations of the local wavenumber/dielectric constant ($\tilde{k^2} = (\omega/c)^2\tilde{\varepsilon}$), $E = E_0 + \tilde{E}$ is the total electric field and it is assumed that the fluctuations are small so the non-linear terms are neglected ($\tilde{k^2} << k^2$ and $\tilde{E} << E_0$). This inhomogeneous equation is solved using the Green's function method. At the antenna/vacuum region, the signal is a sum of a forward wave with a backward wave, $B = B_0 + \tilde{B}$. The perturbed backward wave amplitude is given by.

$$\delta\tilde{B} = -2j\delta B_0 \left( \int_{x_0}^{\infty} \tilde{k^2}(x') \frac{E_0^2(x')}{W} dx' \right) \tag{2.126}$$

and a the phase angle of $B$ relative $B_0$ is

$$\tilde{\varphi} = 2\text{Re} \left( \int_{x_0}^{\infty} \tilde{k}^2(x') \frac{E_0^2(x')}{W} dx' \right), \tag{2.127}$$

where $x_0$ is the reference point (far away from the cutoff, e.g. antenna/vacuum region), $B_0$ is the amplitude of the unperturbed backward solution at the reference point, $W$ is the Wronskian constant [130] and Re denotes the real part.

### Localization of the small phase fluctuations

In [123] the authors used the Born approximation to calculate the phase angle analytical expressions of two types of localized perturbations, a sine wave with a Gaussian shape and a square shape. The expressions are derived for the O-mode using a linear equilibrium density profile in the form $n(x) = n_c - (n_c/L)x$, so that the zero order solution $E_0$ is the Airy's function. The perturbations are characterized by a position with respect to the cutoff position, so the localization problem can be studied analytically. There are basically four important results:

1. The phase response is strongly influenced by the shape, size and position of the perturbation.

2. For $k_f < 2k_A$ (small wavenumbers) or $\lambda_f > 2\lambda_A$, the Bragg rule is not satisfied, and the response is localized at the cutoff layer due to its oscillations.

3. For $2k_A < k_f < 2k_0$ (large wavenumbers) or $2_A > \lambda_f > 2\lambda_0$, the resonant Bragg scattering is the dominant mechanism. In this case different regimes can exist, depending if the width of the perturbation is below or above a critical length, $l_c^2 = (L_n k_f)/k_0^2$. In the spatial regime ($l_f < l_c$), the phase response reproduces the spatial shape of the perturbation. In the spectral regime ($l_f > l_c$), it reproduces the spectral shape of the perturbation, and scattering may occur at locations that are far from the

Bragg position. The maximum phase shift amplitude occurs when the perturbation is located at the Bragg position $x_B$, where the Bragg condition $k_f = 2k$ is valid. As we approach the cutoff layer, the wavelength of the probing wave increases and higher fluctuation wavelengths are necessary to fulfill the condition.

4. High fluctuations of density are in general responsible for higher phase fluctuations. A linear relation between the maximum phase perturbation and the perturbation amplitude has been demonstrated within the framework of Born approximation:

$$\delta\varphi_{max} = F(L_n, k_0, k_f)\left(\frac{\delta n_e}{n_c}\right), \tag{2.128}$$

where the $F$ function depends on the case. For example, for the spatial regime (Gaussian or square) with $2k_A < k_f < 2k_0$, this function is

$$F(L_n, k_0, k_f) = \sqrt{2}\pi\left(\frac{L/\lambda_0}{k_f/k_0}\right)^{1/2}. \tag{2.129}$$

This means that depending on the turbulence spectrum, on the vacuum wavenumber $k_0$ and on the plasma gradient, the fluctuations can be localized at the cutoff or coming from different regions of the propagation, where the Bragg condition is valid.

The linear regime of reflectometry is, in general, valid for small turbulence and amplitude levels [131]. In [132] the condition of transition to the non-linear regime of reflectometry was found for a linear density profile with a statistically homogeneous turbulence profile:

$$\left(\frac{\delta n}{n_c}\right)^2 \frac{\omega^2 l_c x_c}{c^2} \ln\left(\frac{x_c}{l_c}\right) \geq 1, \tag{2.130}$$

where $l_c$ is the turbulence correlation length and $x_c$ is the plasma length to the cutoff. This condition shown to be valid in the 2D simulations [133, 134]. The phase perturbations in the non-linear regime shown to be not localized at the cutoff vicinity, carrying information of different regions of the plasma [135, 136].

### Two dimensional effects

The study of the propagation in fluctuations becomes even more difficult in two dimensions [137, 138, 139]. The finite beam width and divergence and the poloidal fluctuations play an important role in the detected reflectometry signal. In [140], it has been shown that the detected signal is sensitive to the poloidal fluctuation wavenumbers $k_y$. Above a limit dependent on the receiver location and on the incident beam width, $k_y \sim 1/w$ ($w$ is the $1/e$ radius of the incident beam intensity), the scattered signal amplitude is proportional to $e^{-k_y^2}$, giving a limitation of poloidal wavenumber to detect fluctuations. Later studies indicated that strong poloidal and probing wave curvatures could have an impact in the sensitivity of the reflectometer when comparing with the slab geometries [141, 142]. Under these conditions, the electric field fluctuations due to a density fluctuation with wavenumber $k_y$ shown to be as strong as the density fluctuation of a much smaller equivalent wavenumber $k'_y$ in the slab plasma case:

$$k'_y = (\rho/2k_0 w^2)k_y, \quad w << \frac{\rho}{2} << k_0 w^2. \tag{2.131}$$

Here $\rho = (2\rho_c\rho_w)/(\rho_c + 2\rho_w)$ is the effective radius of curvature, where $\rho_c$ is the curvature radius of the cutoff layer and $\rho_w$ the curvature radius of the incident beam, which depend on the propagation in the plasma.

Under the presence of turbulence fluctuations, the probing beam has a tendency to suffer widening and changes of phase, leading to the degradation of the diagnostics performance. In [143] the author derives the an analytical expression for a diffusion-like angular beam width variation of a O-mode Gaussian beam due to the density perturbations. In reference [144] it is derived for the X-mode. In [132] the attenuation of the coherent part (with the same phase information) of a O-mode beam as it passes thought the fluctuations is described with 1D simple theory, demonstrating that the averaged electric field amplitude decreases with an increased level of RMS($\tilde{n}$). In [145] the author analyzes numerically the coherence and the widening of a Gaussian beam as it passes thought a 2D turbulent medium. The distribution of the power $\langle E^2 \rangle$ presents a decrease of amplitude at the region where the unperturbed beam power is localized and an increase in the adjacent regions, representing the beam widening. The relative amplitude of the coherent part of the beam is obtained by taking the average of the electric field at fixed $x$ position and time instant over a set of turbulence realizations, $max(\langle E \rangle)/max(E_0)$. This ratio is used to extract the incoherent part of the beam power profile, by $E_I^2 = \langle E^2 \rangle - (max(\langle E \rangle)/max(E_0))^2 E_0^2$. In accordance with the theory, the results confirm (i) the decrease of amplitude of the coherent part of the electric field with the increase of the level of fluctuations, (ii) the beam widening and the (ii) increasing of the incoherent part beam size with the turbulence level.

### 2.2.8 Other physical mechanisms

#### Doppler effect

Doppler effect is a very well known physical phenomena that consists in the change in wave frequency during the relative motion between a wave source and its observer. It has been used in RADAR systems to determine the target velocity [146]. In reflectometry, due to the movement of the reflecting layer and of the backscattering zones, this effect can induce a frequency shift $f_D$ of

$$f_D = \frac{1}{2\pi}\mathbf{k}\cdot\mathbf{v} = \frac{1}{2\pi}\left[k_\parallel v_\parallel + k_r v_r + k_\perp v_\perp\right]. \tag{2.132}$$

Since the refractive index is a function of the wave frequency, the phase-shift of the wave can be modified after being affected by the Doppler effect. If a wave is propagating in one dimension time-varying density profile, the frequency shift of the detected wave is [147]

$$f_D = -\frac{2\omega}{c}\int_0^{x_c}\frac{\partial n}{\partial t}dx. \tag{2.133}$$

#### Relativistic effects

In the context of reflectometry, the kinetic effects due to the velocity distribution do not play an important role in the propagation of the probing wave. However, the relativistic effects can contribute significantly to the plasma dielectric tensor, changing the cutoff expressions and the refractive index of each mode of propagation [112, 148, 149, 150].

The hot plasma dielectric tensor is derived from the Vlasov equation (see section 1.2.1) [49]. The electron velocity distribution function is divided in two parts, the equilibrium term $f_0$ and the perturbation $f_e(\mathbf{r},\mathbf{v}_e,t) = f_0(\mathbf{r},\mathbf{v}_e) + f_1(\mathbf{r},\mathbf{v}_e,t)$, with $|f_1| << f_0$. The linearization of the Vlasov equation yields

$$\frac{df_1}{dt} = \frac{\partial f_1}{\partial t} + \mathbf{v}_e\cdot\nabla f_1 - \frac{e}{m_e}(\mathbf{v}_e\times\mathbf{B}_0)\cdot\frac{\partial f_1}{\partial \mathbf{v}_e} = \frac{e}{m_e}\left[\mathbf{E}_1 + \mathbf{v}_e\times\mathbf{B}_1\right]\cdot\frac{\partial f_0}{\partial \mathbf{v}_e} \tag{2.134}$$

The perturbed velocity distribution is directly calculated by

$$f_1(\mathbf{r},\mathbf{v}_e,t) = \frac{e}{m_e}\int_{-\infty}^{t} e^{j(\mathbf{k}\cdot\mathbf{r}-\omega t')}\left[\mathbf{E}_1(\mathbf{k},\omega) + \frac{\mathbf{v}_e}{\omega}\times(\mathbf{k}\times\mathbf{E}_1(\mathbf{k},\omega))\right]\cdot\frac{\partial f_0}{\mathbf{v}_e}dt' \tag{2.135}$$

Using the perturbed electric current, the dielectric tensor for a Maxwellian distribution is obtained:

$$\varepsilon_{ij}(\mathbf{k},\omega) = \delta_{ij} - 2\pi\frac{\omega_p^2}{\omega^2}\int_{-\infty}^{+\infty}\frac{e^{-u^2}}{\sqrt{\pi}}du\int_0^{\infty}\frac{e^{-w^2}}{\pi}dw\times\left[\sum_{n=-\infty}^{+\infty}\frac{\omega}{\omega-n\omega_c-k_\parallel v_{th}}u\right]Q_{ij}^n(u,w). \tag{2.136}$$

Here the functions $Q_{ij}^n(u,w)$ are given by the nth-order Bessel functions, $w = v_\perp/v_{th}$ and $u = v_\parallel/v_{th}$. In contrast to the cold plasma model, resonances at $\omega = n\omega_c + k_\parallel v_{th}$ are taken into account due to the continuous velocity distribution. In the $T_e \to 0$ limit, the cold plasma model dielectric tensor is obtained.

The reason why the relativistic effects are important in reflectometry is because the dielectric tensor terms depend on the plasma and cyclotron frequency, which depend on the electron mass. The mass of part of the electrons of the distribution function increases, and this introduces the variations in these characteristic frequencies, which affects the refractive index. With the relativistic description, equation 2.137 gets

$$\frac{\partial f_1}{\partial t} + \mathbf{v}_e\cdot\nabla f_1 - e(\frac{\mathbf{v}_e}{c}\times\mathbf{B}_0)\cdot\frac{\partial f_1}{\partial\mathbf{p}_e} = e\left[\mathbf{E}_1 + \frac{\mathbf{v}_e}{c}\times\mathbf{B}_1\right]\cdot\frac{\partial f_0}{\partial\mathbf{p}_e} \tag{2.137}$$

where $\mathbf{p}_e = \gamma m_e\mathbf{v}_e$ is the relativistic momentum, with $\gamma = (1-(v_e/c)^2)^{-1/2}$. The relativistic Maxwellian distribution is defined as

$$f_0 = \frac{m_ec^2/k_BT_e}{4\pi(mc)^3K_2(m_ec^2/k_BT_e)}\exp\left[-\frac{m_ec^2}{k_BT_e}\gamma\right] = \frac{\alpha}{4\pi(mc)^3K_2(\alpha)}\exp(-\alpha\gamma), \tag{2.138}$$

where $K_n$ is the modified Bessel function of the second kind and order $n$ and $\alpha = (m_ec^2)/(k_BT_e)$. The expression for the relativistic dielectric tensor is complicated and can be found in [35, 148]. In [149] the author derives the relativistic expression of the cutoff frequencies:

$$\frac{\omega_s^2}{\omega_p^2} = \frac{\mu^2}{3K_2(\mu)}\int_0^{\infty}\frac{p^4\exp(-\mu\gamma)}{\gamma(\gamma-s\Omega)}dp, \tag{2.139}$$

where $\Omega = \omega_c/\omega_s$, $s = 0$ for the O-mode, $s = 1$ for the X-mode R-cutoff $(0 \leq \Omega \leq 1)$ and $s = -1$ for the X-mode L-cutoff $(0 \leq \Omega)$. In [112], the author gives an approximate version of the relativistic dielectric tensor, valid in the expected range of temperatures in the current experiments and fusion machines. The relativistic refractive index is obtained by changing the electron mass $m_e$ of the cold plasma model to

$$m_e^* = m_e\sqrt{1+5/\mu}, \tag{2.140}$$

where $\mu = \alpha^{-1}$. The change in the cutoff density $\Delta n_c = n_c - n_c^*$ is given by

$$\frac{\Delta n_c}{n_c} = \frac{(1+5/\mu)^{1/2}-1}{1-s\Omega}. \tag{2.141}$$

The deviation starts to be significant at high temperatures. For example, a temperature of 15 KeV in O-mode $(s = 0)$ can induce a shift of 7%. But for temperatures of 1-5 KeV, this error is 0.5-2%. With the exception of the SOL region where the temperature are usually low, the relativistic effects should be taken into account in the analysis of the propagation of electromagnetic waves in the plasma [148].

## 2.3 The basics of microwave reflectometry

### 2.3.1 Sweeping reflectometry for density profile measurements

The conventional application of reflectometry is the measurement of density profiles [83]. This is possible if the phase shift of the wave is measured for different frequencies. The O-mode has a very simple dispersion relation and the density profile inversion can be calculated directly from the Abel inversion method [151]. According to equation 2.100, the O-mode round-trip phase-shift is

$$\varphi = \frac{4\pi}{c}\int_{x_0}^{x_c(f)} \sqrt{f^2 - f_{pe}^2(x)}dx - \frac{\pi}{2}. \tag{2.142}$$

The wave is reflected when

$$f_{pe}(x_c) = f, \tag{2.143}$$

and the cutoff density layer is

$$n_c = n_e(x_c) = 4\pi^2\frac{\varepsilon_0 m_e}{e^2}f^2 \underbrace{= \alpha_0^{-1}f^2}_{\alpha_0=e^2/(4\pi^2\varepsilon_0 m_e)} \simeq \frac{f^2}{80.6164}\ \ [\mathrm{m}^{-3}]. \tag{2.144}$$

If $x_c(f)$ is known in the $0-F$ range, the density profile $[x_c(f), n_e(f)]$ is obtained. Dividing equation 2.142 by $\frac{4\pi}{c}$ and taking the derivative with respect to the frequency $f$, we obtain

$$\frac{c}{4\pi}\frac{\mathrm{d}\varphi}{\mathrm{d}f} = \frac{\mathrm{d}x_c}{\mathrm{d}f}\underbrace{\sqrt{f^2 - f_{pe}^2(x_c)}}_{f=f_{pe}(x_c)\rightarrow\sqrt{f^2-f_{pe}^2}=0} + \int_{x_0}^{x_c(f)}\frac{f}{\sqrt{f^2 - f_{pe}^2(x)}}dx = \int_{x_0}^{x_c(f)}\frac{f}{\sqrt{f^2 - f_{pe}^2(x)}}dx \tag{2.145}$$

Multiplying by $(F^2 - f^2)^{-\frac{1}{2}}$ and integrating $\int_0^F$ the both sides,

$$\int_0^F \frac{c}{4\pi}\frac{\mathrm{d}\varphi}{\mathrm{d}f}\frac{1}{\sqrt{F^2 - f^2}}df = \int_0^F\int_{x_0}^{x_c(f)}\frac{f}{\sqrt{f^2 - f_{pe}^2(x)}}\frac{1}{\sqrt{F^2 - f^2}}dxdf. \tag{2.146}$$

Assuming a monotonic density, the integration order can be changed,

$$\begin{aligned}\int_0^F\int_{x_0}^{x_c(f)}\frac{f}{\sqrt{f^2 - f_{pe}^2(x)}}\frac{1}{\sqrt{F^2 - f^2}}dxdf &= \int_{x_0}^{x_c(F)}\int_{f_{pe}(x)}^{F}\frac{f}{\sqrt{f^2 - f_{pe}^2(x)}}\frac{1}{\sqrt{F^2 - f^2}}dfdx \\ &= \int_{x_0}^{x_c(F)}\int_{u=0}^{\sqrt{u=F^2-f_{pe}(x)^2}}\frac{1}{\sqrt{F^2 - f_{pe}^2(x) - u^2}}dudx \\ &= \frac{\pi}{2}[x_c(F) - x_0]\end{aligned} \tag{2.147}$$

The change of integration order of the right side of the first line is represented in figure 2.6 (left). The second line is obtained changing the frequency coordinates to $f = (u^2 + f_{pe}^2)^{1/2}$. Comparing the last line with the first side of equation 2.146, the cutoff position is

$$x_c(F) = x_0 + \frac{c}{2\pi^2}\int_0^F\frac{\mathrm{d}\varphi}{\mathrm{d}f}\frac{1}{\sqrt{F^2 - f^2}}df, \tag{2.148}$$

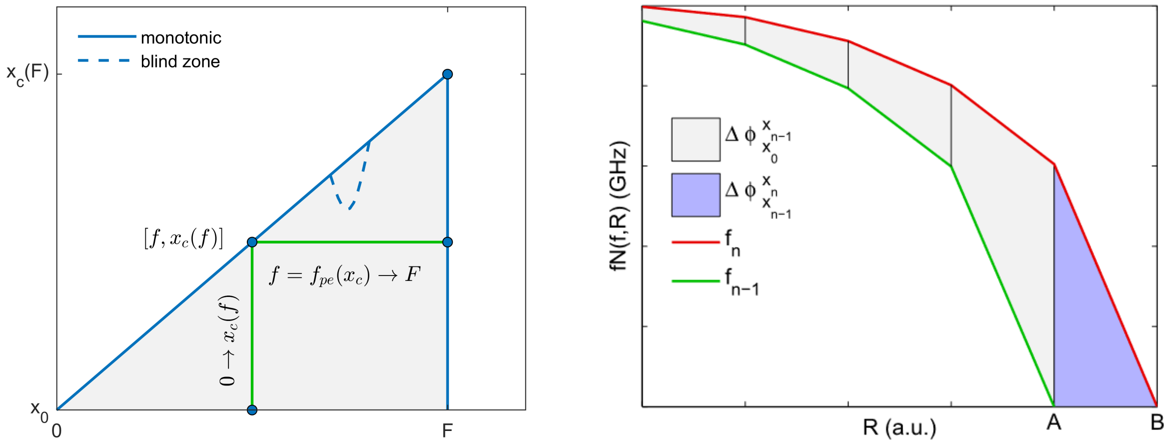

Figure 2.6: Illustration of the integration zone and change of integration order of equation 2.147 (left). Representation of th Bottollier-Curtet iterative method for inversion of the X mode [152] (right)

where $x_0$ is the initial position. This is known as the O-mode Abel inversion. The assumption of monotonic density profile (plasma frequency) is an essential step in this derivation (see figure 2.6, left). If the density profile is a monotonic function, all the density layers before the plasma center where the wave is not absorbed are accessible. In the regions where the monotony is not verified, the propagation stills possible if it satisfies the conditions. However, the reflection does not occur in these layers, the associated probing frequencies are reflected before. Since finding the density profile by sweeping the probing frequency requires reflection in the target layers, the density profiles of these regions are not accessible. The result can be, however, approximated, under small amplitudes of density negative variation. And its effect on the final result is weaker as the frequency increases. The regions where the monotony is not verified are called the blind zones.

The analytical inversion of the X mode is not possible due to its complicated dispersion relation (see equation 2.67) and a numerical technique need to be implemented to find the position of the reflecting layer. The Bottollier-Curtet iterative method assumes a linear refractive index profile between the known positions [153], according to figure 2.6 (right). The area under the refractive index in the last step is calculated by the area of a right triangle. The phase-shift corresponding to this zone is $\Delta\varphi_{x_{n-1}}^{x_n} = W(2\pi f_n/c)N(f_n, x_{n-1}) \times (x_n - x_{n-1})$, where $W = 1/2$. The position of the cutoff is

$$x_n = x_{n-1} + \frac{c\Delta\varphi_{x_{n-1}}^{x_n}}{W2\pi f_n N(f_n, x_{n-1})} \tag{2.149}$$

The $\Delta\varphi_{x_{n-1}}^{x_n}$ term can be written as

$$\Delta\varphi_{x_{n-1}}^{x_n} = \Delta\varphi_{f_{n-1}}^{f_n} - \left[\varphi_{x_0}^{x_{n-1}}(f) - \varphi_{x_0}^{x_{n-1}}(f-1)\right], \tag{2.150}$$

being $\Delta\varphi_{f_{n-1}}^{f_n}$ experimentally measured and $\left[\varphi_{x_0}^{x_{n-1}}(f) - \varphi_{x_0}^{x_{n-1}}(f-1)\right]$ numerically computed. It was later proposed that a modification of $W = 1/2$ to $W = 2/3$ could improve the convergence of the method [154]. In [152] different integration shapes (parabolic, $x^a$) are studied and compared with the Bottollier-Curtet method. The Bottoloier-Curtet method can be applied for O-mode, and also with the possibility reconstruct blind areas [155].

### Accessibility in tokamaks

In a tokamak or other magnetic fusion machine, the characteristic cutoff and absorption frequencies of each mode vary with the position in the line of view. The wave propagates while no absorptions and cutoffs exist locally. This results in intrinsic accessibility regions that limit the measurements [112]. The identification of the accessibility zones is done by plotting the cutoff and absorption frequencies as function of the line of view position and evaluate the intersection with the lines of constant frequency. Figure 2.8 shows the characteristic accessibility diagram for a tokamak with a DEMO-like plasma.

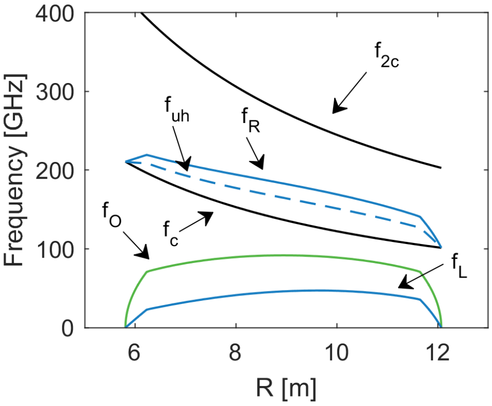

Figure 2.7: Accessibility diagram on the equatorial plane of an DEMO-like plasma. O mode: $f_O$; X-mode: $f_R$, $f_L$, $f_{uh}$. Cyclotron absorption frequencies: $f_c$ and $f_{c2}$.

The O-mode refractive index does not depend on the magnetic field. The propagation only requires that the probing wave frequency is above the plasma frequency, proportional to the square root of the electron density (equation 2.66). The maximum probing frequency should be below the harmonics of the electron cyclotron resonances, otherwise the wave is absorbed (equation 1.44). The magnetic field varies with $1/R$, giving in general to the LFS a lower accessibility than the HFS. Another important aspect of the O-mode is that the Abel integral (see equation 2.148) requires in principle the integration in the $0 - F$ range. Technically, this is difficult to achieve experimentally, since there is no microwave generators that can go from 0 to 100 GHz, although we can use a combination of multiple generators. Another difficulty is to transport the electromagnetic waves to the vacuum vessel in waveguides (see section 2.3.4). Besides that, the condition $\lambda > \lambda_D$ should be valid. This problem is solved using an initialization method, introducing some error in the measurements. This aspect is covered in the next topic.

The X-mode cutoffs and absorptions depend on the magnetic field. The Lower cutoff region has better accessibility that the O-mode since the cutoff is below the plasma frequency and the upper hybrid resonance is above the cyclotron absorption. However it is accessible directly only from the high field side and the wave has to cross before the absorption layer. Similarly to the O-mode, it needs to be initialized due to the fact the probing frequencies start in zero. The upper cutoff region is above the first harmonic of the cyclotron resonance and above the upper hybrid resonance, $\omega_L < \omega_{UH} < \omega_R$. However, in some cases, the second harmonic of the cyclotron resonance can limit the access, especially due to the relativistic down shift. Since the upper cutoff region depends on the magnetic field, the measurements of the layers with very low densities are possible, which is an advantage experimentally. This requires higher probing frequencies when comparing to the O-mode or the lower cutoff, above the cyclotron frequency.

### Initialization

In the O-mode and in the lower-cutoff of the X-mode, the frequency is swept in the range $0 - F$. The phase derivative must be initialized from 0 to $F_i$ (initialization frequency or first probing frequency), which is usually the initial frequency of the first band. This means that the phase derivative used to obtain the density profile is given by a piecewise function,

$$\frac{\partial\varphi}{\partial f} = \begin{cases} \frac{\partial\varphi_i}{\partial f} & \text{if } f < F_i \\ \frac{\partial\varphi_m}{\partial f} & \text{if } f > F_i, \end{cases} \tag{2.151}$$

where $\partial\varphi_i/\partial f$ is the initializing function and $\partial\varphi_m/\partial f$ the measured phase derivative [156]. In this case, the O-mode inversion becomes

$$\begin{aligned} x_c(F) &= \frac{c}{2\pi^2}\int_0^F \frac{\partial\varphi}{\partial f}\frac{1}{\sqrt{F^2-f^2}}df \\ &= \frac{c}{2\pi^2}\int_0^{F_i} \frac{\partial\varphi_i}{\partial f}\frac{1}{\sqrt{F^2-f^2}}df + \frac{c}{2\pi^2}\int_{F_i}^{F} \frac{\partial\varphi_m}{\partial f}\frac{1}{\sqrt{F^2-f^2}}df \end{aligned} \tag{2.152}$$

This results in a contribution of the initialization function to the measurement error, depending on the difference between the initialization function and the real phase derivative. The contribution of the first term, decreases as $F$ is greater than $F_i$. There are basically three different ways of initializing a phase derivative profile [157]. The first possibility is to use data from other diagnostic. A second option is the use of data from the X-mode density profile reconstruction. The last option is the use of a physical model for the phase derivative, as it is proposed in [158]. Assuming a density profile in the form of equation 2.101 for the frequencies below $F_i$, the phase derivative is directly calculated from equation 2.102. The initialization profile is assumed to be in the form

$$\frac{\partial\varphi}{\partial f} = \frac{4\pi^{3/2}\Gamma\left(\frac{2}{s}\right)(x_M - x_0)}{x\Gamma\left(\frac{2}{s}+\frac{1}{2}\right)}\left(\frac{f}{f_M}\right)^{2/s} \rightarrow \frac{\partial\varphi}{\partial f} = A\left(\frac{f}{F_i}\right)^{2/s}, \tag{2.153}$$

where the $A$ and $s$ parameters are adjusted according the measured data. If the initial plasma position $x_p$ is known/estimated, a term of $4\pi(x_p - x_a)/c$ can be added to equation 2.153, contributing to reduce the error.

### Frequency sweeping effects

Due to the conservation of the electromagnetic flux, the sweeping rate of a microwave source may induce amplitude variations in the probing signals [159]. For a sweeping rate of $\partial\varphi/\partial t$, the amplitude of the electric field as function of time is

$$E(t) = E_0\left[1 + \frac{\partial\tau}{\partial t}\right]^{1/2} = E_0\left[1 + \frac{1}{2\pi}\frac{\partial}{\partial t}\left(\frac{\partial\varphi}{\partial t}\right)\right]^{1/2} \tag{2.154}$$

where $E_0$ is the initial amplitude. For typical tokamak plasma parameters this effect may have a significative impact for frequency sweep rates greater than 300 GHz/$\mu$s for the O-mode and greater than 100 GHz/$\mu$s for the X-mode. In the other hand, sweeping rates need to be faster than the characteristic velocities of propagation of the density perturbations, in the order of the acoustic velocity, $c_s$. For the typical values, $c_s \sim 10^3 ms^{-1}$, a frequency range $\Delta f$ of 100 GHz and a plasma displacement of $d_p \sim 1$ cm, the lower sweeping rates must be approximately $(c_s\Delta f)/(2d_p) \sim 5$ GHz/$\mu$s [93].

### Plasma position reflectometry

In this work the DEMO plasma position reflectometry system is studied. As described in section 1.4.2, plasma position reflectometry (PPR) is just an extension to the conventional sweeping frequency reflectometry for density profile measurements. Instead of having a density profile as output, the separatrix density is provided as additional input or identified directly in the density profile with physical considerations and the result of the measurement is the position of the separatrix. From the point of view of the hardware techniques, there is no difference to the conventional reflectometry. The last section of this chapter is dedicated to the study of plasma position reflectometry systems, which is the theoretical input to the other chapters of this work.

## 2.3.2 Other reflectometry types

Apart from conventional reflectometry (density profile measurements), reflectometry is widely used to measure other parameters such as the plasma position, the density fluctuations, the plasma position, turbulence spectrum or the velocity of the fluctuations [160]. The classification of each type depends on the physical principle that relates the initial and final state of the probing wave with the plasma parameters.

### Fixed frequency reflectometry

A temporal variation of the phase $\varphi$ can result from the variation of the probing frequency or of the optical path length,

$$\frac{\partial \varphi}{\partial t} = \frac{4\pi}{c}\left(\frac{\partial f}{\partial t}\right)\int_{x_p}^{x_c} N(f,x)dx + \frac{4\pi}{c} f \frac{\partial}{\partial t}\left[\int_{x_p}^{x_c} N(f,x)dx\right]. \tag{2.155}$$

If the cutoff density layer is displaced inwards or outwards the plasma, the evolution of the phase shift will vary according to this movement. By fixing the frequency of the probing wave, the phase variations of the reflected signal can be used to measure the cutoff position changes and the turbulent fluctuations of the plasma.

### Correlation reflectometry

Correlation reflectometry uses the correlation of different measurements to determine plasma properties. In the radial correlation reflectometry (RCR) signals with frequencies $f_0$ and $f_0 + \Delta f$ probe the plasma simultaneously at the same line of view. $f_0$ is called the reference frequency, and $\Delta f$ is swept. If the distance between the reflection of each wave is small enough, it is possible to measure the radial correlation length $l_r$ of the density fluctuations from cross-correlation analysis [121, 161, 162]. Alternatively, signals can be measured at the same reflection layer, but from different poloidally or toroidally positions/antennas [163, 164]. If the density fluctuations propagate in poloidal direction, the delay between signals from different measured volumes allow to measure its velocity. Using several antennas distributed poloidally and toroidally, it is possible to measure the perpendicular correlation length, the decorrelation time and the propagation velocity.

### Density fluctuations measurements with different type reflectometers

Another application of sweep frequency reflectometry is the measurement of the density fluctuations spectrum and amplitude [165, 166]. When the frequency is swept over an extended range, a set of perturbed phases is measured, corresponding to the set of cutoff positions of each frequency. The incident waves are scattered at different radial positions according to the Bragg rule. It can be shown that for the O-mode there is a relation between the spectra of the phase fluctuations $S_\varphi(k)$ and of the density fluctuations $S_n(k)$:

$$S_\varphi(k) = \pi k_0^2 \frac{L_n}{k} \frac{S_n(k)}{n_c^2}. \tag{2.156}$$

Consequently, the measurement of the phase spectrum leads to the knowledge of the turbulence spectrum. The X-mode is more complicated due to the dispersion relation. A numerical transfer function $f_t(k)$ computed with simulations is typically used to connect the phase fluctuations spectrum to the density fluctuations spectrum as follows $S_\varphi(k) = f_t(k)(S_n(k)/n_c^2)$. The root mean square value is then calculated with the the Parseval's theorem, $\Delta n(< r >)_{k_{min},k_{max}} = (1/N_p)\left[S_n(k_r, < r >)\right)^{1/2}$, so the RMS$(\delta n_e)/n_e$ level can be calculated.

### Doppler reflectometry

In Doppler reflectometry the probing beam is launched into the plasma at a tilt angle $\theta_0$ different from 0 and is scattered on the rough surface [105, 167, 66, 168]. A simple model of the Doppler reflectometry principle is illustrated in figure 2.6.

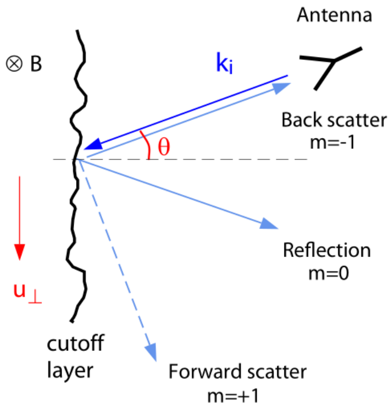

Figure 2.8: Doppler reflectometry principle [168].

Part of the wave that fulfills the Bragg condition $k_\perp = 2k_0 \sin\theta_0$ is backscattered at the cutoff. $k_\perp$ is selected by the probing beam frequency or by the tilt angle $\theta_0$. Since the fluctuations are moving, the back-scattered signal frequency is Doppler shifted by $\omega_D = \mathbf{k}\cdot\mathbf{v}$ (see equation 2.132). It is known that fluctuations stretch out in the field lines, so $k_\| << k_\perp$. Furthermore, the radial term can be neglected due $u_r << u_\perp$. The final frequency shift is

$$f_D = v_\perp \left(\frac{2}{\lambda_0}\right) \sin\theta_0. \tag{2.157}$$

The perpendicular velocity is composed by two components, the $E \times B$ drift and the velocity of the turbulent structures, $v_\perp(k_\perp) = E_r/B + v_{trb}(k_\perp)$. In real plasmas, where the beam experiences a strong refraction due to not propagate parallel to the density gradient, a ray or beam tracing codes are required to determine the cutoff layer position and incident wavenumber [169]. After looking at the different reflectometry types it becomes to detail the different pieces constituting a reflectometer and the associated data analysis processes.

### 2.3.3 Reflectometer set-up and data aquisition

A reflectometer consists in the device with all the physical components necessary to make a reflectometry measurement. A generic reflectometer is composed by:

- Microwave sources - the microwave sources are responsible for generating the signal to probe the plasma with the desired frequency range.
- Transmission lines - the transmission lines are used to guide electromagnetic waves from one place to another. They guide the electromagnetic signals from the source to the probing location, from the detecting antenna to the signal detecting region or between different microwave components of the system.
- Antennas - the antennas are the interface between the reflectometer and the plasma that capture and/or transmit the microwaves.
- Detector - the detector is responsible for converting the electromagnetic signal that comes from the plasma into a voltage signal that can be converted to a digital signal and analyzed to deduce the plasma properties.
- Other microwave components - additional microwave components such as tapers, directional couplers, reference pins are required to make the necessary operations to the electromagnetic signals before being detected.

Similarly to a radar, reflectometers can be monostatic, bi-static or multistatic, depending on the number of antennas involved in the measurement. In the monostatic reflectometers, the emitting antenna is also used to detect the reflected signal. In the bi-static system, one antenna is used to emit and other to detect it. In a multistatic reflectometer, different antennas are used to detect the signal. In some systems, there are multiple emitting antennas, each one emitting different bands. Single antenna (monostatic) has advantages over the double antenna (bi-static) arrangement because the signal reception is optimized for the perpendicular propagation and the space needed for emission/reception is minimized.

The general scheme of a bi-static reflectometer setup for phase detection is shown in figure 2.9.

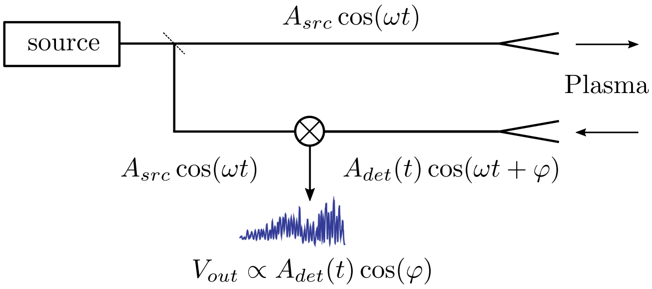

Figure 2.9: Bi-static homodyne detection scheme. Adapted from [82].

The microwave circuit mixes the reference signal with the signal coming from the plasma. The reference signal is given by

$$S_{src}(t) = A_{src}\cos[\omega t]. \qquad (2.158)$$

and the signal reflected from the plasma by

$$S_{det}(t) = A_{det}(t)\cos[\omega t + \phi(t)]. \tag{2.159}$$

The mixed signal is

$$S_{mix}(t) = S_{src}(t)S_{det}(t) = \frac{1}{2}A_{src}A_{det}(t)\cos[\phi(t)] + \frac{1}{2}A_{src}A_{det}(t)\cos[2\omega t + \phi(t)]. \tag{2.160}$$

By applying a low-pass filter (LPF) in the mixed signal, a component proportional to $\cos[\phi(t)]$ is obtained,

$$S(t) = S_{mix} * h_{LP}(t) = \frac{1}{2}A_{src}A_{det}(t)\cos[\phi(t)]. \tag{2.161}$$

This is known as homodyne detection. In practice, the final expression will depend on the concrete microwave circuit and on the detector input to output signal behavior. For example, using a silicon low barrier Schottky Diode working in the square-law regime (output voltage is proportional to the power of the input voltage squared) as a detector, the low frequency component of the output signal is [157]

$$V_{out} = \frac{S_{src}^2(t) + S_{det}^2(t)}{2} + S_{src}(t)S_{det}(t)\cos[\phi(t)]. \tag{2.162}$$

The measure of the absolute phase shift is possible with the in-phased and quadrature detection scheme (I/Q detection), represented in figure 2.10.

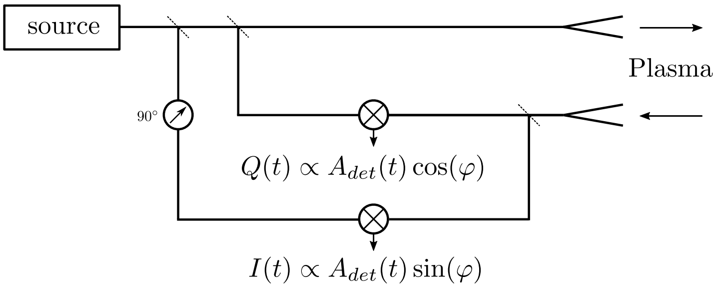

Figure 2.10: The I/Q detection scheme. Adapted from [82].

This scheme introduces a third signal corresponding to $S_{src}(t)$ or $S_{det}(t)$ shifted 90°. There are different ways of combine the three signals to obtain the phase and the amplitude. For example, if the new reference signal is

$$S_{src}^{\pi/2}(t) = A_{src}\cos[\omega t + \pi/2] = A_{src}\sin[\omega t], \tag{2.163}$$

the I/Q signals are

$$I(t) = S_{det}(t)S_{src}^{\pi/2}(t) \tag{2.164}$$
$$Q(t) = S_{det}(t)S_{src}(t), \tag{2.165}$$

which filtered with a LPF become

$$Q(t) = \frac{1}{2}A_{src}A_{det}(t)\cos[\varphi(t)] \tag{2.166}$$

$$I(t) = \frac{1}{2}A_{src}A_{det}(t)\sin[\varphi(t)]. \tag{2.167}$$

From this system of equations the phase and the amplitude are directly deduced from

$$\varphi(t) = \arctan\left(\frac{Q(t)}{I(t)}\right) \tag{2.168}$$

$$A_{det}(t) = 2\sqrt{I^2(t) + Q^2(t)}. \tag{2.169}$$

This system is limited due to the fact that experimentally the phase shift of $\pi/2$ can be done to a limited number of frequencies, so the operation in a frequency band is not possible. To increase the dynamic range of the reflectometers and the signal noise ratio, the heterodyne detection techniques have been used [157]. In the heterodyne detection scheme the signals to be detected are mixed with a signal from a local oscillator (LO) operating at a slightly different stable frequency $\omega_{LO}$. This shifts the high frequency band to a lower one $\omega_{IF} = \omega_{LO} - \omega$, keeping the relevant spectral information. The signal can then be easily detected and the effect of the frequency shift removed later in the data analysis. The detailed description of the microwave circuits used in reflectometry is far behind this dissertation. The reader can find the principal microwave circuits and engineering aspects of reflectometry in [47, 157, 170].

On important aspect in fast sweeping reflectometry is reducing the sweeping time as much as possible, so the frozen plasma approximation is valid. Several hardware techniques such as ultra-fast frequency sweeping [171, 172], pulse compression [173, 174], differential phase reflectometry [175], amplitude modulation reflectometry [176, 177] or short pulse reflectometry [178, 179] have been developed and implemented with this propose. The most used technique is the FMCW (Frequency Modulated Continuous Wave) broadband reflectometry. In this technique the frequency changes continuously in a frequency range $[F_{min}, F_{max}]$. The instantaneous frequency is typically given by a linear time dependence in the form

$$\omega(t) = 2\pi\left[F_{min} + \frac{F_{max} - F_{min}}{\Delta t}t\right] = 2\pi k_w t, \tag{2.170}$$

where $\Delta t$ is the sweeping time and $k_w$ is the sweeping rate. The probing signal (equation 2.158) is

$$S_{src}(t) = A_{src}\cos[\omega(t)t] = A_{src}\cos\left[2\pi F_{min}t + 2\pi\frac{F_{max} - F_{min}}{\Delta t}t^2\right] \tag{2.171}$$

and the detected signal (equation 2.159) becomes

$$S_{det}(t) = A_{det}(t)\cos[\omega(t)t + \varphi(t)]. \tag{2.172}$$

The stationary state of each frequency is assumed be be achieved fastly when compared with the sweeping time, so there is a correspondence approximately direct between the time of measurement and the time of the emission. Thus is possible associate a given phase and group delay with the respective frequency.

The first FM-CW broadband profiles were obtained in the TFR tokamak with sweeping rates in the order of 5 ms [100]. Later, reflectometry systems with lower sweeping rates were implemented in the ASDEX (2ms, O-mode) [180, 181], Tore Supra (1ms, O-mode) [182, 183], Petula-B (200 $\mu$s, X-mode) [153], TJ-1 (850 $\mu$s, X-mode) [184] and DIII-D (500 $\mu$s, X-mode) [185] tokamaks. All these systems had limitations due to the effect of fluctuations changes during the sweeping time. As microwave oscillator technology improved, FM-CW reflectometry sweeping times have been reduced from the order of ms down to $\mu$s. In 1993 the first ultra-fast frequency system with sweeping rates in the order of 10-50 $\mu$s has been developed and implemented in ASDEX [171, 186], allowing the extraction of cleaner phase derivative profiles ($< 10$ $\mu$s). In present day devices and in the expected ITER and DEMO fusion plasmas, the probing frequency covers the standard bands K (18-26.5 GHz), Ka (26.5-40 GHz), Q (33-50 GHz), V (50-75 GHz), W (75-110 GHz) and D (110-170 GHz) with sweeping times in the order of 10 $\mu$s [157, 82, 187]. The fast sweep sources are built using hyperabrupt tuned oscillators (HTO) and programmable voltage ramp generators [188]. Depending on the necessary frequency range, a broadband sweepable source or separate frequency sources can be used.

#### Detector effect

The detected analogical signal is acquired with fast data acquisition systems. The hardware must be capable of measuring during the fast sweeping times and perform the data analysis algorithms to signal at the measurement rate of the reflectometer. The density resolution of the reflectometer depends on the frequency resolution of the acquisition,

$$\Delta F = k_w \frac{1}{f_s} \tag{2.173}$$

where $f_s$ is the sampling frequency. In O-mode, the cutoff density depends only on the frequency, so the resolution is directly calculated ($\Delta n = 2f\Delta F/\alpha_0$). In X-mode, the resolution depends on the magnetic field.

### 2.3.4 The in-vessel microwave components

In a fusion reactor, the access to the vacuum vessel is done thought specific ports. The probing signals are conducted thought waveguides that can have several meters until the antennas, where the electromagnetic field is emitted to the plasma with a certain radiation pattern. The reflected signal is captured by the receiving antenna and the waveguides conduct the reflected waves to the detecting region. The other elements of the reflectometer are located far away from the first wall, where there are conditions to implement the sources, the detectors and the data acquisition systems. The antennas and the waveguides are the in-vessel microwave components of the reflectometer. As the other in-vessel components of the machine, they experience space restrictions and adverse fusion conditions, requiring specific materials that can hold these temperatures. Due to the spacial constraints, the mono-static systems are preferable over the bistatic/multistatic. We make a brief overview of their principal characteristics.

#### Waveguides

In microwave engineering, transmission lines are structures designed to conduct electromagnetic energy from one place to another [111]. These structures use the principle of reflection of the electromagnetic fields in the interfaces of different materials to redirect the energy to the desired direction. Depending on their constitution and geometry, they can support three different type of waves. The transverse electromagnetic (TEM) waves do not have neither electric nor magnetic field in the direction of propagation. These modes require at least two separated conductors to propagate. The transverse electric

(TE) waves have no electric field in the direction of propagation. The transverse magnetic (TM) waves have no magnetic field in the direction of propagation. A fourth type of waves, known as hybrid mode, consists in Non-zero electric and magnetic fields in the direction of propagation, corresponding to the simultaneous propagation of the TE and TM modes.

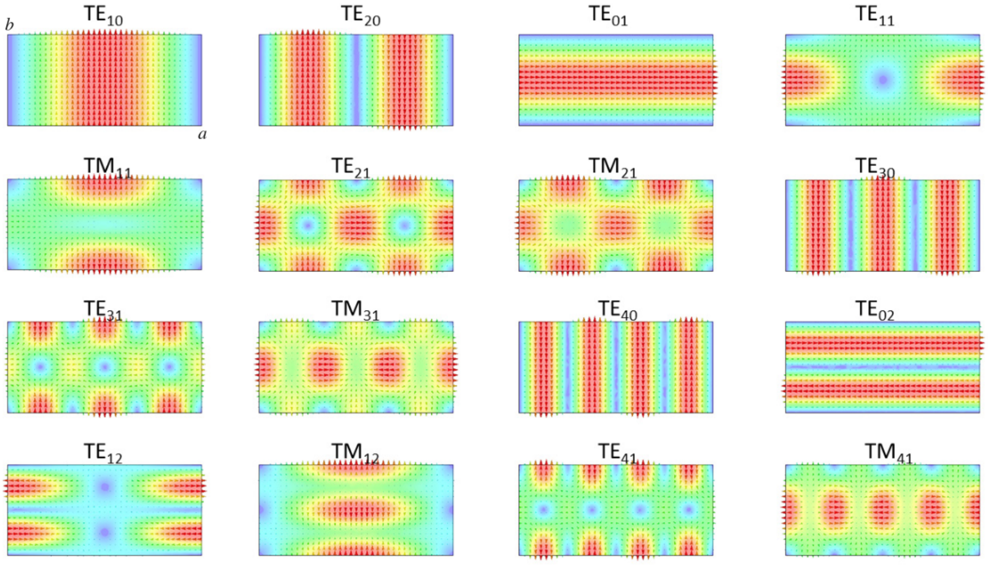

Figure 2.11: Representation of the transverse electric field of the first TE and TM modes of a rectangular hollow waveguide. Adapted from [189].

Waveguides are transmission lines constituted only by one conductor, typically hollow. For this reason, they only support TE and TM waves. They are characterized by a cross section, typically rectangular or circular, constant in the direction of propagation. The conductor material attenuates the electric field, keeping the energy inside the metallic structure. Due to their simplicity, robustness and ability to carry high power waves of high frequency, they are the ideal solution to transport the microwave signals in fusion devices. Due to the boundary conditions, only some configurations of the electromagnetic fields are allowed to propagate, known as waveguide modes. These components represent the different solutions of the Helmholtz equation in the respective waveguide geometry. Assuming propagation in the $z$ direction, the electromagnetic field of each mode is written in the form $f(x,y)e^{j(\beta z-\omega t)}$, where $f(x,y)$ depends on the field component and on the waveguide geometry. $\beta=\sqrt{k_c^2-k_0^2}$ is the propagation constant, where $k_c$ depends on the waveguide cross section geometry [111]. This results in minimum necessary frequencies for propagation ($\beta>0$), defined by $f_c=(c/2\pi)k_c$. The wave propagates if $f>f_c$. Figure 2.11 shows the the transverse electric field of the first TE and TM modes of a ideal rectangular hollow characterized by a width $a$ and height $b$, with $a>b$. The cutoff frequencies of the rectangular waveguide are given by

$$f_c^{mn}=\frac{c}{2\pi}\sqrt{\left(\frac{m\pi}{a}\right)^2+\left(\frac{n\pi}{b}\right)^2}, \tag{2.174}$$

where $m$ and $n$ are the integers that label each mode and appear on the field expressions indicating the number of half-waves that fit transversely in the width $a$ and height $b$ of the waveguide. This expression is valid for the TE and TM waves, however in TM waves the modes characterized by $m=0$ or $n=0$ are not supported due to the fact that the electric field component in the propagation direction vanishes. The fundamental mode of a waveguide is the mode that has the lowest cutoff frequency. Due to the simple structure of the fundamental mode (see figure 2.174) with the power localized at one region, the fundamental mode is typically used to at the emitting antenna and to detect the received signal. Depending if the reflectometer is O or X mode, the waveguide orientation and the antenna geometry are chosen to fulfill the electric field requirements. The waveguide dimension determines the minimum frequency $F_i$ that is possible to send to the vacuum chamber, limiting the frequency sweep range. The waveguide is fundamental if the only the fundamental mode can propagate in the respective frequency range for which it was designed. If not, the waveguide is said to be oversized.

In real waveguides, the wave suffers attenuation due to the finite conductivity of the wall. The amplitude of the wave decreases proportionally to $e^{-\alpha_c}$. The attenuation constant $\alpha_c$ of the fundamental mode ($\mathrm{TE}_{10}$) of a rectangular waveguide is

$$\alpha_c^{10} = \frac{R_s}{a^3 b \beta k \eta}(2b\pi^2 + a^3 k^2), \tag{2.175}$$

where $R_s$ is the is the wall surface resistance and $\eta = \sqrt{\mu_0/\varepsilon_0}$ the vacuum wave impedance. The implementation of waveguides in the vacuum-vessel of a fusion reactor faces several problems. Firstly, since the power must be transported to locations far away from the plasma, the waveguide dimensions are increased to reduce the attenuation (see equation 2.175). However, due to the spacial constraints, this solution is limited. Furthermore, since the mono-static systems are preferable, a unique waveguide transport waves of all the probing frequency range. The solution often implies that the in-vessel waveguides are oversized. The wave is typically excited in a fundamental waveguide and then adapted to the oversized dimensions with a taper. Even that the probing wave corresponds to the fundamental mode, the electric field of the reflected wave can excite high order modes when is adapted from the receiving antenna to the oversized waveguide. Another taper is used to adapt the reflected wave to a fundamental waveguide where is can be detected. One of the main problems that occurs during the propagation in oversized waveguides is the mode conversion in the waveguide bends that exist due to the spatial constraints. When the fundamental mode propagates inside the bend, different modes can be excited, resulting in losses that can be significant. Fortunately, by choosing different functions of curvature the bends can be optimized [190, 84, 191].

### Antennas

The antennas are the interface between the reflectometer and the plasma. The emitting antenna redirects the energy from the input waveguide mode to the desired probing location and the receiving antenna tapers the reflected signal from the plasma the waveguide, so it can be conducted to the detection zone. Each emitting antenna is characterized by a radiation pattern $F(\theta, \phi)$ that represents the directional (angular) dependence of the emitted electric field amplitude, typically in spherical coordinates. Most antennas show a pattern of lobes (local maximums of radiation), and the one where the most power is concentrated is used to probe the plasma. The secondary lobes are in general emitted to different directions, being reflected to different locations. At the far-field condition (Fraunhofer region), the field distribution is independent of the distance from the antenna. This distance $R$ corresponds to the condition

$$R > \frac{2D^2}{\lambda} \quad (\text{if } D > \lambda), \tag{2.176}$$

where $D$ is the overall dimension of the antenna and $\lambda$ the wavelength in vacuum. This is the condition of the probing zone, in order to avoid phase interference.

From the theory of radiation of aperture antennas, the beam width of the main lobe is of the order of $2\lambda/D$. This means that the beam width at the beginning of the Fraunhofer region is $BW \sim (2D^2/\lambda)\tan(2\lambda/D) \simeq 4D$. Note that for $\lambda < D$, $\tan(2\lambda/D) \simeq 2\lambda/D$. If $D$ is too small, the beam cross-section would be smaller at the beginning of the probing zone, but quickly broaden as the wave propagates into the plasma, decreasing the spatial resolution. If $D$ is too high, the antenna should be placed far away from the plasma, which is not possible in the context of a fusion experiment. What is gained by increasing $D$ to decrease the beam width is lost because the antenna must be placed farther away.

Horn antennas of different forms have been used in microwave reflectometry and other microwave diagnostics due to its simplicity in construction, ease of excitation, versatility, gain, performance and robustness. They consist in a simple hollow pipe that is tapered to a larger opening [192]. The geometry of its opening determines the electromagnetic performance, depending on the input waveguide mode. One fundamental parameter of the antenna is the gain $G(\theta, \phi)$, which describes how well the antenna converts input power into output power in a specified direction. Reflectometry and other microwave diagnostics require high gain antennas and axial symmetric beams since high space resolution in measurements is required. Figure 2.12 shows the representation of one pyramidal horn antenna. The design of a pyramidal Horn antenna, involves finding the $(a_1, b_1, \rho_e, \rho_h, P_E, P_h)$ dimensions determined by $a$,$b$ and the desired gain $G_0 \simeq \frac{2\pi}{\lambda^2}\sqrt{3\lambda\rho_h}\sqrt{2\lambda\rho_e}$. This can be done by solving the pyramidal Horn antenna equation [192]. Nowadays, with the vast offer of microwave engineering software, the antennas are optimized numerically.

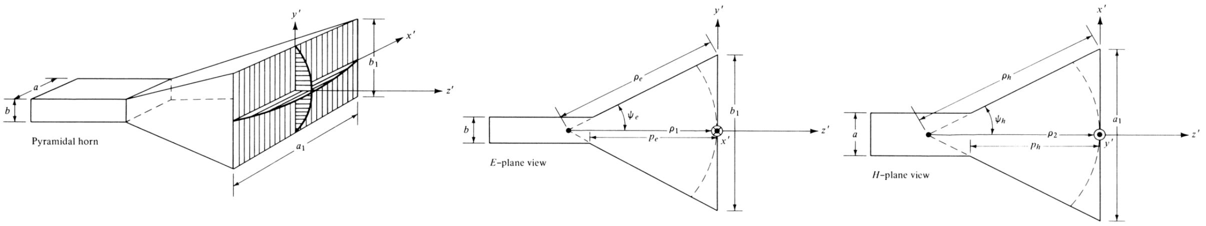

Figure 2.12: Pyramidal Horn geometry and dimensions [192].

A typical solution to reduce beam divergence is the use of focused antennas, which shifts the radiation characteristics of the Fraunhofer region of an antenna to a certain range around the focal length [193]. This solution has been adopted in some bands of the ASDEX-U O-mode reflectometer [157]. Since the focusing distance of each band is different, this implies the use of a different antenna per band, which is undesired a fusion machine. Recently, a frequency-independent horn antenna was designed for plasma positioning reflectometers [194].

One of the precautions to be taken into account in the reflectometer operation is the stray radiation that can eventually enter in the antennas and reach the detectors, leading to wrong measurements and causing damage to the reflectometer components. The plasma itself emits radiation in the electromagnetic spectrum, including in the microwave region. However the power density at the detected polarizations is typically lower than the probing beam, turning the measurement possible. If the radiation comes from the an external source as an ECRH heating system, the system must be protected [195]. In the case of a PPR, the probing frequencies are typically lower than the cyclotron frequency.

### 2.3.5 Signal processing techniques for profile measurements

Different methods have been developed to extract the group delay from the detected signals [196, 82, 197, 198]. When the phase is directly obtained by the detection method as in the I/Q signals, the time-delay is obtained by taking the time derivative of the phase and multiplying it by the inverse of the sweeping rate:

$$\tau_g = \frac{1}{2\pi}\frac{\partial\varphi}{\partial f} = \left(\frac{\partial f}{\partial t}\right)^{-1}\frac{\partial\varphi}{\partial t}. \tag{2.177}$$

The sweeping rate is known a priori, and the time derivative of the phase is directly calculated from the $\varphi(t)$ function. When the signals are proportional to $\cos(\varphi)$, as in the homodyne-detection scheme, the most common method to find the time-delay is compute the frequency distribution with a technique such as the sliding fast Fourier transform (SFFT). The time derivative of the phase is the instant frequency of the $\cos[\varphi(t)]$ term, corresponding to the instantaneous beating frequency, $f_B(t)$. The group delay is

$$\tau_g = \frac{\partial\varphi}{\partial\omega} = \frac{1}{2\varphi}\frac{\partial\phi}{dt}\left(\frac{\partial f}{\partial t}\right)^{-1} = \frac{1}{2\pi}\left(\frac{\partial f}{\partial t}\right)^{-1} f_B. \tag{2.178}$$

The standard spectral techniques use the main frequency of each Fourier transform to estimate the beating frequency (maximum peak technique).

#### Group delay calibration

Once the group-delay $\tau_m(f)$ is obtained, the component $\tau_c(f)$ that is correspondent to the propagation inside the microwave circuit is removed, so the inversion technique can be applied with respect to the reference point, typically at the antenna mouth or at the wall, if the antenna is placed inside a cavity. The corrected time delay is

$$\tau(f) = \tau_m(f) - \tau_c(f), \tag{2.179}$$

where $\tau_c(f) = \tau_{x_s\to x_a}(f) + \tau_{x_a\to x_d}(f)$ is the time-delay round-trip correspondent to the propagation in the microwave circuit (see equation 2.107). One of the ways to do this experimentally is place a metallic mirror at a known distance in front of the reflectometry antennas. The time delay is measured for different mirror positions to minimize the error of free space propagation. The propagation delay due to the distance between the antenna and the metallic mirror is removed from each measurement. The delays are then fit to the delay function,

$$\tau_c(f) = a + \frac{b}{\sqrt{1-\left(\frac{f_c}{f}\right)^2}}, \tag{2.180}$$

where $a$ and $b$ are the fit parameters. The delay function considers the propagation is mainly affected by the propagation in the waveguides. The velocity group in waveguides is (see equation 2.174)

$$v_g = \left[\frac{\partial\beta}{\partial\omega}\right]^{-1} = \frac{c}{k}\beta = c\sqrt{1-\left(\frac{f_c}{f}\right)^2}, \tag{2.181}$$

which suggest the time delay should be in the form $\tau_g \sim l/v_g$. Another aspect to have into account in the system calibration are the non linearities of the sweeping rate. Recently, a technique to monitor and re-calibrate in real-time the linearity of the frequency sweeps of FMCW reflectometers was developed [188].

### Finding the unperturbed time-delay round-trip

Alternatively to the maximum peak method, the beating frequency can be estimated with the first moment of the beating frequency,

$$f_b(t) = \frac{\int f S_h(t,f)df}{\int S_h(t,f)df}, \tag{2.182}$$

where $S$ is the spectrogram amplitude. These techniques work well for a low turbulence plasma, where the interference signal is essentially a mono-component signal with the energy concentrated at the beat frequency [82]. As the plasma perturbations increase, the signal suffers phase and amplitude modulations, and the main peak may not correspond to the unperturbed beat frequency. When the group delay is used as input for the inversion technique, the fluctuation term produces an error in the reconstructed density profile. Based on the principle that the unperturbed group delay profile should be a slow varying function, different techniques have been developed to find the unperturbed group delay $\tau_0$ [196]. One of the most used technique is the best path method. This method considers different local maximums of the discrete Fourier transform above a given threshold. Then it finds all the possible paths and selects the shortest one. A common practice before applying a reconstruction technique is to use multiple measurements and take the average before applying the beat frequency selection technique. This is known as the *burst-mode analysis*. Figure 2.13 shows an example of the average spectrogram of four consecutive sweeps where three methods to find the final group delay are compared (maximum peak: MP; the first moment: 1st M; best path: BP). The best path method gives the best choose of a slow varying unperturbed group velocity profile.

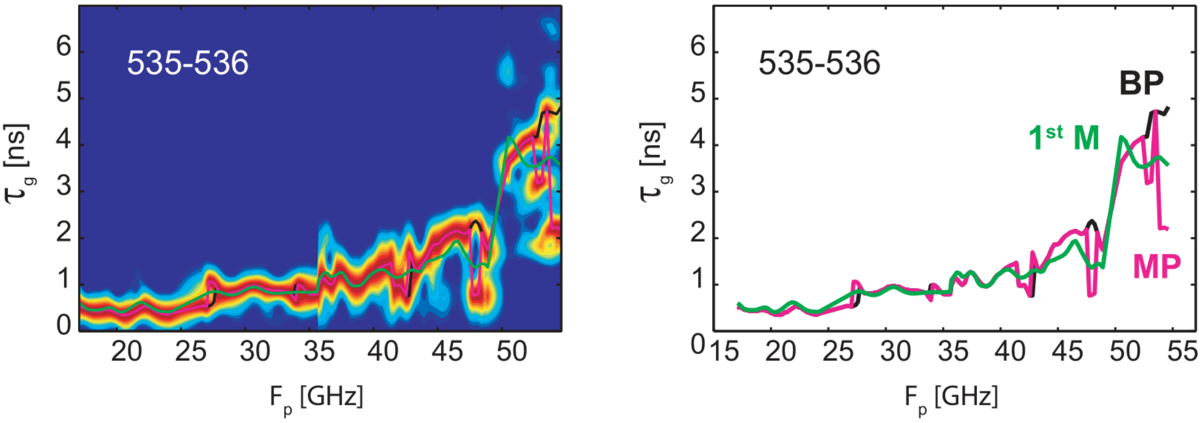

Figure 2.13: Example of spectrogram with the average of four consecutive measurements (maximum peak: MP; the first moment: 1st M; best path: BP) [82].

Understanding how minimize the effect of the group delay irregularities is an essential area of research in reflectometry. Artificial neural networks (NN) have been used in reflectometry signal analysis to obtain smooth density profile reconstructions [199, 82, 200, 170]. In [155] a new reconstruction scheme that uses a database with the perturbation shapes has been applied to density profiles with non-monotonic regions, improving the description of the density profiles. In the present days, the reconstruction techniques continues to be topic of research in reflectometry. After reviewing the principal topics of reflectometry, the PPR systems and the data processing methods are described with a generic formalism.

## 2.4 Plasma position reflectometry

### 2.4.1 Plasma position reflectometry systems

Plasma position reflectometry (PPR) uses the density profiles measured with fast-sweeping reflectometry to obtain the separatrix position. If the frequency associated with the separatrix layer $F_{sep}$ is known, the relative plasma position is given by

$$r_{sep} = r(F_{sep}), \tag{2.183}$$

where $r(F)$ is the measured position of the cutoff layer calculated with the inversion technique and $F_{sep}$ is the separatrix density (section 2.3). For O-mode reflectometry, the separatrix frequency $F_{sep}$ is (see equation 2.144)

$$F_{sep} = \sqrt{\alpha_0 n_{sep}} \simeq 8.9787\sqrt{n_{sep}[\mathrm{m}^{-3}]} \;\; [\mathrm{Hz}], \tag{2.184}$$

while for X-mode it depends on the magnetic field configuration. The separatrix density can be provided with the help of other diagnostic or directly in the density profile with physical considerations. Therefore, a position reflectometer consists technically in a conventional fast sweeping reflectometer, with some differences in the data analysis software. By measuring in different positions of the machine, it is possible to reconstruct the separatrix shape.

The principal application of PPR systems is the substitution or complement of the magnetic diagnostics in the future fusion machines. For this reason, the position reflectometers are preferable work in the O-mode, which is independent of the magnetic field. The principle of this technique has been demonstrated in ASDEX Upgrade at the high and low field side [82, 85, 86, 87]. A multi-reflectometers system to measure the plasma position and shape based purely in reflectometry was not tested in any experimental device and is, for now, just a concept. There are many questions regarding the measurement performance of such system and its stability under the perturbations of the plasma parameters that may occur during the discharge. The most important quantity to evaluate the measurement performance of a position reflectometer is the position error $e(F)$,

$$e(F) = r_m(F) - r_0(F), \tag{2.185}$$

also known as the measurement error. $r_0(F)$ is the position of the plasma layer that is being measured and $r_m$ is the measured position, resulting from the application of the algorithms in the detected signals. An ideal reflectometer corresponds to

$$e(F) = 0. \tag{2.186}$$

The measurement error is inherently inaccessible, since the propose of the diagnostic is to obtain an estimation of the real position, which is unknown a priori. It is assumed that if the conditions of validity of the reflectometry model are approximately valid, then $e(F) \simeq 0 \rightarrow r_m(F) \simeq r_0(F)$. In a system of reflectometers located at different positions of the machine and measuring different plasmas during the discharge, this condition may not be valid. The theoretical calculation of the error is in not possible, in general, due to the complexity of the description of 3D electromagnetic propagation in the plasma and in the detection setup. However, if the expected plasma is known, the error can be calculated with the help of numerical simulations. The plasma scenario is given a priori by the plasma modeling team, so the numerical simulations can be used to find the configurations with better measurement performance. This involves testing different poloidal views, antenna assemblies, emitting angles and plasma configurations and select the best solution, depending on the measurement and geometry requirements.

### 2.4.2 Description of multi reflectometers systems (MRS)

Due to the complexity associated with the high number of variables involved, the analysis of a PPR system, or, in general, of a multiple reflectometers system (MRS), requires the description of the important variables in a simplified way. For this reason, we propose a simple notation to describe the variables and the signals of a multiple reflectometer system and its dependencies. We refer to this notation as the multiple reflectometer systems notation (MRS notation). Each signal or variable $a$ used in the description of a reflectometer is written in the form

$$a^{\text{MRS indexes}}_{\text{variable label}}(\text{independent variables}). \tag{2.187}$$

The MRS indexes identify the reflectometer and other important variables of the system. Each index is numbered in the form $i = 1, ..., N_i$, where $N_i$ is the number of elements associated to the index $i$, dependent on the previous indexes. Thus the order of index is, in general, important. For example, if there are three indexes, $i, j$ and $k$, $N_i$ is independent since it is the first one, but $N_j(i)$ and $N_k(i, j)$ are functions of the previous index. If for some reason the index $k$ is independent, then $N_k(i, j) = N_k$. This should be implicit in the definition.

If the variable corresponds to the solution of a physical process described by a set of differential equations $f$ and by a set in input variables, we write

$$a^{\text{reflectometer indexes}}_{\text{variable label}}(\text{independent variables}) = f[\text{input variables of f of interest}], \tag{2.188}$$

The input variables of $f$ can be scalars, vectors, or other mathematical entity used in the description of the physical process. If the function is written with capital letter, this means the variable $a$ is calculated by a set of operations/algorithms applied to the signals and other inputs variables:

$$a^{\text{reflectometer indexes}}_{\text{variable label}}(\text{independent variables}) = F[\text{input variables of F of interest}], \tag{2.189}$$

This is also used if the variables are the output of a numerical code. In this case, the output is a scalar or a discrete function.

If a vector with all the elements associated to a given index $i$ is needed, the index is represented at the left side and the variable symbol becomes bold (usual notation for vector in the rest of this work):

$$a^i \to {}^i\boldsymbol{a} = [a^1, ..., a^{N_i}] \tag{2.190}$$

In this notation, it is implicit that $i$ is the index that distinguish the vector elements. This can also be written in a simplest form,

$$a^i \to \boldsymbol{a} = [a^1, ..., a^{N_i}] \tag{2.191}$$

In this case, by writing $\boldsymbol{a}$ it is necessary to know that previously the elements were labeled by $i$. If the variable is a vector the same notation is valid, but instead of representing a vector, it represents a matrix.

If the variable is a function of multiple indexes and only a part of them enters in the vector, the vector elements are organized according to the order of the indexes and the dependences. Let's suppose a variable dependent on three indexes, $i$, $j$ and $k$, and only the indexes $i$ and $j$ are suppressed:

$$a^{ijk} \to \boldsymbol{a}^k = {}^{ij}\boldsymbol{a}^k = [a^{11k}, ..., a^{1N_j(1)k}, ..., a^{N_i 1k}, ..., a^{1N_j(N_i)k}] \tag{2.192}$$

The total number of elements of a variable in the MRS system is

$$N[a^{ijk...n}] = N[i, j, k, ..., n] = \sum_{i=1}^{N_i} \sum_{j=1}^{N_j(i)} \sum_{k=1}^{N_k(i,j)} ... \sum_{n=1}^{N_n(i,j,k,...)} 1 \tag{2.193}$$

This notation is used during the description of the design and optimization techniques, as well is the basis for the framework of functions necessary to optimize MRSs developed in chapter three.

### The reflectometer

A reflectometer of a system of $N_R$ reflectometers is labeled by the index $i = 1, ..., N_R$. A general reflectometer is composed by $N_S$ sources, $N_D$ detectors and $N_A$ antennas. A microwave circuit connects all these elements, and their dependence is given by the particular architecture of the reflectometer. The sources are the elements responsible for the emission of the probing wave. Each source is typically associated with a frequency band. By definition, each detector detects the signal associated to the emission of a specific source, and multiple detectors can detect the signals of the same source. For example, in the situations in which the signals come from multiple receiving antennas, or when the phase-shifted signals are required, as in the case of the I/Q detection scheme. In this description, detector means all the physical hardware that transforms the reference signal and the detected signal from the plasma in an output electric signal with the desired form to be digital converted and analyzed. Thus this description works for the different reflectometer architectures. The total number of detectors associated to a specific source is represented by $N_d(i, j)$. The total number of detectors of a reflectometer is

$$N_D(i) = \sum_{j}^{N_B(i)} N_d(i, j) = N[j, k] \tag{2.194}$$

During the operation, the system provides the measurement at each instant $t_k = kT_m$, with $k = 1, ..., N_m$, where $T_m$ is the measurement duration and $N_m$ the total number of measurements during the process. The reflectometer operation time duration $T_O = N_m T_m$ is not necessarily the same as the plasma discharge time, and typically the diagnostic systems start before the plasma formation and ends its operation after the plasma discharge finishes. Each measurement consists in two different phases. At the instant $t_k$, the output is available in the respective hardware physical location. The order for a new measurement starts, and all the necessary mechanisms to the microwave emission are activated and the probing signal emitted from the sources. At the same time, the reflected signal is being detected and recorded digitally. These processes are defined as the probing phase, occurring during the time interval $T_{prob}$, and ending at the instant $t_k + T_{prob}$, when the signal detection of all the bands ends. In the second phase, during the time interval $T_{proc}$, the signals are processed and the position measurement is calculated using the necessary algorithms. The result must be ready to use at the instant $t_{k+1}$, when the next measurement starts. The sum of the time durations of the two phases determines the full measurement duration, written with the extended subscripts as

$$T_{measuring} = T_{probing} + T_{processing}. \tag{2.195}$$

The rate of measurement is given by $f_m = 1/T_{measuring}$. In an ideal MRS, it is assumed that all the reflectometers are synchronized, each reflectometer provides a measurement at the same time, $t_k$. This is not obvious to reach in experiments. The time variable is referent to the measurement time interval,

$$t = t_k + \underline{t}T_{measuring}, \tag{2.196}$$

with $\underline{t} \in [0, 1]$. The principal MRS indexes are four, $i, j, l, k$, corresponding, respectively, to the reflectometer, source, detector and measurement number. A schematic view of the different signals and variables of a reflectometer used in the description of a MRS is shown in figure 2.14. The different signals are analyzed as follows.

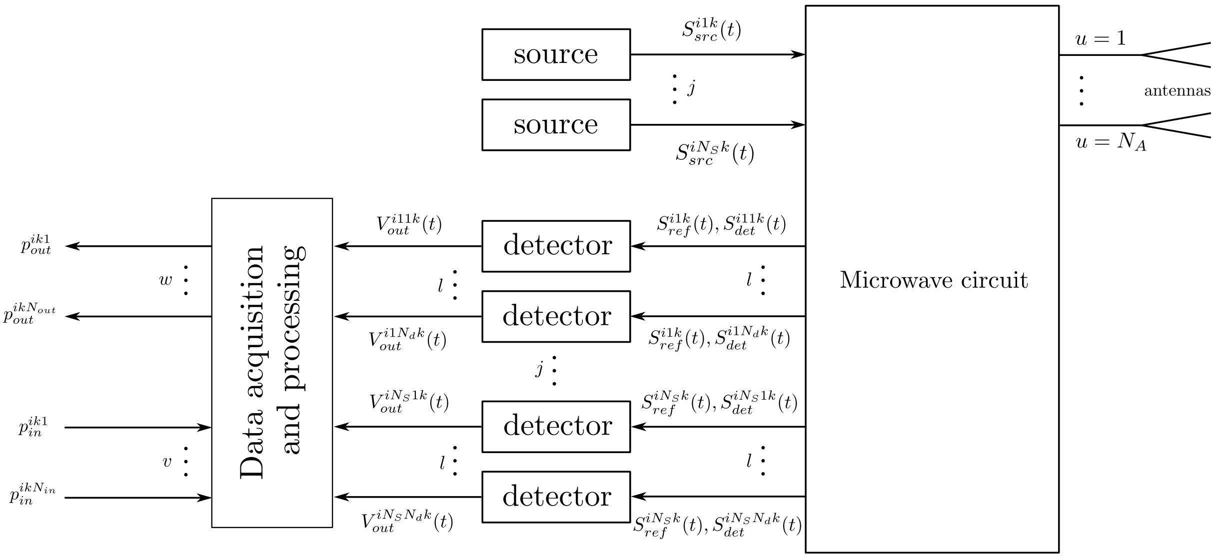

Figure 2.14: Schematic view of the different signals and variables of a reflectometer used in the description of a MRS.

The microwave sources, excite the fundamental mode of a fundamental waveguide, $\mathbf{E}_S^{kij}(\mathbf{r}, t)$ with a characteristic temporal dependence at the source position, $S_{src}^{ijk}(t)$, the source electromagnetic signal. The spectral component of this signal is above the first cutoff frequency of the waveguide and below the second mode, otherwise it can excite additional modes. The fundamental mode is written as

$$\mathbf{E}_S^{ijk}(\mathbf{r}, t) = \mathbf{E}_S^{ijk}(\mathbf{r}) S_{src}^{ijk}(t), \tag{2.197}$$

where, by definition, $\mathbf{E}_S^{j}(\mathbf{r})$ is normalized to its maximum value in the waveguide cross section. Thus, $S_{src}^{ijk}(t)$ includes information on the maximum field amplitude. In FMCW reflectometry, we expect that this function corresponds to equation 2.171 and $A_{src}(t)$ corresponds to the amplitude of the electric field. In general, there is a source per band, so the number of bands $N_B$ is the same as the number of sources, $N_B = N_S$, and the bands are also labeled by $j$. The source signal can be written as a function of the minimum and maximum frequency of the respective band, and of the sweeping time $T_{sw}$:

$$S^{ijk}_{src}(t) = S^{ijk}_{src}[t, f^{ij}_{min}, f^{ij}_{max}, T^{ij}_{sw}] \tag{2.198}$$

If the emission is done in one frequency, this notation stills working, since $f_{max} = f_{min}$.

The detector provides the output electric signal $S^{ijlk}_{out}(t)$ from the reference electromagnetic signal $\mathbf{E}^{ijk}_{R}(\mathbf{r}, t)$ and from the signal that comes from the plasma, $\mathbf{E}^{ijlk}_{D}(\mathbf{r}, t)$. The electromagnetic signals correspond to a fundamental waveguide mode and can be written in the form of equation 2.197,

$$\mathbf{E}^{ijk}_{R}(\mathbf{r}, t) = \mathbf{E}^{ijk}_{R}(\mathbf{r}) S^{ijk}_{ref}(t). \tag{2.199}$$

$$\mathbf{E}^{ijlk}_{D}(\mathbf{r}, t) = \mathbf{E}^{ijlk}_{D}(\mathbf{r}) S^{ijlk}_{det}(t). \tag{2.200}$$

where $S^{ijk}_{ref}(t)$ and $S^{ijlk}_{det}(t)$ are the reference and detected signals which include information on the amplitude of the electric field. The output electric signal is given by

$$S^{ijlk}_{out}(t) = D\left[S^{ijlk}_{ref}(t), S^{ijk}_{det}(t)\right] \tag{2.201}$$

where $D$ is the detector operator that depends on the detector architecture. The reference signal is typically the source signal, or a phase-shifted version of it like in the I/Q detection scheme. Now it is convenient to write the dependences of $S^{ijlk}_{out}(t)$ regarding the reflectometer geometry and the plasma parameters.

From the point of view of electromagnetic propagation, the reflectometer hardware is described by the polarization, magnetization and current vectors. We are interested in describing the propagation of the fields since they are created until being detected, so the analysis is focused in the dependence of the reflectometer variables with the conductivity of the reflectometry system and its surroundings, which is in general high. The permittivity is considered approximately the vacuum permittivity. The propagation of the electromagnetic fields is described by the macroscopic Maxwell equations and the plasma dynamic by a fluid/kinetic model. For now, we assume the cold plasma equation of motion without the collisional term (see equation 2.30), where the density and the magnetic field is the only input plasma parameters. These are also the assumptions behind the reflectometry simulations discussed in the next chapter.

The solution of the system of differential equations that described the propagation of the electromagnetic field is dependent on the boundary conditions: the $\mathbf{E}^{ijk}_{S}(\mathbf{r}, t)$ field, the conductivity $\sigma(\mathbf{r})$, the electron density $n_e(\mathbf{r}, t)$ and the confinement magnetic field $\boldsymbol{B}_0(\mathbf{r}, t)$. We write the detected signal as a function of the main physical quantities involved in the process:

$$S^{ijlk}_{det}(t) = f[S^{ijk}_{src}(t), \sigma(\mathbf{r}), n_e(\mathbf{r}, t), \boldsymbol{B}_0(\mathbf{r}, t)] \tag{2.202}$$

The total number of detected signals in the system during a measurement period is

$$N^k_S = \sum_i^{N_R} \left[\sum_j^{N_B} N_B(i) N_d(i, j)\right]. \tag{2.203}$$

The total number of detected signals in $N_M$ measurements is $N_S = N_M N^k_S$. If all the reflectometers are equal with the same number of detectors per band,

$$N^k_S = N_R N_B N_d. \tag{2.204}$$

With the components of the system and the detected signal dependences defined, we proceed to the acquisition and data processing.

### Acquisition and data processing

The output signals from the different detectors are converted to discrete-time signals with the analog-to-digital converters (ADC) working at a sampling frequency $f_s$. The data are treated with different signal analysis techniques to estimate the plasma parameters. This process is described by the operator $F$. In some cases, additional input data is required from the exterior, namely the data of other diagnostics. In the case of the plasma position reflectometry, the separatrix density is an input variable. The initialization function is another example of an input parameter. Considering $N_{in}(i)$ input parameter functions $p_{in}^{ikv}$, labeled with $v$, and $N_{out}(i)$ output parameters, labeled by $w$, the output plasma parameter $p^{ikw}$ is given by

$$p_{out}^{ikw} = F^{iw}\left[\boldsymbol{S}_{ref}^{ik}, \boldsymbol{S}_{out}^{ik}, \boldsymbol{p}_{in}^{ik}\right], \tag{2.205}$$

where the operation $F$, in general, depends on the reflectometer and on the parameter to be calculated. The reference signal is obtained by $\boldsymbol{S}_{ref}^{ik} = {}^{j}\boldsymbol{S}_{ref}^{ik}$ and the output signal by $\boldsymbol{S}_{out}^{ik} = {}^{jl}\boldsymbol{S}_{out}^{ik}$. The input parameters and the $F^{iw}$ operator depends on the data analysis technique, on the geometry and architecture of the machine and on plasma considerations.

### Plasma position reflectometry data analysis

The measurement of the plasma position involves four phases:

1. **Definition of the line of view** - The inversion method finds the relative cutoff position with the measured group delay. The definition of the final position of the plasma requires the definition of a line of view. If multiple antennas are involved, each one can have a different line of view. In a general description, a line of view is associated to each detection, being described by the parametrization

   $$\mathbf{r}_{lv}^{ijl} = \mathbf{r}_{lv0}^{ijl} + \alpha^{ijl}\mathbf{v}_{lv}^{ijl}, \tag{2.206}$$

   where $\alpha$ is the parametrization variable, $\mathbf{r}_{lv0}$ the reference point and $\mathbf{v}_{lv}$ a normalized vector with the desired direction. Since we do not know the how the propagation occurs in the plasma, this line can be arbitrary. However, it is a good practice define it in the direction of the probing beam main lobe. Thus, if the propagation is ideal, the measured position matches the real position of the plasma in the line of view.

   The way how these lines are defined depends on the reflectometer architecture. Two different detectors can have the same line of view. The simplest case is the monostatic reflectometer, where only one line is required, independently of the number of detectors.

2. **Group delay extraction** - The group delay of each band is obtained applying a phase derivative extraction method (P):

   $$\tau^{ijk}(F) = P^{i}\left[\boldsymbol{S}_{ref}^{ik}, \boldsymbol{S}_{out}^{ijk}(t), \boldsymbol{\tau}_{c}^{ij}(F), \boldsymbol{p}_{P}^{ik}\right] \tag{2.207}$$

   Here $\boldsymbol{\tau}_{c}^{ij}(F) = {}^{l}\boldsymbol{\tau}_{c}^{ij}(F)$ is the group delay correction relative to the propagation in the reflectometer microwave circuit. $\boldsymbol{p}_{P}^{ik}$ are the parameters associated with the P operation, for example filter parameters.

In the case of multiple receiving antennas in different positions, the group delay correction is done separately. If the antennas are supposed to measure similar density profiles and the signals are used directly in the calculation of the same group delay, $\mathbf{r}_{lv}^{ijl}$ should be included the plane perpendicular to the reference line of view containing $\mathbf{r}_{ref}^{ijl}$. The reference line is given by

$$\mathbf{r}_{lvref}^{ijl} = \mathbf{r}_{ref}^{ijl} + \alpha^{ijl}\mathbf{v}_{ref}^{ijl}, \tag{2.208}$$

where $\mathbf{r}_{ref}^{ijl}$ is used by the inversion method as the initial position ($x_a$ point of the reflectometry model 2.84). Alternatively, if there are different sets of antennas measuring different plasma positions independently, they can have independent lines of views, although each sub-system should have one reference line of view.

3. **Group delay assembly** - The group delays of the different bands and antennas are joined and an initialization technique is applied, if required. This operation is described by $J$:

$$\tau^{ik}(F) = J^i\left[\boldsymbol{\tau}^{ik}(F), \boldsymbol{p}_J^{ik}\right]. \tag{2.209}$$

   $\boldsymbol{p}_J^{ik}$ are other necessary input parameters associated with $J$. If the reflectometer consists in a sub group of measurements, each group is characterized by a different group delay, another index can be used to describe the $N_s$ independent subsystems, $s = 1, ..., N_s$.

4. **Inversion technique** - The relative position is obtained from the group delay by the inversion technique $I$:

$$r_m^{ik}(F) = I^i\left[\tau^{ik}(F), \boldsymbol{p}_I^{ik}\right] \tag{2.210}$$

   where $\boldsymbol{p}_I^{ik}$ are other necessary input parameters associated with $I$. The final cutoff layer position is

$$\mathbf{r}^{ik}(F_{sep}) = \mathbf{r}_{ref}^{i} + r_m^{ik}(F_{sep})\mathbf{v}_{ref}^{i} \tag{2.211}$$

   In the case of a multiple sub-systems of measurement, each position can be calculated in a different reference line of view. The final result, depends on the multiple position measurements.

### 2.4.3 The measurement error and the detected power amplitude

Defining the real position of the plasma in the reference line of view as

$$\mathbf{r}_0^{ik}(F_{sep}) = \mathbf{r}_{ref}^{i} + r_0^{ik}(F_{sep})\mathbf{v}_{ref}^{i}. \tag{2.212}$$

The difference of the measured position and the real position is

$$\mathbf{r}^{ik}(F_{sep}) - \mathbf{r}_0^{ik}(F_{sep}) = [r_m^{ik}(F_{sep}) - r_0^{ik}(F_{sep})]\mathbf{v}_{ref}^{i}, \tag{2.213}$$

the position error is defined as

$$e^{ik}(F) = [\mathbf{r}^{ik}(F) - \mathbf{r}_0^{ik}(F)] \cdot \mathbf{v}_{ref}^{i} = r_m^{ik}(F_{sep}) - r_0^{ik}(F_{sep}). \tag{2.214}$$

Based on the chain of dependences of the different variables, it is written in the form

$$e^{ik} = F^i[\boldsymbol{p}_{in}^{ik}, \boldsymbol{S}_{src}^{ik}(t), \boldsymbol{\tau}_c^{i}(F), \sigma(\mathbf{r}), n_e(\mathbf{r}, t), \boldsymbol{B}_0(\mathbf{r}, t), \mathbf{r}_{ref}^{i}, \mathbf{v}_{ref}^{i}]. \tag{2.215}$$

The Abel inversion algorithm assumes the validity of the reflectometry phase-shift model (see section 2.2.6) and the monotony of the density profile. However, in a real reflectometer, none of these conditions are exactly valid. The measurement is possible if all the conditions are approximately verified everywhere, so the error is below the acceptable uncertainty. Let's summarize and analyse the possible causes that contribute to the position error during measurement:

1. **Probing beam** - The beam spatial and temporal shape have an impact on how the interaction with the plasma occurs, resulting in different reflected signals for the same probed plasma. The probing beam is not a plane wave with a monochromatic frequency, it is given by the radiation pattern of the reflectometer antenna and it has a finite time duration, resulting in a frequency spectrum. If the antenna is placed at a cavity, surrounded by a metallic structure, the radiation pattern can be modified and the beam reaches the plasma with a more complex structure. Another assumption is that the probing frequency is linear. However, in practice, there are non-linearities that affect change the temporal component of the beam (see 2.3.5).

2. **Propagation in plasma** - The cold plasma model is in general valid for the order of probing frequencies and low temperatures. However different physical effects such as the relativistic propagation or the Doppler effect can change the nature of the propagation. The frozen plasma condition is achieved with the decrease of the sweeping time duration. However a real plasma does not correspond, in general, to a one-dimensional slow varying monotonic density profile with reflection at a linear dielectric zone. Firstly, the equilibrium/smooth plasma has intrinsically a density gradient that changes its direction according to the probing zone of the machine. Secondly, the plasma shape changes during the different phases of the discharge (ramp up and ramp down phases, plasma displacement). Different phenomena (e.g. turbulence, ELMs, etc...) can occur during the discharge and deform the local smooth density profile.

   If the plasma density gradient (and magnetic field gradient for X-mode) is approximately parallel to the probing direction in the region where the probing beam power is more concentrated, then the reflectometry model is a good approximation and the reflected beam has information similar to the propagation in the 1D ideal plasma [141]. When this does not happen due to any plasma deformation, there is an intrinsic error associated to the propagation. The structure of the electromagnetic field can become complex and several different phenomena like refraction, tunneling effect or scattering can occur. The beam may not propagate in a straight line, while the profile inversion assumes it. However, the reflected wave stills carrying useful information on the plasma properties if the average and standard deviation of the group delay do not impact significantly the final result for the expected range of plasma parameters variation. This degradation can then be reduced with data processing algorithms.

3. **Multiple Plasma-wall reflections** - when the power is reflected from the plasma, part of it enters at the receiving antenna(s) to be detected, part of it is reflected at the surrounding wall to the plasma again, and part of it is lost in other directions. The energy that is reflected to the plasma again passes thought the same process of propagation after being reflected by the plasma again. This process can occur multiple times to part of the energy. The electromagnetic energy can be trapped in

this plasma-wall cavity during some time, and later reach the detector. This affects the detected signal and interfere in the estimation of the group delay. However it is expectable that most of the signal energy comes from the first reflection, carrying the important information.

4. **Magnetic field** - if the electromagnetic field of the probing beam is not aligned with the magnetic field according to the probing mode requirements, the propagation can is affected. The magnetic fluctuations are typically small, and its effect in the signal is neglectable.

5. **Beam detection** - the reflected wave is a superposition of electric field coming from different locations. Depending on the form of the reflected beam and on the geometry of the detecting antennas, part of the electromagnetic field enters in the antenna and propagates in the oversized waveguide until is converted to a fundamental waveguide where it can be detected. All these structures are not ideal and can induce resonances and reflections. Part of the electromagnetic energy that enters in the receiving antenna is reflected again to the plasma. The non linear behavior of the detector can also affect the final result. With the correct calibration of the system, it is expected that the error associated to this part of the propagation is low. The detected signal amplitude should be above the noise limit and the detector limitation.

6. **Data processing and inversion algorithm** - the discretization induces an intrinsic error in the final result. However it is expected that if high sampling frequencies are used, this effect is minimized. The data processing algorithms may also induce an error to the group delay, which is expected to be lower than the the original one. The inversion algorithm, especially in the O-mode, depends on the initialization. This may introduce an error in the final position result. Its effect can be estimated apriori, knowing the expected plasma shape.

7. **Line of view** - the inversion method returns a scalar distance that assumes the group delay comes from a one dimensional plasma. In a real experiment, the line of view must be defined by $\mathbf{r}^i_{ref}$ and $\mathbf{v}^i_{ref}$. For the same detected signals, the position error can increase or decrease, if the line of view is different. For example, fixing the reference point, and changing its direction. This error can be minimized if the line of view coincides with the line of propagation. This may not be possible when the beam changes considerably its direction due to the plasma shape.

These error sources can be separated in two categories:

- Propagation - occurs since the signal is excited in the reflectometer until being detected.

- Detection and data processing - occurs in the detection process, during the group delay estimation, the implementation of the inversion algorithm and with the definition of the Line of view.

The final measurement resulting from the propagation and from the data processing before the profile inversion is seen as an equivalent group delay, written as the sum of the unperturbed/smooth term with the perturbed one:

$$\tau = \tau_0(F) + \tilde{\tau}(F) \tag{2.216}$$

The final position can also be seen as the sum of two terms. For O-mode:

$$\begin{aligned} r(F) &= \frac{c}{\pi}\int_0^F \frac{\tau(f)}{\sqrt{F^2-f^2}}df = \frac{c}{\pi}\int_0^F \frac{\tau_0(f)+\tilde{\tau}(f)}{\sqrt{F^2-f^2}}df \\ &= \frac{c}{\pi}\int_0^F \frac{\tau_0(f)}{\sqrt{F^2-f^2}}df + \frac{c}{\pi}\int_0^F \frac{\tilde{\tau}(f)}{\sqrt{F^2-f^2}}df \\ &= r_0(F) + \underbrace{\frac{c}{\pi}\int_0^F \frac{\tilde{\tau}(f)}{\sqrt{F^2-f^2}}df}_{\tilde{r}(F)} \end{aligned} \tag{2.217}$$

where $r_0$ is the wanted position corresponding to the plasma equilibrium with a possible slow time evolution. One important consideration to have into account is that despite the unperturbed position is associated with a slow varying smooth group delay, it can have an intrinsic error associated. The data analysis techniques try to minimize the effect of $\tilde{\tau}(f)$ with the assumption the group delay should be smooth. But there is no technique associated with the improvement of the unperturbed profile of a specific measurement.

### 2.4.4 Error evaluation

The measurement performance of a reflectometer is not only classified by the position error, but also by the amplitude of the received electromagnetic signal and by the stability of the measurement under different plasmas. If the source and the reflected signals are written as

$$S_{src}^{ijk}(t) = A_{src}(t)\cos[\omega(t)t] \tag{2.218}$$

$$S_{det}^{ijlk}(t) = A_{det}(t)\cos[\omega(t)t+\varphi(t)], \tag{2.219}$$

the amplitude loss of the measurement is defined as

$$a^{ik}(F) = \frac{A_{det}(F)}{A_{src}(F)}. \tag{2.220}$$

The power losses by

$$a_{dB}^{ik}(F) = -20\log_{10}\left[a^{ik}(F)\right] = -20\log_{10}\left[\frac{A_{det}^{ik}(F)}{A_{src}^{ik}(F)}\right]. \tag{2.221}$$

Each detector is sensitive to a minimum value of losses. The signal should also be above the existing noise.

For a set of $N_m$ measurements, the position, the error and the detected amplitude are represented by a statistical distribution. The mean value of the variable $a$ is represented by $A = \langle a\rangle$ and the standard deviation by $\sigma_A = \langle (a-A)^2\rangle$ [201]. The average position error is

$$E(F) = \frac{1}{N_m}\sum_{i=1}^{N_m} \mathrm{e}_i(F), \tag{2.222}$$

and the standard deviation,

$$\sigma_E(F) = \sqrt{\frac{1}{N_m-1}\sum_{i=1}^{N_m}\left[\mathrm{e}_i(F)-E(F)\right]^2}, \tag{2.223}$$

The same definitions are applied for the detected amplitude,

$$A(F) = \frac{1}{N_m} \sum_{i=1}^{N_m} \mathrm{a}_i(F), \tag{2.224}$$

$$\sigma_A(F) = \sqrt{\frac{1}{N_m - 1} \sum_{i=1}^{N_m} [\mathrm{a}_i(F) - A(F)]^2}. \tag{2.225}$$

The rate of successful measurements of the position error is

$$E_R(F) = \frac{1}{N_s} \sum_{i=1}^{N_s} H[-(e_{min}(F) - e_i)] H[e_{max}(F) - e_i(F)], \tag{2.226}$$

where $e_{min}$ and $e_{min}$ are, respectively, the minimum and maximum position error and $H$ is the Heaviside function. The failure rate is calculated by

$$E_F(F) = [1 - E_R(F)] \times 100 \ (\%). \tag{2.227}$$

For the amplitude, the rate of successful measurements is

$$A_R(F) = \frac{1}{N_s} \sum_{i=1}^{N_s} H[-(a_{min}(F) - a_i)], \tag{2.228}$$

and the failure rate is

$$A_F(F) = [1 - A_R(F)] \times 100 \ (\%). \tag{2.229}$$

The total number of successfull measurements depends if both position error and detected amplitude are in the requirements. The success rate of measurements is

$$SR(F) = \frac{1}{N_s} \sum_{i=1}^{N_s} H[-(e_{min}(F) - e_i)] H[e_{max}(F) - e_i(F)] H[-(a_{min}(F) - a_i)]. \tag{2.230}$$

The total failure rate is

$$FR(F) = [1 - SR(F)] \times 100 \ (\%). \tag{2.231}$$

One important question is how the mean and standard devation of the group delay affect the position measurements. In O-mode, it is useful to define the function $G(F, f)$ by

$$G(F, f) = \frac{c}{\pi} \frac{1}{\sqrt{F^2 - f^2}}. \tag{2.232}$$

The mean relative position is the relative position calculated with the mean group delay:

$$\langle r \rangle (f) = \left\langle \int_0^F G(F, f) \tau(f) df \right\rangle = \int_0^F G(F, f) \langle \tau(f) \rangle \, df = r[F, \langle \tau \rangle (f)] \tag{2.233}$$

The standard deviation of the position is not a linear function of $\tau$. The standard deviation is

$$\sigma_r^2(F) = \left\langle (r[F, \tau(f)] - \langle r[F, \tau(f)] \rangle)^2 \right\rangle = \left\langle \left[ \int_0^F G(F, f) \left[ \tau(f) - \langle \tau(f) \rangle \right] df \right]^2 \right\rangle. \tag{2.234}$$

Using the cauchy-schwarz inequality, $\left(\int_a^b f(x)g(x)dx\right)^2 \leq \left(\int_a^b f^2(x)dx\right)\left(\int_a^b g^2(x)dx\right)$,

$$\left\langle \left[\int_0^F G(F,f)\left[\tau(f)-\langle\tau(f)\rangle\right]df\right]^2\right\rangle \leq \left\langle \int_0^F G^2(F,f)df \int_0^F \left(\tau(f)-\langle\tau(f)\rangle\right)^2 df\right\rangle$$
$$= \int_0^F G^2(F,f)df \int_0^F \left\langle\left[\tau(f)-\langle\tau(f)\rangle\right]^2\right\rangle df. \tag{2.235}$$

This yields

$$\sigma_r^2(F) \leq \Lambda(F)\int_0^F \sigma_\tau^2(f)df, \tag{2.236}$$

where $\Lambda(F) = \int_0^F G^2(F,f)df$ is a constant that depends on the frequency. The standard deviation of the position will be lower or equal that the accumulation of the standard deviation of the group delay, times a constant that depends on the frequency.

Given the description of a MRS for one plasma configuration, this analysis is extended for a set of plasma conditions and configurations.

### 2.4.5 Description of multiple configurations of reflectometers

The study of the measurement performance of an existing PPR system consists in the use of numerical simulations to find its error and the detected amplitude. In contrast, the design of a PPR system involves testing different plasmas in multiple configurations of reflectometers. For this reason we describe the variables with two new indexes, the plasma index, labeled by $p = 1, ..., N_p$ and the configuration index, labeled by $c = 1, ..., N_c$. Both indexes are independent. Equation 2.202 can be written as

$$S_{det}^{ijlcpk}(t) = f[S_{src}^{ijk}(t), \sigma^c(\mathbf{r}), n_e^p(\mathbf{r},t), \boldsymbol{B}_0^p(\mathbf{r},t)], \tag{2.237}$$

and the position error and detected power by 2.215 and 2.220

$$e^{icpk}(F) = E[\boldsymbol{S}_{src}^{ik}(t), \boldsymbol{\tau}_c^i(F), \sigma^c(\mathbf{r}), n_e^p(\mathbf{r},t), \boldsymbol{B}_0^p(\mathbf{r},t), \mathbf{r}_{ref}^i, \mathbf{v}_{ref}^i, \boldsymbol{p}_E^{ispk}] \tag{2.238}$$

$$a^{icpk}(F) = A[\boldsymbol{S}_{src}^{ik}(t), \sigma^c(\mathbf{r}), n_e^p(\mathbf{r},t), \boldsymbol{B}_0^p(\mathbf{r},t), \boldsymbol{p}_A^{ispk}], \tag{2.239}$$

where $\boldsymbol{p}_E^{icpk}$ and $\boldsymbol{p}_A^{icpk}$ are the input parameters of the operation that depend also on the plasma and reflectometer geometry, in general. The evaluation of multiple configurations of PPR system requires the simulation of all the $S_{det}^{ijlcpk}(t)$ signals and the calculation of $e^{icpk}$ and $a^{icpk}(F)$.

### 2.4.6 Simulation of multiple configurations of reflectometers

In practice, the numerical method solves the Maxwell equations and the physical model for the plasma dynamics in a finite region of the space. The principal assumption behind the numerical simulation of reflectometry is that the simulated signals (labeled by sim) correspond to the solutions of the analytical models:

$$S_{sim}^{ijlcpk}(t) \simeq S_{det}^{ijlcpk}(t) \tag{2.240}$$

Consequently, we assume that the error bars are representative of those expected in experiments (labeled by exp):

$$e_{sim}^{icpk}(F) \simeq e_{exp}^{icpk}(F) \tag{2.241}$$

$$a_{sim}^{icpk}(F) \simeq a_{exp}^{icpk}(F) \tag{2.242}$$

These conditions are valid if:

1. The numerical algorithm is stable and precise in solving the differential equations of the physical model that describes the propagation.
2. The limitation of the space associated with the numerical simulation includes the relevant elements, impacting the detected signals significantly.

### 2.4.7 Design and optimization of Plasma position reflectometry systems

The design of a PPR system consists in defining the geometry and the constitution of a system of reflectometers is capable of measure the plasma position and shape of the plasma and fulfills the constraints. In general, this process involves the interaction of three different teams:

1. **Thermomechanical performance team (TMP team)** - The TMP team is responsible for analysing the thermomechanical properties of a given reflectometer system under the expected conditions (heat flux, particles flux, neutrons flux, halo current, dilatation) and design the structure of the reflectometer, typically with a CAD program.
2. **Electromagnetic performance team (EMP team)** - The EMP team is responsible for analysing the electromagnetic performance of the in-vessel systems (wave guide and antenna geometry, losses, mode conversion, reflection at the window air-vacuum, waveguide bends, position error).
3. **Experimental team (EXP team)** - The EXP team is responsible for designing the reflectometer hardware (source, detector, microwave circuit, waveguides) and software and test the mockup.

Given the constraints of the system imposed by external entities responsible for the design of the fusion device, these three teams work together to find the best solution amongst the avaiable options. The best solution fulfills all the constraints and optimizes the measurement performance.

#### Constraints of a PPR system

The constraints of a PPR system are divided in six types:

1. **Plasma constraints** - the plasma constraints consist in the expected plasma configurations for which the PPR system will measure. This includes the definition of the magnetic field, of the poloidal flux and of the density profile associated to the equilibrium scenario, to the transient states and to the perturbations/instabilities that may occur during the discharge including the limiting cases.

2. **Geometry constraints** - the geometry constraints define the available space for the implementation of the plasma position reflectometry system (wall, ports, blankets, thermal protections).

3. **Thermomechanical constraints** - the thermomechanical constraints define the temperature and stress limits for the mechanical structure of the reflectometer.

4. **Control system constraints** - the control system constraints defines the minimum/ideal number of measurements, its position and the limits of the measurement error (minimum and maximum error, rate of failure).

5. **Hardware constraints** - the hardware constraints (e.g. ADC sampling frequency, microwave source) impose the physical limits on the sweeping rate, determine the measurement time, the resolution of the detection and the minimum amplitude of detection.

6. **Computational resources** - the design of the reflectometer involves the simulations of many possible configurations. However there is a limit on the computational resources. The simulations should be planned according to these limitations.

7. **Project duration** - in general, the project of a PPR has a pre-defined duration. This means that a strategy of selection of the interesting configurations must be applied, allowing to find the solution in useful time.

The design of a PPR system involves supposing different possible reflectometry configurations (geometries, emission angles, positions) of the reflectometers, testing different plasmas in every configuration and choosing the best combination. Taking into account the limited computational resources and the project duration, next we discuss the optimization of multiple configurations of reflectometers.

### Optimization of multiple configurations of reflectometers

The optimization of multiple configurations of reflectometers is one of the main operation in the design of a PPR system. This operation consists in finding the performance of $N_R$ reflectometers changing its geometry $N_G$ times. Each combination is a configuration. For example, if we are studying $N_R$ reflectometers located at different positions of the machine, and we want to change the angle of incidence of the respective antennas in $N_\theta$ different angles, there are $N_\theta^{N_R}$ different configurations. Neglecting the influence of each reflectometer geometry in each other, the number of configurations is reduced to $N_\theta \times N_R$, which an important consideration for the numerical simulations. For each configuration, $N_P$ plasmas are tested. In the end, the configurations that respect the measurement constraints are selected:

$$e_{min}^{icpk}(F) < e^{icpk}(F) < e_{max}^{icpk}(F), \tag{2.243}$$

$$a^{icpk}(F) > a_{min}^{i}(F). \tag{2.244}$$

The min and max subscripts represent the limit values (minimum and maximum) of the error and of the detected amplitude. From the total number of configurations that respect the measurement constraints, we should select the best option.

An ideal PPR system has a performance of

$$e^{icpk}(F) = 0, \tag{2.245}$$

$$a^{icpk}(F) = 1. \tag{2.246}$$

However, this does not happen due to the losses of energy and error sources mentioned in section 2.4.3.

A good criteria for configuration selection is to assume that the best option for the system safety is the one which has the maximum detected amplitude over the total frequency range, since it will in principle have a better performance under turbulence and other effects that can lead to the signal losses. This condition is valid if the error is within the requirement.

### Fixed wall position (FWP) and fixed separatrix position (FSP) optimization

For a given plasma state, there are two different optimization operations that are useful to perform to the reflectometer geometry to optimize the measurement:

1. **Fixed wall position (FWP) optimization** - In this situation, the intersection point between the line of propagation and the wall is fixed. The region where the reflectometer in-vessel components can be is limited. For a reference antenna setup geometry, there are two options of optimization based in the changes of the reflectometer geometry:
   - **Antenna setup** - Keeping the direction of propagation and changing the antenna setup allows to have beams with different radiation pattern acting on the amplitude criterion.
   - **Angle of incidence** - For the same intersection point with the wall, the angle of incidence of the probing beam in the plasma is changed keeping the antenna setup approximately the same may have a significant impact in the measurement performance.
2. **Fixed separatrix position (FSP) optimization** - In this situation, the separatrix point is fixed and the reflectometer changes its position and angle of incidence to satisfy this condition.

The position error of one reflectometer relatively to one plasma of a given measurement can be written as

$$e^c(F) = e[F, \sigma^c(\mathbf{r}), \mathbf{r}_{ref}, \mathbf{v}_{ref}]. \tag{2.247}$$

If we assume the reference point is in the wall surface, $\mathbf{r}_{wall}$ and that $\mathbf{v}_{ref}$ is defined as a normalized vector with the direction of the probing wave $\mathbf{v}_{prob}$, then

$$e^c(F) = e[F, \sigma^c(\mathbf{r}), \mathbf{r}^c_{wall}, \mathbf{v}^c_{prob}]. \tag{2.248}$$

The $\mathbf{r}^c_{wall}$ position can be parametrized by two constants, since it lies on a surface.

A normalized vector perpendicular to the wall is defined at $\mathbf{r}^c_{wall}$ with the direction pointing to the inner side of the vessel, $\mathbf{v}^c_{wall}$. The angle between the probing direction and the vector perpendicular to the wall $\theta_{wall}$ is

$$\theta^c_{wall} = \cos^{-1}\left(\frac{\mathbf{v}^c_{wall} \cdot \mathbf{v}^c_{prob}}{|\mathbf{v}^c_{wall}||\mathbf{v}^c_{prob}|}\right). \tag{2.249}$$

Each $\mathbf{v}^c_{prob}$ that corresponds to the same angle is identified by an additional angle $\phi_{wall} \in [0, 2\pi]$ defined in the plane perpendicular to $\mathbf{v}^c_{wall}$, similarly to the spherical coordinate system.

The line defined by $\mathbf{r}^c_{wall}$ and $\mathbf{v}^c_{prob}$ intersects the separatrix at $\mathbf{r}^c_{sep}$, by definition. In fact, it can intersect in more than one point (separatrix is a closed surface), so we choose the one closest to $\mathbf{r}^c_{wall}$. We can now define a vector perpendicular to separatrix at $\mathbf{r}^c_{sep}$, pointing to the the outer side of the separatrix, $\mathbf{v}^c_{sep}$. This vector is not defined in all the separatrix points, for example in the X points. The angle between the $-\mathbf{v}^c_{prob}$ and vector perpendicular to the separatrix $\theta_{sep}$ is defined as

$$\theta^c_{sep} = \cos^{-1}\left(\frac{\mathbf{v}_{sep} \cdot -\mathbf{v}^c_{prob}}{|\mathbf{v}_{sep}||\mathbf{v}^c_{prob}|}\right). \tag{2.250}$$

Similarly to the $\theta_{wall}$, there is an additional angle $\phi_{sep} \in [0, 2\pi]$ to specify the direction. In tokamaks, the plasma is approximately symmetric in the toroidal direction, so the problem of optimization is, in general, a two dimensional problem. Figure 2.15 shows the representation of the different vectors and angles for the two dimensional case.

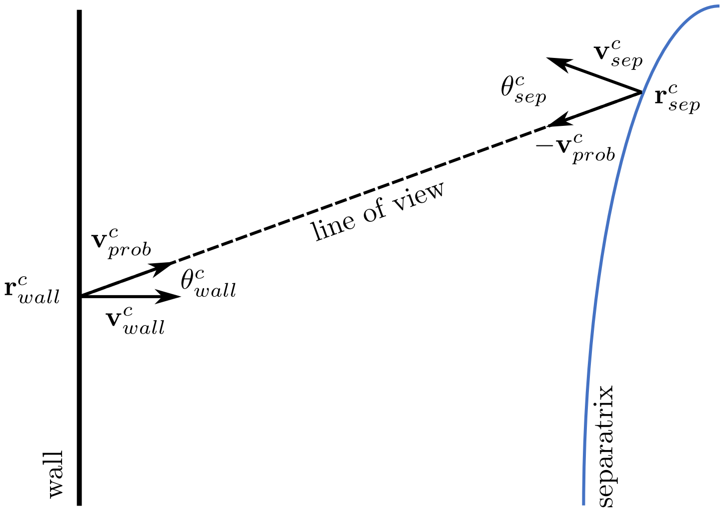

Figure 2.15: Representation of $\theta^c_{wall}$ and $\theta^c_{sep}$.

In this case, the vector can be given only by $\theta^c_{wall}$ or $\theta^c_{sep}$, but it must be identified by a signal to distinguish the two cases with the same angle.

If the reflectometer geometry is defined by a function of the wall position and probing beam direction, $\sigma^c(\mathbf{r}^c_{wall}, \mathbf{v}^c_{prob})$, then

$$e[F, \mathbf{r}^c_{wall}, \mathbf{v}^c_{prob}] = e[F, \mathbf{r}^c_{sep}, \mathbf{v}^c_{prob}] \tag{2.251}$$

In the FWP optimization $\mathbf{r}^c_{wall}$ is fixed and $\mathbf{v}^c_{prob}$ is swept, changing the $\mathbf{r}^c_{sep}$ position. The error can be written as a function of $\theta^c_{wall}$ and $\phi^c_{wall}$:

$$e[F, \mathbf{r}^c_{wall}, \mathbf{v}^c_{prob}] = e[F, \mathbf{r}^c_{wall}, \theta^c_{wall}, \phi^c_{wall}]. \tag{2.252}$$

This function is referred as the FWP error function and is defined all around the machine surface. For a two dimensional plasma, it is a function of two parameters, the separatrix parametrization constant and the $\theta^c_{wall}$.

In the FSP optimization, the $\mathbf{r}^c_{sep}$ is fixed and $\mathbf{v}^c_{prob}$ is swept, changing the $\mathbf{r}^c_{wall}$ position. The error can be written as a function of $\theta^c_{sep}$ and $\phi^c_{sep}$:

$$e[F, \mathbf{r}^c_{sep}, \mathbf{v}^c_{prob}] = e[F, \mathbf{r}^c_{wall}, \theta^c_{sep}, \phi^c_{sep}] \tag{2.253}$$

This function is referred as the FSP error function and is defined all around the separatrix surface. For a two dimensional plasma, it is a function of two parameters, the separatrix parametrization constant and the $\theta^c_{sep}$.

The two error functions are equivalent. However from the point of view of the numerical simulations, it is useful to distinguish and use them depending on the kind of optimization that is needed. Since the discretization occurs, the resolution in which the FWP error function is calculated may not be enough to cover an interesting region of parameters in the discretized FSP error function. The same occurs if the FSP error function is calculated by the simulations.

Summarizing, if the geometry of one reflectometer is given by a function of the wall position and probing direction, the optimization problem can be parametrized by 2-3 geometry parameters (position, probing angle), depending on the dimension of the problem. If the influence of the multiple reflectometers of the system is neglected, the optimization of a PPR system for a given plasma scenario is reduced to the study of this function, which is much less demanding from the computational point of view.

### The principle of the optimization of PPR systems for fixed plasma scenarios

In principle, all the possible probing directions should be swept in order to find the optimized solution. However, this can be a very demanding operation from the computational point of view. It is known that, in the ideal reflectometry model, the direction of the probing beam is parallel to the plasma gradients. Since we are measuring the separatrix and the measurement of the position of a layer depends strongly in the adjacent layers, it is expectable that the optimized solution is around the configuration that respects the condition

$$\mathbf{v}^c_{prob} \cdot \nabla N^2(\mathbf{r}_{sep}) = 0, \tag{2.254}$$

where $\omega_c$ is the cutoff frequency. In the ideal case, the equality is valid.

For the O-mode, this is equivalent to $\mathbf{v}^c_{prob} \cdot \nabla n_e(\mathbf{r}_{sep}) = 0$. If the density if a function of the poloidal flux and $\nabla n_e = \partial n_e / \partial \rho \nabla \rho$, this expression becomes

$$\mathbf{v}^c_{prob} \cdot \nabla \rho(\mathbf{r}_{sep}) = 0. \tag{2.255}$$

The calculation of the FWP/FSP error functions should start with probing directions around respect approximately these conditions.

Discussed the principal aspects of optimization of PPR systems, the procedure for the design of a PPR system is described in appendix A. In the next chapter, we study the process of simulation of the reflectometry measurements and we develop the necessary framework to perform the optimization of multiple configurations of reflectometers.

# Chapter 3

# Reflectometry Simulations

## 3.1 The Finite-Differences Time-Domain method

### 3.1.1 Brief introduction on reflectometry simulation and on the Finite-Differences Time-Domain (FDTD) method

The numerical simulation of reflectometry is considered fundamental in the understanding of the experimental results, in the verification of the theoretical models and in the design of reflectometry systems [202]. To simulate the process of measurement requires solving numerically a physical model that describes the propagation of the electromagnetic fields within a studied plasma and antenna setup geometry. Several numerical methods have been used for reflectometry simulations, including: ray tracing [113, 35], paraxial approximation [203], Helmholtz method [123], transmission line matrix method (TLM) [204], Finite element method (FEM) [205] and finite-differences time-domain (FDTD) method [206, 207]. Each method has its own advantages and limitations, determining the validity of the numerical results [93]. The choice of the method depends on the application, on the desired accuracy of the results and on the available computational resources.

The simulation of conventional reflectometry requires (i) wide frequency bandwidth, (ii) time-varying probing frequency and the (iii) possibility of time evolution of the plasma properties. Due to its versatility, the FDTD method has been one of the most adopted solutions to study the electromagnetic performance of FMCW reflectometry systems [126, 208, 93]. Finite-Differences Time-Domain, based on Yee's method, is a numerical technique for modeling computational electrodynamics that discretizes the Maxwell's equations with the finite-difference approximation [206]. This method has become popular over the last decades of research, being used in a wide range of applications such as radiating structures (e.g. simple antennas, horn antennas, antennas for pulse radiation), guiding structures and microwave components (e.g. transmission lines, waveguides, resonators) and in material modeling (e.g. dispersive material, human tissues) [209]. With the decrease of the computer costs, new applications of FDTD have been developed, making it an important area of research with constant extensions and improvements in diverse areas [93].

In section 2.4.7 we discussed the principal aspects of the optimization and design of PPR and systems. Since reflectometry applications use probing frequencies in the range of 10-200 GHz and volumes in the order of 1-10 $m^3$, the numerical simulations of reflectometry systems with the FDTD algorithm scheme requires, in general, high-performance computing (HPC) systems as supercomputers to perform the simulations.

The optimization and design of PPR systems requires the simulation of multi-reflectometer systems with different geometrical configurations and different plasmas. Preparing the necessary scripts and input models for the simulations and analyse the results are, in general, complex tasks that involve a considerable amount of time. This impacts the cost of the system design and the project duration, which are two fundamental aspects to minimize in fusion research. Strictly speaking, one of the main technical problems in reflectometry research is how to minimize the time involved in the process of optimization of a PPR system.

This chapter is dedicated to this problem. We start with a review of the fundamental aspects related with the FDTD method that are necessary to understand the basic structure of the FDTD codes. In section 3.2 we introduce the the REFMUL* family of codes that has been used to design reflectometry systems in ITER and DEMO [92, 208]. This includes the description of the input models and of other parameters that must be considered. In section 3.3 we analyse the most important steps in the process of simulations with an example. In section 3.4 we develop the general structure of a high level framework to automatize all the simulation process for a general multiple reflectometer system. We introduce the Multi Reflectometry Simulations (MRS) framework that was developed to implement the concept and we discuss some techniques and tools that are necessary to run the simulations in the HPC systems. This framework is essential in the study of the DEMO PPR system that is addressed in chapter 4.

### 3.1.2 The Yee algorithm

The FDTD method is based in the algorithm proposed by Kane Yee in 1966 [210]. It solves each component of the electric and magnetic field in time and space using the Maxwell curl equations for linear isotropic material. In these conditions, $\mathbf{D} = \varepsilon\mathbf{E}$ and $\mathbf{B} = \mu\mathbf{H}$. The Maxwell's curl equations become:

$$\mu\frac{\partial \mathbf{H}}{\partial t} = -\nabla\times\mathbf{E} - (\mathbf{M}_{src} + \sigma^*\mathbf{H}) \tag{3.1}$$

$$\varepsilon\frac{\partial \mathbf{E}}{\partial t} = -\nabla\times\mathbf{H} - (\mathbf{J}_{src} + \sigma\mathbf{E}). \tag{3.2}$$

Here $\mathbf{J}_{src}$ is any independent source of current of the medium (e.g. the plasma), $\mathbf{M}_{src}$ the equivalent magnetic current density and $\sigma^*$ the equivalent magnetic loss [206]. The Yee's algorithm uses centered finite difference expressions for the spatial and time derivatives of equations 4.26-4.27 with second-order accuracy. We follow the chapter 3 and 4 of reference [206]. The position is discretized in the form $(x_i, y_j, z_k) = (i\Delta x, j\Delta y, k\Delta z)$ and the time by $t_n = n\Delta t$. The increments $(\Delta x, \Delta y, \Delta z, \Delta t)$ are assumed constant over the interval of observation. The equations are written in the FDTD notation. The variable $u$ dependent on the position and time is represented by

$$u(i,j,k) = u(i\Delta x, j\Delta y, k\Delta z, n\Delta t) = u^n_{i,j,k}. \tag{3.3}$$

The first partial space derivative of the function $u(\mathbf{r}, t)$ in the $x$ direction, evaluated at $t_n = n\Delta t$ is given by:

$$\frac{\partial u}{\partial x}(i\Delta x, j\Delta y, k\Delta z, n\Delta t) = \frac{u^n_{i+1/2,j,k} - u^n_{i-1/2,j,k}}{\Delta x} + O\left[(\Delta x)^2\right]. \tag{3.4}$$

The derivative is centered at the position with integer subscript, but is calculated with the fields at the adjacent positions, given by $i \pm 1/2\Delta x$. The first partial time derivative of the function $u(\mathbf{r}, t)$ evaluated at $t_n = n\Delta t$ is

$$\frac{\partial u}{\partial t}(i\Delta x, j\Delta y, k\Delta z, n\Delta t) = \frac{u_{i,j,k}^{n+1/2} - u_{i,j,k}^{n-1/2}}{\Delta t} + O\left[(\Delta t)^2\right] \tag{3.5}$$

Figure 3.1 shows the Yee's cell, where is possible to observe the relative location of the field components in the grid, according to the FDTD discretization of the Maxwell's equations.

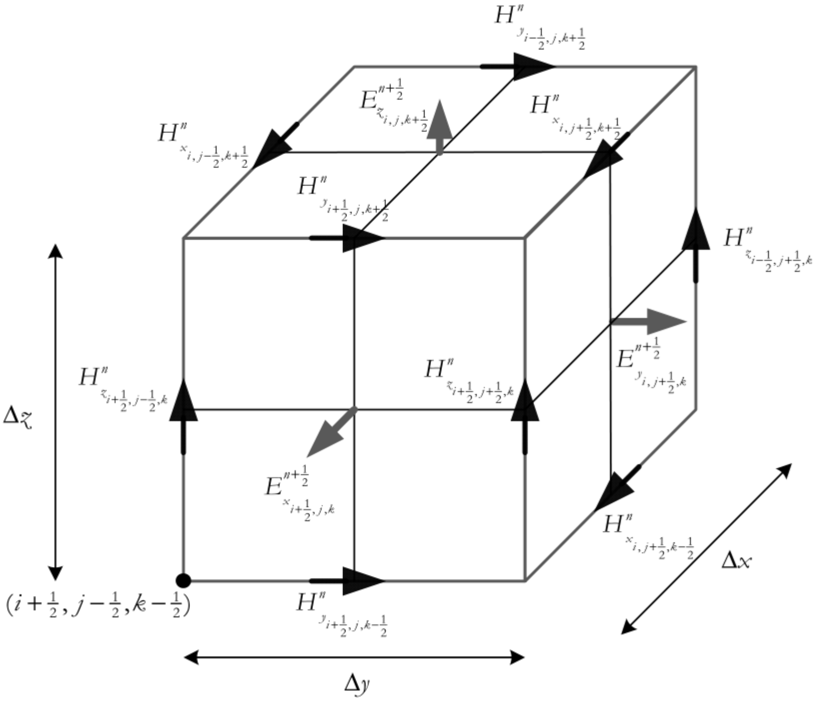

Figure 3.1: Representation of the Yee's grid [211].

The first component of equation 4.26 is

$$\varepsilon\frac{\partial E_x}{\partial t} = \frac{\partial H_z}{\partial y} - \frac{\partial H_y}{\partial z} - J_{src_x} - \sigma E_x. \tag{3.6}$$

Using the discretized expressions for the derivatives we get

$$\frac{E_x|_{i,j+1/2,k+1/2}^{n+1/2} - E_x|_{i,j+1/2,k+1/2}^{n-1/2}}{\Delta t} = \\ \frac{1}{\varepsilon_{i,j+1/2,k+1/2}}\left(\begin{array}{c}\frac{H_z|_{i,j+1,k+1/2}^{n} - H_z|_{i,j,k+1/2}^{n}}{\Delta y} - \frac{H_y|_{i,j+1/2,k+1}^{n} - H_y|_{i,j+1/2,k}^{n}}{\Delta z} \\ -J_{src_x}|_{i,j+1/2,k+1/2}^{n} - \sigma_{i,j+1/2,k+1/2}E_x|_{i,j+1/2,k+1/2}^{n}\end{array}\right) \tag{3.7}$$

The conductivity term includes the electric field evaluated at $n$. However, from the time derivatives of the left side of the equation, it is known that the electric field is evaluated for $n+1/2$ and $n-1/2$. This is solved using the semi-implicit approximation:

$$E_x|_{i,j+1/2,k+1/2}^{n} = \frac{E_x|_{i,j+1/2,k+1/2}^{n+1/2} + E_x|_{i,j+1/2,k+1/2}^{n-1/2}}{2}. \tag{3.8}$$

Using 3.8 on 3.7 and simplifying the equation, one obtains

$$\begin{aligned} E_x\big|^{n+1/2}_{i,j+1/2,k+1/2} &= \left( \frac{1 - \frac{\sigma_{i,j+1/2,k+1/2}\Delta t}{2\varepsilon_{i,j+1/2,k+1/2}}}{1 + \frac{\sigma_{i,j+1/2,k+1/2}\Delta t}{2\varepsilon_{i,j+1/2,k+1/2}}} \right) E_x\big|^{n-1/2}_{i,j+1/2,k+1/2} \\ &+ \left( \frac{\frac{\Delta t}{\varepsilon_{i,j+1/2,k+1/2}}}{1 + \frac{\sigma_{i,j+1/2,k+1/2}\Delta t}{2\varepsilon_{i,j+1/2,k+1/2}}} \right) \left( \begin{array}{c} \frac{H_z|^{n}_{i,j+1,k+1/2} - H_z|^{n}_{i,j,k+1/2}}{\Delta y} \\ -\frac{H_y|^{n}_{i,j+1/2,k+1} - H_y|^{n}_{i,j+1/2,k}}{\Delta z} \\ -J_{src_x}\big|^{n}_{i,j+1/2,k+1/2} \end{array} \right). \end{aligned} \tag{3.9}$$

The equations for the other components are shown in appendix B.1. At each instant, the electric field components are calculated by a linear combination of its value with the respective components of the magnetic fields calculated in the previous instants. The same is valid for the magnetic field. From the point of view of computation, this means that the local value of $\varepsilon$ and $\sigma$ and of each field component needs to be stored in a 3D matrix that is updated at each iteration. The transverse-magnetic mode with respect to z (TM$_z$ mode) is composed by the $H_x$, $H_y$ and $E_z$ fields. The transverse-electric mode with correspondent to z (TE$_z$ mode) mode is composed by the $E_x$, $E_y$ and $H_z$ fields.

In general, the FDTD simulations require saving in (RAM) memory all the components of the electromagnetic field and of the medium properties. In many problems, the two and one dimensional descriptions can produce accurate results, with the advantage of consuming less computational and time resources. The 1D and 2D version of the FDTD equations can be found in appendix B.2. They are obtained by suppressing the indexes associated to the high order dimension.

### 3.1.3 The Courant–Friedrichs–Lewy stability condition

Due to the discretization, the FDTD algorithms cause nonphysical dispersion of the waves. The FDTD dispersion relation is obtained applying the Fourier analysis in the discrete version of the Maxwell's equation:

$$\left[\frac{1}{c\Delta t}\sin\left(\frac{\tilde{\omega}\Delta t}{2}\right)\right]^2 = \left[\frac{1}{\Delta x}\sin\left(\frac{\tilde{k}_x\Delta x}{2}\right)\right]^2 + \left[\frac{1}{\Delta y}\sin\left(\frac{\tilde{k}_y\Delta y}{2}\right)\right]^2 + \left[\frac{1}{\Delta z}\sin\left(\frac{\tilde{k}_z\Delta z}{2}\right)\right]^2. \tag{3.10}$$

Here $\tilde{\omega}$ and $\tilde{k}$ are the frequency and wave-number associated to the FDTD equations. The reader can find the details of the derivation in [206]. One important aspect of this equation is that the grid resolution impacts in the numerical phase velocity. The resolution is tipically represented by the number of points per wavelength for each dimension,

$$N_\lambda = \frac{\lambda}{\Delta x} \tag{3.11}$$

and by the number of points per period,

$$N_T = \frac{T}{\Delta t}. \tag{3.12}$$

This is defined with the real characteristics of the wave, not with the numerical wavelength. In general, with the increase of the number of points per wavelength and period, the phase velocity becomes close to the speed of light and independent on the direction [206].

The stability of the method is assured with the non-existence of the complex component of the frequency. Defining $\xi$ as

$$\xi = c\Delta t\sqrt{\left[\frac{1}{(\Delta x)^2}\sin^2\left(\frac{\tilde{k}_x\Delta x}{2}\right)\right]^2 + \left[\frac{1}{(\Delta y)^2}\sin^2\left(\frac{\tilde{k}_y\Delta y}{2}\right)\right]^2 + \left[\frac{1}{(\Delta z)^2}\sin^2\left(\frac{\tilde{k}_z\Delta z}{2}\right)\right]^2}, \tag{3.13}$$

the frequency is given by $\tilde{\omega} = \frac{2}{\Delta t}\sin^{-1}(\xi)$. It is verified that

$$0 \le \xi \le c\Delta t\sqrt{\frac{1}{(\Delta x)^2} + \frac{1}{(\Delta y)^2} + \frac{1}{(\Delta z)^2}} \equiv \xi_{upper} \tag{3.14}$$

for all the real values of $\tilde{k}$. $\xi_{upper}$ is defined as the value of $\xi$ when all the terms of the sin functions are 1. This situation occurs for

$$\mathbf{k}_{upper} = (\tilde{k}_x, \tilde{k}_y, \tilde{k}_z)_{upper} = \pm\left(\frac{\pi}{\Delta x}, \frac{\pi}{\Delta y}, \frac{\pi}{\Delta z}\right) \tag{3.15}$$

Depending on the choice of $\Delta t$, $\xi_{upper}$ can exceed 1, leading to complex values of $\sin^{-1}(\xi)$. This results in numerical instability. Generally speaking, we can divide the $\xi$ range in two different regimes: (i) a stable range: $0 \le \xi \le 1$ and a (ii) unstable range: $1 < \xi < \xi_{upper}$. If $\xi_{upper} < 1$, the algorithm is stable. This is known as the Courant–Friedrichs–Lewy condition. For a three-dimensional cubic-cell space lattice with $\Delta x = \Delta y = \Delta z = \Delta$, $\xi_{upper}$ is

$$\xi_{upper} = c\Delta t\sqrt{\frac{1}{(\Delta)^2} + \frac{1}{(\Delta)^2} + \frac{1}{(\Delta)^2}} = \left(\frac{c\Delta t}{\Delta}\sqrt{3}\right) = S\sqrt{3} \tag{3.16}$$

where $S$ is the Courant factor, given by

$$S = \frac{c\Delta t}{\Delta} = \frac{N_\lambda}{N_T}. \tag{3.17}$$

In this case, the condition becomes $S < S_{max} = 1/\sqrt{3} \simeq 0.5774$. This factor depends on the dimension of the problem. For 2D grids, $S_{max} = 1/\sqrt{2} \simeq 0.7071$. For 1D grids, $S_{max} = 1$.

### 3.1.4 Grid properties

Typically, the codes that use Cartesian coordinates compute the algorithm in a region defined by a parallelepipede-rectangle characterized by the length of each side, $l_x$, $l_y$ and $l_z$. This region, known as the region of the interest (ROI), contains the most relevant elements for the final physical results. Another common practice that simplifies the implementation of the algorithm is the use of the same spacial step in each dimension, $\Delta = \Delta x = \Delta y = \Delta z$. The number of points of the grid is calculated depending on the simulated frequencies. Given a grid reference frequency, $f_0$, the number of points of each grid dimension is (see equations 3.11 and 3.12):

$$N_{x,y,z} = \frac{l_{x,y,z}}{\Delta} = \frac{l_{x,y,z}}{c}N_\lambda f_0. \tag{3.18}$$

The number of iterations $N_{it}$ depends on the simulated physical time $T_{sim}$,

$$N_{it} = \frac{T_{sim}}{\Delta t} = T_{sim}N_T f_0. \tag{3.19}$$

# 3.2 Reflectometry simulation with REFMUL* codes

## 3.2.1 Simulation of the propagation in the plasma

The reflectometry simulations require a couple of the propagation equations with the plasma. This is done with the equation of movement [212],

$$\frac{\partial \mathbf{J}}{\partial t} = \varepsilon_0 \omega_p^2(\mathbf{r})\mathbf{E} + \omega_c(\mathbf{r})\left[\mathbf{b} \times \mathbf{J}\right] - \nu \mathbf{J}, \tag{3.20}$$

where **b** is a unitary vector with the direction of the magnetic field and $\nu$ is the collision frequency. A model for the discretization of equation 3.20 is derived in [213]. The main equations are in the appendix B.3. In [214] it has been shown that the X-mode (TE$_z$) algorithm can be unstable for strong gradients of the plasma parameters after a number of time-steps in the order of 100 thousand iterations, worsening with the level of turbulence. The authors propose new coupling schemes that proved to be able to extend the stable time steps for values in the order of millions of iterations. For O-mode ($\omega_x = \omega_y = 0$) the $J_z$ current equation becomes simpler,

$$J_z^{n+1/2} = e^{-\nu \Delta t} J_z^{n-1/2} + \Delta t e^{-\nu \Delta t/2} \varepsilon_0 \omega_p^2 E_z^n. \tag{3.21}$$

This is the equation to be used in the study of a O-mode PPR, with $\nu = 0$.

## 3.2.2 The REFMUL* family of codes and the simulation setup

REFMUL* is a family of time-dependent codes that (i) consider the wave propagation in a given time-dependent plasma, (ii) the structure of the vacuum vessel and (iii) the wave guides and antennas of the reflectometer. The REFMUL* family includes (i) REFMUL, a 2D O-mode (TM$_z$) code [207], (2) REFMULX/REFMULXp, a 2D X-mode (TE$_z$) simulation code [215], (iii) REFMULF, a 2D OpenMP [216] full polarization code and (iv) REFMUL3, a 3D hybrid OpenMP/MPI [217] full-wave code that is in an advanced stage of development [94]. The REFMUL* family of codes is primarily aimed at microwave reflectometry research, being an indispensable tool in the design of the reflectometry systems of the future tokamaks and fusion machines that may use this diagnostic. REFMUL* codes have been used to support studies in ASDEX Upgrade and Tore Supra [94], in ITER for the design of PPR [208] and for the first assessment of microwave diagnostics for DEMO [92, 218]. Figure 3.2 shows the scheme of a 2D REFMUL simulation setup:

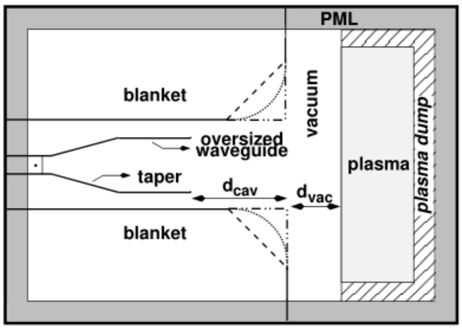

Figure 3.2: Scheme of a general simulation setup. Adapted from [93].

The simulation setup is common to the different versions/dimensions. It is composed by four different elements: (i) the metallic structure, (ii) the plasma, (iii) the vacuum region and (iv) the perfect matched layer (PML) [93]. The input is defined in Cartesian coordinates, according to the FDTD formulation.

The metallic structure that includes the antenna and of the surrounding structure is considered to be a perfect conductor. From the computational point of view, a perfect conductor is easily implemented if the structure is described by a matrix of 0 and 1. In this case, the electric field values are multiplied by the elements of this matrix, becoming zero at the perfect conductor region and simplifying the algorithm. The conductivity values are required in different positions of each Yee's cell (see FDTD equations) but it is assumed that the metallic structure have the same value at the cell's volume. This matrix is denoted by $\sigma_S(i,j,k)$, and has the FDTD grid dimensions.

Since the FDTD algorithm implies the knowledge of the fields at the adjacent cells, the simulated waves would be reflected at the boundary due to the electric field at the limit cells be always zero (perfect conductor) [206]. In order to solve this problem, the FDTD grid is surrounded by a perfect matched layer (PML) that absorbs all the incident waves if they come from vacuum [219]. The basic equations of a PML are shown in appendix B.4 with the 2D TM mode example. The plasma is described by a density matrix, $n_e(i,j,k)$. The collisions are neglected ($\nu = 0$). The equilibrium magnetic field is also defined at each cell, $\mathbf{B}_0(i,j,k)$. The PML requires the incident waves are in vacuum. For this reason, a frame of transition is applied in the plasma, ensuring there is vacuum before the PML [93]. The frame function is described in B.4.

The wave is excited in a fundamental waveguide, so the fundamental mode can be detected and emitted. When the electromagnetic field is excited locally in the grid to generate a probing signal, the excited electromagnetic field propagates in all the possible directions [206]. The excitation of the fundamental mode inside the waveguide generates two waves propagating in opposite directions, making difficult the measurement of the reflected signal in mono-static systems. The solution to this problem is the use of a unidirectional transparent source (UTS) [207]. This algorithm allows to emit the signal in one direction and receive the detected signal in the other, being ideal for reflectometry simulations. The principle behind the UTS algorithm is that if a mirror is placed before the source position, the electromagnetic field is emitted in only one direction. With the knowledge of impulse response of this system, the electromagnetic field of the initial setup without mirror can be corrected at each iteration as the mirror was there, emitting in only one direction and allowing the detection of the reflected signal. This process is illustrated in appendix B.5 with the 1D TM case.

Following, we discuss the principal aspects of the signal injection and detection.

### 3.2.3 Signal injection

The signal is injected in the fundamental waveguide by summing a field with the form of the desired mode to the existing field values. The mode is excited and the signal propagates along the waveguide with the time variation of the injected signal. If the magnetic field is aligned with the z direction, the TE mode corresponds to O-mode reflectometry and the TM mode to the X mode. The waveguide cross-section is assumed to be rectangular, since most of the antennas involve this geometry and the fundamental mode expression is easier to implement. Other geometries can be excited but the code must be adapted. The source dimensions are given by the number of points of each rectangle side.

The field is excited in a y-z plane defined by $i_{src}$ and by a minimum and maximum $j$ and $k$ index values, $[j_{min}, j_{max}]$ and $[k_{min}, k_{max}]$ respectively. By definition, the first and last point of the source is located at the metallic structure, where the field value is zero.

Before exciting the mode, the mirror necessary for the UTS is implemented before the source position and the impulsive response of the system is evaluated during $n_{UTS}$ iterations. For the 1D simulations, the impulsive response of each magnetic field component is saved in a vector with $n_{UTS}$ elements. In the 2D simulations, the values associated with each field are saved in memory in a 2D matrix with $n_{UTS} \times l_{src_y}$ elements. And in the 3D simulations, in a matrix with $n_{UTS} \times l_{src_y} \times l_{src_z}$ elements.

The TM mode is excited with the $E_z$ component of the electric field in the form [111]:

$$E_z(i_{src}, j, k) = \sin\left[\frac{m\pi}{(j_{max} - j_{min})}(j - j_{min})\right] \sin\left[\frac{n\pi}{(k_{max} - k_{min})}(k - k_{min})\right], \tag{3.22}$$

where $m$ and $n$ are the mode indexes, $j_{min} \leq j \leq j_{max}$ and $k_{min} \leq k \leq k_{max}$. The source amplitude is 1 V/m, by default. The TE mode expression is excited with the $H_z$ field which has a similar form ( described by the cos function instead of sin). The source lengths at the y and z direction ($l_{wg_y}$ and $l_{wg_z}$) are given by:

$$l_{wg_y} = j_{max} - j_{min} + 1 \tag{3.23}$$

$$l_{wg_z} = k_{max} - k_{min} + 1. \tag{3.24}$$

In REFMUL* codes, the source lengths have an odd value. This is preferable from the numerical point of view due to the symmetry and allows to probe the amplitude of the electric field at the center position, making sure it is its maximum value. For this reason, it is preferable to describe the source by the center positions $j_{src}$ and $k_{src}$, and by the half width of the waveguide, $h_{wg_y}$ and $h_{wg_z}$. The relation with the minimum and maximum indexes of the waveguide is

$$[j_{src}, h_{wg_y}] = [j_{min} + h_{wg_y}, (l_{wg_y} - 1)/2], \tag{3.25}$$

$$[k_{src}, h_{wg_z}] = [k_{min} + h_{wg_z}, (l_{wg_z} - 1)/2]. \tag{3.26}$$

The designation is the same for the other dimensions.

The time dependence of the signal for FMCW reflectometry is divided in five phases. Each phase has a different phase and amplitude behavior. In the first phase ($T_{s1}$) the amplitude of the signal increases to 1 with an hyperbolic tangent frame. The frequency is the minimum frequency of the range, $f_{min}$. In the second phase ($T_{s2}$), the frequency is the same but the amplitude is constant. In the third phase, ($T_{s3}$), the frequency is swept from $f_{min}$ to $f_{max}$. In the fourth phase ($T_{s4}$), the amplitude is constant but the frequency is constant at $f_{max}$. In the last phase, the frequency is the same but the amplitude decreases with an hyperbolic tangent frame. The size of each phase is determined by the correspondent number of time iterations. In REFMUL* these times are defined by five variables,

$$n_{rise} = T_{s1}/dt \tag{3.27}$$

$$n_{fall} = T_{s5}/dt \tag{3.28}$$

$$n_{pre} = (T_{s1} + T_{s2})/dt \tag{3.29}$$

$$n_{pos} = (T_{s4} + T_{s5})/dt \tag{3.30}$$

$$n_{ramp} = (T_{s1} + T_{s2} + T_{s3} + T_{s4} + T_{s5})/dt. \tag{3.31}$$

One of the principal concern with the signal excitation is the dimensions of the fundamental waveguide. The band frequencies should be between the first (fundamental/dominant) and the second mode of the waveguide. However, the waveguide dimensions are discretized. This means that even that the continuous waveguide is fundamental for the considered band, it may not be when is converted to the FDTD grid. The condition for fundamental waveguide is

$$f_1 < f_{min} < f_{max} < f_2, \tag{3.32}$$

where $f_1$ and $f_2$ are the cutoff frequencies of the first and second mode that is intended to propagate and $f_{min}$ and $f_{max}$ the initial and final band frequencies. These cutoff frequencies depend on $h_{wg_y}$ and $h_{wg_z}$. The design of the fundamental waveguide implies to plot $f_1$ and $f_2$ for different values of $h_{wg_y}$ and $h_{wg_z}$ (1,2,...) and find a combination that respects the condition 3.32. We illustrate it with the example of the 2D TM mode. The first two cutoff frequencies of a 2D waveguide with width $a = 2hw_{wg}dx$ are

$$f_1 = \frac{f_2}{2} = \frac{c}{2a} = \frac{N_\lambda f_0}{4}\frac{1}{h_{wg}}. \tag{3.33}$$

This implies a maximum value of the bandwidth $\Delta f|_{max}$ admitted by the grid:

$$\Delta f|_{max} = f_2 - f_1 = \frac{N_\lambda f_0}{4}\frac{1}{h_{wg}}. \tag{3.34}$$

In the ideal case, the frequency bands and the fundamental waveguides correspond to the real ones. The simulation of the entire measurement process requires several simulations of the same plasma with different grids, changing the fundamental waveguide in each one. When the real bandwidths are not compatible with the grid, they need to be divided in different virtual bands. This introduces an error associated with the new fundamental waveguides (different physical system). In some cases the real waveguides support the band but the discrete versions do not. In these cases the real bands also must be divided.

### 3.2.4 Signal detection

With the UTS implemented, the detection point at a mono-static reflectometer can be done at

$$(i_{det}, j_{det}, k_{det}) = (i_{src}, j_{src}, k_{src}) - (1, 0, 0). \tag{3.35}$$

The signal that comes from the plasma is typically adapted to the fundamental waveguide by a taper. One problem that exists in the detection is that the signal that comes from the plasma can excite high order modes at the beginning of the fundamental waveguide. Therefore, the detection must be placed at a position where its attenuation is high compared with the fundamental mode. In the case of the rectangular waveguide, the $\beta$ constant is

$$\beta = \frac{2\pi}{\lambda_{wg}} = \sqrt{\left(\frac{2\pi f}{c}\right)^2 - \left(\frac{m\pi}{a}\right)^2 - \left(\frac{n\pi}{b}\right)^2} = j\sqrt{\left(\frac{m\pi}{a}\right)^2 + \left(\frac{n\pi}{b}\right)^2 - \left(\frac{2\pi f}{c}\right)^2} \tag{3.36}$$

for a decaying mode. Higher order modes decay faster. Therefore the condition for detection is

$$A_2(i_{det}, j_{det}, k_{det}) = A_2(i_{iwg}, j_{det}, k_{det})e^{j\beta_2 d_{det}} << A_1(i_{det}, j_{det}, k_{det}), \tag{3.37}$$

where $i_{iwg}$ is the position of the waveguide interface with the taper, $A_2$ is the second mode amplitude, $A_1$ the amplitude of the fundamental mode, $\beta_2$ the amplitude decaying constant of the second order mode, and $d_{det}$ the distance that the detection should be placed from the fundamental waveguide-taper interface. For the 2D TM case,

$$\beta_2 = j\sqrt{\left(\frac{\pi}{2h_{wg}dx}\right)^2 - \left(\frac{2\pi f}{c}\right)^2} \tag{3.38}$$

Condition 3.37 must be valid in all the frequencies of the band. $\beta_2$ is lower for higher frequencies, increasing the decay length. This means that the distance should be calculated for $f_{max}$. The minimum distance where the detection should be placed is given by

$$e^{\beta_2 d_{det}} = a_2 = \frac{A_2(i_{det}, j_{det}, k_{det})}{A_2(i_{iwg}, j_{det}, k_{det})} \rightarrow d_{det} = -\frac{\ln(a_2)}{\sqrt{\left(\frac{\pi}{2h_{wg}\Delta x}\right)^2 - \left(\frac{2\pi f_{max}}{c}\right)^2}}. \tag{3.39}$$

where $A_2$ is the amplitude of the second mode and $a_2$ is defined. This distance is then converted to a number of grid points using $\Delta x$ to be implemented in the grid. The 3D case implies the knowledge of the $a$ and $b$ dimensions the describe the second mode. The procedure is the same.

### 3.2.5 The dimension of simulation and computational resources

The dimension of the simulation is chosen according to the available computational resources and project duration. Each dimension has its advantages and limitations.

One-dimensional simulations take into account several one dimensional plasma effects. They are used to evaluate the changes in the phase-shift due to the propagation in one-dimensional plasmas. However, they do not include the description of the antenna setup. The wave is excited at one point and the wave is totally reflected in the plasma if no collisions take in place. They have the advantage of do not require huge computational resources, at least for the most applications.

Two-dimensional simulations include the description of the reflectometer geometry and some plasma characteristics that are not possible with the one-dimensional model (e.g. poloidal gradient). This results in a more accurate determination of the phase-shift and, in contrast to the one-dimensional simulations, it is possible to estimate the power losses. The two-dimensional simulations require more computational resources. The optimization of a PPR where multiple simulations are involved requires the use of HPCs.

Three dimensional simulations include realistic descriptions of the reflectometer geometry and of the plasma. All the components of the Maxwell's equations are calculated, allowing a realistic estimation of the detected amplitude. However, these simulations require huge computational resources to run, being indispensable the use of HPCs. The optimization of a PPR is not possible with the present time computers.

The best solution to optimize PPRs is the use of two-dimensional codes. They combine several effects of the reflectometer geometry and plasma and require acceptable computational resources for multiple simulations. A great part of the effects that contribute to the perturbation of the group delay are well described in the poloidal plane. Although the detected amplitude has not a realistic value in two-dimensional simulations, it is expected that an increasing in the 3D detected amplitude corresponds to an increasing of the 2D detected amplitude, leading to the same optimized solution.

In this work we use REFMULF (2D) to optimize the DEMO PPR. In the next section we verify step by step the necessary operations to run a simulation and obtain the results.

## 3.3 Simulation and data analysis of plasma position reflectometry

In this section we discuss the necessary steps to simulate an O-mode reflectometry measurement with REFMULF (2D) and obtain the plasma position. Simulating a PPR system consists in applying these steps multiple times for different plasmas or configurations. The procedure is similar for the other dimensions of simulation.

### 3.3.1 Defining the FDTD grid parameters

There are several variables that constraint the reflectometry simulations. The maximum size of the grid is limited by the available RAM memory. The maximum number of iterations for a given grid is limited by the number of available core-hours and project duration. Since the study of a entire MRS involves many simulations, the grid dimensions must be minimized as much as possible. The physical constraints impose the minimum area/volume for the simulation and the minimum frequency that is required to probe the plasma separatrix. The minimum frequency is calculated with the density and magnetic field profiles depending on the probing mode. The region of interest must contain the antenna model, the area where the separatrix density is defined, and should include the expected region of propagation of the probing beam, at least referent to the first plasma-wall reflections. The plasma-wall reflections are expected to have less impact in the final result, if a great part of the detected signal comes from the first plasma reflection. The bands are choose according to the separatrix frequency, as well as the frequency associated to the grid discretization. Given the minimum geometric area and the minimum discretization step, the minimum size of the FDTD grid is defined.

The maximum frequency sweeping rates determine the minimum number of iterations. In this section we simulate an O-mode measurement of a slab plasma similar to those simulated for DEMO in chapter 4 ($L_{SOL}$ = 1.5 cm at LFS), with the density profile illustrated in figure 3.32:

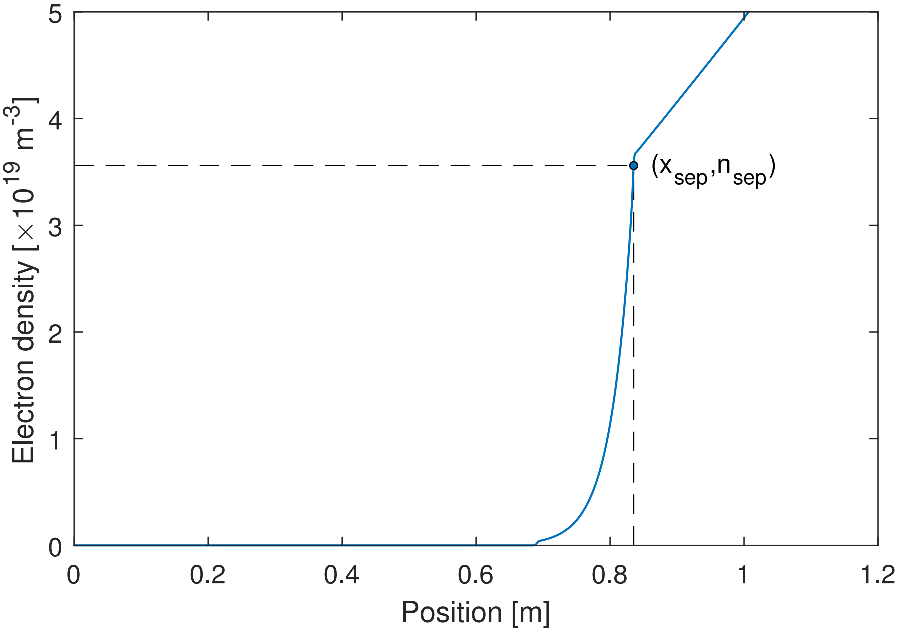

Figure 3.3: The simulated density profile.

The grid has $l_x = 1.2$ m and $l_y = 1$ m. The separatrix density is $n_{sep} \simeq 3.56 \times 10^{19}$ m$^{-3}$, corresponding to a probing frequency of $f_{sep} \simeq 53.57$ GHz. We defined four different bands: K$_1$ = $[18, 29]$ GHz, Ka$_1$ = $[27, 42]$ GHz, Q$_1$ = $[39, 51]$ GHz and V$_1$ = $[48, 57]$ GHz. These bands do not correspond to any specific designation system, they are created to cover the separatrix frequency and to have a solution for the discrete fundamental waveguides as mentioned in section 3.2.3. Along this work, since we use different bands in different studies, we label them with a number. The following table summarizes the variables associated with each band:

| Band | $f_{min}$ [GHz] | $f_{max}$ | $f_0$ | $f_{min,d}$ | $f_{max,d}$ | $N_\lambda$ | $N_T$ | $a_{wg}$ [mm] | $h_{wg}$ |
|---|---|---|---|---|---|---|---|---|---|
| K$_1$ | 18 | 29 | 29 | 18 | 28 | 20 | 40 | 10 | 10 |
| Ka$_1$ | 27 | 42 | 42 | 28 | 40 | 20 | 40 | 7 | 10 |
| Q$_1$ | 39 | 51 | 51 | 40 | 49 | 20 | 40 | 5.8 | 10 |
| V$_1$ | 48 | 57 | 57 | 49 | 54 | 20 | 40 | 5.2 | 10 |

All the frequencies are given in GHz. The first three columns correspond to the minimum, maximum and grid frequencies. $f_{min,d}$ and $f_{max,d}$ correspond to the bandwidth used in the data analysis. The reasons why these values are different will become clear later. $N_\lambda$ and $N_T$ are the same during all the simulations in this work. They provide a good spatial-temporal resolution with $S = 0.5$. The fundamental waveguide width that is proposed to each band is $a_{wg}$ and $h_{wg}$ is the half width of the waveguide, given in number of points after the geometry conversion. Figure 3.4 shows the $f_{c1}$ and $f_{c2}$ modes as function of the fundamental waveguide width (left) and the wavelength $\lambda_{1,2}$ of the selected width as function of the frequency (right). The $g$ and $d$ subscripts mean, respectively, the geometrical or the discrete value. At the left side, it is possible to verify the interval of possible widths by the intersection points of $f_1$ and $f_2$ with the minimum and maximum frequency lines. The discrete value must be in this interval. If it is not, the bands should be divided, increasing the interval of possible widths. At the right side, it is possible to verify the differences of wavelength between the waveguides with the continuous or discrete width. In the considered range of frequencies, the selected waveguide widths produce wavelengths in the order of 1-2 cm. In the following table it is possible to observe the cutoff frequencies, the decaying factor for $d_{det} = 10$ cm (see section 3.2.4), the discretization parameters and the sweeping rate of each band. Increasing $d_{det}$ increases the grid size, leading to higher computer resources.

| Band | $f_{c1}$ | $f_{c2}$ | $f_{c1,d}$ | $f_{c2,d}$ | $\exp(\beta_2 d_{det})$ | dx [mm] | dt [0.1 ps] | $k_w$ [GHz/$\mu$s] |
|---|---|---|---|---|---|---|---|---|
| K$^1$ | 14.99 | 29.98 | 14.50 | 29.00 | 0.0806 | 0.52 | 8.62 | 79.75 |
| Ka$^1$ | 21.41 | 42.83 | 21.00 | 42.00 | 0.0140 | 0.36 | 5.95 | 157.50 |
| Q$^1$ | 25.84 | 51.69 | 25.50 | 51.00 | 0.0089 | 0.30 | 4.90 | 153.00 |
| V$^1$ | 28.83 | 57.65 | 28.50 | 57.00 | 0.0023 | 0.26 | 4.38 | 128.25 |

The sweep occurs in 160000 iterations, and the signal is initialized and finalized with $n_{pre} = n_{fall} = 20000$. For this range of frequencies, the order of the FDTD time step is $10^{-13}$ s, leading to simulation times in the order of 0.01 $\mu s$. Using simulation times in the order of 1-10 $\mu s$ as in the real experiments would be too demanding from the computational point of view. Since the $N_\lambda / n_{ramp}$ is low, it is assumed that at each instant, the stationary is approximately reached. The decaying factor of the second order mode, calculated for the maximum frequency of each band, is defined in the range 0.1-8%. By placing the detection position 10 cm before the taper to the oversized waveguide, most of the detected signal comes from the fundamental mode.

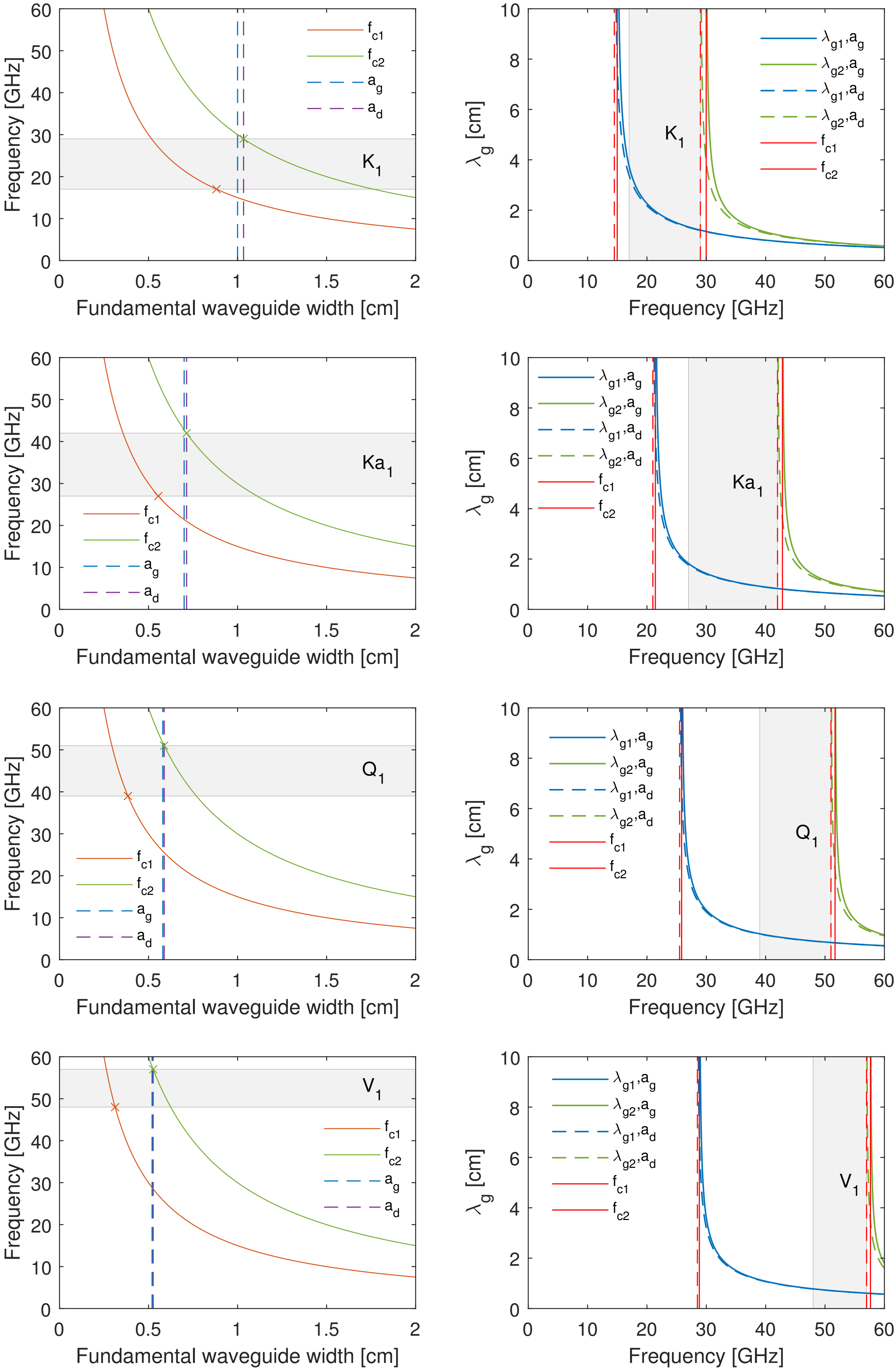

Figure 3.4: Fundamental waveguide design.

### 3.3.2 The antenna and the plasma model

The FDTD grid is defined with the ROI dimensions and with the $dx$ of each band. The following table shows the grid dimensions and the number of grid points per mm (ppmm) for each simulated band:

| Band | $N_x$ | $N_y$ | ppmm |
|---|---|---|---|
| $K_1$ | 2323 | 1936 | 2 |
| $Ka_1$ | 3363 | 2803 | 3 |
| $Q_1$ | 4084 | 3403 | 3 |
| $V_1$ | 4564 | 3804 | 4 |

When the geometry is converted to a grid, $ppmm > 1$ ensures that an object in the order of 1 mm$^2$ is represented in the grid. Figure 3.5 shows the metallic structure model (red) and the area covered by the slab plasma for the $K_1$ band (grey).

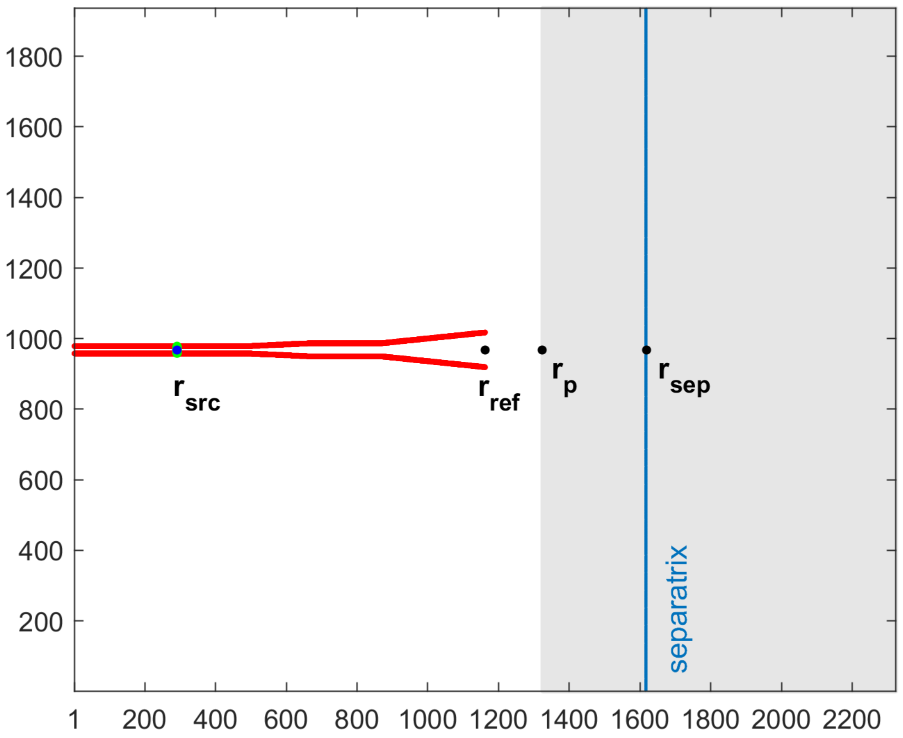

Figure 3.5: The antenna (red) and plasma model (grey).

The axis represent the grid point index. The plasma, defined in the grey region, was obtained by interpolating linearly the density profile. The antenna setup was choose with the same dimensions that are going to be used on DEMO simulations in the next chapter. The horn antenna has an input dimension of 1.9 cm, an output dimension of 5 cm and a length of 15 cm. The oversized waveguide has a width of 10 cm. The taper has 10 cm, corresponding to at least approximately 5 waveguide wavelengths for frequencies higher than 20 GHz. The whole structure has a thickness of 1 mm. The source position and the detection are placed 10 cm before the taper. The reference point is assumed to be in the center of the antenna's mouth. The initial plasma position and the separatrix position are calculated to be used on data analysis. Figure 3.6 shows the zoom in the source region.

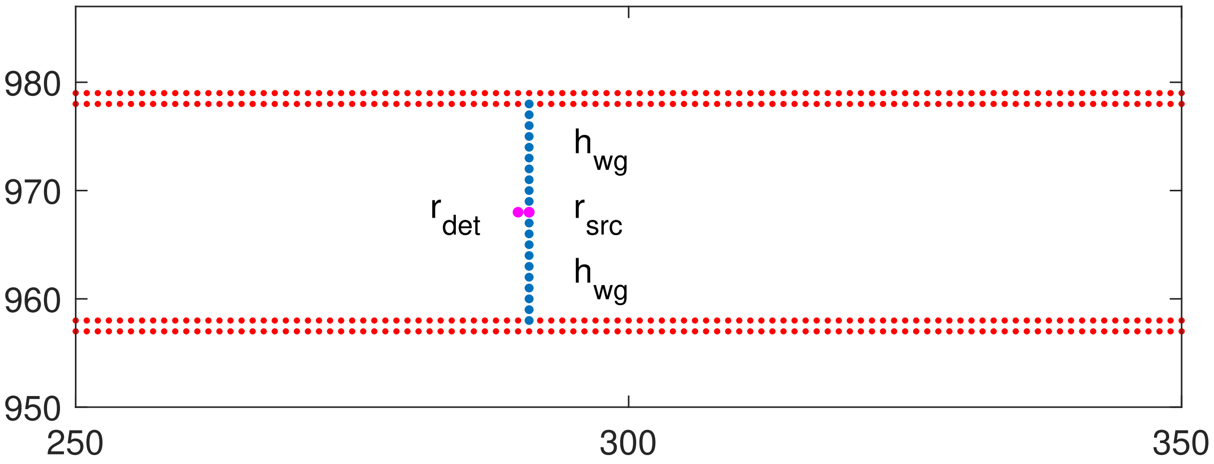

Figure 3.6: Zoom at the fundamental waveguide model.

The detection is one point before the source position, and the half waveguide width includes the first point of the metallic structure. The reference position, the initial plasma position and the separatrix position are calculated in the grids of the other bands.

### 3.3.3 UTS impulsive response

For the O-mode, the impulsive response of the magnetic field $H_z$ is calculated during a few thousands of iterations for all the positions associated with the excitation line ($n_{UTS} = 5000$). Figure 3.11 shows the impulsive response for the $K_1$ band, relative to the model of figures 3.5 and 3.6.

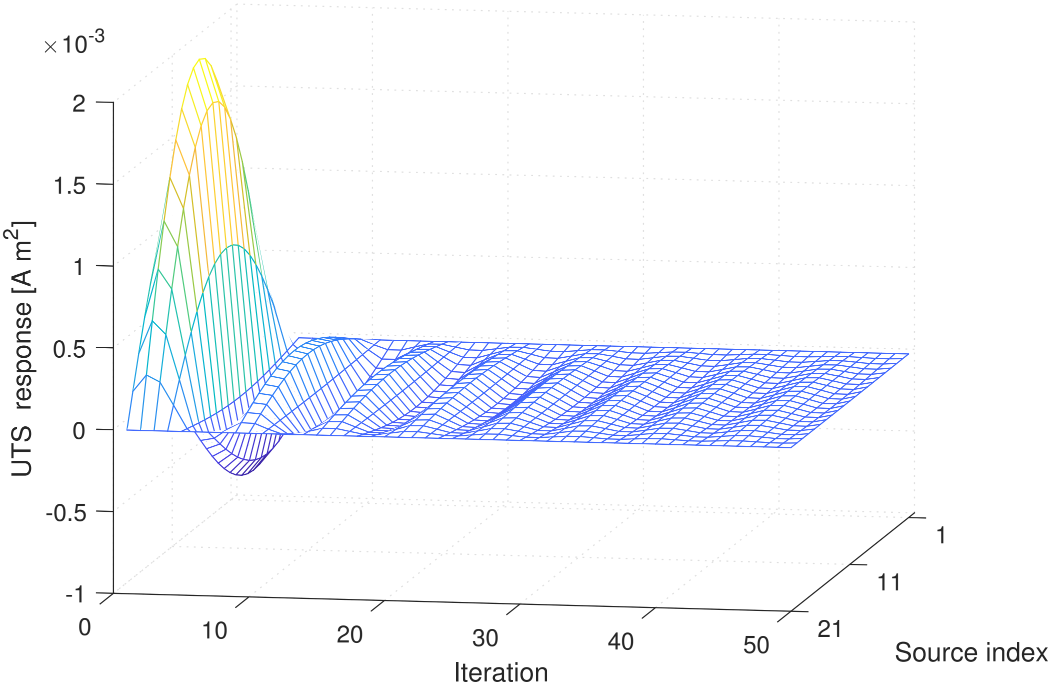

Figure 3.7: The first 50 iterations of the impulsive response for the $K_1$ band.

Its maximum amplitude depends on the excitation position, being zero at the waveguide wall. After some hundreds of iterations, the impulsive response decays to a residual value.

### 3.3.4 Simulation in vacuum

In order to verify if the UTS calibration is correct and the antenna model is emitting the expected probing beam, the emission in vacuum is simulated. Figure 3.8 shows the snapshot of the positive part of the electric field at different frequencies. The color scale is the same in all the figures. As expected the beam width decreases with the frequency.

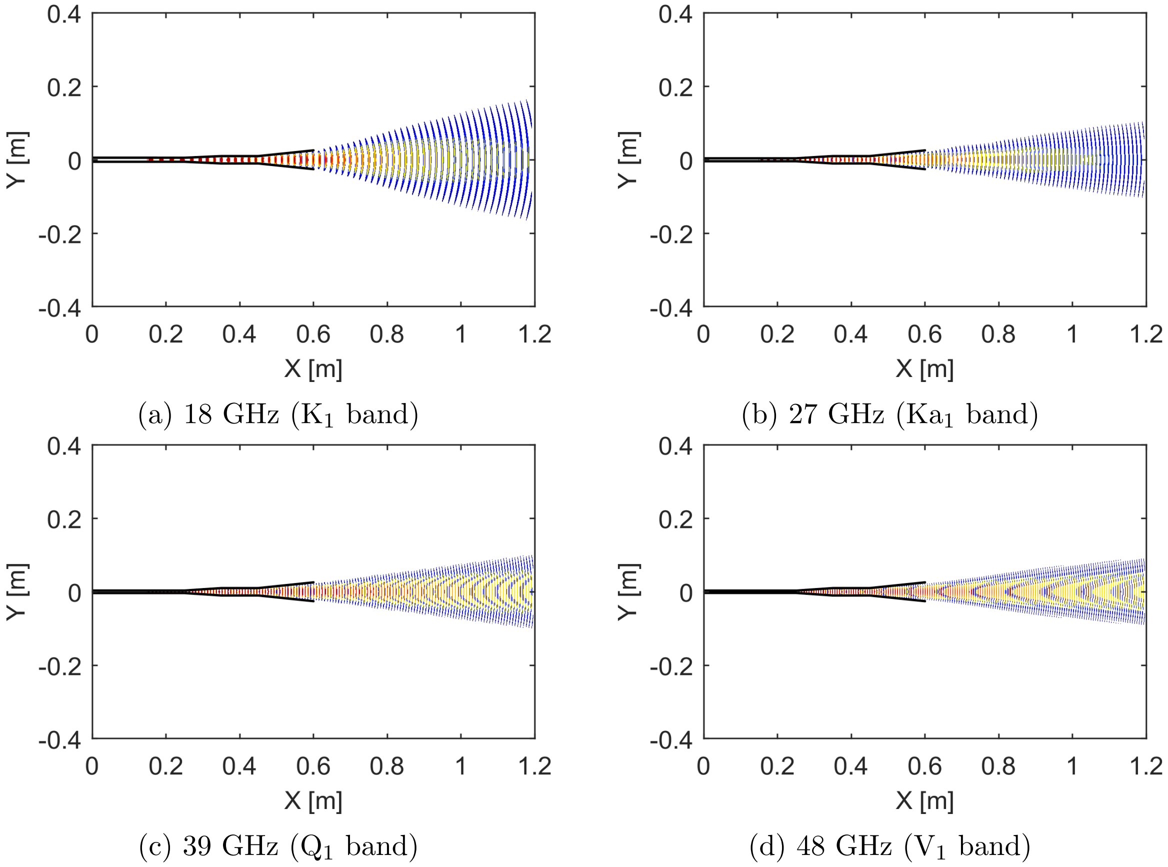

(a) 18 GHz ($K_1$ band)

(b) 27 GHz ($Ka_1$ band)

(c) 39 GHz ($Q_1$ band)

(d) 48 GHz ($V_1$ band)

Figure 3.8: Snapshot of the positive part of the electric field at different frequencies.

Figure 3.9 shows the maximum electric field evaluated in two periods for $x = 0.7$ m.

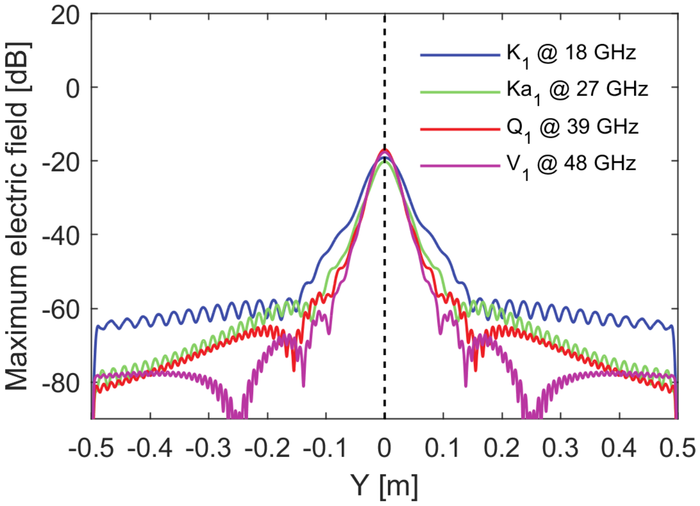

Figure 3.9: The maximum electric field evaluated in two periods of time at $x = 0.7$ m.

This profile is similar to the radiation pattern of an antenna, but it is calculated for fixed $x$ position. The antenna's mouth is located at $x = 0.6$ m, and the measured position corresponds approximately to the initial plasma position. The results show that most of the power is concentrated at approximately 20 cm. Using $l_x = 1$ m allows to take into account the multiple reflections if a wall is considered. As the frequency increases, the power becomes located at $x = 0$ m. Figure 3.10 shows the result of the simulation for the $V_1$ band and the zoom at the first 10000 iterations where is possible to observe the effect of the hyperbolic tangent frame in the amplitude.

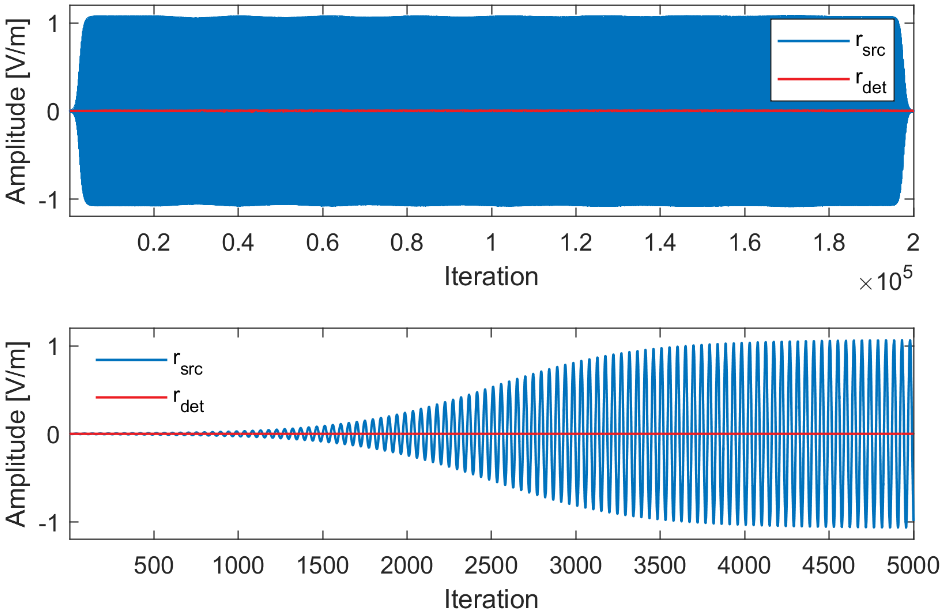

Figure 3.10: Signal at the source and detection position for the $V_1$ band.

One simple form of validating the metallic structure model is plotting the detected signal and the signal at the source and check if the detected values are residual ($< 1\%$) and the mean is zero. For multiple simulations, this can be verified with the plot of the mean, minimum and maximum values for all the simulations:

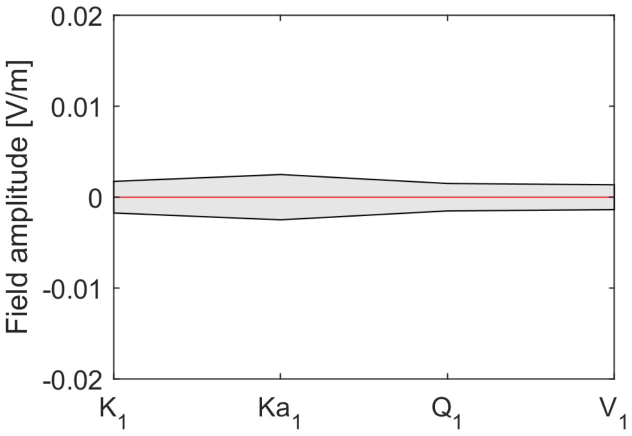

Figure 3.11: Mean (red), minimum and maximum values of the detected electric signal in the case of emition in vacuum.

The source signal is excited with an amplitude of 1 V/m. As observed in figure 3.10, there are some fluctuations above this value. This occurs due to the implementation of the UTS. The source signal $S_{src}(t)$ is plotted in figure 3.12 for the $Q_1$ band in the 1-4000 range. The signal with a phase-shift of 90 degrees is also saved in memory to be used in the I/Q detection scheme.

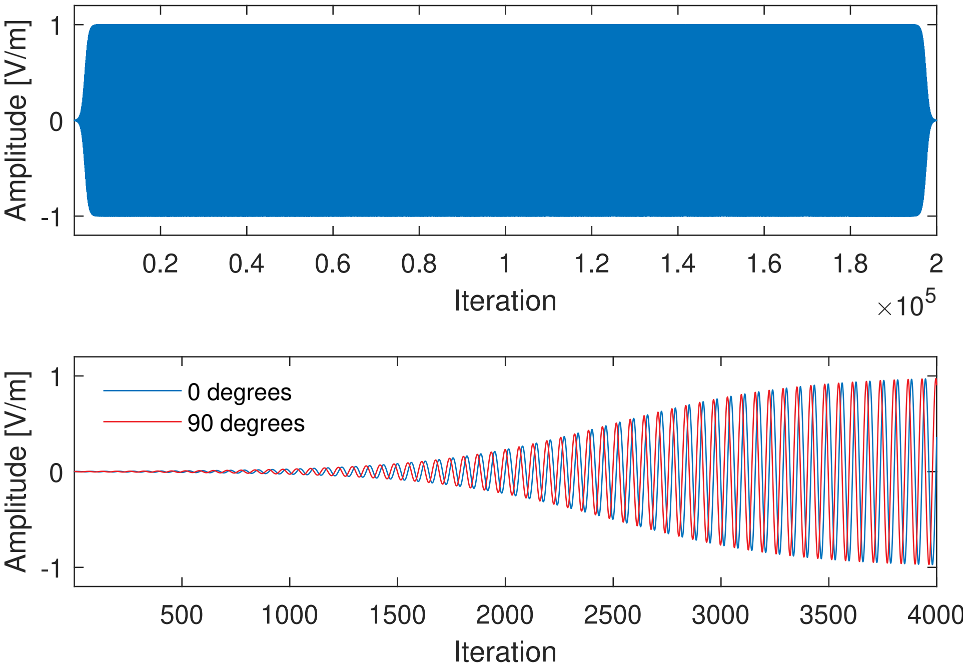

Figure 3.12: Source excitation function $S_{src}(t)$ and $S_{src}^{\pi/2}(t)$ for the $Q_1$ band.

Figure 3.13 shows a comparison of the spectra of the signal emitted by the UTS and $S_{src}(t)$ for the $\mathrm{Q}_1$ band:

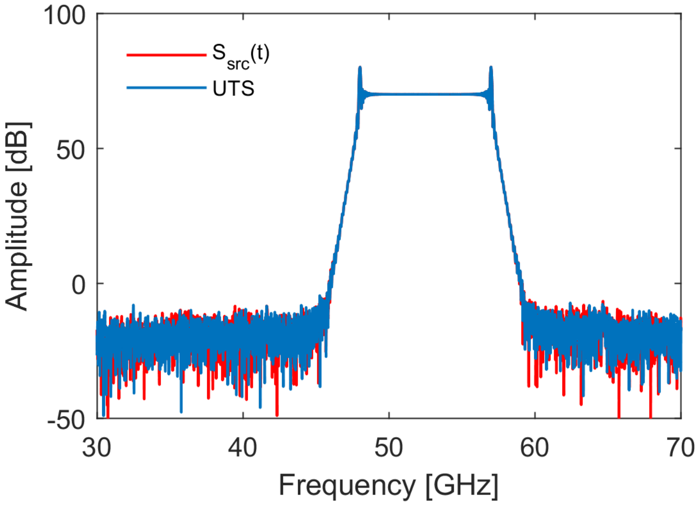

Figure 3.13: Comparison of the $S_{src}(t)$ spectrum with the signal at the source position.

It is possible to identify the spectrum correspondent to the frequency sweep and that the frequency components of the signal emitted by the UTS source are identical to $S_{src}(t)$.

### 3.3.5 Simulation with the mirror

Figure 3.14 shows the snapshot of the electric field of the simulations with the mirror to measure the group delay due to the propagation inside the antenna setup.

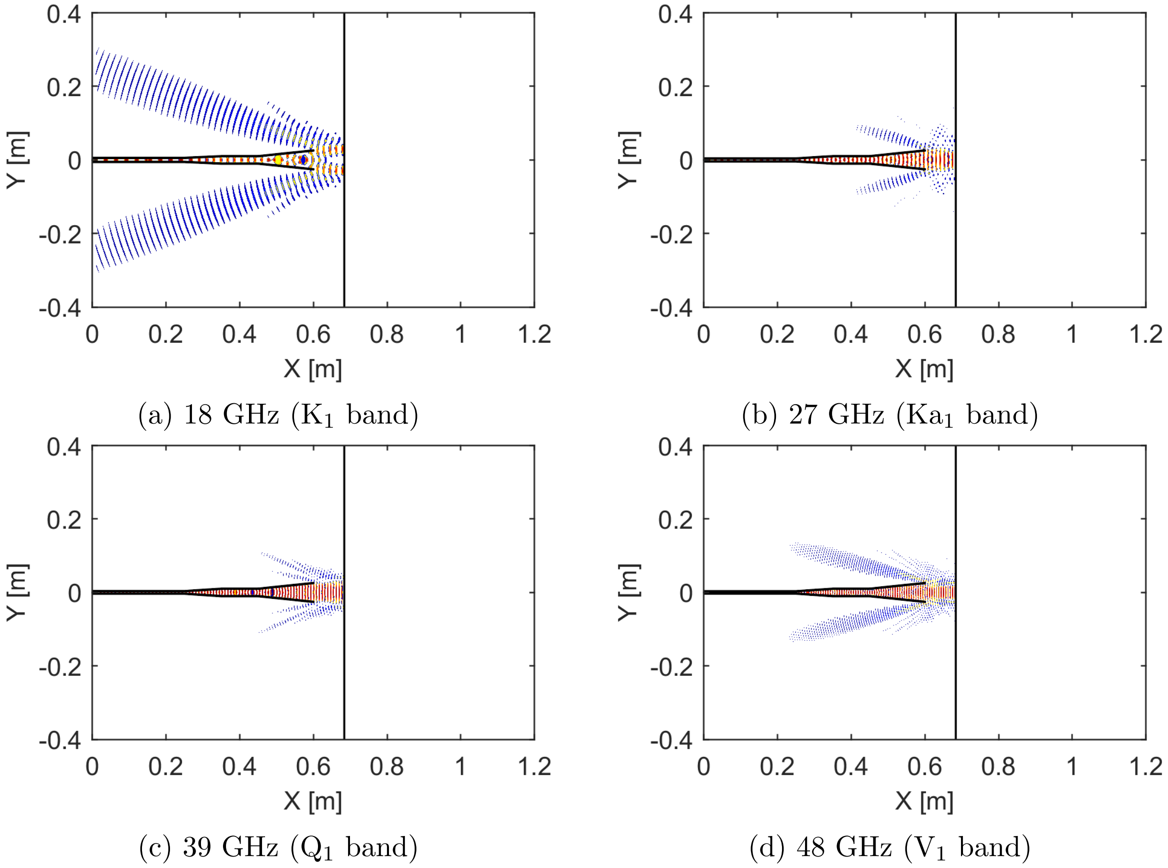

(a) 18 GHz ($K_1$ band) (b) 27 GHz ($Ka_1$ band)

(c) 39 GHz ($Q_1$ band) (d) 48 GHz ($V_1$ band)

Figure 3.14: Snapshot of the positive part of the electric field at different frequencies with the mirror placed at the initial plasma position.

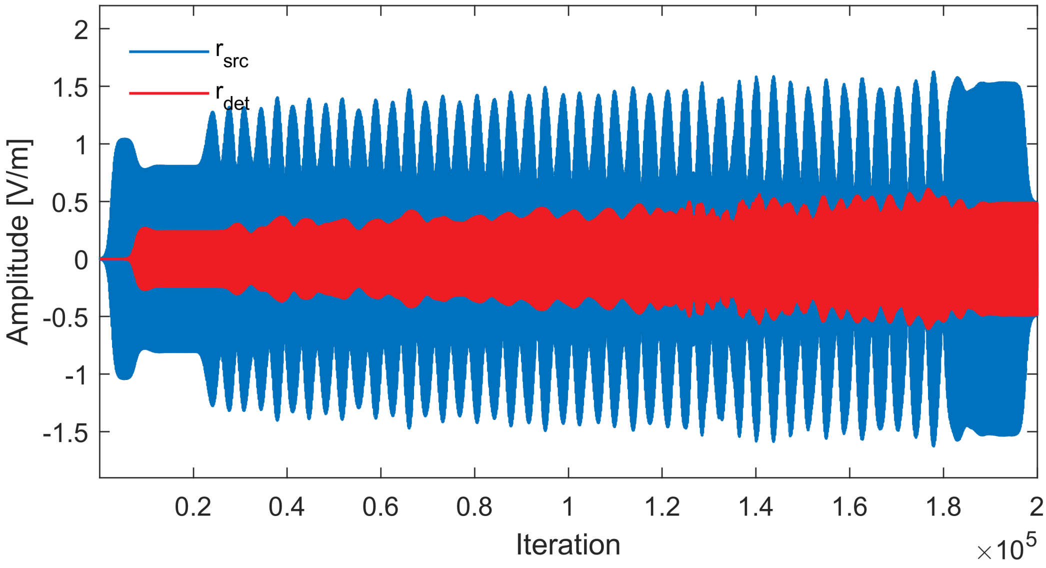

Figure 3.15: Signal at the source and detection position for the $K_1$ band.

The signal peaks at $r_{src}$ correspond to the beats originated by the sum of the excited field with the reflected signal. The gain increases with the frequency, leading to the detection of higher amplitude.

### 3.3.6 Simulation with the plasma

Figure 3.16 shows the electric field of the simulations with the plasma. Figure 3.17 shows the signal at the source and detection position for the $K_1$ band.

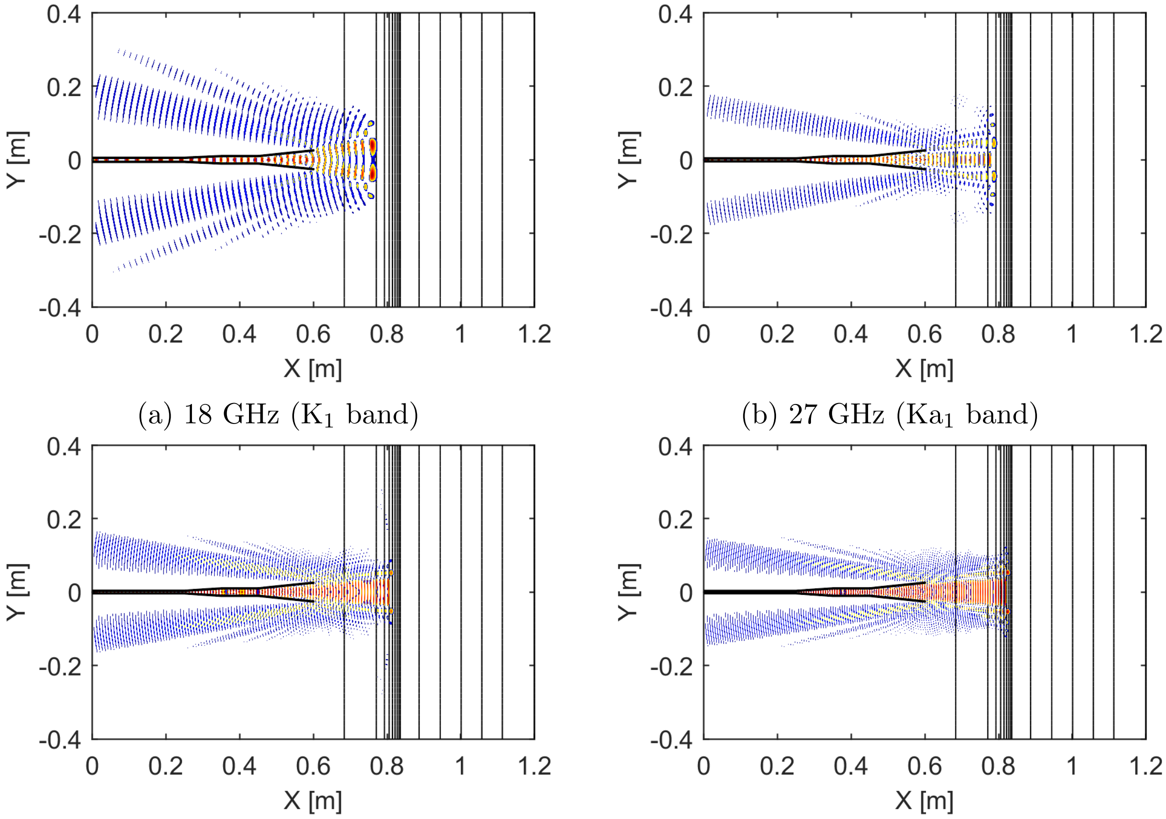

(a) 18 GHz ($K_1$ band)

(b) 27 GHz ($Ka_1$ band)

(c) 39 GHz ($Q_1$ band)

(d) 54 GHz ($V_1$ band)

Figure 3.16: Snapshot of the electric field at different frequencies with the plasma.

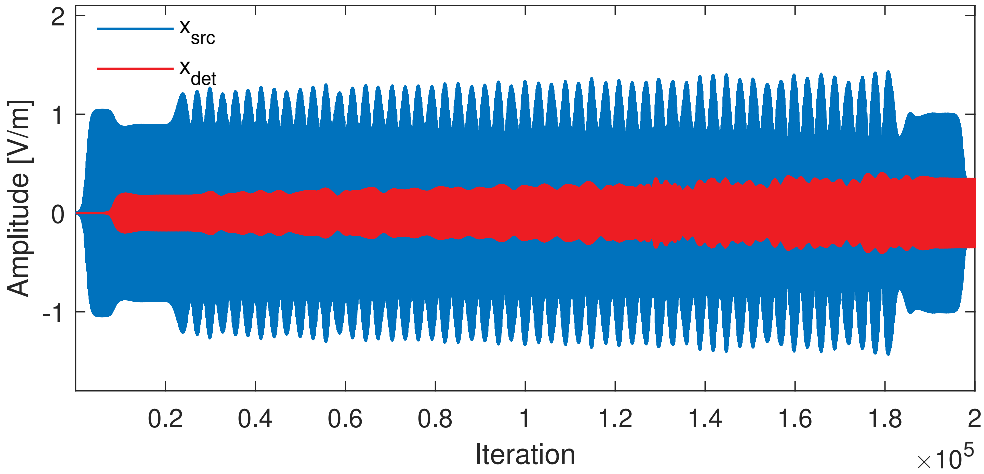

Figure 3.17: Signal at the source and detection position for the $K_1$ band.

The reflection position changes with the frequency, by contrast with the simulations with the mirror.

If at a given instant, the emitted electric field in vacuum is subtracted to the electric field resulting from the interaction of the beam with the plasma, it is possible to observe the structure of the reflected electromagnetic field from the plasma in the region with vacuum. If the obtained electromagnetic field is normalized by

$$\mathbf{E}^N(x,y) = \frac{abs[\mathbf{E}(x,y)]}{max[abs[\mathbf{E}(x,y)]]_{src}}, \tag{3.40}$$

it is possible to verify if the mode is purely fundamental at the detecting position if the contour plot at the fundamental waveguide is composed by straight lines. Thus the position of the detection is set to be always in the area where only the fundamental mode exists for the studied frequency bandwidth. Here *abs* is the absolute value and *max* the maximum value inside the waveguide at fixed y position. If the field is zero outside the antenna (e.g. with a metallic structure around the antenna), the maximum value can be calculated in all the y axis. Figure 3.18 shows the contour plot of the normalized electric field at 28 GHz for the studied case.

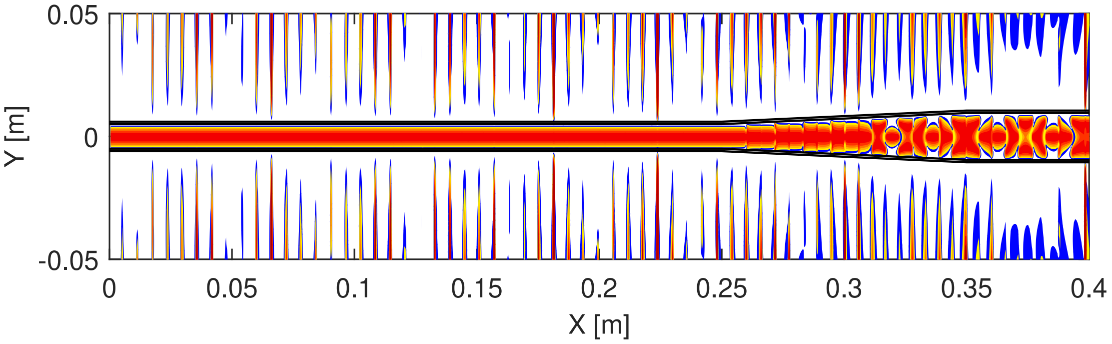

Figure 3.18: The normalized electromagnetic field at 28 GHz.

As expected, the contour lines are straight 10 cm before the taper. This behavior confirms that only the fundamental mode is measured as it is in an experiment.

### 3.3.7 Characteristic propagation inside the setup

The phase derivative due to the propagation in the setup is calculated with I/Q detection scheme studied in section 2.3.3. In the rest of this work we designate this technique as the IQ method. In reflectometry simulation it is useful the use of a shifted source function $S_{src}^{\pi/2}$ (see figure 3.12), so only one simulation of $S_{det}(t)$ is required to define the I and Q signals. The first step in the IQ method is to apply a filter to remove the high frequency components of the I and Q signals. In this case and in the rest of this work we use a 4th order Butterworth low-pass filter. Figure 3.19 shows the Q signal spectrum before and after applying the filter.

The spectrum of the I/Q signals is typically composed by a characteristic frequency peak associated with the propagation. The cutoff frequency is selected manually and the high frequency components are removed, allowing to obtain a smooth phase derivative. With the filtered signals, the phase and its derivative are calculated.

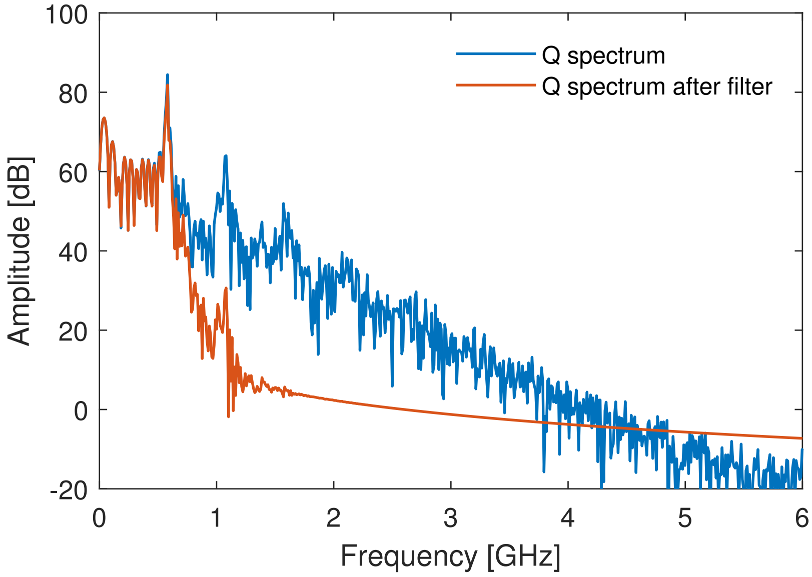

Figure 3.19: Q signal spectrum of the $Q_1$ band.

Figure 3.20 shows the extracted phase derivative during the sweeping time. Due to the short simulation times, there is a delay between the emitted and the detected signal must be taken into account. This results in an increasing phase derivative profile with an accentuated slope at the beginning of each profile. When there is enough detected power, the result stabilizes in the expected slow varying profile. The transition time between the beginning of the sweep and the detection of the first frequencies, $t_0$, is measured and the beginning of the profile is corrected. The resulting phase derivative is then fitted to the expression for the propagation in the setup, so its parameters can be used to correct the result of any plasma that is simulated (equation 2.180).

Figure 3.21 shows the result of the fits to equation 2.180 of all the bands. The term due to the propagation between the antenna's mouth and the mirror is subtracted to $\tau_c$, corresponding to the vacuum correction profile in the figure. This term corresponds to $4\pi(x_p - x_{ref})/c$.

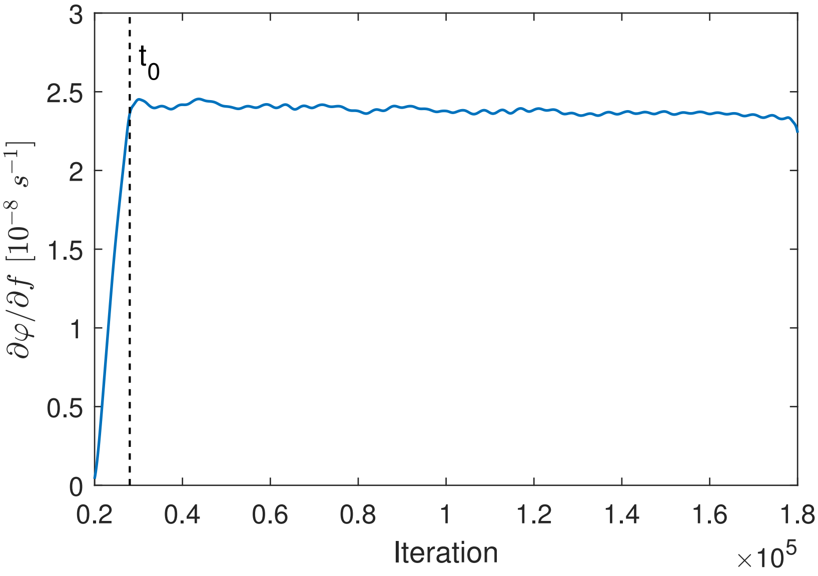

Figure 3.20: Characteristic group delay calculated with the IQ method for the $Q_1$ band.

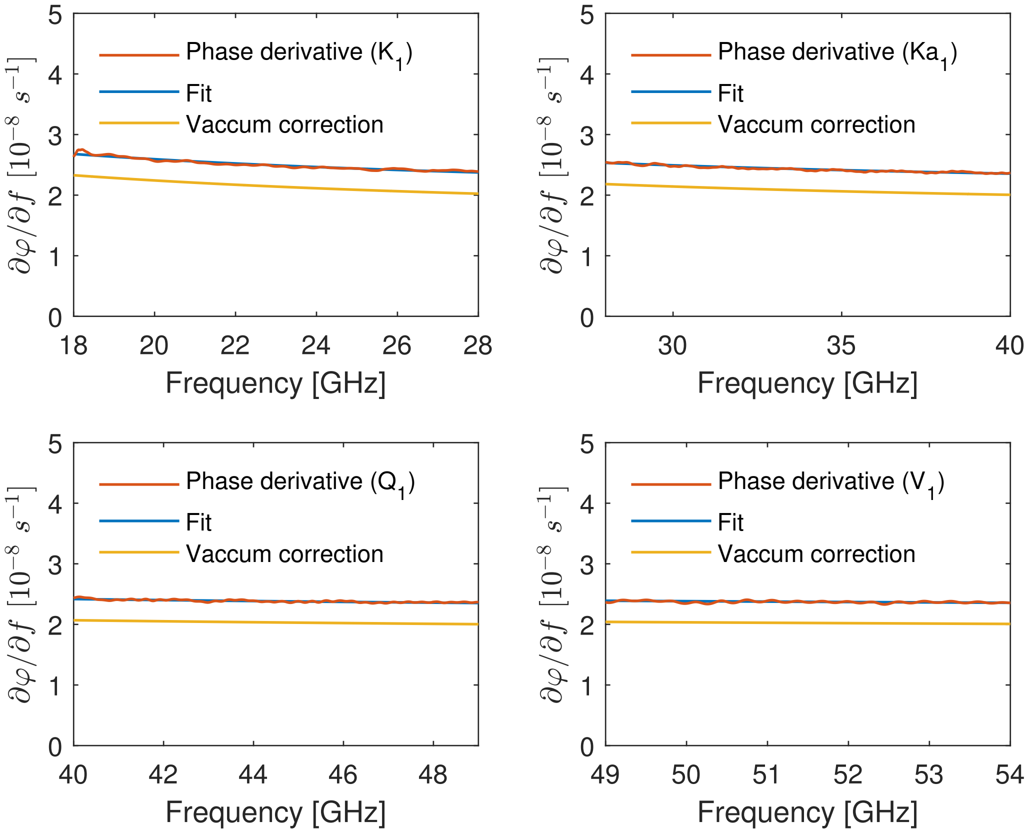

Figure 3.21: Fitting the SFFT signals for all the bands.

### 3.3.8 The phase derivative

With the phase derivative calculated for all the simulations with the mirror, the phase derivative referent to the simulations with the plasma was extracted. As reference, the phase derivative profiles were also calculated with the WKB approximation. A line of view with the (1,0) direction was defined, centered at the antenna's mouth. The WKB phase-shift was calculated with the discrete version of the 2.100 expression. The phase derivative due to the propagation in the plasma is obtained directly by the discrete phase derivative and subtracting the vacuum term, $4\pi x_p/c$.

Figure 3.22 shows the phase derivatives obtained with the IQ method. Figure 3.23 shows the phase derivatives obtained with the spectogram technique, in the same range. This technique, designed as SFFT method, consists in taking the instantaneous beating frequency from the mix of $S_{det}(t)$ with $S_{src}(t)$ as described in the section 2.3.5. The high frequency component of the mixed signal is filtered before the spectrogram calculation. The mixed signal uses a source signal with a frequency shift of 10 GHz, allowing the correct calculation of the beating frequency. The signals are defined in the range of hundreds of iterations, so a decimation is done before the spectogram computation. We use the default MATLAB function to compute the spectrograms [220]. The results were analysed using $n_{window} = 512$, $n_{overlap} = n_{window}/2$ and $n_{fft} = 1024$ for a decimation with a factor of $Q_f = 30$.

The phase derivatives obtained with the IQ and SFFT methods correspond approximately to the WKB profile. The small discrepancies that exist result from the antenna-plasma interaction, of the method used to extract the phase derivative and from the numerical nature of the simulations. At the last frequencies of the profiles, the deviation is typically higher in absolute value. This is due to the initial delay, since the last frequencies of the detected signal are mixed with the signal associated to the fourth phase of $S_{src}(t)$ (see section 3.2.3). At the initial frequencies of the profiles the error is typically associated with a wrong $t_0$ definition or with the use of a low cutoff frequency that removes part of the characteristic frequencies, affecting the reconstruction of the signal. Futhermore, the delay correction can remove some points at the end. These are the reasons why the simulated frequencies should be different from the data analysis ones. The error observed in the IQ method results in the region where the slope changes after the separatrix ($V_1$ band) is the effect of filtering the frequency components after the characteristic peak.

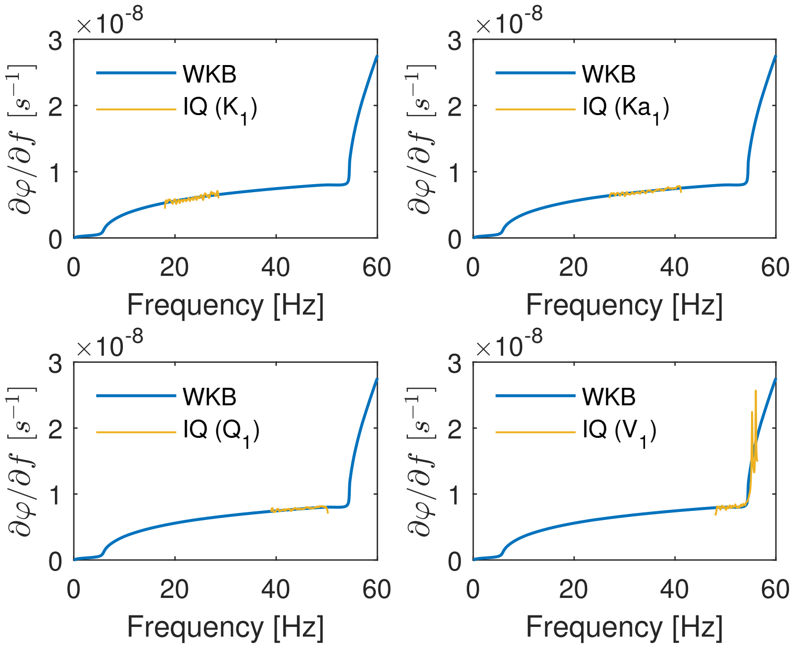

Figure 3.22: Phase derivatives obtained with the IQ method.

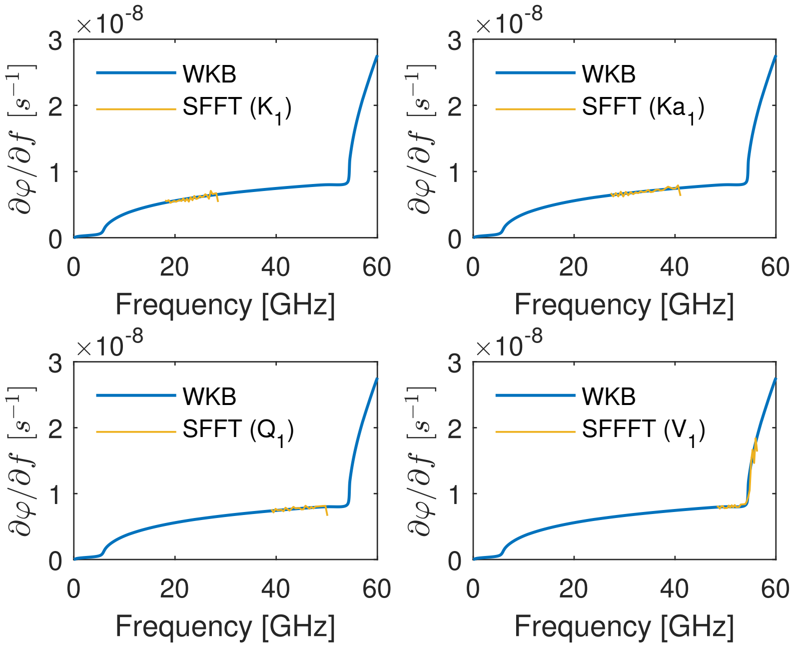

Figure 3.23: Phase derivatives obtained with the SFFT method.

### 3.3.9 The initialization method

With the results of each simulation, the phase derivative of each band is joined in one single profile and the initial frequencies are initialized. Figure 3.24 shows the full-band (FB) phase derivative of both methods.

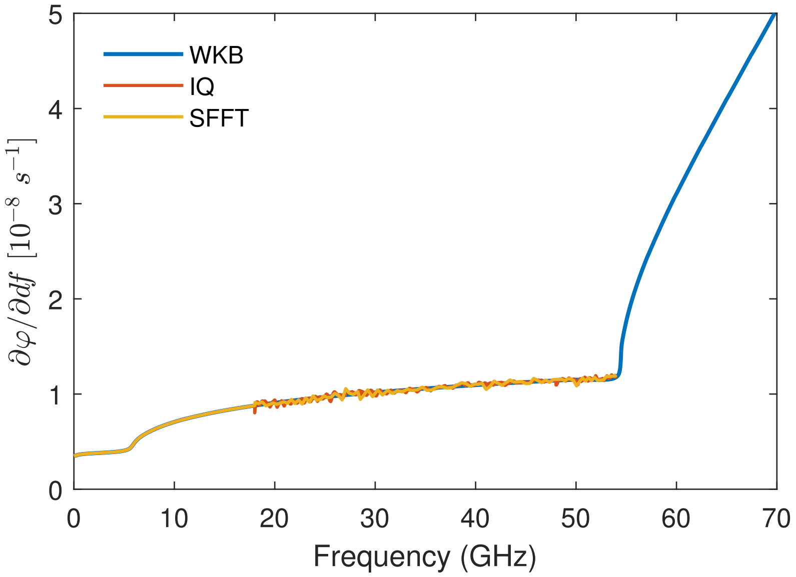

Figure 3.24: The full-band (FB) phase derivative of both methods.

The phase derivative due to the propagation in the setup is included. The profiles of each band are limited to the $[f_{min,d}, f_{max,d}]$ frequency range before being joined. The signal is initialized with the WKB phase derivative profile, removing the error associated with this part. The initialization is a topic by it-self and will be the further work.

### 3.3.10 The plasma position and the measurement error

The FB phase derivative profiles are defined in a set of $f_k$ frequencies, with $k = 1, ..., N$. The numerical Abel inversion is calculated by [82]:

$$r(F) = \frac{c}{2\pi^2} \sum_{k=2}^{N} \int_{f_{k-1}}^{f_k} \frac{\partial\varphi}{\partial f}(f_k) \frac{1}{\sqrt{F^2 - f^2}} df \tag{3.41}$$

With the rectangle rule, this expression becomes:

$$\begin{aligned} r(F) &\simeq \frac{c}{2\pi^2} \sum_{k=2}^{N} \frac{\partial\varphi}{\partial f}(\bar{f}_k) \int_{f_{k-1}}^{f_k} \frac{1}{\sqrt{F^2 - f^2}} df \\ &= \frac{c}{2\pi^2} \sum_{k=2}^{N} \frac{\partial\varphi}{\partial f}(\bar{f}_k) \left[\arcsin\left(\frac{f_k}{F}\right) - \arcsin\left(\frac{f_{k-1}}{F}\right)\right], \end{aligned} \tag{3.42}$$

where $f_{k-1} \leq \bar{f} \leq f_k$. Alternatively, this can be calculated with the trapezoidal rule (see appendix B.6). In this work we compute $r(F)$ with the rectangle rule using 10000 points. The obtained density profile is plotted in figure 3.25.

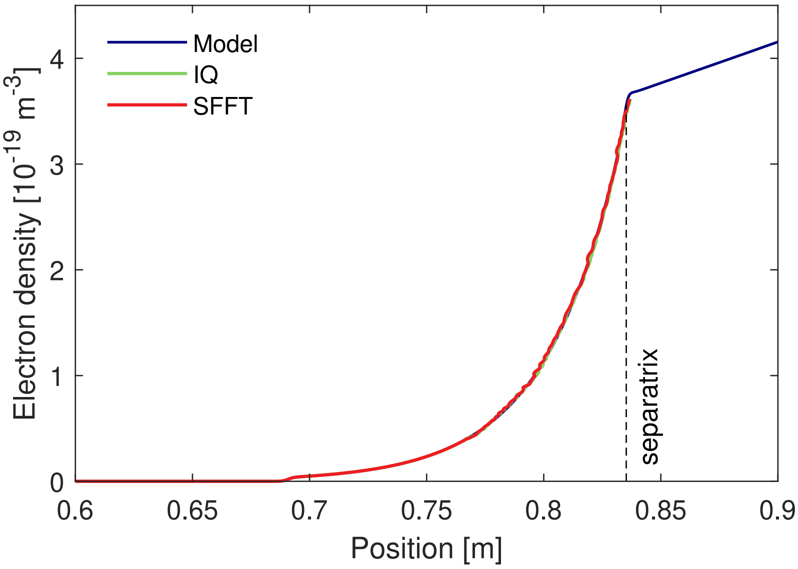

Figure 3.25: Density profile calculated with $r(F)$.

The position error $e(F)$ is shown in figure 3.26. The yellow area corresponds to the reference error requirements for DEMO, 1 cm.

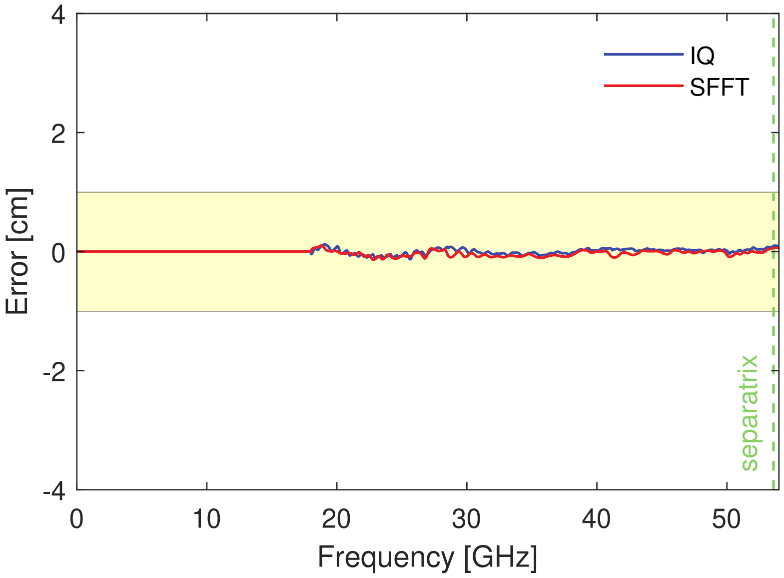

Figure 3.26: The error profile $e(F)$. The yellow region corresponds to the DEMO error requirements. The yellow area corresponds to the reference error requirements for DEMO.

The error is lower than 0.2 mm over all the frequency range. This is the expected order of values for simulations with plasmas that respect the reflectometry model conditions.

### 3.3.11 The plasma-wall multi reflections

If the blanket is added to the antenna assembly, multiple plasma-wall reflections can occur, affecting the detected signals. Figure 3.27 shows a snapshot of the electric field at approximately the separatrix frequency of a setup with a wall implemented.

When the electromagnetic field is reflected by the plasma, part of the energy enters directly in the receiving antenna, part of it is reflected at the wall and returns to the

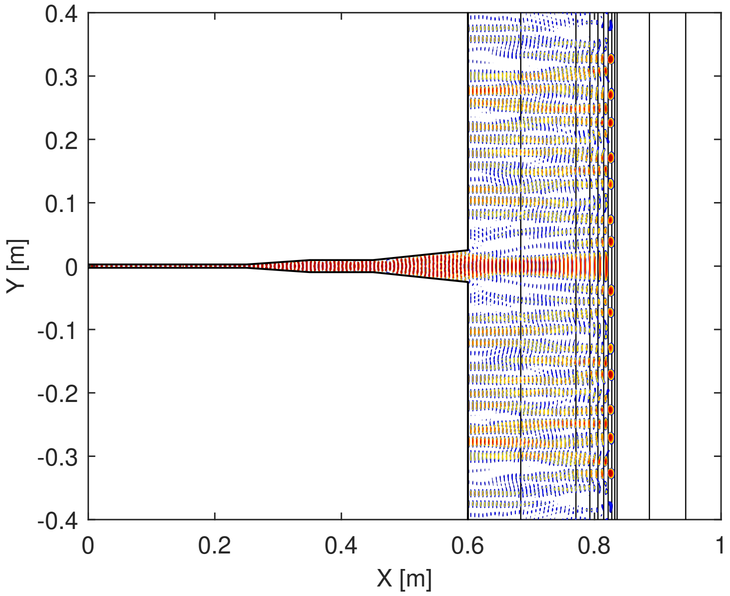

Figure 3.27: Snapshot of the electric field with a wall implemented ($F \sim F_{sep}$).

plasma/antenna and another part is absorbed by the PML at the top and the bottom of the grid. As result of the complex interaction that occurs inside this cavity composed by the metallic structure and the plasma, the spectrum of the I/Q signals gets additional frequency peaks. The comparison between the Q signal spectrum of the two setups (antenna and antenna with blanket) for the $Q_1$ band is shown in figure B.3 of appendix B.7. The information of the characteristic peak correspondent to the first reflection in the plasma stills in the signal. The higher frequency peaks need to be removed by adjusting the cutoff frequency of the applied filter. When these peaks are close, it is difficult to remove them without affecting the first one. This results in spurious oscillations in the phase derivative profiles associated with the method. In the SFFT method, the additional peaks obtained in each FFT can also lead to the wrong estimation of the beat frequency. Figure 3.28 shows this effect in the position error.

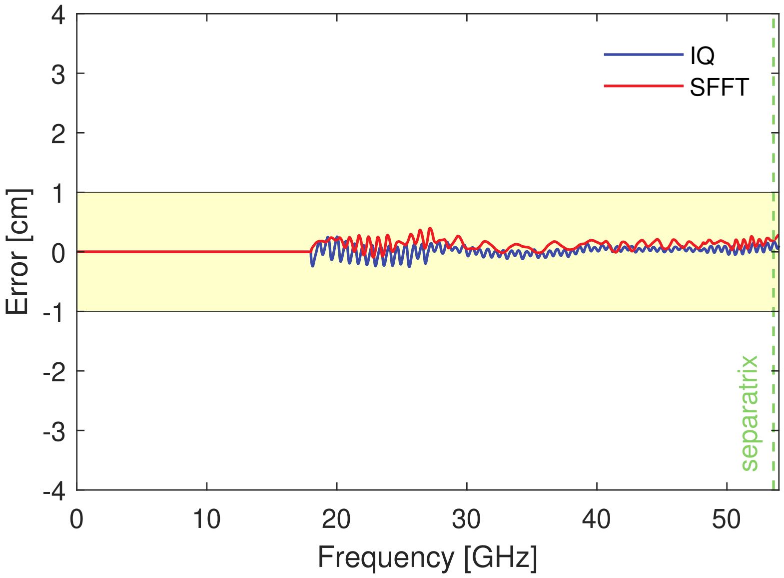

Figure 3.28: Position error in the setup with the blanket for he IQ and SFFT methods.

## 3.4 Simulation of multi reflectometers systems

### 3.4.1 The need for a high level framework

As discussed in chapter 2.4, the study and optimization of MRS/PPR systems involves testing different reflectometers configurations and plasmas. This requires repeating the steps of simulation and data analysis studied in the previous section for different regions of interest, plasmas, metallic structures and bands. In general, this a demanding task from the point of view of computational resources and time for producing the models and the necessary scripts for the simulations. For this reason, the optimization of PPRs requires a high-level framework that simplifies and automate the different operations that needed to be done in the simulation process, including the management of the simulations in HPCs. The simulation of a reflectometry measurement for one plasma configuration involves five elementary operations:

1. **Input models** - Creating the input models of the plasma and of the metallic structure from the input data relative to the region of interest. Define the source dimensions, the detection points and the reference point for the line of view. The fundamental waveguide must be adapted to the simulated band.

2. **UTS impulse response** - Obtain the UTS impulse response in vacuum.

3. **Mirror calibration** - Run the setup in vacuum and place a mirror at a reference position to find the group delay associated to the propagation in the antenna setup.

4. **Simulation with the plasma** - Run the setup with the plasma.

5. **Obtain the source signal** - Obtain the source signal so it can be used as reference.

These operations must be repeated for each band. Supposing the reflectometer works for $N_B$ bands, the simulation involves producing $N_B$ models for the metallic structure and $N_B$ plasma models, obtain $N_B$ UTS impulse responses, $N_B$ simulations with mirror and $N_B$ simulations with plasma. The data analysis follows the steps described in 2.4.2. In this section we propose a general structure of a code to automate the simulation of MRSs and the data analysis. In section 3.4.5 we present the MRSF framework that was developed with the discussed structure to optimize the DEMO PPR.

### 3.4.2 Formulation of a high-level framework for multiple multi-dimensional reflectometry simulations

The structure of the framework should be designed to:

- Automate the production of the necessary discretized models to the simulations from the plasma and reflectometer geometry models.

- Automate the simulation process. This includes create the necessary scripts to simulate the UTS impulse response, the simulation with the mirror and with the plasma for the different grids associated with each band.

- Simplify the process of input definition. Define a set of regions of interest, of metallic structures or plasmas should be an easy task, with minimal operations.

- Allow the use of different REFMUL* versions, with different dimensions (1D, 2D, 3D).
- Create the necessary scripts to support the simulations. This includes scripts to run the simulations, to run them in the HPCs, to verify the data, and other operations.
- Automation of data analysis.
- Facilitate the integration of different users. Different elements of the research team can contribute to the project. The structure of the framework should be designed to accept easily different functions to design the input models.

We propose a structure that is compatible with all these conditions. Simulating a MRS and obtaining the results is a question of defining the input data and run a few scripts that can be eventually needed as intermediary steps. The procedure to run and analyse a set of independent simulations is represented in figure 3.29.

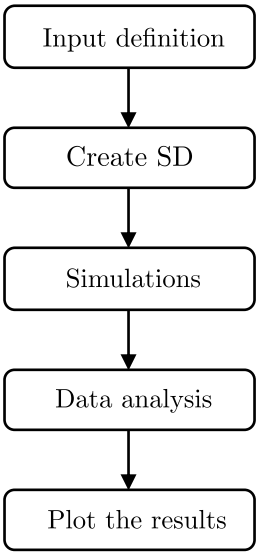

Figure 3.29: The five phases of the procedure simulation with the dedicated framework.

It consists in five phases. In the first phase, the input data is defined by the user. This includes setting all the variables that are relevant to the simulations, such as the set of regions of interest, the plasmas, the geometries of the reflectometers, the probing bands, and others. In the second phase, a script runs over this data and creates the simulation directory (SD script). This directory contains all the information that is needed to run the set of simulations that was predefined in the input. It also includes scripts to run all the simulations in HPCs or any other computer and check the data of necessary (SIM scripts). The next phase is run the simulations with these scripts. When they are finished, the data analysis scripts (DATA scripts) read the input data and run over the simulation results, writing the final results in the simulation directory. This corresponds to the fourth phase. Finally, in the last phase, the user plots the results according to the problem that is intended to study.

A basic concept for the simulation automation would be to have a list of simulations as input, where each variable would be defined in a different column of a list. The code would produce the necessary scripts to run the simulations one by one. However, this approach stills not optimizing the necessary time to define the input as much as it is possible because there are many variables to define in each simulation and there are simulations that share the same parameters. If we are simulating a set of $N_R$ reflectometers probing $N_P$ plasmas with $N_B$ bands, this would require the definition of $N_R \times N_B \times N_P$ independent input lines, which would be a time-consuming task. Therefore, a good approach is to find a set of main variables from which the variables of the problem are dependent, writing the list of each one instead of the list of simulations. Then, by defining the dependence between them, the list of simulations can be generated automatically.

An important condition to simplify the scripts is admitting that the source excitation is done in a plane, in contrast to the alternative, the use of an oblique UTS source. This allows to simplify the definition of the source position and the calculation of many variables, allowing to optimize many parts of the code. It also allows a pure mode definition and the UTS algorithm is faster than in oblique case.

### Finding the main variables of the problem

In section 2.4 the variables of a general multiple reflectometers system were described with the MRS notation. We also studied the description of multiple configurations of reflectometers and the most important aspects of the optimization of PPR systems. Considering the model in which the reflectometer geometry is described by the $\sigma^c(\mathbf{r})$ function, the plasma by the density $n_e^p(\mathbf{r}, t)$ and magnetic field $\boldsymbol{B}_0^p(\mathbf{r}, t)$, the detected signal of one measurement is represented in the MRS notation is:

$$S_{det}^{ijlcpk}(t) = f[S_{src}^{ijk}(t), \sigma^c(\mathbf{r}), n_e^p(\mathbf{r}, t), \boldsymbol{B}_0^p(\mathbf{r}, t)]. \tag{3.43}$$

The index $i$ labels the reflectometer number, $j$ the source, $l$ the detector associated with the $j$ source, $c$ the reflectometer system configuration, $p$ the plasma and $k$ the measurement time. These indexes are useful to describe the mathematical conditions of the system from the formal point of view. However, in the context of simulations, they are not useful due to several reasons:

- Usually only a region of interest (ROI) is simulated instead of the entire system. The region of interest is the fraction of volume to be simulated from the entire system. It should contain the elements of the physical model that are relevant to the final result.

- The measurement index is associated with the simulated plasma.

- Only one source (band) is simulated each time. All the associated detectors can be simulated at the same time. Each simulation produces $N_l$ detected signals. This corresponds to save in memory the field values at different fundamental waveguides.

- Depending on the application, the dimension of the simulation can be different (1D, 2D, 3D).

We are interested in finding a change of variables that facilitates the simulation process. Too many variables increase the complexity of the code. A lower number of variables increase the complexity of the input definition.

One important variable to consider is the dimension of the simulation. Depending on the dimension (1D, 2D, 3D), the REFMUL* version that runs the simulations is different, and the production of the models from the input data should be done with different parameters and routines. The dimension is represented by the index $D$, going from 1 to 3. Its value represents the number of dimensions, by definition.

In the simulation of a MRS, a different ROI is defined for each reflectometer to reduce the required computational power. Each ROI is associated with a different set of simulations, with different plasma and metallic structure models. Therefore, the ROI is an important variable from which the REFMUL* input models depend of. It is denoted by the index $R$.

The geometry of the metallic structure is also an important variable of the problem. Note that when the geometry is mentioned, it is not associated with any specific input matrix for simulation, but with the geometry of the entire system, defined by the $\sigma^c(\mathbf{r})$ function. The final model of the metallic structure to be used in the simulations depends on the region of interest, on the geometry and on the band which is being simulated. The metallic structure variable is represented by the $S$ index, which corresponds to the $c$ index used in the description of multiple configurations of reflectometers.

The plasma, described by the $n_e^p(\mathbf{r}, t)$ and $\boldsymbol{B}_0^p(\mathbf{r}, t)$ functions (and eventually by the temperature), is another important variable of the problem. The final plasma REFMUL* input models depend on the region of interest, on the plasma variable and on the grid resolution, which is a function of the simulated band. The plasma is associated to the index $P$, equivalent to $p$ used in the MRS description. The measurement index ($k$) is irrelevant, since it is directly associated to the plasma model.

The final variable is the source/band, labeled by the $B$ index (instead of $j$). Given the region of interest, the grid matrix is calculated depending on the simulated bandwidth. Since the different detections associated with a given band can be simulated at the same time, the detector index is not an important variable of the system. Introduce it as a main variable would increase the complexity of the code.

So far, we identified five main variables that are important to describe each simulation, labeled by the indexes $D$, $R$, $S$, $P$ and $B$. The fundamental idea to build the framework is to consider every function or variable used in the code as a function of the a combination of these five main variables (or less). Thus, instead of defining the list of simulations, the user defines the list of elements of each variable and its dependent variables separately, and how they are related with each other. The script creates the simulation list with the programed combinations.

### 3.4.3 Automating the simulations

#### Combination of the main variables

In order to automate the simulations it is necessary to define the order of the dependence and how the elements of each variable are associated. We chose the D-R-S-P-B order. The dependence is described by the definition of the vectors $\mathbf{D}$, $\mathbf{R}$, $\mathbf{S}$, $\mathbf{P}$ and $\mathbf{B}$. These vectors contain a set of elements of the respective variable and depend on the previous ones. The dependence is defined by writing the dependent vectors as function of the variables thought the function $C$:

$$\mathbf{R} = C[D] \tag{3.44}$$

$$\mathbf{S} = C[D, R] \tag{3.45}$$

$$\mathbf{P} = C[D, R, S] \tag{3.46}$$

$$\mathbf{B} = C[D, R, S, P] \tag{3.47}$$

The $D$ variable is independent. The number of elements of each vector is also an important quantity:

$$N_D = N[\mathbf{D}] \tag{3.48}$$

$$N_R = N[\mathbf{R}] = N[D] \tag{3.49}$$

$$N_S = N[\mathbf{S}] = N[D, R] \tag{3.50}$$

$$N_P = N[\mathbf{P}] = N[D, R, S] \tag{3.51}$$

$$N_B = N[\mathbf{B}] = N[D, R, S, P] \tag{3.52}$$

where the $N$ function represents the number of elements of a vector. In general, a variable $a$ of the problem is written in the form

$$a = f[D, R, S, P, B, ...], \tag{3.53}$$

or, in MRS notation,

$$a^{DRSPB} = f(...). \tag{3.54}$$

Each simulation corresponds to a $D$-$R$-$S$-$P$-$B$ combination.

Following we present a list of the principal variables of the problem for a general 3D case. The other dimensions follow the same kind of dependence. The coordinates of the ROI in the frame of simulation are:

$$(x_i, x_f, y_i, y_f, z_i, z_f) = f[R]. \tag{3.55}$$

The spatial and temporal resolution,

$$(N_\lambda, N_T) = f[B], \tag{3.56}$$

the minimum and maximum frequencies of the band, and the grid frequency,

$$(f_{min}, f_{max}, f_0) = f[B]. \tag{3.57}$$

The conductivity function is a function of $S$,

$$\sigma(x, y, z) = f[S]. \tag{3.58}$$

The emission and the detection is done at

$$x_{src} = f[S] \tag{3.59}$$

$$(x_{det}, y_{det}, z_{det}) = f[S]. \tag{3.60}$$

The plasma density and magnetic field are functions of $P$,

$$n_e(x, y, z) = f[P] \tag{3.61}$$

$$B_0(x, y, z) = f[P]. \tag{3.62}$$

These variables are directly obtained with the main variables and the other variables of the problem are dependent on them. The spatial (dx) and temporal (dt) discretization steps are given by:

$$dx = \frac{c}{N_\lambda[B] f_0[B]} = f[B] \tag{3.63}$$

$$dt = \frac{1}{N_T[B] f_0[B]} = f[B]. \tag{3.64}$$

The grid dimensions,

$$N_x = \frac{x_f[R] - x_i[R]}{dx[B]} = f[R, B] \tag{3.65}$$

$$N_y = \frac{y_f[R] - y_i[R]}{dx[B]} = f[R, B] \tag{3.66}$$

$$N_z = \frac{z_f[R] - z_i[R]}{dx[B]} = f[R, B]. \tag{3.67}$$

The metallic structure model depends on the continuous $\sigma$ function, on the region of interest and on the grid properties calculated with the band,

$$\sigma(i, j, k) = f[R, S, B], \tag{3.68}$$

as well as the discrete positions of the excitation and detection,

$$i_{src} = x_{src}/dx = f[R, S, B] \tag{3.69}$$

$$(i_{det}, j_{det}, k_{det}) = (x_{det}, y_{det}, z_{det})/dx = f[R, S, B]. \tag{3.70}$$

The result of each division is rounded to the integer. The plasma model depends on the continuous model of the density and magnetic field, but also on the region of interest and on the grid properties,

$$n_e(i, j, k) = f[R, P, B] \tag{3.71}$$

$$B_0(i, j, k) = f[R, P, B]. \tag{3.72}$$

The other variables of the problem can be represented in the same way. After setting the main parameters, the manage of the inputs is analysed.

### Defining the input data

The best way to define and organize the input data is write it in the form of tables/lists of the dependent variables of each main variable. There are 5 principal lists, one for each main variable. These lists contain the variables of the problem that have the dependences with the main variables in the form $a[R]$, $a[S]$, $a[P]$, $a[B]$. Since mixing variables of different dimensions increase the complexity of the input definition, it is a good practice to split the input in three different data sets, one for each dimension.

These lists are represented by $L_i$, where $i$ is the index. In terms of programming, these lists are structures of data. They can be easily stored in a datasheet, which is also easy to visualize and write. Each list is written in the form

$$L_i = \begin{array}{l|c|l|lcl} \text{Name} & \text{flag} & \text{dependences} & a_1[i] & ... & a_n[i] \\ \hline \text{Name}[i=1] & 0/1 & \text{STR}[i=1] & a_1[i=1] & ... & a_n[i=1] \\ \text{Name}[i=2] & 0/1 & \text{STR}[i=2] & a_1[i=2] & ... & a_n[i=2] \\ \text{Name}[i=...] & 0/1 & \text{STR}[i=...] & a_1[i=...] & ... & a_n[i=...] \\ \text{Name}[i=N_i] & 0/1 & \text{STR}[i=N_i] & a_1[i=N_i] & ... & a_n[i=N_i] \end{array}. \tag{3.73}$$

Each line corresponds to one element of the variable $i$. Each column to a variable dependent of $i$ ($a_1 ... a_n$). Instead of a numerical index, the elements of the main variables can be identified by a name, which is much easier to identify. The second column is a variable that allows to activate the element (1/0), which can be useful in some situations (e.g. tests). The third column is where the dependences to the other main variables are defined. This can be done in multiple forms, for example with a string with a predefined structure. One predefined string can be assigned to indicate this element is used to every combination of the other main variables (e.g. the string ALL). In the last columns all the $a[i]$ variables are defined. For example, if $i = R$, these variables can be the coordinates of the ROI, or the coordinates of the region of interest in other frame of reference.

After defining $L_R$, $L_S$, $L_P$, $L_B$, there are other lists of input data that are necessary to define to the problem variables that are function of a combination of main variables. This would require a list for each combination ($C_2^5 + C_3^5 + C_4^5 + C_4^5$ different lists, where $C$ is the usual combination operator). One of the best ways to simplify the input is reduce this to one list, where, in general, all the variables have the dependence of the five main variables. This list (refereed as $L_0$) has the form:

$$L_0 = \begin{array}{l|llllllll} \text{Name} & \text{value} & \text{Exceptions} & \text{Excep.}[1] & \text{Value}[1] & ... & \text{Excep.}[n] & \text{Value}[n] \\ \hline \text{Var}_1 & \text{VAL}_1 & \text{VAL} & \text{STR}[1] & \text{Value}[1] & ... & \text{STR}[n] & \text{Value}[n] \\ ... & ... & ... & ... & ... & ... & ... & ... \\ \text{Var}_n & \text{VAL}_n & \text{VAL} & \text{STR}[1] & \text{Value}[1] & ... & \text{STR}[n] & \text{Value}[n] \end{array} . \tag{3.74}$$

Each line corresponds to a dependent variable. The second column corresponds to its default value. One of the ways of defining the dependence is assume all the combinations of the main variables have the default value, and then define exceptions (Excep.). In general, a set of exceptions can be added. For example, if there is a variable to save the electric field matrix, and if we are interested in turn it on only for the simulations with vacuum, then we select the default value 0 and we add an exception for the vacuum plasmas with value 1.

A list with definitions related with REFMUL* (denoted by $L_R$) and another with the computer parameters where the simulations run is also necessary (denoted by $L_H$). It is useful to create different computer profiles, so the scripts can be produced and run in the respective computer just by changing the necessary variables. This is useful for local tests, to run simulations in HPC, etc.

Since defining the geometry of the metallic structure or of the plasma depends in general of many variables (e.g. path to the input files, displacement, turbulence level), it is also useful to define the variables of each one in a separated file. The $L_S$ and $L_P$ lists have a variable pointing to these configuration files. Thus, generating a set of plasmas or a set of models, can be also easily fully automated.

Summarizing, the input is defined by four different elements:

- The main lists: $L_R$, $L_S$, $L_P$, $L_B$.
- The secondary lists: $L_0$, $L_R$, $L_H$.
- Structure configuration files.
- Plasma configuration files.

### SD script - creating the simulation directory

The SD script reads the input data and creates a directory with the all the information that is necessary to run the simulations and analyze the data. This process is composed by 10 different phases:

- **phase 1** - Declaration of SD variables.
- **phase 2** - Definition of the lists of variables of the problem.
- **phase 3** - Production of the metallic structure models.
- **phase 4** - Production of the plasma models.
- **phase 5** - Write the simulation scripts (UTS scripts, MCAL scripts, SIM scritps, SRC scripts).
- **phase 6** - Write the verification scripts (CHK scripts).
- **phase 7** - Copy REFMUL* to the SD so it can be compiled and run the simulations.
- **phase 8** - Copy the input data, data analysis functions, pre-defined plot codes, other useful files that can be useful to save in memory.
- **phase 9** - Write the compilation script (CMP scripts).
- **phase 10** - Write the HPC scripts (HPC scripts) and prepare the data to send to the HPC if necessary.

The detailed description of each phase can be found in appendix B.8. After these tasks are completed, the user can run the CHK scripts. These scripts verify the existence of all the necessary files, the simulation variables, and other parameters. If they are correct, the user runs the scripts for the simulations. The UTS scripts must run before the others. All these intermediary steps can also be automated.

### 3.4.4 Changing the coordinates of the region of interest

The ROI is a rectangular parallelepiped defined in the frame of simulation ($S_0$) by two points, $(x_i, y_i, z_i)$ and $(x_f, y_f, z_f)$. $S_0$ is the frame of simulation, with the x axis perpendicular to the excitation plane (y-z plane) by convention. Independently of the antenna shape, the region of interest must be aligned with the fundamental waveguide in such way that the propagation direction is parallel with the x axis. One way of doing it is placing the origin of $S_0$ at the center of the waveguide cross-section, allowing to adjust the ROI dimensions easily.

In most of the applications, the geometry of the system or the plasma parameters are given in the machine frame of reference, $S_m$. In this case, it is necessary to convert the coordinates in several operations (e.g. models creation, position calculation, plotting). Figure 3.30 (a) shows the representation of the ROI and change of coordinate system.

Since REFMUL* works in Cartesian coordinates and the models are typically given Cartesian coordinates, the necessary transformation of coordinates is represented by a translation $\mathbf{T}$ and a rotation matrix $\mathbf{R}$. A point $\mathbf{p}_0 = (p_{0x}, p_{0y}, p_{0z})$ defined in the $S_0$ frame has coordinates

$$\mathbf{p}_m = (p_{mx}, p_{my}, p_{mz}) = \mathbf{T} + \mathbf{R}\mathbf{p}_0 \tag{3.75}$$

in the $S_m$ frame. If the coordinates are given in the $S_m$ frame, $\mathbf{p}_0$ is given by

$$\mathbf{p}_0 = \mathbf{R}^{-1}(\mathbf{p}_m - \mathbf{T}). \tag{3.76}$$

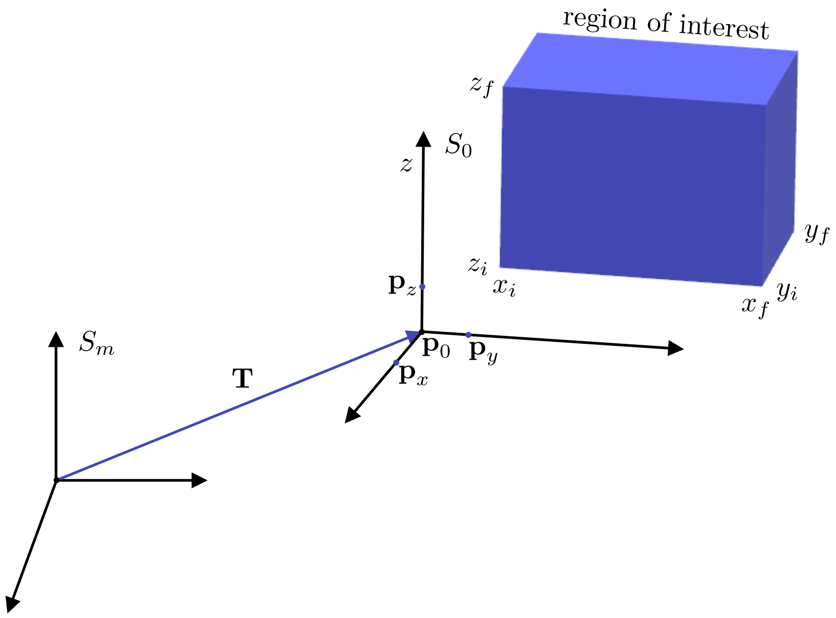

Figure 3.30: Illustration of the ROI and of the coordinate systems.

The $S_0$ frame is defined in terms of an origin $\mathbf{p}_0$ and by a point in each axis, $\mathbf{p}_x$, $\mathbf{p}_y$ and $\mathbf{p}_z$, measured in $S_m$. They can be easily determined, for example, with a CAD software. Thus it is of interest to write $\mathbf{T}$ and $\mathbf{R}$ in terms of these points. The translation is given by the origin of $S_0$:

$$\mathbf{T} = \mathbf{p}_0 = (p_{0x}, p_{0y}, p_{0z}), \tag{3.77}$$

The unit vectors referent to the three axis of $S_0$ are given by

$$\mathbf{v}_x = \frac{\mathbf{p}_x - \mathbf{p}_0}{\sqrt{|\mathbf{p}_x - \mathbf{p}_0|^2}} = \frac{(p_{xx} - p_{0x}, p_{xy} - p_{0y}, p_{xz} - p_{0z})}{\sqrt{(p_{xx} - p_{0x})^2 + (p_{xy} - p_{0y})^2 + (p_{xz} - p_{0z})^2}} \tag{3.78}$$

$$\mathbf{v}_y = \frac{\mathbf{p}_y - \mathbf{p}_0}{\sqrt{|\mathbf{p}_y - \mathbf{p}_0|^2}} = \frac{(p_{yx} - p_{0x}, p_{yy} - p_{0y}, p_{yz} - p_{0z})}{\sqrt{(p_{yx} - p_{0x})^2 + (p_{yy} - p_{0y})^2 + (p_{yz} - p_{0z})^2}} \tag{3.79}$$

$$\mathbf{v}_z = \frac{\mathbf{p}_z - \mathbf{p}_0}{\sqrt{|\mathbf{p}_z - \mathbf{p}_0|^2}} = \frac{(p_{zx} - p_{0x}, p_{zy} - p_{0y}, p_{zz} - p_{0z})}{\sqrt{(p_{zx} - p_{0x})^2 + (p_{zy} - p_{0y})^2 + (p_{zz} - p_{0z})^2}}. \tag{3.80}$$

The matrix $\mathbf{R}$ is given by

$$\mathbf{R} = \begin{bmatrix} v_{xx} & v_{yx} & v_{zx} \\ v_{xy} & v_{yy} & v_{zy} \\ v_{xz} & v_{yz} & v_{zz}. \end{bmatrix} \tag{3.81}$$

The components of the $\mathbf{R}^{-1}$ matrix as function of $\mathbf{v}_{xyz}$ can be found in appendix B.9. In many situations the models for the simulation are defined in one or two dimensions. If the input models are in 1-2D, the transformation is the same, and the output should be only a line or a plane from one of the frames. For the 2D case the transformation has the same form, with $\mathbf{T} = (p_{0x}, p_{0y})$ and

$$R = \begin{bmatrix} v_{xx} & v_{yx} \\ v_{xy} & v_{yy} \end{bmatrix}. \tag{3.82}$$

### 3.4.5 The development of the MRSF framework

In order to study the DEMO PPR, the MRSF framework was created with the structure discussed in the previous sections. The code is written in MATLAB [220], with some of the functions in $C$. The input is written in a data-sheet format.

The metallic structure matrix is obtained creating closed shape objects and verify if the points of the ROI grid are inside. A $F_S$ function was created to deal with any 2D model of the machine geometry composed by a set of points. Defined $\mathbf{r}_{wall}$ and a direction of probing $\mathbf{v}_{prob}$, a box with predefined dimensions is created, intercepting the wall in two points, $\mathbf{r}_{w1}$ and $\mathbf{r}_{w2}$. The antenna model (or multiple antenna setup) is then placed at the box and connected with $\mathbf{r}_{w1}$ and $\mathbf{r}_{w2}$. This allows to place different forms of antennas with cavities keeping the angle of emission and the connection with the wall. The fundamental waveguide of the emitting antenna is aligned with $\mathbf{v}_{prob}$.

The continuous and discrete width of the fundamental waveguide is a function of the band properties, so they are declared as dependent variables of the $L_B$ list. After producing the model, the source length is verified. If it is even, a line is removed to become odd. This gives an error of $dx$ to the metallic structure shape, which impacts the propagation in the setup and its radiation pattern. Due to the fact that $dx$ increases with frequency to values below the 1 $mm$, this effect can be neglected. If it is odd, a line of the matrix correspondent to the waveguide length is turned metallic or vacuum according to the defined discrete width. The slope of the taper to the oversized waveguide is kept. This is done above and below the waveguide geometry.

The plasma models are created by a physical model for the density or by interpolating an existing grid. The impact of the interpolation is very small compare to those associated to the numerical dispersion. This is done in the $S_0$ frame, being necessary convert the coordinates if $n_e$ is defined in the machine frame. Two different $F_P$ functions were created. The first one introduces vacuum in REFMUL*. The second, receives a two dimensional density and a magnetic field profile (that can come from the poloidal flux maps provided by the MHD simulations) and produces plasma models in the $S_0$ frame. The $\mathbf{p}_0$, $\mathbf{p}_x$, $\mathbf{p}_y$ and $\mathbf{p}_z$ coordinates are defined as dependent variables of $R$. Thus they are defined only one time and can be used by $F_S$ or $F_P$ functions multiple times.

Different dependent variables of $P$ (defined in the $L_P$ list) can be defined to automate some operations. For example, in many studies it is necessary to run a slab plasma with the density profile correspondent to the profile at the probing line. This can be automatized with one single variable which is turned on or off directly from the $L_P$ list.

With these two functions is possible to study the FWP and FSP optimization functions (see section 2.4.7) of a given 2D tokamak model.

### 3.4.6 Automating the input data setting

The input of the framework is a set of lists of the main variables with the respective dependent variables and a set of plasma and metallic structure configuration files. In many cases, its setting can also be automated, depending on how the lists and the configuration files are defined. With the $F_S$ and $F_P$ functions defined as described in the previously section, part of the input files can be produced automatically. This reduces the necessary time to configure the system to the definition of a set of positions, probing directions and regions of interest according with the optimization that is intended to do.

Given the shape of the wall, a script can generate a set of points in the wall (FWP optimization) or in the separatrix (FSP optimization). The $\theta_{sep}$ and $\theta_{wall}$ angles and the probing direction are then defined (see section 2.4.7) to each one. Each ROI can be adjusted manually according to the needs, taking the plasma frame into account. Figure 3.31 shows an example of the definition of the wall positions for a general tokamak geometry. The positions, or gaps, are labeled by G1-5. For each position a rectangular box is defined, where the setup is placed. The simulation frame axis is defined by the $\mathbf{v}_x = \mathbf{v}_{prob}$ and $\mathbf{v}_z$ vectors, with $\mathbf{v}_z \cdot \mathbf{v}_x = 0$. Each vertex of the region of interest (blue larger rectangular boxes in the figure) corresponds to the sum of the wall position with a linear combination of $\mathbf{v}_x$ and $\mathbf{v}_z$. The constants are adjusted to make sure the separatrix line is inside the ROI. The G1-2 gaps represent two different positions where the angle was aligned perpendicularly to the separatrix. The G3-5 gaps correspond to the same position with three different probing angles. This function is used for FWP optimization, where a set of positions is defined with different probing angles.

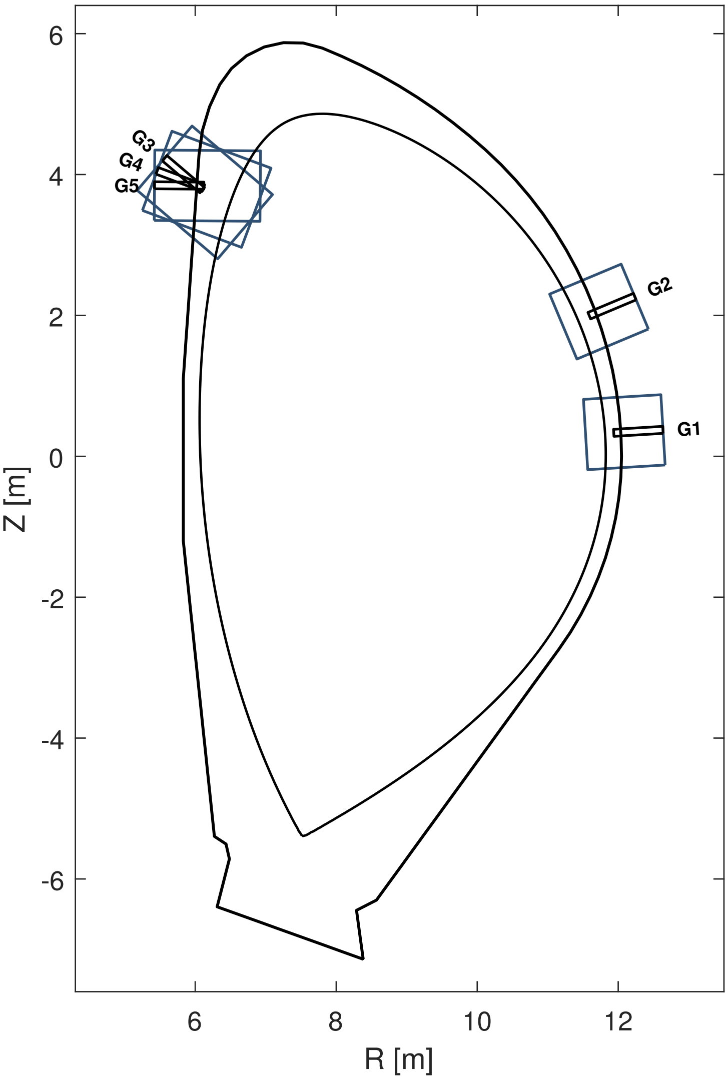

Figure 3.31: Definition of wall positions and model boxes in the FWP optimization. The emitters, the separatrix and the vessel are also represented.

Figure 3.32 shows an example of the definition of wall positions in FSP optimization.

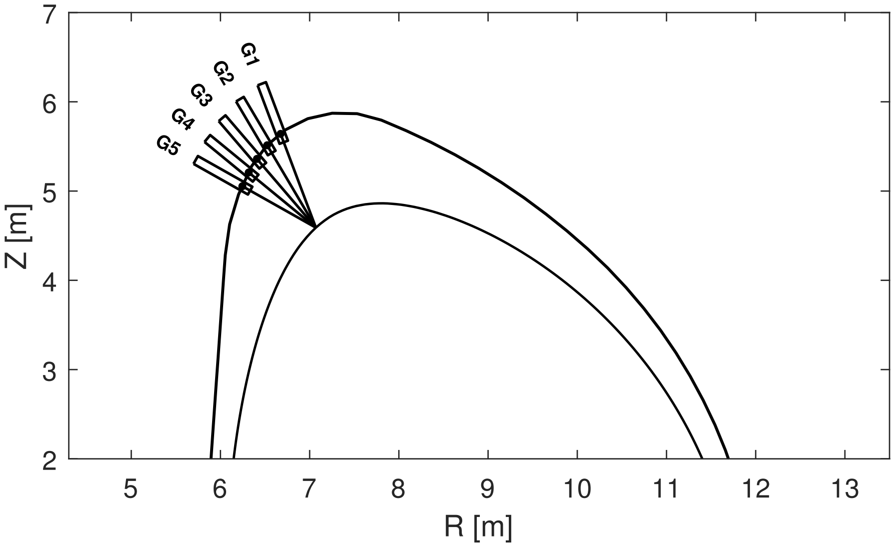

Figure 3.32: Definition of wall positions in FSP optimization. The emitters, the optical axis, the separatrix and the vessel are also represented.

In this case, the separatrix point is fixed, and the algorithm finds the intersection point with the wall, creating a set of setup boxes with the respective direction.

The definition of the configuration files for metallic structures can also be automated. The $F_S$ function connects a general antenna setup to the wall geometry independently to the probing direction. In many cases, like in the calculation of the FWP and FSP functions, the antenna model is the same. The only parameters to change are the wall position and probing direction. A script can produce these configuration files. The plasma list and configuration files can also be automated, especially in cases which involve sweeping plasma parameters or statistical studies (e.g. turbulence).

### 3.4.7 Automating the data analysis

Taking advantage of the main variables, the data analysis, in particular for position reflectometry, can also be automated for a given set of simulations. All the results can be saved in a SD sub-folder with a organized structure, so the plot scripts can be written for a general set of simulations.

In the context of the simulations, the process studied in section 2.4.2-2.4.2 is described by the following steps:

- **step 1** - The reference position and the initial plasma position in the line of view are obtained:

$$x_{ref}(x) = f[D, R, S, P, B] \tag{3.83}$$

$$x_{pls}(x) = f[D, R, S, P, B], \tag{3.84}$$

  $x$ represents the position along the line of view. The density and magnetic profile along the line of view are calculated:

$$n_e(x) = f[D, R, S, P, B] \tag{3.85}$$

$$B_0(x) = f[D, R, S, P, B]. \tag{3.86}$$

The WKB phase-shift and group delay is calculated with $n_e(x)$ and $B_0(x)$,

$$\varphi_{WKB}(F) = f[D, R, S, P] \tag{3.87}$$

$$\tau_{WKB}(F) = f[D, R, S, P], \tag{3.88}$$

as well as the separatrix density,

$$n_{sep} = f[D, R, S, P], \tag{3.89}$$

and the separatrix position,

$$x_{sep}(x) = f[D, R, S, P]. \tag{3.90}$$

These operations are done for a set of $N_{lv}$ line of views and can be fully automated. The $\varphi_{WKB}(F)$ is calculated for the two modes if both are active.

- **step 2** - The group delay relative to the propagation inside the antenna setup is obtained with the simulations with the mirror,

  $$\tau_M(F) = f[D, R, S, B]. \tag{3.91}$$

  This can be done with $N_{\tau_M}$ different methods, as the I/Q detection or the SFFT method. $\tau_M(F)$ is calculated for the O and X modes if both were simulated.

- **step 3** - The measured group delay is obtained with the simulated signals,

  $$\tau_m(F) = f[D, R, S, P, B]. \tag{3.92}$$

  This can be done with $N_{\tau_m}$ different methods. They can consider different mirror calibrations, detection methods, etc. If the I/Q detection is used, the detected amplitude can also be calculated,

  $$a_{det}(F) = f[D, R, S, P, B]. \tag{3.93}$$

  $\tau(F)$ and $a_{det}(F)$ are defined for the two modes.

- **step 4** - Each group delays associated to a $\tau_m$ method is joined in one full-bandwidth $\tau_n(F)$ profile,

  $$\tau_{FB}(F) = f[D, R, S, P]. \tag{3.94}$$

  This operation is done with $N_{\tau_{FB}}$ different methods (FB methods), including different forms of initialization. The same occurs for the amplitude, if it is calculated,

  $$a_{det}(F) = f[D, R, S, P]. \tag{3.95}$$

- **step 5** - The relative position $r(F)$ is calculated for each FB method,

  $$r(F) = f[D, R, S, P]. \tag{3.96}$$

- **step 6** - The error is calculated for each line of view, and FB method,

  $$e(F) = f[D, R, S, P]. \tag{3.97}$$

Each variable can be stored in memory organized by the step, method and name of the main variables. Both modes of propagation are calculated independently. The plot of the results is also easily scripted with the results organized. Plotting a set of data is a question of load the list of combinations of the main variables and plot the entries of interest with a *for* cycle.

The only step that is not automated after the input definition is the input parameters of the analysis methods (IQ and SFFT). If it is possible to automate their selection, in particular the IQ method (due to the possibility of calculating the detected amplitude), the optimization process and the study of the measurement performance for different plasmas can be fully automated. This opens the possibility of automate any dependent set of simulations and using decision algorithms or artificial intelligence AI systems to find the optimal configuration and make the all the necessary simulations to design the machine just by the definition of some input constraints.

Discussed the principal aspects of the simulation and data analysis automation and the MRSF code, the simulations that were conducted in the context of the DEMO PPR design and optimization are presented in the next chapter.

# Chapter 4

# The DEMO Plasma Position Reflectometry system (PPR)

## 4.1 Brief introduction to the study and optimization of the DEMO PPR system

Using the optimization concepts developed in chapter 2 and the MRSF framework with the structure proposed in chapter 3, several studies were conducted in the context of the design of the DEMO PPR system. In this chapter we present the most important results by chronological order, including the developed methods for data analysis and some techniques to minimize the complexity of the input definition.

The current reference antenna design for the design of DEMO PPR uses a pyramidal horn with a gain of 11dB at 10 GHz and an aperture of about 50 mm × 35 mm, being possible to fit two of these horns in a 100 mm circular aperture [221]. A low gain antenna is less directive and therefore less sensitive to changes in the probing angle. With these dimensions, the plasma is probed with the $TE_{10}$ mode and the antenna is aligned with the longest side parallel to the poloidal plane. The rectangular waveguide inner dimensions are 19.05 mm × 9.525 mm, corresponding to a standard WR-75 (minimum operation frequency 9.84 GHz) waveguide. At the required frequency range, the waveguide is oversized. This implies a small loss increase of 0.1 dB/m, that is acceptable in terms of the overall losses. The geometry and the radiation diagram is shown in appendix C.2.

The first set of simulations was carried out with the official DEMO 2015 scenario (section 4.2) and were performed at the IST cluster hosted in Lisbon, Portugal. We defined a set of 100 reflectometers located at equidistant positions around the machine and we tested two different system configurations, the first one with the probing beam aligned perpendicularly to the wall and a second one with the probing beam aligned perpendicularly to the separatrix. The first configuration has advantages from the point of view of the implementation of the antenna setup in the wall, however the measurement performance is expected to be lower.

Later, a new model was available for research, the official DEMO 2017 scenario from the EUROfusion database. We defined a new set of reflectometers the measurement performance of the same configurations was evaluated, expecting similar results of the DEMO 2015 scenario (section 4.3). We also studied the configuration without the wall, so it was possible to understand the effect of the plasma curvature without the effects of the plasma-wall reflections. The simulations were carried out in MARCONI, a new high performance computing facility for European nuclear fusion modeling hosted in Bologna, Italy [222]. Based in the results from the thermomechanical studies, we introduced a 10 cm cavity in the wall, where the antenna setup was placed. In section 4.4 we compared the results of this model with the previous ones, without the cavity. In section 4.5 we evaluated the system's sensibility to different scrape-off layer profiles.

The results from the previous studies were analyzed with the IQ/SFFT methods described in section 3.3. These algorithms have some steps that have to be done manually. In section 4.6 we develop an algorithm based in the IQ detection capable of obtaining phase derivative profiles and detected amplitude in an automated form. The algorithm was applied in the previous set of simulations and the results were compared with the manual implementation. With the developed method it was possible to proceed to the optimization of the system for the baseline scenario. In section 4.7, the FWP optimization function was studied for the baseline scenario and the optimal configuration was obtained.

The second phase of the design of a PPR system involves testing different deviations to the equilibrium that can occur during the discharge. This requires the simulation of many different plasma configurations for each reflectometer with the optimized configuration, which is a very demanding task from the point of view of computational resources, requiring an automated algorithm for the data analysis. In section 4.8 the effect of the plasma displacements in the measurement performance of the optimized system was evaluated. In section 4.10 we studied the effect of the plasma turbulence in one HFS equatorial position and the application of the developed algorithms in turbulence studies.

The conclusions of the study and the future work are described in chapter 5.

## 4.2 Analysis of the DEMO 2015 baseline scenario

### 4.2.1 The DEMO 2015 input models

From the EUROFUSION official database we have access to (i) the vacuum vessel geometry, (ii) the poloidal flux $\rho(R, Z)$ for two plasma configurations, the start of the flap top (SOF) and the end of flat top (EOF), (iii) the separatrix line and (iv) the electron density profile $n_e(\rho)$. More information on the plasma configuration can be found in [223]. We selected the EOF configuration, characterized by $R_0 = 9.31$ m, $a = 2.92$ m and $B_0 = 5.63$ T. Figure 4.1 shows the normalized poloidal flux map and the vacuum vessel geometry.

The data presents two limitations: (i) the lack of information in the scrape off layer region and (ii) the poor resolution of the 2D poloidal flux data comparing with the FDTD simulation grid. To overcome the first problem, we extrapolated the density profile linearly. Figure 4.2 shows the extrapolated density profile.

The normalized poloidal flux was measured at the wall. The values can be found in appendix C.1.2. The minimum value out of the divertor region is $\rho_{min} = 1.0258$, higher than the initial plasma position poloidal flux from the density profile. This ensures that there is no plasma inside the antenna setup. Using the density profile and the poloidal flux map, we built the density map, $n_e(R, Z)$, shown in appendix C.1.1. The poor resolution of the poloidal flux was solved by interpolating the density map to the FDTD grid dimensions.

The principal aim of this introductory study was the (i) test the MRSF framework, the (ii) development of an IQ detection code compatible with the list of simulations, (iii) testing the principle of aligning the probing beam perpendicularly to the separatrix and (iv) study the position error in the regions with variable density gradient direction.

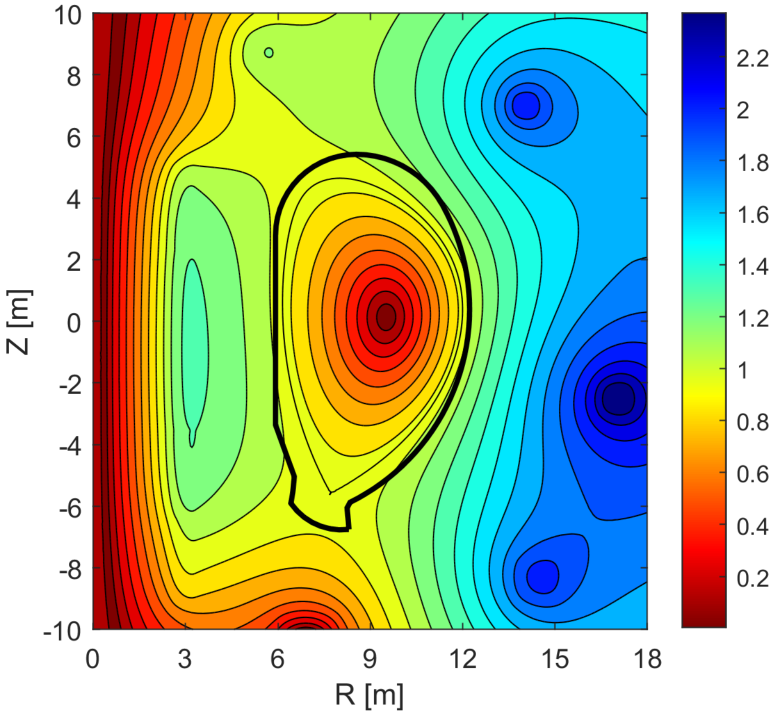

Figure 4.1: Normalized poloidal flux of the 2015 DEMO model.

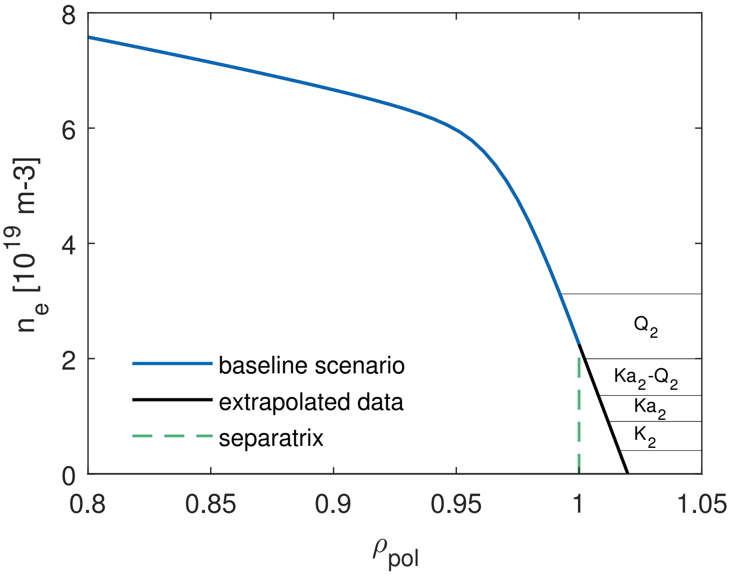

Figure 4.2: Extrapolated density profile.

As discussed in section 1.4.3, at least 15 positions are required for a reliable reconstruction of the DEMO separatrix. In the other hand, there is a limit for waveguides associated with the spatial constraints. Since there is no constraint on the location of each reflectometer, we opted for defining 100 different equidistant positions around the machine. This allows to study the measurement performance of the system independently from the final decision on the location of the reflectometers with an acceptable spatial resolution (the distance between the center of each reflectometer is 24 cm). The positions, designed as gaps, were divided in 16 regions and labeled by the code G[region][letter]. For this system of positions, we defined two different emission configurations, one with the emission line aligned perpendicularly to the wall and the other with the emission line aligned perpendicularly to the separatrix. For each position and configuration, we defined the boxes to place the antenna assembly models (model boxes) and the respective regions of interest for the simulations. The region of interest is the same for all the bands, facilitating its definition. The separatrix density is $n_{sep} = 2.25 \times 10^{19}$ m$^{-3}$, the corresponding probing frequency is $F_{sep} = 42.58$ GHz. The minimum cyclotron frequency is 119.9 GHz at the LFS, guarantying the accessibility to the separatrix. The 18–50 GHz range of frequencies was selected to probe the DEMO separatrix, divided in three different bands: K$_2$=[18,29] GHz, Ka$_2$=[27,45] GHz and Q$_2$=[33,55] GHz. The sweep is done in 100000 iterations. The relativistic effects are not usually taken into account in PPR studies because the temperature is typically low in the SOL.

### 4.2.2 Probing direction perpendicular to the wall

Figure 4.3 shows the position and the direction of the model boxes of each reflectometer in the first configuration where the probing direction is aligned perpendicularly with the wall. Some of the regions of interest used in the simulations are also shown, with the respective plasma decaying frame region (red rectangle).

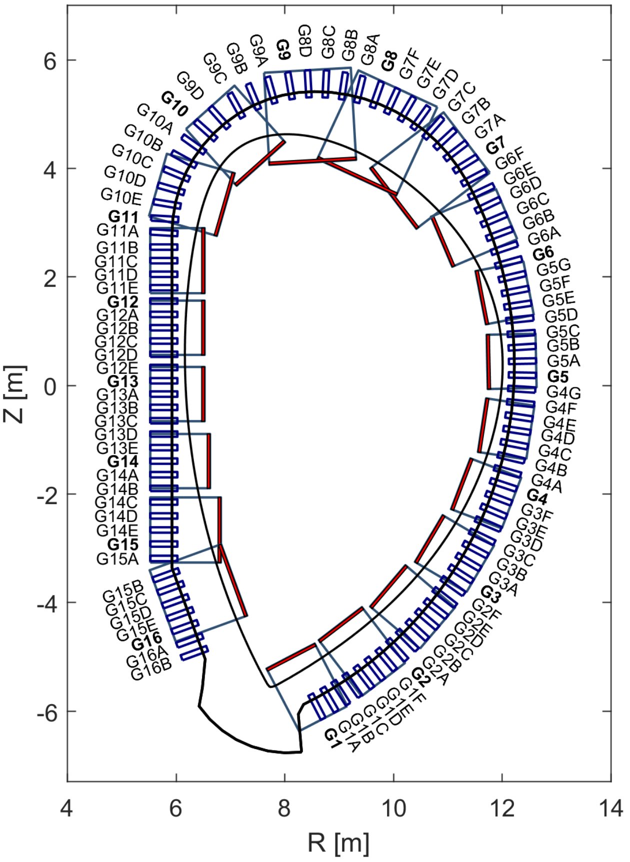

Figure 4.3: Configuration with the antennas aligned perpendicularly to the wall.

This study corresponds to 300 simulations to calibrate the UTS, 300 simulations with the mirror and 300 simulations with the plasma (100 reflectometers, 3 bands each one, 1 plasma). There are essentially two different conditions that simplify and reduce the necessary time to define the input. The first condition is using the same region of interest for all the bands. The second condition is using the same number of iterations and source parameters for each region of interest and for each band. Each region of interest is defined in such way that the plasma decaying frame region is after the separatrix.

The angle of incidence of the probing beam in the plasma and the plasma-wall distance are two important factors that contribute to the final measurement performance. Figure 4.5 shows the plasma-wall distance and the absolute value of $\theta_{sep}$ for this configuration. The discontinuities are due to the separatrix line is composed by a discrete set of points.

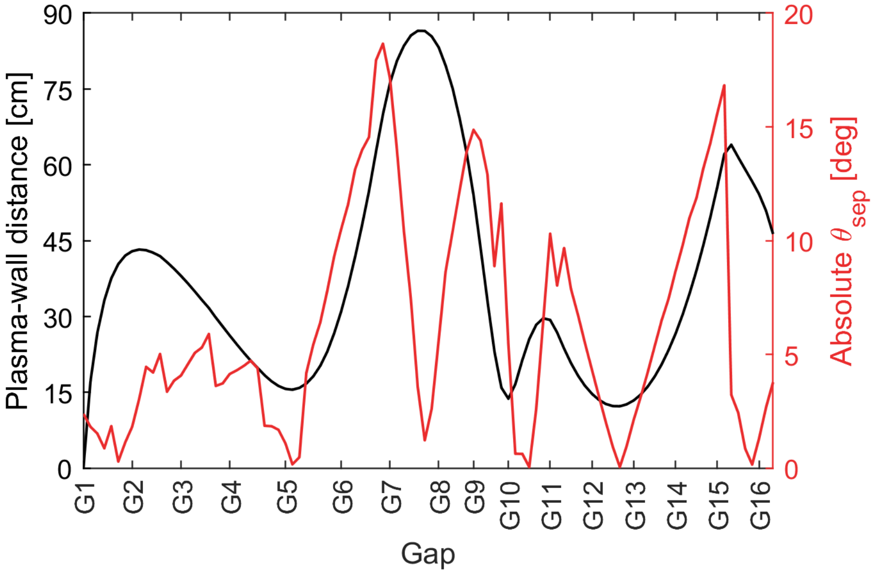

Figure 4.4: The plasma-wall distance and the absolute value of $\theta_{sep}$.

Figure 4.5 shows the absolute position error of this configuration.

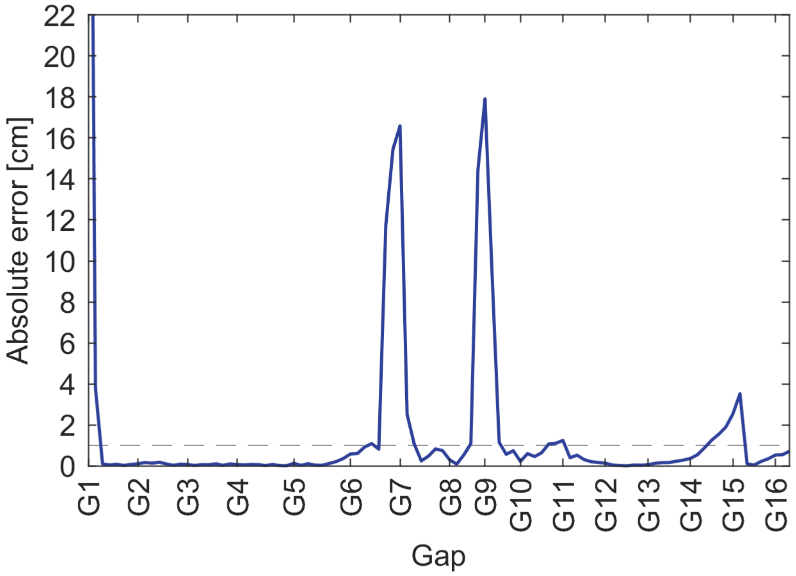

Figure 4.5: The position error with the probing direction perpendicular to the wall.

The results show that the positions in the equatorial plane region and some below (G1C-G6 and G11C-G14) exhibit errors in the order of 1 mm, being in agreement with the requirements for plasma positioning. On the other hand, the positions near the divertor (G1A-B and G14B-G15A) and at the top of the machine (G6B-G7B, G8C-G9B and G10D-G11) have errors in the order or greater than 1 cm. They correspond to the gaps where $\theta_{sep}$ and the distance between the wall and the initial plasma position (the plasma-wall distance) are larger simultaneously (see figure 4.4). In some situations the signal is lost or partially lost, leading to the high errors, without physical meaning in terms of propagation. Figure 4.6 shows the snapshot of the positive part of the electric field at the separatrix frequency for different positions.

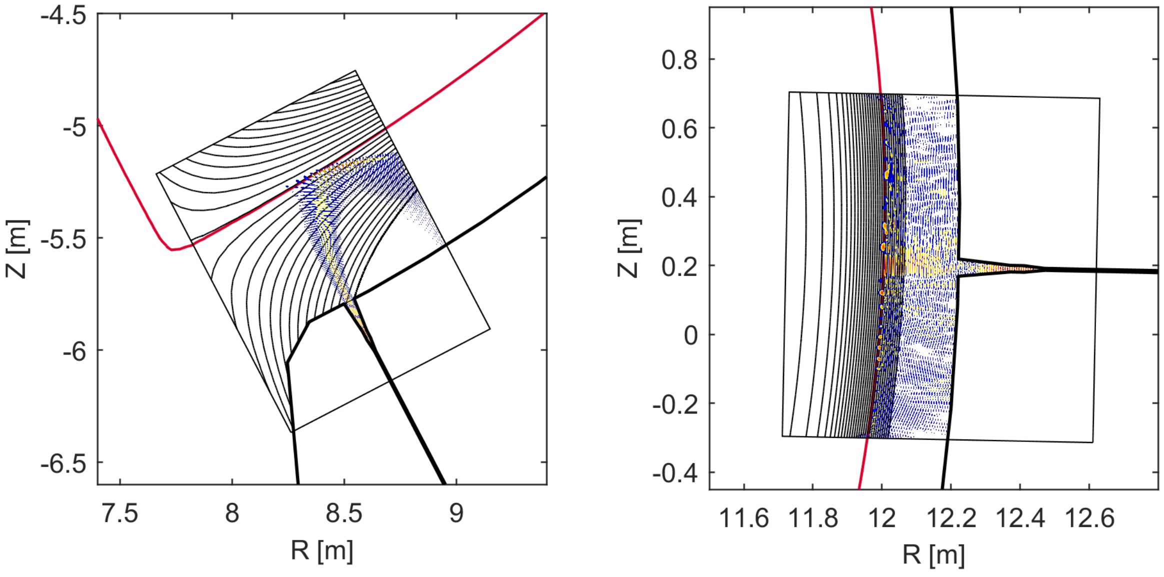

(a) G1.

(b) G5.

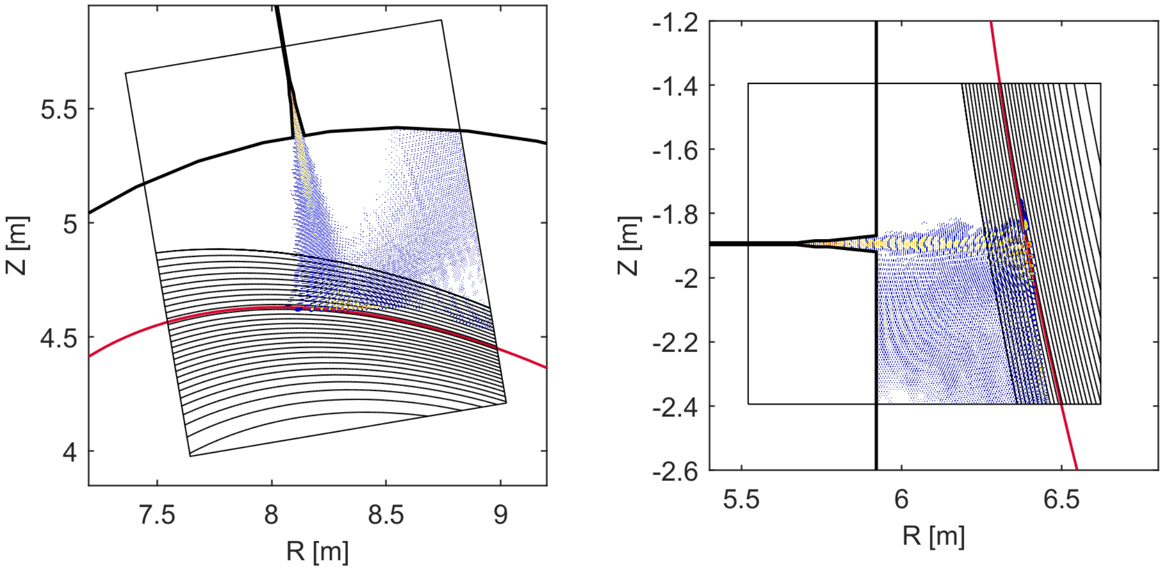

(c) G9.

(d) G14B

Figure 4.6: The snapshot of the electric field at different positions.

The beam deviation due to the divergence of the flux lines is illustrated in figures *a* and *c*. Figure 4.6 *b* shows a gap where the measurement error is low. The density gradient has approximately constant direction, being approximately aligned with the probing direction during all the propagation. Despite the reflections at the wall, most of the signal reflected by the plasma is detected by the antenna. In figure 4.6 we observe a situation where part of the beam is mostly reflected to only one side of the tokamak's wall. In this case, the effects of the plasma-wall reflections are expected to be lower, since most of the reflected signal that comes from the plasma enters directly in the antenna or is conducted to the environment due to the way of how the plasma-wall reflections occur due to the particular plasma configuration and wall geometry.

### 4.2.3 Probing direction perpendicular to the separatrix

In the second configuration the direction of the probing beam was aligned perpendicularly with the separatrix according with the condition studied in section 2.4.7, $\nabla\rho \cdot \mathbf{v}_{prob} = 0$. Since the model boxes have different directions, this study required 300 new simulations with the plasma, with the mirror and the respective UTS calibrations. Figure 4.7 shows the direction of the model boxes of each reflectometer and some examples of regions of interest used in the simulations. Figure 4.8 shows the absolute position error.

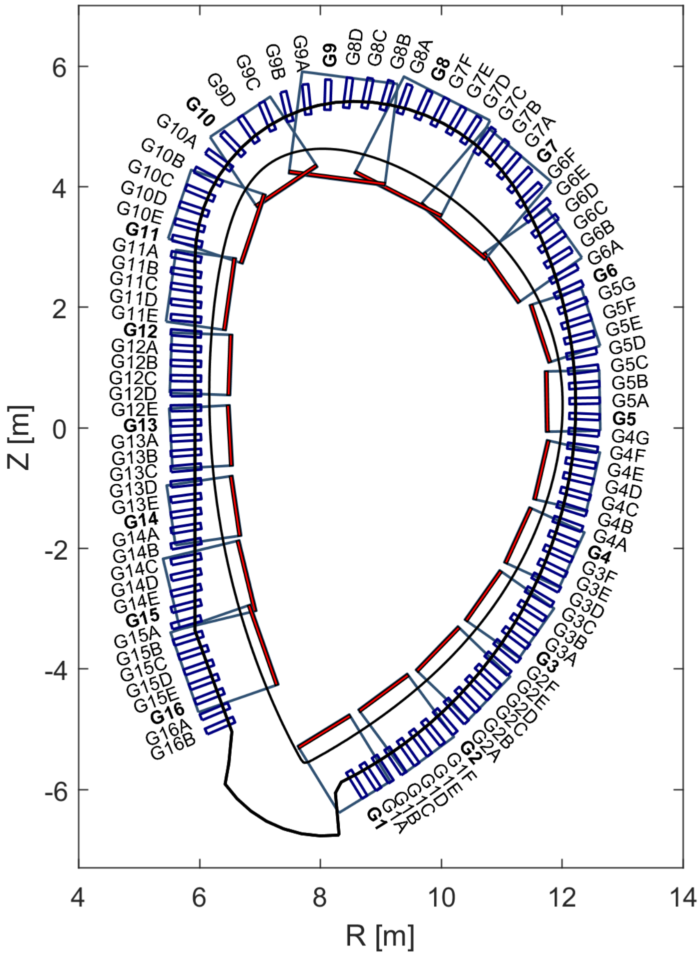

Figure 4.7: Configuration with the antennas aligned perpendicularly to the separatrix.

With the exception of the divertor region where the density gradient variations are higher, the error is lower than 0.5 cm over all the positions, corresponding to the mea-

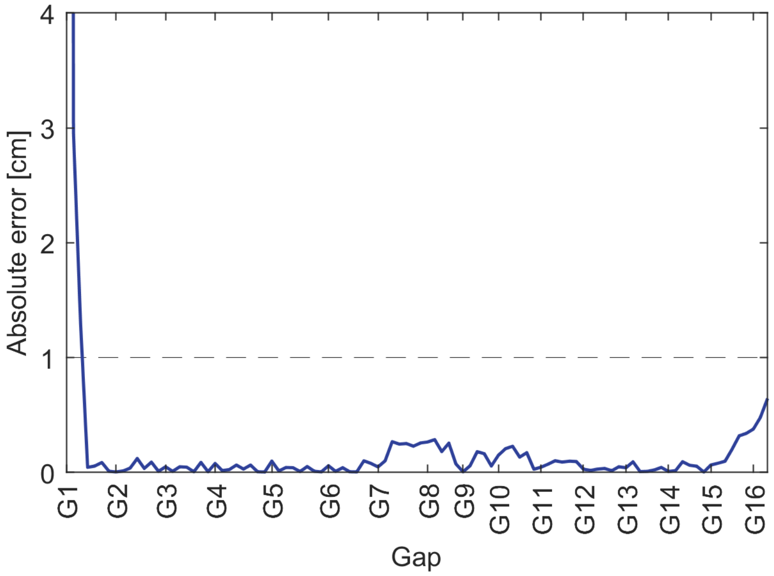

Figure 4.8: The position error for the configuration with the probing direction perpendicular to the separatrix.

surement requirements. This shows that the alignment condition with the separatrix leads is a good choose as first configuration to test in the design of a PPR.

The phase derivatives were obtained with the IQ method implemented with the framework variables. There are essentially three parameters that need to be selected manually: the number of simulation, the signal delay and the filter cutoff. Even with all the remaining operations automated, the process of data analysis of all the simulations consumes a considerable time in its execution.

In 2017 a new DEMO scenario was available in the EUROfusion database. We decided to continue the studies with the new model. There are several aspects that need to be taken into account:

- The density profile was extrapolated by a linear function. The density profile of real plasmas is better described by an exponential decay in the SOL [43].
- A compressive study of the I/Q spectrum is necessary to identify how the signal frequency components change in each gap.
- It necessary the implementation of the SFFT method with the framework variables and the comparison with the IQ results.
- The measurement error is not the unique indicator of measurement performance. A study in the detected amplitude is necessary to conclude if the measurements are viable or not. This can be done with the IQ algorithm.
- If the signal delay is estimated by an algorithm, the IQ method is reduced to the selection of the cutoff parameter. The investigation of a selection criteria is necessary to understand if the full automation of the data analysis is possible.

Next the new geometry and the results of the new configurations are shown.

## 4.3 Analysis of the 2017 DEMO baseline scenario

### 4.3.1 The 2017 input models

The official data from the EUROfusion official database provides the vacuum vessel geometry, the normalized poloidal flux and the electron density profile of the 2017 baseline scenario ($R_0 = 8.938$ m, $a = 2.883$ m and $B_0 = 4.89$ T). Similarly to the 2015 model, the density data lacks information in the scrape-off layer. In this region, the density profile was extrapolated by an exponential decay [43]. Figure 4.9 shows the extrapolated density profile.

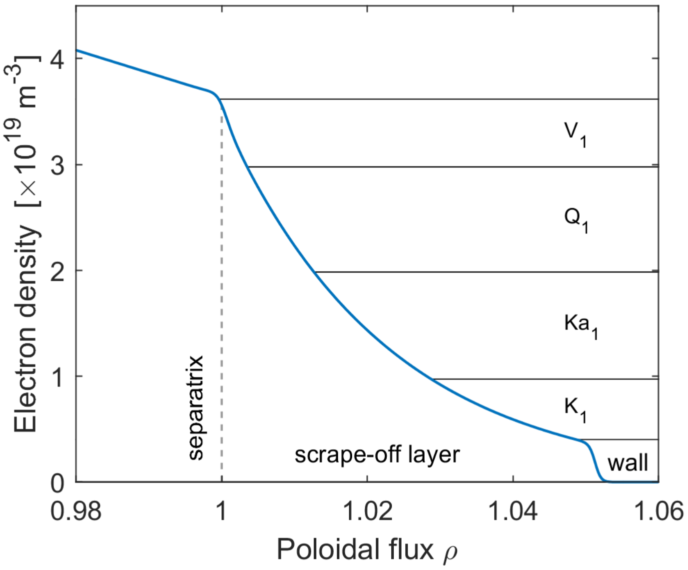

Figure 4.9: Extrapolated density profile for the 2017 baseline scenario.

The final density profile $n(\rho)$ is described by

$$n(\rho) = [n_{\text{ped}}(\rho) + n_{\text{sol}}(\rho)] \times \kappa(\rho_f - \rho, w_f), \tag{4.1}$$

with

$$n_{\text{sol}}(\rho) = \beta n_{\text{sep}} exp\left(-\frac{\rho - 1}{\lambda_{\text{sol}}}\right) \times \kappa(\rho - 1, w_0), \tag{4.2}$$

$$n_{\text{ped}}(\rho) = \left[\frac{n_{\text{ped}} - n_{\text{sep}}}{1 - \rho_{\text{ped}}}(\rho - 1) + n_{\text{sep}}\right] \times \kappa(1 - \rho, w_0), \tag{4.3}$$

and

$$\kappa(x, w) = \frac{1}{2}\left[1 + tanh\left(\frac{x}{w}\right)\right], \tag{4.4}$$

where $w_f = 0.0004$ is the width and $\rho_f = 1.0271 - 3w_f$ is the central position of the hyperbolic tangent decay to the wall, $n_{\text{sep}} = 3.65 \times 10^{19}\,\text{m}^{-3}$ is the input separatrix density, $n_{\text{ped}} = 6.21 \times 10^{19}\ m^{-3}$ is the pedestal density, $\rho_{\text{ped}} = 0.94$ the pedestal position, $\lambda_{\text{sol}} = 0.0114$ is the decay constant at the scrape-off layer and $\beta = 0.95$ and $w_0 = \lambda_{\text{sol}}/18$ are smoothing constants. The decaying length is approximately 3 cm at the equatorial zone, compatible to the order of values that is observed in experiments [43, 224, 44, 45].

An hyperbolic tangent frame centered at the plasma wall position (the minimum poloidal flux at the wall is 1.0542) is applied to ensure the density is zero inside the antenna setup. These parameters create a smooth profile between the pedestal and the scrape-off layer zone, as shown in figure 4.9. With this model, where the continuity of the density derivative is ensured, the final separatrix density is $n(\rho = 1) = 3.56 \times 10^{19}\,\mathrm{m}^{-3}$, slightly lower than the input one. Another limitation from the data is the poor resolution of the normalized poloidal flux map $\rho(R, Z)$. The equilibrium density profile $n_0(R, Z)$ was calculated with $n_e(\rho)$ by extrapolating the normalized poloidal flux to the FDTD grid as it was done for the 2015 model. Figure 4.10 shows the obtained density map.

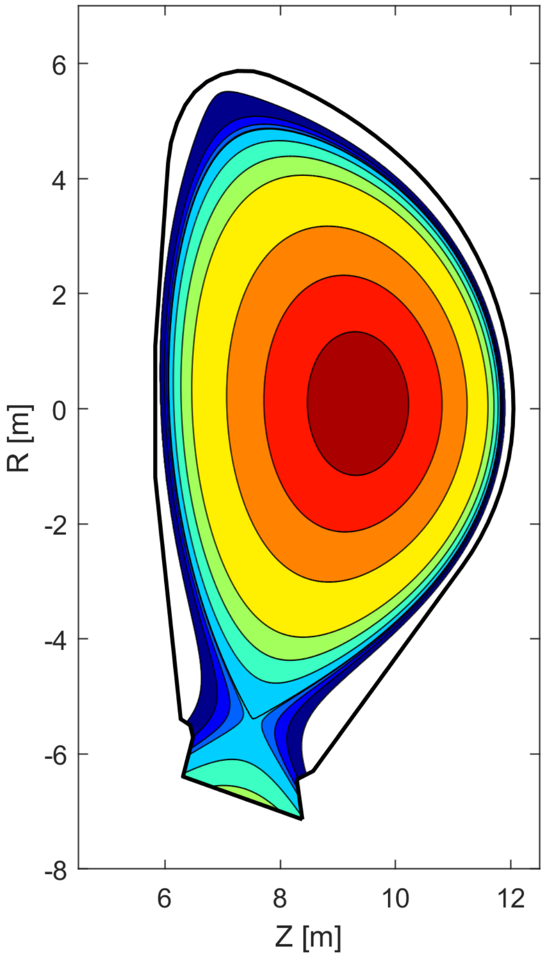

Figure 4.10: Density map for the 2017 baseline scenario.

Similarly to the previous studies, we defined 100 different positions divided them in 16 regions and labeled by the code G[region][letter]. We also defined the configuration with the probing direction aligned perpendicularly to the wall and perpendicularly to the separatrix. For each position and configuration, the model boxes and the respective regions of interest (ROI) were defined for each simulation. Figure 4.11 shows the second configuration and some of the regions of interest.

The separatrix density corresponds to a probing frequency of $F_{sep} = 53.57$ GHz. The 18–54 GHz frequency range was selected to probe the separatrix, divided in four bands, the same that were used in the example illustrated in section 3.3 ($\mathrm{K}_1$ = [18,29] GHz, $\mathrm{Ka}_1$ = [27,42] GHz, $\mathrm{Q}_1$ = [39,51] GHz, $\mathrm{V}_1$ = [48,57] GHz). The frequency range for data analysis is $\mathrm{K}_{d1}$ = [18,28] GHz, $\mathrm{Ka}_{d1}$ = [28,40] GHz, $\mathrm{Q}_{d1}$ = [40,49] GHz, $\mathrm{V}_{d1}$ = [49,54]

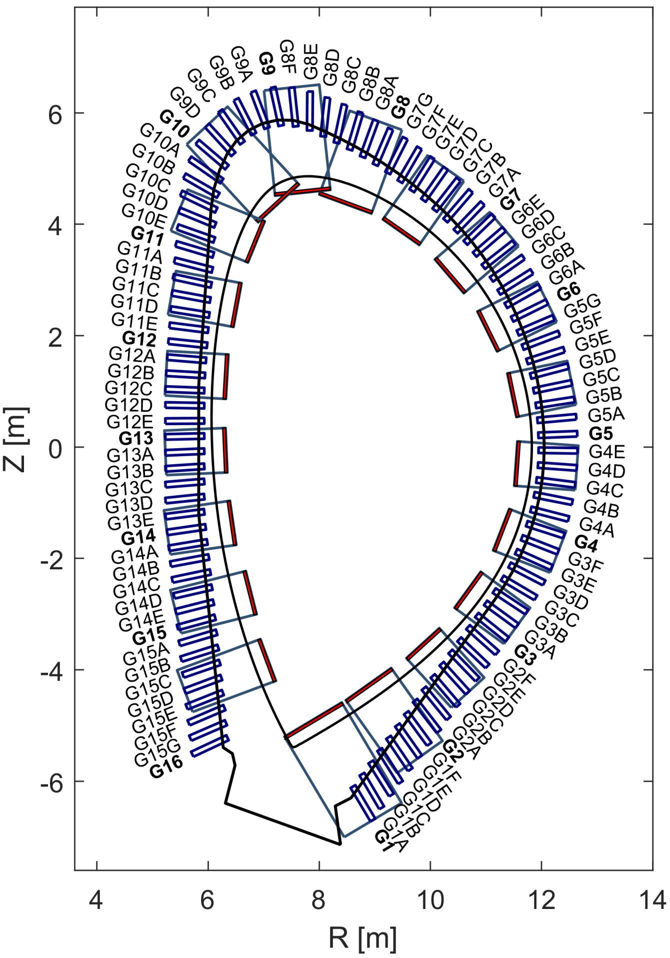

Figure 4.11: Configuration with the probing direction aligned perpendicularly to the separatrix for the DEMO 2017 model.

GHz. The cyclotron frequency at $R_0 + a$ is $f_c = 103$ GHz, guarantying the accessibility to the separatrix position. The relativistic effects are not included. The sweep occurs in 160000 iterations and the signal is initialized and finalized with $n_{pre} = n_{fall} = 20000$. The profiles are initialized with the WKB phase derivative.

### 4.3.2 Probing beam perpendicular to the separatrix

The data of the two configurations was analysed with the IQ method. Figure 4.12 shows the absolute position error of the two configurations (*sep* for the alignegment perpendicularly to the separatrix and *wall* for the alignement perpendicularly to the wall). The wall-separatrix distance and the absolute $\theta_{sep}$ angle are shown in appendix C.3. Similarly to the 2015 model, we verify that the regions where these parameters are higher are susceptible to higher error. Aligning the gaps perpendicularly to the separatrix improves the measurement performance in most of the positions.

As we approach the divertor region, the error increases fastly since flux lines have a gradient with variable direction. This effect is worst in the configuration with the probing direction perpendicular to the wall and leads to the loss of the signal or a part of it. For most of the gaps at the equatorial zone (G2-G8, G11-G15b) the error remains within the requirements, at a low level (∼ 0.1 cm). At the top of the machine, the change in configuration allows to decrease the error to values in the order of 1 cm or below.

By looking to the error plots, it is not possible to determine directly if the error is due to the propagation in the plasma, due to the spurius signals from the plasma-wall reflections, to the data analysis, or to a combination of them.

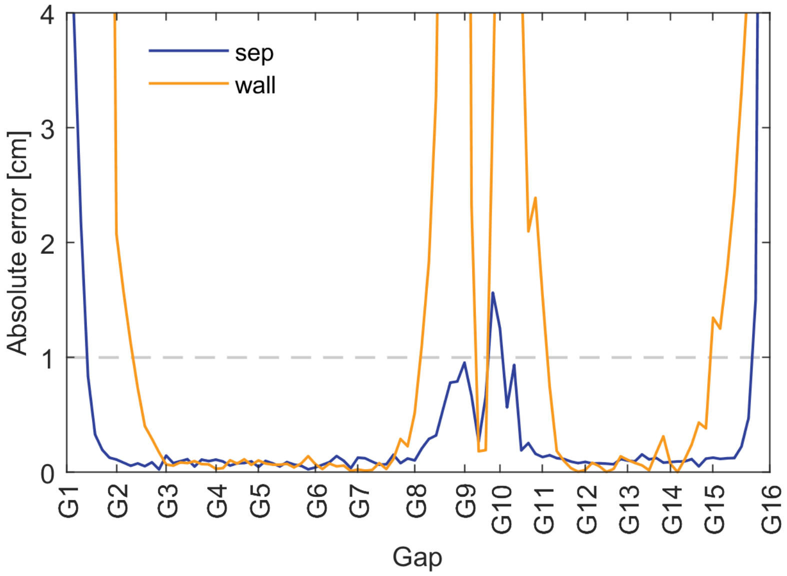

Figure 4.12: The position error of the two configurations, calculated with the IQ method.

### 4.3.3 The maximum detected amplitude

Figure 4.13 shows the maximum detected absolute amplitude of each band in each gap for the configuration for with the probing direction aligned perpendicular to the separatrix.

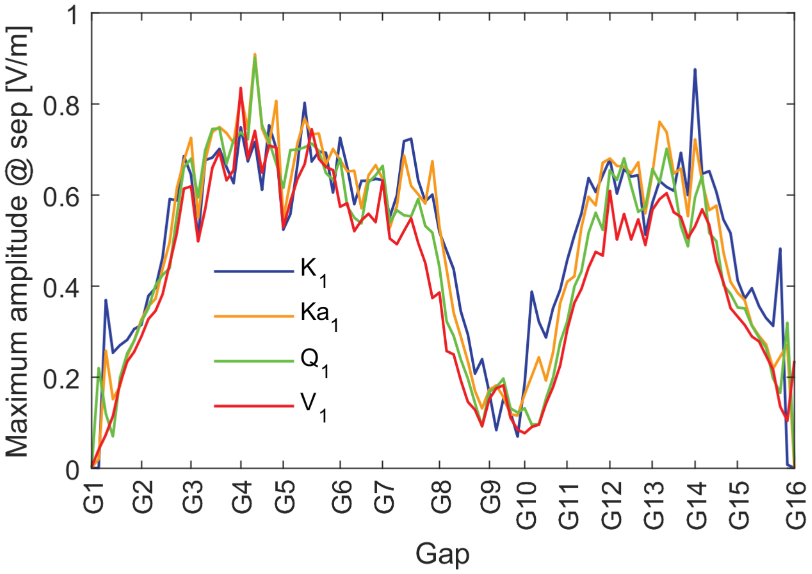

Figure 4.13: Maximum absolute amplitude of the detected field for each band.

Although this analysis does not provide the detected amplitude as function of frequency, it is easily implemented and gives information where the gaps with low signal amplitude are located, which is a first indicator where the poor quality of measurement can be. It is verified that in the first gaps of the divertor region the maximum amplitude is practically zero, corresponding to the situation where the signal is lost. At the top of the machine, the maximum amplitude is around one quarter of the equatorial zone values. In this region there is divergence of the flux lines and a density gradient with variable direction that can affect the measurements, especially the lower frequencies. Therefore, it is of interest to study the contribution to the error of each band of the phase derivative profiles. This allows to identify what are the most affected frequency ranges.

### 4.3.4 Contribution to the position error

Here we prove that the error of a phase derivative profile function can be decomposed in a sum of errors of a set of piecewise functions generated by a part of the measured phase derivative profile and a part with the WKB theoretical profile. The error (the relative scalar error) associated to a phase derivative profile is calculated by

$$e_i(F) = r_i(F) - r_0(F), \tag{4.5}$$

where $r_i(F)$ is given by the analysis of the simulation results and $r_0$ is the position of the density $n_e(F)$ taken from the model. For O-mode, $r_i(F)$ is given by the Abel Inversion, assuming the WKB conditions are valid and a monotonic profile,

$$r_i(F) = \frac{c}{2\pi^2}\int_0^F \frac{d\phi_i}{df}(f)\frac{1}{\sqrt{F^2 - f^2}}df. \tag{4.6}$$

Considering $N$ errors ($i = 1...N$) calculated for the same $r_0(F)$,

$$\begin{aligned} e_1(F) &= r_1(F) - r_0(F) \\ &\;\;... \\ e_i(F) &= r_i(F) - r_0(F) \\ &\;\;... \\ e_N(F) &= r_N(F) - r_0(F), \end{aligned} \tag{4.7}$$

its sum is:

$$\sum_{i=1}^{N} e_i(F) = \sum_{i=1}^{N}[r_i(F) - r_0(F)] = \sum_{i=1}^{N} r_i(F) - Nr_0(F). \tag{4.8}$$

A piecewise function $\frac{d\varphi_i}{df}(f)$ of $M'$ parts is defined in the form

$$\frac{d\varphi_i}{dt}(f) = \begin{cases} \frac{d\varphi_{i,1}}{dt}(f) & \text{if } f_{i,0} < f < f_{i,1} \\ \;\;\;... & \\ \frac{d\varphi_{i,j}}{dt}(f) & \text{if } f_{i,j-1} < f < f_{i,j} \\ \;\;\;... & \\ \frac{d\varphi_{i,M'}}{dt}(f) & \text{if } f_{i,M-1} < f < f_{i,M'} \end{cases}, \tag{4.9}$$

where $[f_{i,j-1}, f_{i,j}]$ defines the domain of each sub function $\phi_{ij}(f)$, with $j = 1...M'$. The function is zero for $f \leq f_{i,0}$ and $f \geq f_{i,M'}$. Considering a given frequency $F$, we define a new domain composed by $f_{i,k} = f_{i,j}$ if $f_{i,j} < F$ and $f_{i,M} = F$, where $k = 1, ..., M$. The Abel inversion of $\frac{d\varphi_i}{df}(f)$ is given by

$$r_i(F) = \frac{c}{2\pi^2} \int_0^F \frac{d\varphi_i}{dt}(f) \frac{1}{\sqrt{F^2 - f^2}} df = \frac{c}{2\pi^2} \sum_{k=1}^{M} \int_{f_{i,k-1}}^{f_{i,k}} \frac{d\varphi_{i,k}}{dt}(f) \frac{1}{\sqrt{F^2 - f^2}} df. \tag{4.10}$$

Considering a set of $N$ piecewise functions with the same domain division, the sum of the errors is:

$$\begin{aligned} \sum_{i=1}^{N} e_i(F) &= \sum_{i=1}^{N} r_i(F) - N r_0(F) \\ &= \frac{c}{2\pi^2} \sum_{i=1}^{N} \sum_{k=1}^{M} \int_{f_{k-1}}^{f_k} \frac{d\varphi_{i,k}}{dt}(f) \frac{1}{\sqrt{F^2 - f^2}} - N r_0 \\ &= \frac{c}{2\pi^2} \sum_{i=1}^{N} \sum_{k=1}^{M} \int_{f_k}^{f_{k+1}} \frac{d\varphi_{i,k}}{dt}(f) \frac{1}{\sqrt{F^2 - f^2}} - N r_0 \end{aligned} \tag{4.11}$$

The WKB position $r_{\mathrm{WKB}}(F)$ is defined by

$$r_{\mathrm{WKB}}(F) = \frac{c}{2\pi^2} \int_0^F \frac{d\varphi_{\mathrm{WKB}}}{df}(f) \frac{1}{\sqrt{F^2 - f^2}} df. \tag{4.12}$$

For a monotonic profile that fulfills the WKB condition,

$$r_{\mathrm{WKB}}(F) = r_0(F). \tag{4.13}$$

Additionally, a piecewise function $\varphi^T(f)$ that can be written in the form of equation 4.9 is defined. Each part of the function is represented by $\varphi_j^T(f)$. In the same frequency domain, the WKB modified function (WMF) $d\varphi_p^{\mathrm{WMT}}/dt(f)$ of index $p$ is defined by

$$\frac{d\varphi_p^{\mathrm{WMT}}}{dt}(f) = \begin{cases} \frac{d\varphi_{j=p}^T}{dt}(f) & \text{if } j = p \\ \frac{d\varphi_{\mathrm{WKB}}}{dt}(f) & \text{if } j \neq p \end{cases}, \tag{4.14}$$

Given a phase derivative profile $d\varphi_j^T/dt(f)$, a set of WKB modified functions can be generated with $p = 1...M'$. It is necessary to demonstrate that the O-mode position error of a given phase derivative function $d\phi^T/dt(f)$ is the sum of the errors of each WKB modified function generated by $p = 1, ..., M$:

$$e\left(\frac{d\varphi^T}{dt}, F\right) = \sum_{p=1}^{M} e\left(\frac{d\varphi_p^{\mathrm{WMT}}}{dt}, F\right). \tag{4.15}$$

For a given frequency range $f_{k-1}^{f_k}$,

$$\begin{aligned} \int_{f_{k-1}}^{f_k} \sum_{p=1}^{M} \frac{d\varphi_p^{\mathrm{WMT}}}{df} \frac{1}{\sqrt{F^2 - f^2}} df &= \sum_{p=1}^{M} \int_{f_{k-1}}^{k_j} \frac{d\varphi_p^{\mathrm{WMT}}}{df} \frac{1}{\sqrt{F^2 - f^2}} df \\ &= \int_{f_{k-1}}^{k_j} \frac{d\varphi_k}{df} \frac{1}{\sqrt{F^2 - f^2}} df \qquad (4.16) \\ &+ (M-1) \int_{f_{k-1}}^{f_k} \frac{d\varphi_{\mathrm{WKB}}}{df} \frac{1}{\sqrt{F^2 - f^2}} df \qquad (4.17) \end{aligned}$$

Here $\phi_{p,k}^{\text{WMT}}$ is the $k$ piece of the $\phi_p^{\text{WMT}}$ function. Using this equality and equation 4.11 the demonstration of equality 4.15 is obtained:

$$\begin{aligned}
\sum_{p=1}^{M} e\left(\frac{d\varphi_p^{\text{WMT}}}{dt}, F\right) &= \frac{c}{2\pi^2} \sum_{p=1}^{M} \sum_{k=1}^{M} \int_{f_{k-1}}^{f_k} \frac{d\varphi_{p,k}^{\text{WMT}}}{df} \frac{1}{\sqrt{F^2 - f^2}} df - M r_0 \\
&= \frac{c}{2\pi^2} \sum_{k=1}^{M} \left( \sum_{p=1}^{M} \int_{f_{k-1}}^{f_k} \frac{d\varphi_{p,k}^{\text{WMT}}}{df} \frac{1}{\sqrt{F^2 - f^2}} df \right) - M r_0 \\
&= \frac{c}{2\pi^2} \sum_{k=1}^{M} \left[ \int_{f_{k-1}}^{f_k} \frac{d\varphi_k}{df} \frac{1}{\sqrt{F^2 - f^2}} df + (M-1) \int_{k-1}^{f_k} \frac{d\varphi_{\text{WKB}}}{df} \frac{1}{\sqrt{F^2 - f^2}} df \right] - M r_0 \\
&= \frac{c}{2\pi^2} \sum_{k=1}^{M} \int_{f_{k-1}}^{f_k} \frac{d\varphi_k}{df} \frac{1}{\sqrt{F^2 - f^2}} df + (M-1) r_0 - M r_0 \\
&= \frac{c}{2\pi^2} \int_0^F \frac{d\varphi^T}{df} \frac{1}{\sqrt{F^2 - f^2}} df - r_0 = e\left(\frac{d\varphi^T}{df}, F\right) \qquad (4.18)
\end{aligned}$$

This decomposition is also useful in the study of the error associated to the O-mode initialization function. The study of $N_I$ different initializations in $N_D$ different phase derivative profiles (for example given by different analysis) is reduced from $N_I \times N_D$ different error functions to $N_I + N_D$. The initialization error can be calculated separately if the measured range is substituted by the WKB profile.

Figure 4.15 (next page) shows an example of WMF decomposition for the gap 9C. Each index $p$ corresponds to the profile of a different band ($p = 1 \rightarrow$K, $p = 2 \rightarrow$Ka,...), by order of frequency. The separatrix position error of each $d\phi_p^{\text{WMT}}/dt(f)$ profile is shown in figure 4.14, labeled by the respective band.

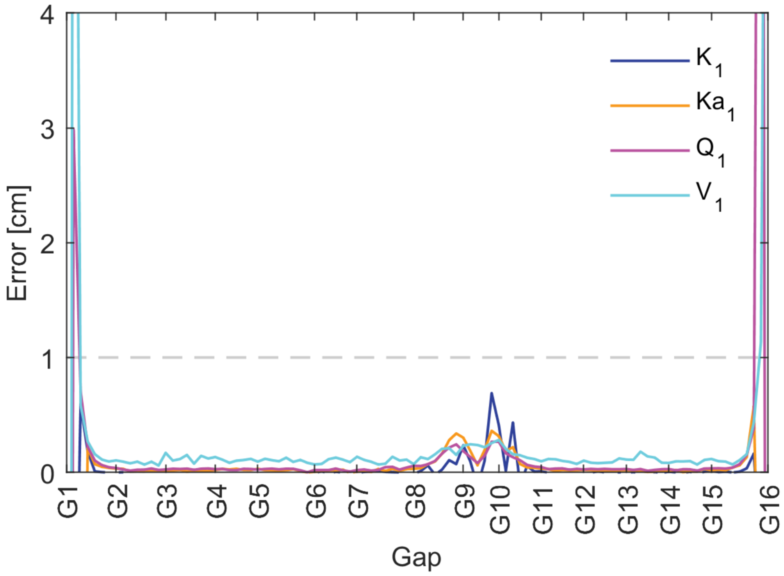

Figure 4.14: Error at the separatrix of each $d\phi_p^{\text{WMT}}/dt(f)$ profile.

Since the direction of the probing beam was aligned perpendicularly to the separatrix, the density regions associated with the lower frequencies where the density gradient direction can be easily variable are, in principle, susceptible to higher errors for the lower

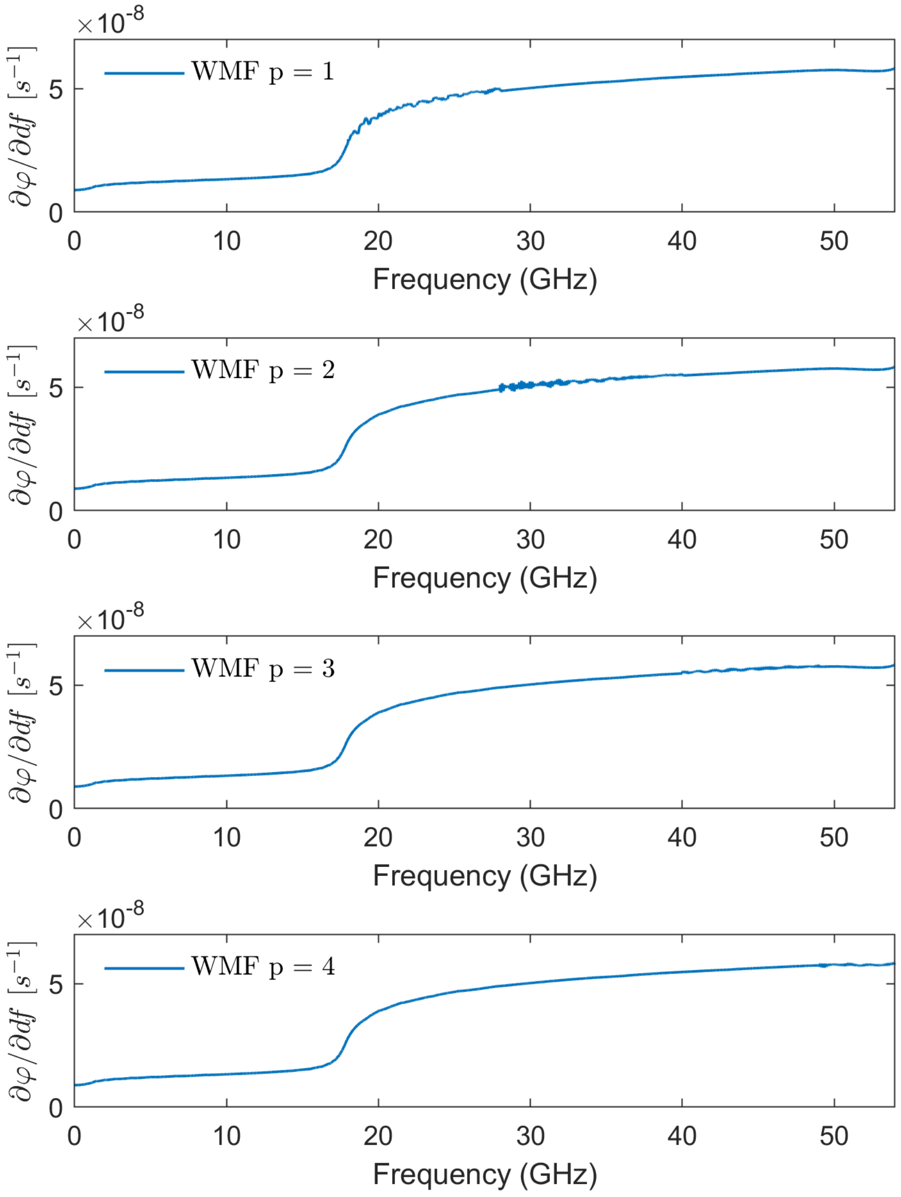

Figure 4.15: The WMF decomposition of the phase derivatives for the gap 9C.

frequencies. On the other hand, these frequencies have a lower contribution to the separatrix position error. The contribution of the $K_1$ and $Ka_1$ bands to the position error is higher at the top of the machine. In the equatorial region, where the flux lines are approximately parallel in the simulation frame, all the bands have a low contribution to the error. The $V_1$ band has the higher contribution in most of the positions since it corresponds to the layers closer to the cutoff. In the divertor region there are gaps where the absolute contribution to the error is higher than 1 cm for all the bands. This corresponds to the situation where the signal is lost.

The signal of the error function indicates if the measured position is closer to the antenna (negative) or closer to the plasma center (positive) when compared with the plasma position in the line of view associated with the frequency. The variable signal at the divertor has no physical meaning. It depends on how the filters are applied in the detected signal, which has no useful information.

### 4.3.5 Q-spectrum analysis

The Q signal spectrum (Q-spectrum), or, alternatively, the spectrum of the I signal (I-spectrum) of the IQ detection, is a fundamental tool to analyze the results. By convention, we use the Q-spectrum. The Q signal is related with the cosine of the phase-shift by $Q = [A_{det}(t)/2]\cos[\varphi(t)]$. Figure 4.16 shows the spectrum-gap diagram, where the normalized Q-spectrum of each band is shown. The relative amplitude is 1 for dark red and low ($< 0.1$) for blue.

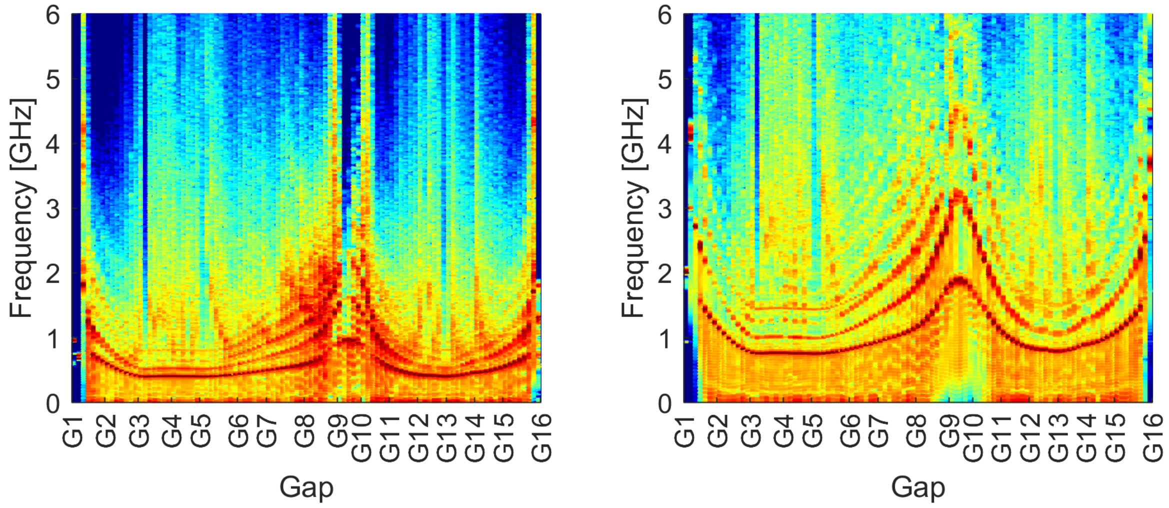

(a) $K_1$ band.

(b) $Ka_1$ band.

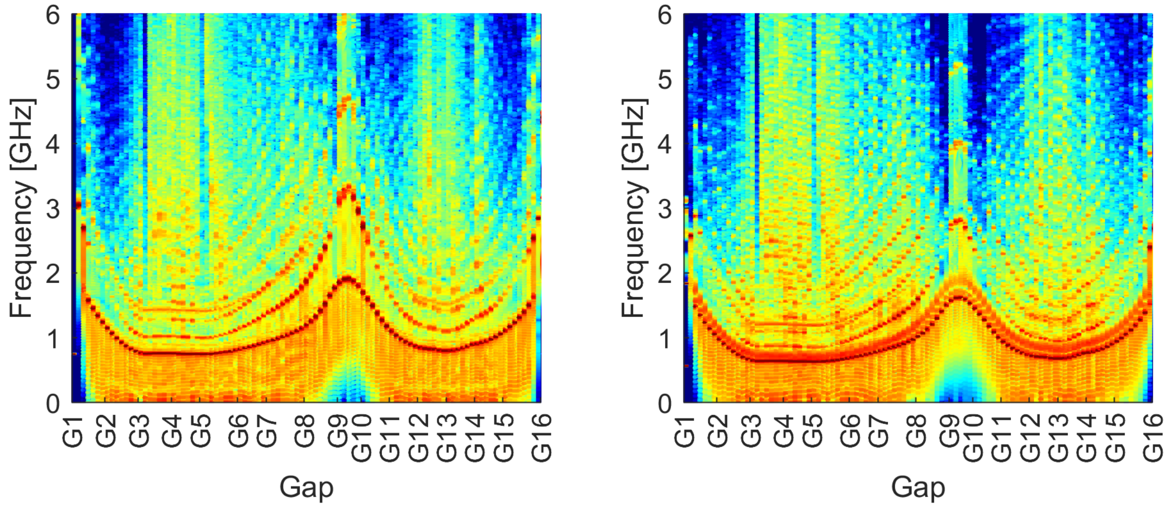

(c) $Q_1$ band.

(d) $V_1$ band.

Figure 4.16: Normalized Q-spectrum of each band. The relative amplitude is 1 for dark red and lower ($< 0.1$) for blue.

Each Q-spectrum is in general composed by different local maximums of relative amplitude. If most of the electric power is reflected in the plasma and detected, the maximum of the Q-spectrum is expected to be the characteristic frequency associated with the propagation in the plasma. If the cos term is written in the form $\cos[2\pi f't]$, the respective group delay $\tau_g(f')$ is calculated thought the relation

$$f' = \frac{1}{2\pi}\frac{\partial\varphi}{\partial t} = \frac{1}{2\pi}\frac{\partial f}{\partial t}\frac{\partial\varphi}{\partial f} = k_w\tau_g(f'). \tag{4.19}$$

Therefore is expected that the dominant frequencies of its spectrum are proportional to the group delay of the dominant components of the detected signal. By definition, we call the maximum associated with the propagation in the plasma as the characteristic peak and its frequency as the characteristic frequency. With the use of 100 gaps equally distributed along the wall, it is possible to observe the continuous variation of the characteristic frequency value. It corresponds to the darker red line in the diagram. Its value changes according to the location, since the characteristic group delay is different. Higher antenna-cutoff layer distance implies a characteristic peak of higher frequency ($f' \propto \tau_g$). The frequency peaks above the characteristic frequency are called the higher order maximums/peaks.

It is known that the spectrum of a well behaved Q-signal can be intrinsically composed by multiple local maximums of lower amplitude. In order to illustrate this with an example, we defined a phase-shift in the form

$$Q(t) = A\cos[\varphi(t)] \times H[t] \times H[-(t-T)] = A\cos[Bt] \times H[t] \times H[-(t-T)], \tag{4.20}$$

according to equation 2.102 for $s = 2$ and $F(t) \propto t$. $H[t]$ is the Heavyside function, that creates an envelope with the sweeping duration, $T$. Its Fourier transform is

$$Q(\omega) = \frac{-jA\omega + Ae^{jT\omega}(j\omega\cos[BT] + B\sin[BT])}{\sqrt{2\pi}(B-\omega)(B+\omega)}. \tag{4.21}$$

From this expression it is possible to identify an oscillatory term $Ae^{jT\omega}$ which decays with $(B-\omega)(B+\omega)$. This is not, however, the unique effect capable of generating multiple peaks with a periodic-like behavior. The multi-reflections in the wall can also generate different frequency components, depending on the form how they occur. A simple model that considers the delay of a reflection as the time-delay round-trip between the wall and the cutoff layer can identify the Q-spectrum frequencies associated with the plasma-wall reflections. If $\tau_0 = k_w f'_0$ is the group delay due to the first reflection in the plasma, the group delay associated with the plasma-wall reflection in the wall of order $m$ is

$$\tau_m = \tau_0 + m\tau_r, \tag{4.22}$$

where $\tau_r$ is the delay associated with one reflection and $\tau_m$ the delay of the $m$ reflection. Dividing equation 4.22 by $k_w$, the frequency of each local maximum $f'_k$ associated with the $k$ plasma-wall reflection is

$$f'_m = f'_0 + m(\tau_r/k_w) = f'_0 + m\frac{k_w}{2\pi}\left\langle\frac{\partial\varphi_{\mathrm{WKB}}}{\partial f}\right\rangle, \tag{4.23}$$

where $\varphi_{\mathrm{WKB}}$ is calculated with the reference at the wall position. Since the Q-spectrum contains information of all the sweep, an average over the sweeping frequency range is applied to $\varphi_{\mathrm{WKB}}$. Using this model, we calculated the first 12 frequencies associated with each reflection in the gap G4 for the Ka$_1$ band. Figure 4.17 shows the frequency of each local maximum associated with the $m$ plasma-wall reflection given by equation 4.23.

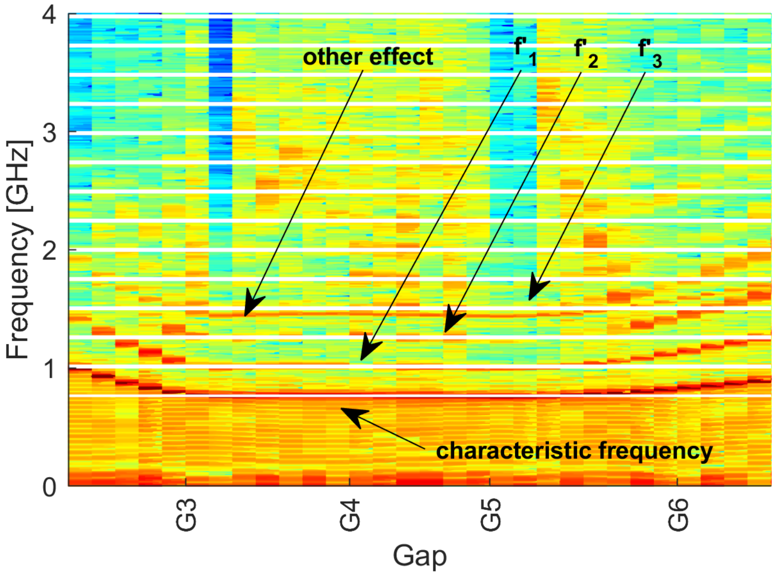

Figure 4.17: Q-spectrum frequencies associated with the multiple reflections (Ka$_1$ band).

The theoretical $f'_m$ frequencies coincide with a great part of the high order peaks observed in the diagram, including for the positions surrounding gap G4, where the plasma-wall distance is approximately the same. The peaks of lower amplitude that are observed between the principal ones may correspond to other reflections associated to the particular setup geometry and plasma or to the propagation of the other lobes emitted by the antenna. Part of the field that is reflected by the plasma to the antenna is also reflected again to the plasma and by the microwave components of the detecting system, contributing to the final obtained spectrum. Below $f'_3$ there is a well defined peak which is associated with other effect. One possibility is that this peak corresponds to one of the high order maximums associated with the spectrum of the signal due to the propagation. By removing the wall from the model, the origin of this effect becomes clear. This is studied in section 4.3.7.

When the characteristic peak has higher amplitude than the higher order maximums, the I/Q signals are easier to filter and a smooth profile is obtained with the proper data analysis. This is the situation for most of positions in the equatorial region, explaining why the error is low here. In the V$_1$ band, the characteristic peak is wider. This occurs because this band uses probing frequencies above the separatrix frequency, where a density profile with a different slope is defined, changing the expected spectrum form. In the divertor region, the Q-spectrum has not a similar form comparing with the other positions since the propagation of the probing beam is highly affected by the plasma shape or is lost.

At the top of the machine, specially for the K$_1$ and Ka$_1$ bands, there are positions where the higher order peaks have amplitudes of the same order or higher that the characteristic peak. This corresponds to the situation where most part of the signal does not come from the first reflection in the plasma and it is difficult to extract useful information. Figure 4.18 shows the Q-spectrum of the K$_1$ band for three gaps, G8, G8B and G8D.

It is possible to verify that the characteristic peak, that has the higher amplitude in gap G8, becomes the second maximum in gap G8B. In gap G8D, its amplitude decreases 20 dB and is almost not possible to distinguish it without a reference. Figure 4.19 (a) shows the snapshot of the electric field in the simulation frame for this case at two different

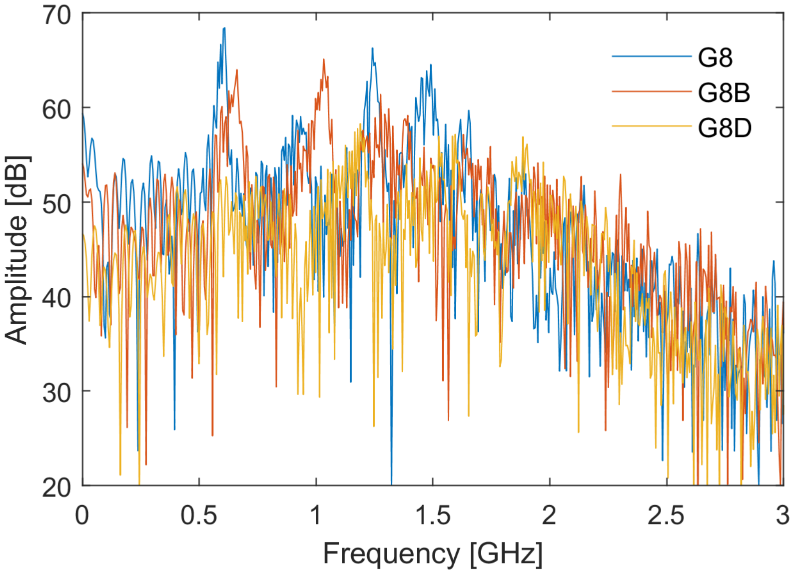

Figure 4.18: Q-spectrum of gaps G8, G8B and G8D.

frequencies (18 and 28 GHz).

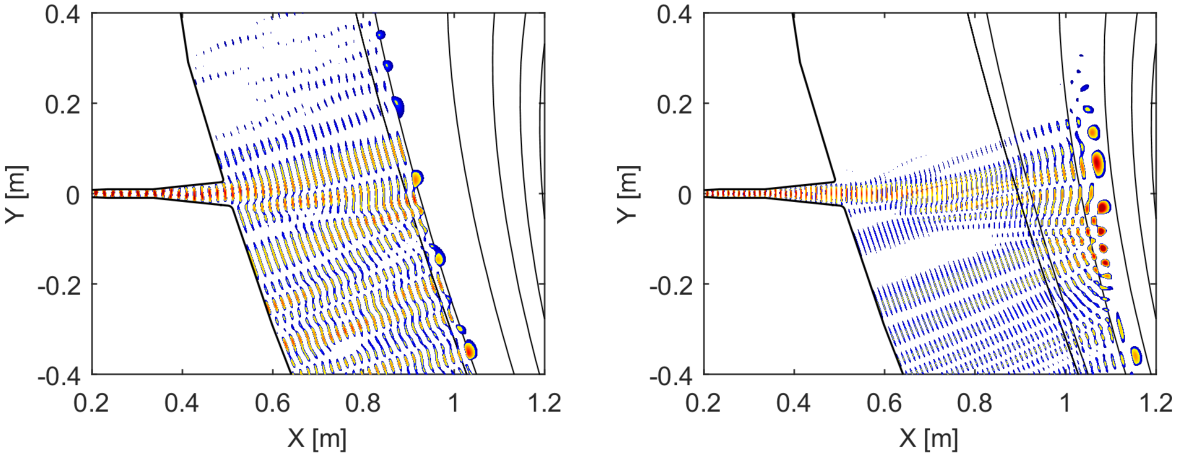

(a) Gap 8D, $K_1$ band, 18 GHz.

(b) Gap 8D, $Ka_1$ band, 28 GHz.

Figure 4.19: Electric field snapshot in gap G8D for the $K_1$ and $Ka_1$ band.

With this particular configuration of reflectometer and plasma shape, part of the electric field is deviated by the plasma, is reflected by the wall, and is reflected by the plasma again until reaches the antenna. This can explain the prevalence of higher frequency components that do not correspond to the characteristic peak, resulting in more difficulty in filtering and obtaining smooth phase derivative profiles. Figure 4.16 (b) shows the electric field snapshot for the $Ka_1$ band. The beam is less wide for these probing frequencies and propagates until different cutoff layers, originating a different reflection pattern where this effect is weaker. In this case, the characteristic peak of propagation has the same order of amplitude of the second maximum.

In this studied case the effect of the multiple reflections in the wall plays an important role in the spectrum of the detected signal. The opposite situation occurs in many other situations: depending on the plasma shape and wall geometry, the losses of energy from the cavity to the environment can be higher, decreasing the detected spurious signals. Most of the gaps before the divertor and between the equatorial zone and the top of the machine are characterized by cleaner spectrum above 4 GHz. Figure 4.20 shows two examples of configurations in these regions and where it is possible to observe part of the electric field propagating to the environment thought one of the cavity openings.

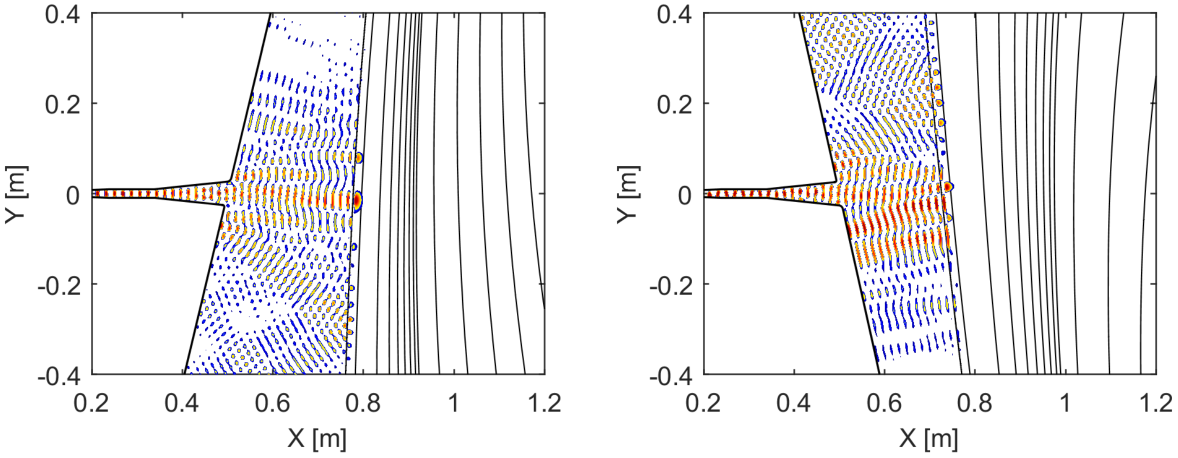

(a) Gap G2B, $K_1$ band, 18 GHz.

(b) Gap G11, $K_1$ band, 18 GHz.

Figure 4.20: Electric field snapshot in gap G2B and G11 for the $K_1$ and $Ka_1$ band.

In these configurations where $\theta_{wall}$ is higher due to the alignment with the separatrix, it is important to take into account that the probing beam may not be perfectly symmetric.

### 4.3.6 Error profile calculated with the SFFT method

Figure 4.21 shows the comparison of the position error calculated with the SFFT and IQ methods with the probing beam is aligned perpendicularly to the separatrix.

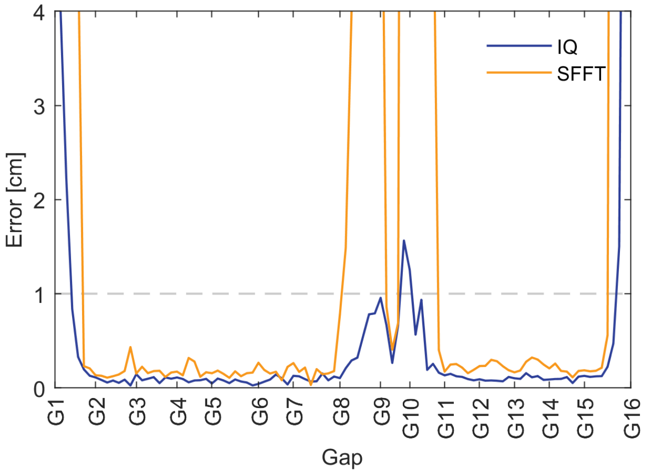

Figure 4.21: Comparison of the position error calculated with the SFFT and IQ methods.

Figure 4.22 shows different spectrogram of the Ka$_1$ band corresponding to four adjacent gaps (8A-D).

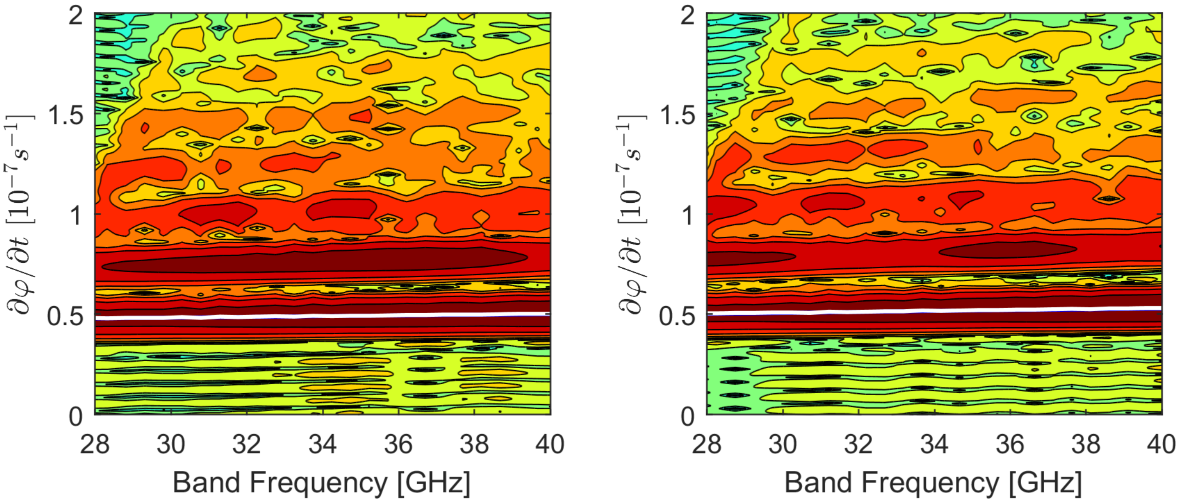

(a) Gap 8A, Ka$_1$ band.

(b) Gap 8B, Ka$_1$ band.

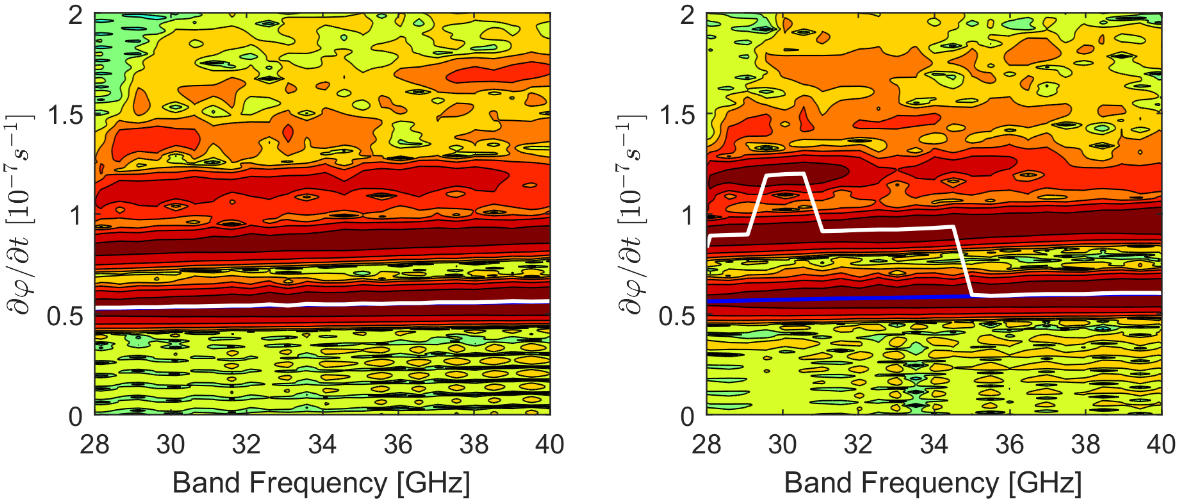

(c) Gap 8C, Ka$_1$ band.

(d) Gap 8D, Ka$_1$ band.

Figure 4.22: Spectogram of the Ka$_1$ signal in different gaps, 8A-8D.

The SFFT method was adapted to the MRSF framework variables. The results have, in general, a higher level of absolute error than the results with the IQ method. In the top of the machine and in the divertor region, the error is few cm higher. This can be explained by the way of how the SFFT method selects the beat frequency, proportional to the phase derivative. Unlike the IQ method, the maximums are selected locally at each spectrogram window. If the characteristic peak is not the maximum, the method selects the wrong beating frequency, leading to wrong phase derivatives and consequently higher errors.

The different evolutions of second order maximums are shown in gaps 8A-8C, with different amplitudes for different probing frequencies. In these gaps, the first order maximum stills the dominant component for all the frequencies, resulting in lower position errors. In gap 8D there are frequencies where the dominant frequency is not the first order peak. In the 28-35 GHz range, the second and third order peaks are dominant, resulting in higher errors. The application of a technique to correct the beating frequency selection (e.g. best path method) could improve the error results.

### 4.3.7 Removing the wall from the setup

By removing the blanket/wall from the setup it is possible to remove most of the the contributions from the plasma-wall reflections. Since part of the wave that is reflected by the plasma is also reflected by the antenna setup, it is expected that some components of the plasma-wall reflections appear, but with lower amplitude when compared with the configuration with the blanket. The effect of the plasma shape in the propagation can be studied using a slab plasma with this configuration. The absolute position error for this antenna configuration is shown in figure 4.23 for both plasma configurations. SOL1 describes the results for the 2017 scenario that was used in the previous section. SLAB describes the results for the slab plasma, where the the density profile was assumed to be constant in the $y$ direction of the simulation frame, the same existing in line of view.

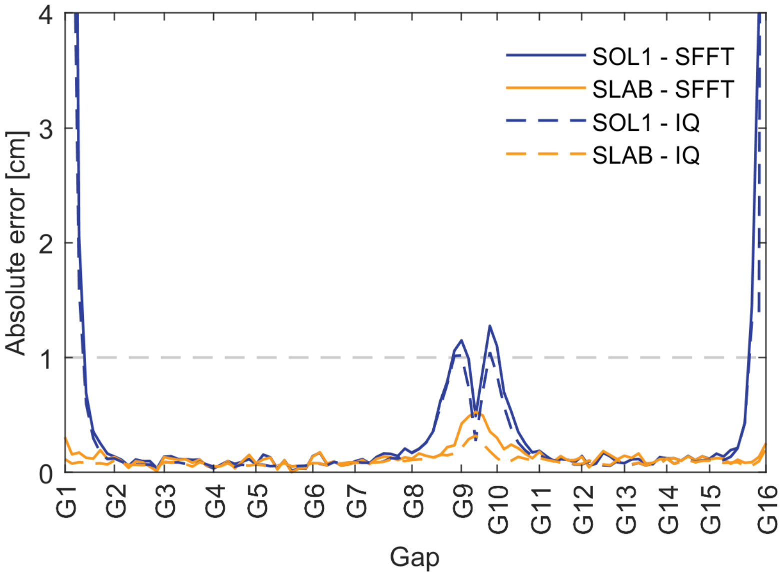

Figure 4.23: Absolute position error for both plasma configurations.

By contrast to the previous simulations where the wall was included, the results from the IQ and SFFT methods are similar. Since most of the signal components associated with plasma-wall reflections are now removed, the SFFT method chooses the characteristic frequency correctly.

In the top of the machine, the error calculated with the IQ method is slightly different to the previous configuration. Analyzing the difference between the error calculated with the SOL1 and the SLAB plasma, it is possible to conclude that at in the region G8-G9 and G9D-G11, the error is associated with the plasma shape and not only with the plasma-wall reflections.

In G9A-D, the position error obtained with the SOL1 and SLAB plasmas are approximately the same and are above the equatorial zone level. This means that the 1D effects are important to consider in this region, as well as in the divertor. One possible explanation for this effect is that in these positions, the reflection at the cutoff layer is not approximately metallic. Figure C.6 (appendix C.3.2) shows the Airy's wavelength at the separatrix frequency. At the exact positions where the error of the simulations with the slab plasma are higher, the Airy's wavelength is also. Figure C.7 (appendix C.3.2) shows the density profile of gap G8E, where the Airy's wavelength is in the order of 5 cm. Since the distance between the separatrix position and the change of slope is approximately 0.5-1 cm, the reflection does not occurs in a region described approximately by a linear dielectric constant. The 1D reflectometry model is only approximately valid, leading to considerable position errors due to the measurements in this region.

Figure 4.24 shows the Q-spectrum relative to the SOL1 plasma simulations.

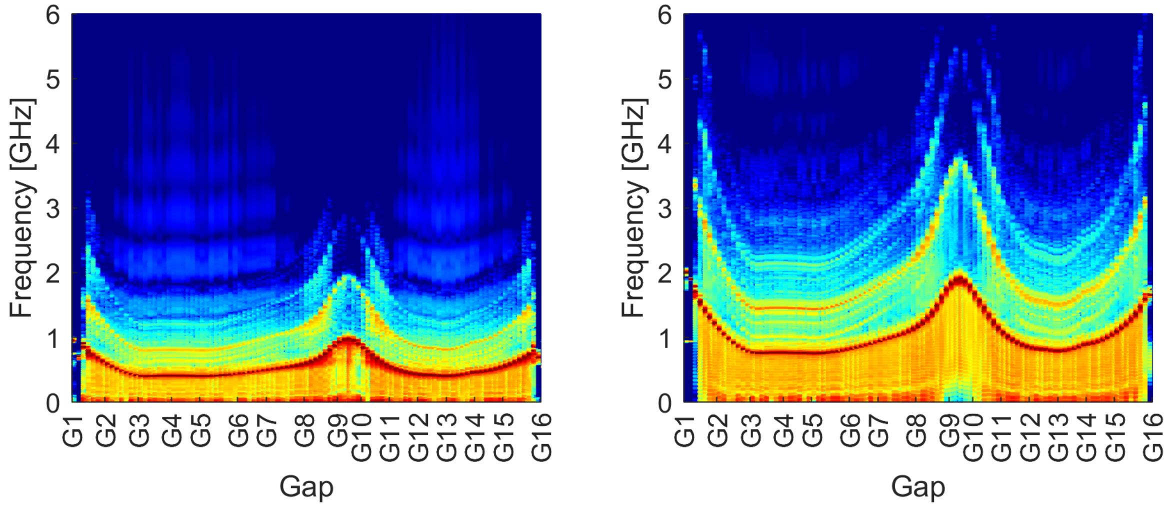

(a) $K_1$ band.

(b) $Ka_1$ band.

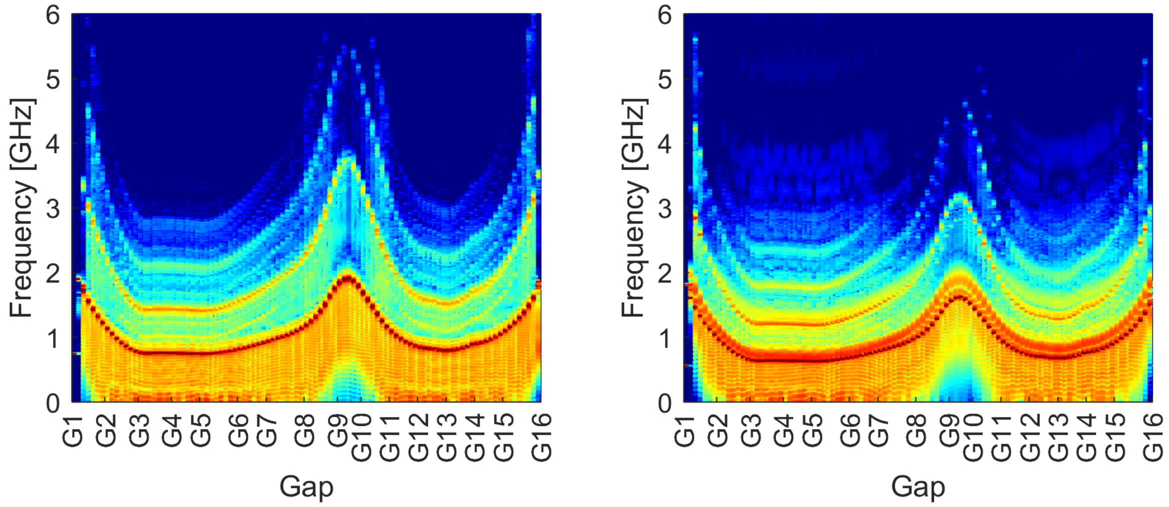

(c) $Q_1$ band.

(d) $V_1$ band.

Figure 4.24: Q-spectrum/gap diagram for the SOL1 plasma.

The results show that most of frequency peaks associated to the plasma-wall reflections are not detected or have a reduced amplitude. Some of them still present due to the reflections in the antenna. The second maximum correspond to the peak identified in figure 4.17 below the $f_3'$ reflection, in the case of the $Ka_1$ band. These periodic-like peaks correspond to the different components of a typical Q signal, as discussed in the previous section. The analysis of the Q-spectrum for the slab plasma is shown in appendix C.3.3.

## 4.4 Effect of the cavity in the measurements

The models that were used in the first studies with the DEMO 2015 and 2017 baseline scenarios consisted in simple antennas placed at the wall surface. Thermomechanical studies concluded that a cavity of 10 cm × 10 cm with rounded corners and the proper cooling system can hold the expected order of wall temperatures. All the gaps were simulated for the same bands of frequency with this reflectometer configuration. Figure 4.25 shows a snapshot of the positive part of the electric field at 33 GHz for this configuration.

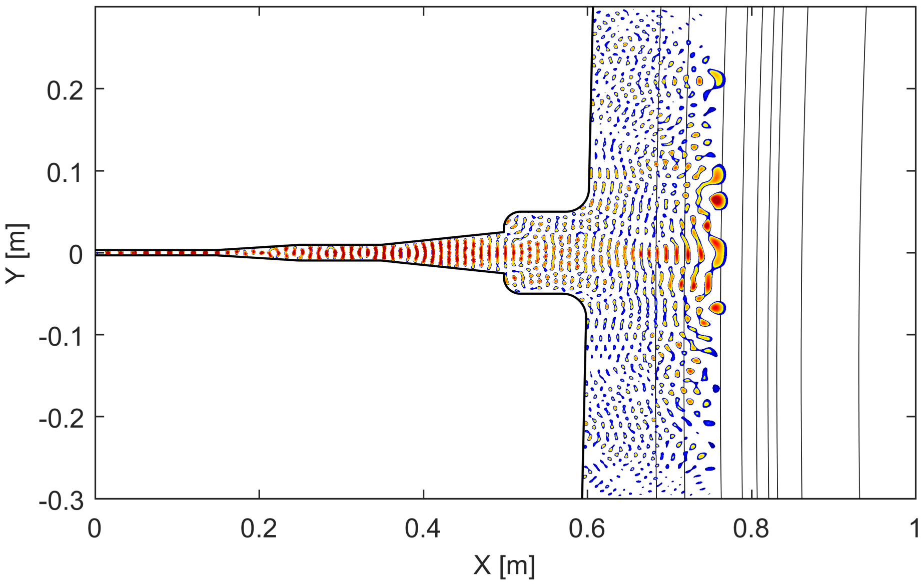

Figure 4.25: Snapshot of the positive part of the electric field at 33 GHz.

Figure 4.26 shows the comparison of the position error calculated with the IQ method for the different setups (A - antenna; AB - antenna and blanket; CAV - cavity).

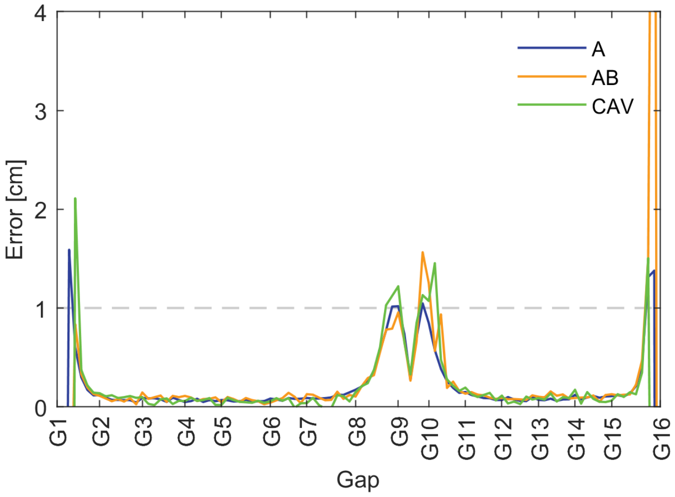

Figure 4.26: Comparison of the position error calculated with the IQ method (A - antenna; AB - antenna and blanket; CAV - cavity).

The results are similar to antenna-wall setup. Since the cavity setup has the detection 10 cm before the other setups, it is expected the characteristic frequency is shifted to a higher frequency, corresponding to a higher group delay. In the other hand, the effect of the plasma-wall reflections can be weaker due to the cavity geometry. Figure 4.27 shows the Q-spectrum diagram for this configuration.

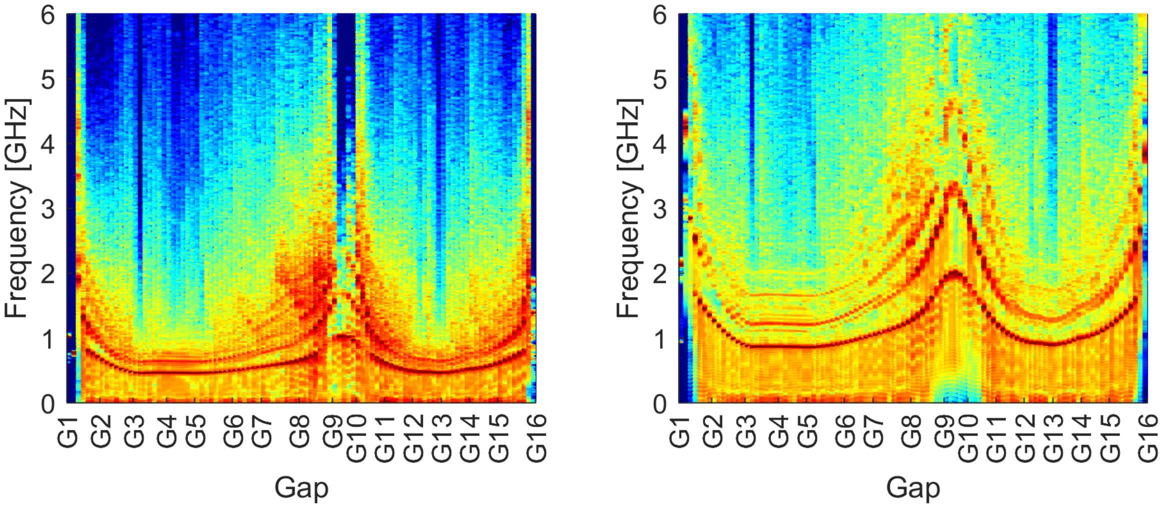

(a) $K_1$ band.

(b) $Ka_1$ band.

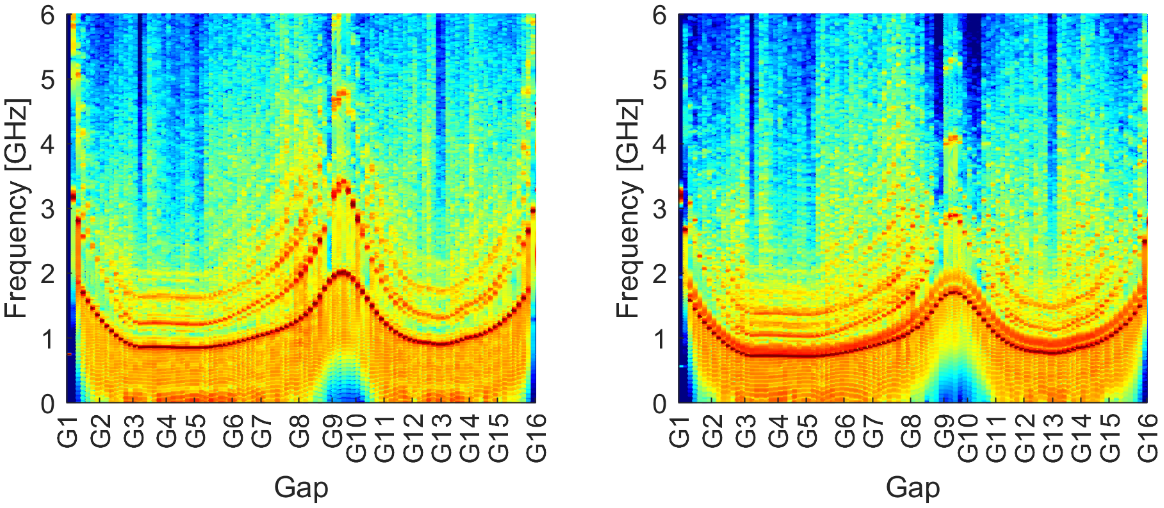

(c) $Q_1$ band.

(d) $V_1$ band.

Figure 4.27: Q-spectrum analysis for the cavity configuration.

The diagrams are similar to the antenna-wall configuration in terms of the distribution of the different frequency peaks. Each Q-spectrum is, in general, cleaner for the higher frequencies. The dominant frequency of each configuration are shown in appendix C.3.4, where the shift of the characteristic frequency due to the higher detection distance and the wrong characteristic frequency selection is observed.

The conclusion of the previous studies is that plasma-wall reflections are an important mechanism that can modify the Q-spectrum, leading to higher measurement errors, in particular when the SFFT method is applied. The plasma shape can also contribute to a higher measurement error, but its effects is not clearly represented in the Q-spectrum diagrams. The simulations with the slab plasma are important to verify the validity of conditions assumed in the reflectometry model.

## 4.5 Propagation in different density profiles

The scrape-off layer of the density profile used in the simulations of the previous studies was extrapolated to an exponential decay using values in the order of the observed experimentally in tokamaks. In order to study the sensitivity of the measurements to the scrape-off layer decay, we defined three different profiles, characterized by three different characteristic lengths. They are represented in figure 4.28.

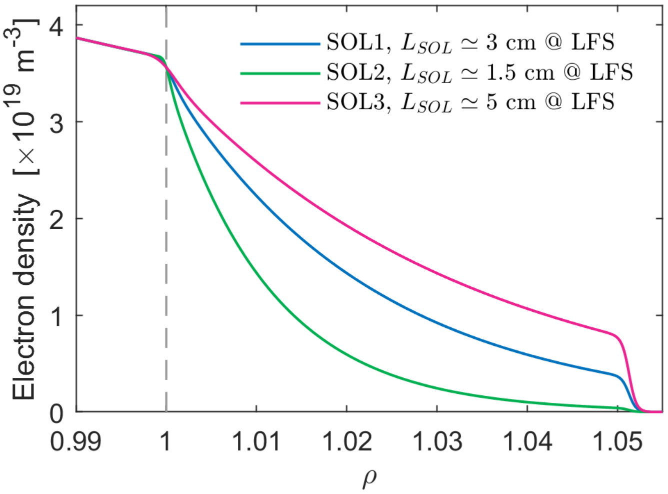

Figure 4.28: Different density profiles for the 2017 baseline scenario.

The absolute error is shown in figure 4.29.

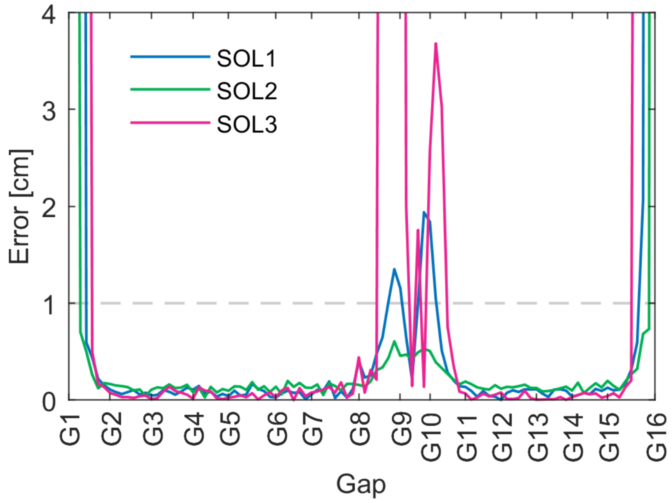

Figure 4.29: Absolute error of each density profile.

In the equatorial zone where the flux lines are approximately perpendicular to the probing direction, the error associated to each decay is low (0-0.2 cm). In the divertor region and in the top of the machine, the error is sensitive to the decaying length. Since in this reflectometer configuration the direction of the probing beam was aligned perpendicularly to the separatrix, it is expectable that the flux lines near the separatrix are approximately parallel, in contrast to the lines associated to the lower frequencies. For this reason, the better performance is given by the shortest decay.

## 4.6 Data analysis automation

### 4.6.1 Automating the data analysis

The study of the measurement performance of a multi-reflectometer system involves the data analysis of many different simulations. With the framework introduced in the previous chapter, we concluded that many steps can be automated with the main variables of the problem. In the previous section, the IQ and SFFT methods were implemented in this framework with part of the parameters defined manually. Even with this implementation, the data analysis was a demanding process from the duration point of view due to the need to define three parameters manually. The optimization of a system or the statistical study of different plasma configurations requires the automation of the entire process. Next, we analyze the characteristics and the performance of each method for determining the phase derivative:

- **SFFT** - In this method the user defines the lag of the detected signal, the cutoff frequency of a LP filter that is applied to the beating signal and the spectrogram parameters. Without any modification in the form how the method chooses the beating frequency associated with the propagation in the unperturbed plasma, the SFFT has shown to be susceptible to higher errors in the regions where the detected of the plasma-wall reflections is higher. Furthermore, since the simulation times are in general in the order of 0.01 $\mu s$, the window sizes that are necessary to reconstruct the spectrogram produce profiles with a low probing frequency resolution. The final phase derivative profile is calculated by a linear interpolation between each point. When the group delay is wrongly estimated, a region with phase derivative above/-below the WKB curve is created and may affect the error calculation considerably.
- **IQ** - In this method the user defines the lag of the detected signal and the cutoff frequency of a LP filter that is applied to the I and Q signals. This cutoff frequency is typically after the characteristic peak. The remaining components related with the undesired effects are removed, leading to smooth phase derivative profiles. This method has shown to be less sensitive to the local fluctuations of phase derivative, the filter is applied to the entire signal.

The IQ method is the only one that calculates the detected amplitude, which is an essential variable to optimize PPRs or in the statistical studies of turbulence. Its automation is of crucial interest to reflectometry simulation. In this section we developed an automated version of the IQ method and the results are compared with the manual data analysis results from the previous studies.

### 4.6.2 Determination of the signal lag

Both IQ and SFFT methods require the determination of the signal lag. This can be done by comparing the detected signal and determining the instant where its amplitude is above the level of noise. Figure 4.30 shows the detected amplitude ($S_{det}(t)$ signal) and the beating signal ($S_{beat}(t)$ signal) at the source position, before the UTS position, with the respective lag. The signals corresponds to the simulation with the antenna-setup in gap G13, for the $Q_1$ band and are decimated with a 10 factor.

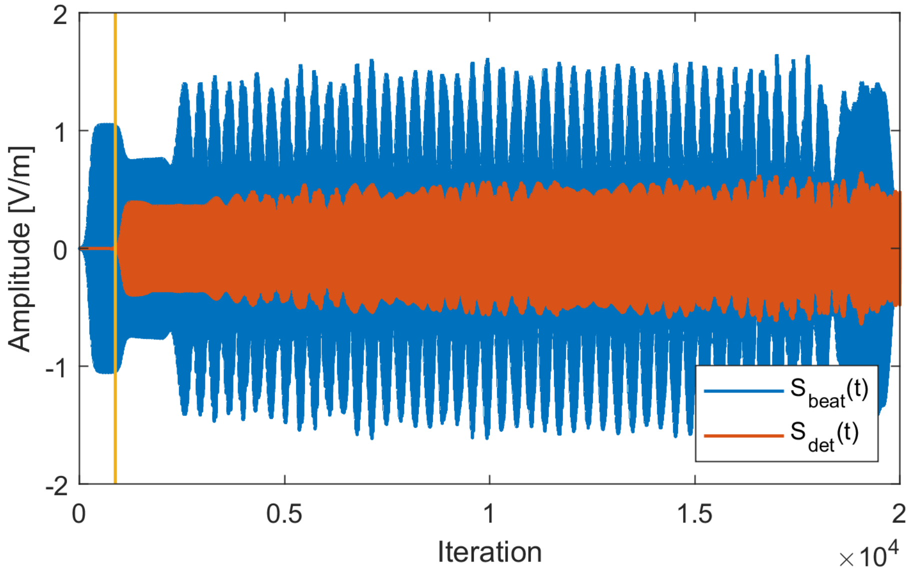

Figure 4.30: Detected amplitude ($S_{det}(t)$ signal) and the beating signal at the source position ($S_{beat}(t)$ signal), before the UTS position, with the respective lag. The signals correspond to the simulation with the antenna-setup in gap G13, for the $Q_1$ band.

One form of automate the process of lag selection is using a cross-correlation [225]. The signal lag is chosen by the cross-correlation displacement parameter where the cross-correlation is maximum. Figure 4.31 shows the cross-correlation of the signals shown in figure 4.30, where the maximum at the signal lag is observed.

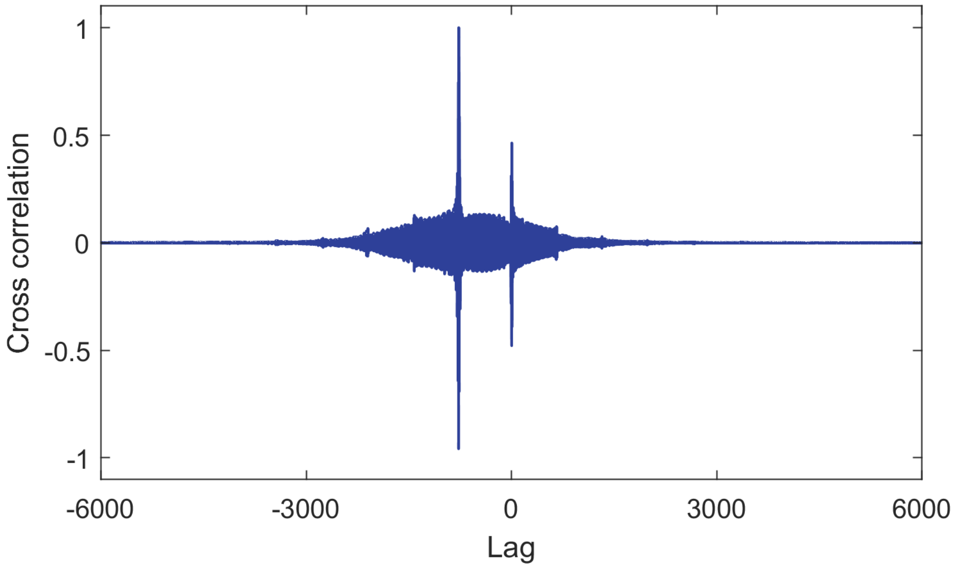

Figure 4.31: The cross-correlation of the $S_{det}(t)$ and $S_{beat}(t)$ signals shown in figure 4.30.

Although this technique works in most of the signals, there are cases where the lag is wrongly calculated, typically when the detected signal is more affected by the propagation and includes spurious signals of considerable amplitude. This occurs typically for the $K_1$ or $Ka_1$ bands, in the setups with blanket, in the divertor and top regions. A shift in the phase derivative profiles is introduced, leading to an error in the final measurement.

### 4.6.3 Automating the IQ method

With the lag calculated with the cross correlation, the IQ method is fully automated if the filter parameter can be selected by some criteria. In this section we propose a method to the automate the IQ detection, abbreviated by IQA.

In the previous section, we studied that a typical I/Q signal is characterized by a spectrum with a characteristic frequency, followed by other components related with the propagation in the setup, with the plasma or with the plasma-wall reflections. As the cutoff frequency $f_c$ is swept, three different regions are identified. In the first region, there is no enough frequency components to form a smooth profile. The phase derivative is composed by multiple oscillations, with increasing mean value. The second region, when the characteristic peak is included, is characterized by a smooth phase derivative profile. This is the region that we are interested. As higher frequencies are included in the I/Q-spectrum, the oscillations in the smooth phase derivative profile increase.

The second region is well described by the minimum of the the standard deviation of the phase derivative, $\sigma(\partial\varphi/\partial f)$. In the first region the spectrum is incomplete, resulting in phase derivative oscillations that are associated to a higher standard deviation than when the profile is smooth. In the third region, the standard deviation increases as we add the higher frequencies associated with the spurious signals, resulting in higher standard deviation. The standard deviation of the sum of two functions $f_1$ and $f_2$ is

$$\sigma^2(f_1+f_2) = \sigma^2(f_1) + \sigma^2(f_2) + 2[\langle f_1 f_2\rangle - \langle f_1\rangle\langle f_2\rangle], \tag{4.24}$$

where $\langle ...\rangle$ is the mean over the sample set. If $f_1$ is a smooth phase derivative defined by the characteristic peak and $f_2$ is the component introduced by increasing the cutoff frequency, the condition $\sigma(f_1+f_2) > \sigma(f1)$ is satisfied if

$$\langle f_1 f_2\rangle - \langle f_1\rangle\langle f_2\rangle > -\frac{\sigma^2(f_2)}{2}. \tag{4.25}$$

If $f_1$ is a positive constant, this condition is always satisfied if $\sigma(f_2) > 0$. For a slowly varying positive phase derivative profile $f_1$ and a noise-like $f_2$ function, this condition is still being met, since $\langle f_1 f_2\rangle \simeq \langle f_1\rangle\langle f_2\rangle$. Dividing the frequency range in $N$ intervals of width $df$ and taking constant the values of $f_1$ in each interval, $c_i$, we get

$$\langle f_1 f_2\rangle = \frac{\int_{\Delta f} f_1 f_2 df}{\Delta f} \simeq \frac{\sum_i^N c_i}{\Delta f}\int_{df} f_2 df. \tag{4.26}$$

Assuming a uncorrelated noise-like function where

$$\int_{\Delta f} f_2 df \simeq N \int_{df} f_2 df, \tag{4.27}$$

the same expression is obtained for the $\langle f_1\rangle\langle f_2\rangle$ term,

$$\langle f_1\rangle\langle f_2\rangle = \frac{\int_{\Delta f} f_1 df}{\Delta f}\frac{\int_{\Delta f} f_2 df}{\Delta f} \simeq \frac{\sum_i^N c_i}{\Delta f}\int_{df} f_2 df. \tag{4.28}$$

This shows that the minimum standard deviation of the phase derivative is a good selection criteria for the type of signals that are expected. Alternatively, an higher order derivative of the phase can also be used to find the minimum standard deviation. When the characteristic peak is not well defined or when its amplitude is lower than other components, the algorithm can have some problems applying this principle. However, these cases are not interesting from the point of view of the measurement.

### Simulation with the mirror

Figure 4.32 shows the standard deviation as a function of the normalized cutoff (to the sampling frequency) for the $Q_1$ band signal of the gap G13 with the blanket removed, for the configuration with the probing direction perpendicular to the separatrix. In the rest of this work, the normalized cutoff frequency is also referred simply by cutoff frequency. Only the data relative to the frequencies used in the data analysis are used to the calculations. Figure 4.33 shows the respective phase derivative profiles associated with the points A, B, C and D. Each point represents a region (A,B - region 1, C - region 2, D - region 3).

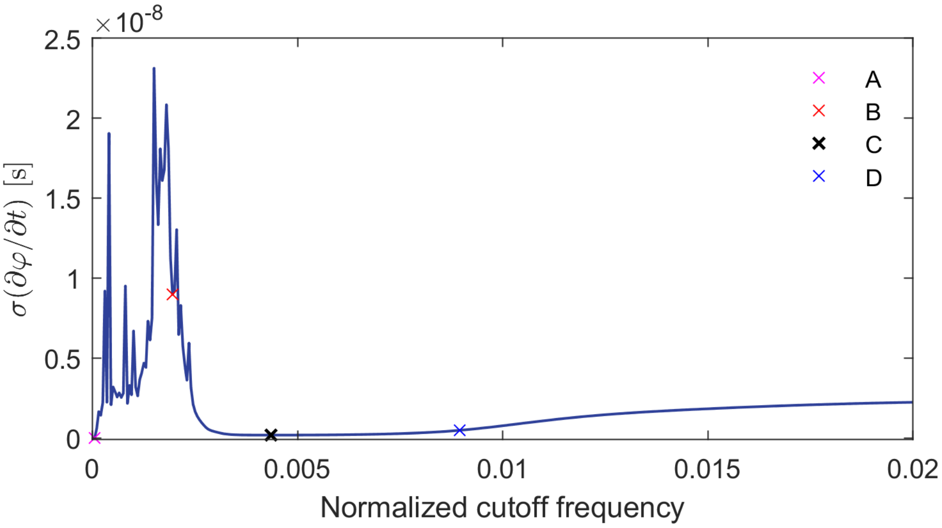

Figure 4.32: The standard deviation as a function of the normalized cutoff for the $Q_1$ band signal of the gap G13 with the wall removed, for the configuration with the probing direction perpendicular to the separatrix.

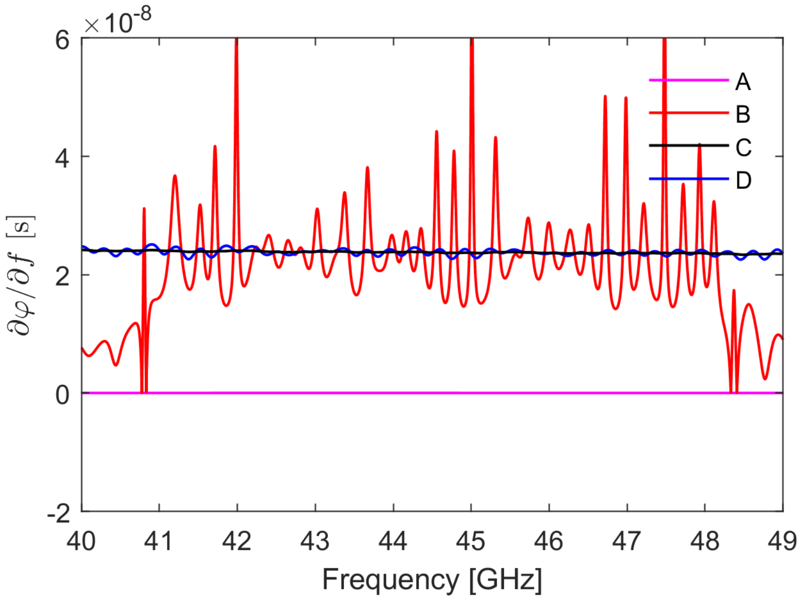

Figure 4.33: Phase derivative profile associated with the points A, B, C and D.

Beyond the three regions that were mentioned, the first frequencies have a lower standard deviation since all the spectrum is filtered, resulting in a constant signal with mean zero in the limit. Therefore, for the simulations with the mirror, the minimum standard deviation condition does not work to select the optimal cutoff frequency.

Another condition must be added to the selection process. One possibility, is the use of the maximum standard deviation position to determine the minimum value of cutoff frequency to find the minimum standard deviation, $f_{c\,min}$. However, depending on the case and on the limit of the normalized cutoff that is being used in the sweep, the maximum value of standard deviation is not guaranteed to be before the interesting point with minimum standard deviation. This problem can be solved with the derivative of the mean phase derivative profile as function of the cutoff frequency. Figure 4.34 shows the mean phase derivative as function of the cutoff frequency and its derivative for the considered signals.

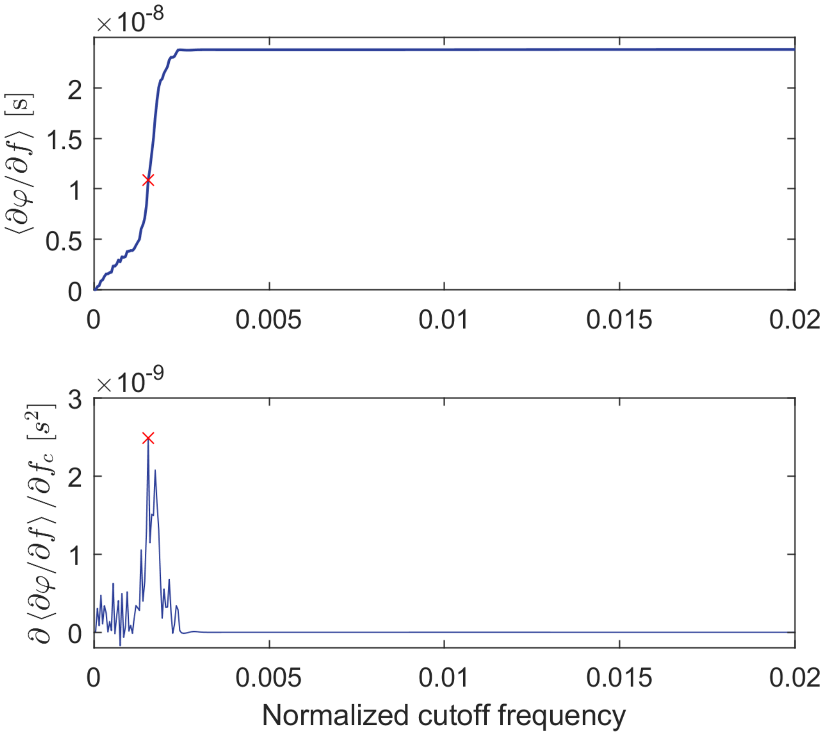

Figure 4.34: Mean phase derivative as function of the cutoff frequency and its derivative for the considered signals.

The mean phase derivative increases for the first cutoff frequencies as the smooth profile is formed. After the characteristic peak is included, its value stabilizes. Even that additional frequencies are added to the spectrum, the mean tends to increase slowly. Thus, the position of the maximum of its derivative can be used as $f_{c\,min}$. The procedure is summarized in five steps:

- The lag is calculated with the cross correlation.
- The standard deviation of the phase derivative is calculated,

$$s\left(f_c\right) = \sigma\left(\frac{\partial\varphi}{\partial f}\right) \tag{4.29}$$

- The mean $m\left(f_c\right)$ of the phase derivative and its derivative $d\left(f_c\right)$ are calculated,

$$m\left(f_c\right) = \left\langle \frac{\partial \varphi}{\partial f} \right\rangle \tag{4.30}$$

$$d\left(f_c\right) = \frac{\partial}{\partial f_c}\left(\left\langle \frac{\partial \varphi}{\partial f} \right\rangle\right) \tag{4.31}$$

- The cutoff frequency of the maximum of $d\left(f_c\right)$ is selected, $f_{c\,min}$.
- The selected cutoff frequency to filter the I/Q signals, $f_{c0}$, is determined by the frequency of the minimum standard deviation after $f_{c\,min}$.

### Simulation with the plasma

In the simulations with the plasma, the term correspondent to the propagation in the setup is subtracted to the phase derivative. When the filter cutoff frequency is set to zero, its mean is negative and the standard deviation low. The values are calculated with the reference in the wall, explaining why for higher cutoff frequencies the mean is approximately the same for all the configurations. Figure 4.35 shows the phase derivative standard deviation and the mean in the three different setups (A - antenna, AB - antenna with blanket, CAV - cavity), for the $Q_1$ band. The selected points with the minimum standard deviation are also shown.

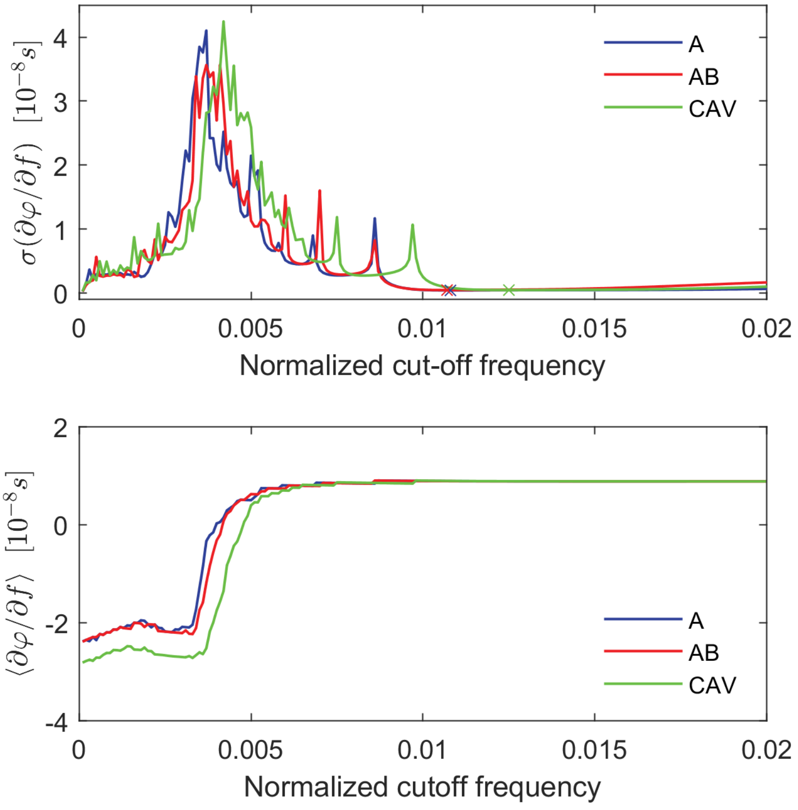

Figure 4.35: The standard deviation and the mean for the three different setups (A - antenna, AB - antenna with blanket, CAV - cavity).

By contrast to the simulations with the mirror, the cutoff frequency is selected by the frequency of the minimum standard deviation $s(f_c)$, if $m(f_c) > 0$. Figure 4.36 shows the phase derivative profiles for different values of cutoff frequency in the case of the setup with the antenna and the blanket removed. As it is shown in the example, lower cutoff frequencies lead to negative group delays. Although this situation is not physical, it is useful to simplify the algorithm.

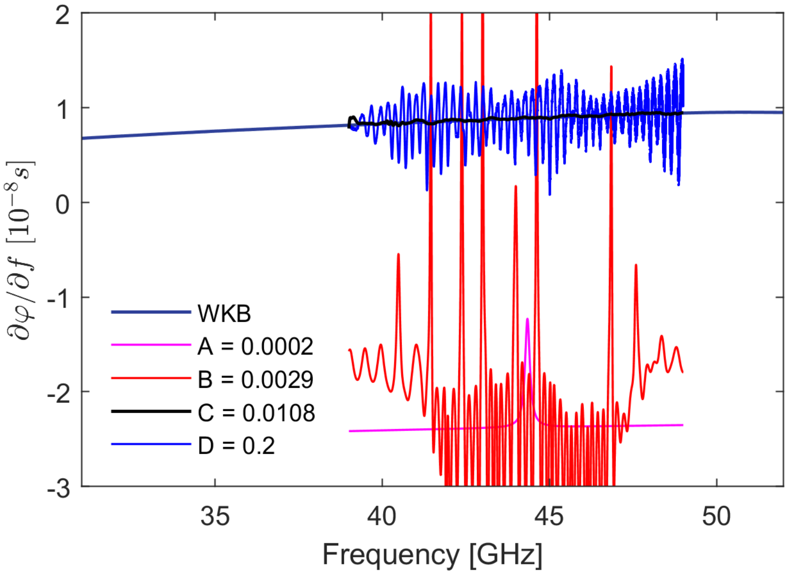

Figure 4.36: Phase derivative profiles for different values of cutoff frequency in the case of the setup with the blanket removed.

The detected amplitude $a_{det}(f) = 2\sqrt{Q^2(f) + I^2(f)}$ is also dependent on the cutoff frequency. Figure 4.37 shows the mean detected power and its derivative for this example.

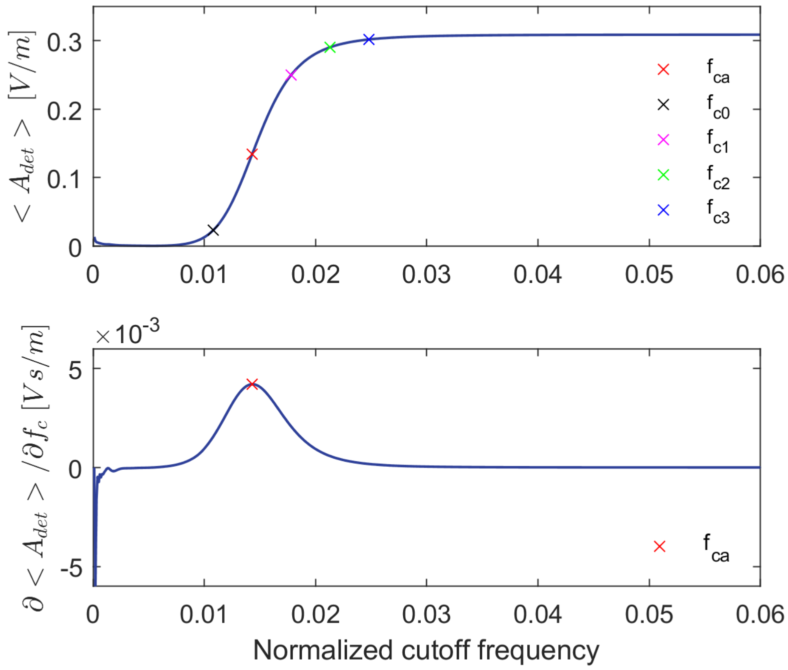

Figure 4.37: The mean detected power $\langle a_{det}(f) \rangle$ and its derivative.

As the cutoff frequency is increased, the mean detected amplitude increases and stabilizes when the characteristic components of the I and Q signals are included. Its derivative has a maximum in this transition, and its positive part has a Gaussian-like shape. The frequency of this maximum, $f_{ca}$, is, in general, slightly different from the cutoff frequency selected for phase derivative calculation, $f_{c0}$. Figure 4.38 shows the Q-spectrum and the filtered spectrum for $f_c = 0.02$, when the mean value stabilizes after including the characteristic components.

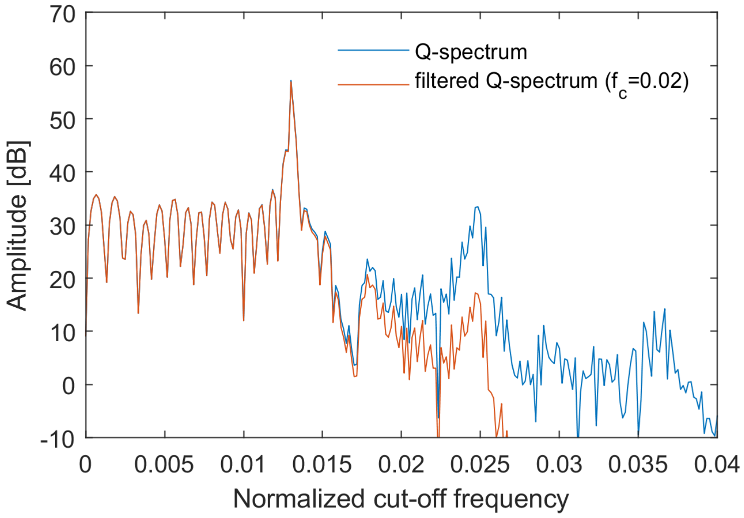

Figure 4.38: The Q-spectrum of the example signal and the filtered spectrum for $f_c = 0.02$.

Figure 4.39 shows the detected amplitude for different cutoff frequencies, including multiples of the full width at half maximum ($\Delta f_{c\,\mathrm{FWHM}}$),

$$f_{cn} = f_{ca} + n\Delta f_{c\,\mathrm{FWHM}}. \tag{4.32}$$

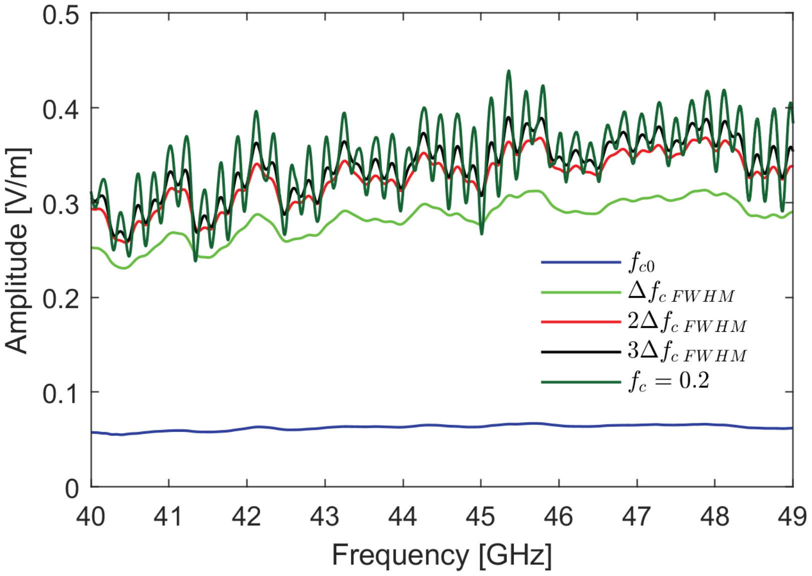

Figure 4.39: The detected amplitude with different values of cutoff frequency.

These frequencies are also represented in figure 4.37. As the cutoff frequency increases to values above the characteristic frequency, the level of amplitude stabilizes. The $f_{c0}$ cutoff does not take into account all the power associated with the characteristic peak. When the spurious components are included, the $a_{det}(f)$ profile can be seen as the sum of a smooth profile with the fluctuations. The $f_{c2}$ or $f_{c3}$ frequencies are ideal to compute the detected amplitude. Figure 4.40 shows the of amplitude for the antenna and cavity setups, calculated with the last cutoff frequency of the sweep. Figure 4.41 shows the amplitude profiles calculated with $f_{c2}$.

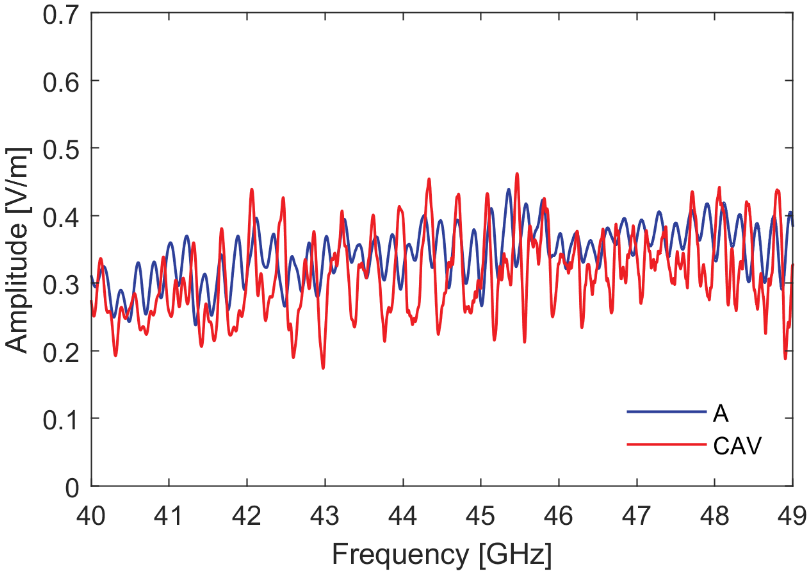

Figure 4.40: Amplitude profile for different setups, calculated with the last cutoff frequency of the sweep.

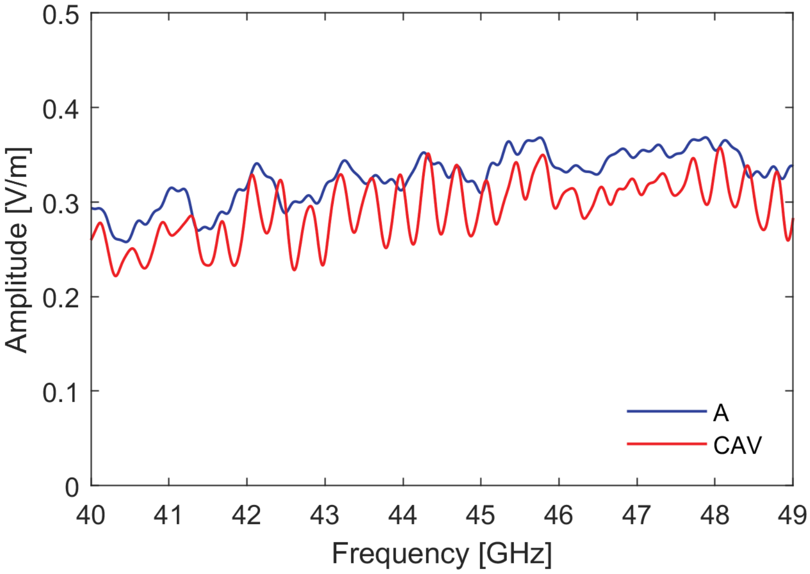

Figure 4.41: Level of power for the three different antenna setups, calculated with $f_{c2}$.

The cavity setup has a vertical shift of the level of amplitude, explained by the change in the detection position.

### 4.6.4 Comparison with the manual data analysis

So far we introduced the IQA algorithm with some examples. Before using it in the study of the optimization of the system, the results from the application of the algorithm are compared with the results obtained manually in the studies effectuated in the previous section. Figure 4.42 shows the fit parameters of the waveguide propagation function ($\tau(f) = a + b/\sqrt{1-(2h_{wg}dx/f)^2}$) in the antenna setup for the $Q_1$ band. Figure 4.43 shows the same parameters for the cavity setup.

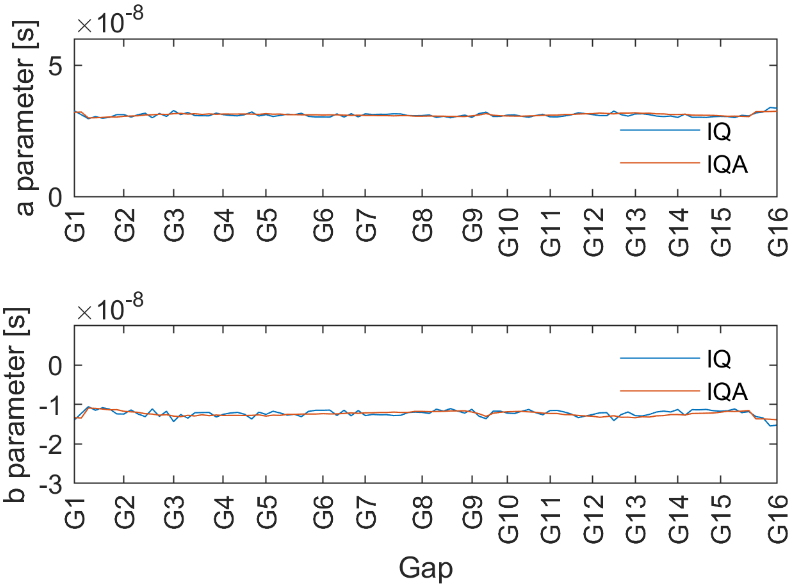

Figure 4.42: Comparison of the fit parameters of the waveguide propagation function.

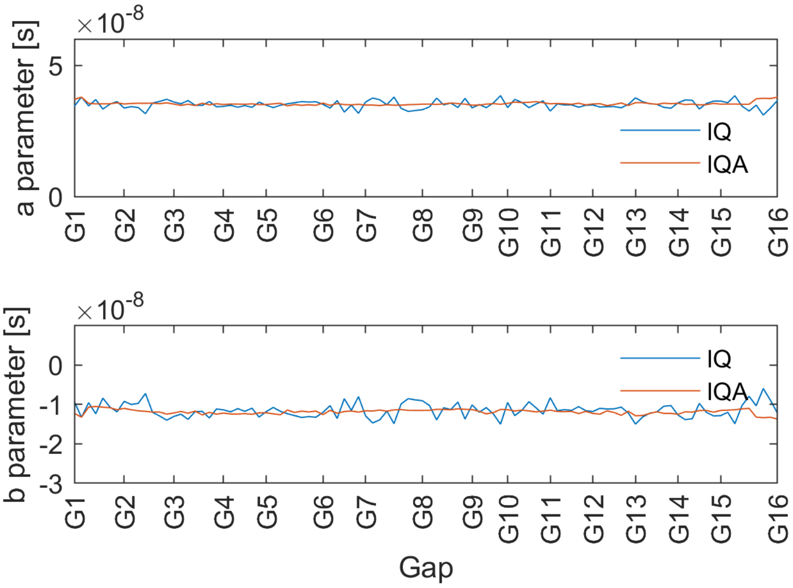

Figure 4.43: The fit parameters of the waveguide propagation function for the cavity setup.

The results show a low error between the parameters calculated with the IQA method and with the manual selection for both setups. In the simulations with the mirror, the correlation usually provides an accurate estimation of the signal lag. Both parameters are almost constant in the different gaps, since the differences between the different antenna models is practically in the connection with the blanket and the distance to the wall position. The position error for the setup with the antenna without blanket is shown in figure 4.44.

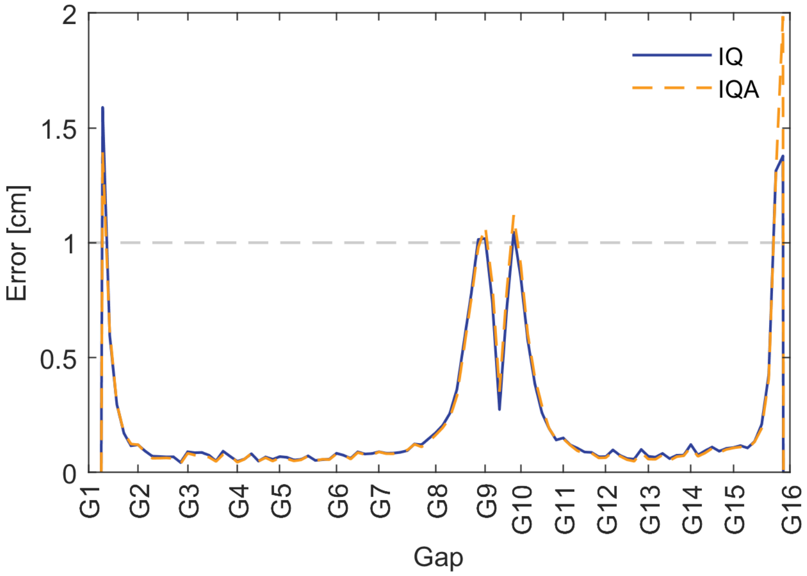

Figure 4.44: The position error calculated with the IQ and IQA methods.

For this configuration, the signal lag is well estimated with the cross correlation. The IQA method selected similar frequencies to the manual selection in practically all the gaps, including in the divertor and top of the machine.

Figure 4.45 shows the position error calculated for the setup with the cavity.

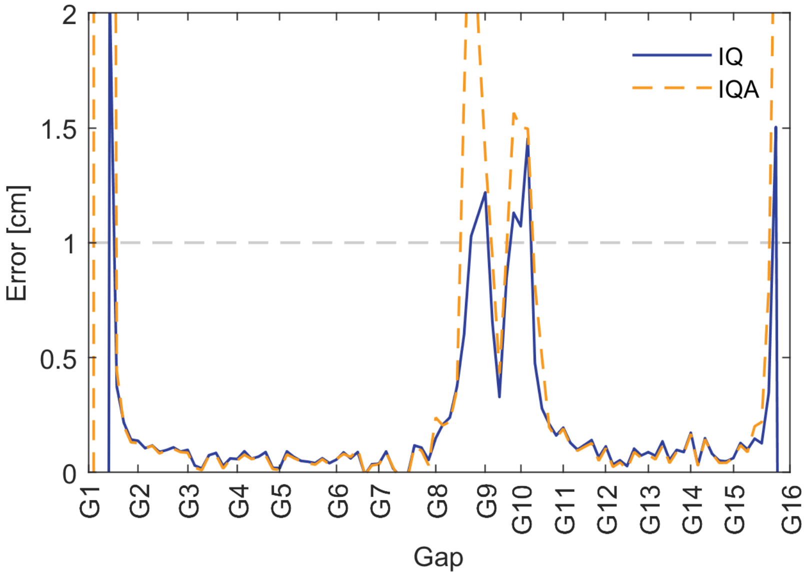

Figure 4.45: The position error calculated with the IQ and IQA methods for the cavity setup.

The results are similar in the gaps G1D-G8C and G10D-G15C. In the divertor and in the top of the machine, they have a considerable difference. This is explained by the wrong lag calculation and difficulty in finding smooth phase derivative profiles with the minimum standard deviation criteria.

### 4.6.5 Calculation of the power losses

Figure 4.46 shows the power losses at the separatrix, and the mean power in the range 50-54 GHz for the two setups, calculated with $f_{c2}$. If the power losses calculated with $f_{c1} - f_{c3}$ are represented by its exact value, some fluctuations occur when different measurements are compared (see figure 4.40 and 4.41). By using the mean in a small frequency range, smoother profiles are obtained.

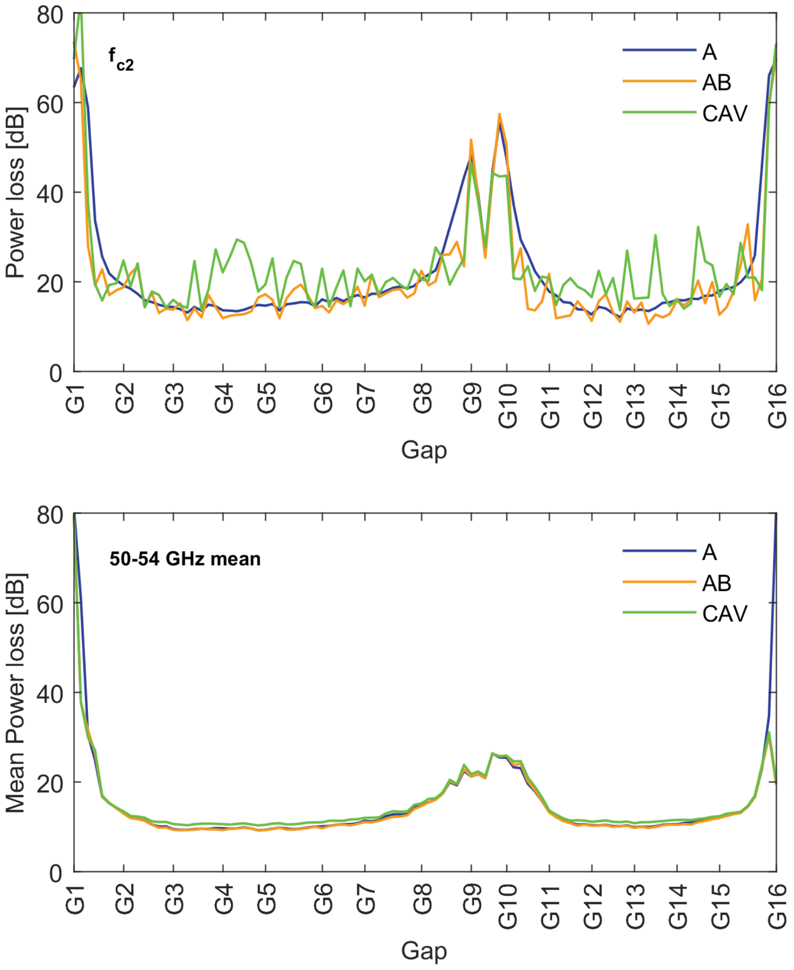

Figure 4.46: The power losses and mean power losses for the different setups.

The results show mean losses in the order of 10-30 dB in the equatorial zone and at the top of the machine, in agreement with the order of values that in the experiments [221]. In the divertor region, the losses increase to values above 40 dB when the signal is lost. In these cases, there is no characteristic components associated with the propagation, and the interpretation of the value returned by the IQA algorithm is not trivial.

## 4.7 Optimization for the baseline scenario

With the automated data analysis it was possible to find the FWP optimization function for the baseline scenario (see section 2.4.7). For each position, $\theta_{sep}$ was swept in the interval $[-10, 10]$ degrees, in steps of 1 degree. Figure 4.47 shows the superposition of the lines of view of each position.

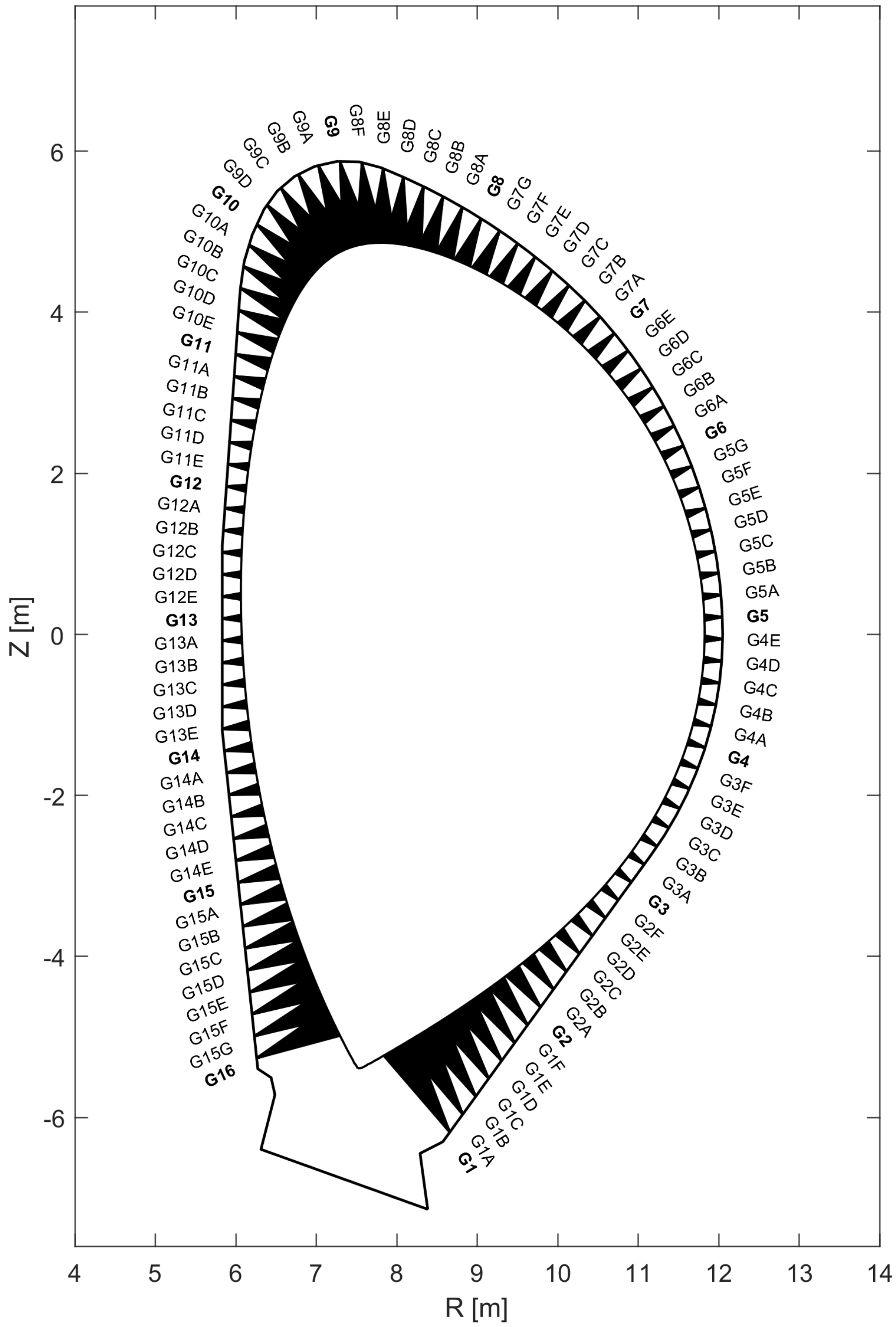

Figure 4.47: Lines of view of the configurations used to study the system optimization.

The simulations were performed with three different bands, $K_3 = [18, 30]$ GHz, $Ka_3 = [28, 48]$ GHz, $Q_3 = [45, 58]$ GHz. This results in 6300 UTS calibrations, 6300 simulations with the mirror and 6300 simulations with the plasma. The simulations were separated in 10 different sets to simplify the data analysis, the simulation management and the storage. The FWP error function is shown in figure 4.48.

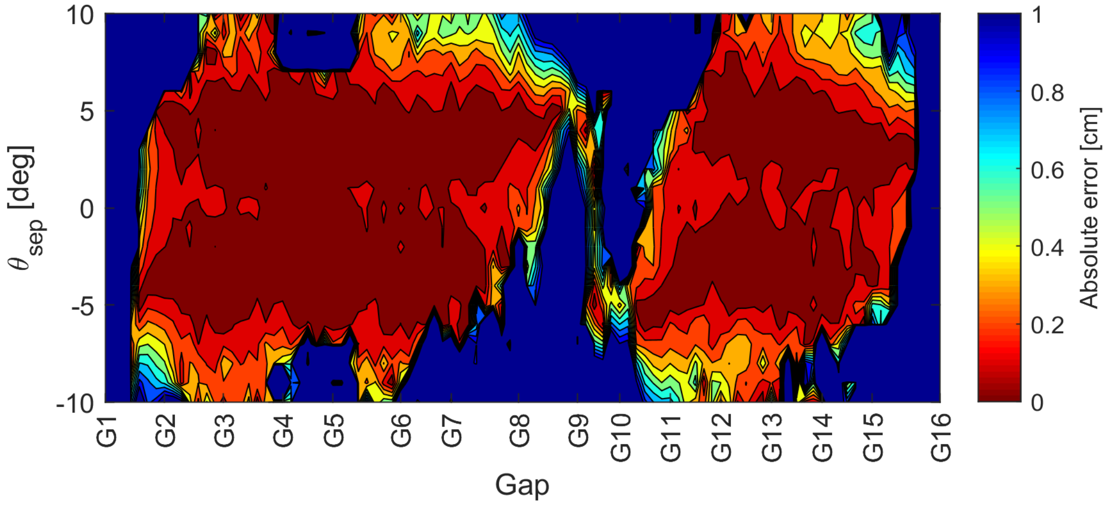

Figure 4.48: The FWP error function.

In the equatorial zone (LFS and HFS), there is an angular region between -5 and 5 degrees where the absolute error is in the 0-0.3 cm range. In this region, aligning the direction of the probing beam perpendicularly to the separatrix is a good criteria for optimization, as expected from the principle of optimization. It is also expected to be less sensitive to deviations to the equilibrium. As we approach the divertor or the top of the machine, the error is low to specific values of $\theta_{sep}$, depending on the plasma and wall geometry. The power losses at the separatrix function is represented in figure 4.49.

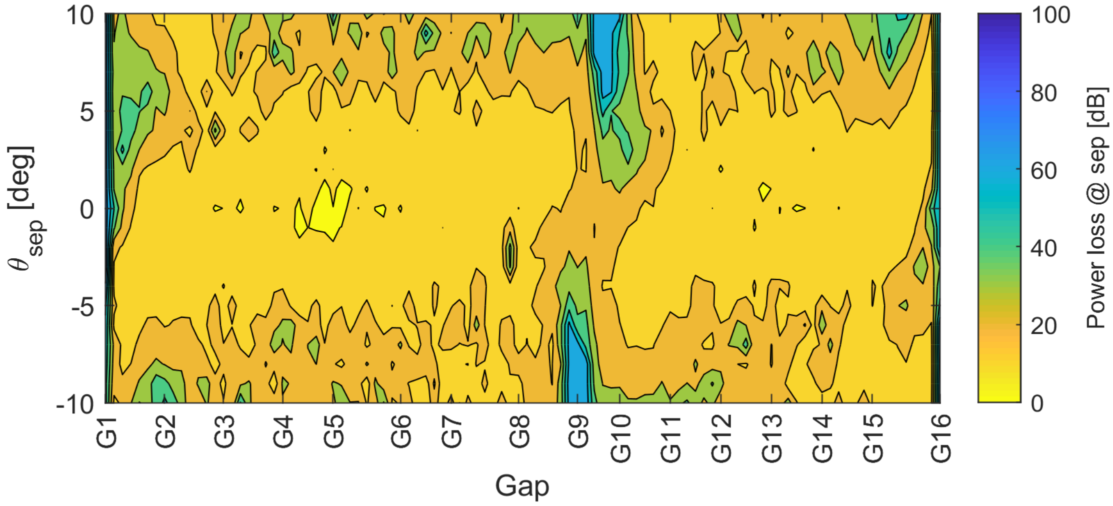

Figure 4.49: FWP optimization power loss at the separatrix function.

Similarly to the error function, the power losses are in the 0-30 dB range in the equatorial zone. The optimized solutions for the top of the machine and divertor appear in specific values of $\theta_{sep}$.

The signal of $\theta_{sep}$ is defined positive when it is in the first quadrant of the frame of simulation. The x axis of the frame of simulation points to the plasma, and the y axis points has a positive component in $Z$ from G1 to gap G8E and then changes the orientation to the opposite direction from G8F to G16. Figures 4.48 and 4.49 have the data relative to the gaps G8F-G16 inverted, so the error and the detected amplitude are continuous functions. In appendinx C.4 are shown the same figures with the original signal. The following results use the correct signal. After obtaining the error and amplitude profile for probing angles in the $[-10, 10]$ degrees range, the divertor positions and the top of the machine were simulated in higher angular ranges. In the top of the machine (gaps G8A-G11B) and in the last 10 gaps (G14E-G16A) the $\theta_{sep}$ swept in the [-20,20] degrees range. In the first 10 gaps, the angle was swept in the [-35,35] range, and the simulations were done with 4 different bands ($K_4 = [17, 29]$ GHz, $Ka_4 = [27, 42]$ GHz, $Q_4 = [39, 51]$ GHz, $V_4 = [48, 57]$ GHz). Figure 4.50 shows the performance of gap G1.

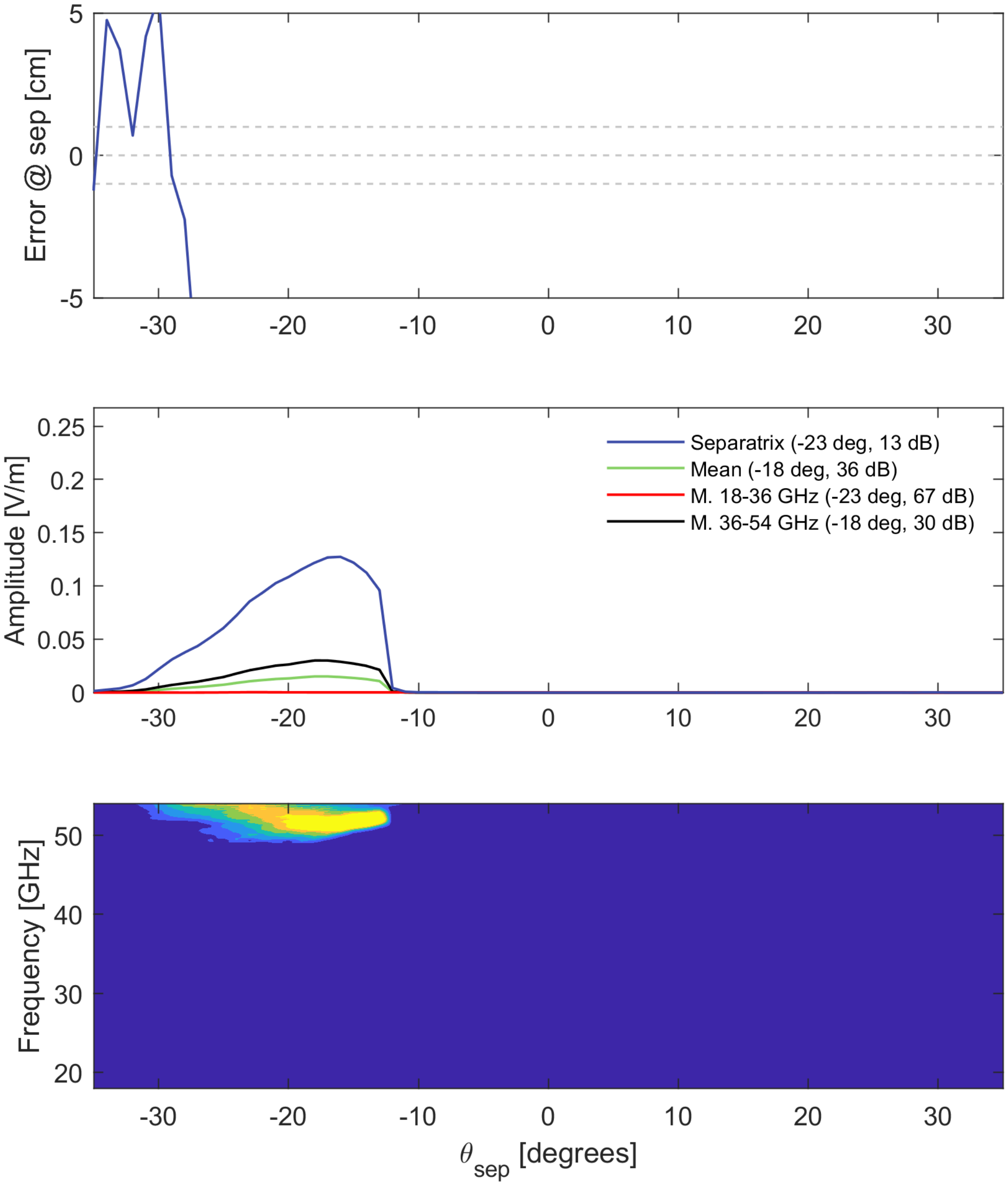

Figure 4.50: Performance of gap G1.

The detected amplitude at the separatrix frequency corresponds to the mean value in the 50-54 GHz range. The mean was also calculated for the 18-36 and 36-54 GHz ranges. The last diagram represents the power amplitude as function of the frequency and $\theta_{sep}$. The maximum and the respective detected power are identified for each profile. The yellow color is used to values above half of the maximum amplitude. The blue is used to values near 0. In the G1 gap, the signal is deviated by the strong curvature existing in this region, independently on $\theta_{sep}$. There is no solution for a reflectometry measurement with a mono-static reflectometer. Around $\theta_{sep} = 20°$, it is possible to detect signal at the separatrix frequencies, which can be used as an indicator of plasma presence. As we advance to gap G1D, different frequency ranges start to be detected. Figure 4.51 shows the measurement performance of gap G1B.

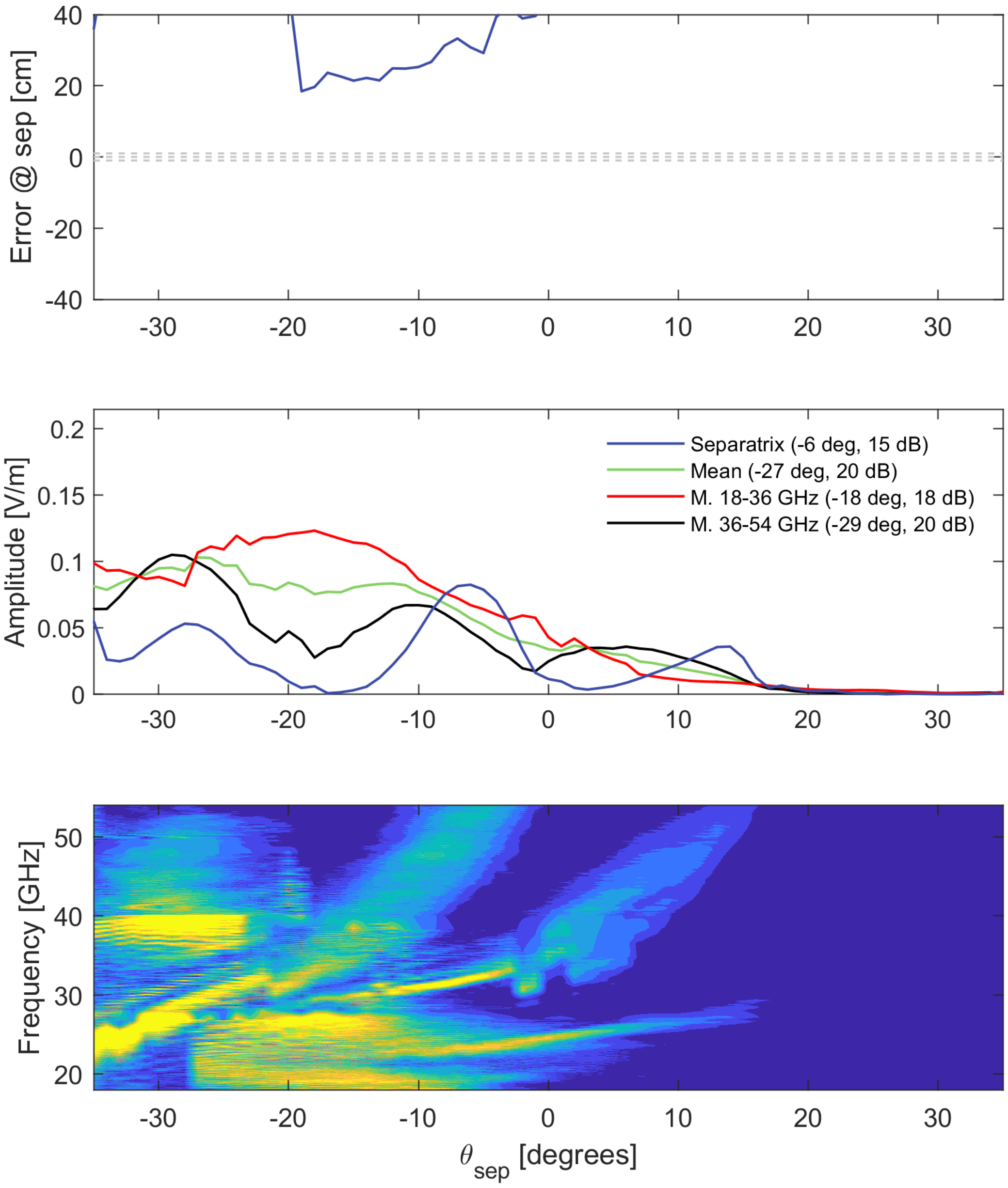

Figure 4.51: Performance of gap G1B.

In this case, even with the signal detection present in different frequencies for negative $\theta_{sep}$, there is no a solution that covers most of the frequency range. The position measurements are not possible with a mono-static system. Figure 4.52 shows the performance of gap G1D. The discontinuities in the power map are due to the change of physical system that occurs in each band with a different taper and fundamental waveguide.

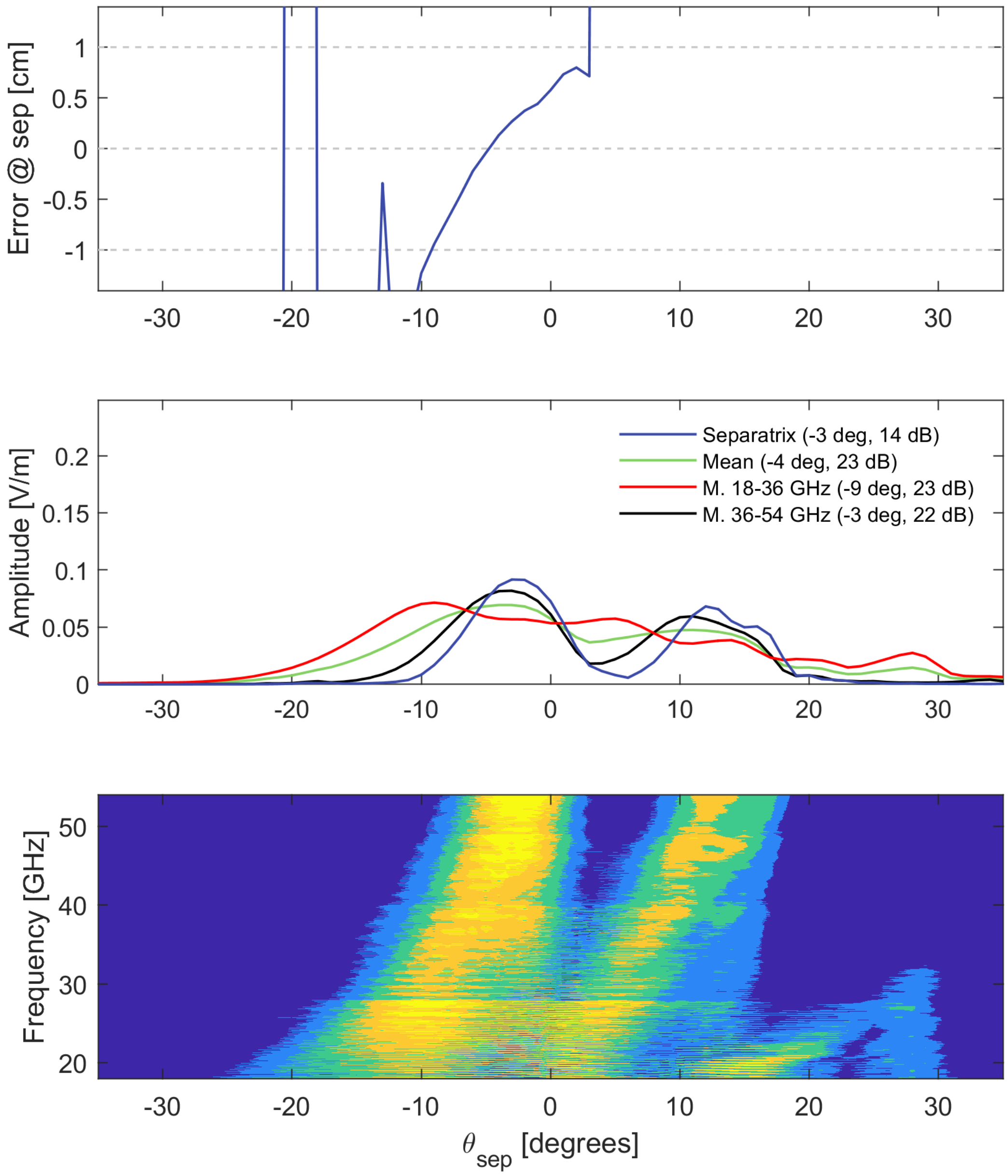

Figure 4.52: Performance of gap G1D.

In this gap, the power map shows high detected amplitude levels for all the bands at some angular regions. By looking to the position error, it is verified that only the [-10,0] angular region has a position error in the required range, including some angular positions with absolute error below 0.1 cm. In this particular example, it is clear that depending on the probing beam trajectory, the error can become positive or negative. The other regions with detected amplitude correspond to the detection of the plasma-wall reflections. Since these signals do not carry useful information in the first reflection in the plasma, the position error is not in the desired range.

The maximum of the mean detected amplitude is located at $\theta_{sep} = -4°$. The maximum of the 18-36 GHz, 36-54 GHz mean and separatrix mean do not coincide. The detected amplitude in the separatrix is not an ideal criteria of selection for the optimized configuration. The position depends on the integration over all the frequency range, and therefore the other bands must be taken into account. The maximum mean detected amplitude over the total frequency range was selected as criteria to select the optimal position, taking into account the detected amplitude profile of the lower frequencies. As we advance to the equatorial zone, the region with lower losses gets located at a $\theta_{sep} = 0°$ according to the optimization principle. Figure 4.53 shows the performance of gap G2F.

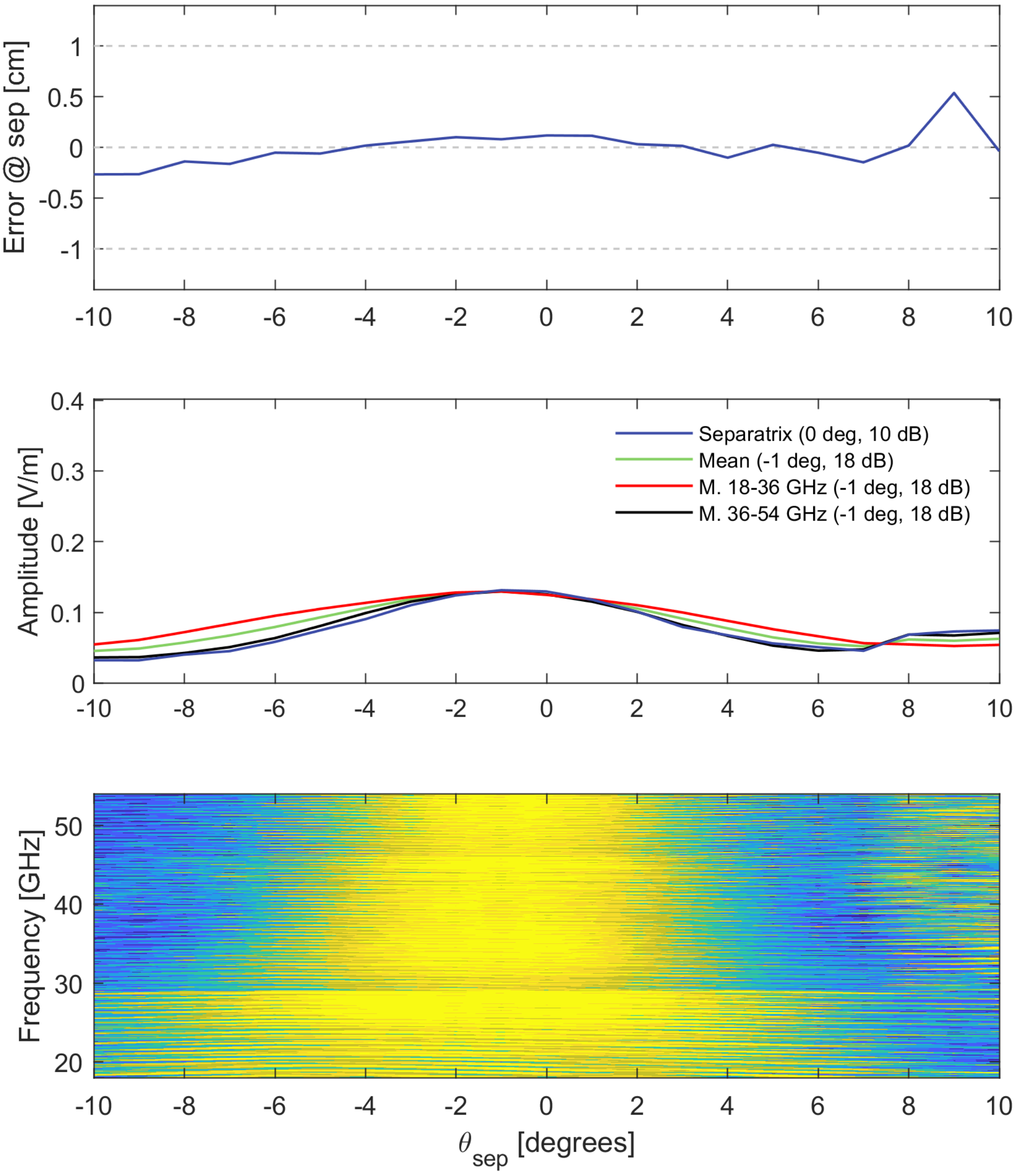

Figure 4.53: Performance of gap G2F.

In these positions located at the equatorial zone, there is a wider $A_{det}(\theta_{sep})$ profile, with a wider region of $\theta_{sep}$ where the error is low.

In the top of the machine the profiles are characterized by a higher difference between the lower and higher frequencies due to the shape of each density layer. Figure 4.54 shows the performance of gap G8F.

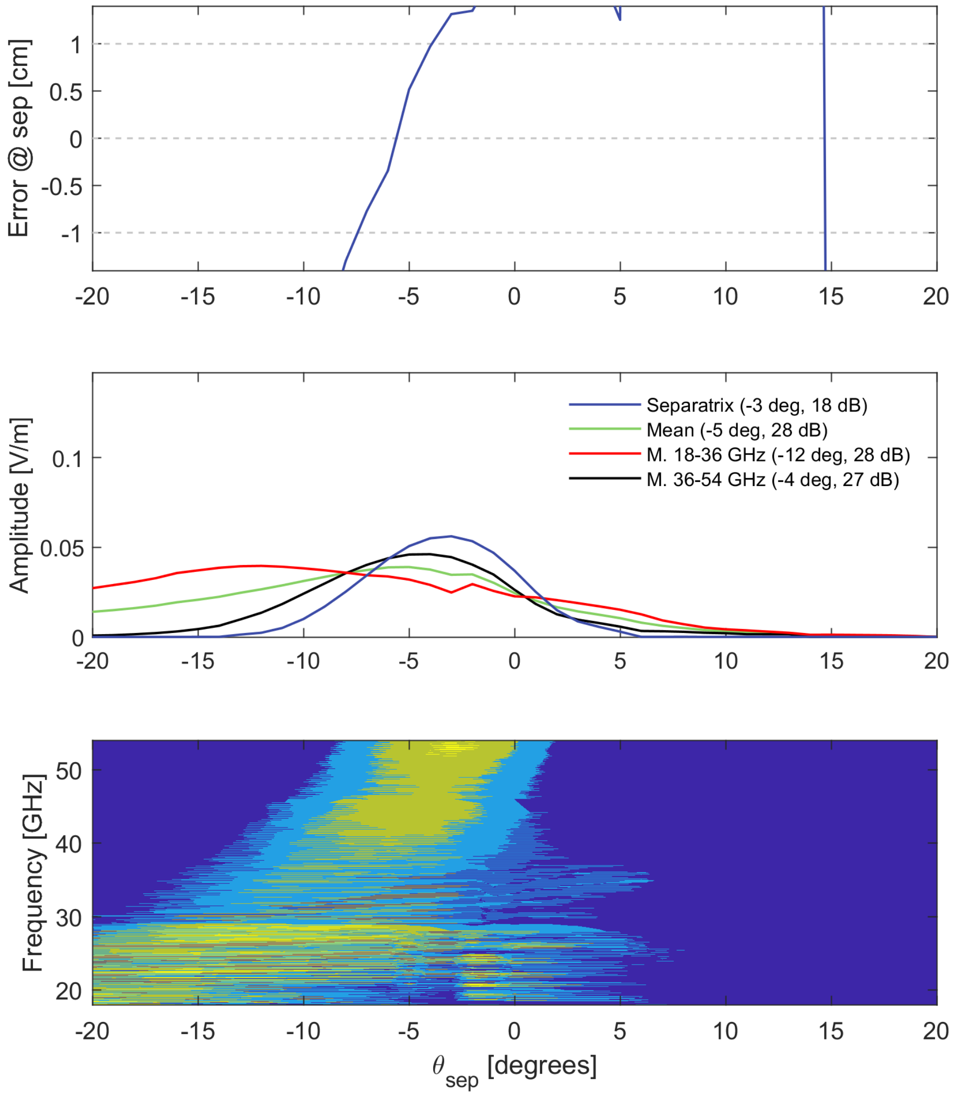

Figure 4.54: Performance of gap G8F.

Figure 4.55 shows the performance of gap G9B. In this region of the machine, characterized by a higher plasma-wall distance and curvature, the $e(\theta_{sep})$ has a symmetric quadratic-like shape. The solution with less losses does not correspond to the solution with lower absolute error.

Looking to the different amplitude and error profiles and using the maximum mean detected amplitude value as criteria to select the optimized configuration if the error is in the requirement, the optimal angles were selected and the optimized configuration was selected. Figure 4.56 shows the selected $\theta_{sep}$ values.

The lines of view of the optimized system are shown in appendix C.6. Figure 4.57 shows the position error of the optimized (opt) and original configuration (psep). The optimized system improves the measurement error in all the positions in the top of the machine to values below 0.5 cm. Some positions in the divertor region also improve the measurement performance.

Given the optimized configuration, it is necessary to demonstrate its stability under deviations to the equilibrium. Next we study the effect of the plasma displacement at the measurement performance of the system.

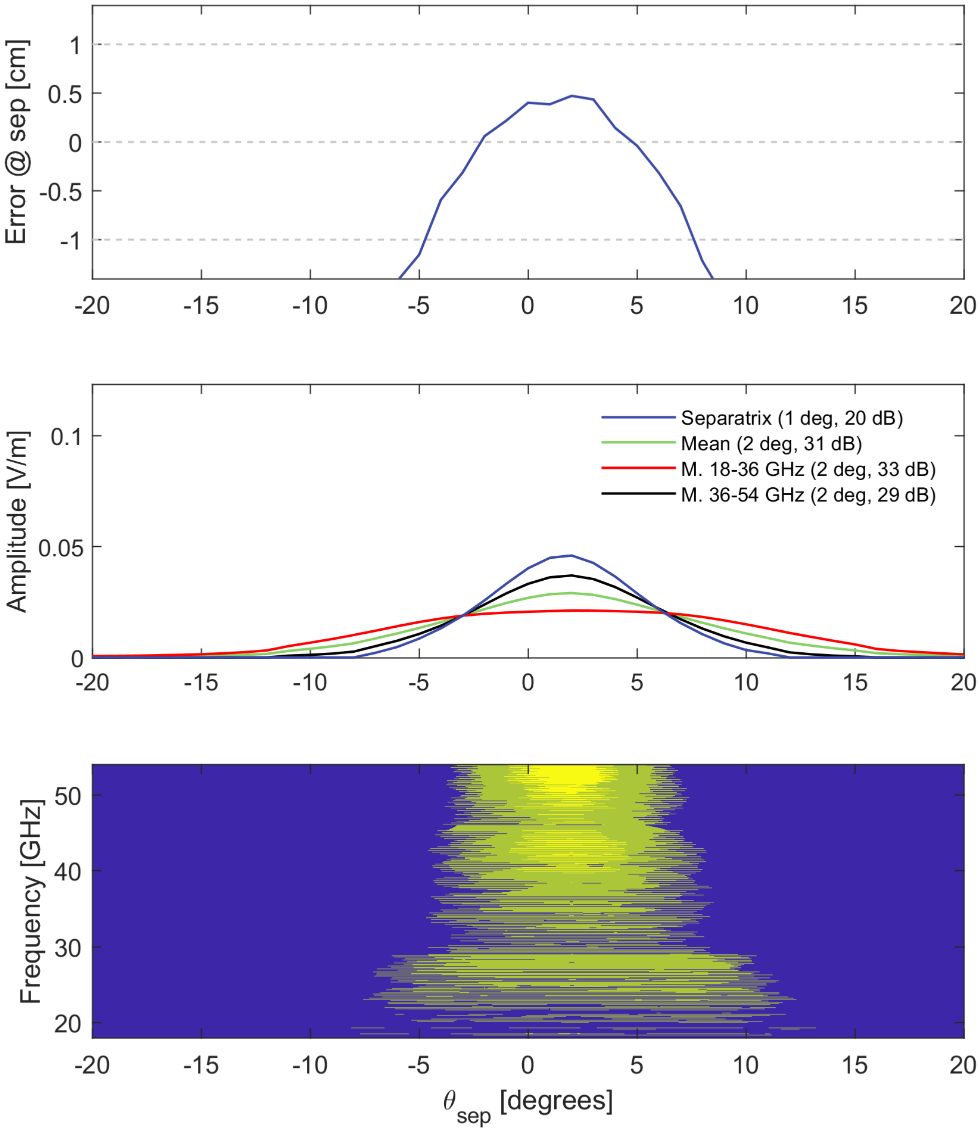

Figure 4.55: Performance of gap G9B.

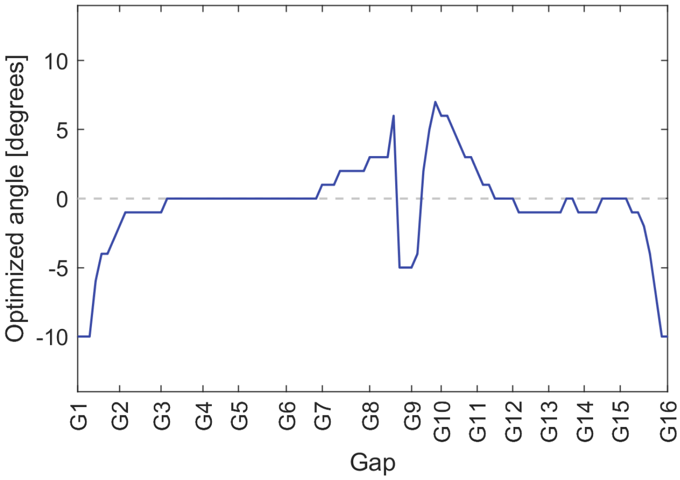

Figure 4.56: The optimal angle as function of the gap.

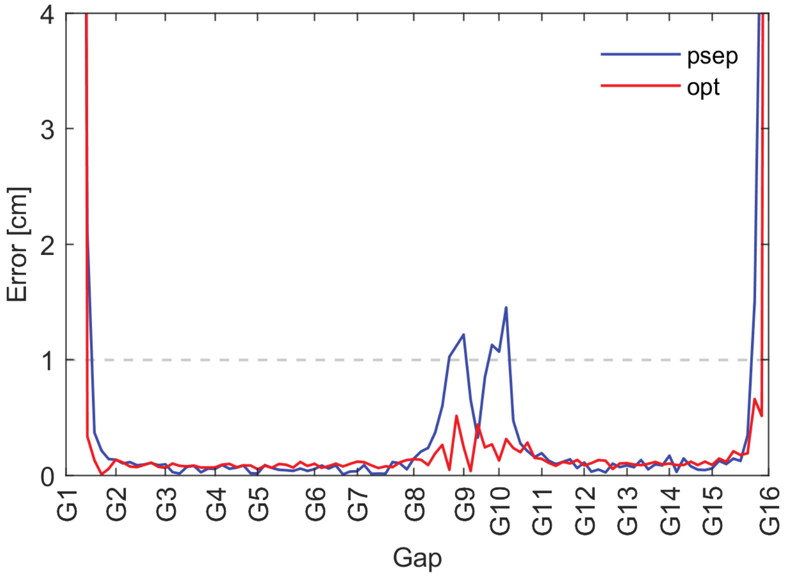

Figure 4.57: Position error of the optimized (opt) and original configuration (psep).

## 4.8 Effect of the plasma displacement in the measurements

In a situation of failure of the control system or other off-normal occurrences, the system must be able to measure the possible plasma displacements. Due to the lack of information on the plasma state during these events, the effect of the plasma displacement in the system performance was described with a translation in the form

$$\mathbf{D} = D[\cos(\theta), \sin(\theta)]. \tag{4.33}$$

The plasma model is easily obtained by applying the symmetric translation in the region of interest coordinates and using the same function to extract the plasma matrix.

In the first study, we used the non optimized configuration. 24 different plasmas were simulated, corresponding to plasma displacements of 5, 10 and 15 cm, for 8 different directions, $\theta = [0, 45, 90, 135, 180, 225, 270, 315]$ degrees. The regions of interest are the same for each reflectometer and were defined to be compatible with all the displacements. This consumes more computational resources, however the input definition is less complex. The results are in appendix C.7 and show that in the equatorial zone the system is stable under all the simulated displacements. In the top of the machine, the results show position errors above the requirements for most of the displacement configurations. In the second study, we used the optimized configuration and calculated the error and the detected amplitude to plasma displacements of 5 (typical case) and 15 cm (limit case), for $\theta = [0, 90, 180, 270]$ degrees. Figure 4.58 shows the position error for $D = 5$ cm.

In the top of the machine, the vertical (90° and 270°) and the horizontal (0° and 180°) displacements are characterized by errors equal or below of 1 cm. Figure 4.59 shows the average losses at the separatrix frequency for each displacement. The shadow region represents the interval between the minimum and maximum value.

With the optimized configuration, the system keeps the same order of average losses for all the positions, with the exception of the divertor region where the signal is lost. This means that the optimized configuration is stable under displacements of 5 cm. Figure 4.60

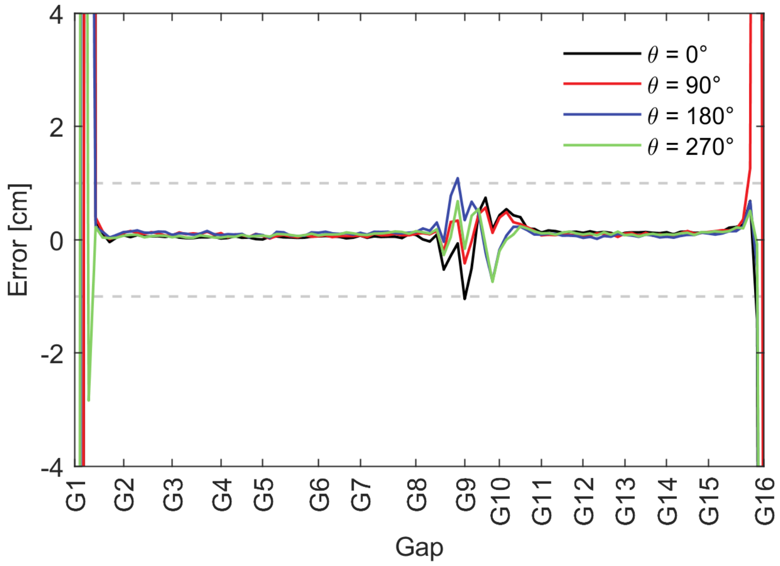

Figure 4.58: Position error for $D = 5$ cm ($\theta = [0, 90, 180, 270]$ degrees).

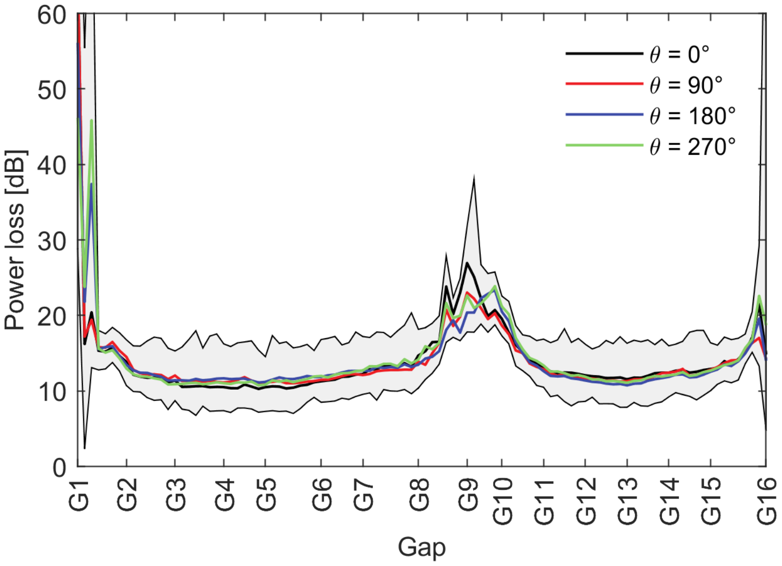

Figure 4.59: Power losses for a 5 cm plasma displacement.

shows the position error for $D = 15$ cm. In this case, the error can reach absolute values above 1 cm in the top of the machine. The signal changes according to the direction of the displacement and with the considered location. In the equatorial zone the system is capable of measuring with a low error, similar to the results for a displacement of 5 cm. Figure 4.61 shows the average power losses.

At the equatorial zone the power losses have the same order of values comparing with the 5 cm displacements. For $\theta = 0°$, the losses are higher in the HFS and lower at the LFS, as expected due to the increasing or decreasing antenna-plasma distance. For $\theta = 180°$, the opposite situation occurs, the losses are higher in the LFS and lower at the HFS. At the top of the machine, some displacements cause average losses above 20 dB.

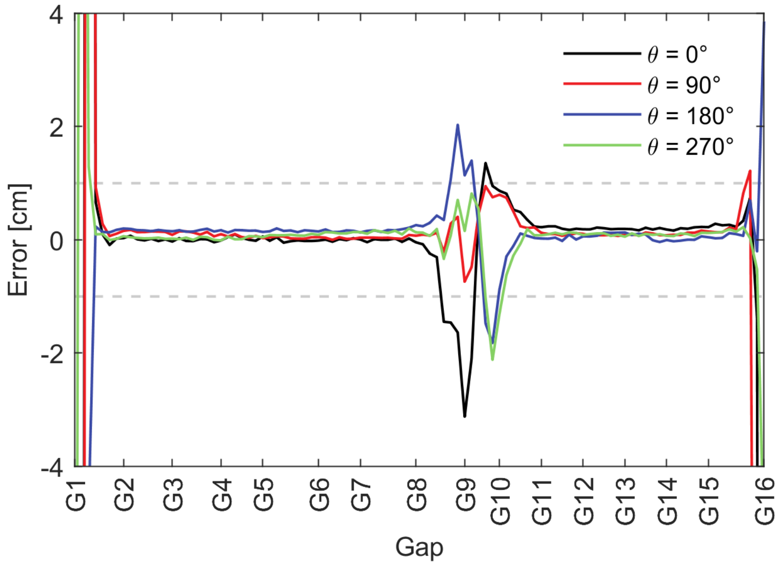

Figure 4.60: Position error for $D = 15$ cm.

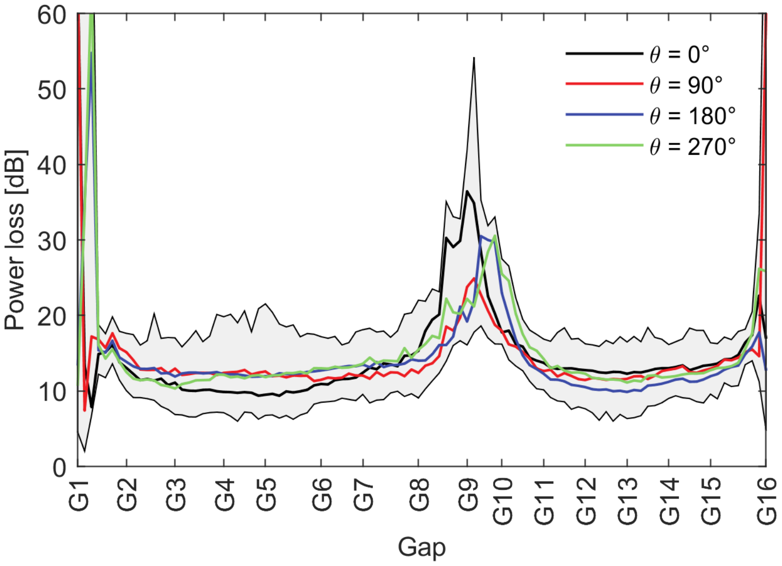

Figure 4.61: Average power losses for a 15 cm plasma displacement.

## 4.9 Effect of the initialization in the position error

With the optimized system, an introductory study on the effect of the O-mode signal initialization in the measurement error was done. The initialization is defined by the initial plasma position and by a function to connect the initial point with the phase derivative of the first probing frequency. In a fusion machine where the scenario is predefined, the initial plasma position uncertainty is expected to be low. We added a term of $4\pi\Delta d_p/c$ to the initial point of the WKB phase derivative (with the vacuum distance included), where $\Delta d_p$ is the uncertainty in the plasma position. We also used a linear initialization function [82], connecting it to the WKB phase derivative of the first probing frequency. Figure 4.62 shows the phase derivative profiles relative to values of $\Delta d_p$ in the $[-5, 5]$ cm range, in steps of 1 cm. It is assumed that there is no error in the measurements of the initial probing frequency.

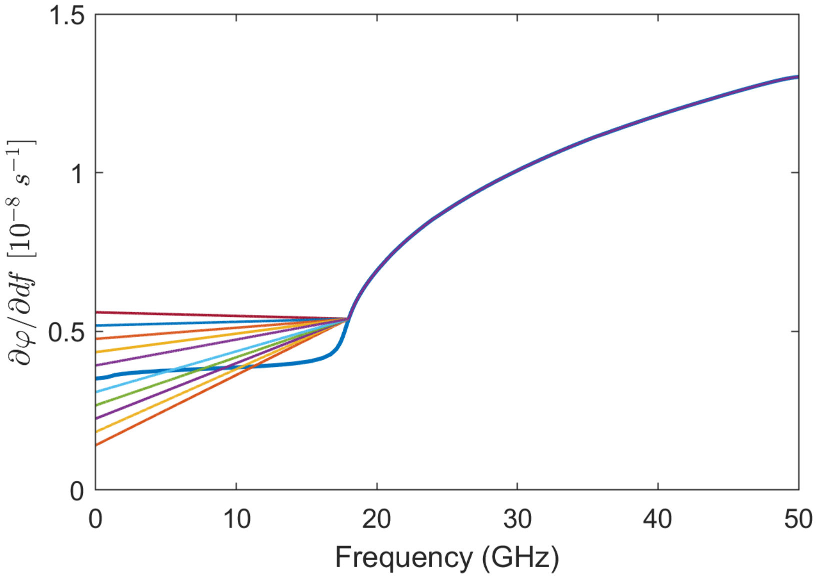

Figure 4.62: Phase derivative profiles for plasma position uncertainties.

Figure 4.63 shows the measurement error associated with the initialization for $\Delta d_p = [-5, 1, 0, 1, 5]$ cm (see section 4.3.4).

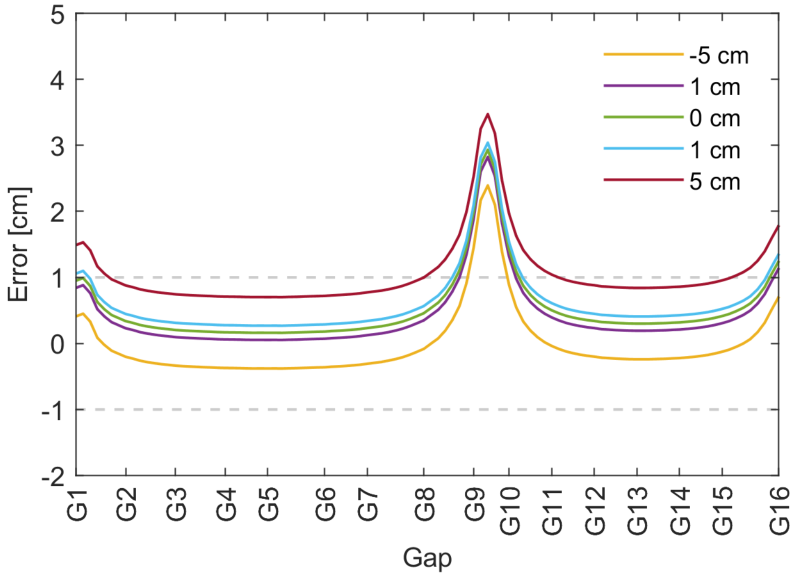

Figure 4.63: The measurement error associated with the initialization.

The results show the position error below 0.5 cm in the equatorial zone, with the exception of +5 cm uncertainty where it is approximately 0.8 cm. In the top of the machine, the error can reach values of 1-3 cm. These gaps are characterized by higher distance between the initial plasma position and the first probing frequency layer. In this region it is fundamental to define different initialization functions that minimize the position error.

## 4.10 Effect of turbulence in the measurements

In a real plasma confinement experiment, the electron density and the other plasma parameters have fluctuations. The smooth profiles are obtained by averaging the plasma parameters over a large period compared with the turbulence time-scale. The effects of the turbulence in the measurements were discussed in chapter 2.2.7. Turbulence affects the measured group delay and the amplitude of the detected signal, leading to higher position errors. The characteristic scales of the turbulent structures and its amplitude are different in each region of the machine and changes during the different phases of the discharge. The design of a PPR system requires the study of the effects of turbulence in the measurements for all the positions of the optimized solution with the baseline scenario. A large number of density profile samplings needs to be simulated to obtain the statistical parameters of the position error with an acceptable statistical error.

There are essentially two problems related with the study of the effect of turbulence in the position reflectometry measurements. The first problem is the necessary computational resources. The standard error of the mean is proportional to $1/\sqrt{N_s}$, where $N_s$ is the number o samples. At least 400 samples are required to have errors of 5% in the study a given turbulence profile. Since different profiles of turbulence should be tested for all the reflectometers, this kind study is very demanding from the computational point of view, even performed with the 2D models. The second problem is the data analysis. The study of turbulence is only possible in useful time with the automated analysis methods. One important question is to understand if the IQA method developed in the section 4.6 is able to extract the phase derivative in this kind of study, where the characteristic Q-spectrum peak can suffer deformations due to the fluctuations. Another question is the to understand the utility of the SFFT method in the evaluation of the error mean. This method is easily automated in a study of deviations to a reference plasma, since the order of the applied filter, signal lag and spectrogram parameters is the same. Since this method selects the group delay by the frequencies with higher spectral amplitude, the error can become higher in absolute value if a great part of the power is lost relatively to the spurious signals due to the plasma-wall propagation or phase-shift induced by the fluctuations. In this case, if some physical effect creates an intrinsic negative error, it is possible that this method does not provide accurate results.

In this section we evaluate the measurement performance of gap G13 with the IQA method for different amplitudes of turbulence. An accurate estimation of the error in all the positions of the machine would require computational resources that were not available. Each level of amplitude was studied statistically with 400 samples. This number of samples allows to have an acceptable standard error and is compatible with the available computational time. The region of interest was reduced to a 1 m × 0.6 m rectangle and was used in all the simulations of this study. The plasma was probed in three different bandwidths, $\mathrm{K}_5 = [17, 30]$ GHz, $\mathrm{Ka}_5 = [29, 46]$ GHz and $\mathrm{Q}_5 = [45, 56]$ GHz with a lower number of time iterations, 160000.

### 4.10.1 Modeling density fluctuations

The plasma density is written as the sum of the equilibrium density term $n_0$ with the fluctuations $dn_e$,

$$n(x, y) = n_0(x, y) + dn_e(x, y). \tag{4.34}$$

The fluctuations are locally described by a characteristic spectrum and an amplitude/level with respect to the equilibrium plasma. Due to the lack of information on the turbulence properties of DEMO plasmas, we define the fluctuations with a Kolmogorov-like spectrum [226, 227], following [228]. The spectrum is described by the function

$$S(k) = H(k_{knee} - k) + H(k - k_{knee}) \times k_{knee}^3 k^{-3}, \tag{4.35}$$

where $H(k)$ is the Heaviside function and $k$ is the density fluctuations wavenumber. This model assumes the electron drift waves as the predominant instability at the edge and uses a characteristic scale of $k_{knee} \sim 1/\rho_S$ according to its maximum growth rate [229]. $\rho_S$ is the Larmor radius calculated with the sound speed. Considering the provided values of magnetic field at the separatrix position (7.2 T) and the expected values for the electron temperature around the separatrix (3-4 keV or lower), we selected a characteristic scale of $k_{knee} = 8\ \text{cm}^{-1}$. The aim of this study is the study of the kind of behavior of the measurement error under the variations of the turbulence amplitude. The accuracy of the results can be improved using realistic density profiles from gyrokinetic simulations, as done in [230]. The fluctuations term is defined as

$$dn_e(x, y) = n_0(x, y)\text{Frm}(x, y)\frac{dn(x, y)}{\text{RMS}[dn(x, y)]}, \tag{4.36}$$

where $dn(x, y)$ is the inverse Fourier transform in the form of the spectrum amplitude $S(k_x, k_y) = S[k_x]S[k_y]$, with spectral phase $\phi(x, y)$ and $\text{Frm}(x, y)$ is the frame function. This function localizes the turbulence and defines its amplitude. The turbulence is assumed to be homogeneous and isotropic in the poloidal plane. By defining a random spectrum phase profile $\phi(x, y)$ a different fluctuation matrix $dn(x, y)$ is generated with the equation (4.36). One of the $dn(x, y)/\text{RMS}[dn(x, y)]$ matrices is shown in figure 4.64.

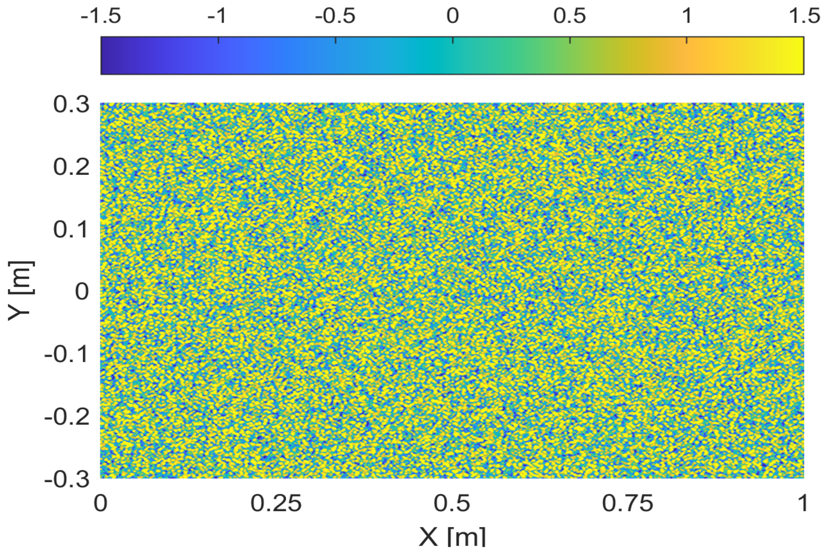

Figure 4.64: The $dn(x, y)/\text{RMS}[dn(x, y)]$ matrix for the selected k-spectrum.

Due to the RMS normalization, most of the values are in the [-1,1] range. Sixteen levels of turbulence were defined, from 1% to 16% in steps of 1%. Eight are shown in figure 4.65.

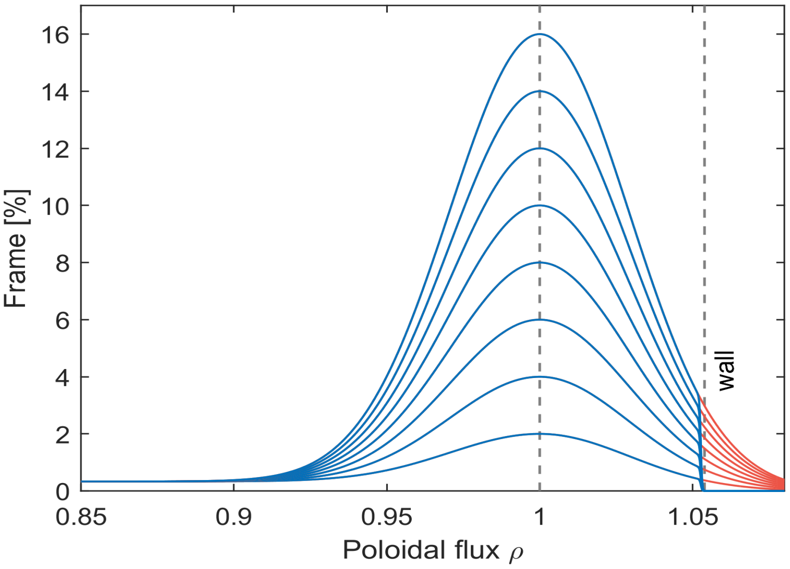

Figure 4.65: Eight of the sixteen defined frames.

Each frame has a Gaussian shape in the form

$$\mathrm{Frm}(\rho) = B + C\exp\left\{-\frac{(\rho-1)^2}{2D^2}\right\}, \tag{4.37}$$

where $A_{trb} = B+C$ is the maximum amplitude and $D$ the standard deviation, taken as 0.02. The $C$ parameter is adjusted in the SOL region and in the pedestal region to set the maximum value of amplitude. A hyperbolic tangent frame is applied at the wall position, similarly to the density profile. The turbulence level is low at the core and increases until the separatrix, where it can reach values above 10 % [166, 74, 145]. In the rest of this work, the maximum amplitude $A_{trb}$ is also referred as level/amplitude of turbulence. Figure 4.66 shows a frame function corresponding to a density fluctuation level of 10 %.

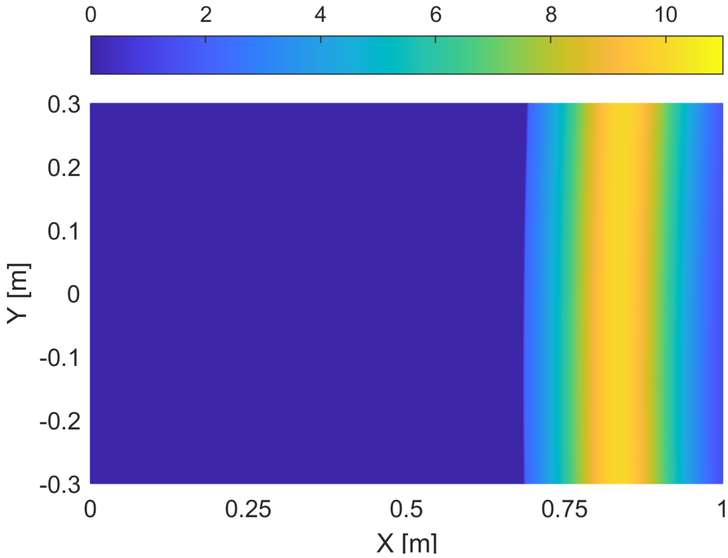

Figure 4.66: Frame function corresponding to a density fluctuation level of 10 %.

### 4.10.2 The effect of turbulence in the position error

Figure 4.67 shows the electric field snapshot as result of probing one turbulent plasma sample with $A_{trb} = 10\%$ at 53 GHz. A complex configuration of the electromagnetic field is formed in the between the wall and the plasma cavity due to the superposition of the emitted and reflected field with the scattered field.

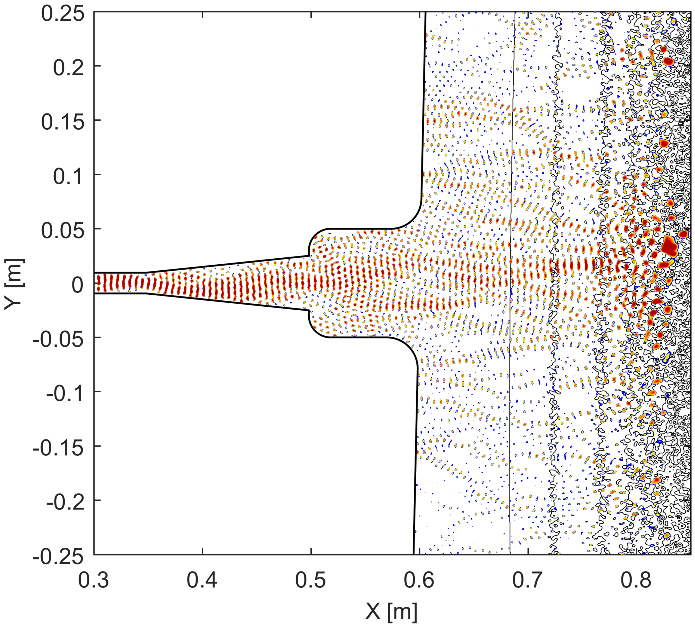

Figure 4.67: Electric field snapshot at 53 GHz for $A_{trb} = 10\%$.

The measurement error $e_i$ and the amplitude $a_i$ of every sample $i$ were obtained and the statistical quantities were calculated. Figure 4.68 shows the mean error at the separatrix as function of the turbulence level. The bars correspond to the standard deviation.

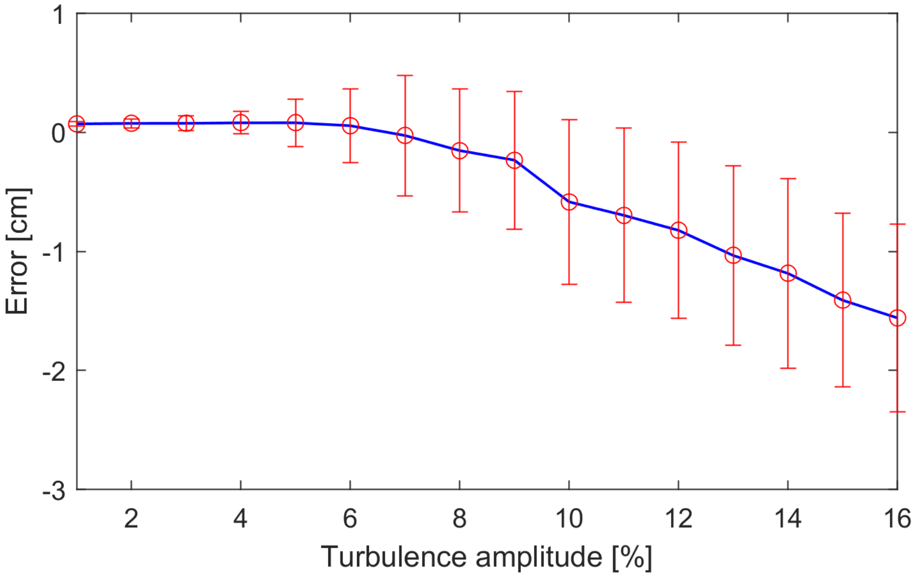

Figure 4.68: The mean error at the separatrix as function of the turbulence amplitude.

The respective histogram is shown in figure 4.69 for different levels of turbulence and the standard deviation and the rate of failure is shown in figure 4.70.

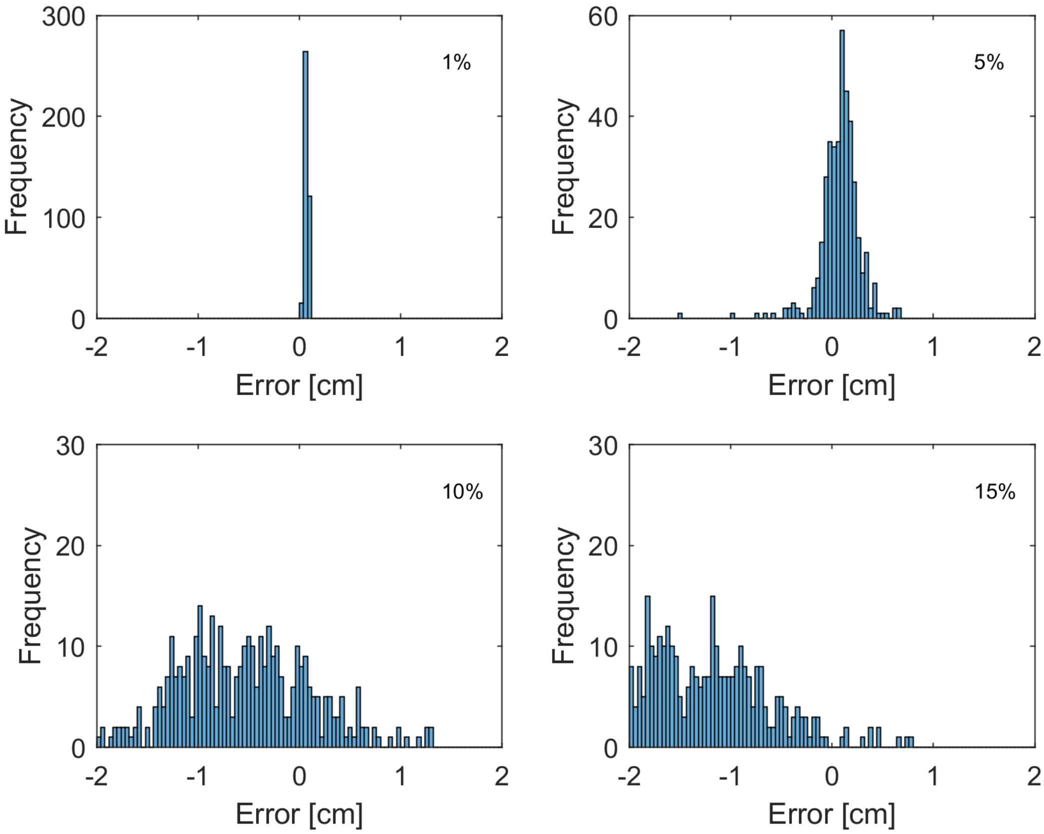

Figure 4.69: The error distribution for diferent turbulence levels.

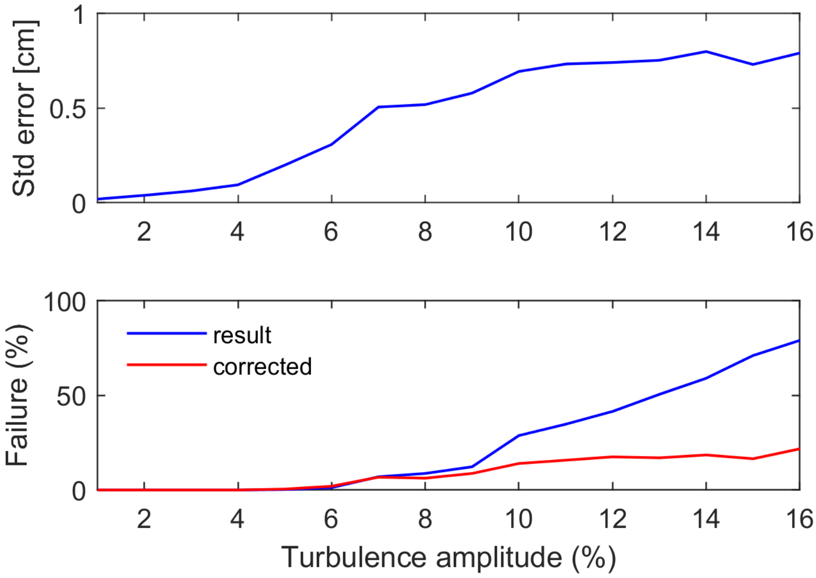

Figure 4.70: The standard deviation and the rate of failure.

The corrected rate of failure is discussed later. The first observation is that the mean becomes negative and decreases with the turbulence level, corresponding to an higher absolute error. The standard deviation increases with the turbulence level until stabilize for turbulence amplitudes above 10%. The appearance of failed measurements (out of the 1 cm error requirement) starts at $A_{trb} = 5\%$, and for the maximum fluctuation level (16%) reaches 50%. Figure 4.71 shows a sample of the phase derivative for a turbulence level of 10% and the respective Q-spectrum for the $Q_3$ band.

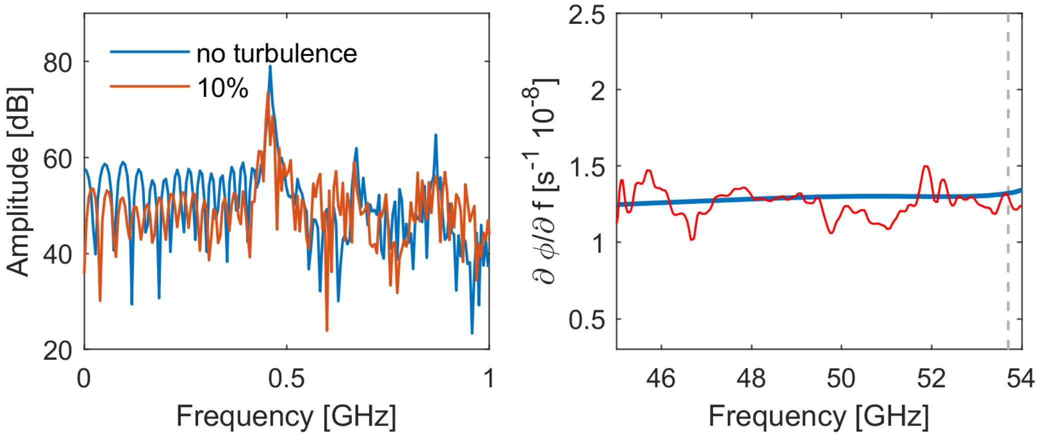

Figure 4.71: Sample of phase derivative for a turbulence level of 10% and the respective Q-spectrum for the $Q_3$ band.

The Q-spectrum shows that the turbulence modifies the shape and amplitude of the characteristic peak and of the lower frequencies. By filtering the higher frequency components with the IQA algorithm, the fluctuations due to turbulence appear in the phase derivative profile. The negative mean implies that the group delay is predominant below the WKB curve. This means that the waves reach the antenna before what they would with the unperturbed density profile. The reason for this effect is that high levels of fluctuations change the cutoff position to a position closer the antenna.

Even though the propagation in a turbulent plasma is a complex phenomena, a one dimensional simple model can explain this tendency to negative errors. First, lets consider a one dimensional density profile in the form

$$n(x) = mx + A_{trb}\cos(k_f x + \phi_0), \tag{4.38}$$

where the first term is a linear density profile with slope $m$ and the second term is an oscillation with amplitude $A_{trb}$, wavelength $k_f$ and phase $\phi_0$. By selecting a probing frequency and consequently a cutoff density $n_c$, the cutoff position is $x_c = n_c/m$ if $A_{trb} = 0$ (equilibrium case). By increasing the oscillation amplitude, the new cutoff position $x'_c$ resulting from the interception of the new profile with the same cutoff density line changes. For low amplitude, it can oscillate around $x_c$, depending on $k_f$ and $\phi_0$. As we increase the amplitude of the oscillation, there is a limit where, for a given $k_f$, whatever is the phase there is always a fringe before $x_c$ that corresponds to a density higher than the cutoff density. In a plasma with a realistic turbulence profile, this corresponds to the situation in which a great part of the errors become negative as it is observed in the simulations. Since the time delay is decreased due to the reflection occurs before the expected position, there is a tendency on the phase derivative to be below the WKB curve, although in many frequencies it is above or centered, depending on the propagation before the cutoff region.

For a fixed frequency the mean phase derivative of all the samples is below the WKB curve, leading to a negative mean (see section 2.4.3).

Using the density profiles from the simulations, we calculated the mean cutoff deviation ($x_c' - x_c$) and the respective standard deviation as function of the frequency for different turbulence levels. The line of view centered at the antenna was used as reference to obtain the cutoff position. Figure 4.72 shows the result. Similarly to the measurement error, the mean is approximately zero initially and becomes negative for higher turbulence levels. The standard deviation also increases as observed in the error distribution. The effect of the failed measurements in the separatrix reconstruction must be studied to understand what is the range of turbulence that is acceptable naturally by the reconstruction algorithms. This range of turbulence can be extended if a position correction in the form

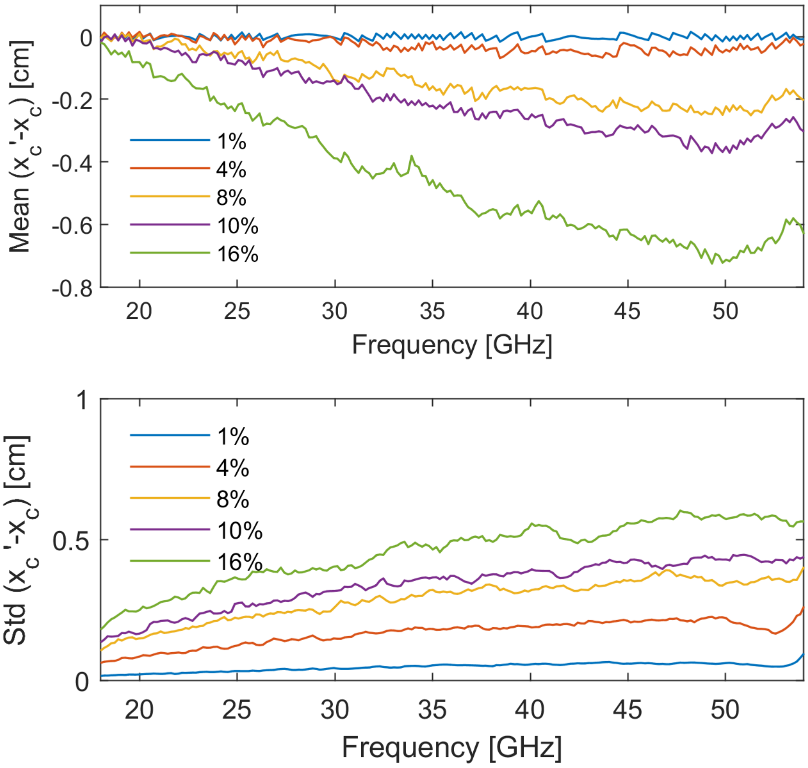

Figure 4.72: Mean and standard deviation of the cutoff deviation of the models that were used for simulation.

$$r'(F) = r(F) - E(F, A_{trb}) \tag{4.39}$$

is applied. $r'(F)$ is the corrected position, $r(F)$ is the obtained position and $E(F, A_{trb})$ is the mean error obtained with the simulations. This correction works if the standard deviation of the error is lower than the measurement requirement, $\sigma_E(F_{sep}) < \Delta e$, and if the value of failed measurements is accepted.

Figure 4.70 shows the failure rate of the corrected error. In a real application, the level of turbulence can be also measured with reflectometry, and this could be adjusted dynamically [231].

### 4.10.3 The effect of turbulence in the detected amplitude

The power losses were calculated with the IQA algorithm. Figure 4.73 shows some samples of the the detected amplitude profile for the $Q_3$ band, where is possible to identify higher losses at specific frequency ranges.

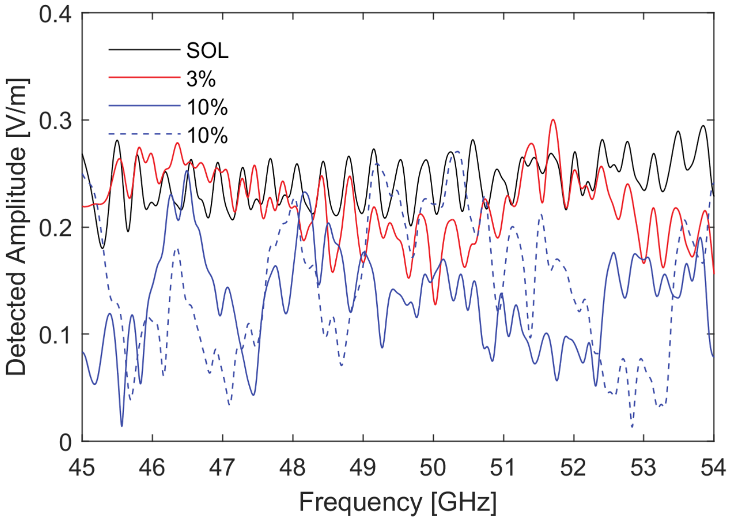

Figure 4.73: Detected amplitude profile of different samples for the $Q_3$ band.

As the turbulence level increases, it is possible to identify frequency regions where the detected amplitude is lower when comparing with the unperturbed. These regions depend on the form of how the turbulence scatters the probing wave, having a different behavior in each sample. They are the principal cause for the wrong selection of the beating frequency in the SFFT method. Figure 4.74 shows the mean power loss at the separatrix (50-54 GHz average) as function of $A_{trb}$.

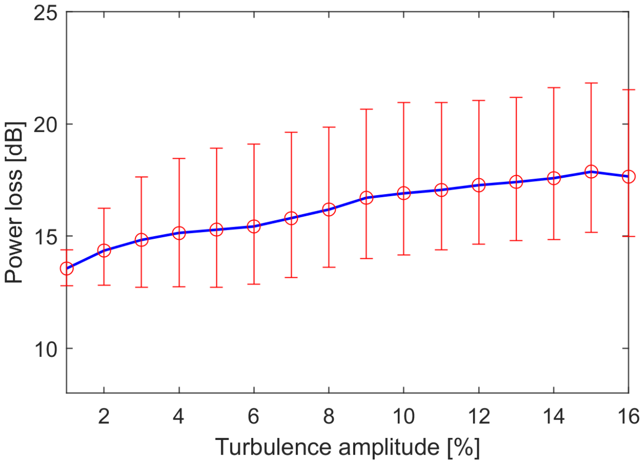

Figure 4.74: The power loss as function of the turbulence amplitude.

As expected, the power losses increase with the turbulence amplitude. For levels of 10-16%, it can reach values of 22 dB, approximately a difference of 5-10 dB from the unperturbed losses. This effect can be problematic in situations where the detected power without turbulence is low or for higher levels of turbulence.

### 4.10.4 Using SFFT method in turbulence studies

An important question related with turbulence studies is to understand if the SFFT algorithm identifies the negative mean error due to the change of cutoff position. Figure 4.75 shows the spectrogram of two $A_{trb} = 10\%$ samples for the $Q_3$ band where the wrong beating frequency selection is visible. The propagation in the setup is included.

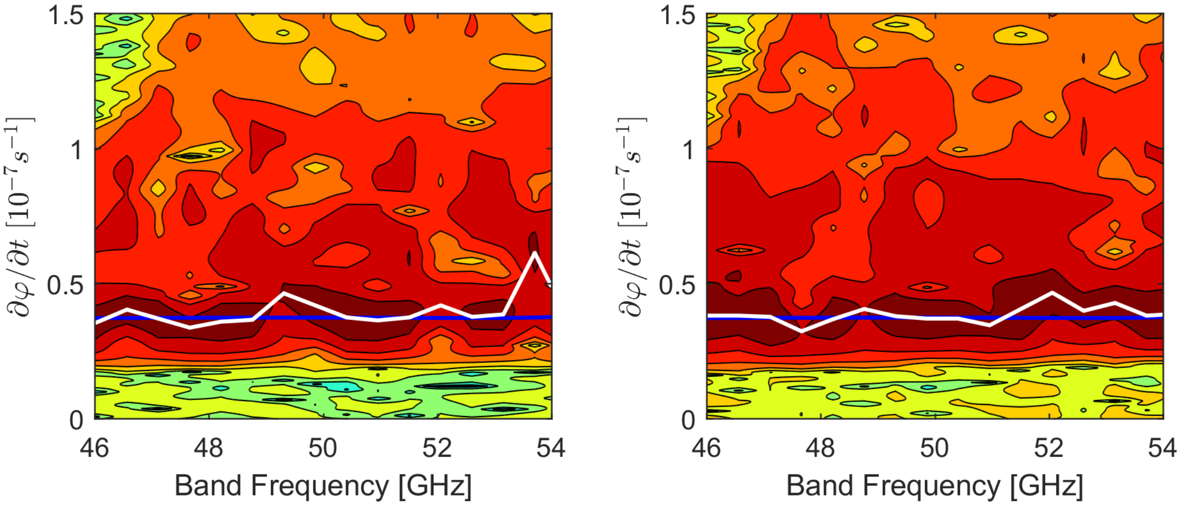

(a) Spectrogram of a $A_{trb} = 10\%$ sample.

(b) Gap G11B, $\theta_{sep} = 10°$

Figure 4.75: Spectrogram of two $A_{trb} = 10\%$ samples.

This leads to a systematic positive error that can overcome the effective cutoff effect. Figure 4.76 shows the separatrix position error distribution calculated with the SFFT method for $A_{trb} = 10\%$ where it is possible to observe this effect, the mean error becomes positive.

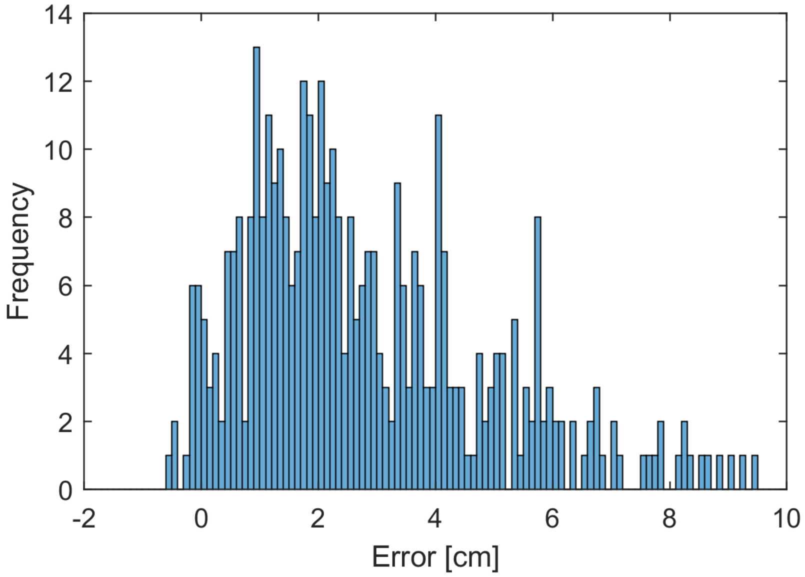

Figure 4.76: Distribution of $e_i(F_{sep})$ calculated with the SFFT algorithm for $A_{trb} = 10\%$.

A technique of beating frequency selection as the best path method can decrease this effect.

# Chapter 5

# Conclusions and future work

## 5.1 Conclusions

DEMO and the future fusion reactors require a reliable diagnostic system to complement or substitute the magnetic diagnostics in the measurement of the plasma position. The principal candidate that fulfills the requirements to the operation with the necessary resolution is microwave reflectometry, known by its reduced access, robustness and reliability. Reflectometry uses the reflection of electromagnetic waves in the plasma to measure the electron density profiles by sweeping the frequency and measuring the round-trip time-delay. The plasma position is estimated with the knowledge of the separatrix density or identified directly in the density profile with physical considerations.

A plasma position reflectometry system consists in a set of reflectometers distributed along the machine's wall at different positions that provide the separatrix position measurements that are used to reconstruct the separatrix shape. A plasma position reflectometer has an ideal measurement performance if the position error is zero and the detected signal amplitude is the same as the emitted by the source. In a real system, these conditions are never fulfilled. The measurement error and the detected power amplitude depend on several factors such as the plasma shape, the reflectometer geometry, the data analysis methods and the definition of the line of view. Different phenomena that can occur during the plasma confinement and affect the measure performance of the reflectometers such as the plasma displacement, turbulence or MHD activity.

This dissertation was focused in the study and optimization of the DEMO plasma position reflectometry system (DEMO PPR). The final solution must be optimized for the operation scenario and stable under the possible deviations to its equilibrium that may occur during the long discharges. The optimization of such system requires the simulation of the measurement process for different poloidal views, emitting angles, antenna assemblies and plasma configurations. Taking into account the future changes in the geometry and plasma scenario, we studied the process of optimization of PPR systems with a general approach. The important variables of a general multiple reflectometers system were identified and the techniques and the procedures to the optimization were developed.

The simulation of such systems is in general a complex task that requires the definition of several different regions of interest and testing different antenna models and plasmas, which is a very demanding task from the computational point of view and of necessary time to build the simulation scripts. For this reason, we developed the structure of a high-level framework for multiple reflectometry simulations that is capable of automatizing all the simulation process of a multiple reflectometers system for the REFMUL* codes, a family of full-wave FDTD codes that has been used for reflectometry simulations. The user defines the configuration files of the system geometry and plasma, the probing bands and the dependence between the main variables of the problem. With this information, a framework of high-level functions create all the necessary models and scripts to run and manage all the simulations in the HPCs.

Using the developed framework, we studied the DEMO PPR system measurement performance using the official DEMO scenarios from EUROFUSION database. We started by defining 100 different gaps around the tokamak and testing two different configurations. In the first configuration, the antennas were aligned perpendicularly with the wall. This configuration has advantages from the point of view of the implementation of the antenna setup in the wall. However, the results shown that there are positions in the top of the machine and in the divertor region that have a very poor measurement performance and in some cases the signal is totally lost. In the second configuration, the antennas were aligned perpendicularly to the separatrix. In this case, since the direction of the probing beam is approximately parallel to the density gradient, a better measurement performance is expected. The results confirmed this principle, improving the position measurement in several gaps. At the divertor region, some of the gaps continued to have a poor measurement performance, being necessary to sweep the probing angle to find the optimized configuration. The data was analysed with the two different methods, the IQ and SFFT methods. The position error calculated by the SFFT method shown to be higher in the regions where the components due to the plasma-wall reflections have higher amplitude than the characteristic frequencies associated with the propagation in the plasma, leading to the wrong selection of the beating frequency. The representation of the Q signal spectrum (Q-spectrum) of each band as function of the gap shown to be a very useful way to identify the components associated to the plasma-wall reflections and its relative amplitude with the characteristic frequency, allowing the identification of the regions where the measurements have useful information.

One of the problems associated with the optimization is that is necessary to extract the phase derivative and calculate the amplitude of the detected signal for many different configurations. The analysis of the simulation results requires the manual adjustment of some data analysis parameters, as the cutoff frequencies of the applied filters or the signal delay. Using the principle that a slow varying phase derivative profile has a minimum standard deviation if it is ideally filtered, an automated version of the the I/Q detection was developed, designated by IQA method. With this technique, it was possible sweeping the probing angle at all the gaps and analyze the results in useful time. The maximum average detected amplitude shown to be a good selection criteria to define the optimized configuration. The results show that, with the exception of some positions in the divertor region, there is an optimized configuration with low position error ($< 1$ cm) and the power losses minimized.

With the optimized configuration, the stability of the system was tested for plasma displacements of 5 (reference case) and 15 cm (limiting case). The results show that, in contrast to the configuration with the antennas perpendicular to the separatrix, the system is stable for plasma displacements of 5 cm in different directions (0°,90°,180° and 270°). For displacements of 15 cm, some of the gaps in the top of the machine can have position errors above 1 cm, with mean power losses of 30-40 dB. The effect of having this order of error in some gaps and plasma configurations in the separatrix reconstruction must be studied to prove that the system is stable in the limiting case of a disruption. The effect of the profile initialization was also studied. The positions at the top of the machine, where the plasma-wall distance is higher, are more sensitive to the initialization function, being necessary to have better phase derivative descriptions in the first frequencies.

The effect of turbulence in the position error was studied in one gap of the equatorial region, in the high field side. Due to the lack of information on the turbulence properties of DEMO plasmas, the fluctuations were defined with an analytical model. A Kolmogorov-like spectrum was used to generate 400 random plasma samples for 16 different levels of amplitude (1-16%), compatible with the order of values observed in the experiments. Using the IQA algorithm, the principal statistical parameters were calculated. The results show that for higher levels of turbulence ($> 5\%$), the mean position error becomes negative due to the change of the effective cutoff position. This effect occurs for all the frequencies, leading to an accumulative error that can affect the position measurement in the order of accuracy requirements. The power losses were estimated to be in the order of 5-10 dB above the equilibrium case for the higher turbulence levels, which is an acceptable value from the experimental point of view. In order to prove the reliability of the entire system, it is necessary to apply the same procedure to the other positions of the system, which requires a huge amount of computation time on HPCs to be done. The power losses can be problematic for the gaps with high plasma-wall distance and for higher levels of turbulence.

In general, the results of the two dimensional simulations show that a PPR system is possible for the expected order of parameters in DEMO. Since there is no analytical solution for the propagation equations, designing a reflectometer in general is a numerical problem. It is possible, however, take some general conclusions regarding the scalability of the implementation of PPR systems based on the obtained results. Firstly, the regions with parallel poloidal flux lines are in general regions where the position error is low if the $n_e(\rho)$ profile follows the ideal reflectometry conditions. Different decaying lengths have a low impact in the measurement error. The regions with divergence in the flux lines and/or plasma curvature are sensitive to higher decaying lengths. By optimizing the probing angle, it is possible to minimize the power losses and the position error. In the divertor and in the top of a D-shaped plasma where the shape effects are stronger, it is possible to have a limiting case where no measurements are possible with a monostatic system because the signal can be lost in a large frequency range. By scaling the dimension of the plasma (keeping the same order of densities and the same geometry of the flux lines), it is expected that smaller plasmas are associated with higher measurement errors since the curvature and flux lines divergence needs to occur in a smaller region (assuming an antenna setup with similar geometric characteristics due to the use of the same frequencies), as well as a reduced minimum number of measurements. Secondly, the plasma-wall reflections are an important effect to have into consideration and need to be filtered from the signals if the amplitude of its components is the same order of the components due to the propagation in the plasma. This happens typically in the regions where the angle of incidence of the reflected signal is favorable to be reflected to the plasma and return to the antenna again instead of being partially lost to the environment. This condition is in general dependent on the probing frequency. Lastly, the plasma-wall distance affects the measurements in terms of the power losses and the profile of the plasma-wall reflections. Lower distances decrease the power losses, but the characteristic frequencies of the plasma-wall reflections become closer to the characteristic frequency and have higher amplitude, resulting in signals more difficult to filter. Increasing the plasma-wall distance decreases the plasma-wall reflections effect and increases the power losses and the error due to the initialization function.

The techniques and the algorithms developed in this work can be applied in other studies that involve the analysis of a high number of simulations, including studies with other reflectometry techniques. Next we list the highlights of this work:

### Contributions to reflectometry theory

- General description of the variables involved in a system of multiple reflectometers and in the data analysis for position reflectometry.
- Description of the optimization procedure of a PPR system.
- WMF error decomposition.
- Equation to identify the plasma-wall reflections in the Q-spectrum.

### Contributions to reflectometry simulation

- General description of the necessary variables to the simulations.
- Development of a high level framework to automate the simulation of MRS systems.
- Development of a code to convert generic CAD models to an input compatible with REFMUL3.
- Development of a code to create 3D plasma models from the poloidal flux maps with turbulence included.

### Contributions to data analysis techniques in reflectometry

- Data representation in multiple reflectometer systems.
- Q-spectrum analysis.
- Automation of the I/Q detection method.

### Contributions to the study and design of DEMO PPR system

- Study of the measurement performance of 100 different gaps for different DEMO baseline scenarios (2015/2017 EUROfusion models), antenna setups and plasmas.
- Optimization of all the defined gaps for the 2017 DEMO baseline scenario.
- Study of the effect of signal initialization, plasma displacement, and turbulence in the DEMO PPR system measurement performance.

## 5.2 Future research and work on DEMO PPR

This work represents an introductory study of the DEMO plasma position reflectometer. The final design of the system will depend on the evolution of the DEMO concept in the next years of fusion research. New scenarios and geometries of the machine will be considered, resulting in new configurations of reflectometers and in a different measurement performance of the system.

The techniques developed allow to study and optimize the future plasma position reflectometry systems just by the definition of the input configurations, which is an important technical advance in position reflectometry simulation and research. The process of simulation and data analysis were automated for a general multiple reflectometer system, having direct applications in other reflectometry projects or theoretical studies, where multiple simulations are involved. This includes the simulation of other reflectometry techniques, and it may be necessary to add new modules of data analysis.

An important aspect to have into consideration in the future is the description of the plasma. In this work we used simple models to describe the SOL density profile, the plasma displacement and the turbulence. The future studies on the DEMO PPR performance will require the use of more realistic plasma models, which can be obtained from the gyrokinetic simulations. The turbulence was studied in the HFS, being necessary a statistical study in the other positions of the machine. One important phenomena that was not simulated was the Doppler effect. With the moving turbulent structures, the probing beam may change the characteristic frequency, leading to local changes of the refractive index which may result in different group delays. It is important to verify that the resulting beating signals still being described by a well defined characteristic frequency peak so the automated IQ algorithm can be used in these studies.

The 3D simulations allow a realistic evaluation of the detected signal amplitude and measurement error. However, they cannot be used for the optimization process due to the huge amount of computation time required on HPCs. For now the optimization of PPR systems is only possible with the 2D simulations, where some physical effects such has the toroidal curvature of the plasma or the 3D effects of the geometry are neglected. The use of 2D simulations in the optimization assumes that the configuration with better performance corresponds to the same configuration in 3D. The 3D simulations can be used to test the optimized configuration after being selected from 2D results. The study of the stability of the system (e.g. turbulence effect or plasma displacement) is also a demanding task to be performed with the 3D simulations.

One fundamental aspect to have in consideration in the future simulations with REFMUL3 is the possibility of including realistic models of the metallic structure, where complex antenna assemblies can be implemented in the wall. It is important to study the utility of a reflectometer composed by multiple receiving antennas. This configuration could be useful if some plasma configuration deflects a large part of the reflected power out of the principal antenna's mouth or to have multiple measurements.

As a complement of this work, we developed a code to convert a generic CAD model to an input matrix compatible with the REFMUL3 functions and data structures, named CAD2RFM. The process of conversion is illustrated in figure 5.1 with a simple antenna model. The CAD model is designed with the required shape. The model is then converted to a tetrahedron mesh. The CAD2RFM reads the mesh, the ROI is defined and the model is converted to a FDTD grid.

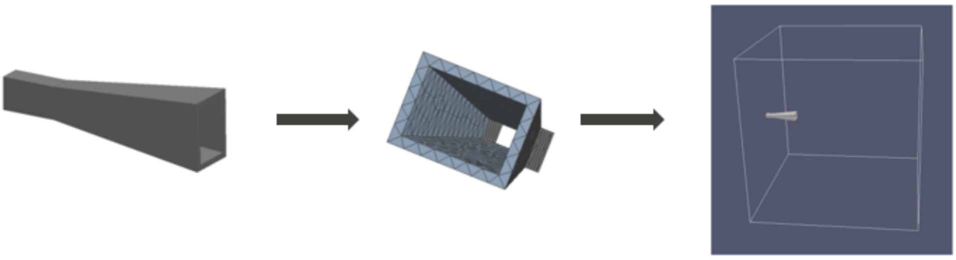

Figure 5.1: The process of conversion with CAD2RFM.

The algorithm of conversion works as follows:

1. The list of nodes and tetrahedrons are loaded from the respective input files.
2. The coordinates of the nodes are converted to the simulation frame in case of needed (see section 3.4.4). The ROI is defined.
3. The algorithm checks if each tetrahedron is inside the simulation box or not. If not, it is not converted. This allows to read meshes of the entire machine dimension. If the tetrahedron is inside the box, the algorithm finds the cube with lower volume that contains it (represented in figure 5.2). The indexes of the cube vertices in the structure matrix are calculated. Therefore, it is not required to check all the matrix elements.
4. Inside the cube, it is verified point by point if it is inside of the tetrahedron. If it is, the value of the respective element is changed.

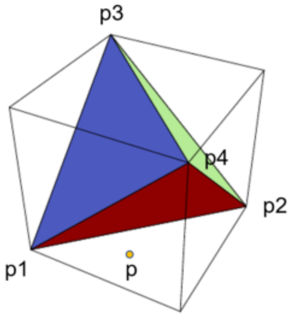

Figure 5.2: Tetrahedron representation and the respective cube with lower volume that contains it.

The operation of checking if a point $p$ of the grid that is inside the cube is inside tetrahedron or not uses the following algorithm:

- The tetrahedron is composed by 4 different nodes (p1,p2,p3,p4). This gives 4 different planes: (p1,p2,p3), (p1,p2,p4), (p1,p3,p4), (p2,p3,p4).
- The equation of each plane is obtained, in the form $ax + by + cz + d = 0$.
- Using the other point of the tetrahedron, the left term is calculated.

- The term is also calculated with the test point, $p = (px, py, pz)$. If the term calculated for both points has the same signal, that means that they are in the same side.
- If the side is the same for all the four planes, this means that the point $p$ is inside the tetrahedron.

An illustrative example of an implementation in the DEMO PPR is illustrated in figure 5.3. We defined the tokamak's wall based in the 2017 DEMO geometry, with a width of 1600 mm and a thickness of 100 mm. The entire model, composed by 16 antennas was designed in a CAD software. The mesh is calculated in the frame of coordinates associated with the machine. By selecting the ROI, in this case in the top of the machine (blue box), and defining a frame with the $x$ axis parallel to the ROI box, the code creates the input metallic structure for REFMUL3.

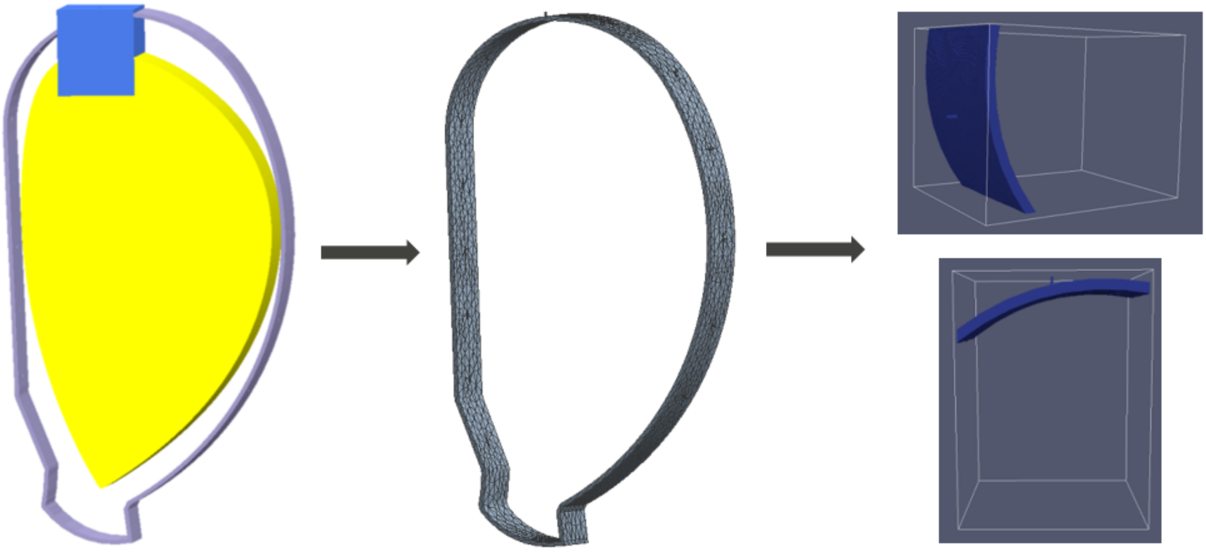

Figure 5.3: Implementation of the CAD2RFM with a 3D DEMO model based in the 2017 geometry from the EUROfusion official database.

For a system of reflectometers with a given configuration, only one mesh is necessary. The models of each reflectometer are given by the definition of different regions of interest. The popt library is implemented [232], allowing to execute all the operations thought the command line. The code is easily implemented in a high level framework with the structure proposed in chapter 3.

A code to produce 3D plasma models based in the poloidal flux maps that are produced by the equilibrium codes was also developed. Each point of the region of interest is converted if necessary to the Cartesian system associated to the machine. The coordinates of each point are converted to cylindrical coordinates and $\rho(R, Z)$ is calculated. Figure 5.4 shows an illustration of different converted plasma models using the DEMO 2017 scenario. The first model was converted in a box larger than the machine and is possible to observe the toroidal curvature. The second model represents a cut, where is possible to observe the different density layers of the model. The last figure is an example of a region of interest located at the HFS of the machine with turbulence. The code allows also to displace the plasma in a given direction. Similarly to the studies with the 2D models, these simple operations are essential to study the system at the initial stage of the project.

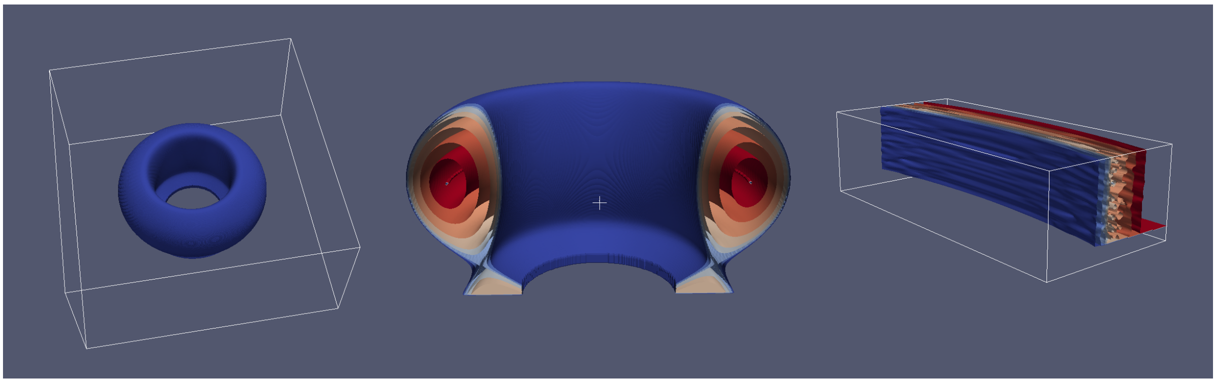

Figure 5.4: Example of converted plasma models using the DEMO 2017 scenario.

The first 3D simulations with metallic structures obtained from a CAD model were performed in the study of reflectometry in the Divertor Test Tokamak. The Divertor Test Tokamak (DTT) facility is a new project for a machine intended to study the exhaust solutions in tokamaks with a special look on DEMO [233, 234]. Figure 5.5 shows the CAD model of a DTT section, with the definition of the region of interest. A system of three antennas was designed and implemented in the wall. The tetrahedron mesh was created and the REFMUL3 input was created with CAD2RFM.

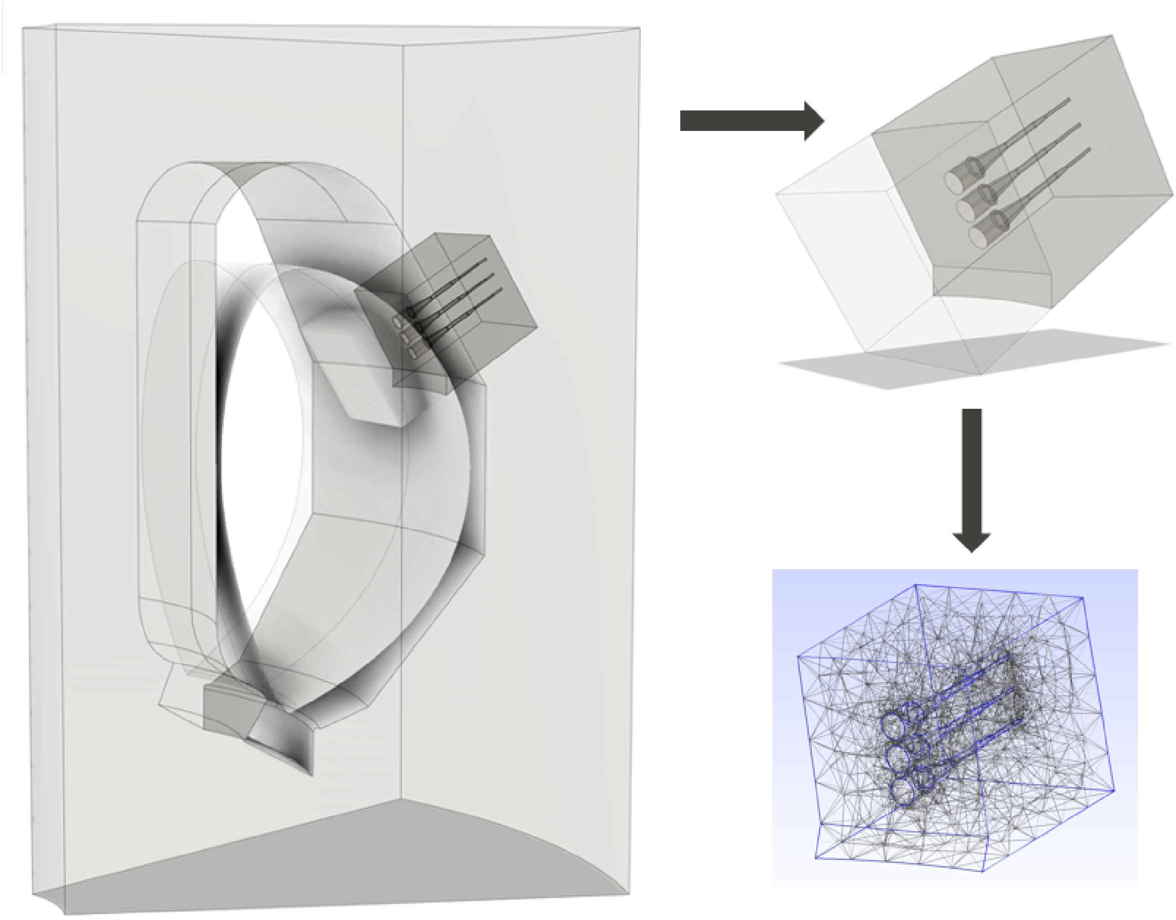

Figure 5.5: Implementatrion of a three antenna configuration model in the DTT vessel and production of the tetrahedron mesh.

Figure 5.6 shows the resulting snapshot of the electric field at 21.2 GHz.

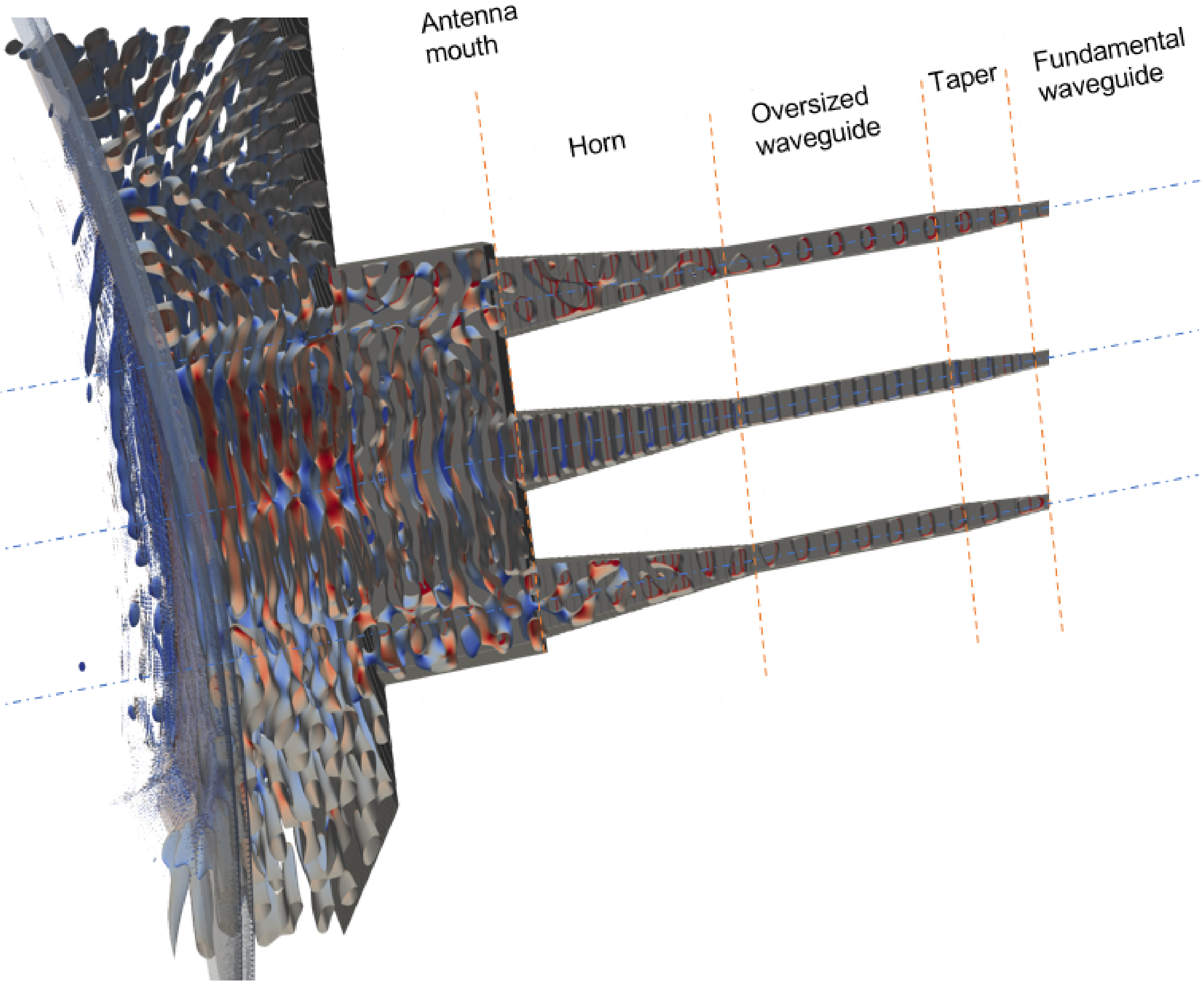

Figure 5.6: Snapshot of the 3D electric field at 21.2 GHz.

With the help of the tools and data analysis methods developed in this work, the future of microwave reflectometry research passes thought the systematic analysis of different reflectometer geometries and plasmas in order to study the measurement performance of the system and find the optimized configurations. With the increasing of the computational performance and with the optimization and parallelization of the simulation framework and of the data analysis codes, the cost and execution time of this task will be reduced, contributing to the development and research of reflectometry systems and consequently to the development and sustainability of thermonuclear fusion.

# Appendix A

# Procedure for the design of a PPR system

In this section we propose a procedure to design a PPR system. The procedure is composed by 7 stages, where the three teams work together in its specific tasks (see section 2.4.7). If there is solution to the problem, the convergence is achieved after some iterations and the final system is obtained. Following, each stage is described and commented:

1. **Definition of the problem** - The first stage consists in defining all the constraints of the problem with the responsible entities.

2. **Test of a reference model of a reflectometer** - The project teams define a reference model of the in-vessel components and geometry (antenna dimensions, waveguide, cavity, cooling system) of one reflectometer, known as reference reflectometer model. The electromagnetic performance of the waveguides, the measurement performance and the thermomechanical properties are evaluated in a position where the error is expected to be lower (e.g. equatorial zone) and it is verified if they are inside the limits imposed by the constraints. If there is a solution with a good performance, the third stage starts. If there is not, the teams identify the problem and find an alternative solution. If they do not find a solution, they communicate with the responsible identity to clarify the problem and find a solution.

3. **Optimization of the measurement performance** - Based on the reference model geometry, the EMP team makes a study of the measurement performance of the system for the equilibrium scenario. This includes testing different configurations with different positions and emission angles, using a FWP/FSP optimization approach, depending on the constraints. Then the best possibilities of each configuration are selected. If there are positions where there are no available options with an acceptable performance, it is verified if the main cause of the problem is the plasma or the reflectometer geometry. If the cause is the plasma it is verified if this measurement is essential to reconstruct the separatrix. If it is not, this position is removed from the possibilities. If it is, the problem constraints must be redefined.

4. **Separatrix reconstruction** - Based on the possibilities given by the study done in the previous phase, the entity responsible for the separatrix reconstruction selects a configuration which minimizes the number of reflectometers (minimizing the access to the machine), but that can reconstruct the separatrix within the accuracy requirements.

5. **Evaluation of the thermomechanical performance** - The TMP team analyses the thermomechanical performance of the selected configuration of reflectometers, with special attention to the changes in the geometry of the reflectometer that must be done to change the angle of emission. If there are problems, a new reflectometer geometry is proposed, keeping the angle of emission. The project returns to the second stage, where this new configuration is tested. If the configuration has an acceptable thermomechanical performance, the sixth stage starts.

6. **Evaluation of the system's stability for other plasma configurations** - The optimized system for the equilibrium scenario is evaluated by the EMP team for the different expected plasma configurations. The system must be stable under the influence of the expected perturbations (e.g. turbulence, MHD activity, plasma displacements, etc) and during the different transient states of the plasma (e.g. ramp up, ramp down). The extreme cases must be tested to ensure the system is secure and resilient. In the end, the position error and detected amplitude distribution function associated to the expected plasmas is known. If the measurement performance is under the limits, the project advances to the last stage. If not, there are two possibilities:

   - **Position correction** - The position error distribution is separated by plasma patterns. Each pattern is composed by a set of plasma variables (e.g. turbulence level, turbulence velocity, ramp up/down plasma, etc). In this case, the position error distribution is a function of the plasma pattern, denoted by $p$. If there is access to these variables thought other diagnostics or methods, then the relative position of a measurement can be corrected by

     $$r^{ik}(F) \to r^{ik}(F) - E^{ik}(F, p) \tag{A.1}$$

     where $E^{ik}(F, p)$ is the mean measurement error calculated by the simulations or adjusted experimentally. This correction works if the standard deviation of the position error associated with each pattern is below the measurement limitations, and if the failure rate of the system is acceptable after the correction. The effect of the line of view in the position error can also be studied, if needed.

   - **Consider multiple systems of reflectometers** - If this correction is not a solution in some positions, there is the possibility of considering another reflectometry system optimized to measure in the patterns where the system fails. For example, if for some reason the machine works under two different equilibrium, there is the possibility of having two independent systems optimized for each one. Or, if the measurement is needed at the ramp up/down phases of the discharge, an independent system can measure during these transient regimes. The choice to have two specific systems is not very attractive for a fusion reactor, since it requires more access to the machine. In the case of this option is selected, the new system must be studied from the second stage.

   If none of these possibilities work, the project must return to the first stage, where the constraints are discussed and the aim of the project is reconsidered.

7. **Finalization of the project** - This task is devoted to verify all the models used to build the final design of the PPR system from the mechanical implementation

to the data processing. When this stage is finished, the system is ready to be manufactured and implemented. Due to the importance of the system in the machine the system should be first tested in laboratory. The performance of the components of the reflectometers are tested in laboratory and compared with the simulations. The system is then implemented in the fusion machine. After the initial calibrations/tests the system is ready to measure during the machine operation.

# Appendix B

# Complement to reflectometry simulations

## B.1 3D FDTD equations

The equations 4.26-4.27 are equivalent to this system of six coupled scalar equations:

$$\mu\frac{\partial H_x}{\partial t} = \frac{\partial E_y}{\partial z} - \frac{\partial E_z}{\partial y} - M_{src_x} - \sigma^* H_x \tag{B.1}$$

$$\mu\frac{\partial H_y}{\partial t} = \frac{\partial E_z}{\partial x} - \frac{\partial E_x}{\partial z} - M_{src_y} - \sigma^* H_y \tag{B.2}$$

$$\mu\frac{\partial H_z}{\partial t} = \frac{\partial E_x}{\partial y} - \frac{\partial E_y}{\partial x} - M_{src_z} - \sigma^* H_z \tag{B.3}$$

$$\varepsilon\frac{\partial E_x}{\partial t} = \frac{\partial H_z}{\partial y} - \frac{\partial H_y}{\partial z} - J_{src_x} - \sigma E_x \tag{B.4}$$

$$\varepsilon\frac{\partial E_y}{\partial t} = \frac{\partial H_x}{\partial z} - \frac{\partial H_z}{\partial x} - J_{src_y} - \sigma E_y \tag{B.5}$$

$$\varepsilon\frac{\partial E_z}{\partial t} = \frac{\partial H_y}{\partial x} - \frac{\partial H_x}{\partial y} - J_{src_z} - \sigma E_z. \tag{B.6}$$

The 3D FDTD equations are:

$$\begin{aligned} E_x\Big|_{i,j+1/2,k+1/2}^{n+1/2} &= \left(\frac{1-\frac{\sigma_{i,j+1/2,k+1/2}\Delta t}{2\varepsilon_{i,j+1/2,k+1/2}}}{1+\frac{\sigma_{i,j+1/2,k+1/2}\Delta t}{2\varepsilon_{i,j+1/2,k+1/2}}}\right) E_x\Big|_{i,j+1/2,k+1/2}^{n-1/2} \\ &+ \left(\frac{\frac{\Delta t}{\varepsilon_{i,j+1/2,k+1/2}}}{1+\frac{\sigma_{i,j+1/2,k+1/2}\Delta t}{2\varepsilon_{i,j+1/2,k+1/2}}}\right) \begin{pmatrix} \frac{H_z|_{i,j+1,k+1/2}^{n} - H_z|_{i,j,k+1/2}^{n}}{\Delta y} \\ -\frac{H_y|_{i,j+1/2,k+1}^{n} - H_y|_{i,j+1/2,k}^{n}}{\Delta z} \\ -J_{src_x}\Big|_{i,j+1/2,k+1/2}^{n} \end{pmatrix} \end{aligned} \tag{B.7}$$

$$\begin{aligned} E_y\Big|_{i-1/2,j+1,k+1/2}^{n+1/2} &= \left(\frac{1-\frac{\sigma_{i-1/2,j+1,k+1/2}\Delta t}{2\varepsilon_{i-1/2,j+1,k+1/2}}}{1+\frac{\sigma_{i-1/2,j+1,k+1/2}\Delta t}{2\varepsilon_{i-1/2,j+1,k+1/2}}}\right) E_y\Big|_{i-1/2,j+1,k+1/2}^{n-1/2} \\ &+ \left(\frac{\frac{\Delta t}{\varepsilon_{i-1/2,j+1,k+1/2}}}{1+\frac{\sigma_{i-1/2,j+1,k+1/2}\Delta t}{2\varepsilon_{i-1/2,j+1,k+1/2}}}\right) \begin{pmatrix} \frac{H_x|_{i-1/2,j+1,k+1}^{n} - H_x|_{i-1/2,j+1,k}^{n}}{\Delta z} \\ -\frac{H_z|_{i,j+1,k+1/2}^{n} - H_y|_{i-1,j+1,k+1/2}^{n}}{\Delta x} \\ -J_{src_y}\Big|_{i-1/2,j+1,k+1/2}^{n} \end{pmatrix} \end{aligned} \tag{B.8}$$

$$
\begin{aligned}
E_z\big|^{n+1/2}_{i-1/2,j+1/2,k+1} = {} & \left( \frac{1 - \frac{\sigma_{i-1/2,j+1/2,k+1}\Delta t}{2\varepsilon_{i-1/2,j+1/2,k+1}}}{1 + \frac{\sigma_{i-1/2,j+1/2,k+1}\Delta t}{2\varepsilon_{i-1/2,j+1/2,k+1}}} \right) E_z\big|^{n-1/2}_{i-1/2,j+1/2,k+1} \\
& + \left( \frac{\frac{\Delta t}{\varepsilon_{i-1/2,j+1/2,k+1}}}{1 + \frac{\sigma_{i-1/2,j+1/2,k+1}\Delta t}{2\varepsilon_{i-1/2,j+1/2,k+1}}} \right) \left( \begin{array}{c} \frac{H_y|^n_{i,j+1/2,k+1} - H_y|^n_{i-1,j+1/2,k+1}}{\Delta x} \\ - \frac{H_x|^n_{i-1/2,j+1,k+1} - H_x|^n_{i-1/2,j,k+1}}{\Delta y} \\ - J_{src_z}\big|^n_{i-1/2,j+1/2,k+1} \end{array} \right)
\end{aligned}
\tag{B.9}
$$

$$
\begin{aligned}
H_x\big|^{n+1}_{i-1/2,j+1,k+1} = {} & \left( \frac{1 - \frac{\sigma^*_{i-1/2,j+1,k+1}\Delta t}{2\mu_{i-1/2,j+1,k+1}}}{1 + \frac{\sigma^*_{i-1/2,j+1,k+1}\Delta t}{2\mu_{i-1/2,j+1,k+1}}} \right) H_x\big|^{n}_{i-1/2,j+1,k+1} \\
& + \left( \frac{\frac{\Delta t}{\mu_{i-1/2,j+1,k+1}}}{1 + \frac{\sigma^*_{i-1/2,j+1,k+1}\Delta t}{2\mu_{i-1/2,j+1,k+1}}} \right) \left( \begin{array}{c} \frac{E_y|^{n+1/2}_{i-1/2,j+1,k+3/2} - E_y|^{n+1/2}_{i-1/2,j+1,k+1/2}}{\Delta z} \\ - \frac{E_z|^{n+1/2}_{i-1/2,j+3/2,k+1} - E_z|^{n+1/2}_{i-1/2,j+1/2,k+1}}{\Delta y} \\ - M_{src_x}\big|^{n+1/2}_{i-1/2,j+1,k+1} \end{array} \right)
\end{aligned}
\tag{B.10}
$$

$$
\begin{aligned}
H_y\big|^{n+1}_{i,j+1/2,k+1} = {} & \left( \frac{1 - \frac{\sigma^*_{i,j+1/2,k+1}\Delta t}{2\mu_{i,j+1/2,k+1}}}{1 + \frac{\sigma^*_{i,j+1/2,k+1}\Delta t}{2\mu_{i,j+1/2,k+1}}} \right) H_y\big|^{n}_{i,j+1/2,k+1} \\
& + \left( \frac{\frac{\Delta t}{\mu_{i,j+1/2,k+1}}}{1 + \frac{\sigma^*_{i,j+1/2,k+1}\Delta t}{2\mu_{i,j+1/2,k+1}}} \right) \left( \begin{array}{c} \frac{E_z|^{n+1/2}_{i+1/2,j+1/2,k+1} - E_z|^{n+1/2}_{i-1/2,j+1/2,k+1}}{\Delta x} \\ - \frac{E_x|^{n+1/2}_{i,j+1/2,k+3/2} - E_x|^{n+1/2}_{i,j+1/2,k+1/2}}{\Delta z} \\ - M_{src_y}\big|^{n+1/2}_{i,j+1/2,k+1} \end{array} \right)
\end{aligned}
\tag{B.11}
$$

$$
\begin{aligned}
H_z\big|^{n+1}_{i,j+1,k+1/2} = {} & \left( \frac{1 - \frac{\sigma^*_{i,j+1,k+1/2}\Delta t}{2\mu_{i,j+1,k+1/2}}}{1 + \frac{\sigma^*_{i,j+1,k+1/2}\Delta t}{2\mu_{i,j+1,k+1/2}}} \right) H_z\big|^{n}_{i,j+1,k+1/2} \\
& + \left( \frac{\frac{\Delta t}{\mu_{i,j+1,k+1/2}}}{1 + \frac{\sigma^*_{i,j+1,k+1/2}\Delta t}{2\mu_{i,j+1,k+1/2}}} \right) \left( \begin{array}{c} \frac{E_x|^{n+1/2}_{i,j+3/2,k+1/2} - E_x|^{n+1/2}_{i,j+1/2,k+1/2}}{\Delta y} \\ - \frac{E_y|^{n+1/2}_{i+1/2,j+1,k+1/2} - E_y|^{n+1/2}_{i-1/2,j+1,k+1/2}}{\Delta x} \\ - M_{src_z}\big|^{n+1/2}_{i,j+1,k+1/2} \end{array} \right).
\end{aligned}
\tag{B.12}
$$

## B.2 1D and 2D FDTD equations

The 1D and 2D FDTD equations are obtained by suppressing the indexes associated to the high order dimension.

### The 2D equations

The two dimensional version of equations B.1-B.6 assume an infinite structure in the z-direction with no change in the shape or position of its transverse cross section. With this assumption, the TM$_z$ mode equations become

$$
\varepsilon \frac{\partial E_z}{\partial t} = \frac{\partial H_y}{\partial x} - \frac{\partial H_x}{\partial y} - J_{src_z} - \sigma E_z \tag{B.13}
$$

$$\mu\frac{\partial H_x}{\partial t} = -\frac{\partial E_z}{\partial y} - M_{src_x} - \sigma^* H_x \tag{B.14}$$

$$\mu\frac{\partial H_y}{\partial t} = \frac{\partial E_z}{\partial x} - \frac{\partial E_x}{\partial z} - M_{src_y} - \sigma^* H_y. \tag{B.15}$$

The 2D TM$_z$ FDTD equations are

$$\begin{aligned}E_z\big|_{i-1/2,j+1/2}^{n+1/2} &= \left(\frac{1-\frac{\sigma_{i-1/2,j+1/2}\Delta t}{2\varepsilon_{i-1/2,j+1/2}}}{1+\frac{\sigma_{i-1/2,j+1/2}\Delta t}{2\varepsilon_{i-1/2,j+1/2}}}\right) E_z\big|_{i-1/2,j+1/2}^{n-1/2} \\ &+ \left(\frac{\frac{\Delta t}{\varepsilon_{i-1/2,j+1/2}}}{1+\frac{\sigma_{i-1/2,j+1/2}\Delta t}{2\varepsilon_{i-1/2,j+1/2}}}\right)\left(\begin{array}{c}\frac{H_y|_{i,j+1/2}^{n} - H_y|_{i-1,j+1/2}^{n}}{\Delta x} \\ -\frac{H_x|_{i-1/2,j+1}^{n} - H_x|_{i-1/2,j}^{n}}{\Delta y} \\ -J_{src_z}\big|_{i-1/2,j+1/2}^{n}\end{array}\right)\end{aligned} \tag{B.16}$$

$$\begin{aligned}H_x\big|_{i-1/2,j+1}^{n+1} &= \left(\frac{1-\frac{\sigma^*_{i-1/2,j+1}\Delta t}{2\mu_{i-1/2,j+1}}}{1+\frac{\sigma^*_{i-1/2,j+1}\Delta t}{2\mu_{i-1/2,j+1}}}\right) H_x\big|_{i-1/2,j+1}^{n} \\ &+ \left(\frac{\frac{\Delta t}{\mu_{i-1/2,j+1}}}{1+\frac{\sigma^*_{i-1/2,j+1}\Delta t}{2\mu_{i-1/2,j+1}}}\right)\left(\begin{array}{c}-\frac{E_z|_{i-1/2,j+3/2}^{n+1/2} - E_z|_{i-1/2,j+1/2}^{n+1/2}}{\Delta y} \\ -M_{src_x}\big|_{i-1/2,j+1}^{n+1/2}\end{array}\right)\end{aligned} \tag{B.17}$$

$$\begin{aligned}H_y\big|_{i,j+1/2}^{n+1} &= \left(\frac{1-\frac{\sigma^*_{i,j+1/2}\Delta t}{2\mu_{i,j+1/2}}}{1+\frac{\sigma^*_{i,j+1/2}\Delta t}{2\mu_{i,j+1/2}}}\right) H_y\big|_{i,j+1/2}^{n} \\ &+ \left(\frac{\frac{\Delta t}{\mu_{i,j+1/2}}}{1+\frac{\sigma^*_{i,j+1/2}\Delta t}{2\mu_{i,j+1/2}}}\right)\left(\begin{array}{c}\frac{E_z|_{i+1/2,j+1/2}^{n+1/2} - E_z|_{i-1/2,j+1/2}^{n+1/2}}{\Delta x} \\ -M_{src_y}\big|_{i,j+1/2}^{n+1/2}\end{array}\right).\end{aligned} \tag{B.18}$$

The TE$_z$ mode equations are

$$\mu\frac{\partial H_z}{\partial t} = \frac{\partial E_x}{\partial y} - \frac{\partial E_y}{\partial x} - M_{src_z} - \sigma^* H_z \tag{B.19}$$

$$\varepsilon\frac{\partial E_x}{\partial t} = \frac{\partial H_z}{\partial y} - \frac{\partial H_y}{\partial z} - J_{src_x} - \sigma E_x \tag{B.20}$$

$$\varepsilon\frac{\partial E_y}{\partial t} = \frac{\partial H_x}{\partial z} - \frac{\partial H_z}{\partial x} - J_{src_y} - \sigma E_y. \tag{B.21}$$

The 2D TE$_z$ FDTD equations are

$$\begin{aligned}H_z\big|_{i,j+1}^{n+1} &= \left(\frac{1-\frac{\sigma^*_{i,j+1}\Delta t}{2\mu_{i,j+1}}}{1+\frac{\sigma^*_{i,j+1}\Delta t}{2\mu_{i,j+1}}}\right) H_z\big|_{i,j+1}^{n} \\ &+ \left(\frac{\frac{\Delta t}{\mu_{i,j+1}}}{1+\frac{\sigma^*_{i,j+1}\Delta t}{2\mu_{i,j+1}}}\right)\left(\begin{array}{c}\frac{E_x|_{i,j+3/2}^{n+1/2} - E_x|_{i,j+1/2}^{n+1/2}}{\Delta y} \\ -\frac{E_y|_{i+1/2,j+1}^{n+1/2} - E_y|_{i-1/2,j+1}^{n+1/2}}{\Delta x} \\ -M_{src_z}\big|_{i,j+1}^{n+1/2}\end{array}\right)\end{aligned} \tag{B.22}$$

$$E_x\big|_{i,j+1/2}^{n+1/2} = \left(\frac{1-\frac{\sigma_{i,j+1/2}\Delta t}{2\varepsilon_{i,j+1/2}}}{1+\frac{\sigma_{i,j+1/2}\Delta t}{2\varepsilon_{i,j+1/2}}}\right) E_x\big|_{i,j+1/2}^{n-1/2} + \left(\frac{\frac{\Delta t}{\varepsilon_{i,j+1/2}}}{1+\frac{\sigma_{i,j+1/2}\Delta t}{2\varepsilon_{i,j+1/2}}}\right) \begin{pmatrix} \frac{H_z|_{i,j+1}^{n} - H_z|_{i,j}^{n}}{\Delta y} \\ -J_{src_x}\big|_{i,j+1/2}^{n} \end{pmatrix} \tag{B.23}$$

$$E_y\big|_{i-1/2,j+1}^{n+1/2} = \left(\frac{1-\frac{\sigma_{i-1/2,j+1}\Delta t}{2\varepsilon_{i-1/2,j+1}}}{1+\frac{\sigma_{i-1/2,j+1}\Delta t}{2\varepsilon_{i-1/2,j+1}}}\right) E_y\big|_{i-1/2,j+1}^{n-1/2} + \left(\frac{\frac{\Delta t}{\varepsilon_{i-1/2,j+1}}}{1+\frac{\sigma_{i-1/2,j+1}\Delta t}{2\varepsilon_{i-1/2,j+1}}}\right) \begin{pmatrix} -\frac{H_z|_{i,j+1}^{n} - H_y|_{i-1,j+1}^{n}}{\Delta x} \\ -J_{src_y}\big|_{i-1/2,j+1}^{n} \end{pmatrix}. \tag{B.24}$$

In the two dimensional case, $\xi_{upper} = S\sqrt{2}$.

### The 1D equations

The one dimensional version of equations B.1-B.6 assume an infinite structure in the $z$ and $y$ directions. The TM$_z$ mode equations become

$$\varepsilon\frac{\partial E_z}{\partial t} = \frac{\partial H_y}{\partial x} - J_{src_z} - \sigma E_z \tag{B.25}$$

$$\mu\frac{\partial H_x}{\partial t} = -M_{src_x} - \sigma * H_x \tag{B.26}$$

$$\mu\frac{\partial H_y}{\partial t} = \frac{\partial E_z}{\partial x} - \frac{\partial E_x}{\partial z} - M_{src_y} - \sigma * H_y. \tag{B.27}$$

and the 1D TM$_z$ FDTD equations are

$$E_z\big|_{i-1/2}^{n+1/2} = \left(\frac{1-\frac{\sigma_{i-1/2}\Delta t}{2\varepsilon_{i-1/2}}}{1+\frac{\sigma_{i-1/2}\Delta t}{2\varepsilon_{i-1/2}}}\right) E_z\big|_{i-1/2}^{n-1/2} + \left(\frac{\frac{\Delta t}{\varepsilon_{i-1/2}}}{1+\frac{\sigma_{i-1/2}\Delta t}{2\varepsilon_{i-1/2}}}\right) \begin{pmatrix} \frac{H_y|_{i}^{n} - H_y|_{i-1}^{n}}{\Delta x} \\ -J_{src_z}\big|_{i-1/2}^{n} \end{pmatrix}$$

$$H_x\big|_{i-1/2}^{n+1} = \left(\frac{1-\frac{\sigma^*_{i-1/2}\Delta t}{2\mu_{i-1/2}}}{1+\frac{\sigma^*_{i-1/2}\Delta t}{2\mu_{i-1/2}}}\right) H_x\big|_{i-1/2}^{n} + \left(\frac{\frac{\Delta t}{\mu_{i-1/2}}}{1+\frac{\sigma^*_{i-1/2}\Delta t}{2\mu_{i-1/2}}}\right) \left( -M_{src_x}\big|_{i-1/2}^{n+1/2} \right) \tag{B.28}$$

$$H_y\big|_{i}^{n+1} = \left(\frac{1-\frac{\sigma^*_{i}\Delta t}{2\mu_{i}}}{1+\frac{\sigma^*_{i}\Delta t}{2\mu_{i}}}\right) H_y\big|_{i}^{n} + \left(\frac{\frac{\Delta t}{\mu_{i}}}{1+\frac{\sigma^*_{i}\Delta t}{2\mu_{i}}}\right) \begin{pmatrix} \frac{E_z|_{i+1/2}^{n+1/2} - E_z|_{i-1/2}^{n+1/2}}{\Delta x} \\ -M_{src_y}\big|_{i}^{n+1/2} \end{pmatrix}. \tag{B.29}$$

The TE$_z$ mode equations are

$$\mu\frac{\partial H_z}{\partial t} = -\frac{\partial E_y}{\partial x} - M_{src_z} - \sigma * H_z \tag{B.30}$$

$$\varepsilon\frac{\partial E_x}{\partial t} = \frac{\partial H_z}{\partial y} - \frac{\partial H_y}{\partial z} - J_{src_x} - \sigma E_x \tag{B.31}$$

$$\varepsilon\frac{\partial E_y}{\partial t} = \frac{\partial H_x}{\partial z} - \frac{\partial H_z}{\partial x} - J_{src_y} - \sigma E_y \tag{B.32}$$

and the 2D TE$_z$ FDTD equations,

$$H_z\big|_{i}^{n+1} = \left(\frac{1-\frac{\sigma^*_{i}\Delta t}{2\mu_{i}}}{1+\frac{\sigma^*_{i}\Delta t}{2\mu_{i}}}\right) H_z\big|_{i}^{n} + \left(\frac{\frac{\Delta t}{\mu_{i}}}{1+\frac{\sigma^*_{i}\Delta t}{2\mu_{i}}}\right) \begin{pmatrix} -\frac{E_y|_{i+1/2}^{n+1/2} - E_y|_{i-1/2}^{n+1/2}}{\Delta x} \\ -M_{src_z}\big|_{i}^{n+1/2} \end{pmatrix} \tag{B.33}$$

$$E_x\big|_i^{n+1/2} = \left( \frac{1 - \frac{\sigma_i \Delta t}{2\varepsilon_i}}{1 + \frac{\sigma_i \Delta t}{2\varepsilon_i}} \right) E_x\big|_i^{n-1/2} + \left( \frac{\frac{\Delta t}{\varepsilon_i}}{1 + \frac{\sigma_i \Delta t}{2\varepsilon_i}} \right) \left( -J_{src_x}\big|_i^n \right) \tag{B.34}$$

$$E_y\big|_{i-1/2}^{n+1/2} = \left( \frac{1 - \frac{\sigma_{i-1/2} \Delta t}{2\varepsilon_{i-1/2}}}{1 + \frac{\sigma_{i-1/2} \Delta t}{2\varepsilon_{i-1/2}}} \right) E_y\big|_{i-1/2}^{n-1/2} + \left( \frac{\frac{\Delta t}{\varepsilon_{i-1/2}}}{1 + \frac{\sigma_{i-1/2} \Delta t}{2\varepsilon_{i-1/2}}} \right) \left( \begin{matrix} -\frac{H_z|_i^n - H_y|_{i-1}^n}{\Delta x} \\ -J_{src_y}\big|_{i-1/2}^n \end{matrix} \right). \tag{B.35}$$

## B.3 The Xu-Yuan kernel (XYK)

Following [213], the authors consider a time-discretization in the form:

$$\varepsilon_0 \frac{\mathbf{E}^{n+1} - \mathbf{E}^n}{\Delta t} = \nabla \times \mathbf{H}^{n+1/2} - \mathbf{J}^{n+1/2} \tag{B.36}$$

$$\mu_0 \frac{\mathbf{H}^{n+1/2} - \mathbf{H}^{n-1/2}}{\Delta t} = -\nabla \times \mathbf{E}^n \tag{B.37}$$

$$\frac{\mathbf{J}^{n+1/2} - \mathbf{J}^{n-1/2}}{\Delta t} = \varepsilon_0 \omega_p^2 \mathbf{E}^n + \omega_c \mathbf{b} \times \frac{\mathbf{J}^{n+1/2} - \mathbf{J}^{n-1/2}}{2} \tag{B.38}$$

The spatial indexes are assumed to be represented with the same labels of equations B.7-B.12. Defining the $C_0$ and $C_1$ constants as

$$C_0 = 1 + \frac{\omega_x^2 \Delta t^2 e^{-\nu \Delta t}}{4} \tag{B.39}$$

$$C_1 = 1 + \frac{\omega_y^2 \Delta t^2 e^{-\nu \Delta t}}{4} - \left( \frac{\omega_x^2 \omega_y^2 \Delta t^4 e^{-2\nu \Delta t}}{16 C_0} - \frac{\Delta t^2 \omega_z^2 e^{-\nu \Delta t}}{4 C_0} \right), \tag{B.40}$$

the $J_x$ component is given by

$$\begin{aligned} J_x^{n+1/2} = {} & \frac{e^{-nu\Delta t}}{C_1} \left[ 1 - \frac{\omega_y^2 \Delta t^2}{4} + \left( \frac{\omega_y^2 \Delta t^2}{4} - \frac{\omega_x^2 \omega_y^2 \Delta t^4 e^{-\nu \Delta t}}{16 C_0} - \frac{\Delta t^2 \omega_z^2}{4 C_0} \right) \right] \times J_x^{n-1/2} \\ & + \frac{\varepsilon_0 \omega_p^2 \Delta t e^{-nu\Delta t/2}}{C_1} \times \left[ E_x^n + \left( \frac{\omega_x \omega_y \Delta t^2 e^{-\nu \Delta t}}{4 C_0} - \frac{\Delta t \omega_z e^{-\nu \Delta t/2}}{2 C_0} \right) E_y^n \right] \\ & + \frac{\Delta t^2 \varepsilon_0 \omega_p^2 e^{-\nu \Delta t}}{2 C_1} \times \left[ \omega_y - \left( \frac{\omega_x^2 \omega_y \Delta t^2 e^{-\nu \Delta t}}{4 C_0} - \frac{\Delta t \omega_z \omega_x e^{-\nu \Delta t/2}}{2 C_0} \right) E_z^n \right] \\ & + \left( \frac{\omega_x \omega_y \Delta t^2 e^{-\nu \Delta t}}{4 C_1} - \frac{\omega_z \Delta t e^{-\nu \Delta t/2}}{2 C_1} \right) \times \left[ 1 + \left( 1 + \left( \frac{1}{C_0} - \frac{\omega_x^2 \Delta t^2}{4 C_0} \right) e^{-\nu \Delta t} \right) \right] J_y^{n-1/2} \\ & + \frac{e^{-\nu \Delta t/2} (1 + e^{-\nu \Delta t})}{2 C_1} \times \left[ \omega_y \Delta t - \frac{\omega_x \Delta t e^{-\nu \Delta t/2}}{C_0} \left( \frac{\omega_x \omega_y \Delta t^2 e^{-\nu \Delta t/2}}{4} - \frac{\Delta t \omega_z}{2} \right) \right] J_z^{n-1/2} \end{aligned} \tag{B.41}$$

The calculation of $J_x$ uses $E_y$, $E_z$, $J_y$ and $J_z$ of the previous iterations. The $J_x$ and $J_y$ components are written in terms of $J_x$ by:

$$\begin{aligned} J_y^{n+1/2} &= \frac{1}{C_0}\left(1-\frac{\omega_x^2\Delta t^2}{4}\right)e^{-\nu\Delta t}J_y^{n-1/2}+\frac{\varepsilon_0\omega_p^2\Delta t}{C_0}e^{-\nu\Delta t/2}E_y^n \\ &\quad -\frac{\omega_x\Delta t}{2C_0}\varepsilon_0\omega_p^2\Delta t e^{-\nu\Delta t}E_z^n-\frac{\Delta t\omega_x}{2C_0}e^{-\nu\Delta t/2}(1+e^{-\nu\Delta t})J_z^{n-1/2} \\ &\quad +\left(\frac{\Delta t\omega_z e^{-\nu\Delta t/2}}{2C_0}+\frac{\omega_x\omega_y\Delta t^2 e^{-\nu\Delta t}}{4C_0}\right)\times\left(J_x^{n-1/2}+J_x^{n+1/2}\right). \end{aligned} \tag{B.42}$$

$$\begin{aligned} J_z^{n+1/2} &= e^{-\nu\Delta t}J_z^{n-1/2} \\ &\quad +\Delta t e^{-\nu\Delta t/2}\times\left[\varepsilon_0\omega_p^2E_z^n+\frac{\omega_x}{2}\left(J_y^{n-1/1/2}+J_y^{n+1/2}\right)-\frac{\omega_y}{2}\left(J_x^{n-1/2}+J_x^{n-1/2}\right)\right]. \end{aligned} \tag{B.43}$$

The discretization of equation 3.20 uses the value of these components in positions that are not compatible with the positions of the FDTD discretization (equations B.7-B.12). An approximation is needed to obtain the final system of equations. In [213] these terms are calculated by

$$E_y|_{i+1/2,j,k}^n = \frac{1}{4}\left[E_y|_{i,j-1/2,k}^n + E_y|_{i,j+1/2,k}^n + E_y|_{i+1,j-1/2,k}^n + E_y|_{i+1,j+1/2,k}^n\right] \tag{B.44}$$

$$J_y|_{i+1/2,j,k}^{n-1/2} = \frac{1}{4}\left[J_y|_{i,j-1/2,k}^{n-1/2} + J_y|_{i,j+1/2,k}^{n-1/2} + J_y|_{i+1,j-1/2,k}^{n-1/2} + J_y|_{i+1,j+1/2,k}^{n-1/2}\right] \tag{B.45}$$

$$E_z|_{i+1/2,j,k}^n = \frac{1}{4}\left[E_z|_{i,j/2,k-1/2}^n + E_z|_{i,j,k+1/2}^n + E_z|_{i+1,j,k-1/2}^n + E_z|_{i+1,j,k+1/2}^n\right] \tag{B.46}$$

$$J_z|_{i+1/2,j,k}^{n-1/2} = \frac{1}{4}\left[J_z|_{i,j,k-1/2}^{n-1/2} + J_z|_{i,j,k+1/2}^{n-1/2} + J_z|_{i+1,j,k-1/2}^{n-1/2} + J_z|_{i+1,j,k+1/2}^{n-1/2}\right] \tag{B.47}$$

This algorithm is referenced in the literature as the Xu-Yuan kernel (XYK).

## B.4 Perfect matched layer

The PML is an artificial absorbing layer that absorbs all the incident power if it comes from vacuum [219]. In this layer, the electromagnetic field is splitted in different components. When the PML medium properties are set to zero, the FDTD equations are obtained. The PML technique is illustrated in figure B.1 for the 2D case:

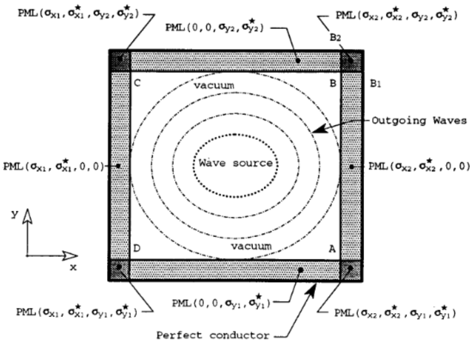

Figure B.1: The PML technique [219].

Each side of the PML has a combination of $\sigma_x$, $\sigma_x^*$, $\sigma_y$, $\sigma_y^*$. Setting $\sigma_y = \sigma_y^* = 0$ will absorb the wave propagating along $x$ but will reflect a wave traveling along $y$. Using $\sigma_x = \sigma_x^* = 0$ the opposite situation occurs. At the corner, both directions are absorbed. The equations that describe the propagation for the 2D TM mode are

$$\mu_0\varepsilon_0\frac{\partial E_{zx}}{\partial t} + \mu_0\sigma_x E_{zx} = \frac{\partial B_y}{\partial x} \tag{B.48}$$

$$\mu_0\varepsilon_0\frac{\partial E_{zy}}{\partial t} + \mu_0\sigma_y E_{zy} = \frac{\partial B_x}{\partial y} \tag{B.49}$$

$$\mu_0\varepsilon_0\frac{\partial B_x}{\partial t} + \sigma_y^* B_x = -\mu_0\frac{\partial (E_{zx}+E_{zy})}{\partial y} \tag{B.50}$$

$$\mu_0\varepsilon_0\frac{\partial B_y}{\partial t} + \sigma_x^* B_y = \mu_0\frac{\partial (E_{zx}+E_{zy})}{\partial x}. \tag{B.51}$$

For a vacuum-PML transition, the absorption without reflection occurs if

$$\frac{\sigma_{xy}}{\varepsilon_0} = \frac{\sigma_{xy}^*}{\mu_0}. \tag{B.52}$$

The amplitude of the wave $\psi$ that enters in the PML is given by

$$\psi(\rho) = \psi(0)\exp\left[-\left(\frac{\sigma_{x,y}\cos\theta}{\varepsilon_0 c}\right)\rho\right], \tag{B.53}$$

where $\theta$ is the angle of incidence and $\rho$ is the distance from the interface. The wave enters in the PML and is attenuated until reaches the border, where is totally reflected by the perfect conductor surrounding the grid. Then, it is attenuated again until reaches the vacuum-PML interface. For a layer of thickness $\delta$, the reflection factor due to this path is

$$R(\theta) = \exp\left[-2\left(\frac{\sigma_{x,y}\cos\theta}{\varepsilon_0 c}\right).\delta\right] \tag{B.54}$$

In the implementation of the PML in a FDTD code, a smooth $\sigma_{x,y}$ is used to ensure numerical stability. If the conductivity that changes along the propagation, the reflection factor becomes

$$R(\theta) = \exp\left[-2\left(\frac{\cos\theta}{\varepsilon_0 c}\right)\int_0^\delta \sigma_{x,y} d\rho\delta\right]. \tag{B.55}$$

Using a conductivity with the form $\sigma(\rho) = \sigma_m\left(\frac{\rho}{\delta}\right)^n$, the equation B.55 becomes

$$R(\theta) = \exp\left[-\frac{2}{n+1}\frac{\sigma_m\delta}{\varepsilon_0 c}\cos\theta\right]. \tag{B.56}$$

The reader can find the detailed calculations of the 2D and 3D PML in [219] and [235]. The 1D PML is easily implemented considering a layer at each side of the grid. In REFMUL* codes the PML is defined by the $\sigma_m$ (typically $\sim 10^{-6}$ S/m), by the $n$ index (2 by default) and by a fixed layer width (e.g. 26 points). The $\sigma(\rho)$ is then defined according to these parameters. Between the plasma and the PML there is a matching layer to match the propagation in the plasma to vacuum, so it can interact to the PML minimizing the reflection.

The plasma frame is given by

$$f_{PML}(i,j,k) = \frac{1}{N_{norm}} \times \{1 - \tanh[\alpha(i - N_x + w_x)] - 2D\}$$
$$\times \left\{\frac{1}{2}\tanh[\beta(j - w_y)] + \frac{1}{2}\tanh[\beta(N_y - w_y - j)] - D\right\}$$
$$\times \left\{\frac{1}{2}\tanh[\beta(k - w_z)] + \frac{1}{2}\tanh[\beta(N_z - w_z - k)] - D\right\}. \tag{B.57}$$

The parameters $w_{x,y,z}$ describe the damping width and the parameters $\alpha$, $\beta$ shape the decay, $N_{x,y,z}$ are the number of points that constitute the grid, $D$ is adjusted to ensure the frame is exactly zero at the border and $N_{norm}$ scales the frame matrix to unit outside the damping layer [93]. For two dimensions, only the first two terms are considered. At the left side of the grid it is assumed that there is no plasma.

## B.5 Unidirectional transparent source (UTS)

When the electric field is excited in the fundamental waveguide, two waves are formed, one propagating in the positive direction of the waveguide and other in the negative. If the detection of the reflected signal occurs in the same waveguide as it happens in the simulation of a mono-static reflectometer, the detected signal contains the signal that is being emitted at the source and is not possible to extract the phase shift due to the propagation in the plasma. The UTS source emits in only one direction (in this case, to the plasma) and allows the detection of the reflected signal that is propagating in the oposite direction. The principle behind the UTS algorithm is that if a mirror is placed before the source position, the electromagnetic field is emitted in only one direction. With the knowledge of impulse response this system, the electromagnetic field of the initial setup without mirror can be corrected at each iteration as the mirror was there, emitting in only one direction. Since the mirror effect is included in the correction term and not in the metallic structure, the reflected signals can propagate in the opposite direction of the emission, being possible to detect the reflected signal from the plasma.

Figure B.2 shows the signal excitation region, with the source located at $i_s$ and the mirror at $i_m = i_s - 1$.

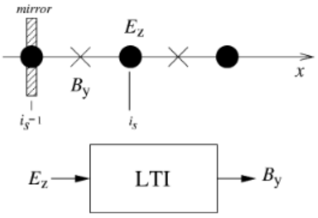

Figure B.2: Representation of a 1D mirrored waveguide as a LTI system [207].

When the electric field is excited at the instant $n$, the magnetic field evaluated at $n + 1/2$ is given by

$$B_y^{n+1/2}(i_s - 1/2) = \frac{\Delta t}{\Delta x} E_z^n(i_s). \tag{B.58}$$

The propagation occurs in vacuum. This equation form a linear time-invariant (LTI) system, where $E_z^n(i_s)$ is the output and $B_y^{n+1/2}(i_s - 1/2)$ the input [207]. Any input function $x[n] = f[n] = f(n\Delta t)$ is written in the form

$$x[n] = \sum_{k=-\infty}^{+\infty} f(k\Delta t)\delta[n-k], \tag{B.59}$$

where $\delta$ is the Dirac function. Since the system is an LTI, the output $y[n]$ can be calculated by

$$y[n] = \sum_{k=-\infty}^{+\infty} f(k\Delta t)h[n-k], \tag{B.60}$$

where $h$ is the impulsive response of the system. Due to the conservation of energy, it is expected that the amplitude of the impulsive system decreases to zero, eventually below the noise level after some iterations. The response of the system can be approximated by a finite impulsive response with $N$ points. The output is simplified to

$$y[n] \simeq \sum_{k=0}^{N-1} f(k\Delta t)h[n-k], \tag{B.61}$$

The choice of the number of samples influences the accuracy of the system response.

Exciting the system with an unitary impulse in the form $E_z^n(i_s) = \delta[n]$, the impulsive response $B_y^{n+1/2}(i_s)$ is obtained and saved in memory. The $B_y$ field can then be calculated by equation B.60, where $f$ is the electric field at the source. With the knowledge of $B_y$ field, the correction of the electric field at each instant $n + 1/2$ at the mirror position $(i_s - 1)$ is done by:

$$E_z^{n+1/2}(i_s - 1) = \frac{\Delta t}{\varepsilon_0 \mu_0 \Delta x} B_y^n(i_s - 1/2). \tag{B.62}$$

If some variables are changed ($\Delta x$, $\Delta t$, $i_s$), the impulse response must be calibrated again. The reader can find the expressions for the 2D UTS and the tests of the spectral characteristics of the signal emitted in [207].

## B.6 Discrete Abel inversion with the trapezoidal rule

The phase derivative is assumed in the form $a_k - b_k f$, with

$$a_k = \frac{f_k}{f_k - f_{k-1}} \frac{\partial \varphi}{\partial f}(f_{k-1}) - \frac{f_k}{f_k - f_{k-1}} \frac{\partial \varphi}{\partial f}(f_k) \tag{B.63}$$

$$b_k = \frac{1}{f_k - f_{k-1}} \left[ \frac{\partial \varphi}{\partial f}(f_{k-}) - \frac{\partial \varphi}{\partial f}(f_{k-1}) \right]. \tag{B.64}$$

In this case, equation 3.41 is given by:

$$\begin{aligned} r(F) &\simeq \frac{c}{2\pi^2} \sum_{k=2}^{N} \left( a_k \int_{f_{k-1}}^{f_k} \frac{1}{F^2 - f^2} df + b_k \int_{f_{k-1}}^{f_k} \frac{f}{F^2 - f^2} df \right) \\ &\simeq \frac{c}{2\pi^2} \sum_{k=2}^{N} \left( a_k \left[ \arcsin\left(\frac{f_k}{F}\right) - \arcsin\left(\frac{f_{k-1}}{F}\right) \right] + b_k \left[ \sqrt{F^2 - f_k^2} - \sqrt{F^2 - f_{k-1}^2} \right] \right). \end{aligned} \tag{B.65}$$

## B.7 Q signal spectrum comparison

The comparison between the Q signal spectrum of the two setups (antenna and antenna with blanket) for the $Q_1$ band is shown in figure B.3.

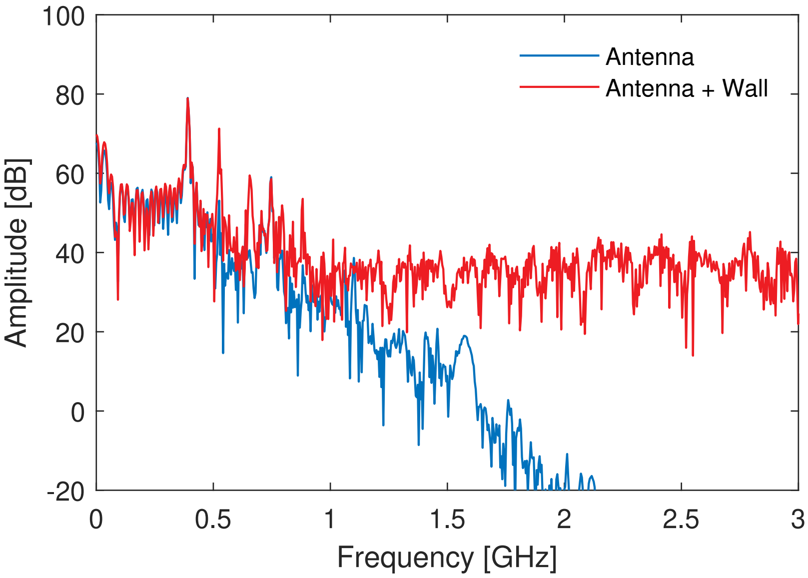

Figure B.3: Comparison of the Q signal spectrum between the two setups ($Q_1$ band).

## B.8 SD script description

### Phase 1 - declaration of SD variables

The first phase consists in the declaration of the SD variables. These variables include:

1. Definition of the project name.
2. Definition of the output directory.
3. Definition of the input data directory.
4. Definition of the number of simulations per script file (useful to run scripts in HPC with limit of job file size).

### Phase 2 - definition of the lists of variables of the problem

The lists of variables contain all the possible combinations of the main variables that are necessary to the different types of simulation and for the data analysis. These lists are saved in the SD, where they can be easily accessed any time to use or to consult.

The list of simulations, represented by $L_{SIM}$, includes all the combinations of the D-R-S-P-B variables. Each combination corresponds to one simulation. To each combination is attributed a number from 1 to $N_{SIM}$, the simulation number. The total number of simulations is given by:

$$N_{SIM} = \sum_{i}^{N_D} \sum_{j}^{N_R(i)} \sum_{k}^{N_S(i,j)} \sum_{n}^{N_P(i,j,k)} \sum_{l}^{N_B(i,j,k,n)} 1 \tag{B.66}$$

If R-S-P-B are independent, the number of simulations per dimension is:

$$N_{SIM} = N_R \times N_S \times N_P \times N_B. \tag{B.67}$$

The list of metallic structures, represented by $L_S$, contains all the combinations of D-R-S-B variables. This list is corresponds to the different metallic structures that are needed to the simulations. The total number of metallic structures is given by:

$$N_S = \sum_{i}^{N_D} \sum_{j}^{N_R(j)} \sum_{k}^{N_S(i,j)} \sum_{l}^{N_B(i,j,k)} 1 \tag{B.68}$$

If R-S-B are independent, the number of metallic structure models per dimension is:

$$N_S = N_R \times N_S \times N_B. \tag{B.69}$$

The list of plasmas, represented by $L_P$, contains all the combinations of D-R-P-B variables. Each combination of this list corresponds to different plasma models that are needed to the simulations. The total number of plasma models is given by:

$$N_P = \sum_{i}^{N_D} \sum_{j}^{N_R(i)} \sum_{n}^{N_P(i,j)} \sum_{l}^{N_B(i,j,k)} 1. \tag{B.70}$$

If R-S-B are independent, the number of plasma models per dimension is:

$$N_P = N_R \times N_P \times N_B \tag{B.71}$$

The list of plasmas and metallic structures, represented by $L_{SP}$, contains all the combinations of D-R-S-P variables. Each combination of this list corresponds to a different combination of plasma and metallic structure models that are needed to the data analysis. The total number of plasma models is given by:

$$N_{SP} = \sum_{i}^{N_D} \sum_{j}^{N_R(i)} \sum_{k}^{N_S(i,j)} \sum_{n}^{N_P(i,j,k)} 1. \tag{B.72}$$

If R-S-B are independent, the number of plasma models per dimension is:

$$N_{SP} = N_R \times N_S \times N_P. \tag{B.73}$$

In many cases, it is necessary to get all the elements of a list with the exception of the ones where the plasma model corresponds to vacuum. For this reason, it is very useful to define a default element for vacuum, for example $P$=VAC. A list $L$ without the elements with $P$=VAC is represented by $L^*$. A list only constituted by the elements with $P = \text{VAC}$, is represented by $L^{**}$. Therefore the lists $L^*_{SIM}$, $L^*_S$, $L^*_P$, $L^*_{SP}$, $L^{**}_{SIM}$, $L^{**}_S$, $L^{**}_P$, $L^{**}_{SP}$ are also important to define. For example, if there is interest in running only the simulations with vacuum to test the metallic structure models, only the simulations corresponding to each combination of $L^{**}_{SIM}$ are selected.

Another important list is the list of sources, $L_{SRC}$. This list contains not only the different bands, but also the different combinations of $n_{rise}$, $n_{fall}$, $n_{pre}$, $n_{pos}$ and $n_{ramp}$ which are required to create the reference signals (see section 3.2.3). There are also other lists of parameters that are useful for consultation. For example, the list of grids, represented by $L_G$, contains all the combinations of D-R-B variables and the respective grid parameters (dimensions, spatial discretization, etc). Each combination of this list corresponds to a different grid dimension used in the simulation. The total number of grids is given by:

$$N_G = \sum_{i}^{N_D} \sum_{j}^{N_R(i)} \sum_{l}^{N_B(i,j)} 1 \tag{B.74}$$

If the variables are independent, the number of different grids per dimension is:

$$N_G = N_R \times N_B \tag{B.75}$$

This list includes the information on the grid dimensions (geometry and discretization), which can be useful for consultation. The same occurs with the list of bands, $L_B$. Each parameter associated with the band like the characteristic frequencies, $dx$, $dt$, $N_T$ or $N_\lambda$ and other parameters are interesting to list for further use.

### Phase 3 - production of the metallic structure models

With the lists of combination of the main variables, producing the metallic structure models is done by reading each combination of the $L_S$ list and use the associated dependent variables. In a generic form, the function $F_S$ that creates the metallic structure is the form

$$[\sigma_S(i,j,k), \text{structure arguments}, \text{other outputs}] = F_S(D, R, S, B, \text{other inputs}) \tag{B.76}$$

Alternatively, instead of using the *D-R-S-B* variables, the *D-R-S-B* index can be used ($L_S$ elements are numerated from 1 to $N_S$). In this case, producing all the models is a question of making a simple for loop. This function needs of information on the input data folder, on the SD folder and on the output folder to save the models. It is a good practice to save the output in a directory three defined by each D-R-S-B combination as well as using the main variables in the file name, for example

```
$SD/STRUCT/$D/$R/$S/$B/DIM[$D]ROI[$R]STRUCT[$S]BAND[$B].dat
```

The $ symbol represents the string associated to the variable. The output of the function is the $\sigma_S$ matrix (whose dimensions depend on $D$) and the arguments that are necessary to run a simulation with this model in REFMUL* (e.g. source parameters, reference points), as well as other output files that can be interesting for other operations (e.g. geometry lines to plot the model later).

If the structure of the input and output of this function is maintained, it is possible to change its content without change the other phases of the process. Different users can define different $F_S$ functions according to its necessity, keeping the rest of the framework code intact. One way to do this is define in the configuration file (for example the first variable) which function should be used to produce the model. Then, inside a unique $F_S$ function, the function is called according to the D-R-S-B combination.

For a large number of simulations, this form of creating the output is very demanding from the point of view of memory space, in particular for the 3D simulations. One solution is to produce the model dynamically at the begining of the simulations. In this case, the form of the function $F_S$ is exactly the same, however the $\sigma_S$ matrix is not produced. The structure arguments for REFMUL* include all the information that is required to produce the model in the beginning of the simulation.

### Phase 4 - production of the plasma models

The production of the plasma works exactly in the same way as the production of metallic structures, but for the combinations of the $L_P$ list. A function $F_P$ in the form

$$[n_e(i,j,k), \mathbf{B}_0(i,j,k), \text{plasma arguments}, \text{other outputs}] = F_P(D,R,P,B,\text{other inputs}) \tag{B.77}$$

runs over each *D-R-P-B* combination and produces the plasma variables. The plasma models can be stored in a folder in the form

```
$SD/PLASMA/$D/$R/$P/$B/DIM[$D]ROI[$R]PLS[$P]BAND[$B].dat
```

The plasma matrix occupies in general more memory space than the metallic structure models. For large number of simulations or 3D simulations, the plasma model should also be created dynamically.

If different $F_S$ and $F_P$ functions produce the same structure of output, all the other parts of the code remain the same.

### Phase 5 - write the simulation scripts

REFMUL* codes run in the form

```
./refmul* $OUT $UTS $PLS $STRUCT $SRC $BAND $WRT $OTHER
```

where $OUT is the output directory, $UTS are the arguments for the UTS impulse response, $PLS the arguments for the plasma, $STRUCT the arguments for the metallic structure, $SRC the arguments for the source parameters, $BAND the arguments for the band, $WRT the parameters to define which fields should be saved (including the different detection points associated to the band) and $OTHER for other parameters.

In this phase all the necessary scripts to the simulations are written. This includes:

- UTS scripts - these scripts run all the necessary simulations to measure the UTS impulsive response. Each UTS simulation is associated to a *D-R-S-B* combination.
- MCAL scripts - these scripts run the necessary simulations for the calibration of the group delay inside the antenna setup. There are different ways of doing this process. One solution is associate a reference position to each *D-R-S-B* combination and use it as mirror position. Another solution is associate a plasma/s to each element of $P$. This produces a *D-R-S-PM-B* list, where $PM$ is a reference plasma. The mirror is placed at the initial position of the reference plasma.
- SIM scripts - these scripts run all the simulations with the plasma associated to each *D-R-S-P-B* combination ($L_{SIM}$ list). If more than one mode is simulated the output files can be written with an additional subscript for each mode (O-X).
- SRC scripts - the SRC scripts create the synthetic reference signal for each combination of $L_{SRC}$.

The scripts (exemplified in bash) are executed in the form:

```
sh script.sh $I $F $EXTRA
```

where $I is the initial number of the simulation and $F the final. These numbers depend on the list associated with each type of simulation. The last line are the extra arguments that are added to REFMUL*. This is useful in some situations, for example if for some reason we want to print the output.

The output of each simulation (MCAL and SIM scripts) is the detected signal at the emitting fundamental waveguide (see equation B.78),

$$S_{det}^{DRSPB}(n) = f[S_{src}^{DB}(n), \sigma_S^{DRSB}(i,j,k,n), n_e^{DRPB}(i,j,k,n), \boldsymbol{B}_0^{DRPB}(i,j,k,n)] \tag{B.78}$$

given by the field value at the central waveguide position before the source position. If multiple detections are associated with each band, these signals are also saved in the respective positions, which are defined in the metallic structure model definition phase. A directory with all the simulation results is created in the SD. The results can be organized according to the type of the simulation (UTS, MCAL, SIM, SRC).

### phase 6 - Write the verification scripts

The verification scripts verify if the simulations are done. They are very useful to run a large number of simulations. Each type of simulation has a script associated.

### phase 7 - Copy REFMUL* to the SD

The necessary REFMUL* versions are copied to the SD.

### phase 8 - Copy other necessary data

Other optional files are copied to the SD, such as pre defined plot codes, other useful scripts and functions.

### phase 9 - Write the compilation script

A script is created to compile the different REFMUL* versions with the definitions associated to the computer profile that were chosen in the input files.

### phase 10 - Write the HPC scripts

In HPCs, the simulations are typically submitted by jobs, where the information about the allocated computer resources is defined. In general, in a large list of simulations, the simulations run in sets and using the simulation number as input of the headers in the UTS/MCAL/SIM/SRC scripts. Then, with an additional script in the form

```
sh script.sh $STYPE $I $D $F $EXTRA
```

a set of jobs is submitted. The $STYPE variable selects the type of simulation to run (UTS/MCAL/SIM/SRC). $I and $F are the initial and final number of the simulations and $D is the number of simulations per job. The last argument adds extra commands to REFMUL*. This form of script can be adapted to any configuration of OPENMP/MPI that is intended to use.

Sometimes due to some technical problem, part of the simulations do not finish. A script is required to run the simulations in the interval $I-$F that are not finished. There is also the case of long simulations, where it is necessary to save the final state of the simulation and start a new simulation with it. This possibility can also be included in the same script.

## B.9 Inverse R matrix

Given the $R$ matrix as function of $\mathbf{v_x}$, $\mathbf{v_y}$ and $\mathbf{v_z}$,

$$\mathbf{R} = \begin{bmatrix} R_{xx} & R_{xy} & R_{xz} \\ R_{yx} & R_{yy} & R_{yz} \\ R_{zx} & R_{zy} & R_{zz} \end{bmatrix} = \begin{bmatrix} v_{xx} & v_{yx} & v_{zx} \\ v_{xy} & v_{yy} & v_{zy} \\ v_{xz} & v_{yz} & v_{zz} \end{bmatrix} \tag{B.79}$$

The components of the inverse matrix are:

$$R^{-1}_{xx} = \frac{-v_{yz}v_{zy} + v_{yy}v_{zz}}{-v_{xz}v_{yy}v_{zx} + v_{xy}v_{yz}v_{zx} + v_{xz}v_{yx}v_{zy} - v_{xx}v_{yz}v_{zy} - v_{xy}v_{yx}v_{zz} + v_{xx}v_{yy}v_{zz}} \tag{B.80}$$

$$R^{-1}_{xy} = \frac{v_{yz}v_{zx} - v_{yx}v_{zz}}{-v_{xz}v_{yy}v_{zx} + v_{xy}v_{yz}v_{zx} + v_{xz}v_{yx}v_{zy} - v_{xx}v_{yz}v_{zy} - v_{xy}v_{yx}v_{zz} + v_{xx}v_{yy}v_{zz}} \tag{B.81}$$

$$R^{-1}_{xz} = \frac{-v_{yy}v_{zx} + v_{yx}v_{zy}}{-v_{xz}v_{yy}v_{zx} + v_{xy}v_{yz}v_{zx} + v_{xz}v_{yx}v_{zy} - v_{xx}v_{yz}v_{zy} - v_{xy}v_{yx}v_{zz} + v_{xx}v_{yy}v_{zz}} \tag{B.82}$$

$$R^{-1}_{yx} = \frac{v_{xz}v_{zy} - v_{xy}v_{zz}}{-v_{xz}v_{yy}v_{zx} + v_{xy}v_{yz}v_{zx} + v_{xz}v_{yx}v_{zy} - v_{xx}v_{yz}v_{zy} - v_{xy}v_{yx}v_{zz} + v_{xx}v_{yy}v_{zz}} \tag{B.83}$$

$$R^{-1}_{yy} = \frac{-v_{xz}v_{zx} + v_{xx}v_{zz}}{-v_{xz}v_{yy}v_{zx} + v_{xy}v_{yz}v_{zx} + v_{xz}v_{yx}v_{zy} - v_{xx}v_{yz}v_{zy} - v_{xy}v_{yx}v_{zz} + v_{xx}v_{yy}v_{zz}} \tag{B.84}$$

$$R^{-1}_{yz} = \frac{v_{xy}v_{zx} - v_{xx}v_{zy}}{-v_{xz}v_{yy}v_{zx} + v_{xy}v_{yz}v_{zx} + v_{xz}v_{yx}v_{zy} - v_{xx}v_{yz}v_{zy} - v_{xy}v_{yx}v_{zz} + v_{xx}v_{yy}v_{zz}} \tag{B.85}$$

$$R^{-1}_{zx} = \frac{-v_{xz}v_{yy} + v_{xy}v_{yz}}{-v_{xz}v_{yy}v_{zx} + v_{xy}v_{yz}v_{zx} + v_{xz}v_{yx}v_{zy} - v_{xx}v_{yz}v_{zy} - v_{xy}v_{yx}v_{zz} + v_{xx}v_{yy}v_{zz}} \tag{B.86}$$

$$R^{-1}_{zy} = \frac{v_{xz}v_{yx} - v_{xx}v_{yz}}{-v_{xz}v_{yy}v_{zx} + v_{xy}v_{yz}v_{zx} + v_{xz}v_{yx}v_{zy} - v_{xx}v_{yz}v_{zy} - v_{xy}v_{yx}v_{zz} + v_{xx}v_{yy}v_{zz}} \tag{B.87}$$

$$R^{-1}_{zz} = \frac{-v_{xy}v_{yx} + v_{xx}v_{yy}}{-v_{xz}v_{yy}v_{zx} + v_{xy}v_{yz}v_{zx} + v_{xz}v_{yx}v_{zy} - v_{xx}v_{yz}v_{zy} - v_{xy}v_{yx}v_{zz} + v_{xx}v_{yy}v_{zz}}. \tag{B.88}$$

# Appendix C

# DEMO design

## C.1 DEMO 2015 baseline scenario

### C.1.1 The poloidal flux at the wall

Figure C.1 shows the density map obtained with the extrapolated density profile.

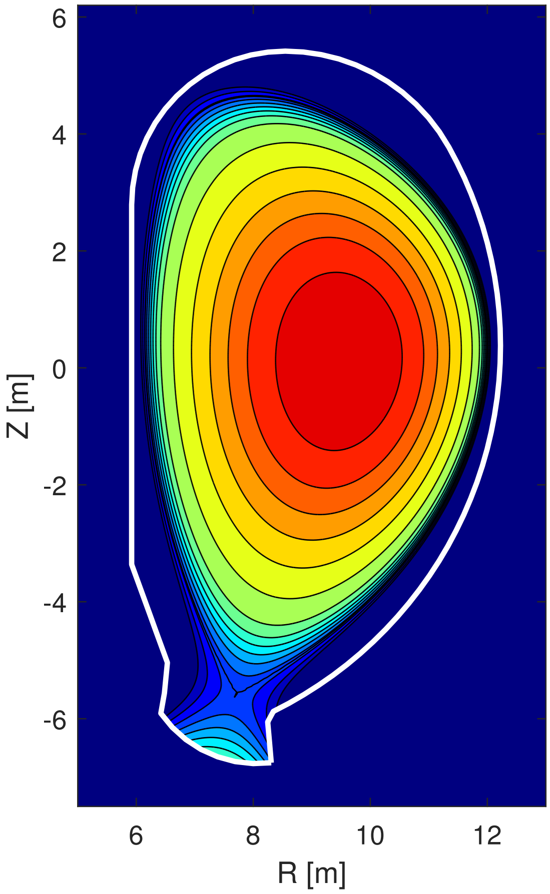

Figure C.1: Density map obtained with the extrapolated density profile.

### C.1.2 The poloidal flux at the wall

The poloidal flux as function of the index of the wall model is shown in figure C.2.

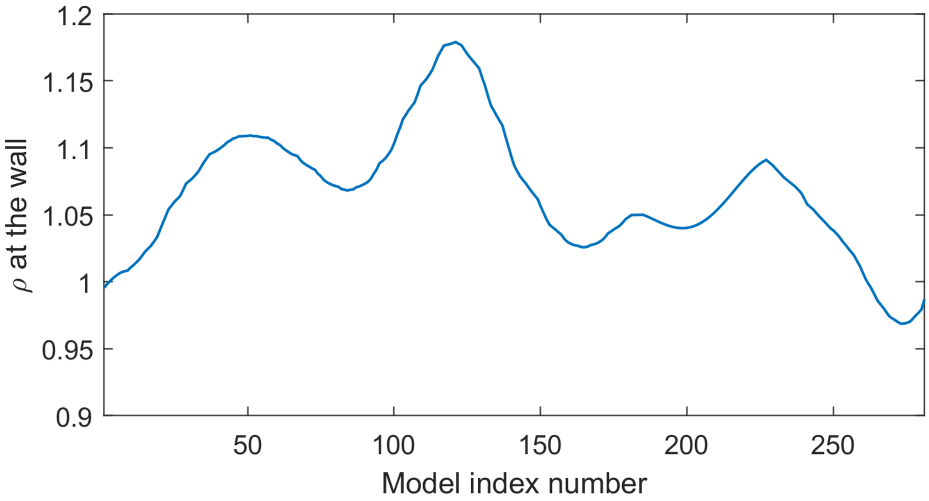

Figure C.2: Normalized poloidal flux at the wall.

The wall model is given in a vector of $(R, Z)$ points. The x axis of this figure corresponds to the index of each point. The index 1 corresponds to the wall point with lower $Z$ coordinate. The minimum value between the indexes 50 and 250 (out of the divertor region) is $\rho_{min} = 1.0258$.

## C.2 Reference antenna geometry

### C.2.1 Antenna geometry

The reference antenna is shown in C.3.

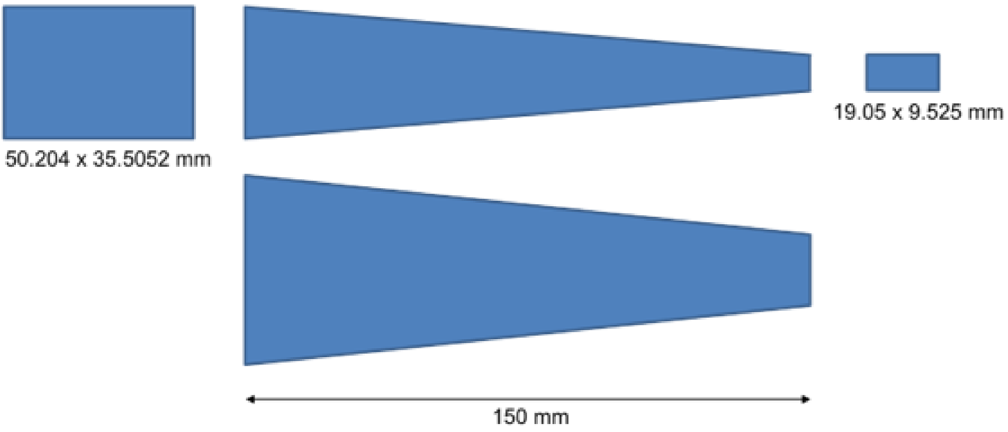

Figure C.3: Dimensions of the reference antenna used in the simulations.

### C.2.2 Radiation diagram

The radiation patterns for different operating frequencies were obtained using CST and are shown in figure C.4.

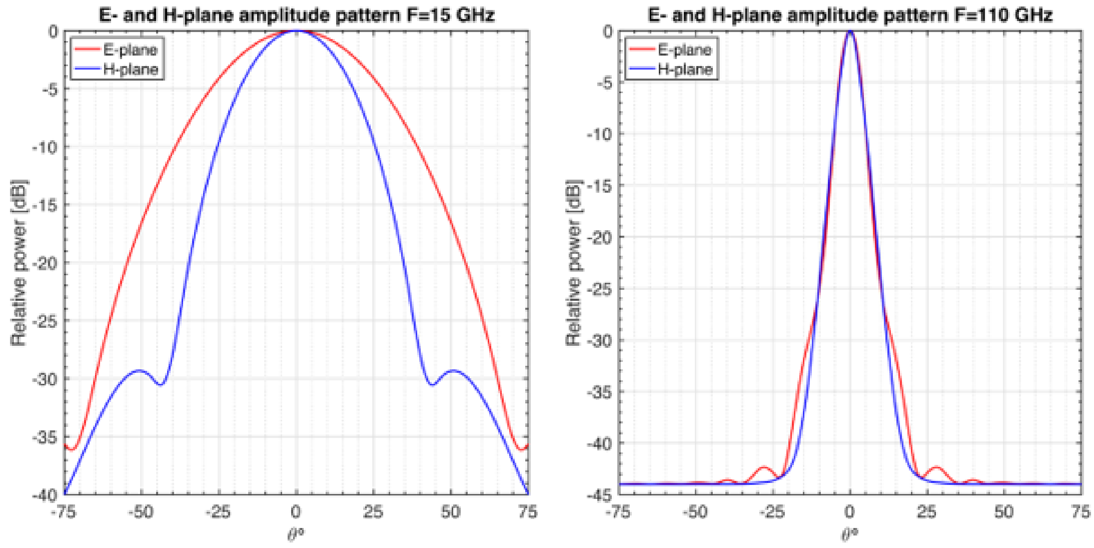

Figure C.4: Dimensions of the reference antenna used in the simulations [221].

## C.3 DEMO 2017 scenario

### C.3.1 Configuration perpendicular to the wall

Figure C.5 shows the wall-separatrix distance and the absolute $\theta_{sep}$ angle for the configuration with the probing beam aligned perpendicularly to the wall.

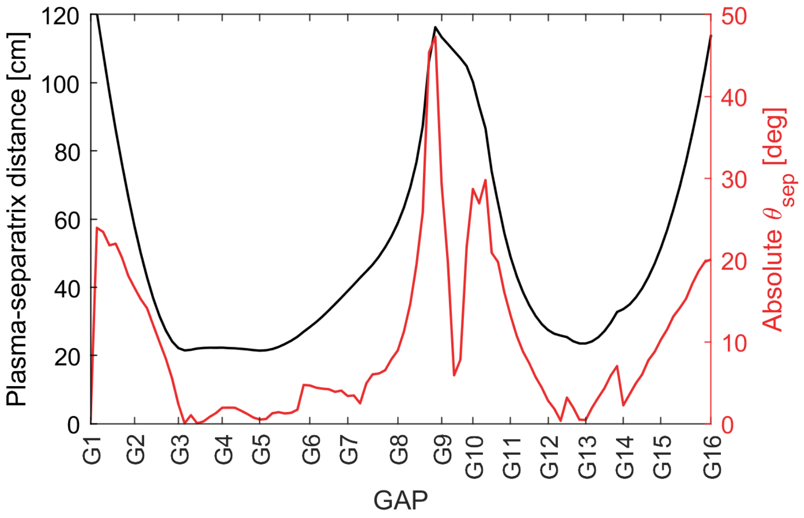

Figure C.5: The wall-separatrix distance and the absolute $\theta_{sep}$ angle for the configuration with the probing beam aligned perpendicularly to the wall.

### C.3.2 Density profile in gap G8E

Figure C.6 shows the Airy's wavelength at the separatrix frequency.

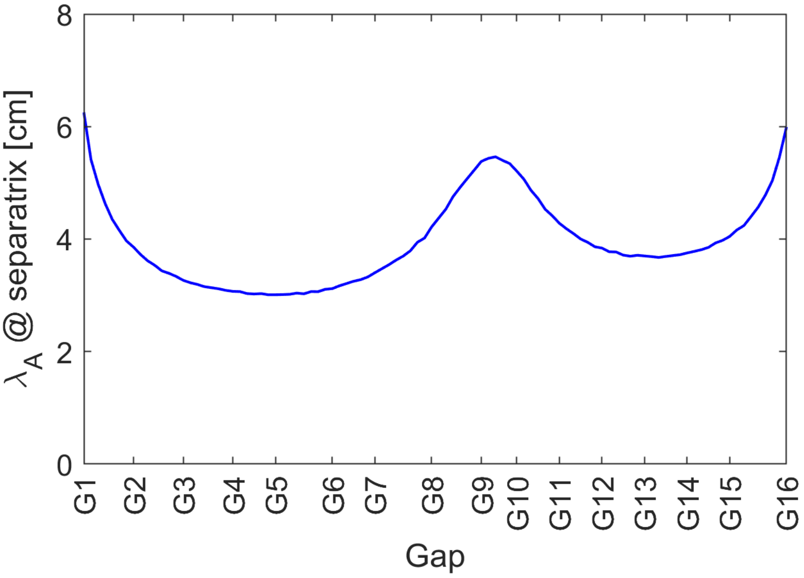

Figure C.6: Airy's wavelength at the separatrix frequency for as function of the gaps.

Figure C.7 shows the density profile in the gap G8E, where the Airy's wavelength is in the order of 5 cm. Since the distance between the separatrix position and the change of slope is approximately 1 cm, the reflection does not occur in a region described approximately by a linear dielectric constant.

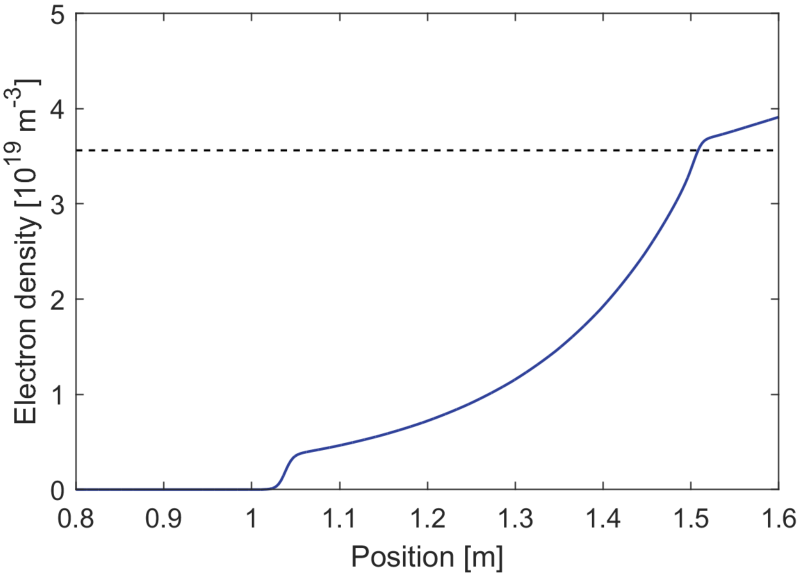

Figure C.7: Electron density in the gap G8E.

### C.3.3 Q-spectrum of the slab plasma

Figure C.8 shows the spectrum-gap diagram for the slab plasma.

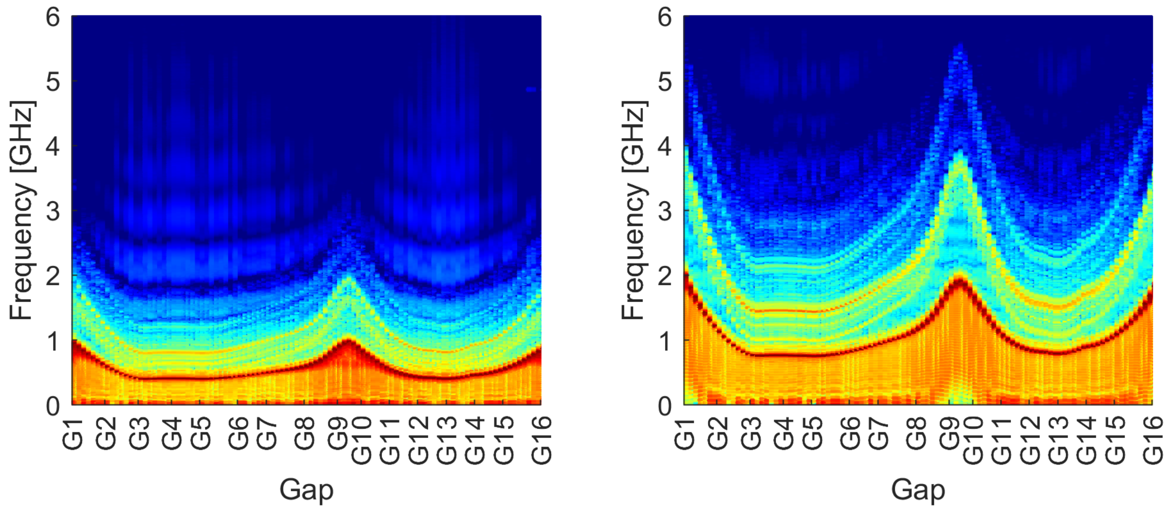

(a) $K_1$ band. (b) $Ka_1$ band.

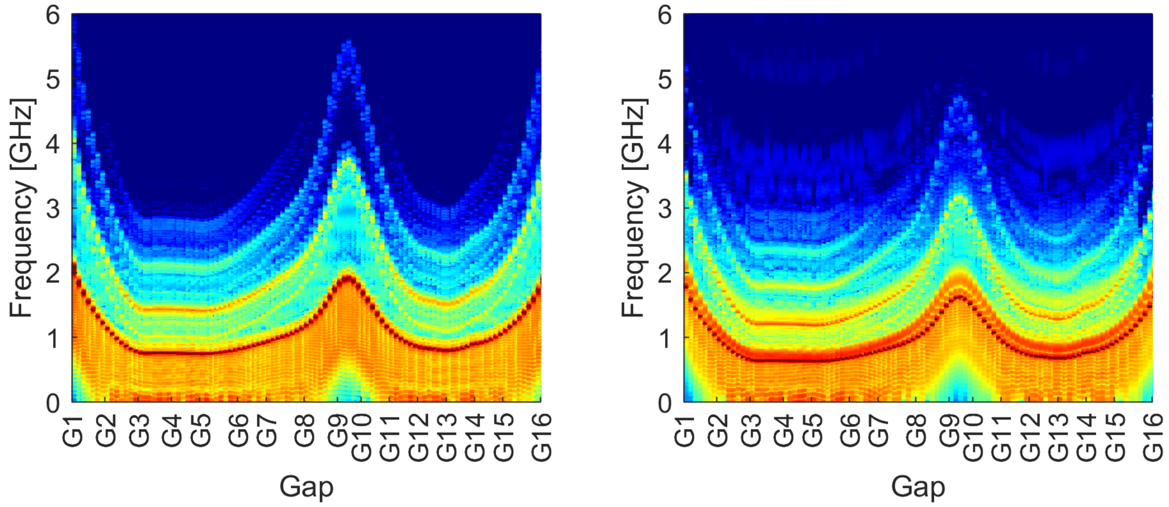

(c) $Q_1$ band. (d) $V_1$ band.

Figure C.8: Spectrum-gap diagram for the slab plasma.

### C.3.4 Dominant frequency of each configuration

The dominant frequency of each configuration is shown in figures C.9-C.10 for the $K_1$ and $Ka_1$ bands.

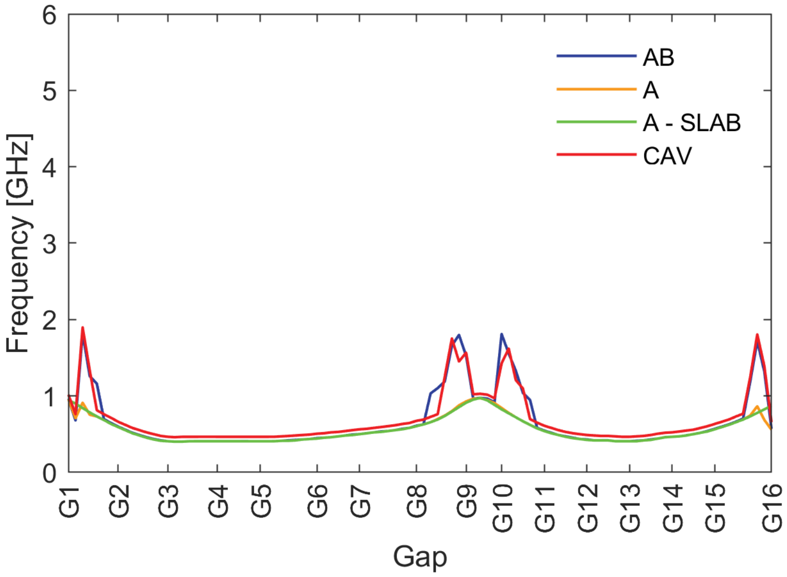

Figure C.9: Dominant frequency of each configuration for the $K_1$ band.

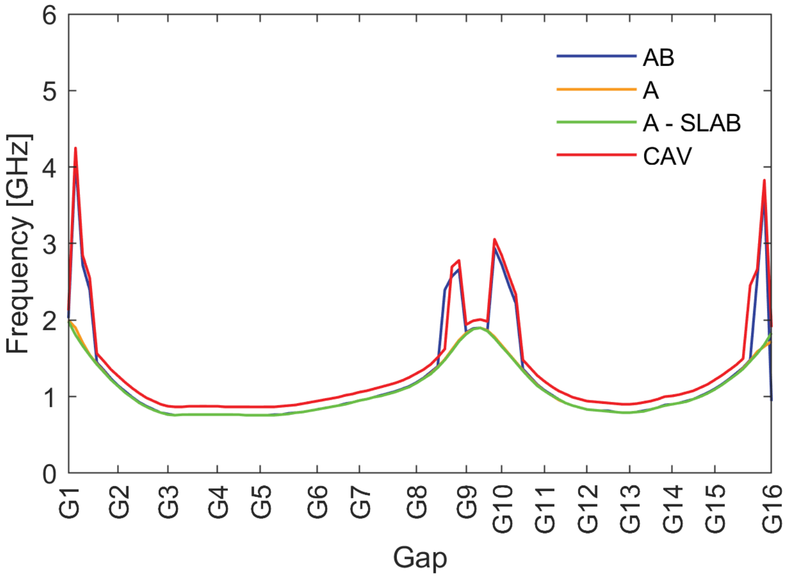

Figure C.10: Dominant frequency of each configuration for the $Ka_1$ band.

The dominant frequency of each configuration is shown in figures C.11-C.12 for the $Q_1$ and $V_1$ bands.

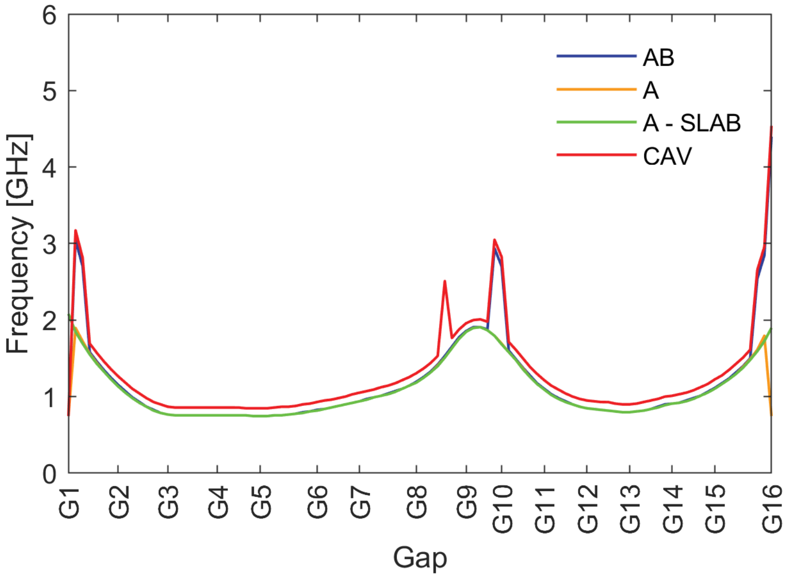

Figure C.11: Dominant frequency of each configuration for the $Q_1$ band.

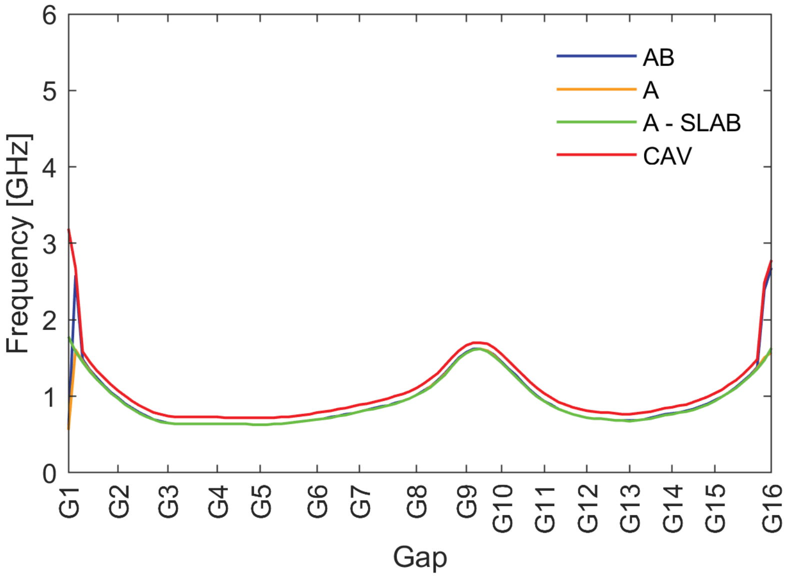

Figure C.12: Dominant frequency of each configuration for the $V_1$ band.

## C.4 Optimization for the baseline scenario

Figure C.13 shows the original FWP optimization separatrix error function, without the correction of the probing angle.

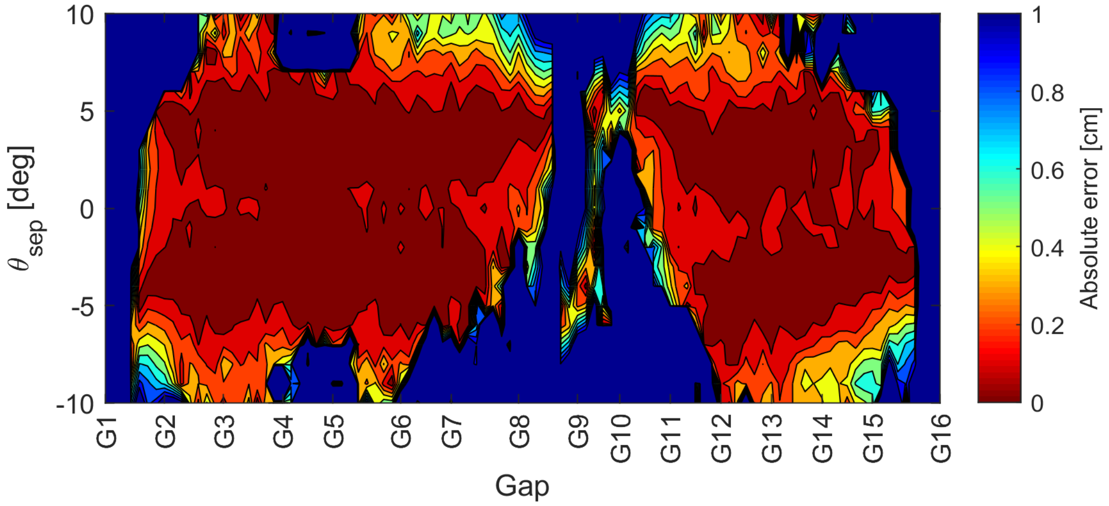

Figure C.13: The FWP optimization separatrix error function.

Figure C.14 shows the power loss at the separatrix position.

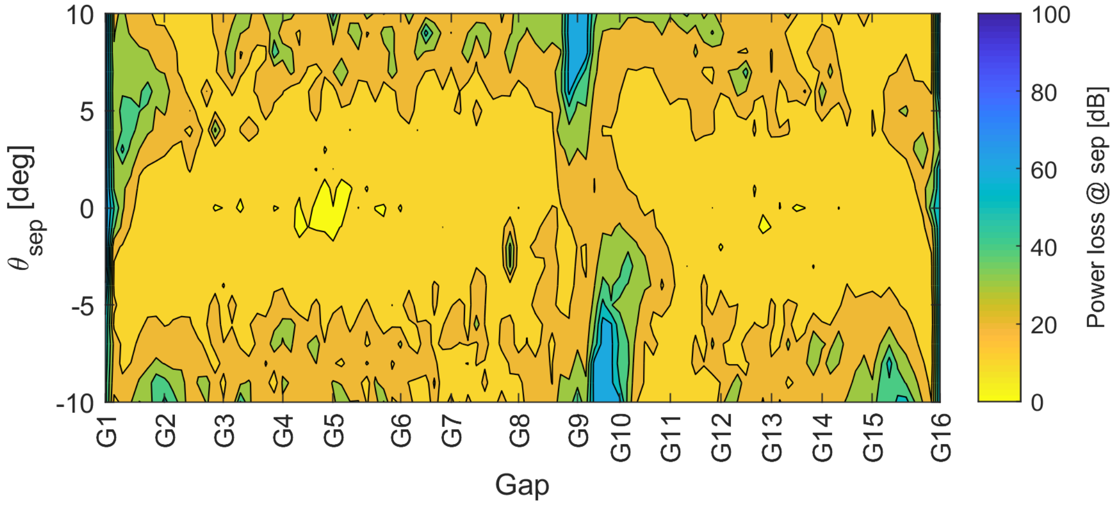

Figure C.14: FWP optimization power loss at the separatrix position.

## C.5 Measurement performance of gap G11B

Figure C.15 shows the measurement performance of gap G11B.

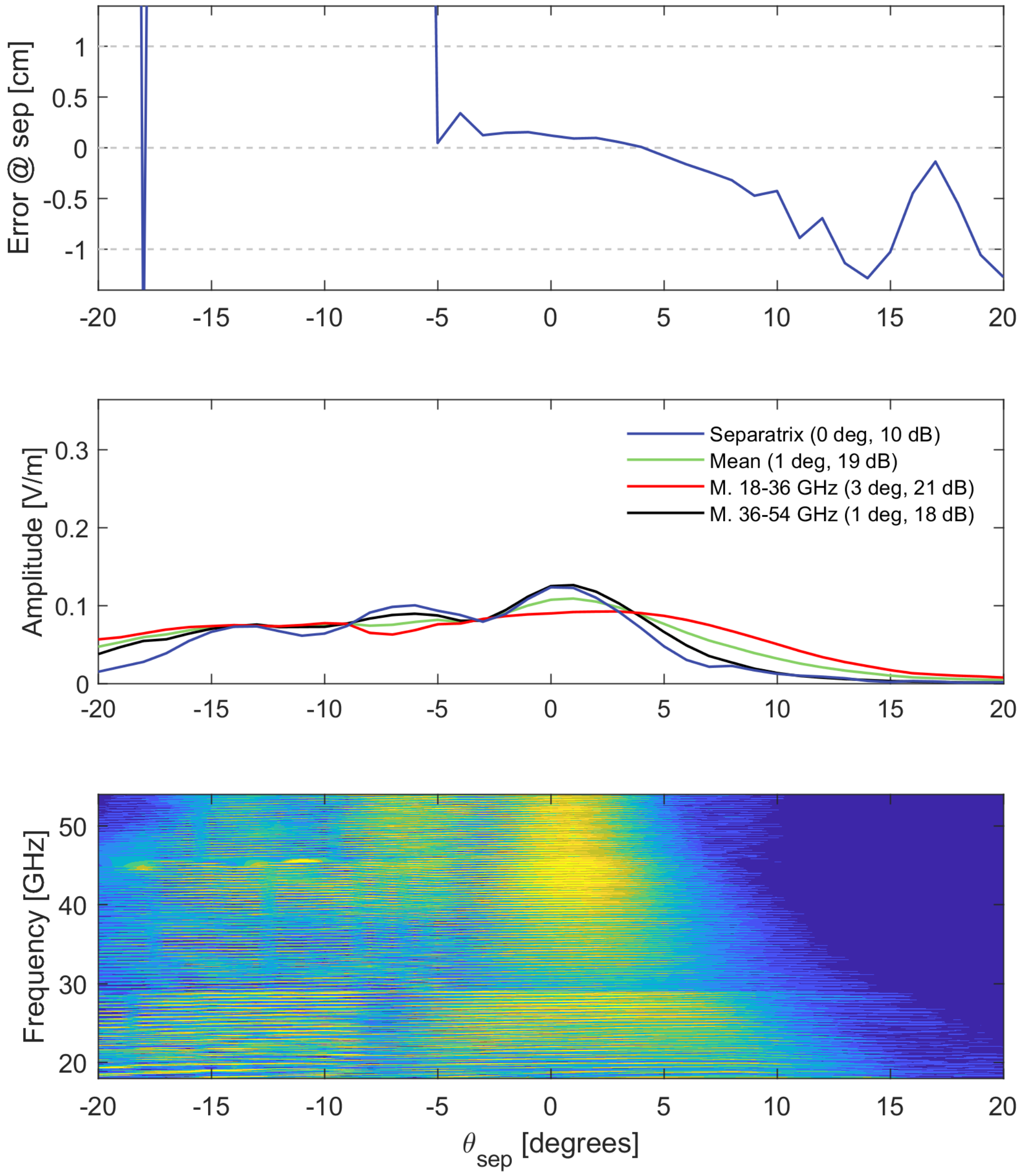

Figure C.15: Measurement performance of gap G11B.

## C.6 Optimized lines of view

Figure C.16 shows the lines of view of the configurations used to study the system optimization.

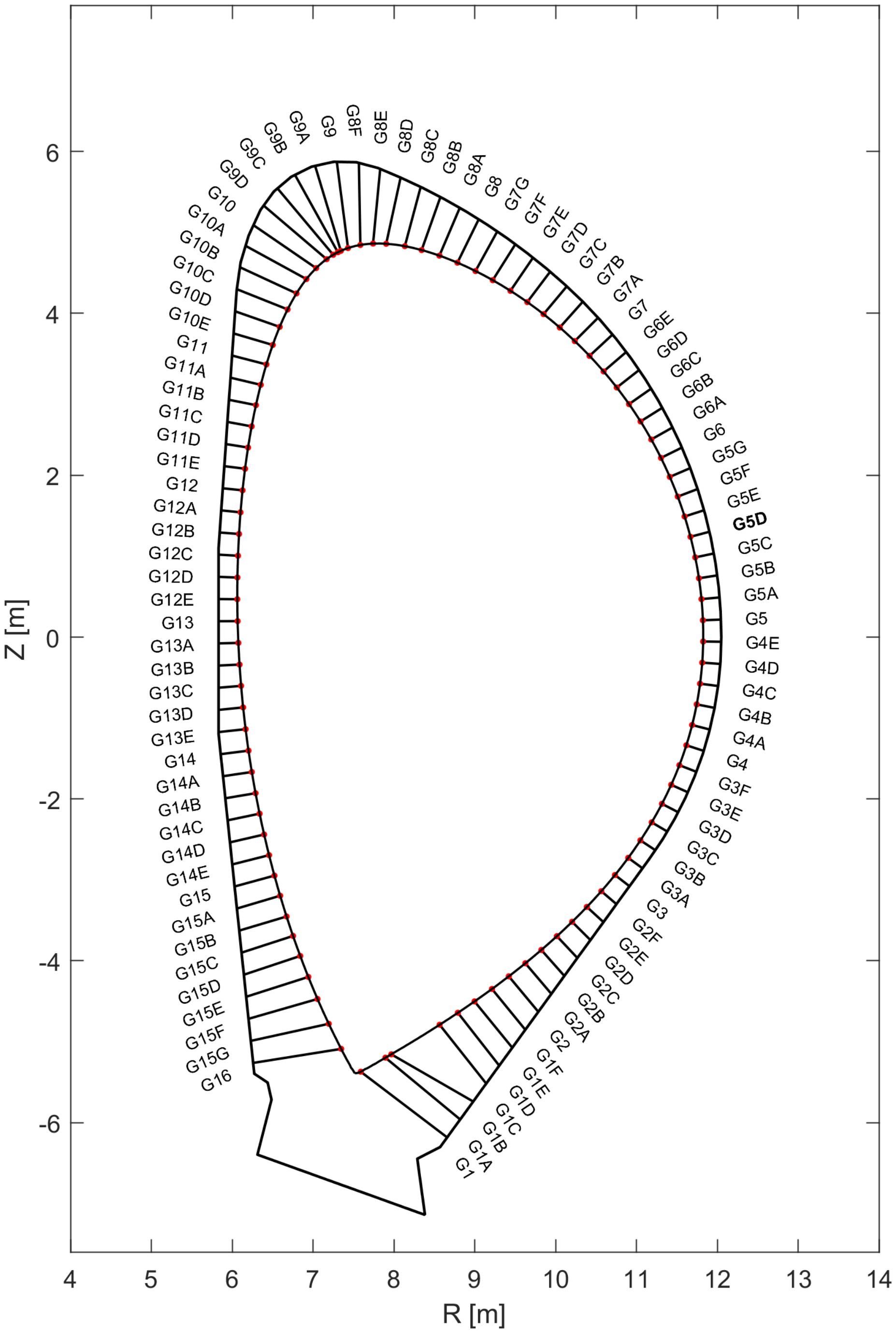

Figure C.16: Lines of view of the configurations used to study the system optimization.

## C.7 Plasma displacement

Figure C.17 shows the results for plasma displacements of 5, 10 and 15 cm, with $\theta = [0, 45, 90, 135, 180, 225, 270, 315]$ deg.

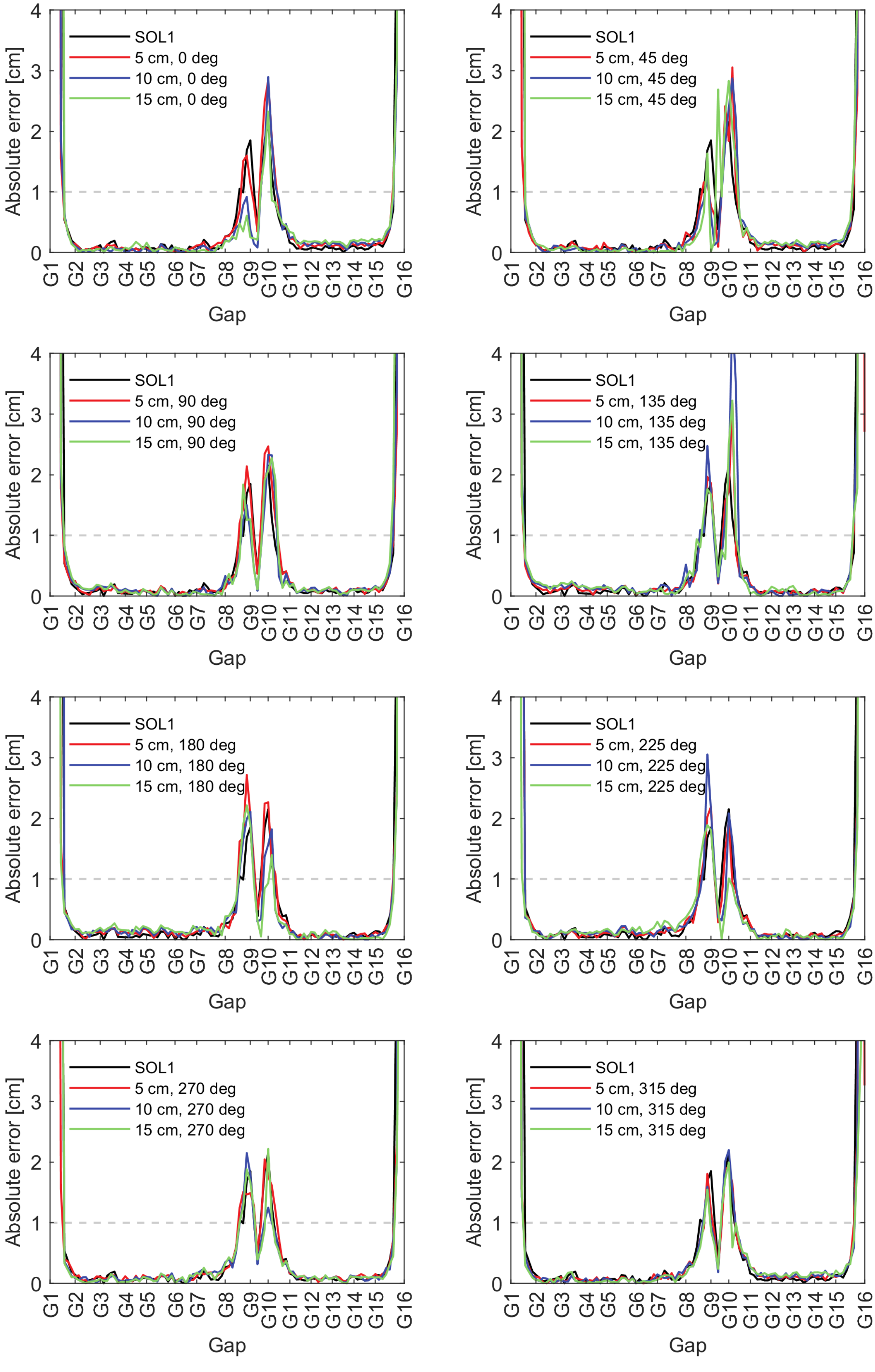

Figure C.17: Position error for different plasma displacements.

# List of Figures

# Bibliography

[1] *International Energy Agency.* `https://www.iea.org`.

[2] P. Zweifel, A. Praktiknjo, and G. Erdmann, *Energy Economics: Theory and Applications.* Springer Texts in Business and Economics, Springer-Verlag Berlin Heidelberg, 1st ed., 2017.

[3] K. Mathis and B. R. Huber, *Energy Law and Economics.* Economic Analysis of Law in European Legal Scholarship 5, Springer International Publishing, 1st ed., 2018.

[4] *United Nations.* `https://www.un.org`.

[5] I. Arto, I. Capellán-Pérez, R. Lago, G. Bueno, and R. Bermejo, "The energy requirements of a developed world," *Energy for Sustainable Development*, vol. 33, pp. 1–13, 08 2016.

[6] *Wikipedia - world population.* `https://en.wikipedia.org/wiki/World_population`.

[7] J. A. Fay and D. S. Golomb, *Energy and the environment.* MIT-Pappalardo series in mechanical engineering, The Oxford series on advanced manufacturing, Oxford University Press, 1st ed., 2002.

[8] J. Freidberg, *Plasma Physics and Fusion Energy.* Cambridge University Press, 1st ed., 2008.

[9] R. L. Nersesian, *Energy Economics: Markets, History and Policy.* Routledge, 1st ed., 2016.

[10] S. Shahriar and T. Erkan, "When will fossil fuel reserves be diminished?," *Energy Policy*, vol. 37, pp. 181–189, 2009.

[11] *World in data.* `https://ourworldindata.org/energy-mix`.

[12] *ITER website.* `https://www.iter.org/`.

[13] W. Biel, R. Albanese, R. Ambrosino, M. Ariola, M. Berkel, I. Bolshakova, K. Brunner, R. Cavazzana, M. Cecconello, S. Conroy, A. Dinklage, I. Duran, R. Dux, T. Eade, S. Entler, G. Ericsson, E. Fable, D. Farina, L. Figini, C. Finotti, T. Franke, L. Giacomelli, L. Giannone, W. Gonzalez, A. Hjalmarsson, M. Hron, F. Janky, A. Kallenbach, J. Kogoj, R. König, O. Kudlacek, R. Luis, A. Malaquias, O. Marchuk, G. Marchiori, M. Mattei, F. Maviglia, G. D. Masi, D. Mazon, H. Meister, K. Meyer, D. Micheletti, S. Nowak, C. Piron, A. Pironti, N. Rispoli, V. Rohde,

G. Sergienko, S. E. Shawish, M. Siccinio, A. Silva, F. da Silva, C. Sozzi, M. Tardocchi, M. Tokar, W. Treutterer, and H. Zohm, “Diagnostics for plasma control – from iter to demo,” *Fusion Engineering and Design*, vol. 146, pp. 465–472, 2019.

[14] K. S. Krane, *Introductory nuclear physics.* Wiley International Editions, Wiley, 1st ed., 1987.

[15] D. J. Griffiths, *Introduction to Elementary Particles.* Wiley, 2nd ed., 2008.

[16] *Of Particular Significance - Conversations About Science with Theoretical Physicist Matt Strassler.* `https://profmattstrassler.com/articles-and-posts/particle-physics-basics/the-known-forces-of-nature/the-strength-of-the-known-forces`.

[17] S. B. Patel, *Nuclear Physics - An Introduction.* New Age International, 1st ed., 2010.

[18] S. Atzeni and J. M. ter Vehn, *The Physics of Inertial Fusion: Beam Plasma Interaction, Hydrodynamics, Hot Dense Matter.* International Series of Monographs on Physics, Oxford University Press, 1st ed., 2004.

[19] M. R. Enzo De Sanctis, Stefano Monti, *Energy from Nuclear Fission: An Introduction.* Undergraduate Lecture Notes in Physics, Springer International Publishing, 1st ed., 2016.

[20] P. A. Sturrock, *Physics of the Sun.* Geophysics and astrophysics monographs, D. Reidel, 1st ed., 1986.

[21] D. J. Mullan, *Physics of the Sun. A First Course.* CRC SERIES in PURE and APPLIED PHYSICS, CRC Press, 1st ed., 2010.

[22] T. Tanabe, *Tritium: Fuel of Fusion Reactors.* Springer, 1st ed., 2016.

[23] J. Wesson, *Tokamaks.* International series of monographs on physics 118 Oxford science publications, Oxford University Press, 3rd ed., 2004.

[24] P. M. Bellan, *Fundamentals of plasma physics.* Cambridge University Press, 1st ed., 2006.

[25] J. A. Bittencourt, *Fundamentals of Plasma Physics.* Springer-Verlag New York, 3rd ed., 2004.

[26] F. F. Chen, *Introduction to plasma physics and controlled fusion.* Springer, 3rd ed., 2016.

[27] S. Nakai and H. Takabe, “Principles of inertial confinement fusion - physics of implosion and the concept of inertial fusion energy,” *Reports on Progress in Physics*, vol. 59, pp. 1071–1131, 09 1996.

[28] S. Pfalzner, *An introduction to inertial confinement fusion.* Series in plasma physics, Taylor and Francis/CRC Press, 1st ed., 2006.

[29] R. P. Drake, *High-Energy-Density Physics: Foundation of Inertial Fusion and Experimental Astrophysics.* Graduate Texts in Physics, Springer International Publishing, 2nd ed., 2018.

[30] J. Freidberg, *Ideal MHD.* CUP, 1st ed., 2014.

[31] A. H. Boozer, "What is a stellarator?," *Physics of Plasmas*, vol. 5, p. 1647, 1998.

[32] H. Bodin, "The reversed field pinch," *Nuclear Fusion*, vol. 30, pp. 1717–1737, 1990.

[33] EFDA, "Safety and environmental impact of fusion," vol. EFDA–S–RE-1, 2001.

[34] J. Mlynář, ""focus on: Jet," european centre of fusion research," vol. EFD-R(07)01, 2007.

[35] D. G. Swanson, *Plasma kinetic theory.* Series in plasma physics, CRC Press, 1st ed., 2008.

[36] B. Scott, *Turbulence and Instabilities in Magnetised Plasmas: Gyrokinetic theory and gyrofluid turbulence*, vol. 2 of *IOP Series in Plasma Physics.* Iop Publishing, 1st ed., 2021.

[37] L. Zakharov and V. Shafranov, "Equilibrium of a toroidal plasma with noncircular cross section," *Soviet Physics Technical Physics*, vol. 18, pp. 151–156, 2019.

[38] Y. Xu, "A general comparison between tokamak and stellarator plasmas," *Matter and Radiation at Extremes*, vol. 1, pp. 192–200, 7 2016.

[39] J. Ongena, R. Koch, and R. W. et al, "Magnetic-confinement fusion," *Physics of Plasmas*, vol. 12, p. 398–410, 2016.

[40] *Landreman Group website.* `https://terpconnect.umd.edu/~mattland/projects/1_stellarators`.

[41] O. Sauter and S. Medvedev, "Tokamak coordinate conventions," *Computer Physics Communications*, vol. 184, pp. 293–302, 2013.

[42] *Fusion in Europe - news views on the progress of fusion research.* `https://www.euro-fusion.org/fileadmin/user_upload/Newsletter/EUROfusion%20Fusion%20in%20Europe/EUROfusion%20Fusion%20in%20Europe%202016%20Mar.pdf`.

[43] P. Stangeby, *The plasma boundary of magnetic fusion devices.* Plasma physics series, Institute of Physics Pub, 1st ed., 2000.

[44] D. Carralero, M. Siccinio, M. Komm, S. Artene, F. D'Isa, J. Adamek, L. Aho-Mantila, G. Birkenmeier, M. Brix, and G. Fuchert, "Recent progress towards a quantitative description of filamentary sol transport," *Nuclear Fusion*, vol. 57, p. 056044, 2017.

[45] A. Wynn, B. Lipschultz, I. Cziegler, J. Harrison, A. Jaervinen, G. F. Matthews, J. Schmitz, B. Tal, and C. G. M. Brix, "Investigation into the formation of the scrape-off layer density shoulder in jet iter-like wall l-mode and h-mode plasmas," *Nuclear Fusion*, vol. 58, p. 056001, 2018.

[46] D. G. Swanson, *Plasma waves.* Series in plasma physics, Institute of Physics Pub, CRC Press, 2nd ed., 2003.

[47] H. L. Pécseli, *Waves and Oscillations in Plasmas.* Series in Plasma Physics, CRC Press, 1st ed., 2012.

[48] I. H. Hutchinson, *Principles of Plasma Diagnostics.* Cambridge University Press, 2nd ed., 2005.

[49] H.-J. Hartfuß and T. Geist, *Fusion Plasma Diagnostics with mm-Waves.* Wiley, 1st ed., 2013.

[50] *EUROfusion website.* `https://www.euro-fusion.org/devices/jet/jets-salient-features`.

[51] J. Hugill, "Transport in tokamaks - a review of experiment," *Nuclear Fusion*, vol. 23, pp. 331–373, 1983.

[52] F. Wagner and U. Stroth, "Transport in toroidal devices-the experimentalist's view," *Plasma Physics and Controlled Fusion*, vol. 35, pp. 1321–1371, 10 1993.

[53] V. Grandgirard, Y. Sarazin, X. Garbet, G. Dif-Pradalier, P. Ghendrih, N. Crouseilles, G. Latu, E. Sonnendrucker, N. Besse, and P. Bertrand, "Gysela, a full-f global gyrokinetic semi-lagrangian code for itg turbulence simulations - aip theory of fusion plasmas: Joint varenna-lausanne international workshop - varenna (italy) aip conference proceedings," vol. 871, pp. 100–111, 2006.

[54] R. Waltz, J. Candy, and M. Rosenbluth, "Gyrokinetic turbulence simulation of profile shear stabilization and broken gyrobohm scaling," *Physics of Plasmas*, vol. 9, p. 1938, 2002.

[55] T. Görler, X. Lapillonne, S. Brunner, T. Dannert, F. Jenko, F. Merz, and D. Told, "The global version of the gyrokinetic turbulence code gene," *Journal of Computational Physics*, vol. 230, pp. 7053–7071, 2011.

[56] S. Zweben, B. Scott, J. Terry, B. LaBombard, J. Hughes, and D. Stotler, "Comparison of scrape-off layer turbulence in alcator c-mod with three dimensional gyrofluid computations," *Physics of Plasmas*, vol. 16, p. 082505, 2009.

[57] *General Atomics Fusion Group.* `https://ccfe.ukaea.uk/research/mast-upgrade`.

[58] D. Prisiazhniuk, *Development and application of poloidal correlation reflectometry to study turbulent structures in the ASDEX Upgrade tokamak.* PhD thesis, Technical University of Munich, 2017.

[59] T. V. Karman, *Aerodynamics.* McGraw-Hill Education, 1st ed., 1963.

[60] G. Falkovich, *Fluid Mechanics: A Short Course for Physicists.* Cambridge University Press, 1st ed., 2011.

[61] F. H. Champagne, "The fine-scale structure of the turbulent velocity field," *Journal of Fluid Mechanics*, vol. 86, p. 67, 1978.

[62] R. H. Kraichnan, “Inertial-range transfer in two- and three-dimensional turbulence,” *Journal of Fluid Mechanics*, vol. 47, pp. 525–535, 6 1971.

[63] P. Hennequin, R. Sabot, C. Honoré, G. Hoang, X. Garbet, A. Truc, C. Fenzi, and A. Quéméneur, “Scaling laws of density fluctuations at high-k on tore supra,” *Plasma Physics and Controlled Fusion*, vol. 46, pp. B121–B133, 2004.

[64] A. Gurchenko and E. Gusakov, “Evolution of etg mode scale turbulence and anomalous electron transport in dynamic tokamak experiments,” *Plasma Physics and Controlled Fusion*, vol. 42, p. 42033046, 2010.

[65] T. Happel, T. Estrada, E. Blanco, C. Hidalgo, G. Conway, U. Stroth, and T. Team, “Scale selective turbulence reduction in h-mode plasmas in the tjii stellarator,” *Physics of Plasmas*, vol. 18, p. 102302, 2011.

[66] T. Happel, *Doppler reflectometry in the stellarator TJ-II: Design of an optimized Doppler reflectometer and its application to turbulence and radial electric field structures.* PhD thesis, Universidad Carlos III de Madrid, 2010.

[67] B. Scott, “Three-dimensional computation of drift alfvén turbulence,” *Plasma Physics and Controlled Fusion*, vol. 39, pp. 1635–1668, 10 1997.

[68] J. Conner and H. Wilson, “Survey of theories of anomalous transport,” *Plasma Physics and Controlled Fusion*, vol. 36, pp. 719–795, 1994.

[69] B. D. Scott, “Computation of electromagnetic turbulence and anomalous transport mechanisms in tokamak plasmas,” *Plasma Physics and Controlled Fusion*, vol. 45, pp. A385–A398, 12 2003.

[70] W. Horton, B. Hu, and J. D. P. Zhu, “Turbulent electron thermal transport in tokamaks,” *New Journal of Physics*, vol. 5, p. 14, 2003.

[71] F. Wagner, G. Becker, K. Behringer, D. Campbell, A. Eberhagen, W. Engelhardt, G. Fussmann, O. Gehre, J. Gernhardt, and G. Gierke, “Regime of improved confinement and high beta in neutral-beam-heated divertor discharges of the asdex tokamak,” *Physical Review Letters*, vol. 49, pp. 1408–1412, 1982.

[72] F. Ryter, T. Pütterich, M. Reich, A. Scarabosio, E. Wolfrum, R. Fischer, M. G. Adamov, N. Hicks, B. Kurzan, C. Maggi, R. Neu, V. Rohde, and G. Tardini, “H-mode threshold and confinement in helium and deuterium in asdex upgrade,” *Nuclear Fusion*, vol. 49, p. 062003, 06 2009.

[73] F. Ryter, S. Rathgeber, L. B. Orte, M. Bernert, G. Conway, R. Fischer, T. Happel, B. Kurzan, R. McDermott, A. Scarabosio, W. Suttrop, E. Viezzer, M. Willensdorfer, and E. Wolfrum, “Survey of the h-mode power threshold and transition physics studies in asdex upgrade,” *Nuclear Fusion*, vol. 53, p. 113003, 2013.

[74] A. Medvedeva, C. Bottereau, F. Clairet, P. Hennequin, U. S. G. Birkenmeier, M. C. G. Conway, T. Happel, and S. Heuraux, “Density profile and turbulence evolution during l-h transition studied with the ultra-fast swept reflectometer on asdex upgrade,” *Plasma Physics and Controlled Fusion*, p. 125014, 2017.

[75] A. Garofalo, K. Burrell, D. Eldon, B. Grierson, J. Hanson, C. Holland, G. Huijsmans, F. Liu, A. Loarte, O. Meneghini, T. Osborne, C. Paz-Soldan, S. Smith, P. Snyder, W. Solomon, A. Turnbull, and L. Zeng, "The quiescent h-mode regime for high performance edge localized mode-stable operation in future burning plasmas," *Physics of Plasmas*, vol. 22, p. 056116, 05 2015.

[76] D. Maisonnier, I. Cook, S. Pierre, B. Lorenzo, D. P. Luigi, G. Luciano, N. Prachai, and P. Aldo, "Demo and fusion power plant conceptual studies in europe," *Fusion Engineering and Design*, vol. 81, pp. 1123–1130, 2006.

[77] A. Donné, A. Costley, and A. Morris, "Diagnostics for plasma control on demo: challenges of implementation," *Nuclear Fusion*, vol. 52, p. 074015, 07 2012.

[78] F. Orsitto, R. Villari, F. Moro, T. Todd, S. Lilley, I. Jenkins, R. Felton, W. Biel, A. Silva, M. Scholz, J. Rzadkiewicz, I. Duran, M. Tardocchi, G. Gorini, C. Morlock, G. Federici, and A. Litnovsky, "Diagnostics and control for the steady state and pulsed tokamak demo," *Nuclear Fusion*, vol. 56, p. 026009, 2016.

[79] G. Federici, W. Biel, M. Gilbert, R. Kemp, N. Taylor, and R. Wenninger, "European demo design strategy and consequences for materials," *Nuclear Fusion*, vol. 57, p. 092002, 2017.

[80] M. Cecconello, S. Conroy, G. Ericsson, H. Hjalmarsson, T. Franke, and W. Biel, "Pre-conceptual study of the european demo neutron diagnostics," *Journal of Instrumentation*, vol. 14, pp. C09001–C09001, 2019.

[81] S. Ciattaglia, G. Federici, L. Barucca, A. Lampasi, S. Minucci, and I. Moscato, "The european demo fusion reactor: Design status and challenges from balance of plant point of view - ieee international conference on environment and electrical engineering and ieee industrial and commercial power systems europe (eeeic / icps europe)," pp. 1–6, 2017.

[82] J. Santos, *Fast reconstruction of reflectometry density profiles on ASDEX Upgrade for plasma position feedback purposes.* PhD thesis, Universidade técnica de Lisboa, 2008.

[83] E. Mazzucato, "Microwave reflectometry for magnetically confined plasmas," *Review of Scientific Instruments*, vol. 69, p. 2201, 1998.

[84] E. Ricardo, P. Varela, A. Silva, and B. Gonçalves, "Assessment and performance optimization of the iter plasma position reflectometry in-vessel oversized waveguide bends," *Fusion Engineering and Design*, pp. 1593–1596, 7 2015.

[85] J. Santos, L. Guimarãis, M. Zilker, W. Treutterer, and M. Manso, "Reflectometry-based plasma position feedback control demonstration at asdex upgrade," *Nuclear Fusion*, vol. 52, p. 032003, 03 2012.

[86] J. M. Santos, G. S. Santos, M. Zilker, L. Guimarãis, C. Rapson, W. Treutterer, and B. Gonçalves, "Enhancement of the asdex upgrade real-time plasma position reflectometry diagnostic diagnostic," *IEEE Transactions on Nuclear Science*, vol. 62.

[87] J. Santos, L. Guimarãis, C. Rapson, G. Santos, A. Silva, W. Treutterer, and M. Zilker, “Real-time reflectometry – an asdex upgrade dcs plugin app for plasma position and shape feedback control,” *Fusion Engineering and Design*, p. S0920379617302193, 3 2017.

[88] G. Porter, S. Davies, B. LaBombard, A. Loarte, K. McCormick, R. Monk, M. Shimada, and M. Sugihara, “Analysis of separatrix plasma parameters using local and multi-machine databases,” *Journal of Nuclear Materials*, vol. 266-269, pp. 917–921, 1999.

[89] G. Marchiori, G. D. Masi, R. Cavazzana, A. Cenedese, N. Marconato, R. Moutinho, and A. Silva, “Study of a plasma boundary reconstruction method based on reflectometric measurements for control purposes,” *IEEE Transactions on Plasma Science*, vol. 46, pp. 1285–1290, 5 2018.

[90] R. Luis, R. Moutinho, L. Prior, P. B. Quental, A. Lopes, H. Policarpo, N. Velez, A. Vale, A. Silva, and A. Malaquias, “Nuclear and thermal analysis of a reflectometry diagnostics concept for demo,” *IEEE Transactions on Plasma Science*, vol. 46, pp. 1–7, 2018.

[91] K. Mergia and N. Boukos, “Structural, thermal, electrical and magnetic properties of eurofer 97 steel,” *Journal of Nuclear Materials*, vol. 373, pp. 1–8, 2008.

[92] A. Silva, F. da Silva, S. Heuraux, and B. Gonçalves, “First assessment of microwave diagnostics for demo,” *Fusion Engineering and Design*, vol. 96-97, pp. 948–951, 10 2015.

[93] F. da Silva, *Finite-Difference Time-Domain Simulation of Reflectometry in Fusion Plasmas.* PhD thesis, 2007.

[94] F. da Silva, S. Heuraux, E. Ricardo, A. Silva, and T. Ribeiro, “Modelling reflectometry diagnostics: finite-difference time-domain simulation of reflectometry in fusion plasmas,” *Journal of Instrumentation*, vol. 14, pp. C08003–C08003, 08 2019.

[95] A. Belous, *Handbook of Microwave and Radar Engineering.* 1st ed., 2021.

[96] K. G. Budden, *Radio Waves in the Ionosphere.* Cambridge University Press, 1st ed., 1961.

[97] V. L. Ginzburg, *Propagation of Electromagnetic Waves in Plasmas.* Pergamon Press, 1st ed., 1970.

[98] A. Anisimov, N. Vinogradov, V. Goland, and B. Konstantinov, “Method of investigating electron spatial distribution in a plasma,” *Soviet Physics*, vol. 56, p. 664–669, 1961.

[99] A. Cavallo and R. Cano, “Proposal for density profile measurements by reflectometry in large tokamaks,” *Technical Report EUR-CEA-FC-1337*, 1982.

[100] F. Simonet, “Measurement of electron density profile by microwave reflectometry on tokamaks,” *Review of Scientific Instruments*, vol. 56, p. 664–669, 1985.

[101] A. E. Hubard, *Measurement of Electron Density on JET by Microwave Reflectometry.* PhD thesis, Imperial College of Science and Technology, 1987.

[102] A. Silva, L. Cupido, M. Manso, F. Serra, I. Nunes, J. Santos, P. Varela, S. V. L. Meneses, V. G. F. Silva, C. Loureiro, F. Nunes, B. Kurzan, and W. Suttrop, "Microwave reflectometry diagnostic for density profile and fluctuation measurements on asdex upgrade," *Review of Scientific Instruments*, vol. 70, p. 1072, 1999.

[103] A. Sips and G. Kramer, "Analysis of reflectometry density profile measurements in jet," *Plasma Physics and Controlled Fusion*, vol. 35, pp. 743–755, 06 1993.

[104] T. Lehecka, W. Peebles, N. Luhmann, S. Burns, E. Olson, and D.-D. Group, "Reflectometry systems for the diii-d tokamak," *Review of Scientific Instruments*, vol. 59, p. 1620, 1988.

[105] M. Hirsch, E. Holzhauer, J. Baldzuhn, and B. Kurzan, "Doppler reflectometry for the investigation of propagating density perturbations," *Review of Scientific Instruments*, vol. 72, p. 324, 2001.

[106] D. Prisiazhniuk, G. Conway, A. Krämer, and U. Stroth, "Density fluctuation correlation measurements in asdex upgrade using poloidal and radial correlation reflectometry," *Plasma Physics and Controlled Fusion*, vol. 60, p. 075003, 07 2018.

[107] M. E. Manso, "Reflectometry in fusion devices," *Plasma Physics and Controlled Fusion*, vol. 35, pp. B141–B155, 12 1993.

[108] C. Laviron, A. Donné, M. Manso, and J. Sanchez, "Reflectometry techniques for density profile measurements on fusion plasmas," *Plasma Physics and Controlled Fusion*, vol. 38, pp. 905–936, 07 1996.

[109] J. D. Jackson, *Classical electrodynamics.* Wiley, 3rd ed., 1999.

[110] K. G. Budden, *The Propagation of Radio Waves: The Theory of Radio Waves of Low Power in the Ionosphere and Magnetosphere.* Cambridge University Press, 1st ed., 1988.

[111] P. D. M., *Microwave Engineering.* Wiley, 4th ed., 2012.

[112] E. Mazzucato, "Relativistic effects on microwave reflectometry," *Physics of Fluids B Plasma Physics*, vol. 4, p. 3460, 1992.

[113] T. H. Stix, *Waves in plasmas.* IoP, 1992.

[114] H. G. Booker, *Cold Plasma Waves.* Developments in Electromagnetic Theory and Applications 2, Springer Netherlands, 1st ed., 1984.

[115] C. Fanack, *Etude analytique et numerique de la Reflectometrie dans un plasma fluctuant: modeles a une et deux dimensions.* PhD thesis, Université Henri Poincaré, 1997.

[116] M. Manso, F. Nunes, A. Silva, J. Leitao, and P. Varela, "Profile evaluation techniques for o-mode broadband microwave reflectometry on asdex," *International*

*Atomic Energy Agency, Vienna (Austria); 264 p; 1992; p. 38-47; IAEA technical committee meeting on microwave reflectometry for fusion plasma diagnostics; Abingdon (United Kingdom); 4-6 Mar 1992*, vol. 25, pp. 38–47, 1992.

[117] A. Medvedeva, A. Biancalani, C. Bottereau, F. Clairet, G. Conway, S. Heuraux, A. Molina, A. Silva, U. Stroth, and A. U. Team, "Density fluctuations measurements with an ultra-fast-swept reflectometer in asdex upgrade," *Materials Science*, 2015.

[118] J. Hillesheim, D. Dickinson, C. Roach, S. Saarelma, R. Scannell, A. Kirk, N. Crocker, W. Peebles, and H. Meyer, "Intermediate-k density and magnetic field fluctuations during inter-elm pedestal evolution in mast," *Plasma Physics and Controlled Fusion*, vol. 58, p. 014020, 2016.

[119] N. Bretz, "One-dimensional modeling of the wavelength sensitivity, localization, and correlation in reflectometry measurements of plasma fluctuations," *Physics of Fluids B: Plasma Physics*, vol. 4, p. 2414, 1992.

[120] S. Baang, C. Domier, N. Luhmann, W. Peebles, and T. Rhodes, "Spatial resolution of microwave/millimeter-wave reflectometry," *Review of Scientific Instruments*, vol. 61, p. 3013, 1990.

[121] T. Rhodes, S. Baang, A. Chou, C. Domier, N. Luhmann, and W. Peebles, "Fundamental investigation of reflectometry as a density fluctuation diagnostic," *Review of Scientific Instruments*, vol. 63, p. 4599, 1992.

[122] X. L. Zou, L. Laurent, and J. M. Rax, "Scattering of an electromagnetic wave in a plasma close to a cut-off layer. application to fluctuation measurements," *Plasma Physics and Controlled Fusion*, vol. 33, pp. 903–918, 07 1991.

[123] C. Fanack, I. Boucher, F. C. S. Heuraux, G. Leclert, and X. L. Zou, "Ordinary-mode reflectometry: modification of the scattering and cut-off responses due to the shape of localized density fluctuations," *Plasma Physics and Controlled Fusion*, vol. 38, pp. 1915–1930, 11 1996.

[124] W. H. Bragg and W. L. Bragg, "The reflection of x-rays by crystals," *Nature*, vol. 88, p. 1913, 1913.

[125] P. Moreau, *Développement d'un reflectometre micro-onde heterodyne a balayage ultra rapide.* PhD thesis, Université Aix-Marseille I, 1997.

[126] F. da Silva, S. Heuraux, and M. Manso, "Studies on o-mode reflectometry spectra simulations with velocity shear layer," *Nuclear Fusion*, vol. 46, p. 816.

[127] S. Heuraux, S. Hacquin, F. da Silva, F. Clairet, R. Sabot, and G. Leclert, "Radial wave number spectrum of density fluctuations deduced from reflectometry phase signals," *Review of Scientific Instruments*, vol. 74, p. 1501, 2003.

[128] M. Colin, *Modélisation d'un réflectomètre mode X en vue de caractériser les fluctuations de densité et de champ magnétique: applications aux signaux de Tore Supra-Muriel.* PhD thesis, Université Henri Poincaré, Nancy, 2001.

[129] I. Boucher, C. Fanack, S. Heuraux, G. Leclert, F. Clairet, and X. Zou, "One-dimensional analytical model of the phase shift due to bragg backscattering of an ordinary wave by large amplitude density fluctuations," *Plasma Physics*, vol. 40, p. 1489, 1998.

[130] I. Hutchinson, "One-dimensional full-wave analysis of reflectometry sensitivity and correlations," *Plasma Physics and Controlled Fusion*, vol. 34, p. 1225, 1992.

[131] J. Vicente, F. D. Silva, T. Ribeiro, S. Heuraux, G. Conway, B. Scott, L. Guimarãis, L. Gil, E. Seliunin, P. Manz, J. Santos, A. Silva, and C. Silva, "Synthetic conventional reflectometry probing of edge and scrape-off layer plasma turbulence," *Journal of Instrumentation*, vol. 14, p. C10043, 2019.

[132] E. Gusakov and A. Popov, "Non-linear theory of fluctuation reflectometry," vol. 44, p. 2327, 2002.

[133] E. Blanco and T. Estrada, "Study of doppler reflectometry capability to determine the perpendicular velocity and the k-spectrum of the density fluctuations using a 2d full-wave code," vol. 50, p. 095011, 2008.

[134] E. Blanco and T. Estrada, "Two-dimensional full-wave simulations of radial correlation doppler reflectometry in linear and non-linear regimes," vol. 55, p. 125006, 2013.

[135] E. Gusakov, S. Heuraux, and A. Popov, "Strong bragg backscattering in reflectometry," *Plasma Physics and Controlled Fusion*, vol. 51, p. 065018, 2009.

[136] E. Sysoeva, E. Gusakov, and S. Heuraux, "Transition into diffusive regime of propagation of probing electromagnetic waves in a turbulent inhomogeneous plasma and limitations for microwave reflectometry in reactor scale devices," *Plasma Physics and Controlled Fusion*, vol. 55, p. 115001, 2013.

[137] G. Conway, L. Schott, and A. Hirose, "Comparison of reflectometer fluctuation measurements from experiment and two-dimensional numerical simulation," *Review of Scientific Instruments*, vol. 67, p. 3861, 1996.

[138] G. Conway, "Beam diameter effects on microwave reflectometer measurements," *Plasma Physics and Controlled Fusion*, vol. 39, p. 1261, 1997.

[139] J. Irby, S. Horne, I. H. Hutchinson, and P. Stek, "2d full-wave simulation of ordinary mode reflectometry," *Plasma Physics and Controlled Fusion*, vol. 35, p. 601, 1993.

[140] E. Gusakov and M. Tyntarev, "The two-dimensional theory of reflectometry diagnostics of plasma fluctuations," *Fusion Engineering and Design*, vol. 34-35, pp. 501–505, 1997.

[141] Y. Lin, R. Nazikian, J. Irby, and E. Marmar, "Plasma curvature effects on microwave reflectometry fluctuation measurements," *Plasma Physics and Controlled Fusion*, vol. 43, 2001.

[142] L. Bruskin, A. Mase, N. Oyama, K. Shinohara, and Y. Miura, "Reflectometry study of mode coupling in fusion plasma turbulence," *Plasma Physics and Controlled Fusion*, vol. 45, p. 1227, 2003.

[143] E. V. Sysoeva, F. da Silva, E. Z. Gusakov, S. Heuraux, and A. Popov, "Electron cyclotron resonance heating beam broadening in the edge turbulent plasma of fusion machines," vol. 55, p. 033016, 2015.

[144] P. Tretinnikov, E. Gusakov, and S. Heuraux, "X-mode beam broadening in turbulent plasma," *Plasma Physics and Controlled Fusion*, vol. 63, p. 085003, 2021.

[145] G. Zadvitskiy, *Experimental and numerical study of turbulence in fusion plasmas using reflectometry synthetic diagnostics.* PhD thesis, Université de Lorraine, 2018.

[146] C. Alabaster, *Pulse Doppler Radar: Principles, Technology, Applications.* SciTech Publishing, 1st ed., 2012.

[147] G. Cunningham, "Use of the absolute phase in frequency modulated continuous wave plasma reflectometry," *Review of Scientific Instruments*, vol. 79, p. 083501, 2008.

[148] H. Bindslev, "Relativistic effects in plasma reflectometry," *Plasma Physics and Controlled Fusion*, vol. 34, p. 1601, 1992.

[149] H. Bindslev, "Relativistic expressions for plasma cutoffs," *Plasma Physics and Controlled Fusion*, vol. 35, pp. 1093–1102, 1993.

[150] H. Bindslev, *On the Theory of Thomson Scattering and Reflectometry in a Relativistic Magnetized Plasma.* PhD thesis, Balliol College, Oxford, 1992.

[151] P. Stott, "Basic and advanced diagnostic techniques for fusion plasmas: Proceedings of the course and workshop held in varenna," vol. 1, 1987.

[152] R. Morales, S. Hacquin, S. Heuraux, and R. Sabot, "New density profile reconstruction methods in x-mode reflectometry," *Review of Scientific Instruments*, vol. 88, p. 043503, 04 2017.

[153] H. Bottollier-Curtet and G. Ichtchenko, "Microwave reflectometry with the extraordinary mode on tokamaks: Determination of the electron density profile of petula-b," *Review of Scientific Instruments*, vol. 58, p. 539–546, 1987.

[154] H. Bottollier-Curtet, *Microwave reflectometry for the determination of electron density and its fluctuations in the PETULA-B tokamak.* PhD thesis, L'université de Paris XI, 1986.

[155] R. Morales, S. Heuraux, R. Sabot, S. Hacquin, F. Clairet, and the Tore Supra Team, "Reconstruction of hollow areas in density profiles from frequency swept reflectometry," *Plasma Science and Technology*, vol. 22, p. 064005, 2020.

[156] P. E. Stott, G. Gorini, P. Prandoni, and E. Sindoni, *Diagnostics for Experimental Thermonuclear Fusion Reactors 2 —— Status and Prospects of Pulse Radar Reflectometry on the Start Tokamak*, pp. 587–596. 1998.

[157] A. Silva, *The ASDEX Upgrade broadband microwave reflectometry system.* PhD thesis, Universidade técnica de Lisboa, 2006.

[158] P. Varela, M. Manso, A. Silva, J. Fernandes, and F. Silva, “Initialization of plasma density profiles from reflectometry,” *Review of Scientific Instruments*, vol. 66, p. 4937, 1995.

[159] S. Heuraux and S. Hacquin, “Amplitude variation and frequency shift of a reflectometer signal propagating in a time varying plasma,” in *32nd EPS Conference on Plasma Physics. Tarragona 27 June - 1 July 2005*, vol. 29C, pp. P–4.085, 2005.

[160] G. Conway, “Microwave reflectometry for fusion plasma diagnosis,” *Nuclear Fusion*, vol. 46, p. S665, 2006.

[161] G. Conway, G. Vayakis, J. Fessey, and D. Bartlett, “A reflectometer for fluctuation and correlation studies on the joint european torus tokamak,” *Review of Scientific Instruments*, vol. 70, p. 3921, 1999.

[162] G. Hornung, F. Clairet, G. Falchetto, R. Sabot, H. Arnichand, and L. Vermare, “Turbulence correlation properties measured with ultrafast sweeping reflectometry on tore supra,” vol. 55, p. 125013, 2013.

[163] E. Gusakov and A. Popov, “Measurements localization in poloidal correlation reflectometry,” *Nuclear Fusion*, vol. 46, p. S829, 2006.

[164] H. Qu, T. Zhang, X. Han, F. Wen, S. Zhang, D. Kong, Y. Wang, Y. Gao, C. Huang, J. Cai, and X. Gao, “Radial and poloidal correlation reflectometry on experimental advanced superconducting tokamak,” *Review of Scientific Instruments*, vol. 86, p. 083503, 2015.

[165] L. Vermare, S. Heuraux, F. Clairet, G. Leclert, and F. da Silva, “Density fluctuation measurements using x-mode fast sweep reflectometry on tore supra,” *Nuclear Fusion*, vol. 46, p. S743, 2006.

[166] T. Gerbaud, F. Clairet, R. Sabot, , and A. Sirinelli, “Comparison of density fluctuation measurements between o-mode and x-mode reflectometry on tore supra,” *Review of Scientific Instruments*, vol. 77, p. 10E928, 2006.

[167] G. Conway, E. POLI, T. Happel, and the ASDEX Upgrade Team, “Interaction of mean and oscillating plasma flows across confinement mode transitions,” vol. 5, p. S2005, 2010.

[168] C. Tröster, *Development of a flexible Doppler reflectometry system and its application to turbulence characterization in the ASDEX Upgrade tokamak.* PhD thesis, LMU München: Faculty of Physics, 2008.

[169] C. Lechte, G. Conway, T. GÖRLER, T. Happel, and the ASDEX Upgrade team, “Fullwave doppler reflectometry simulations for density turbulence spectra in asdex upgrade using gene and ipf-fd3d,” *Plasma Science and Technology*, vol. 22, p. 064006, 2020.

[170] D. Aguiam, *Implementation of a X-mode multichannel edge density profile reflectometer for the new ICRH antenna on ASDEX Upgrade.* PhD thesis, Universidade técnica de Lisboa, 2018.

[171] A. Silva, L. Cupido, M. Manso, F. X. Söldner, and A.-U. Team, “Fast sweep multiple broadband reflectometer for asdex upgrade,” in *Fusion Technology 1992: Proceedings of the 17th Symposium on Fusion Technology*, pp. 747–750, 1993.

[172] F. Clairet, C. Bottereau, A. Medvedeva, D. Molina, G. Conway, A. Silva, and U. Stroth, “1$\mu$s broadband frequency sweeping reflectometry for plasma density and fluctuation profile measurements,” *Review of Scientific Instruments*, vol. 88, p. 113506, 11 2017.

[173] C. Laviron, P. Millot, and R. Prentice, “First experiments of pulse compression radar reflectometry for density measurements on jet plasmas,” *Plasma Physics and Controlled Fusion*, vol. 37, p. 975–987, 1995.

[174] P. Millot in *Proc. IAEA Technical Meeting on Microwave Reflectometry for Fusion Plasmas Diagnostics (Culham,Abingdon, UK)*, 1992.

[175] G. Hanson, J. Wilgen, T. Bigelow, I. Collazo, A. England, M. Murakami, D. Rasmussen, and J. Wilson, “Differential-phase reflectometry for edge profile measurements on tokamak fusion test reactor,” *Review of Scientific Instruments*, vol. 66, p. 863, 1995.

[176] J. Sanchez, B. Branas, T. Estrada, E. de la Luna, and V. Zhuravlev, “Amplitude modulation reflectometry for large fusion devices,” *Review of Scientific Instruments*, vol. 63, p. 4654, 1992.

[177] M. Hirsch, H. Hartfuss, T. Geist, and E. de la Luna, “Amplitude modulated heterodyne reflectometer for density profile and density fluctuation profile measurements at w7-as,” *Review of Scientific Instruments*, vol. 67, p. 1807–1813, 1996.

[178] C. J. Hugenholtz and S. Heijnen, “Pulse radar technique for reflectometry on thermonuclear plasmas,” *Review of Scientific Instruments*, vol. 62, pp. –, 1991.

[179] C. Domier, N. Luhmann, A. Chou, W. Zhang, and A. Romanowsky, “Ultrashort-pulse reflectometry,” *Review of Scientific Instruments*, vol. 66, pp. 399–401, 1995.

[180] M. Manso, F. Serra, J. Barroso, J. Comprido, C. Teixeira, A. Monteiro, A. Silva, J. Neves, J. Pereira, L. Cupido, A. Cardoso, C. Costa, and A. Garrett, “Broadband microwave reflectometry on asdex,” *In Proceedings on 16th European Conference on Controlled Fusion and Plasma Physics*, pp. 1517–1520, 1989.

[181] M. Manso, F. Serra, A. Silva, J. Matias, F. Nunes, J. Leitão, J. Mata, P. Varela, S. Vergamota, and F. Söldner, “Localized density measurements on asdex using microwave reflectometry,” *In Proceedings on 17th European Conference on Controlled Fusion and Plasma Heating*, pp. 1560–1563, 1990.

[182] P. Millot and F. Simonet, “A broadband microwave reflectometer for tore supra,” in *In Proceedings on 14th European Conference on Controlled Fusion and Plasma Physics*, p. 1303–1305, European Physical Society, 1987.

[183] F. Clairet, M. Paume, and J. Chareau, “Electron density profile measurements by microwave reflectometry on tore supra,” in *In Proceedings on 21st European Conference on Controlled Fusion and Plasma Physics*, vol. 18B, p. 1172–1175, European Physical Society, 1994.

[184] E. Anabitarte, E. Bustamante, M. Calderon, J. Sentiles, A. Navarro, and J. Sanchez, “Determination of the electron density profile and its fluctuations by broad-band microwave reflectometry in the tj-1 tokamak,” *Journal of Physics D: Applied Physics*, vol. 21, p. 1384–1390, 1988.

[185] E. Doyle, T. Lehecka, N. L. Jr., W. Peebles, and D.-D. Group, “X-mode broadband reflectometric density profile measurements on diii-d,” vol. 61, p. 2896–2898, 1990.

[186] *First density measurements with microwave reflectometry on ASDEX Upgrade*, vol. 17C, 1993.

[187] A. Silva, M. Manso, L. Cupido, M. Albrecht, F. Serra, P. Varela, J. Santos, S. Vergamota, F. Eusebio, J. Fernandes, T. Grossmann, A. Kallenbach, B. Kurzan, C. Loureiro, L. Meneses, I. Nunes, F. Silva, W. Suttrop, and the ASDEX Upgrade Team, “Ultrafast broadband frequency modulation of a continuous wave reflectometry system to measure density profiles on asdex upgrade,” *Review of Scientific Instruments*, vol. 67, p. 4138, 1996.

[188] J. Santos and A. Silva, “Real-time detection and correction of frequency sweeping non-linearities of fmcw reflectometry microwave sources,” *Journal of Instrumentation*, vol. 14, pp. C11017–C11017, 11 2019.

[189] *RF Cavity Design, E. Jensen, CERN, Geneva, Switzerland.* `https://arxiv.org/ftp/arxiv/papers/1601/1601.05230.pdf`.

[190] J. L. Doane, “Hyperbolic secant coupling in overmoded waveguide,” *IEEE Transactions on Microwave Theory and Techniques*, vol. 32, pp. 1362–1371, 1984.

[191] J. Belo, P. Varela, E. Ricardo, A. Silva, and P. Quental, “Performance assessment of critical waveguide bends for the iter in-vessel plasma position reflectometry systems,” *Fusion Engineering and Design*, vol. 123, pp. 773–777, 2017.

[192] C. A. Balanis, *Antenna Theory: Analysis and Design.* Wiley, 3rd ed., 2005.

[193] M. Moresco, A. Vendramin, and E. Zilli, “A focussing hog-horn antenna for microwave diagnostics in plasma machines,” vol. 51, p. 1071–1074, 1980.

[194] J. Lips, S. Heuraux, C. Lechte, and B. Plaum, “On frequency-independent horn antenna design for plasma positioning reflectometers, from simulation to prototype testing,” *Nuclear Fusion*, vol. 16, p. P07040, 2021.

[195] M. Hirsch, H. Laqua, D. Hathiramani, J. Oosterbeek, J. Baldzuhn, C. Biedermann, H. Brand, A. Cardella, V. Erckmann, R. Jimenez, R. König, M. Köppen, S. Parquay, and D. Zhang, “The impact of microwave stray radiation to in-vessel diagnostic components,” in *AIP Conference Proceedings: Proceedings of the International Conference - Villa Monastero, Varenna (Lc), Italy (9–13 September 2013)*, 2014.

[196] P. Varela, M. Manso, A. Silva, the CFN Team, and the ASDEX Upgrade Team, “Review of data processing techniques for density profile evaluation from broadband fm-cw reflectometry on asdex upgrade,” *Nuclear Fusion*, vol. 46, pp. S693–S707, 09 2006.

[197] B. Boashash, “Estimating and interpreting the instantaneous frequency of a signal. i. fundamentals,” *Proceedings of the IEEE*, vol. 80, pp. 520–538, 1992.

[198] B. Boashash, “Estimating and interpreting the instantaneous frequency of a signal. ii. algorithms and applications,” *Proceedings of the IEEE*, vol. 80, pp. 540–568, 1992.

[199] J. Santos, F. Nunes, M. Manso, and I. Nunes, “Neural network evaluation of reflectometry density profiles for control purposes,” *Review of Scientific Instruments*, vol. 70, p. 521, 1999.

[200] J. Santos, F. Nunes, M. Manso, and P. Varela, “A neural network approach to evaluate density profiles from reflectometry in asdex upgrade discharges with internal transport barriers,” *Fusion Engineering and Design*, vol. 48, pp. 119–126, 2000.

[201] A. M. Mathai and H. J. Haubold, *Probability and Statistics: A Course for Physicists and Engineers.* De Gruyter, 1st ed., 2018.

[202] L. Shi, E. Valeo, B. Tobias, G. Kramer, L. Hausammann, W. Tang, , and M. Chen, “Synthetic diagnostics platform for fusion plasmas,” *The Review of scientific instruments*, vol. 87, p. 11D303, 2016.

[203] E. Valeo, G. Kramer, and R. Nazikian, “Two-dimensional simulations of correlation reflectometry in fusion plasmas,” *Plasma Physics and Controlled Fusion*, vol. 44, p. L1, Valeo2002.

[204] P. Johns and R. Beurle, “Numerical solution of 2-dimensional scattering problems using a transmission-line matrix,” *Proceedings of the Institution of Electrical Engineers*, vol. 118, p. 1203–1208, 1971.

[205] P. P. Silvester and L. R. Ferrari, *Finite Elements for Electrical Engineers.* Cambridge University Press, 3rd ed., 1996.

[206] A. Taflove and S. C. Hagness, *Computational Electrodynamics: The Finite-Difference Time-Domain Method.* 3rd ed., 2005.

[207] F. da Silva, S. Heuraux, S. Hacquin, and M. Manso, “Unidirectional transparent signal injection in finite - difference time-domain electromagnetic codes - application to reflectometry simulations,” *Journal of Computational Physics*, vol. 203, 2005.

[208] F. da Silva, S. Heuraux, E. Ricardo, P. Quental, , and J. Ferreira, “Assessment of the measurement performance of the in-vessel system of gap 6 of the iter plasma position reflectometer using a finite-difference time-domain maxwell full-wave code,” *Review of Scientific Instruments*, vol. 87, p. 11E727, 2016.

[209] A. selective survey of the finite-differences time-domain literature, “Kurt l. shlager and john b. schneider,” *IEEE Antennas Propagation Magazine*, vol. 37, 1995.

[210] K. Yee, “Numerical solution of initial boundary value problems involving maxwell’s equations in isotropic media,” *IEEE Transactions on Antennas and Propagation*, vol. 14, p. 302–307, 1966.

[211] S. Narayan, K. M. Divya, and V. K. Kanth, *FDTD Modeling of EM Field inside Microwave Cavities.* SpringerBriefs in Electrical and Computer Engineering, Springer Singapore, 1st ed.

[212] F. da Silva, S. Heuraux, T. Ribeiro, and B. Scott, "Development of a 2d full-wave je-fdtd maxwell x-mode code for reflectometry simulation," *9th International Reflectometry Workshop (IRW9)*, 2009.

[213] L. Xu and N. Yuan, "Fdtd formulations for scattering from 3-d anisotropic magnetized plasma objects," *IEEE Antennas and Wireless Propagation Letters*, vol. 5, pp. 335–338, 2006.

[214] F. da Silva, M. C. Pinto, B. Després, and S. Heuraux, "Stable explicit coupling of the yee scheme with a linear current model in fluctuating magnetized plasmas," *Journal of Computational Physics*, vol. 295, pp. 24–45, 2015.

[215] F. da Silva, S. Heuraux, B. Després, and M. C. Pinto, "Numerical advances in kernels for fdtd maxwell codes using the yee algorithm in proceedings of the 11th international reflectometry," *Workshop for fusion plasma diagnostics — IRW11*, 2013.

[216] *Openmp website.* https://www.openmp.org.

[217] *MPI website.* https://www.open-mpi.org.

[218] E. Ricardo, F. da Silva, S. Heuraux, and A. Silva, "Assessment of the measurement performance of demo plasma position reflectometry gaps perpendicular to the separatrix," *presented at the 12o Congresso do Comité Português da URSI "Inteligência artificial e as ciências rádio", Lisbon*, 2018.

[219] J. Berenger, "A perfectly matched layer for the absorption of electromagnetic waves," *Journal of Computational Physics*, vol. 114, p. 185–200.

[220] *MathWorks website.* https://www.mathworks.com/products/matlab.html.

[221] *Final report on deliverables (D001) Advanced simulation studies on microwave diagnostics under DEMO conditions, (D002) Advanced concept on in vessel and ex vessel components, (D003) Complete set of expected performance data of all MW diagnostics. EUROfusion IDM reference No* $EFDA_{D2}PHYUD$.

[222] F. Iannone, G. Bracco, C. Cavazzoni, R. Coelho, D. Coster, O. Hoenen, A. Maslennikov, S. Migliori, M. Owsiak, A. Quintiliani, B. Palak, V. Pais, F. Robin, E. Rossi, and I. Voitsekhovitch, "Marconi-fusion: The new high performance computing facility for european nuclear fusion modelling," *Fusion Engineering and Design*, p. S0920379617309018, 11 2017.

[223] *EUROFUSION databse - WPPMI-2015-DEMO*$_3d1_equilibrium_definition_final.docxfile$.

[224] D. Carralero, G. Birkenmeier, H. Müller, P. Manz, P. deMarne, S. Müller, F. Reimold, U. Stroth, M. Wischmeier, and E. Wolfrum, "An experimental investigation of the high density transition of the scrape-off layer transport in asdex upgrade," *Nuclear Fusion*, vol. 54, p. 123005, 12 2014.

[225] M. Khan, S. K. Hasnain, and M. Jamil, *Digital Signal Processing: A Breadth-First Approach.* River Publishers Series in Signal, Image and Speech Processing, River Publishers, 1st ed., 2016.

[226] T. Happel, T. Görler, P. Hennequin, C. Lechte, M. Bernert, G. D. Conway, S. J. Freethy, C. Honoré, J. R. Pinzón, and U. Stroth, “Comparison of detailed experimental wavenumber spectra with gyrokinetic simulation aided by two-dimensional full-wave simulations,” *Plasma Physics and Controlled Fusion*, vol. 59, p. 054009, 2017.

[227] P. H. Diamond, *Modern Plasma Physics*, vol. 1. Cambridge University Press, 1st ed.

[228] J. Vicente, F. da Silva, S. Heuraux, G. Conway, C. Silva, and T. Ribeiro, “Turbulence level effects on conventional reflectometry using 2d full-wave simulations,” vol. 89, p. 10H110, 2018.

[229] F. Jenko, D. Told, T. Görler, J. Citrin, A. B. Navarro, C. Bourdelle, S. Brunner, G. Conway, T. Dannert, and H. Doer, “Global and local gyrokinetic simulations of high-performance discharges in view of iter,” *Nuclear Fusion*, vol. 53, p. 073003, 2013.

[230] J. Vicente, T. Ribeiro, F. D. Silva, S. Heuraux, G. D. Conway, B. Scott, and C. Silva, “2d full-wave simulations of conventional reflectometry using 3d gyro-fluid plasma turbulence,” *Plasma Physics and Controlled Fusion*, vol. 62, p. 2, 2020.

[231] E. Gusakov, S. Heuraux, A. Popov, and M. Schubert, “Reconstruction of the turbulence radial profile from reflectometry phase root mean square measurements,” *Plasma Physics and Controlled Fusion*, vol. 54, p. 045008, 2012.

[232] *popt page*. https://github.com/rpm-software-management/popt.

[233] *Divertor Test Tokamak*. https://www.dtt-project.it/.

[234] F. da Silva, J. Ferreira, G. D. Masi, S. Heuraux, E. Ricardo, T. Ribeiro, O. Tudisco, R. Cavazzana, O. D’Arcangelo, and A. Silva, “A first full wave simulation assessment of reflectometry for dtt,” *Journal of Instrumentation*, vol. 14, p. C08011, 2019.

[235] J. Berenger, “Three-dimensional perfectly matched layer for the absorption of electromagnetic waves,” *Journal of Computational Physics*, vol. 127, pp. 363–379, 1996.